UNIVERSITY OF CALIFORNIA SAN DIEGO

Polymer Injection for Mitigating Ground Liquefaction and Associated Deformations

A Dissertation submitted in partial satisfaction of the requirements
for the degree Doctor of Philosophy

in

Structural Engineering

by

Athul Prabakaran Parayancode

Committee in charge:

Professor Ahmed Elgamal, Chair
Professor Joel P Conte
Professor John S McCartney
Professor Gilberto Mosqueda
Professor Sutanu Sarkar

2023

The Dissertation of Athul Prabakaran Parayancode is approved, and it is acceptable in quality and form for publication on microfilm and electronically.

University of California San Diego

2023

DEDICATION

To my family

EPIGRAPH

"In engineering practice, difficulties with soils are almost exclusively due to not the soils themselves, but to the water contained in their voids. On a planet without any water, there would be no need for soil mechanics".

- Karl von Terzaghi in his 1939 James Forrest Lecture

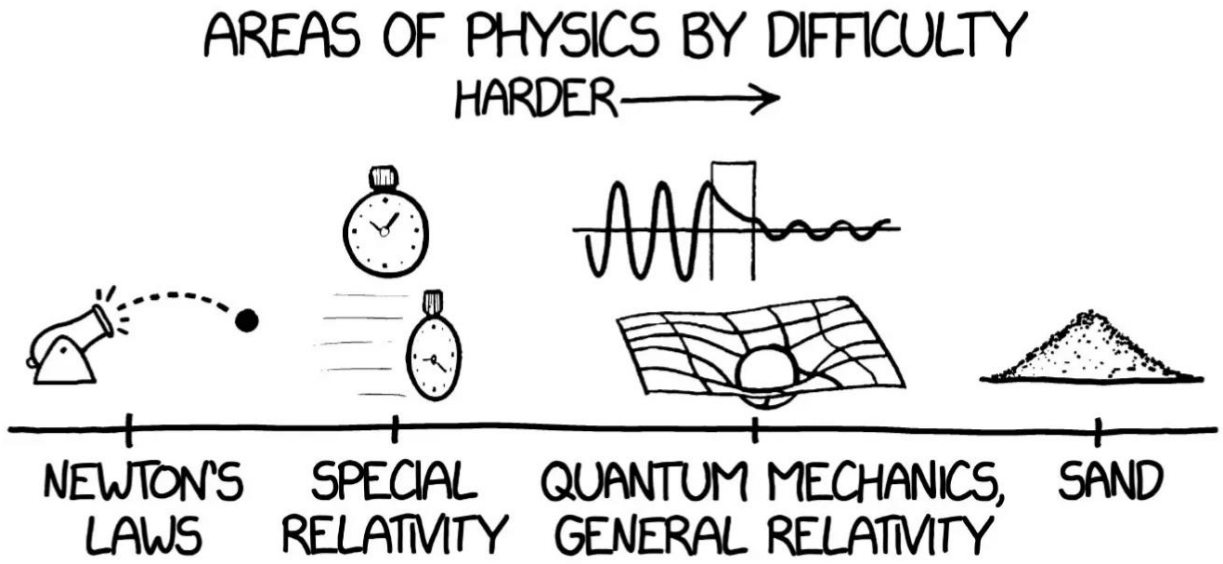

- New York Times, 2020

TABLE OF CONTENTS

LIST OF FIGURES

LIST OF TABLES

LIST OF SYMBOLS

$\gamma_{d,\,soil}$	Soil dry unit weight
$\gamma_{d,\,min}$	Soil minimum dry unit weight
$\gamma_{d,\,max}$	Soil maximum dry unit weight
ρ	Soil dry density
ρ_{min}	Soil minimum dry density
ρ_{max}	Soil maximum dry density
e	Soil void ratio
e_{min}	Soil minimum void ratio
e_{max}	Soil maximum void ratio
D_r	Soil relative density
G_0	Low strain shear modulus
V_s	Shear wave velocity
V_{s30}	Average shear wave velocity in the top 30m of soil
CPT	Cone penetration test

q_c	Cone tip resistance from a cone penetration test
PWP	Pore water pressure
EPWP	Excess pore water pressure
r_u	Excess pore pressure ratio
g	Acceleration due to gravity (9.81 m/s^2)
CSR	Cyclic Stress Ratio
$CRR_{7.5}$	Cyclic Resistance Ratio for an equivalent magnitude 7.5 M_w event
M_w	Moment magnitude scale
V_p	Volume of injected polymer
K_o	Lateral earth pressure coefficient
PDMY02	Pressure Dependent Multi Yield 02
PDMY03	Pressure Dependent Multi Yield 03
PIMY	Pressure Independent Multi Yield
$(N_1)_{60}$	Normalized standard penetration test blow count
FS_{Liq}	Factor of safety against initial liquefaction
$s_{u,liq}$	Post liquefaction residual shear strength

HWB	Highway Bridge
RRB	Railroad Bridge
FE	Finite Element
LE	Limit Equilibrium
k_y	Yield acceleration
ν	Poisson's ratio
μ	Friction coefficient between bridge deck and bent
τ	Shear stress
ϕ	Curvature
σ'_{v0}	Initial vertical effective shear stress
p'	Current confinement
p'_0	Initial confinement
γ	Shear strain
I_a	Arias Intensity
CAV	Cumulative Absolute Velocity

ACKNOWLEDGEMENTS

"If I have seen any further, it is by standing on the shoulders of giants".

- Bernard of Chartres

As I pause and look back at a decade of what continues to be a deeply enriching journey into the field of earthquake geotechnical engineering, I realize that I haven't traveled alone. I have been fortunate to meet a great number of people who have shaped my interest, informed my decisions, and guided me along the right path. I would like to take this opportunity to thank them.

First and foremost, I am forever indebted to Professor Ahmed Elgamal. I remember walking into your office in the Winter of 2017, fresh from India - a stranger in an alien land, and trying hard to convince you to take me on as your master's student. Thank you for recognizing my desire to learn and for the faith you reposed in me. You have been a constant source of encouragement, technical guidance, and support throughout my time at UC San Diego. I am a better communicator, thanks to you, and your words of advice helped me hone my technical writing skills. Among the things I will treasure the most is working alongside and learning from you for the SE180 (Earthquake Engineering) undergraduate class. Serving as a teaching assistant for the class for five years and assisting in developing a small part of it gave me immense self-belief and reinforced my interest in teaching subjects that I am passionate about.

Being the youngest member of our research group in 2017, I benefitted greatly from the experience, knowledge, and camaraderie of former group members: Dr. Kyungtae Kim, Dr. Jinchi Lu, Dr. Zhijian Qiu, Dr. Ahmed Ebeido, Dr. Muhammad Zayed, Dr. Abdullah Almutairi, and

Dr. John Li. Your friendship and support mean a lot to me. I will forever remember conversations with Muhammad and Kyungtae during walks around the SME building later in the evenings.

If I had to choose the favorite part of my PhD journey, it would be the time I spent at the Powell Structural Engineering Laboratories at UC San Diego. I came to the United States to an entirely new system of measurement units, with little feel for what an object weighing 1 kip actually looked like. The staff at the Powell lab took me in as one of their own, taught me their ways, gave me confidence, and provided me with invaluable hands-on experience. Darren McKay, Michael Sanders, Noah Aldrich, Andrew Sander, Abdullah Hamid, and Dr. Christopher Latham, thank you for giving so selflessly. To this day, I see myself largely as an experimentalist thanks to my experience in the labs. During my time at the Powell lab, I also worked alongside an army of dedicated undergraduate aids: Kim-Chi Nguyen, Angel Gonzales, Marvin Machado, Gustavo Ramirez, Javi Puyat and Jaysen Zapata. It was a pleasure spending time with you on top of the laminar soil container, and I look forward to seeing you scale greater heights.

I would like to thank Prof. Ramin Motamed, Dr. Milad Jahed Orang, and Dr. Reza Boushehri at the University of Nevada Reno for helping me with my test series and facilitating a productive collaboration. Milad and Reza, in particular, were extremely kind to help me finish the excavation of the polymer test. I hope this experience does deter you from enjoying future trips to San Diego.

I would like to thank Cliff Frazao and Donald Moody at EagleLift for supporting the polymer experiments. Cliff Frazao, in particular, was instrumental in providing feedback from the practice standpoint.

I would like to thank Prof. Suresh R Dash (at IIT Bhubaneswar) for introducing me to the discipline of earthquake geotechnical engineering. If not for you taking me under your wing in the Summer of 2012 and instilling interest in the subject, this journey would never have happened. A special shout out to Prof. Suby Bhattacharya and Dr. Sadra Amani at the University of Surrey. Prof. Bhattacharya was instrumental in developing my interest in the field of offshore wind turbines. During the Covid lockdown (2019), meetings with the research group were a source of constant motivation and support. For that, I am grateful.

Prof. Paul Mayne, I will never forget your generous feedback on the CPT, particularly at low confining pressures, during your visit to UC San Diego. I would like to acknowledge the support I received from Prof. Anbazhagan P at the Indian Institute of Science, Bangalore for a very productive year and a half (2015-2016) following my undergraduate degree.

My time at UC San Diego was possible with the support of several agencies including the California Department of Transportation (Caltrans), Pacific Earthquake Engineering Research Center (PEER), United States Bureau of Reclamation (USBR). I would also like to thank Roman Koltuniuk at the USBR for very fruitful technical discussions over the past year.

My committee members - Prof. Joel Conte, Prof. John McCartney, Prof. Gilberto Mosqueda and Prof. Sutanu Sarkar – I cannot thank you enough for being so generous with your time and valuable feedback for this dissertation.

During my time at UC San Diego, I have served as an instructional assistant in 15 undergraduate and graduate level courses. I have thoroughly enjoyed this experience and would like to thank Nicholas Abi-Samra (ECE Dept.), Prof. Tara Hutchinson, Prof. Joel Conte,

Prof. Veronica Eliasson, Prof. Petr Krysl, and Prof. Benson Shing for the opportunity. I believe your feedback has helped me develop into a more rounded engineer.

San Diego is a great city, and good company makes it even greater. I am lucky to have Dr. Angshuman Deb, Dr. Mukesh Ramancha, Dr. Amanpreet Singh, Aditya Vijay Ramanitharapandian, Sachin Jagarlamudi, Rahul Hazra, Dr. Patrick Phaneuf, Dylan McNamara and Chris Lin Sun as friends. A special shout-out to Dr. Jeffery Newgard, Dr. Raghavendra Sivapuram, and Dr. Sumit Gupta for sharing their wealth of knowledge. I would also like to acknowledge the support of my cohorts - Krishna Adusumili, Tejas Baid, Sneha Raj, Elesh Lakhani, Aneri Seth, Masood Inamdar, Soum Dutta, Srikar Gunisetty, Michael Morano, Karan Taneja and Lucas Deyglun.

Finally, to my family. Words are insufficient to describe the constant support, love, and encouragement offered by my family. I am extremely grateful to my parents Dr. Bindu C S, Dr. Prabhakaran P B, and in-laws Adv. Jayakumar Parameswaran and Jayalakshmi Jayakumar for their constant support and immense patience. My siblings (Nishant, Sachin, Diya, Gautam, Jayakrishnan and Sonia) were my biggest cheerleaders and kept my spirit alive. Rekha Remadevi and Arun C S, Geetha and Taj Anand, Priya and Rajesh, Savitha and Sidharth – Thank you for making me feel at home in a foreign land. I would like to thank my grandmother (V Bhavani), late grandfather (C S Sivasankaran), late grandparents (P B Balakrishnan and Parukutty) for their prayers and immense love.

Last, I would like to thank my wife, Jayasudha Jayakumaran for her absolute support and unconditional love. She keeps reminding me that I saw the light at the end of the PhD tunnel a year

(or 2) too soon and was extremely patient and supportive at every setback. This success is as much hers as it is mine. I look forward to the exciting journey ahead of this tunnel.

This dissertation contains a mix of published journal and conference articles and new papers being prepared for publication. A summary is provided below:

Chapter 2, in full, is a reprint of the material as it appears in Prabhakaran, A., Kyungtae, K., Ebeido, A., Jahed Orang, M., Motamed, R., Elgamal, A., and Frazao, C. (2021). "Polymer injection and associated site liquefaction remediation mechanisms." *17th World Conference on Earthquake Engineering*, Sendai, Japan. The dissertation author was the primary investigator and author.

Chapter 4, in part, is a reprint of the material as it appears in a forthcoming article: Prabhakaran, A., Kim, K., Orang, M. J., Qiu, Z., Ebeido, A., Zayed, M., Boushehri, R., Motamed, R., Elgamal, A., and Frazao, C. *Forthcoming*. "Polymer Injection and Liquefaction-Induced Foundation Settlement: a Shake Table Testing Investigation", Journal of Geotechnical and Geoenvironmental Engineering, ASCE. The dissertation author was the primary investigator and author.

Chapter 4, in part, is a reprint of the material as it appears in the article: Prabhakaran, A., Kim, K., Orang, M. J., Qiu, Z., Ebeido, A., Zayed, M., Boushehri, R., Motamed, R., Elgamal, A., and Frazao, C. (2020). "Polymer Injection and Liquefaction-Induced Foundation Settlement: A Shake Table Test Investigation." *ASCE Geo-Congress 2020*, American Society of Civil Engineers, Minneapolis, MN. The dissertation author was the primary investigator and author.

Chapter 5, in part, is a reprint of the material as it appears in the article: Prabhakaran, A., Kim, K., Qiu, Z., Elgamal, A., and Frazao, C. (2022). "Polymer Injection to Remediate Liquefaction-Induced Foundation Settlement: Numerical Simulation of Shake Table

Experiments." *ASCE Lifelines Conference*, American Society of Civil Engineers, Los Angeles, CA. The dissertation author was the primary investigator and author.

Chapter 6, in part, is a reprint of the material as it appears in the article: Prabhakaran, A., Kim, K., Qiu, Z., Elgamal, A., and Frazao, C. (2022). "Polymer Injection to Remediate Liquefaction-Induced Foundation Settlement: Numerical Simulation of Shake Table Experiments." *ASCE Lifelines Conference*, American Society of Civil Engineers, Los Angeles, CA. The dissertation author was the primary investigator and author.

Chapter 7, in full, is currently being prepared for submission for publication of the material as it may appear in the following publication: Prabhakaran, A., Qiu, Z., and Elgamal, A. "Response of the San Felipito bridge-ground system during the 2010 El Mayor-Cucapah Earthquake: Computational Simulation, Insights and Remediation". The dissertation author will be the primary investigator and author of this paper.

VITA

2011 - 2015	Bachelor of Technology (Honors) in Civil Engineering Indian Institute of Technology Bhubaneswar
2015 - 2016	Research Assistant, Indian Institute of Science Bangalore
2021	Master of Science in Structural Engineering University of California San Diego, La Jolla, United States
2023	Doctor of Philosophy in Structural Engineering University of California San Diego, La Jolla, United States

PUBLICATIONS

Published Journal/Conference Papers

Prabhakaran, A., Kim, K., Orang, M. J., Qiu, Z., Ebeido, A., Zayed, M., Boushehri, R., Motamed, R., Elgamal, A., and Frazao, C. (2023). "Polymer Injection and Liquefaction-Induced Foundation Settlement Mitigation: a Shake Table Testing Investigation". *Journal of Geotechnical and Geoenvironmental Engineering*, American Society of Civil Engineers, 149(8), 04023054. https://doi.org/10.1061/JGGEFK.GTENG-10840

Prabhakaran, A., Kim, K., Qiu, Z., Elgamal, A., and Frazao, C. (2022). "Polymer Injection to Remediate Liquefaction-Induced Foundation Settlement: Numerical Simulation of Shake Table Experiments." *ASCE Lifelines Conference*, American Society of Civil Engineers, Los Angeles, CA. https://doi.org/10.1061/9780784484449.023

Prabhakaran, A., Kyungtae, K., Ebeido, A., Jahed Orang, M., Motamed, R., Elgamal, A., and Frazao, C. (2021). "Polymer Injection and Associated Site Liquefaction Remediation Mechanisms." *17th World Conference on Earthquake Engineering*, Sendai, Japan.

Prabhakaran, A., Kim, K., Orang, M. J., Qiu, Z., Ebeido, A., Zayed, M., Boushehri, R., Motamed, R., Elgamal, A., and Frazao, C. (2020). "Polymer Injection and Liquefaction-Induced Foundation Settlement: A Shake Table Test Investigation." *ASCE Geo-Congress 2020*, American Society of Civil Engineers, Minneapolis, MN, 1–9. https://doi.org/10.1061/9780784482810.001

Prabhakaran, A., Sreenivasulu, S., Dash, S. R. (2015). "Kinematic Bending of Pile Foundations in Layered Liquefiable Soils". 6th International Conference on Earthquake Geotechnical Engineering (6ICEGE), Christchurch, New Zealand. https://www.issmge.org/uploads/publications/59/60/568.00_Dash.pdf

Jahed Orang, M., Motamed, R., **Prabhakaran, A.**, and Elgamal, A. (2021). "Large-Scale Shake Table Tests on a Shallow Foundation in Liquefiable Soils." *Journal of Geotechnical and Geoenvironmental Engineering*, American Society of Civil Engineers, 147(1), 04020152. https://doi.org/10.1061/(ASCE)GT.1943-5606.0002427

Jahed Orang, M., R Boushehri, Motamed, R., **Prabhakaran, A.**, and Elgamal A. (2021). "An experimental evaluation of helical piles as a liquefaction-induced building settlement mitigation measure." *Soil Dynamics and Earthquake Engineering,*151(12), 106994, https://doi.org/10.1016/j.soildyn.2021.106994

Motamed, R., Orang, M. J., **Parayancode, A.**, and Elgamal, A. (2022). "2018 PEER Blind Prediction Contest on Numerical Simulation of a Large-Scale Liquefaction Shaking Table Test: Lessons Learned and Practical Insights." *12th National Conference on Earthquake Engineering*, EERI, Salt Lake City, Utah.

Motamed, R., Orang, M. J., **Parayancode, A.**, and Elgamal, A. (2020). "Results of a Class C Blind Prediction Competition on the Numerical Simulation of a Large-Scale Liquefaction Shaking Table Test." *ASCE Geo-Congress 2020*, American Society of Civil Engineers, Minneapolis, MN, 334–342. https://doi.org/10.1061/9780784482780.032

Zayed, M., Kim, K., **Prabhakaran, A.**, and Elgamal, A. (2023) "Shake table testing and computational framework for seismic response of utility-scale bucket foundation offshore wind turbines". *Soil Dynamics and Earthquake Engineering. 171 (8), 107939.* https://doi.org/10.1016/j.soildyn.2023.107939

Zayed, M., Ebeido, A., **Prabhakaran, A.**, Kim, K., Qiu, Z., and Elgamal, A. (2021). "Shake Table Testing: A High-Resolution Vertical Accelerometer Array for Tracking Shear Wave Velocity." *Geotechnical Testing Journal*, ASTM International, 44(4), 20190066. https://doi.org/10.1520/GTJ20190066

Zayed, M., Ebeido, A., **Prabhakaran, A.**, Qiu, Z., and Elgamal, A. (2020). "Asymmetric Input Motion for Accumulation of Lateral Ground Deformation in Laminar Container Shake Table Testing." *Canadian Geotechnical Journal*, Canadian Science Publishing, 58(2) cgj-2018-0647. https://doi.org/10.1139/cgj-2018-0647

Qiu, Z., **Prabhakaran, A.,** and Elgamal, A. (2023) "A three-dimensional multi-surface plasticity soil model for seismically-induced liquefaction and earthquake loading applications". *Acta Geotechnica*. https://doi.org/10.1007/s11440-023-01941-1

Qiu Z., Yu Z., Su L., **Prabhakaran A**, Elgamal A. and Wang X. (2023) "Longitudinal seismic fragility assessment of an integral bridge-ground system in liquefaction-induced lateral spreads". *Soil Dynamics and Earthquake Engineering* 168 (5), 107838 https://doi.org/10.1016/j.soildyn.2023.107838

Amani S, **Prabhakaran A.**, Bhattacharya S (2022). "Design of monopiles for offshore and nearshore wind turbines in seismically liquefiable soils: Methodology and Validation" *Soil Dynamics and Earthquake Engineering*,157(6), 107252, https://doi.org/10.1016/j.soildyn.2022.107252

Rohit D., Hazarika H., Qin C., Maeda T., Kokusho T., Yahiro Y., and **Prabhakaran A.** (2022). "Simulation of Water Film Formation during the 2018 Sulawesi Earthquake, Indonesia." *Forensic Engineering,* Proceedings of the Institution of Civil Engineers. https://doi.org/10.1680/jfoen.21.00024

Bhattacharya S, Lombardi D, **Prabhakaran A,** Mistry HK, Biswal S, Aleem M, Amani S, Prakhya G, Jindal S, Macabuag J., Qiu, Z. (2023). "Risks and Vulnerabilities in the Design, Construction, and Operation of Offshore Wind Turbine Farms in Seismic Areas". *7th International Conference on Recent Advances in Geotechnical Earthquake Engineering (7ICRAGEE)*, Bangalore. https://doi.org/10.1007/978-981-19-3330-1_1

Dash, S. R., Bhattacharya, S., **Prabhakaran, A.,** Sreenivasulu, S. (2014). "Generation and Dissipation of Pore Water Pressure Near to Pile and Far Field in Liquefiable Soils". *4th International Conference on Geotechnique, Construction Materials and Environment (Geomate 2014)*, Brisbane, Australia.

Anbazhagan, P., Rohit, D., **Prabhakaran, A.,** Vidyaranya B. (2018). Identification of Karstic Features in Lateritic Soil by an Integrated Geophysical Approach. *Pure and Applied Geophysics* 175 (4515-4536). https://doi.org/10.1007/s00024-018-1908-8

Technical Reports

Prabhakaran A., Kim K., Koltuniuk R., and Elgamal A. (2022) "Verification of UCSDSand3 in LS-DYNA". Technical Report submitted to the United States Bureau of Reclamation under contract 2016041.

Magazine Articles

Jeffrey T Newgard and **Prabhakaran A.**, (2022) "Lessons Learned from Geo Legends - George Gazetas, PhD., M. ASCE". ASCE Geostrata Magazine 26 (4). https://doi.org/10.1061/geosek.0000435

ABSTRACT OF THE DISSERTATION

Polymer Injection for Mitigating Ground Liquefaction and Associated Deformations

by

Athul Prabakaran Parayancode

Doctor of Philosophy in Structural Engineering

University of California San Diego, 2023

Professor Ahmed Elgamal, Chair

A well-established ground improvement approach, the polymer injection technique has the advantages of being durable, hydro-insensitive, fast curing, and easy to deploy in dense urban environments. It is being widely employed with much success, primarily for uplifting embankments, releveling slabs and foundations, and erosion control. In view of the aforementioned advantages, its potential as a soil liquefaction countermeasure is of current

interest. In this regard, the main objective of this dissertation is to explore viability of the polymer injection technique as a soil liquefaction countermeasure.

This objective is achieved in three phases. First, a large-scale shake table test series is conducted to assess potential of the polymer injection technique as a countermeasure against seismically induced soil liquefaction. Specifically, mitigation of settlement for a shallow foundation supported on a liquefiable sand deposit is explored. In a series of two shake table experiments, system response is studied first without (baseline) and subsequently with the injection of polymer into the liquefiable stratum. Upon application of the polymer injection countermeasure, results show a significant reduction in the tendency for liquefaction and resulting foundation settlement. After the test, careful excavation of the deposit provided additional insights into the injected polymer configuration, creating solidified zones that further support the shallow foundation load and increasing the overall stratum strength (relative density and confinement).

In the second phase, insights gained from the test series are leveraged to calibrate a nonlinear solid-fluid coupled finite element model. In this regard, stress-strain properties of the solidified polymer zones and surrounding strengthened ground are developed. This calibrated model was then extended to explore additional scenarios beyond the scope of the original test series. Effects of geometric configuration of the solidified polymer zones, and state of compacted soil around the solidified zones were explored in detail.

Finally, within a computational framework, a representative practical application of the polymer injection technique as a liquefaction countermeasure is addressed. For that purpose, numerical modeling scenarios of polymer injection are studied to mitigate the damage reported in a well-documented bridge seismic response case history, where large lateral spreading ground deformations ultimately resulted in unseating of a railroad bridge-deck span. Detailed post-

earthquake reconnaissance surveys and observations are used to computationally simulate the bridge-ground system, and capture the documented damage mechanisms. Three different polymer injection configurations are studied, and the response of the remediated bridge-ground system is explored. In these configurations, injections of the order of 10 % (volume of liquid polymer to soil) resulted in a major reduction of lateral spreading deformations, precluding the observed bridge-deck unseating damage mechanism. Overall, the insights gained from this research indicate that the polymer injection technique has considerable potential for mitigating soil liquefaction.

Chapter 1. Introduction and Literature Review

1.1 Outline of Chapter

This dissertation focuses on the exploration, development, and application of a novel ground remediation measure, polymer injection. The effectiveness of this technique for soil liquefaction mitigation is investigated through large scale experimental and computational simulations. On this basis, this chapter provides 1) a concise introduction to the earthquake induced soil liquefaction, 2) possible soil liquefaction mitigation measures for existing structures, and 3) a brief overview of prior research on polymer remediation and 5) an outline of this dissertation.

1.2 Introduction

In the last 25 years (between 1998 and 2023), earthquakes were directly responsible for over 750,000 deaths around the world. These events have affected over 125 million people, who have been either displaced, injured, or made homeless (Guha-Sapir *et al.* 2023). Such disasters, including the recent February 2nd 2023, 7.8 M_w Turkey-Syria earthquake, clearly indicate the devastation and human suffering inflicted by such seismic events.

During earthquakes, several mechanisms contribute to observed geotechnical failures from past events. These mechanisms can broadly be categorized into 1) inertial effects i.e., failures due to strong shaking e.g., slope stability type failures, site response (resonance), and 2) kinematic effects i.e., failures due to ground deformations, including earthquake fault rupture, and soil liquefaction-induced ground deformations, or 3) a combination thereof, e.g., soil structure interaction. Past events in India (Jain *et al.* 2002), United States (NCEER 1994), Japan (Ashford *et al.* 2011), Turkey (Bray *et al.* 2000), Greece (GEER/EERI/ATC Reconnaissance 2014), New Zealand (Cubrinovski *et al.* 2010), Mexico (EERI 2010) and Chile (GEER 2010b) have

demonstrated soil liquefaction to be among the main response mechanisms that contribute to widespread failures.

In this chapter, the following sections briefly discuss: 1) the community's consensus regarding the mechanics of the soil liquefaction process and past observed failures, 2) a brief overview of possible mitigation measures, and 3) the polymer injection technique, and 4) past research/applications using this method.

1.3 Soil Liquefaction

Natural or artificially placed granular soil deposits tend to settle and densify when subjected to ground vibrations that induce cyclic shearing (Silver and Seed 1971). If the deposit is saturated and the shear stresses are applied "quickly" such that drainage is impeded (during this short duration), there is limited time for the sand grains to settle and densify (and the deposit to undergo volume change). This tendency for the soil grains to contract (densify) transfers loads from the interparticle forces between sand grains to the pore fluid (water) surrounding them. As such, the pressure in the pore fluid increases and separates individual particles away from each other, i.e., causing the sand grains to essentially float in the fluid (Ishihara 1985) as seen in Figure 1.1. Since the resistance to applied loads in cohesionless granular soils arises largely from particle-particle friction, the developed pore pressure can be high enough to cause a temporary loss of soil strength and stiffness, changing the behavior of the deposit from solid to a heavy fluid. This mechanism of soil response has long been recognized within the community and is termed soil liquefaction.

During earthquakes, the propagation of seismic waves from the source of rupture to ground surface generates cyclic shear stresses within the deposit. If ground is saturated and composed primarily of loose cohesionless soil, depending on the extent of induced cyclic shear stresses, the

deposit can liquefy, affecting structures within/above the ground. As such, soil liquefaction has led to several dramatic failures including settlement and tilting of buildings (Figure 1.2), the buoyant rise of utility access holes/underground structures (Figure 1.3), failures of bridges (Figure 1.4), road networks (Figure 1.5), farmland (Figure 1.6), retaining walls (Figure 1.7), marine ports, quay walls, and wharves (Figure 1.8) in several past seismic events. Therefore, appropriate characterization, recognition, and remediation of liquefaction-susceptible soil remain a high priority in many seismic regions around the world.

1.4 Soil Liquefaction Mitigation

Broadly, current techniques to remediate soil liquefaction for new construction include:

1. Soil densification, including deep dynamic compaction, rapid impact compaction, vibro-compaction (sand compaction piles), blasting, compaction grouting etc.
2. Soil replacement, including excavation and replacement. This method can also encompass solidification measures i.e., the use of additives to improve cohesion (such as chemical or cementitious grouts such as permeation grouting).
3. Reinforcement by creation of inclusions (jet grouting, deep soil mixing, stone columns, vibro-concrete columns) to improve the native soil.
4. Enhancement of soil drainage using stone columns, gravel/prefabricated vertical drains, etc.
5. Reduction in the soil's degree of saturation by air injection or lowering of ground water levels.

The selection of an appropriate measure relies on the type of the structure (extent of necessary remediation), economic factors (cost and efficiency of the employed method), technical applicability dictated by the particle size (Figure 1.9) and the chemical composition of the insitu

soil, and ease of deployment (i.e., depth considerations, site working conditions, environmental impact etc.). However, a large proportion of the available methods for soil liquefaction remediation are targeted at new construction. As such, options for liquefaction remediation underneath existing structures are quite limited.

The extent of this issue was evident following the 2011 Tohoku earthquake where more than 27,000 wooden homes (which were not explicitly designed for the liquefaction hazard) suffered damage (Yasuda and Ishikawa 2018) as seen in Figure 1.10. In addition, several homes that suffered little to no structural damage exhibited high settlement and tilt, leading to their demolition. The nature of the remediation measure was chosen primarily based on site access conditions, economy, and degree of damage (Yasuda 2014).

1. For residential areas with a large number of demolished structures, current soil remediation techniques for new construction (e.g., compaction piles, deep soil mixing) were readily employed to prevent liquefaction in future events.

2. Dense urban environments with existing construction, public utilities, roads, and lifelines, were remediated using specialized methods to avoid liquefaction-induced damage in future events. The Japanese government established an "Urban liquefaction countermeasure project" using dewatering, and lattice-type underground walls to limit liquefaction-induced foundation settlement and tilt during future events (Figure 1.11),

3. For dense urban environments with demolished individual homes (with narrow access areas), liquefaction countermeasures were employed prior to their reconstruction. This led to the development of newer, more economical methods from contractors using smaller, quieter machines. For example, the 'gravel drain with compaction' was employed at several sites in Urayasu city.

4. For existing undamaged homes in residential areas, that exhibited settlement and tilt, the structures were first uplifted (to grade and correct tilt) and advanced methods (insitu liquefaction countermeasures) were employed to improve the soil beneath the structure (Figure 1.12). For example, a few homes were retrofitted using compaction grouting, and sheet piles were installed as a containment system along the perimeter of the house and foundation system. However, as seen in Figure 1.13, based on data from JGS Kanto Branch (2013) and Yasuda (2014), grouting methods are not often economically viable and only a limited number of homes were treated using this technique. As such further efforts should be directed toward making such methods amenable to practice.

Detailed surveys of available methods for liquefaction mitigation under existing structures over the past 40 years can be found in (Andrus and Chung 1995, Kramer and Holtz 1991, Ledbetter 1985, Towhata 2021, Yasuda 2007). As such, these remediation measures can be categorized into two main categories:1) methods to reduce soil liquefaction potential by strengthening the soil, and 2) methods to retrofit foundations to provide additional support if the native soil liquefies.

Recent studies of liquefaction mitigation under existing structures, include model tests using both the centrifuge (Conlee *et al.* 2012, Kirkwood and Dashti 2019, García-Torres and Madabhushi 2019, Paramasivam *et al.* 2020) and shake table experiments (Jahed Orang *et al.* 2021, Rasouli *et al.* 2016). A number of mitigation measures employ a form of grouting for soil remediation at locations which might otherwise be difficult to treat with conventional techniques. Commonly employed grouting methods and their applicability to different soil types is provided in Figure 1.14 and Figure 1.15, respectively. Among these grouting techniques, polymer (resin) injection has proven to be a method that shows considerable promise (Erdemgil *et al.* 2007, Traylen *et al.* 2017).

As such, the mechanisms contributing to soil remediation, and previous literature on the polymer injection technique is detailed in the section below.

1.5 Polyurethane Injection

Polyurethane (Polymer) or resin injection has been used to underpin, lift, and re-level structures since the last half a century (Naudts 2003). Since the early 1990's this technique was deployed to construct grout curtains (as containment walls), improve karsts in soil, reduce permeability, improve soil strength, particularly to prevent subsidence during excavation or tunneling, and relevel structures exhibiting differential settlement, and control erosion in sea walls. The method primarily involves the injection of liquid polymer into the ground. The polymer is injected through thin cold form steel tubes with either an opening at the tip or using sleeved tubes (tube á manchette), which offer a distributed surface (Soga *et al.*, 2004). The tubes are typically deployed at a spacing of 0.9 m-1.0 m on center and are easy to install in dense urban environments as it does not require an excavation (Traylen *et al.* 2017).

On injection, the liquid mixture expands (based on the degree of confinement) and solidifies, filling any voids or cracks in the soil (Figure 1.16 and Figure 1.17). In the polymer grouting industry, two-component polymer foams have become the preferred choice for many engineering applications due to their effectiveness and versatility. These two-component foams are typically composed of a curative phase (poly-isocyanate) and a resin phase (polyol) which are mixed together in a specific ratio immediately prior to injection into the soil or structure being treated. Upon mixing, rapid polymerization occurs forming polyurethane, which expands (due to released CO_2 as a by-product), and cures into a hardened foam (Rao *et al.* 2017). As such, this technique offers significant advantages over current ground remediation measures:

1. Ability to tailor polymer to client specific needs: Variations of the ratio of each phase before mixing leads to polymers with different density, strength, and stiffness characteristics. Further, varying the temperature and pressure of injection can control the degree of expansion, and mixing of the foam. For example, such an improvement strategy could even be adopted in the presence of underground utilities, whereby a low viscosity polymer would be injected to allow for permeation without damage to buried infrastructure. If more mixing is required, the foam is typically injected at a lower temperature to allow for more cementation. As such, there is great control over the final product to meet client-specific requirements.
2. Ground remediation can be performed without an excavation: Contrary to other methods that require excavations to improve soil at depth, this technique can specifically target select areas for remediation. Typically, the structure can stay functional during the remediation process.
3. Ability to access areas with limited overhead/access.
4. Environmentally compatible (as it does not react with ground water)
5. Long term product life: Typically, the design life is of the order of 100 years.

As such, the technique shows considerable promise as a soil remediation measure underneath existing structure. The following section presents a brief literature review on past applications of this technique for soil remediation.

1.6 Brief Literature Review

Past research on this method has focused on the material-level stress-strain characteristics of the pure polyurethane foam and the polymer-soil composite. Several laboratory studies demonstrated the beneficial effects of polymer remediation across various soil types (Barma *et al.* 2008, Buzzi *et al.* 2008, Coppola *et al.* 2016, Gatto *et al.* 2019, Golpazir *et al.* 2016, Hussain *et al.* 2014, Kim *et al.* 2017, Komurlu and Kesimal 2015, Koyama *et al.* 2022, Lee *et al.* 2017b, a, Li *et*

al. 2020, Liu *et al.* 2019, Maher *et al.* 1994, Sabri and Shashkin 2020, Saleh *et al.* 2019, Shigang *et al.* 2013, Tu *et al.* 2001, Valentino *et al.* 2014, 2023, Wang *et al.* 2021, Xiao *et al.* 2015, 2018, Yamazaki *et al.* 2005)

In the context of field applications, the technique has long been used to correct excessive settlement and tilt in buildings (Dominijanni *et al.* 2022, Fakhar and Asmaniza 2016, Gatto and Montrasio 2022, Lavín *et al.* 2018, Miroshnichenko *et al.* 2018, Santarato *et al.* 2011), strengthen weak soils below pavements (Cong *et al.* 2019, Fakhar and Asmaniza 2016, Koyama *et al.* 2023, Popik *et al.* 2010, Priddy *et al.* 2010, Van Reenen 2006, Vennapusa *et al.* 2016) and railroads (Bian *et al.* 2021, Wan *et al.* 2020, Wei *et al.* 2017), slope stability (Chun *et al.* 1997, Zhang *et al.* 2016), groundwater control (Kucuk *et al.* 2009, Li *et al.* 2016), vibration isolation (Gatto *et al.* 2021), remediate expansive soil (Al-Atroush and Sebaey 2021, Buzzi *et al.* 2010) and for erosion control in sea walls (Sanchez *et al.* 2019).

More recently, a few studies have indicated that the polymer injection technique could be deployed as a soil liquefaction countermeasure, particularly applicable to existing structures due to its non-invasive nature. Field trials in Turkey (Erdemgil *et al.* 2007) reported significant increases in the post-injection standard penetration test blow counts (SPT-N value, and subsequently liquefaction resistance) at sites which suffered extensive damage in the 1999 Kocaeli earthquake. In 2013, the Earthquake Commission (EQC) of New Zealand deployed the polymer injection technique (along with a number of other ground improvement methods) at a few sites that were 'red-zoned' (Earthquake Commission, 2016) following the 2010-2011 Canterbury earthquake sequence. The study observed clear increases in CPT tip resistance (qc), shear wave velocity (V_s), and lateral earth pressure coefficient (K_0) over the improvement depth. As such, reduced cyclic shear strains (generated through a vibroseis machine), and soil surface settlement

measurements (after blasting) were noted at the test site. The study showed the promise of the polymer injection technique and noted that further exploratory experiments were warranted. Following the EQC trials, additional studies were undertaken (Van Ballegooy *et al.* 2016 and Traylen *et al.* 2017) using full production test panels at these red zone sites (Figure 1.18a). Extensive instrumentation was deployed using pre and post injection cone penetration tests, dilatometer tests, plate load tests, and seismic cross-hole tests to quantify the extent of ground remediation and is detailed in Traylen (2017). Attention was paid to the mechanisms involved in the improved liquefaction resistance through a detailed excavation post-injection. The hardened composite (Traylen *et al.* 2016) was observed as dendritic veins/dykes, with thickness of few centimeters oriented along the direction of the lateral spread observed during the 2010-2011 Canterbury earthquake sequence (Figure 1.18b). In addition, the technique was deployed to retrofit several commercial buildings in New Zealand after the 2010-2011 canterbury earthquake sequence. The results were extremely effective with applications in the Supa Centa shopping center (Figure 1.19) in Christchurch, Seaview Wastewater treatment plant (Wellington), and Christchurch art gallery attaining international acclaim (Mainmark 2016).

In the context of liquefaction remediation, the technique offers two-fold benefit in terms of: 1) improvement in soil confinement and related liquefaction resistance (cyclic resistance ratio), through densification (Blake 2022, Traylen *et al.* 2017), cementation (Clough *et al.* 1981), and increase in soil confinement (Hynes and Olsen 1999) , and 2) reduction in the shear demand (cyclic shear stress ratio), through the addition of solid inclusions within the ground(Adalier *et al.* 2003, Baez 1995, Rayamajhi *et al.* 2016). A limited extent of improvement could also be attributed to the partial saturation of soil, as polymerization process occurs releasing CO_2.

As such, the polymer injection technique shows considerable promise. However, the performance of sites improved by this technique during realistic ground excitation are not fully detailed. Towards this end, this dissertation focuses on the development of a novel soil liquefaction mitigation measure (polymer injection) applicable to existing structures. Emphasis is placed on the liquefaction mitigation of shallow foundations and the research entrails large-scale experimental and computational components to highlight the potential of this technique.

1.7 Outline of Dissertation

The objectives and scope of the dissertation are detailed in the outline of the chapters below:

1. Chapter 1 focuses on surmising existing literature on soil liquefaction, available methods for soil liquefaction remediation, and past work on the polymer injection technique.
2. Chapter 2 focuses on the development of a pilot test program to assess the potential of the technique with an emphasis on contributing mechanisms and the extent of required remediation.
3. Chapter 3 focuses on the experimental response of a shallow foundation seated on a large liquefiable stratum (termed Baseline test) during shake table testing. This test provides a baseline to compare the efficacy of the polymer injection technique.
4. Chapter 4 focuses on the experimental response of a shallow foundation seated on a large liquefiable stratum remediated using polymer injection (termed Polymer test), during shake table testing.
5. Chapter 5 focuses on the calibration process and computational simulation of the baseline test.

6. Chapter 6 focuses on the calibration process and computational simulation of the polymer test, with comparisons made to the baseline test. Mechanisms contributing to the improved foundation response after injection are further highlighted using a set of parametric studies.

7. Chapter 7 focuses on the seismic response of a pair of adjacent bridges during the 2010 7.2 M_w El Mayor-Cucapah (Mexico) earthquake. Strategies to remediate liquefaction-induced foundation deformations using the polymer injection technique are proposed. As such, it is shown that the technique shows considerable promise to remediate liquefaction-induced foundation deformations in existing structures.

8. Chapter 8 focuses on the developed conclusions from this study. Avenues for further research are then provided.

1.8 References

Adalier, K., Elgamal, A., Meneses, J., and Baez, J. I. (2003). "Stone columns as liquefaction countermeasure in non-plastic silty soils." *Soil Dynamics and Earthquake Engineering*, Elsevier BV, 23(7), 571–584.

Al-Atroush, M. E., and Sebaey, T. A. (2021). "Stabilization of expansive soil using hydrophobic polyurethane foam: A review." *Transportation Geotechnics*, Elsevier, 27, 100494.

Andrus, R. D., and Chung, R. M. (1995). *Ground Improvement Techniques for Liquefaction Remediation Near Existing Lifelines*. *National Institute of Standards and Technology Report NISTIR 5714*, Gaithersburgh.

Ashford, S. A., Boulanger, R. W., Donahue, J. L., and Stewart, J. P. (2011). "Geotechnical Quick Report on the Kanto Plain Region during the March 11, 2011, Off Pacific Coast of Tohoku Earthquake, Japan." *Geotechnical Extreme Events Reconnaissance*, GEER-025a(April), 1–20.

Baez, J. (1995). "A design model for the reduction of soil liquefaction by vibro- stone columns." University of Southern California, Los Angeles.

Bardet, J. P., Deaton, S., Frost, D., Goel, P., Lettis, W., Moss, R., Patel, U., Rathje, E., Seed, R., Singh, J. P., Stewart, J., Vandhana, S. V., and Wright, R. H. (2001). *Initial Geotechnical Observations of the Bhuj, India, Earthquake of January 26, 2001*.

Barma, P., Rhodes, M. B., and Salovey, R. (2008). "Mechanical properties of particulate-filled polyurethane foams." *Journal of Applied Physics*, American Institute of PhysicsAIP, 49(10), 4985.

Bian, X., Duan, X., Li, W., and Jiang, J. (2021). "Track settlement restoration of ballastless high-speed railway using polyurethane grouting: Full-scale model testing." *Transportation Geotechnics*, Elsevier, 26, 100381.

Blake, D. H. (2022). "Performance of Resin Injection Ground Improvement in Silty Sand Based on Blast-Induced Liquefaction Testing in Christchurch, New Zealand." Brigham Young University, Provo.

Bray, J. D., Stewart, J. P., Baturay, M. B., Durgunoglu, T., Onalp, A., Sancio, R. B., Ural, D., Ansal, A., Bardet, J. B., Barka, A., Boulanger, R., Cetin, O., and Erten, D. (2000). "Damage Patterns and Foundation Performance in Adapazari." *Earthquake Spectra*, SAGE PublicationsSage UK: London, England, 16(SUPPL. A), 163–188.

Buzzi, O., Fityus, S., Sasaki, Y., and Sloan, S. (2008). "Structure and properties of expanding polyurethane foam in the context of foundation remediation in expansive soil." *Mechanics of Materials*, 40(12), 1012–1021.

Buzzi, O., Fityus, S., and Sloan, S. W. (2010). "Use of expanding polyurethane resin to remediate

expansive soil foundations." *Canadian Geotechnical Journal*, 47(6), 623–634.

Chun, B.-S., Ryu, D.-S., Shin, C.-B., Im, G.-S., Choi, J.-K., Lim, H.-S., and Son, J.-Y. (1997). "The Performance of Polyurethane Injection Method with Soil Nailing System for Ground Reinforcement." *Ground improvement geosystems Densification and reinforcementeosystems Densification and reinforcement*, 445–451.

Clough, G. W., Sitar, N., and Bachus, R. C. (1981). "Cemented Sands under Static Loading." *Journal of the Geotechnical Engineering Division*, American Society of Civil Engineers, 107(6), 799–817.

Cong, L., Yang, F., Guo, G., Ren, M., Shi, J., and Tan, L. (2019). "The use of polyurethane for asphalt pavement engineering applications: A state-of-the-art review." *Construction and Building Materials*, Elsevier Ltd.

Conlee, C. T., Gallagher, P. M., Boulanger, R. W., and Kamai, R. (2012). "Centrifuge Modeling for Liquefaction Mitigation Using Colloidal Silica Stabilizer." *Journal of Geotechnical and Geoenvironmental Engineering*, American Society of Civil Engineers, 138(11), 1334–1345.

Coppola, O., Magliulo, G., and Maio, E. Di. (2016). "Mechanical Characterization of a Polyurethane-Cement Hybrid Foam in Compression, Tension, and Shear." *Journal of Materials in Civil Engineering*, American Society of Civil Engineers, 29(2), 04016211.

Cubrinovski, M., Green, R. A., Allen, J., Ashford, S., Bowman, E., Brendon, Bradley, Cox, B., Hutchinson, T., Kavazanjian, E., Orense, R., Pender, M., Quigley, M., and Wotherspoon, L. (2010). "Geotechnical reconnaissance of the 2010 Darfield (Canterbury) earthquake." *Bulletin of the New Zealand Society for Earthquake Engineering*, 43(4), 243–320.

Dashti, S., Bray, J. D., Pestana, J. M., Riemer, M., and Wilson, D. (2010). "Mechanisms of Seismically Induced Settlement of Buildings with Shallow Foundations on Liquefiable Soil." *Journal of Geotechnical and Geoenvironmental Engineering*, American Society of Civil Engineers, 136(1), 151–164.

Dominijanni, A., Gabassi, M., Kopf, F. F., Minardi, A., and Pasquetto, A. (2022). "Improvement of foundation soil behavior for Gründerzeit buildings in Austria using polyurethane resin injections." *Geotechnical Engineering for the Preservation of Monuments and Historic Sites III - Proceedings of the 3rd International Issmge TC301 Symposium, 2022*, CRC Press/Balkema, 964–976.

Earthquake Commission (EQC). (2016). *Residential Ground Improvement - Findings from trials to manage liquefaction vulnerability*.

EERI. (2010). *The Mw 7.2 El Mayor Cucapah (Baja California) Earthquake of April 4, 2010*.

Erdemgil, M., Sağlam, S., and Bakır, B. S. (2007). "Utilization of Highly Expansive Polymer Injection to Mitigate Seismic Foundation Failure for Existing Structures." *8th Pacific Conference on Earthquake Engineering*, Singapore.

Fakhar, A. M. M., and Asmaniza, A. (2016). "Road Maintenance Experience Using Polyurethane (PU) Foam Injection System and Geocrete Soil Stabilization as Ground Rehabilitation." *IOP Conference Series: Materials Science and Engineering*, Langkawi.

García-Torres, S., and Madabhushi, G. S. P. (2019). "Performance of vertical drains in liquefaction mitigation under structures." *Bulletin of Earthquake Engineering*, Springer Netherlands.

Gatto, M. P. A., Lentini, V., Castelli, F., Montrasio, L., and Grassi, D. (2021). "The use of polyurethane injection as a geotechnical seismic isolation method in large-scale applications: A numerical study." *Geosciences (Switzerland)*, Multidisciplinary Digital Publishing Institute, 11(5), 201.

Gatto, M. P. A., and Montrasio, L. (2022). "The geotechnical seismic isolation of historical buildings through polyurethane injections: A numerical study." *Geotechnical Engineering for the Preservation of Monuments and Historic Sites III - Proceedings of the 3rd International Issmge TC301 Symposium, 2022*, CRC Press/Balkema, 917–929.

Gatto, M. P. A., Montrasio, L., Tsinaris, A., Pitilakis, D., and Anastasiadis, A. (2019). "The dynamic behaviour of polyurethane foams in geotechnical conditions." *Earthquake Geotechnical Engineering for Protection and Development of Environment and Constructions- Proceedings of the 7th International Conference on Earthquake Geotechnical Engineering, 2019*, F. Silvestri and N. Moraci, eds., Rome, Italy, 2566–2573.

GEER/EERI/ATC Reconnaissance. (2014). *January 26th and February 2nd, 2014 Cephalonia, Greece Earthquakes*.

GEER. (2010a). *Geotechnical Engineering Reconnaissance of the 2010 Haiti Earthquake*.

GEER. (2010b). *Geo-Engineering Reconnaissance of the 2010 Maule, Chile Earthquake*.

Golpazir, I., Ghalandarzadeh, A., Jafari, M. K., and Mahdavi, M. (2016). "Dynamic properties of polyurethane foam-sand mixtures using cyclic triaxial tests." *Construction and Building Materials*, Elsevier Ltd, 118, 104–115.

Guha-Sapir, D., Below, R., and Hoyois, P. (2023). *EM-DAT: The CRED/OFDA International Disaster Database – www.emdat.be*. Brussels, Belgium.

Hussain, H. K., Liu, G. W., and Yong, Y. W. (2014). "Experimental study to investigate mechanical properties of new material polyurethane–cement composite (PUC)." *Construction and Building Materials*, Elsevier, 50, 200–208.

Hynes, M. E., and Olsen, R. S. (1999). "Influence of confining stress on liquefaction resistance." *Physics and mechanics of soil liquefaction. Proceedings of the international workshop, Baltimore, September 1998.*

Ishihara, K. (1985). "Stability of natural deposits during earthquakes." *Proc. 11th international conference on soil mechanics and foundation engineering, San Francisco, August 1985. Vol. 1, (Balkema)*, San Francisco, 321–376.

Jahed Orang, M., Boushehri, R., Motamed, R., Prabhakaran, A., and Elgamal, A. (2021). "An experimental evaluation of helical piles as a liquefaction-induced building settlement mitigation measure." *Soil Dynamics and Earthquake Engineering*, Elsevier Ltd, 151.

Jain, S. K., Lettis, W. R., Murty, C. V. R., and Bardet, J.-P. (2002). "2001 Bhuj, India Earthquake Reconnaissance Report." *Earthquake Spectra*, SAGE Publications, 18(1_suppl), 1–4.

JGS Kanto Branch. (2013). *Guideline to Mitigate Liquefaction-induced Damage to Wooden Houses*.

Kang, G. C., Tobita, T., and Iai, S. (2013). "Damage to sewerage systems during the 2004 earthquake in niigata-ken chuetsu, japan." *Engineering Geology*, Elsevier, 164, 230–242.

Kim, T. R., Shin, J. K., Goh, T. S., Kim, H. S., Lee, J. S., and Lee, C. S. (2017). "Modeling of elasto-viscoplastic behavior for polyurethane foam under various strain rates and temperatures." *Composite Structures*, Elsevier Ltd, 180, 686–695.

Kirkwood, P., and Dashti, S. (2019). "Influence of prefabricated vertical drains on the seismic performance of similar neighbouring structures founded on liquefiable deposits." *Geotechnique*, ICE Publishing, 69(11), 971–985.

Komurlu, E., and Kesimal, A. (2015). "Experimental study of polyurethane foam reinforced soil used as a rock-like material." *Journal of Rock Mechanics and Geotechnical Engineering*, Elsevier, 7(5), 566–572.

Koyama, A., Akira, Y., Mitabe, H., Fukubayashi, Y., and Suetsugu, D. (2023). "Field experiment of vibration characteristics of lightweight embankments converted from bridges using rigid polyurethane foam-filling under traffic load." *Case Studies in Construction Materials*, Elsevier, 18, e01756.

Koyama, A., Suetsugu, D., Fukubayashi, Y., and Mitabe, H. (2022). "Experimental study on the dynamic properties of rigid polyurethane foam in stress-controlled cyclic uniaxial tests." *Construction and Building Materials*, Elsevier Ltd, 321.

Kramer, S. L., and Holtz, R. D. (1991). *Soil Improvement and Foundation Remediation with Emphasis on Seismic Hazards*. Seattle, Washington.

Kucuk, K., Genis, M., Onargan, T., Aksoy, C. O., Guney, A., and Altindağ, R. (2009). "Chemical injection to prevent building damage induced by ground water drainage from shallow tunnels." *International Journal of Rock Mechanics and Mining Sciences*, Pergamon, 46(7), 1136–1143.

Lavín, J. R. S., Sánchez, F. E., and de la Serna, A. M. (2018). "Chemical Injections Realized with Null Pressure for Underpinning the Foundation of an 18th Century Building Located in the Historical City of Cuenca (Spain)." *Applied Sciences 2018, Vol. 8, Page 1117*, Multidisciplinary Digital Publishing Institute, 8(7), 1117.

Ledbetter, R. H. (1985). *Improvement of Liquefiable Foundation Conditions Beneath Existing*

Structures. *Technical Report - US Army Engineer Waterways Experiment Station*, Vicksburgh.

Lee, K. S., Choi, J. Il, Kim, S. K., Lee, B. K., Hwang, J. S., and Lee, B. Y. (2017a). "Damping and mechanical properties of composite composed of polyurethane matrix and preplaced aggregates." *Construction and Building Materials*, Elsevier Ltd, 145, 68–75.

Lee, S. H., Lee, S. J., Park, J. G., and Choi, Y. T. (2017b). "An experimental study on the characteristics of polyurethane-mixed coarse aggregates by large-scale triaxial test." *Construction and Building Materials*, Elsevier Ltd, 145, 117–125.

Li, M., Du, M., Wang, F., Xue, B., Zhang, C., and Fang, H. (2020). "Study on the mechanical properties of polyurethane (PU) grouting material of different geometric sizes under uniaxial compression." *Construction and Building Materials*, Elsevier Ltd, 259.

Li, S., Liu, R., Zhang, Q., and Zhang, X. (2016). "Protection against water or mud inrush in tunnels by grouting: A review." *Journal of Rock Mechanics and Geotechnical Engineering*, Elsevier, 8(5), 753–766.

Lincoln, M. (2020). "The Story Behind This Car in Silt Photo." *nzraw.co.nz*, <https://nzraw.co.nz/photography/this-car-in-silt-photo/> (Mar. 1, 2023).

Liu, K., Li, Y., Wang, F., Xie, H., Pang, H., and Bai, H. (2019). "Analytical and Model Studies on Behavior of Rigid Polyurethane Composite Aggregate under Compression." *Journal of Materials in Civil Engineering*, American Society of Civil Engineers (ASCE), 31(3), 04019007.

Maher, M. H., Ro, K. S., and Welsh, J. P. (1994). "High strain dynamic modulus and damping of chemically grouted sand." *Soil Dynamics and Earthquake Engineering*, Elsevier, 13(2), 131–138.

Mainmark. (2016). "Mainmark." <https://mainmark.com/mainmark-wins-at-2016-ground-engineering-awards-in-london/> (Mar. 1, 2023).

Miroshnichenko, S., Plugin, D., Kalinin, O., Zvierieva, A., and Reznichenko, I. (2018). "Improved bearing resistance of soil foundations of buildings with injectable polyurethane composites." *MATEC Web of Conferences*, EDP Sciences, 03013.

Mitchell, J. K. (1981). "Soil Improvement - State-of-the-Art Report." *10th International Conference on Soil Mechanics and Foundation Engineering*, ISSMGE, Stockholm.

Mitchell, J. K. (2008). "Recent Developments in Ground Improvement for Mitigation of Seismic Risk to Existing Embankment Dams." American Society of Civil Engineers, 1–20.

Naudts, A. (2003). "Irreversible Changes in the Grouting Industry Caused by Polyurethane Grouting: An Overview of 30 Years of Polyurethane Grouting." Third Internatioanl Conference on Grouting and Ground Treatment, American Society of Civil Engineers, New Orleans, 1266–1280.

NCEER. (1994). *The Northridge California Earthquake of January 17, 1994: General Reconnaissance Report*. Buffalo.

Paramasivam, B., Dashti, S., and Liel, A. B. (2020). "In-Ground Gravel–Rubber Panel Walls to Mitigate and Base Isolate Shallow-Founded Structures on Liquefiable Ground." *Journal of Geotechnical and Geoenvironmental Engineering*, American Society of Civil Engineers (ASCE), 146(9), 04020087.

Popik, M., Trout, M., and Brown, R. W. (2010). "Improving Soil Stiffness Beneath Pavements using Polyurethane Injection." *Proceedings of the TAC/ATC 2010 Annual Conference and Exhibition of the Transportation Association of Canada: Adjusting to New Realities*, Transportation Association of Canada, Halifax, Nova Scotia.

Priddy, L. P., Jersey, S. R., and Reese, C. M. (2010). "Full-Scale Field Testing for Injected Foam Stabilization of Portland Cement Concrete Repairs." *https://doi.org/10.3141/2155-03*, SAGE PublicationsSage CA: Los Angeles, CA, (2155), 24–33.

Rao, R. R., Mondy, L. A., Long, K. N., Celina, M. C., Wyatt, N., Roberts, C. C., Soehnel, M. M., and Brunini, V. E. (2017). "The kinetics of polyurethane structural foam formation: Foaming and polymerization." *AIChE Journal*, John Wiley and Sons Inc., 63(7), 2945–2957.

Rasouli, R., Towhata, I., and Akima, T. (2016). "Experimental Evaluation of Drainage Pipes as a Mitigation against Liquefaction-Induced Settlement of Structures." *Journal of Geotechnical and Geoenvironmental Engineering*, American Society of Civil Engineers (ASCE), 142(9), 04016041.

Rayamajhi, D., Asce, A. M., Ashford, S. A., Asce, M., Boulanger, R. W., Asce, F., and Elgamal, A. (2016). "Dense Granular Columns in Liquefiable Ground. I: Shear Reinforcement and Cyclic Stress Ratio Reduction." *Journal of Geotechnical and Geoenvironmental Engineering*, American Society of Civil Engineers, 142(7), 04016023.

Van Reenen, R. (2006). "Uretek Deep Injection Method: Lifting of settled foundations Analysis of full scale test results." TU Delft, Delft.

Sabri, M. M., and Shashkin, K. G. (2020). "The mechanical properties of the expandable polyurethane resin based on its volumetric expansion nature." *Magazine of Civil Engineering*, St-Petersburg State Polytechnical University, 98(6).

Saleh, S., Yunus, N. Z. M., Ahmad, K., and Ali, N. (2019). "Improving the strength of weak soil using polyurethane grouts: A review." *Construction and Building Materials*, Elsevier, 202, 738–752.

Sanchez, M. A., Zavichi, A., Pan, M., Varatharaj, R. S., and Herrmann, J. (2019). "Repair of a Deteriorated Timber Seawall at the Port of Los Angeles, Berth 240 A, B, C." *Ports 2019: Port Engineering - Papers from Sessions of the 15th Triennial International Conference*, American Society of Civil Engineers, 468–477.

Santarato, G., Ranieri, G., Occhi, M., Morelli, G., Fischanger, F., and Gualerzi, D. (2011). "Three-

dimensional Electrical Resistivity Tomography to control the injection of expanding resins for the treatment and stabilization of foundation soils." *Engineering Geology*, Elsevier, 119(1–2), 18–30.

Shigang, A., Liqun, T., Yiqi, M., Yongmao, P., Yiping, L., and Daining, F. (2013). "Effect of aggregate distribution and shape on failure behavior of polyurethane polymer concrete under tension." *Computational Materials Science*, Elsevier, 67, 133–139.

Silver, M. L., and Seed, H. B. (1971). "Deformation characteristics of sands under cyclic loading." *ASCE J Soil Mech Found Div*, American Society of Civil Engineers, 97(SM8), 1081–1098.

Towhata, I. (2021). "Liquefaction Mitigation Measures: A Historical Review." Springer, Singapore, 41–86.

Traylen, N. J. (2017). *Resin Injection Ground Improvement Research Trials-Avondale and Bexley red zone*. Christchurch.

Traylen, N. J., Van Ballegooy, S., and Wentz, R. (2016). "Liquefaction Mitigation beneath Existing Structures Using Polyurethane Grout Injection." *NZSEE Conference*, Christchurch.

Traylen, N. J., Wentz, R., Van Ballegooy, S., Hnat, T., and Wotherspoon, L. M. (2017). "Research Results from a Study into Resin Injection for Liquefaction Mitigation 2017 NZSEE Conference." *NZSEE Conference*, Wellington.

Tu, Z. H., Shim, V. P. W., and Lim, C. T. (2001). "Plastic deformation modes in rigid polyurethane foam under static loading." *International Journal of Solids and Structures*, Pergamon, 38(50–51), 9267–9279.

Valentino, R., Bisceglie, F., and Romeo, E. (2023). "Effects of Artificial Aging on Polyurethane Resins Used in Geotechnical Works." *Journal of Materials in Civil Engineering*, American Society of Civil Engineers, 35(5), 04023055.

Valentino, R., Romeo, E., and Stevanoni, D. (2014). "An experimental study on the mechanical behaviour of two polyurethane resins used for geotechnical applications." *Mechanics of Materials*, Elsevier, 71, 101–113.

Vennapusa, P. K. R., Asce, M., Zhang, Y., Asce, S. M., and White, D. J. (2016). "Comparison of Pavement Slab Stabilization Using Cementitious Grout and Injected Polyurethane Foam." *Journal of Performance of Constructed Facilities*, American Society of Civil Engineers, 30(6), 04016056.

Wan, Z., Bian, X., Li, S., Chen, Y., and Cui, Y. (2020). "Remediation of mud pumping in ballastless high-speed railway using polyurethane chemical injection." *Construction and Building Materials*, Elsevier, 259, 120401.

Wang, C., Guo, C., Du, X., Shi, M., Liu, Q., and Xia, Y. (2021). "Reinforcement of silty soil with permeable polyurethane by penetration injection." *Construction and Building Materials*, Elsevier, 310, 124829.

Wei, Y., Wang, F., Gao, X., and Zhong, Y. (2017). "Microstructure and Fatigue Performance of Polyurethane Grout Materials under Compression." *Journal of Materials in Civil Engineering*, American Society of Civil Engineers (ASCE), 29(9), 04017101.

Xiao, Y., Liu, H., and Desai, C. S. (2015). "New Method for Improvement of Rockfill Material with Polyurethane Foam Adhesive." *Journal of Geotechnical and Geoenvironmental Engineering*, American Society of Civil Engineers (ASCE), 141(2), 02814003.

Xiao, Y., Stuedlein, A. W., Chen, Q., Liu, H., and Liu, P. (2018). "Stress-Strain-Strength Response and Ductility of Gravels Improved by Polyurethane Foam Adhesive." *Journal of Geotechnical and Geoenvironmental Engineering*, American Society of Civil Engineers (ASCE), 144(2), 04017108.

Yamazaki, H., Hayashi, K., and Zen, K. (2005). "New liquefaction countermeasure based on pore water replacement." *Proceedings of the 16th International Conference on Soil Mechanics and Geotechnical Engineering: Geotechnology in Harmony with the Global Environment*, Osaka, 2741–2744.

Yasuda, S. (2007). "Remediation methods against liquefaction which can be applied to existing structures." *Geotechnical, Geological and Earthquake Engineering*, Kluwer Academic Publishers, 6, 385–406.

Yasuda, S. (2014). "New liquefaction countermeasures for wooden houses." *Soil Liquefaction during Recent Large-Scale Earthquakes - Selected Papers from the New Zealand: Japan Workshop on Soil Liquefaction during Recent Large-Scale Earthquakes*, R. P. Orense, I. Towhata, and Chouwm N., eds., Taylor and Francis - Balkema, Aukland, 167–179.

Yasuda, S., and Ishikawa, K. (2018). "Appropriate measures to prevent the liquefaction-induced inclination of existing houses." *Soil Dynamics and Earthquake Engineering*, Elsevier, 115, 652–662.

Zhang, Z., Liu, K., and Ye, L. (2016). "Application of polymer grouting reinforcement technology in the treatment of slope collapse." *5th International Conference on Environment, Materials, Chemistry and Power Electronics*, Atlantis Press, Paris, 244–249.

1.9 Tables and Figures

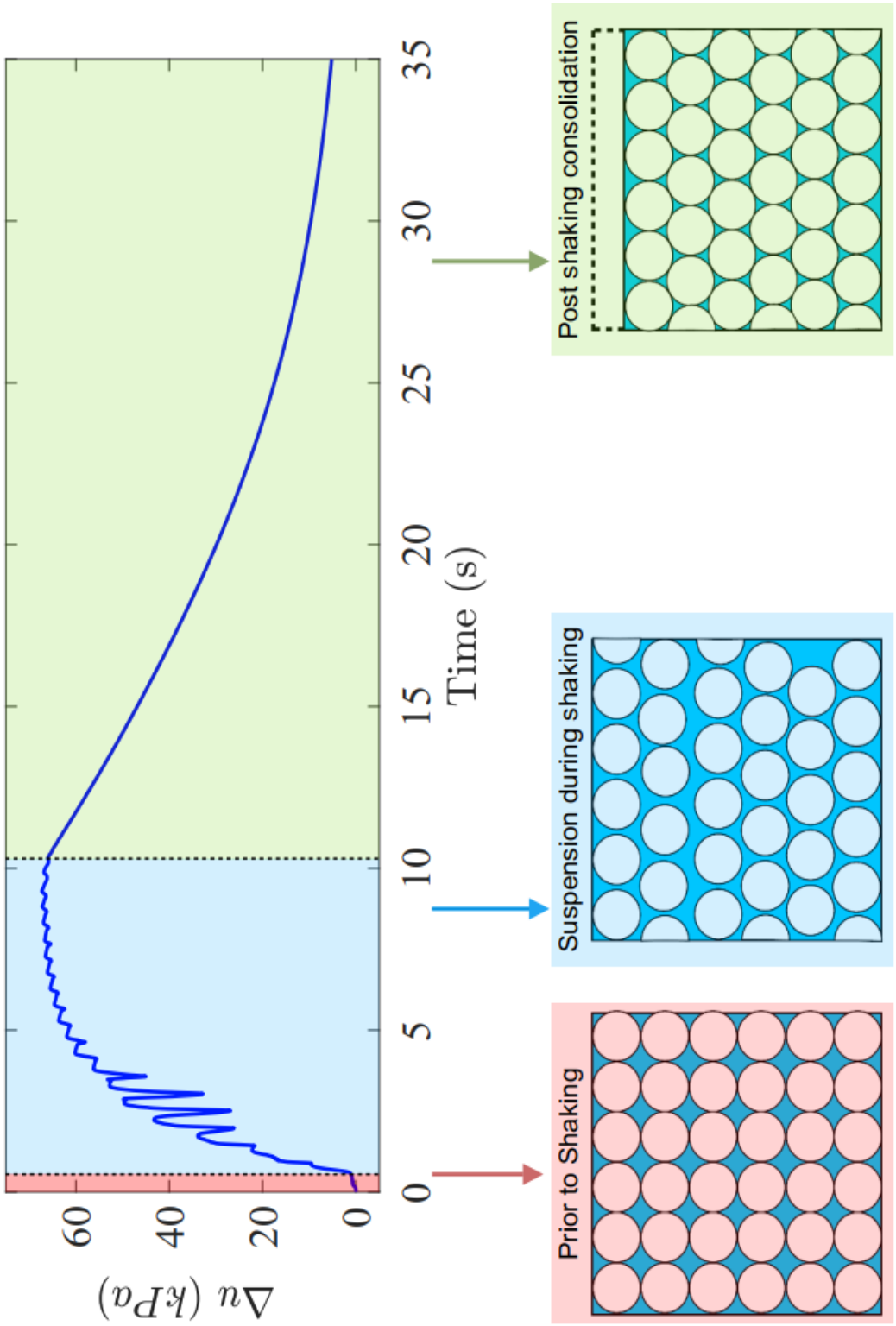

Figure 1.1. Schematic of loss of particle-particle contact during soil liquefaction (modified after National Academies of Sciences, Engineering, and Medicine 2021)

(a) Tilted buildings in Adazapari, Turkey following the 1999 Kocaeli (Turkey) earthquake

(b) Settlement of a car from the 2010-2011 Canterbury earthquake sequence

Figure 1.2. Liquefaction induced bearing failures (settlement): (a) Tilted buildings in Adazapari, Turkey following the 1999 Kocaeli (Turkey) earthquake (from Boulanger 2017), and (b) Settlement of a car from the 2010-2011 Canterbury earthquake sequence (from Lincoln 2020)

(a) Buoyant rise of an underground utility access hole from the 2004 Niigata Ken-Chuetsu (Japan) earthquake

(b) Buoyant rise of an underground tanks from the 2010 Maule earthquake, Chile

Figure 1.3. Liquefaction induced uplift of underground structures (buoyant rise) from past seismic events: (a) Buoyant rise of an underground manhole from the 2004 Niigata Ken-Chuetsu (Japan) earthquake (after Kang *et al.* 2013), and (b) Buoyant rise of an underground tanks from the 2010 Maule earthquake, Chile (after GEER 2010b)

(a) Lateral spreading induced failure of the Showa bridge (lateral soil movement).

(b) Lateral Unseating of the Puente Bio Bio bridge in Concepción in the 2010 Chile earthquake.

Figure 1.4. Lateral spreading (lateral soil movement) induced failure of the Showa bridge in the 1964 Niigata earthquake, (photo creator: Prof. Joseph Penzien, NISEE archives) and Puente Bio Bio bridge from the 2010 Maule Earthquake (GEER 2010b).

(a) Railroad embankment during the 1964 Alaska earthquake

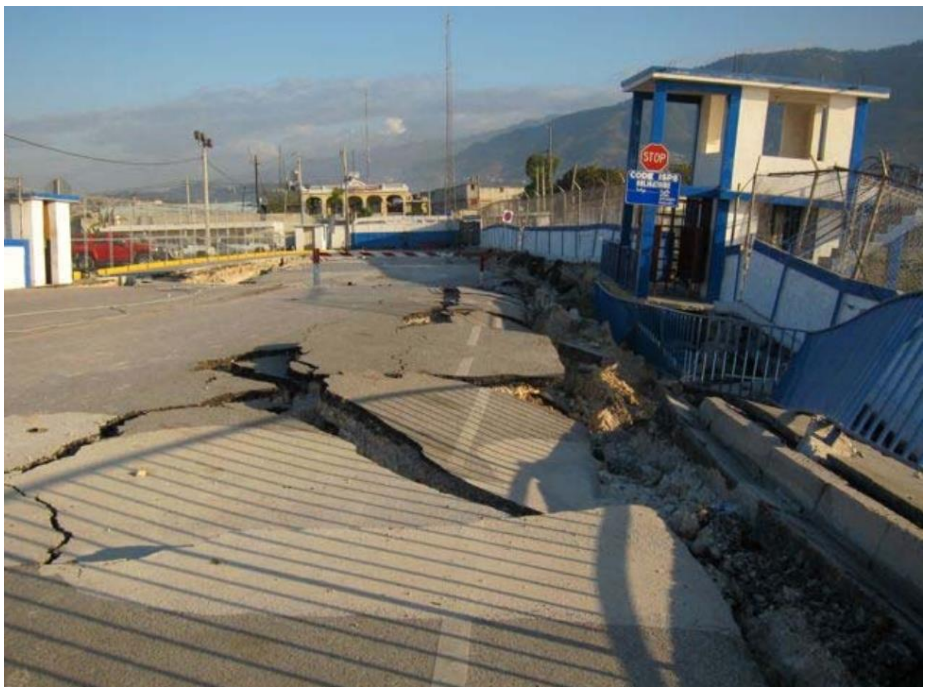

(b) Road embankment during the 2010 Haiti earthquake

Figure 1.5. Liquefaction induced failure of (a) Railroad embankment during the 1964 Alaska earthquake (McCulloch and Bonilla 1980) and (b) road embankments, (b) Road embankment during the 2010 Haiti earthquake (GEER 2010a)

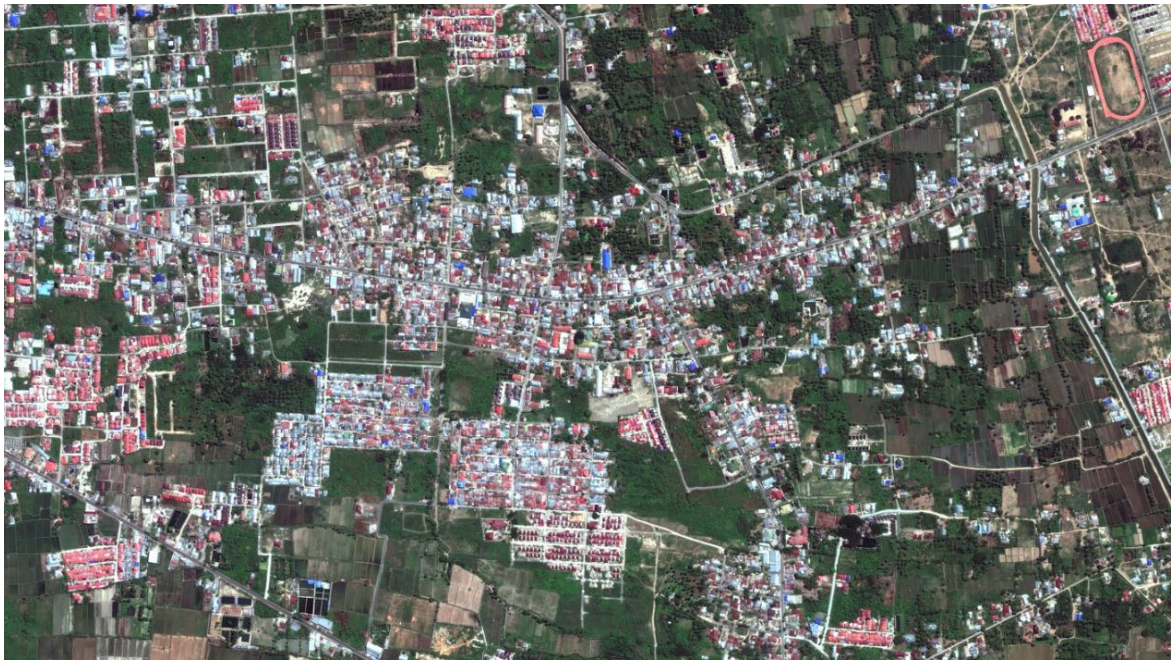

(a) Satellite photo of Palu on August 17, 2018 (about a month before the earthquake)

(b) Satellite photo of Palu on October 1, 2018 (3 days after the earthquake)

Figure 1.6. Liquefaction induced slope failures during the 2018 Sulawesi earthquake Satellite photo of Palu (DigitalGlobe 2018) (a) on August 17, 2018 (about a month before the earthquake), (b) on October 1, 2018 (3 days after the earthquake)

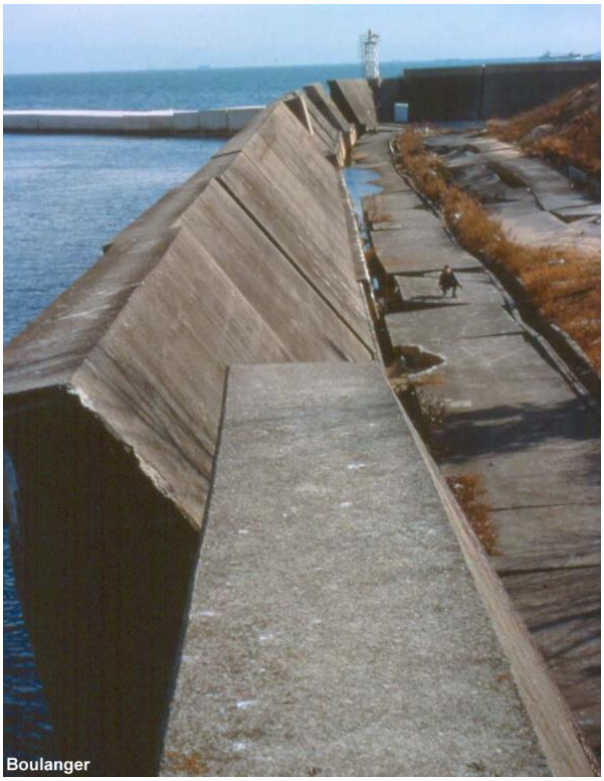

(a) Lateral spreading induced damage to a quay wall after the 1995 Kobe earthquake

(b) Damages to a quay wall during the 2001 Bhuj Earthquake

Figure 1.7. Liquefaction induced failures of quay walls: (a) after the 1995 Kobe earthquake (from Boulanger 2017), and (b) after the 2001 Bhuj earthquake (from Bardet *et al.* 2001)

(a) Lateral spreading induced damage to a pier and cranes during the 1995 Kobe earthquake

(b) Lateral spreading induced damage to a wharf during the 2010 Haiti earthquake

Figure 1.8. Liquefaction induced failures of coastal structures (ports and wharfs): (a) during the 1995 Kobe earthquake (Boulanger 2017), and (b) during the 2010 Haiti earthquake (from Rathje *et al.* 2010)

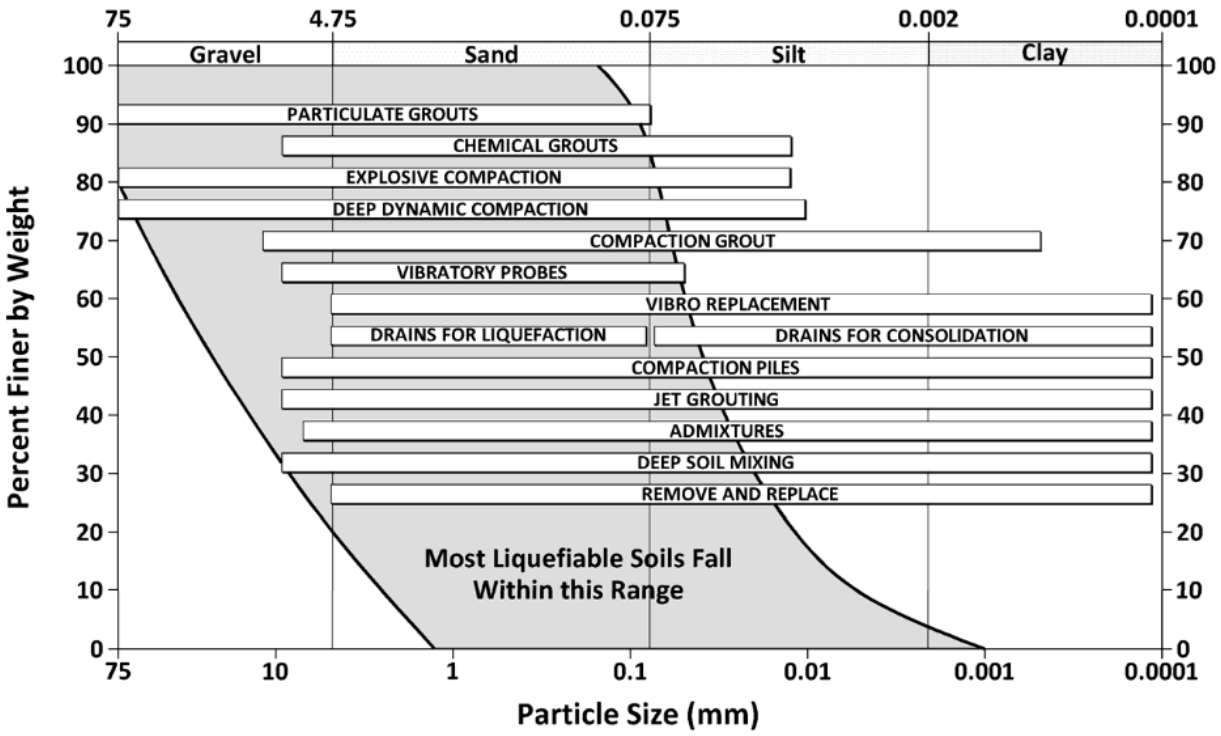

Figure 1.9. Applicability of liquefaction countermeasures with soil particle size (From Mitchell 2008)

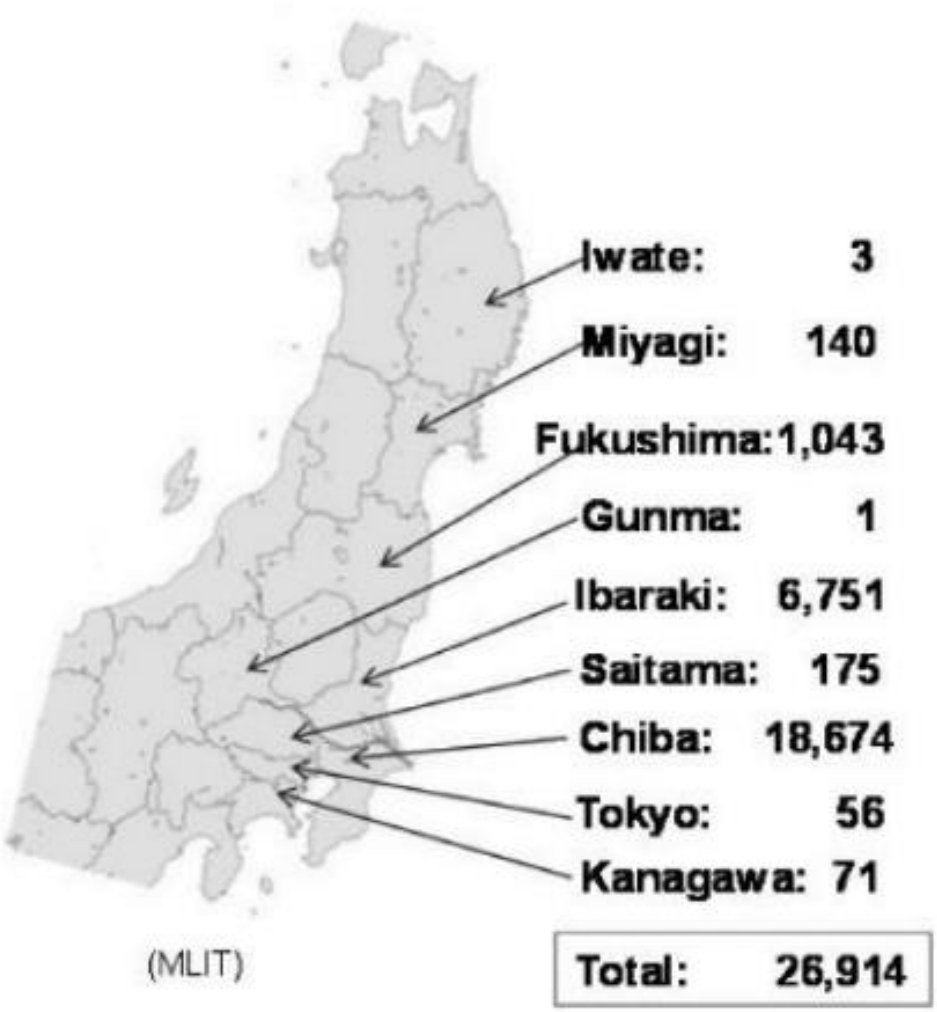

Figure 1.10. Homes damaged due to soil liquefaction during the 2011 Tohoku Earthquake (from Yasuda 2014)

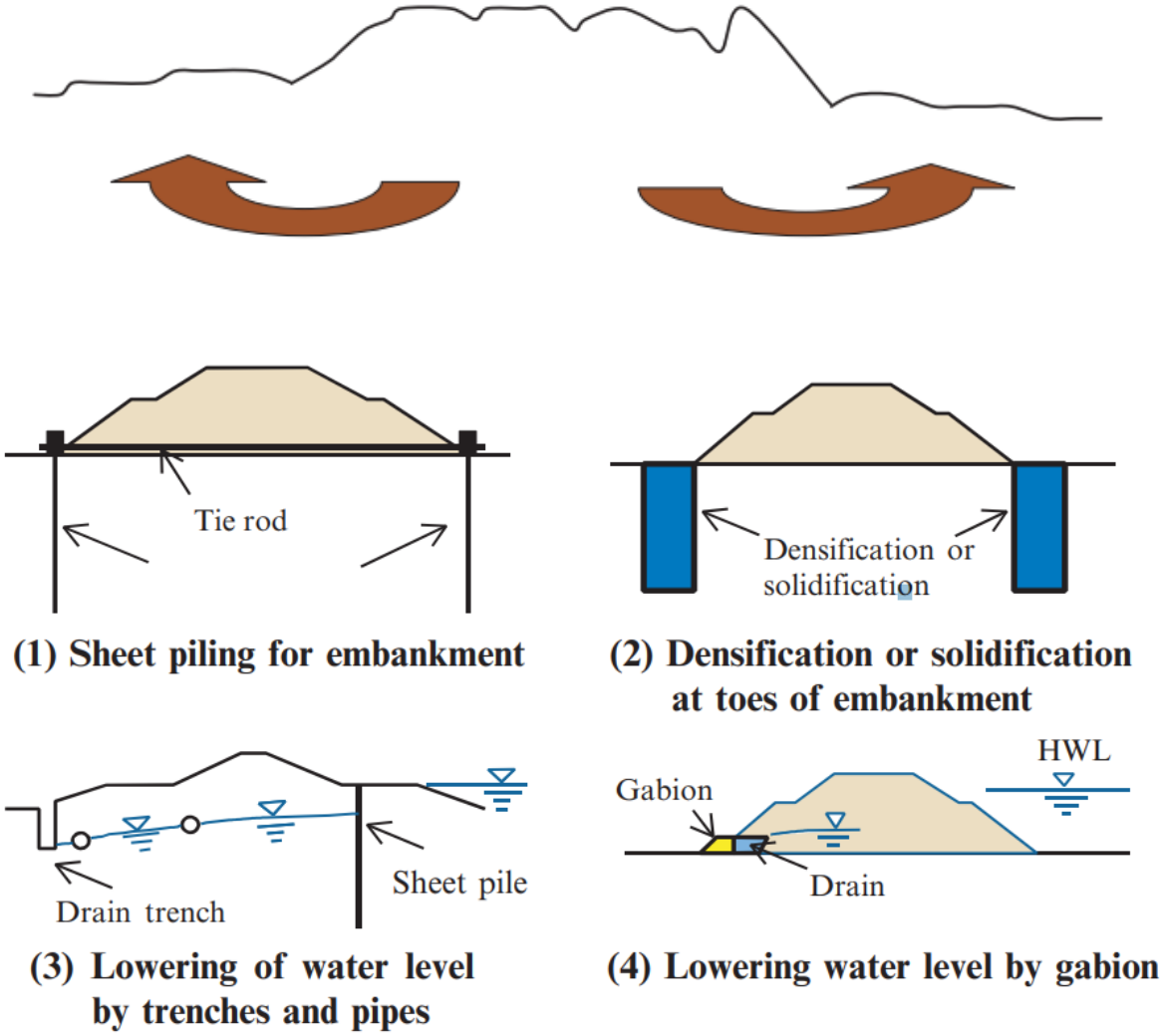

Figure 1.11. Insitu liquefaction countermeasures for embankments (from Yasuda 2014)

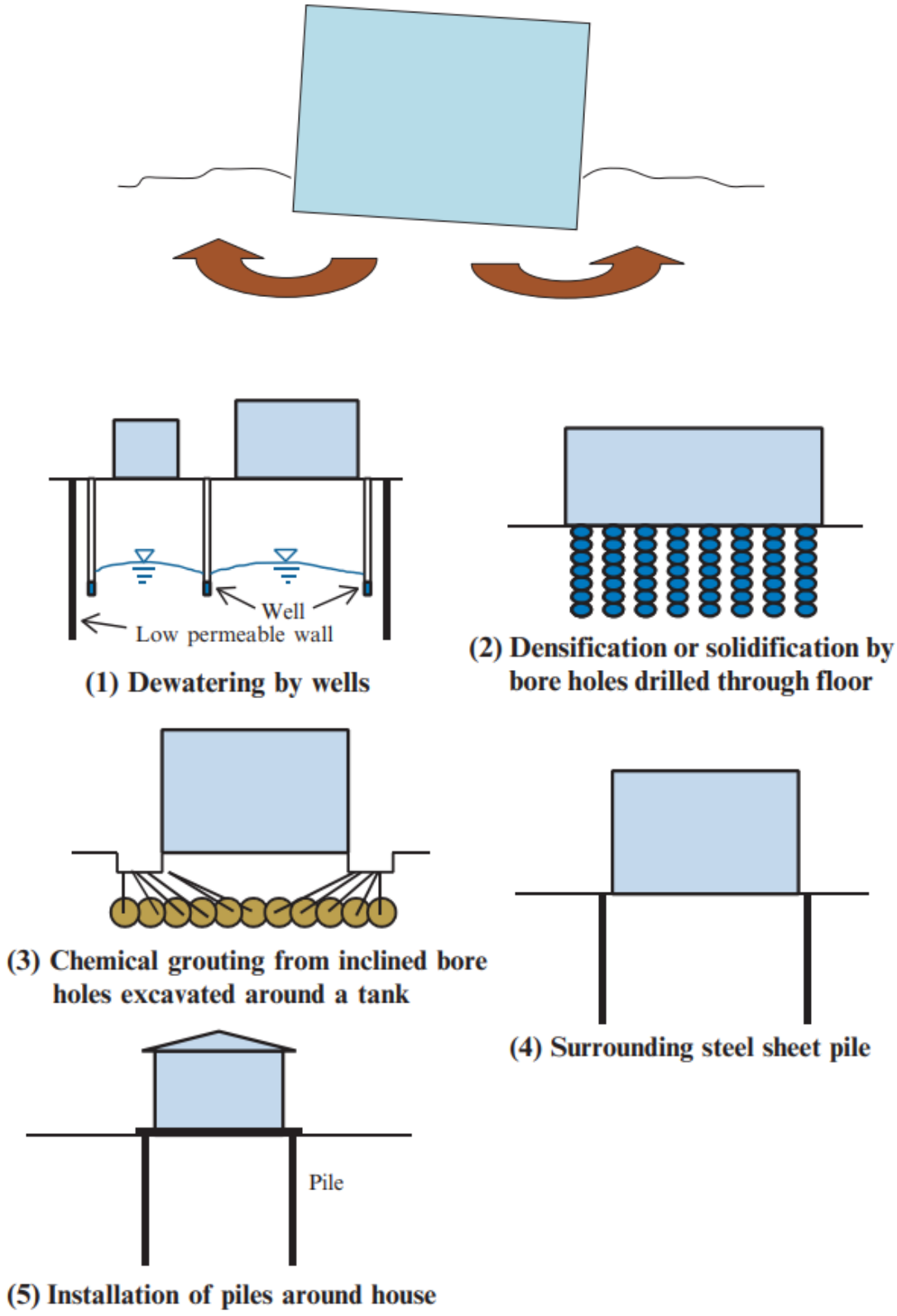

Figure 1.12. Insitu liquefaction countermeasures for existing individual homes (from Yasuda 2014)

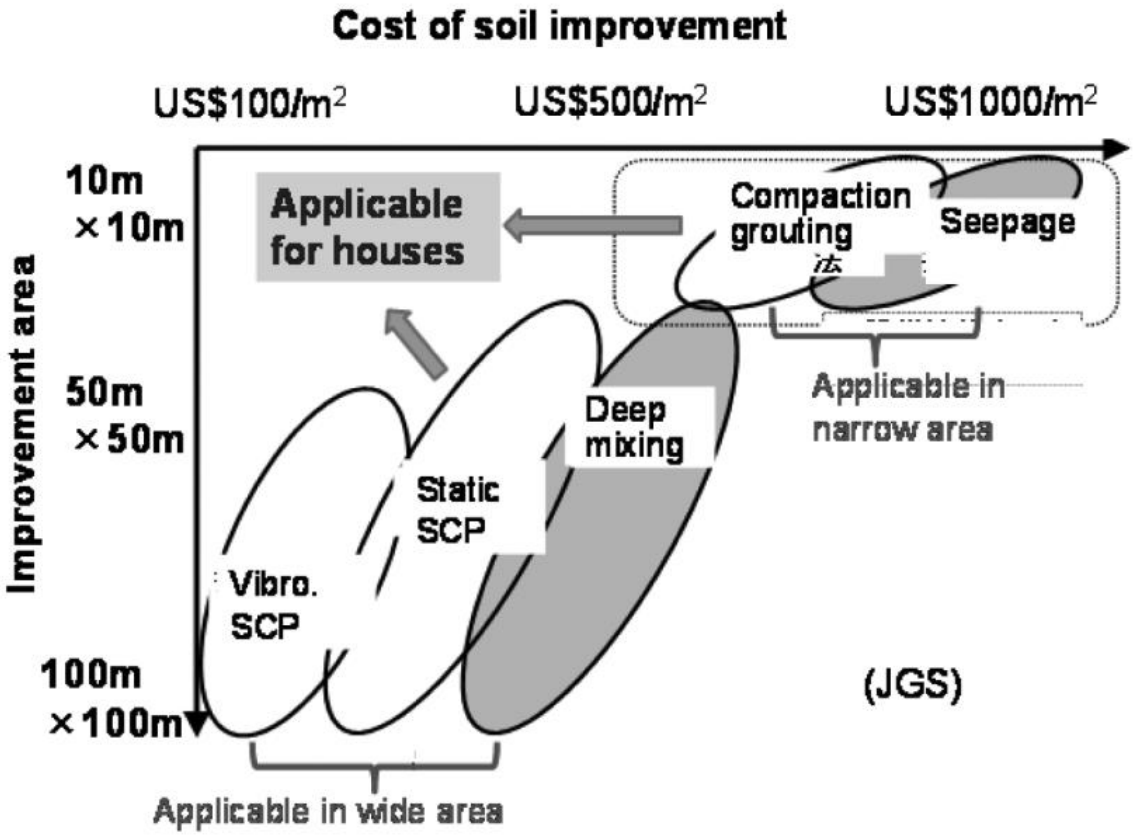

Figure 1.13. Cost of current liquefaction countermeasures for existing individual houses (from Yasuda 2014)

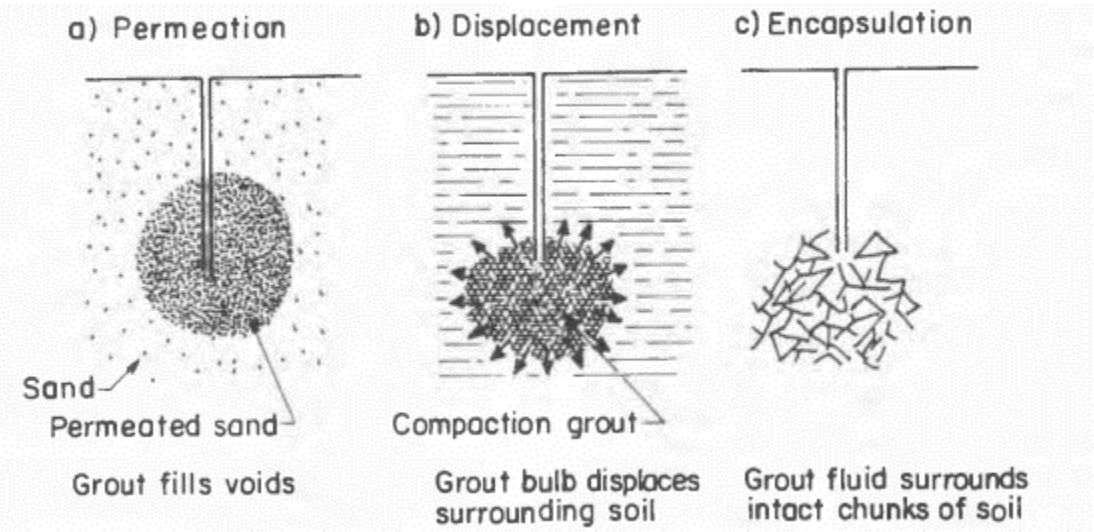

Figure 1.14. Different types of grouts (From Mitchell 1981)

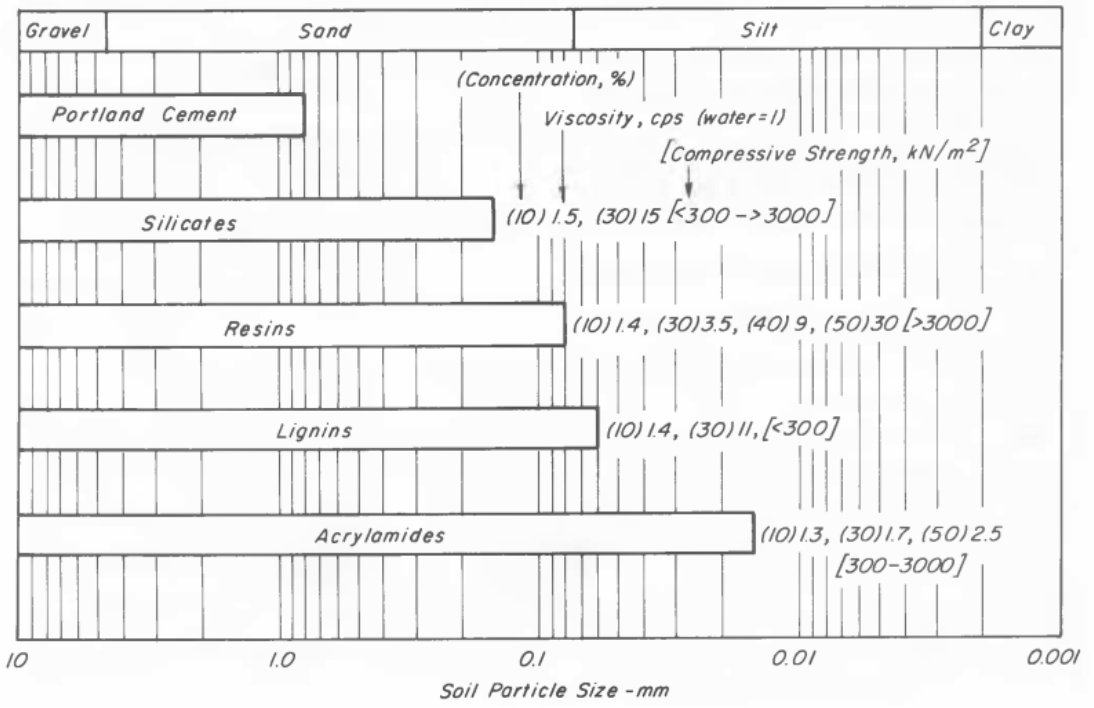

Figure 1.15. Soil particle sizes for different grout mixtures, and resulting mechanical properties (From Mitchell 1981)

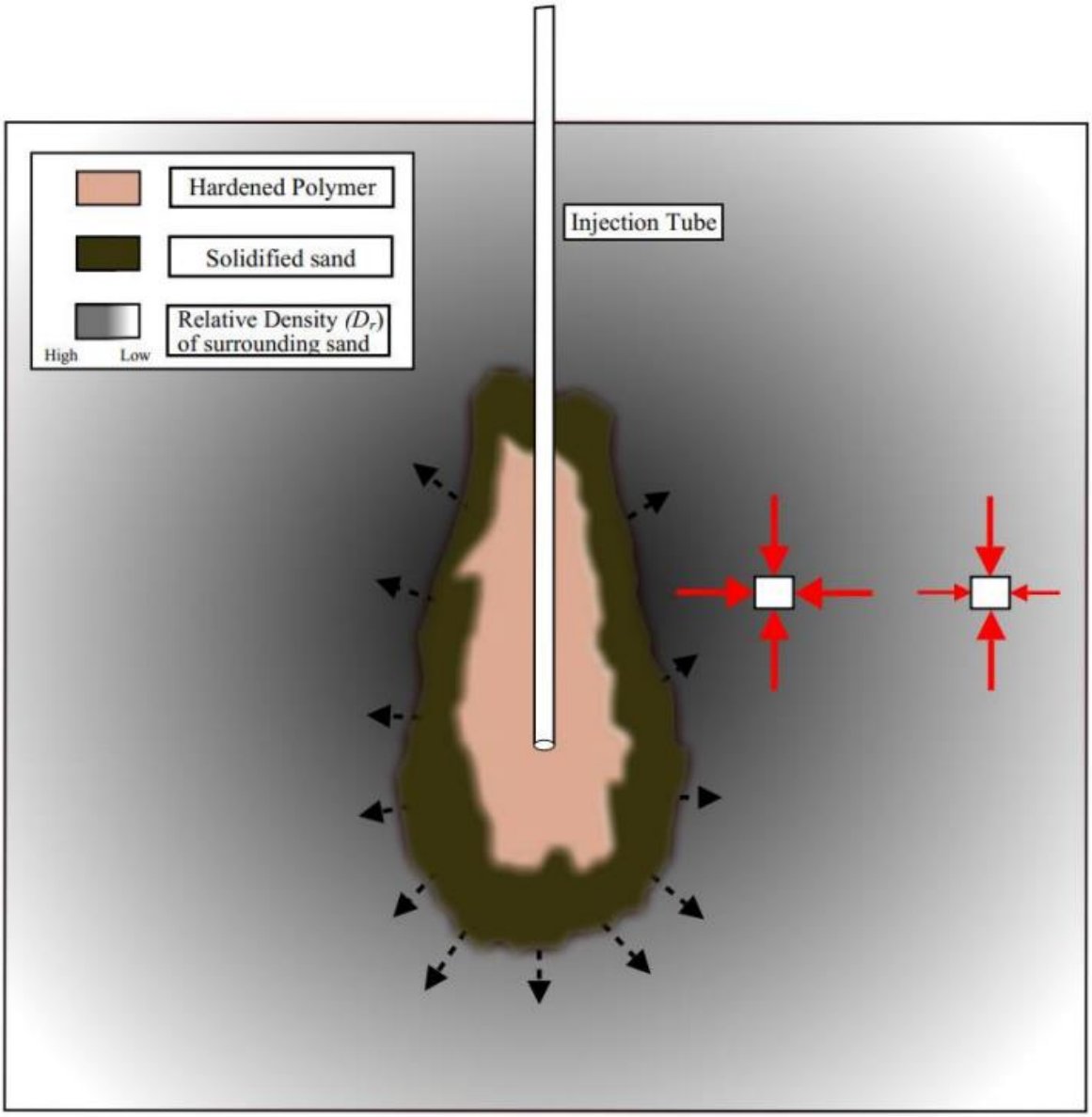

Figure 1.16. Schematic of the polymer-sand composite after injection (thickness of red arrows conceptually indicates magnitude and direction of acting vertical and horizontal stresses)

(a) Shoring the perimeter of the structure prior to polymer injection

(b) Injection of the expansive polymer under the structure.

Figure 1.17. Injection of the expansive polymer underneath an existing structure (Photo from Cliff Frazao)

(a) Polymer injection test panels at the red zone site (site 3)

(b) Exhumed polymer-soil composites after excavation (at site 3)

Figure 1.18. (a) Polymer injection test panels and (b) polymer-sand composite veins following the excavation (From Traylen *et al.* 2017)

Chapter 2. Polymer Injection and Associated Site Liquefaction Remediation Mechanisms

2.1 Abstract

The results from a pilot study performed at the University of California, San Diego to assess potential of the polymer injection technique as a liquefaction countermeasure are presented. Three containers of dimensions about 1.1 m (length) by 0.9 m (width) by 1.0 m (height) are filled with saturated Ottawa F-65 sand at loose, medium-dense, and dense relative densities. An expansive polymer is then injected into each container. Once the polymer material was cured, all three containers are placed on a shake table and subjected to strong dynamic excitation. Post shaking, all three containers are carefully dissected to observe the extent of permeation of the polymer within the saturated sand. On careful examination of the hardened composite polymer-sand inclusion, mechanisms contributing to improved liquefaction resistance including densification, cementation, and increase in lateral confinement are observed. The composite inclusions are characterized based on weight/volume relationships. Further, an initial guideline is proposed to relate amount of polymer to increased level of liquefaction resistance, in preparation for large-scale shake table testing. A recommendation is then made, in the context of an example, towards deploying the developed framework for field applications.

2.2 Introduction

Seismically induced soil liquefaction is a documented mechanism that results in severe damage to structures and foundation systems. Liquefaction-induced loss of soil strength and stiffness and subsequent consequences have been well documented in several major earthquakes including events in Japan, Turkey, India, and New Zealand (Ishihara and Koga 1981, JGS 1996,

Ashford *et al.* 2011, Bray *et al.* 2000, Jain *et al.* 2002, Cubrinovski *et al.* 2010). For example, during the 2010-2011 Canterbury earthquake sequence, severe soil liquefaction affected 3,000 buildings within the Central Business District (CBD) of Christchurch, of which over 50% were to be demolished, being deemed economically unfit for further repairs (Cubrinovski, 2010). Hence in high seismic regions, with loose saturated granular soils, it is vital that remediation measures be undertaken to minimize the consequences of soil liquefaction.

Various techniques currently exist to improve liquefaction susceptible soils, including strategies involving soil densification (Adalier and Sharp 2004, Olarte *et al.* 2018), cementation (Gallagher and Mitchell 2002), drainage, and replacement (Yasuda and Harada 2014). Among the mitigation techniques, the injection of low viscosity polyurethane (polymer) using permeation grouting has proven to be an effective measure for remediation, at locations which might otherwise be difficult to treat with conventional techniques (Erdemgill *et al.* 2007 and Traylen *et al.* 2017). Injection of expansive polymers into the ground has long been used to improve karsts in soil, reduce permeability, improve soil strength, particularly to prevent subsidence during excavation or tunneling, and relevel structures exhibiting differential settlement (Buzzi *et al.* 2008 and Soga *et al.* 2004).

In the context of liquefaction remediation, the technique offers two-fold benefit in terms of a reduction in the shear demand (cyclic shear stress ratio) and improvement in soil confinement and related liquefaction resistance (cyclic resistance ratio) of the insitu soil (Traylen *et al.* 2017). The injection methodology (Figure 2.1) uses either low viscosity grouts injected under pressure to hydro-fracture the soil or high-viscosity grouts that densify soil through compaction. The polymer is injected through thin cold form steel tubes with either an opening at the tip or using sleeved tubes (tube á manchette) which offer a distributed surface (Soga *et al.* 2004). The tubes are

typically deployed at a spacing of 0.9 m-1.0 m on center and are easy to install in dense urban environments as it does not require an excavation (Traylen *et al.* 2017). The ability to tailor polymers with structural and rheological capabilities specific to the ground conditions is a considerable advantage to this technique. For example, such an improvement strategy could even be adopted in the presence of underground utilities whereby a low viscosity polymer would be injected to allow for permeation without damage to buried infrastructure.

In this chapter, the authors discuss the results from a pilot experimental stage of a three-phase testing program. Overall, the aim is to study a number of ground improvement strategies to remediate liquefaction induced settlement of a shallow foundation on loose liquefiable soil through 1g-large scale shake table testing (Jahed Orang *et al.* 2021). The pilot experiment is performed to provide insight into the mechanisms contributing towards improved liquefaction resistance of polymer remediated soils. The results from this phase are then used to develop a methodology to estimate the extent of remediation required in the subsequent large-scale shake table test, with an initial guideline chart for practical applications.

Within this pilot phase, three identical containers are filled with sand at different relative densities (D_r) and polymer is injected thereafter into the containers. The three containers are then subjected to base excitation on the shake table facility at the Powell Structural Engineering Laboratories at UC San Diego (UCSD). Further, the containers are carefully dissected to characterize the extent of polymer permeation and properties of the hardened sand-polymer matrix (composite inclusion). Associated ground improvement mechanisms contributing to the increased liquefaction resistance are explored. Recommendations made from this testing phase are provided to aid in the design of related large-scale testing and applications in practice.

2.3 Specimen Preparation and Polymer Injection

2.3.1 Specimen preparation

Specimen construction involved the preparation of three containers (Figure 2.2), each about 1.10 m (length) by 0.90 m (width) by 1.00 m (height), filled with Ottawa F-65 sand. Different deposition techniques were employed in order to build loose, medium-dense, and dense specimens (in each container). Ottawa F-65 is a clean poorly graded fine sand with minimum and maximum dry densities of 14.02 kN/m^3 (e_{max} = 0.83) and 17.3 kN/m^3 (e_{min} = 0.51) (Bastidas 2016).

Each container is equipped with a u-shaped perforated piping system at its base to saturate the soil specimen. Further, three flexible acrylic tubes of diameter 12 mm are embedded at different depths to monitor the dissipation of excess pore pressure within the specimen (i.e., serving as piezometers). The weight of the dry sand and water deposited into each specimen is noted during each lift. Each container is filled to a specimen height of 0.95 m as follows:

i. **Loose Sand**: The container with loose sand is prepared using the hydraulic fill approach, whereby Ottawa sand is first pluviated into the model while maintaining a clear water head of 125 mm resulting in a specimen relative density (D_r) of about 30%.

ii. **Medium-Dense Sand**: The container with medium-dense sand is prepared using the hydraulic fill approach, whereby Ottawa sand is deposited into the soil model while maintaining a clear water head of 75 mm, resulting in a specimen D_r of about 55%.

iii. **Dense Sand**: The container with dense sand is prepared moist in 5 lifts. Each lift consisted of sand deposition up to a height of 200 mm with further compaction using 10 blows of a 23 kg hammer. The process is repeated till the specimen height is achieved and saturated by adding water slowly through the perforated piping system installed at the base of the container. A specimen D_r of about 80% was achieved using this approach.

Table 2.1 summarizes the achieved relative densities and equivalent corrected standard penetration test $(N_1)_{60}$ blow count based on Eq. (1) proposed by Idriss and Boulanger (2008).

$$D_r = \sqrt{\frac{(N_1)_{60}}{46}} \quad (1)$$

2.3.2 Polymer Injection

Post sample preparation, each container is injected with 18.15 kg of a two-component expansive polymer (designated EagleLift^{TM} EL077), as shown in Figure 2.3. The amount of polymer injected is based on the typical scenario to level-correct buildings on incompetent soil, as a first estimate in this preliminary test.

The structural polyurethane (polymer) used in this study is a two-component chemically blown foam consisting of a curative phase (poly-isocyanate) and a resin phase (including polyol). The two components are mixed in equal parts to produce the expanding foam at a nominal temperature of 43°C. The resulting structural foam has a free rise density of 64 kg/m^3. On injection, the polymer used in this study has a low viscosity and a cream time of 7 s and expands in volume depending on its surrounding state of confinement (thereby increasing in viscosity). In this experiment, the injection is performed only at a single point in each container, at a height of 300 mm from the base of each container. After injection, the polymer was allowed to cure for 72 hours.

2.4 Shake Table Testing and Results

Post injection, all three specimens are carefully lifted and placed on the uniaxial shake table facility at the Powell Structural Engineering Laboratories, University of California, San Diego. The uniaxial shake table platform has dimensions of 4.9 m by 3.1 m and is designed for models that weigh up to 350 kN. Further details concerning the shake and its performance characteristics are reported by Trautner *et al.* (2018). All specimens are subjected to a test protocol that consisted

of two base motions (Figure 2.4), allowing for excess pore pressure dissipation between, as observed through the embedded thin flexible acrylic tubes.

Significant rise in pore water pressure and consequent volumetric settlement were observed in the loose and medium-dense specimens during Shake01. Loss of effective confinement was evident with ground surface oscillation and subsequent tilting of the injection tube in the loose specimen. As such, the amount of polymer that remained within the loose specimen after injection could not prevent liquefaction. Relatively moderate ground oscillation of the pipe was seen in the medium- dense specimen, and no movement was observed in the dense specimen, indicating an adequately sustained level of effective confinement during the shaking phase. Following each shaking event, the volumetric strains developed in each specimen are presented in Figure 2.5.

2.5 Excavation

2.5.1 Polymer Injection

After shaking, the containers were dissected, and the sand was excavated to see the formation of the composite inclusion within each specimen (Figure 2.6). Emphasis is based on the distribution of the polymer around the point of injection. As seen in Figure 2.6, due to the low initial viscosity and high mobility, the orientation of the inclusion is irregular in all three specimens.

However, several salient features of the formation of the inclusion can be delineated (Figure 2.7). In the loose and medium-dense specimens, the polymer is first seen to permeate laterally around the injection point, creating a grout bulb. Veins are then seen to emanate from this bulb, particularly at locations closer to the injection tube. The dense specimen is able to retain more of the polymer within its soil mass and hence the composite inclusion is not localized around the injection tube.

Figure 2.8 presents a cross-section of the composite excavated from the medium dense specimen, where several zones can be observed including a cemented polymer-sand surficial zone and a pure polymer inner zone. The extent of each of these zones can be attributed partially to the variation in fluid viscosity, extent of permeation, and the polymer expansion post injection. The polymer initially fractures through the soil deposit and then permeates into the sand. With cementation a portion of this sand mixes with the polymer and contributes to the cemented interface sand zone. Polymer expansion leads to further separation of surfaces where zones of the pure polymer are sandwiched between layers of cemented sand. After the dissection process, the three composite inclusions are weighed. Volume of each is estimated by immersion into a prismatic container filled with water and measuring the change in the water level pre and post immersion. Table 2.2 presents a comparison of the mass densities of the three composite inclusions, where volume of the inclusion is normalized by volume of the soil in each container (0.93 m^3).

As the range of mass densities of pure polymer (80 kg/m^3- 240 m^3) and deposited sand in each specimen is known beforehand, it is possible to approximately estimate the amount of pure polymer and cemented sand within each composite inclusion from a mass balance calculation. Once obtained, an expansion ratio (volume of expanded solidified polymer compared to its liquid volume) can be established. On this basis, it is seen that on an average, pure polymer encompasses about 60% (by volume) of each composite inclusion (interface sand occupying 40%) in all three specimens. In addition, an average polymer expansion ratio of 2.7 is noted.

2.5.2 Degree of Soil Improvement

As the volumes of pure polymer and cemented sand zones within the composite inclusion are now reasonably obtained, it is possible to estimate the D_r of the remaining sand which

surrounds this inclusion (based on replacement assuming constant volume conditions). In the conducted experiment, this assumption is acceptable, as no significant visible heave was observed in the soil surface during injection.

Post injection, a fraction of granular phase of the sand is assumed to be cemented (obtained from Table 2.2) within the composite inclusion. The volume available for the granular phase uncemented sand (surrounding the inclusion) is hence reduced, assuming the injection occurs at constant volume. Since volume of the inclusion and the cemented sand in each container have been reasonably estimated, the D_r of the uncemented sand surrounding the inclusions can be obtained. As such, Figure 2.9 presents the estimated improvement in the D_r of the surrounding uncemented sand. It is noted that a D_r greater than 100% in the dense specimen represents that a larger portion of the sand had been cemented in comparison with the estimate.

2.6 Application to Large Scale Testing

A framework is developed to derive a family of curves relating the final relative density of the uncemented sand to the volume of polymer injected in its liquid (Figure 2.10), keeping in mind the following assumptions (per the earlier sections):

a. The deposit consists of granular soil

b. Injection takes place under constant volume (no heave or polymer escape through ground surface)

c. Expansion ratio of 2.7 is assumed (average value from the three specimens)

d. 40 % of the composite inclusion consists of cemented sand.

The set of curves in Figure 2.10, specifically address the change in $(N_1)_{60}$ within the uncemented sand of the improved layer. Through injection, the polymer expands (estimated at 2.7 times in this experiment) and a portion of the soil is cemented (therefore non-liquefiable). Due to

this expansion, the remaining uncemented soil occupies less space and the new D_r can be obtained. In a field setting, the assumption of constant volume might be difficult to achieve. Thus, it would be a solution that a perimeter grout curtain could be created to help containment and prevent polymer escape.

In the second phase of this experimental effort, a large-scale shake table test is conducted to study the response of a shallow foundation overlain on surficial liquefiable soils. The soil model in the experiment consisted of a three-layered deposit, consisting of a saturated 1.00 m dense bottom layer underlying a 1.25 m thick saturated liquefiable deposit, overlain by a moist 0.64 m crust. The loose liquefiable layer is constructed at D_r in the range of 35 % - 44 %, corresponding to an $(N_1)_{60}$ of 5-9. The model is subjected to cyclic base excitation and large liquefaction induced settlements are observed as shown in Figure 2.11. Full details of this testing program can be found in Jahed Orang *et al.* (2021). To remediate liquefaction induced foundation settlement in this baseline experiment, an identical model is constructed with the EagleLift EL077 polymer injected into the loose liquefiable stratum (Prabhakaran *et al.* 2020). The methodology is applied specifically to strengthen the loose sand stratum within this large-scale shake table test.

In the polymer remediated experiment, a corrected blow count $(N_1)_{60}$ of 30 (corresponding to a volume ratio of 8.4 %) is selected as the target (Figure 2.10), conceptually to preclude liquefaction. The remediated model post shaking response is presented in Figure 2.12, where the actual achieved volume ratio is about 7.9 % is achieved.

2.7 Conclusions

A testing program was conducted to evaluate the mechanisms associated with improved liquefaction resistance in granular soils remediated with the polymer injection technique. Three containers were filled with sand at loose, medium-dense, and dense relative densities, injected with

polymer, with base excitation imparted. The specimens were then carefully dissected to examine the composite inclusion within the surrounding sand. Within all three composite inclusions, around 60 % by volume of each was estimated as pure polymer. Across the three inclusions, the polymer was seen to expand about 2.7 times as compared to its liquid volume. This ratio could be used to estimate the degree of polymer expansion under similar confinement scenarios.

Several mechanisms are noted to contribute to the observed improved liquefaction resistance. These mechanisms are illustrated via a representative scenario where deposit of clean sand at D_r = 30% (corresponding to $(N_1)_{60}$ = 5) is improved by 6 % volume polymer (in its liquid state).

1. The polymer forms a composite inclusion at relatively constant volume. This inclusion cements a portion of the liquefiable sand and reduces the shear demand on the surrounding soil due to the improved cemented composite stiffness. The 6 % by volume injection will result in about 27 % of the total volume being occupied by the non-liquefiable composite inclusion.
2. Expansion of the polymer provides for an increase of D_r in the surrounding uncemented sand. This mechanism contributes to the increase in liquefaction resistance. Within the context of this representative scenario, an improvement in D_r will take place from 30 % (corresponding $(N_1)_{60}$ of 5) to about 57 % (corresponding $(N_1)_{60}$ of 15). However, we must be mindful of considerations such as uneven distribution of volumetric strain reductions, and the potential for an extent of lateral expansion and/or subsurface heave as briefly discussed by Boulanger and Hayden (1995). These mechanisms can be further accounted for on a case-by-case basis.
3. Furthermore, the expansion of the polymer offers additional lateral confinement (increasing the lateral pressure).

4. The weight volume relationships established from the test are then used to construct a family of curves relating the increase in corrected SPT blow count $(N_1)_{60}$ to the volume of polymer injected in its liquid form. Such a family of curves is specific to the polymer used in this experiment and can be extended for deployment in actual in situ remediation scenarios (by adjusting the polymer expansion ratio as a function of ambient confinement). Based on this family of curves, a large-scale shake table experiment was designed, where significant improvement was observed in the performance of the initially soft liquefiable ground. A similar approach can be taken for any prescribed site condition, to estimate the appropriate amount of polymer to be injected into the ground to mitigate the susceptibility and the consequences of soil liquefaction.

2.8 Acknowledgement

Chapter 2, in full, is a reprint of the material as it appears in Prabhakaran, A., Kyungtae, K., Ebeido, A., Jahed Orang, M., Motamed, R., Elgamal, A., and Frazao, C. (2021). "Polymer injection and associated site liquefaction remediation mechanisms." *17th World Conference on Earthquake Engineering*, Sendai, Japan. The dissertation author was the primary investigator and author.

2.9 References

Ishihara, K., and Koga, Y. (1981). "Case Studies of Liquefaction in the 1964 Niigata Earthquake." *Soils and Foundations*, Elsevier BV, 21(3), 35–52.

Japanese Geotechnical Society (JGS). (1996). *Remedial measures against soil liquefaction*. Rotterdam, the Netherlands.

Ashford, S. A., Boulanger, R. W., Donahue, J. L., and Stewart, J. P. (2011). "Geotechnical Quick Report on the Kanto Plain Region during the March 11, 2011, Off Pacific Coast of Tohoku Earthquake, Japan." *Geotechnical Extreme Events Reconnaissance*, GEER-025a(April), 1–20.

Bray J. D., Stewart J. P., Baturay M. B., Durgunoglu T., Onalp A., Sancio R. B., Stewart J. P., Ural D., Ansal A., Bardet J. B., Barka A., Boulanger R., Cetin O., Erten D. (2000): Damage patterns and foundation performance in Adapazari. *Earthquake Spectra*, 16 (1), Supplement A.

Jain, S. K., Lettis, W. R., Murty, C. V. R., and Bardet, J.-P. (2002). "Bhuj, India Earthquake of January 26, 2001 Reconnaissance Report." *Earthquake Spectra*, 18 (1), Supplement A

Cubrinovski M (2013). Liquefaction-induced damage in the 2010–2011 Christchurch (New-Zealand) earthquakes. *Proceedings of the International Conference on Case Histories in Geotechnical Engineering*, Chicago, IL, USA.

Adalier K, Sharp M K (2004). Embankment dam on liquefiable foundation-dynamic behavior and densification remediation. *Journal of Geotechnical and Geoenvironmental Engineering*, 130 (11), 1214–1224.

Olarte J C, Dashti S, Liel A B (2018). Can ground densification improve seismic performance of the soil–foundation–structure system on liquefiable soils?. *Earthquake Engineering & Structural Dynamics*, 47 (5), 1193–1211.

Gallagher P M, Mitchell J K (2002). Influence of colloidal silica grout on liquefaction potential and cyclic undrained behavior of loose sand. *Soil Dynamics and Earthquake Engineering*, 22 (9), 1017–1026.

Yasuda S, Harada K (2014). Measures developed in Japan after the 1964 Niigata earthquake to counter liquefaction of soil. *10th National Conference on Earthquake Engineering*, Anchorage, Alaska.

Erdemgil M, Saglam, S, Bakir B (2007). Utilization of Highly Expansive Polymer Injection to Mitigate Seismic Foundation Failure for Existing Structures. *Proceedings of the 8th Pacific Conference on Earthquake Engineering*, Singapore.

Traylen N, Wentz R, Van Ballegooy S, Wotherspoon L M (2017). Research results from a study into resin injection for liquefaction mitigation. *Proceedings of the New Zealand Society for Earthquake Engineering Conference*, Wellington, New Zealand.

Buzzi O, Fityus S, Sasaki Y, Sloan S (2008). Structure and properties of expanding polyurethane foam in the context of foundation remediation in expansive soil. *Mechanics of Materials*, 40 (12), 1012–1021.

Soga K, Au S K A, Jafari M R, Bolton M D (2004). Laboratory investigation of multiple grout injections into clay. *Geotechnique*, 54(2), 81–90.

Mitchell J K (1993). *Fundamentals of Soil Behavior*. Wiley & Sons.

Jahed Orang, M., Motamed, R., Prabhakaran, A., and Elgamal, A. (2021). "Large-Scale Shake Table Tests on a Shallow Foundation in Liquefiable Soils." *Journal of Geotechnical and Geoenvironmental Engineering*, American Society of Civil Engineers, 147(1), 04020152.

Bastidas A M P (2016). Ottawa F-65 Sand Characterization. *PhD Dissertation*, University of California Davis.

Idriss I M, Boulanger R W (2008). Soil liquefaction during earthquakes. *Earthquake Engineering Research Institute Monograph* (12). Earthquake Engineering Research Institute, Oakland, CA, USA

Trautner C, Zheng Y, McCartney J S, Hutchinson T (2018). An approach for shake table performance evaluation during repair and retrofit actions. *Earthquake Engineering & Structural Dynamics* 47 (1), 131-146

Prabhakaran A, Kim K, Jahed-Orang M, Qiu Z, Ebeido A, Zayed M, Boushehri R, Motamed R, Elgamal A, Frazao C. (2020). Polymer Injection and Liquefaction induced foundation settlement: a Shake table Test Investigation. *Geo-Congress 2020,* Minneapolis, Minnesota.

Boulanger R, Hayden R (1995). Aspects of Compaction Grouting of Liquefiable Soils. *Journal of Geotechnical Engineering*, 121(12), 844-855.

2.10 Tables and Figures

Table 2.1. Summary of specimen properties

Specimen	**Weight of Sand (kN)**	D_r **(%)**	**Equivalent** $(N_1)_{60}$
Loose Sand	14.3	30	4
Medium-Dense Sand	15	55	14
Dense Sand	15.98	80	29

Table 2.2. Mass and Volume of composite inclusions

Specimen	**Mass of composite (kg)**	**Normalized Volume of Composite (%)**	**Mass Density (kg/m^3)**	**Estimated pure polymer in composite (%)**	**Estimated expansion ratio**
Loose	25.9	3.64	741	(60 - 67)	2.5
Medium-Dense	33.75	4.26	825	(55 – 62)	2.2
Dense	61.1	7.79	816	(56 - 62)	3.5

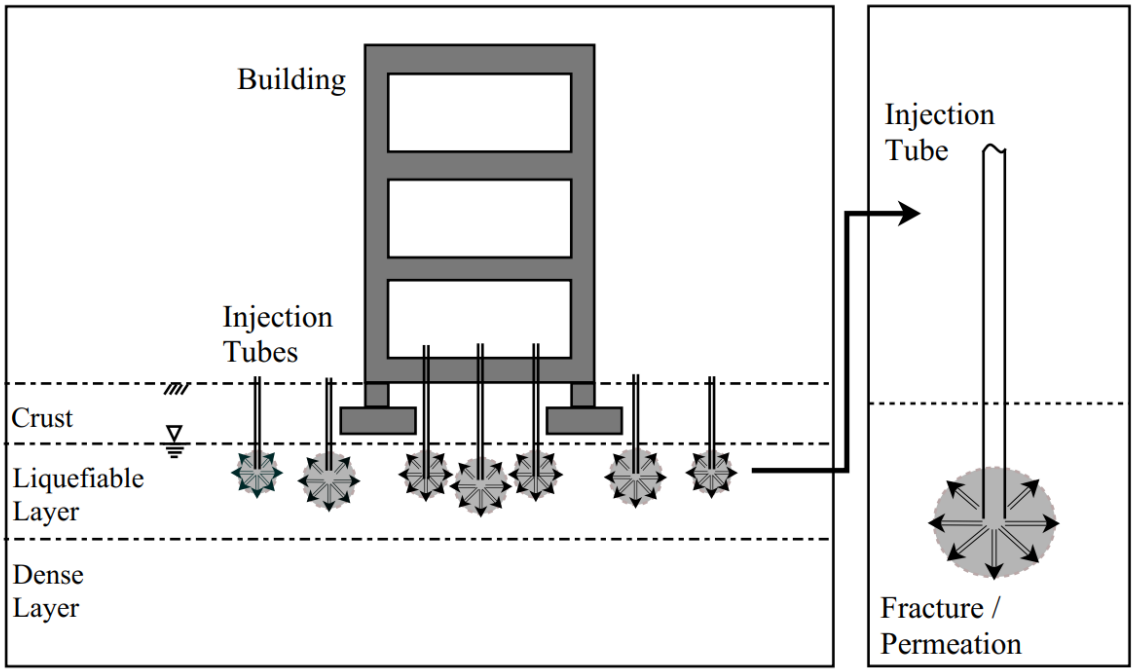

Figure 2.1. Typical Layout and mechanisms in polymer injection

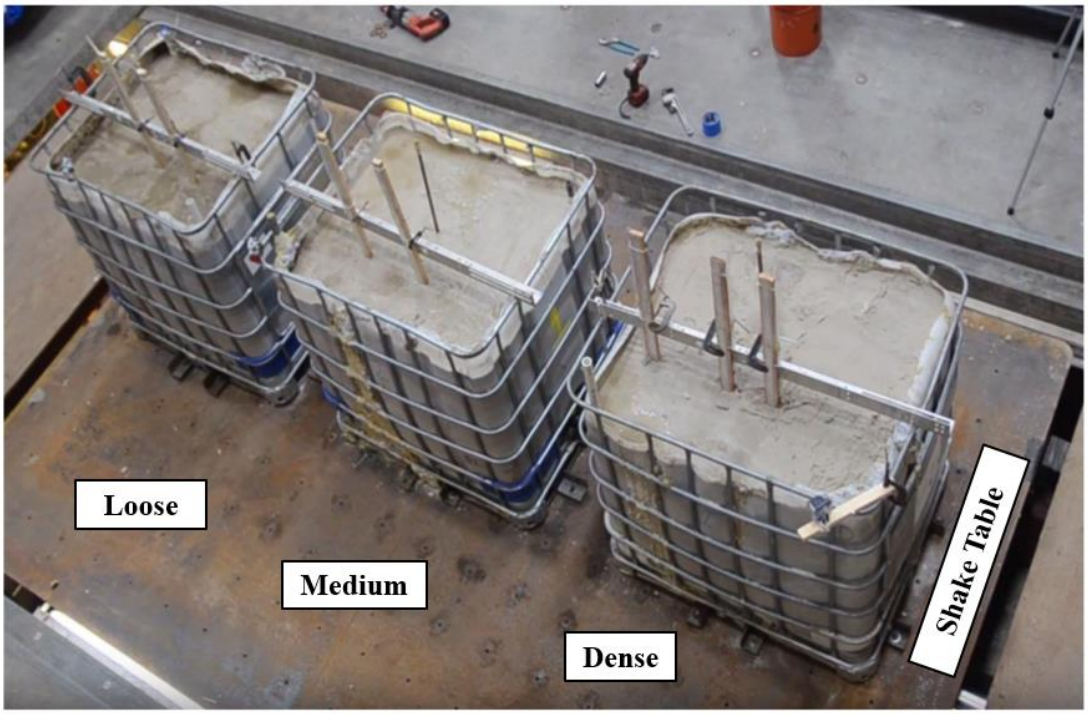

Figure 2.2. Containers placed on the shake table platform

Figure 2.3. Polymer injection in each container

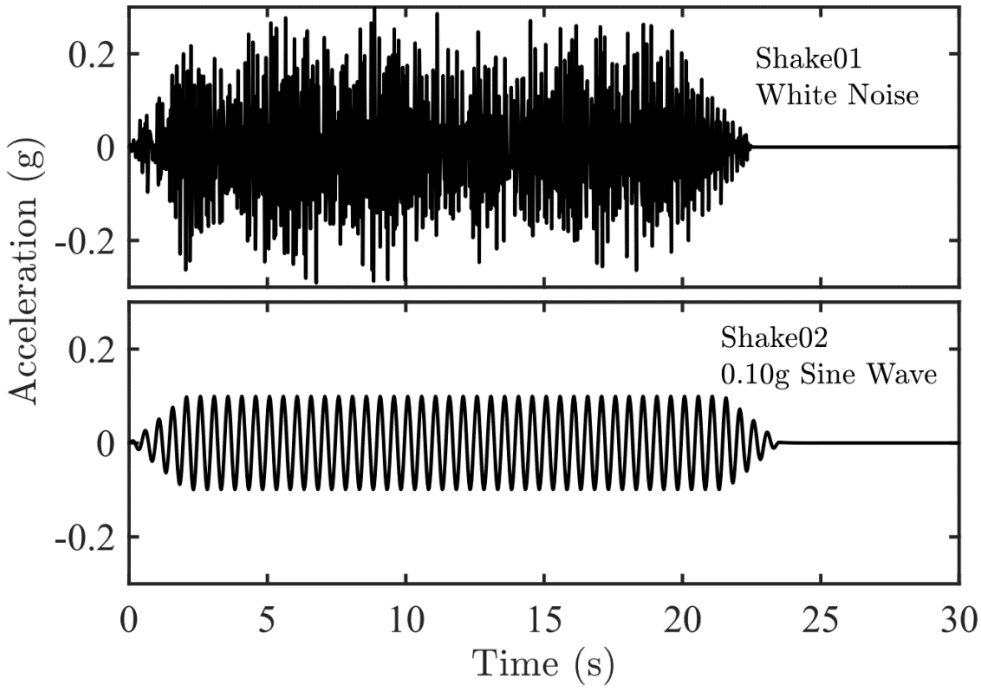

Figure 2.4. Base excitation imparted to the specimen

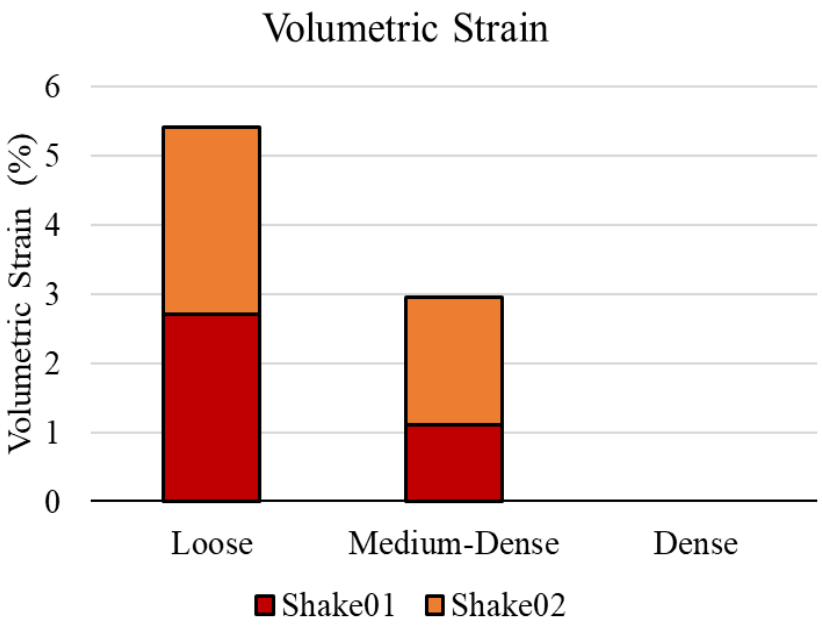

Figure 2.5. Volumetric (settlement) strains after each shaking event in the three specimens

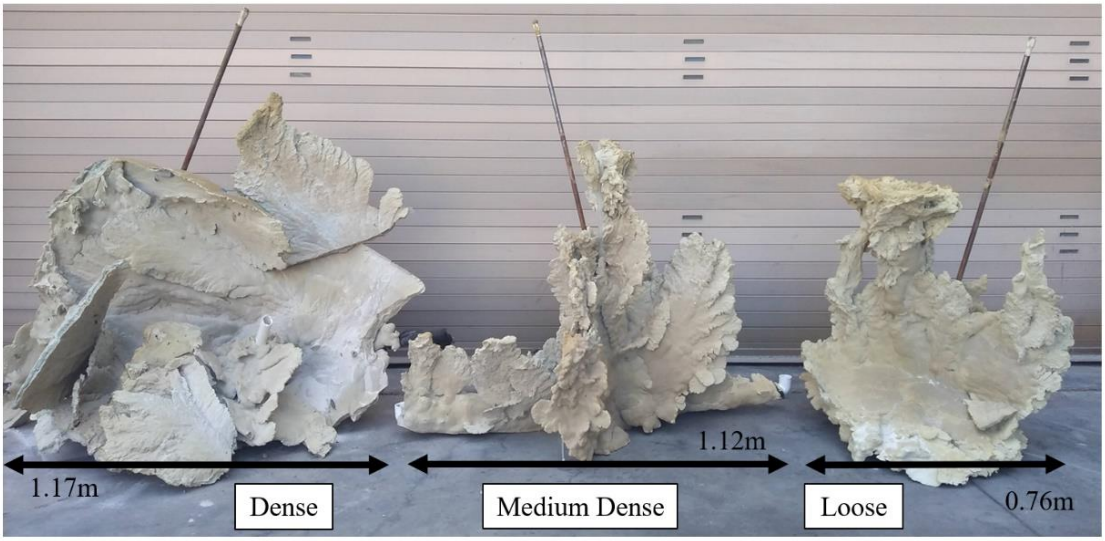

Figure 2.6. Hardened composite inclusions obtained post excavation

Figure 2.7. Observed composite inclusions (veins) after excavation in the dense and medium-dense specimens

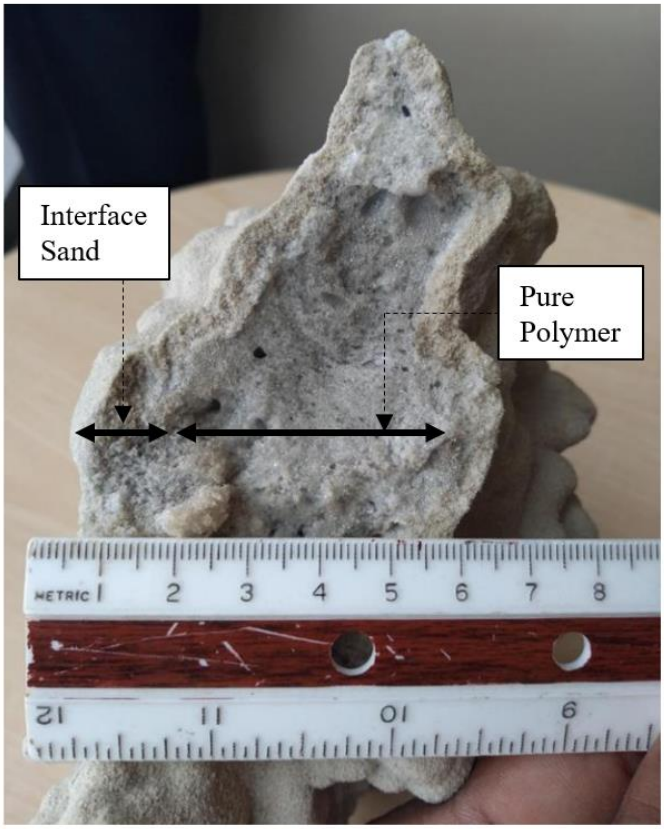

Figure 2.8. Cross section of the hardened polymer sand matrix obtained from the medium-dense specimen

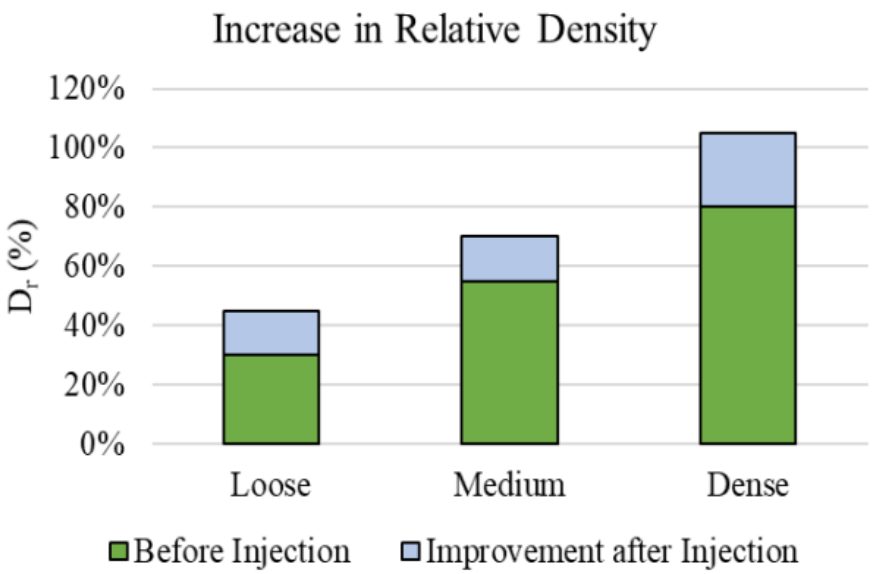

Figure 2.9. Estimated Improvement in relative density (D_r) assuming constant volume conditions

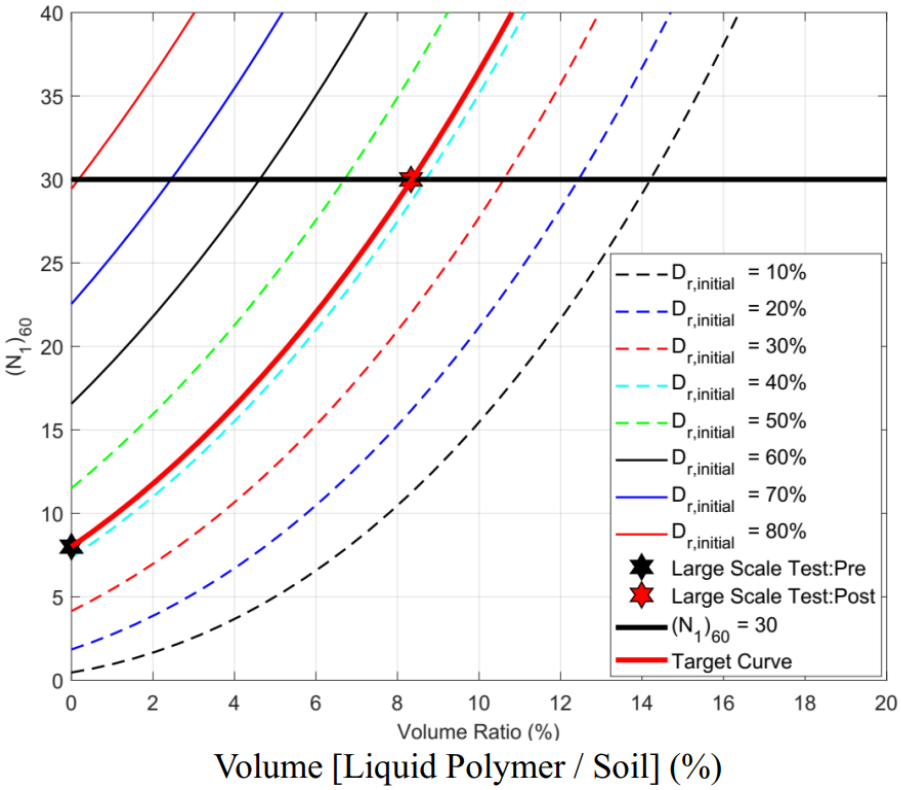

Figure 2.10. Family of curves developed to relate $(N_1)_{60}$ to the volume of injection.

Figure 2.11. Observed soil-foundation system response prior to improvement

Figure 2.12. Observed soil-foundation system response after injection

Chapter 3. Liquefaction Induced Settlement of Shallow Foundations: Baseline Experiment and Interpretation

3.1 Abstract

This chapter presents a detailed analysis of a set of large-scale shake table tests performed to evaluate the liquefaction induced settlement of a shallow foundation founded on top of liquefiable soil. The system response of a rigid foundation, overlain on a three-layer soil deposit with a large liquefiable stratum, is explored through a series of large-scale tests at the University of California San Diego. Each test is instrumented to provide insights into the dynamic response of the soil and foundation system. Details on geotechnical system identification are presented to characterize the deposit prior to shaking. Strong base excitation is then imparted by the shake table in a two-part sequence, resulting in excessive liquefaction and excessive foundation settlement in the test. System response and contributing mechanisms associated with liquefaction induced settlements are explored in both shaking sequences. This series of shake table tests are the first of its kind, in terms of scale, and provide a unique opportunity to serve as a baseline dataset to explore remediation measures and numerical tools to estimate liquefaction induced foundation settlements.

3.2 Introduction

Soil liquefaction is a mechanism that results in severe damage to buried structures and foundation systems during earthquakes as documented in Niigata 1964, Kobe 1995 and Tohoku 2011, Japan (Ashford *et al.* 2011, Hamada *et al.* 1996, Ishihara and Koga 1981), Kocaeli, 1999, Turkey (EERI 2000), Bhuj 2001, India (Jain *et al.* 2002), and 2010-2011 Canterbury earthquake sequence in New Zealand 2010-2011 (Cubrinovski *et al.* 2010). For instance, during the 2010-2011 Canterbury earthquake sequence, severe soil liquefaction affected 3,000 buildings within the

Central Business District (CBD) of Christchurch, of which over 50 % were to be demolished, being deemed economically unfit for further repairs (Cubrinovski 2013). Hence, in high seismic regions with loose saturated granular soils, it is vital that remediation measures be undertaken to minimize the consequences of soil liquefaction.

Documented case histories have been useful to researchers studying the devastating effects of liquefaction during past earthquakes. The 1964 Niigata and 1990 Luzon Philippine earthquakes resulted in extensive damage to structures and the built environment (Seed and Idriss 1967, Tokimatsu *et al.* 1994). More recently, the 2010-2011 Canterbury Earthquake Sequence (CES) in New Zealand and the 2011 Tohoku earthquake in Japan generated widespread liquefaction-induced damage to structures and their foundation systems (Cubrinovski 2013, Cubrinovski *et al.* 2010, Yasuda *et al.* 2012).

Past research on the behavior of shallow foundations in liquefiable soils have encompassed shake table tests (Jahed Orang *et al.* 2021, Yoshimi and Tokimatsu 1977), centrifuge experiments (Adamidis and Madabhushi 2018, Dashti *et al.* 2010, Liu and Dobry 1997, Mehrzad *et al.* 2018, Tokimatsu *et al.* 2019), and field reconnaissance (Cubrinovski 2013, Cubrinovski *et al.* 2010, GEER 2010, Tokimatsu and Katsumata 2012).

This chapter documents the seismic response of a rigid shallow foundation, seated on a layered soil stratum encompassing a shallow liquefiable layer, during 1g large scale shake table testing (Jahed Orang *et al.* 2021). The behavior of the ground-foundation system is examined in detail during 3 seismic events, with attention paid to liquefaction induced foundation settlement. The dataset reported in this paper acts as a compliment to Jahed Orang *et al.* (2021), where salient foundation response mechanisms during 2 motions is reported. In addition, the experiment serves

as a baseline to compare a remediation strategy, where polyurethane polymer is injected into the liquefiable layer, as presented in Chapter 4.

3.3 Specimen Characterization

3.3.1 Experimental Setup

The shake table experiments were performed (Jahed Orang *et al.* 2021) using the laminar soil container (Figure 3.1) of the Powell structural engineering laboratories at the University of California, San Diego. The uniaxial shake table platform has dimensions of 4.9 m by 3.1 m and is designed for models that weigh up to 350 kN with an actuator of capacity 490 kN. Maximum table displacement is ±150 mm with a maximum nominal operating frequency of 20 Hz (Magenes 1989, Trautner *et al.* 2018).

The soil deposit is prepared in the laminar soil container (Figure 3.1) with original internal dimensions of 3.9 m by 1.8 m by 1.9 m built by Ashford and Jakrapiyanun (2001) and extended an additional 1m in height by Ebeido (2019). In such a container, steel laminates are stacked on each other separated by roller bearings, to minimize lateral edge effects thus, facilitating the propagation of one dimensional horizontally polarized shear waves in a periodic boundary condition. A 60 MIL thick Ethylene Propylene Diene Monomer (EPDM) rubber liner was placed to hold soil and water inside the laminar container. Two flexible perforated pipes were placed at the base of the laminar container and water was used to saturate the model. Further details about the shake table and laminar container are reported in Motamed *et al.*(2020) and Zayed *et al.* (2021).

The deposit was instrumented with three arrays of pore pressure sensors and accelerometers as shown in Figure 3.2. The laminar soil container, foundation, and free field soil surface were instrumented with vertical displacement transducers to obtain further insight into the

performance of the system. The experiment consisted of three arrays of sensor deployment within the soil deposit of which the north "free-field" and "under foundation" arrays are presented. The soil surrounding the foundation at 0.6 m from edge of the foundation on each side is referred to as "free-field" condition through this paper (Jahed Orang *et al.* 2021) Data were recorded at a sampling rate of 256 samples/s.

3.3.2 Model Preparation

The soil models for both tests were constructed in three phases using Ottawa F-65 sand (Parra Bastidas 2016), consisting of a saturated 1.00 m dense base layer underlying a 1.25 m thick saturated liquefiable deposit, overlain by a moist 0.64 m crust (Figure 3.2). The methodology of construction of all three layers is described in detail in the following sections.

i. **Dense base Layer**: The dense base layer was built dry in three sublayers, each densified using a plate compactor. Sand cone tests were performed to estimate relative density (D_r) of each sublayer (estimated at about 80 – 95 %). Post construction, this layer was saturated using a perforated piping system installed at the base of the laminar container with care in order to prevent soil disturbance.

ii. **Loose Middle Layer**: The 1.25 m liquefiable stratum was built using hydraulic pluviation to mimic the deposition of a loose young deposit (Dobry *et al.* 2011 and Whitman 1970). The sand was pluviated into the laminar container from a hopper through a number 6 sieve ensuring a clear water head of 0.25 m - 0.5 m, between the screen and the deposit. Estimated relative density (D_r) for this layer based on weight of the sand deposited was in the range of 35 - 44 %.

iii. **Top Crust**: The 0.64 m thick crust was built dry in two stages. An initial 0.24 m thick layer was deposited over the loose liquefiable strata, and the foundation was placed. Thereafter, the remaining 0.4 m layer was built around the foundation system. Upon construction, this crust

layer was in a moist state due to possible capillary action. The relative density of the top crust is estimated at about 50 – 55 % through sand cone tests.

iv. **Foundation System**: The foundation system (Figure 3.1b) consisted of a rigid concrete block of length 1.3 m, width 0.6 m and height 0.4 m, overlain by steel plates designed to produce a surcharge vertical pressure of 41.6 kPa. The concrete block (height of 0.4 m) was fully embedded into the crust.

A summary of properties of Ottawa F-65 sand and properties of the three-layered deposit is presented in Tables 3.1 and Table 3.2, respectively.

3.4 Model Characterization and Geotechnical System Identification

Large scale experimental results provide a unique dataset, complementing element level testing to identify system level characteristics and insitu properties (Oskay and Zeghal 2011, Ramancha *et al.* 2020, Ramancha 2022). Systematic geotechnical system identification procedures were performed to characterize the low strain shear modulus and shear wave velocity of the profile. The system was subjected to three white noise excitations pre and post the base the excitation to characterize the deposit prior to and post each base excitation.

This section discusses the estimated low strain shear modulus and damping ratio by several frequency domain and time domain methods including cross-correlation, identification of site transfer functions, and analysis of free vibration response. The model is further characterized through the back calculated stress strain response during shaking event WN01. Detailed discussions and analyses are provided for the first white noise excitation prior to shaking event WN01. Details of all the base excitations are provided in Table 3.3. Figure 3.3 presents the time histories for recorded for white noise excitation WN01 at several sensor locations along depth of

the model and their corresponding Fourier amplitude spectra. The white noise excitation is performed for 6 s, at root mean square acceleration of 0.05 g.

3.4.1 Time Domain Analysis

i. Free Vibration Analysis

The PCB accelerometers were used to obtain natural frequency of the deposit following the white noise excitation. As seen in Figure 3.3, clear evidence of system response is visible, with the deposit freely vibrating at its natural period of 0.21 s (4.7 Hz). As seen in the figure, the input WN excitation had effectively stopped post 10s, indicating the response after 10 s was effectively dictated by the free vibration of the deposit.

An estimate of the low strain damping ratio was made from the logarithmic decrement method as shown in Figure 3.4 and Figure 3.5. Consistent estimates of (0.01 % - 4 %) are obtained following WN01, with an average estimate of about 1 %.

ii. Cross Correlation

The first peak during each WN excitation was tracked (Figure 3.6) to obtain the relative stiffness (shear wave velocity) between subsequent sensor locations as shown in Figure 3.7. The method is used to obtain the shear wave velocity of the deposit after each main shake and is presented in Figure 3.8.

As seen from Figure 3.8, a consistent 7 % - 13 % increase in shear wave velocity (V_s) was observed across the dense layer following each main shake due to densification after the loose layer consolidated. Corroborating with this, a reduction (6 % - 10 %) in V_s is observed with the bottom of the loose layer. However, in the top of the loose layer (depths between 0.4 m – 1 m) a steady increase in V_s is observed following in each shake (2 % - 48 %) due to the settlement of the upper dry crust and possible void ratio redistribution following each excitation.

3.4.2 Frequency Domain Analysis

The PCB accelerometers are further deployed to estimate the site transfer function (between each sensor and the base input) as seen in Figure 3.9 during WN01. The fundamental mode of response is observed at 5.03 Hz (0.2 s), with an additional peak at 15.6 Hz (0.06 s). Since the model was built in a laminar soil container, a shear beam type response is expected. Therefore, the second natural frequency of the deposit would correspond to 3 f_1, (where, f_1 is the first natural frequency). Hence the energy density at 5.03 Hz and 15.6 Hz agrees with the 1D shear wave propagation assumption. PCB acceleration and the corresponding Fourier Amplitude Spectra during WN02 and WN03 are provided in Figure 3.10 and Figure 3.11, respectively.

Using Dobry *et al.* (1975), based on the Rayleigh method, the theoretical fundamental mode of response is estimated at 0.14 s. The transfer function and free vibration response approaches estimated the first natural period at about 0.2 s. Therefore, it is estimated that an extent of period elongation had occurred due to slight nonlinear response of the soil, particularly towards the end of the WN excitation (7 s – 10 s). The V_s was estimated using only the first peak and hence, would not capture the softened response, whereas the transfer function and free vibration response utilizes the entire time history and hence would reflect the slight softening.

3.4.3 Soil Shear Stress-Strain

Using Zeghal and Elgamal (1994), estimates of the hysteretic stress strain response were used to corroborate the aforementioned system identification methods. The first order approach (linear interpolation) was used to estimate the cyclic shear stress at the mid-point between two sensors. Further, the acceleration response was twice differentiated to obtain the cyclic displacement response and hence the cyclic shear strain between two sensor locations. Estimates of the stress strain response during WN01 are presented in Figure 3.12. The stress strain response

is estimated for the first part of the acceleration time history particularly between (2 – 3 s). As observed from the figure, there exists evidence of slight softening particularly within the upper depth of the soil stratum (within the crust layer at depth of 0.35 m).

From the obtained stress strain response, the low strain shear modulus (G_0) and therefore the shear wave velocity (V_s) is back calculated through the secant of the stress strain curve after the first cycle. Shear strains of the of the order of 10^{-4} % are obtained for this cycle and hence the obtained G is not corrected for strain and is assumed to be equal to G_0.

A summary of the estimates of V_s is presented in Table 3.4. For future shake table tests with similar soil deposits, it is recommended to use an RMS excitation of less than 0.05 g, particularly given the stick slip nature of the Powell structural laboratory shake table bearings. Following each base excitation and the sedimentation consolidation process, the V_s of the dense and upper crust layers increased while the loose layer reduced, possibly due to void redistribution. Due to the importance of V_s in quality control, predicting system stiffness, and liquefaction resistance, use of high-resolution PCB accelerometer arrays is recommended.

3.5 Shake Table Testing Program

The baseline model is subjected to three large base excitations at a peak cyclic acceleration of 0.2 g (referred to as Shake01), 0.4g (referred to as Shake02 and Shake03). The motions and their time-frequency spectra computed using the modified Stockwell transformation (George 2009, Stockwell *et al.* 1996) are shown in Figure 3.13 and Figure 3.14, respectively. Details on the sequence of excitation are provided in Table 3.3.

3.5.1 Excess Pore Pressure

Figure 3.15 presents the excess pore pressures in the baseline test generated during Shake01. In the free field array (FF_2, FF_3), within the liquefiable layer a substantial rise in excess

pore pressure (EPWP) is seen during the first shake, whereby the soil liquefies within 2-3 cycles of strong shaking indicative of its loose nature. Sensors embedded in the dense bottom (FF_4, FF_5) layer indicated gradual increase in EPWP, partially due to the reduced stress demands on the layer as layers above the sensor location fully liquefied and partially due to the slower contraction rates for the dense sand as observed in Elgamal *et al.* (2005). The dry nature of construction of the denser layer may have affected the EPWP in these sensors and can be delineated through observing the stress strain response at these locations.

In the below foundation array (FD_2, FD_3), the peak value of recorded EPWP is similar to the values recorded in the free field at the corresponding sensor depths corroborating with Adalier et al (2003) and Karamitrios *et al.* (2013). This indicates that the loss of lateral confinement of the sand below the foundation clearly contributed to the observed settlements. However, FD_2, indicated strong a sharp rise in EPWP around 20 s, due to the foundation edge shearing through and dilating the surrounding soil leading to redistribution of the EPWP.

Within the liquefiable layer, the EPWP data indicated a steady increase during shaking (up to 20 s) and followed a dissipative trend afterward. However, in the bottom dense layer, the EPWP in the dense layer continued to increase well post shaking, up to 50s, after which the layer started to dissipate. Post 50s, the EPWP records appeared to stabilize indicating uniform values. This trend is strongly indicative that the bottom dense layer continued to act as a reservoir, contributing to the upward flow, well after shaking had ceased.

As seen in Figure 3.15, in the free field, the development of 3D hydraulic gradients underneath the foundations clearly indicates the direction of flow within the liquefiable layer. Towards the bottom of the liquefiable layer, the pore pressure gradient indicates a downward flow into the denser stratum. Whereas, within the liquefiable layer, an upward gradient exists indicating

an upward flow. The direction of artesian flow is particularly significant given the manifestation of ejecta in this test, immediately post strong shaking. Underneath the foundation array, there existed a tendency for the flow to occur away from the foundations (in all directions) as seen in the below foundation array. A similar response was observed for Shake02 (as seen in Figure 3.16).

3.5.2 Foundation and Soil Acceleration

Figure 3.17 displays a comparison between the recorded accelerations of the two test models during Shake01 for the free-field and under foundation arrays. All acceleration records presented here were filtered using a zero phase lowpass fourth order Butterworth with a cutoff of 15 Hz. In general, a significant reduction in the foundation and ground accelerations were observed in the baseline test in both free-field and under foundation accelerometers. The ability of the soil to transfer high-frequency content is significantly reduced in the baseline model. This may be attributed to the extensive softening of the soil within the first few cycles of shaking in the test.

As seen from Figure 3.19, a clear indication of de-amplification is observed in the baseline test in the 5% damped acceleration response spectra. The de-amplified acceleration response in the baseline test is indicative of the reduction in the ability of the soil to transfer shear due to the significant degradation in stiffness that occurs post liquefaction.

During Shake02, extensive dilation is observed in the liquefiable layer as compared to Shake01 observed through the asymmetric nature of the acceleration time history (Figure 3.18). Attenuation of ground acceleration is observed in the response during Shake02 (similar to Shake01), however, there is evidence of higher frequencies being transmitted to the top of the deposit as observed from the response spectra (Figure 3.20). Significant differences in response are seen in AF_3 and AD_3 (located towards the base of the liquefiable layer) between Shake01 and Shake02, whereby attenuation occurs during Shake01 as opposed to amplification in Shake02.

This type of response is partly attributed to the densification following Shake01 (as seen through the V_s) and the higher base acceleration (in Shake02) leading to possible strain excursions and subsequently dilation.

3.5.3 Soil Shear Stress-Strain

String pots on the laminates are used to obtain the lateral displacement of the box during each base excitation (As shown in Figure 3.11). The lateral response of box and laminates are presented in Figure 3.22. The separation of the laminates by bearings facilitates the propagation of 1D horizontally polarized waves within the deposit, ensuring a periodic boundary condition minimizing wave reflections from the laminar box boundary. A second-order approach as proposed by Zeghal and Elgamal (1994) is used to estimate the shear stress/strain response during both excitations. The shear strain in the direction of shaking is estimated through the displacement transducers mounted on the laminates (Figure 3.23). Further, these transducers are used to estimate the relative displacement and subsequently the acceleration response at the location of each transducer. These acceleration histories are then used to estimate the shear stresses at the midpoint between sensor locations.

Significant softening of the system response is seen to occur within the first few cycles of shaking, corroborating with rapid rise in excess pore pressures seen in Figure 3.15. During Shake01, a complete loss of stiffness is observed within up to a depth of about 2.5 m (liquefiable layer and top of dense layer) after 5 - 6 s into the time history. There is evidence of retention of stiffness within the bottom dense layer (depths of 2.5 m and 2.8 m). During Shake01, the maximum shear strain developed within the liquefiable layer was observed at around 1.5 %.

During Shake02 (Figure 3.24), much higher shear strains developed within the liquefiable layer and the dense layer as compared to Shake01 (peak shear strains of about 2.3 % within the

liquefiable layer). There is evidence of slight dilation tendency in the liquefiable layer as observed from depths between 1.6 m - 2.0 m. Within the dense layer, the degree of softening is higher as compared to Shake01 at the same sensor locations (for example, at a depth of 2.8 m). However, post liquefaction and loss of strength in the upper layers (and subsequent reduction in demand), there is no further degradation in stiffness in the bottom dense layer.

Clear evidence of system response of the soil deposit can be observed from Figure 3.23. Within the liquefiable layer in the baseline model, significant vertical continuity exists allowing for pore pressure redistribution, without any permeability contrasts. As pore pressure starts approaching initial liquefaction within the upper layers of the deposit, the ability of the layers to transmit shear stresses to deeper strata decreases and reducing the development of additional shear stress towards the bottom dense layer.

3.5.4 Foundation Settlement

i. Shake01

In the baseline experiment, as noted by Jahed Orang *et al.* (2021), a local shear failure occurs in the foundation system resulting in the foundation punching through the soil. Post injection, a significant reduction in the liquefaction induced foundation settlement and rotation were observed during Shake01 as seen in Figure 3.25 and Figure 3.27, respectively. Upon onset off soil liquefaction, the loss of ground stiffness and strength is visible with a reduction in the ability of the foundation system to undergo cyclic loading. The settlement is largely co-seismic in both base excitations, contributing to about 83% in Shake01.

In the baseline experiment, there is no evidence of soil structure interaction attributed to the height of the surcharge (little to no tendency of cyclic ratcheting) due to the loss of ground stiffness within the first few cycles of shaking. Extensive tilts of the order of 1/60 rad were

observed in the shaking transverse directions respectively in the baseline experiment higher than the 1/300 rad prescribed in standard design codes (JGS 1996 and DFI 2013).

Figures 3.29 and 3.30 present the free field settlement of the soil obtained from the four corners of the laminar soil box. In the free field, soil heave is observed in the test, indicative of the local shear failure of the foundation system post softening as per Vesic (1973). An average heave of about 16 mm is observed post Shake01. The model pre and post Shake01 is presented in Figure 3.31a and Figure 3.31b, respectively. The nature of the co-seismic settlement and heave of surrounding soil indicates that once the free field soil liquefied, the soil underneath the foundation lost its lateral confinement and therefore, its strength (even though the EPP ratio underneath the foundation was much less than EPP ratio in the free field). This suggests that the settlement of the foundation was largely shear induced and occurred due to the movement of soil underneath the foundation to the free field once the soil in the free field liquefied.

ii. Shake02

Post Shake01, the model is subjected to a further excitation, at a peak cyclic acceleration of 0.4 g. The results of the baseline and polymer remediated models post the second shake are presented in Figures 3.26 and Figure 3.28. As with Shake01, the co-seismic settlement largely contributed to the observed deformations with about 92 % in Shake02. This event manifested extensive liquefaction induced damage in the baseline experiment resulting in a cumulative settlement of about 660 mm. Following Shake02, a soil surface heave of about 10 mm is observed during shaking, followed by settlement post shaking of about 20 mm. The model post Shake02 is presented in Figure 3.31c and Figure 3.31d, respectively.

3.6 Conclusions

The experimental program involved conducting a series of large-scale shake table tests to serve as a baseline case (without remediation) scenario of a shallow foundation of a representative 2 story structure seated on a three-layered deposit with a large liquefiable stratum at shallow depth (Jahed Orang *et al.* 2021). The presented test series is the first of its kind (in terms of scale) and reproduced realistic deformation mechanisms contributing to liquefaction induced settlement. This test further serves as a baseline case to compare the effect of mitigation measures, calibration of numerical models, and as a reference dataset to study existing evaluation techniques to obtain estimates of liquefaction induced settlement involving shallow foundations.

1. Large settlements and permanent tilts were observed following each base excitation, the majority of which was co-seismic. The deformation patterns and observed heave of the soil in the free field indicated a local shear failure of the foundation system.
2. The excess pore pressure response within the liquefiable layer indicated the free-field soil reaches initial liquefaction within 2-3 cycles of strong shaking for both base excitations. The soil underneath the foundation experienced marginally higher excess pore pressures compared to the free field. Observation of excess pore pressure isochrones during shaking enabled the estimation of the co-seismic hydraulic gradients and therefore the flow direction. The flow largely emanated away from the foundation in all directions during shaking.
3. Pore pressure in the dense bottom layer continued to rise well after shaking (up to 50 s) and hence this layer continued to supply water to the upward layers (contributing to ejecta manifestation), acting as a reservoir. As such, the contribution of such layers must be accounted for in obtaining realistic estimates of foundation settlement.

4. The acceleration response attenuated in the liquefiable layer, after 2-3 cycles of strong shaking. Estimates of the shear stress and shear strain corroborated with the measured acceleration and pore pressure response for both excitations. After initial liquefaction in the loose layer, the dense layer at the bottom did not develop significant additional stiffness degradation due to the reduced demand on the layer from the top. This clearly indicates the role of system response in performing the liquefaction evaluation of interbedded deposits.
5. A series of system identification procedures were carried out to obtain the natural frequency of the deposit from two dense arrays of PCB accelerometers sampled at high frequencies. In addition, estimates of low strain damping ratio of the soil- foundation system was obtained from white noise excitation. The natural period of the system is estimated at around 0.21 s and a low strain damping ratio of about 1%.
6. Pre and post each large excitation, a series of white noise excitations were performed to study the evolution of shear wave velocity (V_s) of the deposit. Consistent increase in the V_s was observed within the dense (7-13%) and crust layers (2-48%) following each excitation, while the V_s within the liquefiable layer reduced by 6-10%.

The test series is a first of its kind and the dataset serves as a reference, to compare with an additional test (discussed in Chapter 4), performed to evaluate the efficacy of polymer injection as an insitu liquefaction remediation measure to retrofit this foundation system.

3.7 Acknowledgement

A part of the dataset presented in Chapter 3 is obtained from Jahed Orang, M., Motamed, R., Prabhakaran, A., and Elgamal, A. (2021). "Large-Scale Shake Table Tests on a Shallow Foundation in Liquefiable Soils." *Journal of Geotechnical and Geoenvironmental Engineering*,

American Society of Civil Engineers, 147(1), 04020152. The dissertation author is a co-investigator and co-author.

3.8 References

Adalier, K., Elgamal, A., Meneses, J., and Baez, J. I. (2003). "Stone columns as liquefaction countermeasure in non-plastic silty soils." *Soil Dynamics and Earthquake Engineering*, Elsevier BV, 23(7), 571–584.

Adamidis, O., and Madabhushi, S. G. (2018). "Deformation mechanisms under shallow foundations on liquefiable layers of varying thickness." *Geotechnique*, ICE Publishing, 68(7), 1–13.

Ashford, S. A., Boulanger, R. W., Donahue, J. L., and Stewart, J. P. (2011). "Geotechnical Quick Report on the Kanto Plain Region during the March 11, 2011, Off Pacific Coast of Tohoku Earthquake, Japan." *Geotechnical Extreme Events Reconnaissance*, GEER-025a(April), 1–20.

Ashford, S. A., and Jakrapiyanun, W. (2001). *Design and verification of the UCSD laminar container (SSRP282 2001/07)*. La Jolla, CA.

Cubrinovski, M. (2013). "Liquefaction-Induced Damage in the 2010-2011 Christchurch (New Zealand) Earthquakes." *International Conference on Case Histories in Geotechnical Engineering*, Missouri University of Science and Technology, Chicago, Illinois.

Cubrinovski, M., Green, R. A., Allen, J., Ashford, S., Bowman, E., Brendon, Bradley, Cox, B., Hutchinson, T., Kavazanjian, E., Orense, R., Pender, M., Quigley, M., and Wotherspoon, L. (2010). "Geotechnical reconnaissance of the 2010 Darfield (Canterbury) earthquake." *Bulletin of the New Zealand Society for Earthquake Engineering*, 43(4), 243–320.

Dashti, S., Bray, J. D., Pestana, J. M., Riemer, M., and Wilson, D. (2010). "Mechanisms of Seismically Induced Settlement of Buildings with Shallow Foundations on Liquefiable Soil." *Journal of Geotechnical and Geoenvironmental Engineering*, American Society of Civil Engineers, 136(1), 151–164.

DFI-GIC. (2013). "Commentary on the Selection, Design and Specification of Ground Improvement for Mitigation of Earthquake-Induced Liquefaction." *DFI Journal - The Journal of the Deep Foundations Institute*, Informa UK Limited, 7(1), 3–12.

Dobry, R., Oweis, I., and Urzua, A. (1975). "Simplified procedures for estimating the fundamental period of a soil profile." *Bulletin of the Seismological Society of America*, GeoScienceWorld, 66(4), 51–58.

Dobry, R., Thevanayagam, S., Medina, C., Bethapudi, R., Elgamal, A., Bennett, V., Abdoun, T., Zeghal, M., El Shamy, U., and Mercado, V. M. (2011). "Mechanics of Lateral Spreading Observed in a Full-Scale Shake Test." *Journal of Geotechnical and Geoenvironmental*

Engineering, American Society of Civil Engineers, 137(2), 115–129.

Ebeido, A. (2019). "Lateral-Spreading Effects on Pile Foundations: Large-scale Testing and Analysis." University of California San Diego, La Jolla, CA.

EERI. (2000). "Damage Patterns and Foundation Performance in Adapazari." *Earthquake Spectra*, 16(SUPPL. A), 163–188.

GEER. (2010). *Geo-Engineering Reconnaissance of the 2010 Maule, Chile Earthquake*.

George, N. V. (2009). "S Transform: Time Frequency Analysis and Filtering." National Institute of Technology, Rourkela.

Hamada, M., Isoyama, R., and Wakamatsu, K. (1996). "Liquefaction-induced ground displacement and its related damage to lifeline facilities." *Soils and Foundations*, Japanese Soc of Soil Mechanics & Foundation Engineering, 36(Special), 81–97.

Ishihara, K., and Koga, Y. (1981). "Case Studies of Liquefaction in the 1964 Niigata Earthquake." *Soils and Foundations*, Elsevier BV, 21(3), 35–52.

Jahed Orang, M., Motamed, R., Prabhakaran, A., and Elgamal, A. (2021). "Large-Scale Shake Table Tests on a Shallow Foundation in Liquefiable Soils." *Journal of Geotechnical and Geoenvironmental Engineering*, American Society of Civil Engineers, 147(1), 04020152.

Jain, S. K., Lettis, W. R., Murty, C. V. R., and Bardet, J.-P. (2002). "2001 Bhuj, India Earthquake Reconnaissance Report." *Earthquake Spectra*, SAGE Publications, 18(1_suppl), 1–4.

Japanese Geotechnical Society (JGS). (1996). *Remedial measures against soil liquefaction*. Rotterdam, the Netherlands.

Karamitros, D. K., Bouckovalas, G. D., and Chaloulos, Y. K. (2013). "Insight into the Seismic Liquefaction Performance of Shallow Foundations." *Journal of Geotechnical and Geoenvironmental Engineering*, American Society of Civil Engineers, 139(4), 599–607.

Liu, L., and Dobry, R. (1997). "Seismic Response of Shallow Foundation on Liquefiable Sand." *Journal of Geotechnical and Geoenvironmental Engineering*, American Society of Civil Engineers, 123(6), 557–567.

Magenes, G. (1989). "Design, analysis and calibration of the UCSD shake table." University of California San Diego.

Mehrzad, B., Jafarian, Y., Lee, C. J., and Haddad, A. H. (2018). "Centrifuge study into the effect of liquefaction extent on permanent settlement and seismic response of shallow foundations." *Soils and Foundations*, Elsevier, 58(1), 228–240.

Motamed, R., Orang, M. J., Parayancode, A., and Elgamal, A. (2020). "Results of a Class C Blind Prediction Competition on the Numerical Simulation of a Large-Scale Liquefaction Shaking Table Test." *ASCE Geo-Congress 2020*, American Society of Civil Engineers (ASCE), 334–

342.

Oskay, C., and Zeghal, M. (2011). "A survey of geotechnical system identification techniques." *Soil Dynamics and Earthquake Engineering*, Elsevier.

Parra Bastidas, A. M. (2016). "Ottawa F-65 Sand Characterization." *PhD Thesis*, University of California Davis.

Ramancha, M. K., Madarshahian R., Astorza R., and Conte, J. P. (2020). "Non-unique Estimates in Material Parameter Identification of Nonlinear FE Models Governed by Multiaxial Material Models Using Unscented Kalman Filtering" *Model Validation and Uncertainty Quantification, Volume 3.* Conference Proceedings of the Society for Experimental Mechanics Series. Springer.

Ramancha, M. K. (2022). "Bayesian Time Domain Finite-Element Model Updating of Civil Infrastructure Systems" *PhD Thesis*, University of California San Diego.

Seed, H. B., and Idriss, I. M. (1967). "Analysis of Soil Liquefaction: Niigata Earthquake." *Journal of the Soil Mechanics and Foundations Division*, American Society of Civil Engineers, 93(3), 83–108.

Stockwell, R. G., Mansinha, L., and Lowe, R. P. (1996). "Localization of the complex spectrum: the s transform." *IEEE Transactions on Signal Processing*, 44(4), 998–2001.

Tokimatsu, K., Hino, K., Suzuki, H., Ohno, K., Tamura, S., and Suzuki, Y. (2019). "Liquefaction-induced settlement and tilting of buildings with shallow foundations based on field and laboratory observation." *Soil Dynamics and Earthquake Engineering*, Elsevier, 124, 268–279.

Tokimatsu, K., and Katsumata, K. (2012). "Liquefaction-induced damage to buildings in urayasu city during the 2011 Tohoku Pacific earthquake." *The International Symposium on Engineering Lessons Learned from the 2011 Great East Japan Earthquake*, Tokyo, 665–674.

Tokimatsu, K., Kojima, H., Kuwayama, S., Abe, A., and Midorikawa, S. (1994). "Liquefaction-induced damage to buildings in 1990 Luzon earthquake." *Journal of Geotechnical Engineering*, American Society of Civil Engineers, 120(2), 290–307.

Trautner, C., Zheng, Y., McCartney, J. S., and Hutchinson, T. (2018). "An approach for shake table performance evaluation during repair and retrofit actions." *Earthquake Engineering and Structural Dynamics*, John Wiley and Sons Ltd, 47(1), 131–146.

Vesic, A. S. (1973). "Analysis of Ultimate Loads of Shallow Foundations." *ASCE J Soil Mech Found Div*, American Society of Civil Engineers, 99(SM1), 45–73.

Whitman, R. V. (1970). "Hydraulic Fills to Support Structural Loads." *Journal of the Soil Mechanics and Foundations Division*, 96(1), 23–47.

Yasuda, S., Harada, K., Ishikawa, K., and Kanemaru, Y. (2012). "Characteristics of liquefaction

in Tokyo Bay area by the 2011 Great East Japan Earthquake." *Soils and Foundations*, Elsevier, 52(5), 793–810.

Yoshimi, Y., and Tokimatsu, K. (1977). "Settlement of Buildings on Saturated Sand During Earthquakes." *Soils and Foundations*, Elsevier, 17(1), 23–38.

Zayed, M., Ebeido, A., Prabhakaran, A., Kim, K., Qiu, Z., and Elgamal, A. (2021). "Shake table testing: A high-resolution vertical accelerometer array for tracking shear wave velocity." *Geotechnical Testing Journal*, ASTM International, 44(4), 20190066.

Zeghal, M., and Elgamal, A. W. (1994). "Analysis of site liquefaction using earthquake records." *Journal of Geotechnical Engineering*, American Society of Civil Engineers, 120(6), 996–1017.

3.9 Tables and Figures

Table 3.1. Basic Geotechnical Properties of Ottawa F-65 Sand (Parra Bastidas, 2016)

Specific Gravity	2.65
Maximum Void Ratio (e_{max})	0.853
Minimum Void Ratio (e_{min})	0.503
Coefficient of uniformity (C_u)	1.61
Coefficient of curvature (C_c)	0.96
Maximum and minimum voids ratio (e_{max}, e_{min})	0.853, 0.503
Maximum and minimum mass density ρ_{min}, ρ_{max} (kg/m^3)	1446, 1759
Coefficient of uniformity (C_u)	1.61

Table 3.2. Properties of three-layered model

Property	**Crust layer**	**Liquefiable layer**	**Base layer**
Water/soil condition	Moist	Saturated	Saturated
Depth (m)	0-0.64	0.64-1.9	1.9-2.9
Thickness (m)	0.64	1.26	1.0
Estimated D_r (%)	50%-55%	35%-44%	80 – 95%

Table 3.3. Base Excitation Sequence

Shake#	**Shake Identifier**	**PGA (g)**	**Duration (s)**	**Comments**
1	WN01	0.05 (RMS)	5 s	(5-20) Hz
2	**Shake01**	0.15g	18 s	Main Shake01
3	WN02	0.05g (RMS)	20 s	(5-20) Hz
4	**Shake02**	0.3g	18 s	Main Shake02
5	WN03	0.05g (RMS)	20 s	(5-20) Hz
6	WN05	0.05g (RMS)	20 s	TestDay2: Top Layer Saturated
7	**Shake03**	0.3g	18 s	Main Shake03
8	WN06	0.05g (RMS)	20 s	(5-20) Hz

Table 3.4. Summary of V_s Measurements

Shake#	**Shake Identifier**	**V_s (m/s) in loose layer**	**V_s (m/s) in dense layer**
1	WN01	72-101	100-150
3	WN02	60-120	95-168
5	WN03	60-104	100-173

(a)

(b)

Figure 3.1. Laminar soil container at the Powell structural engineering laboratories at UC San Diego: (a) Side view, and (b) Foundation and soi model prior to experiment

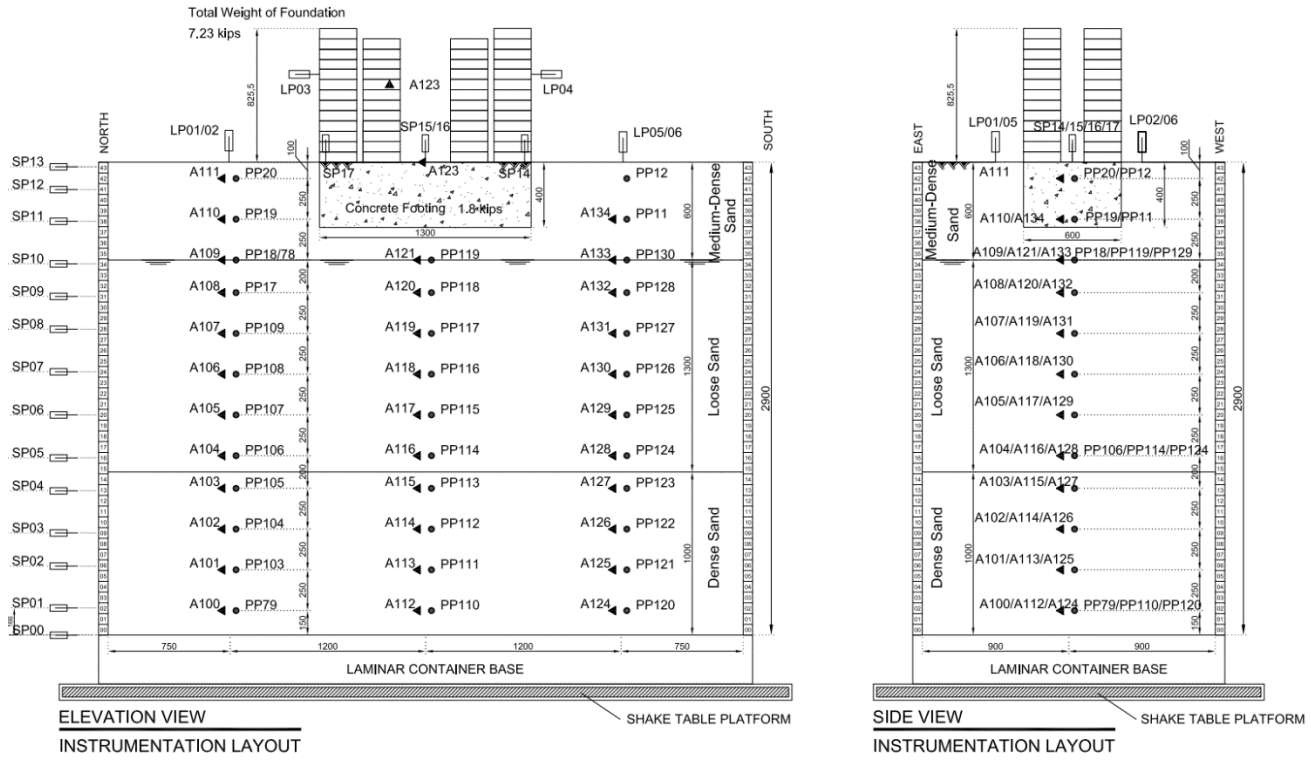

(a)

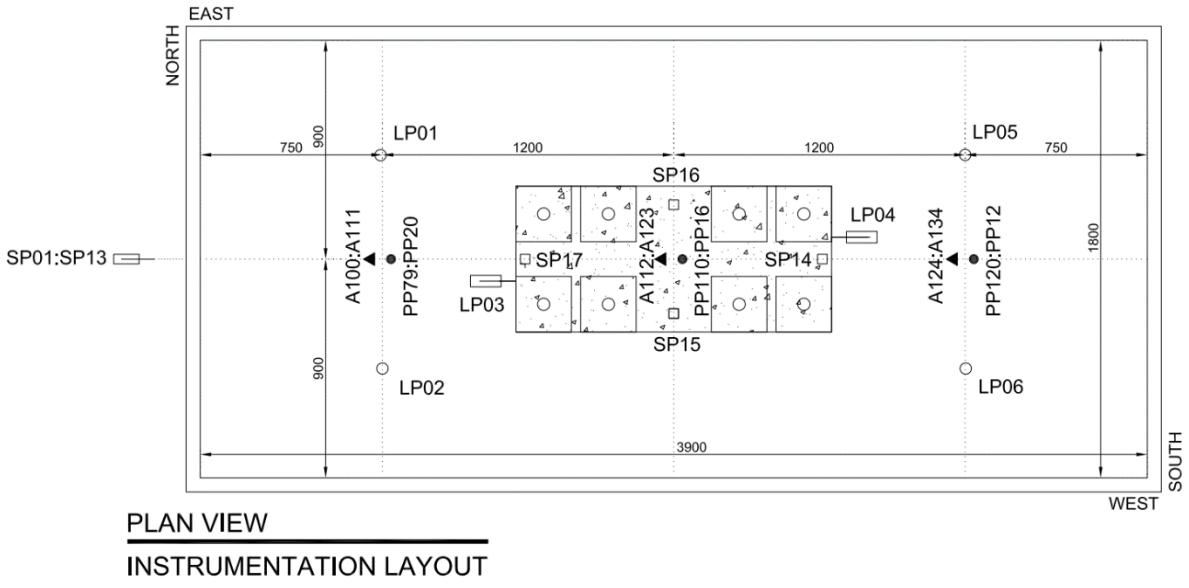

(b)

Figure 3.2. Instrumentation layout (Jahed Orang *et al.* 2021): (a) Elevation and side view, (b) Plan view of baseline model, and (c) Elevation and side view of PCB accelerometers (All units in mm)

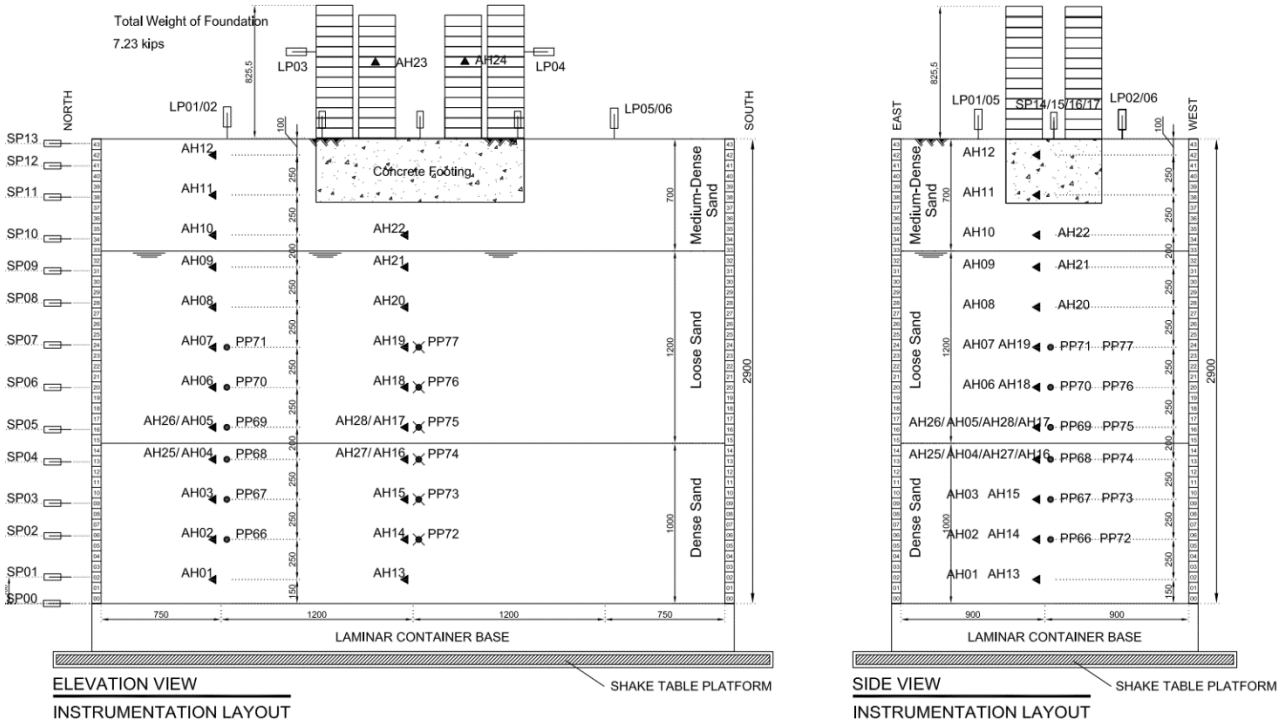

(c)

Figure 3.2. (continued) Instrumentation layout (Jahed Orang *et al.* 2021): (a) Elevation and side view, (b) Plan view of baseline model, and (c) Elevation and side view of PCB accelerometers (All units in mm)

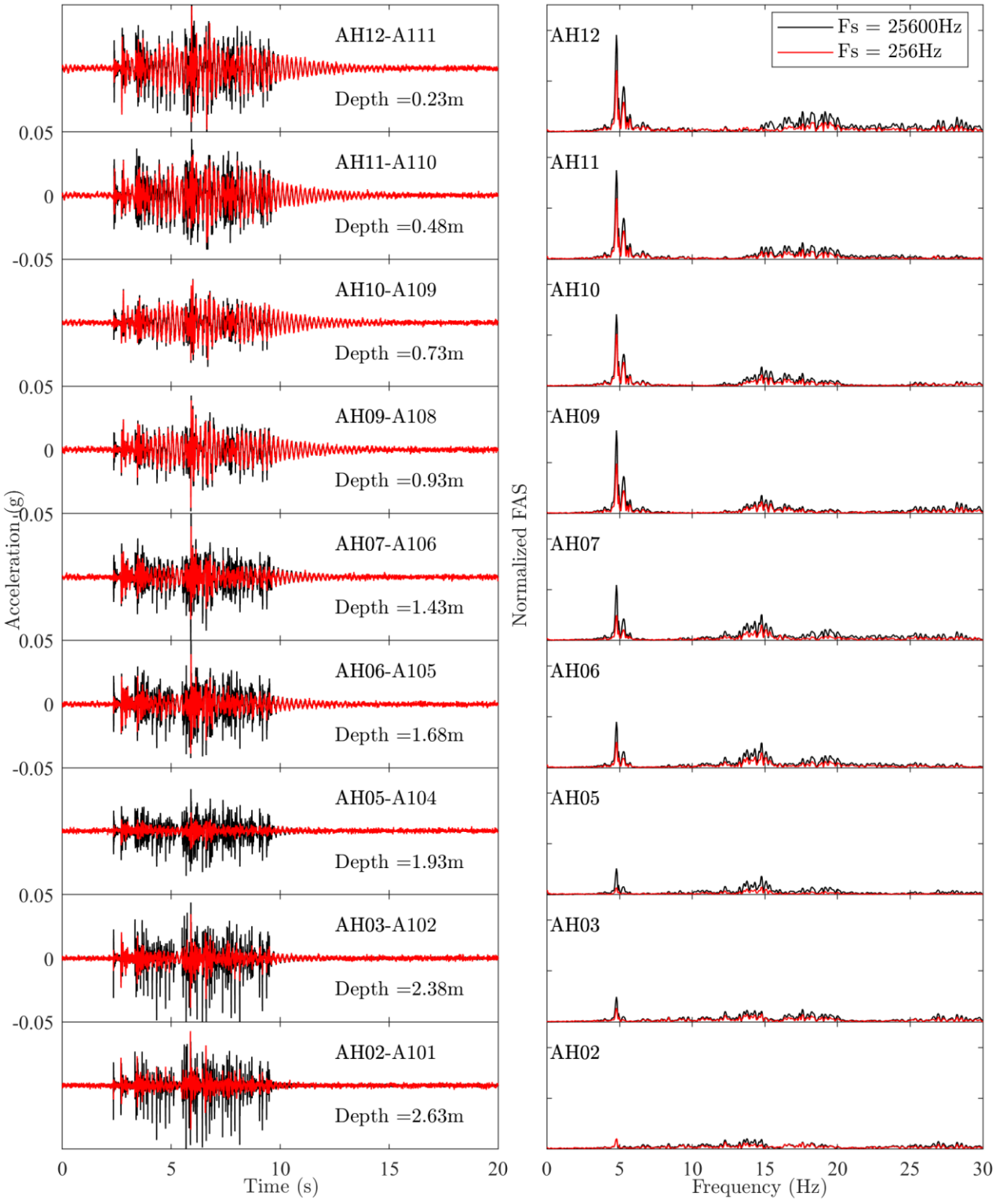

Figure 3.3. Recorded acceleration response and normalized Fourier amplitude spectra during WN01 (Fs refers to the sampling rate)

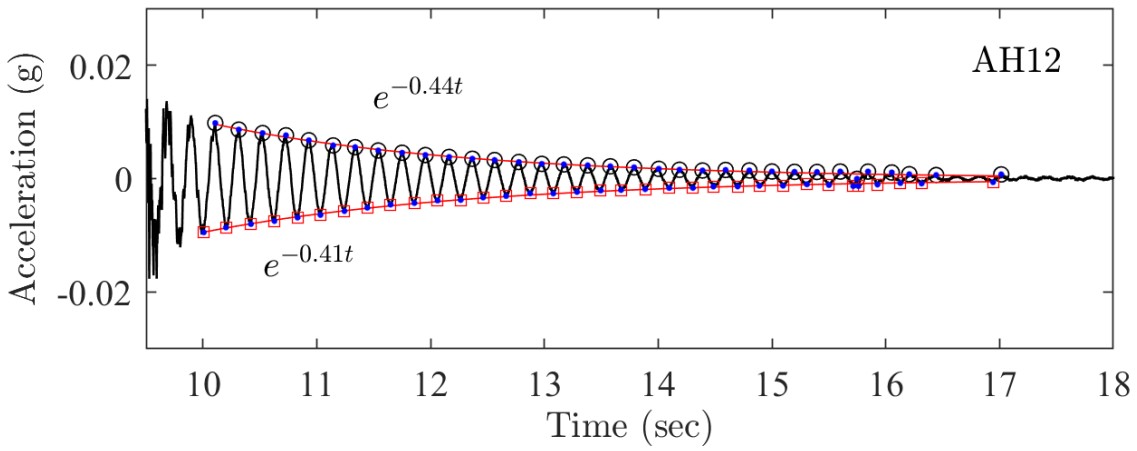

Figure 3.4. Recorded free vibration response at AH12 (PCB Accelerometer) following WN01

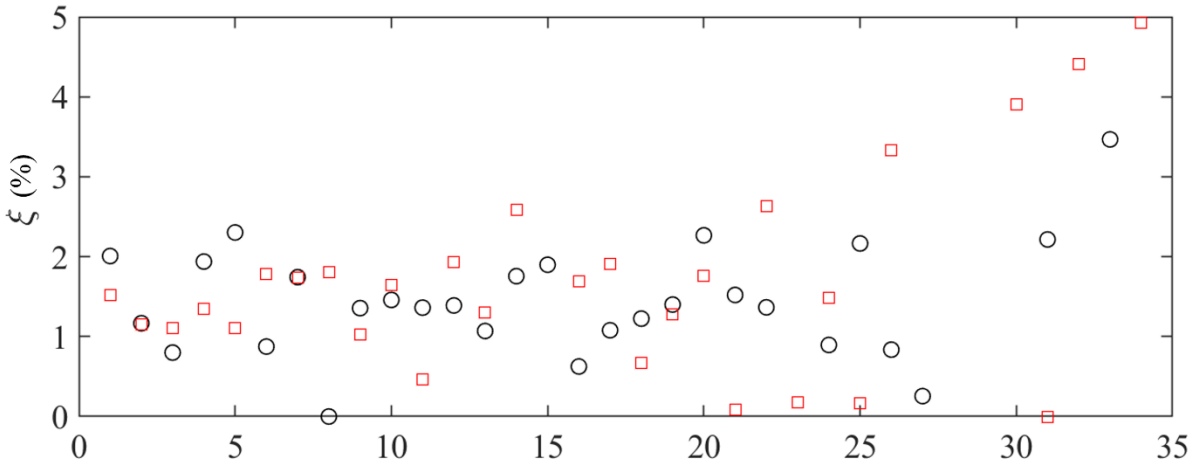

Figure 3.5. Estimates of low strain damping ratio from thefree vibration response at AH12, using logarithmic decrement.

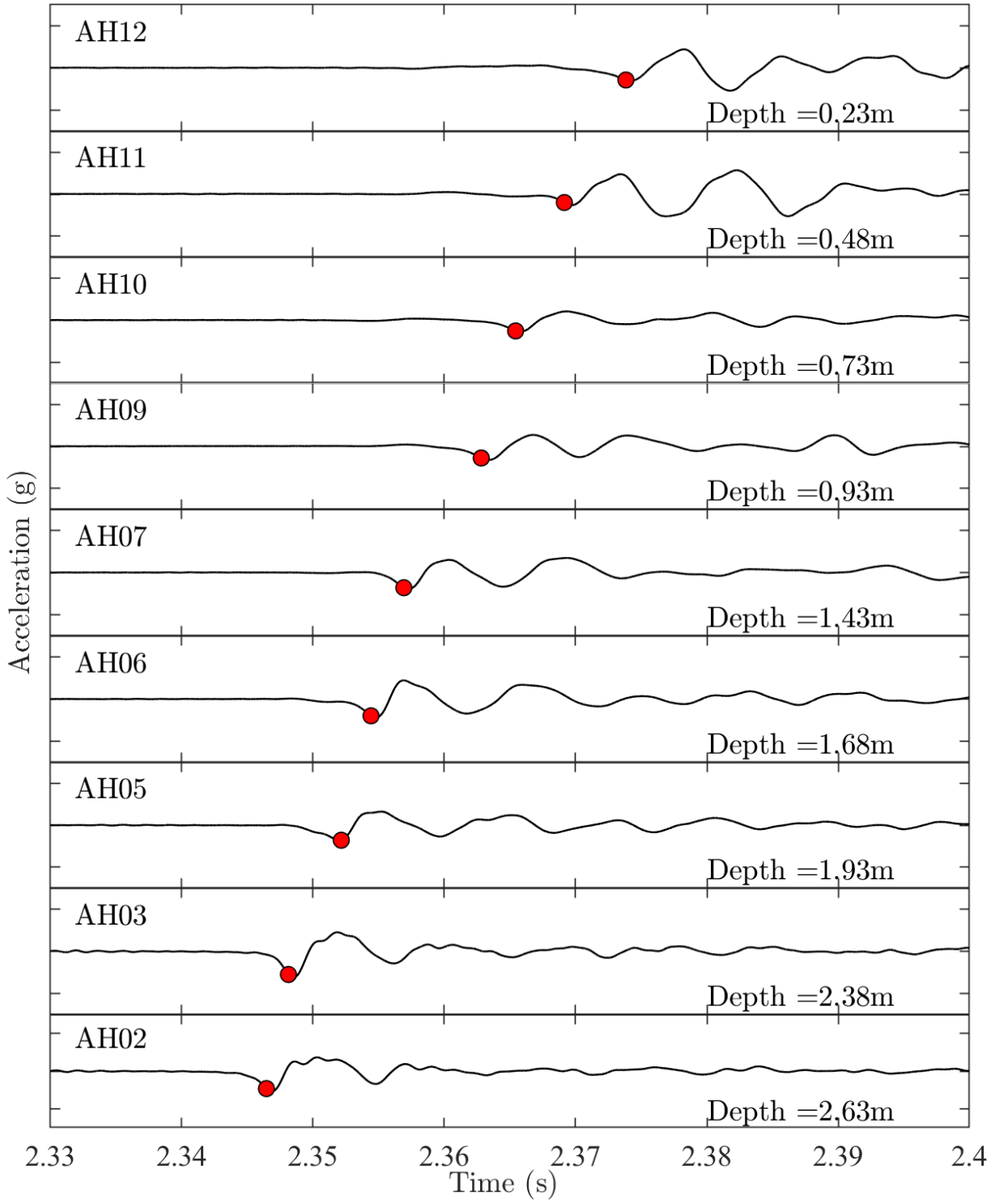

Figure 3.6. Peak picking from WN01 using north array PCB accelerometers

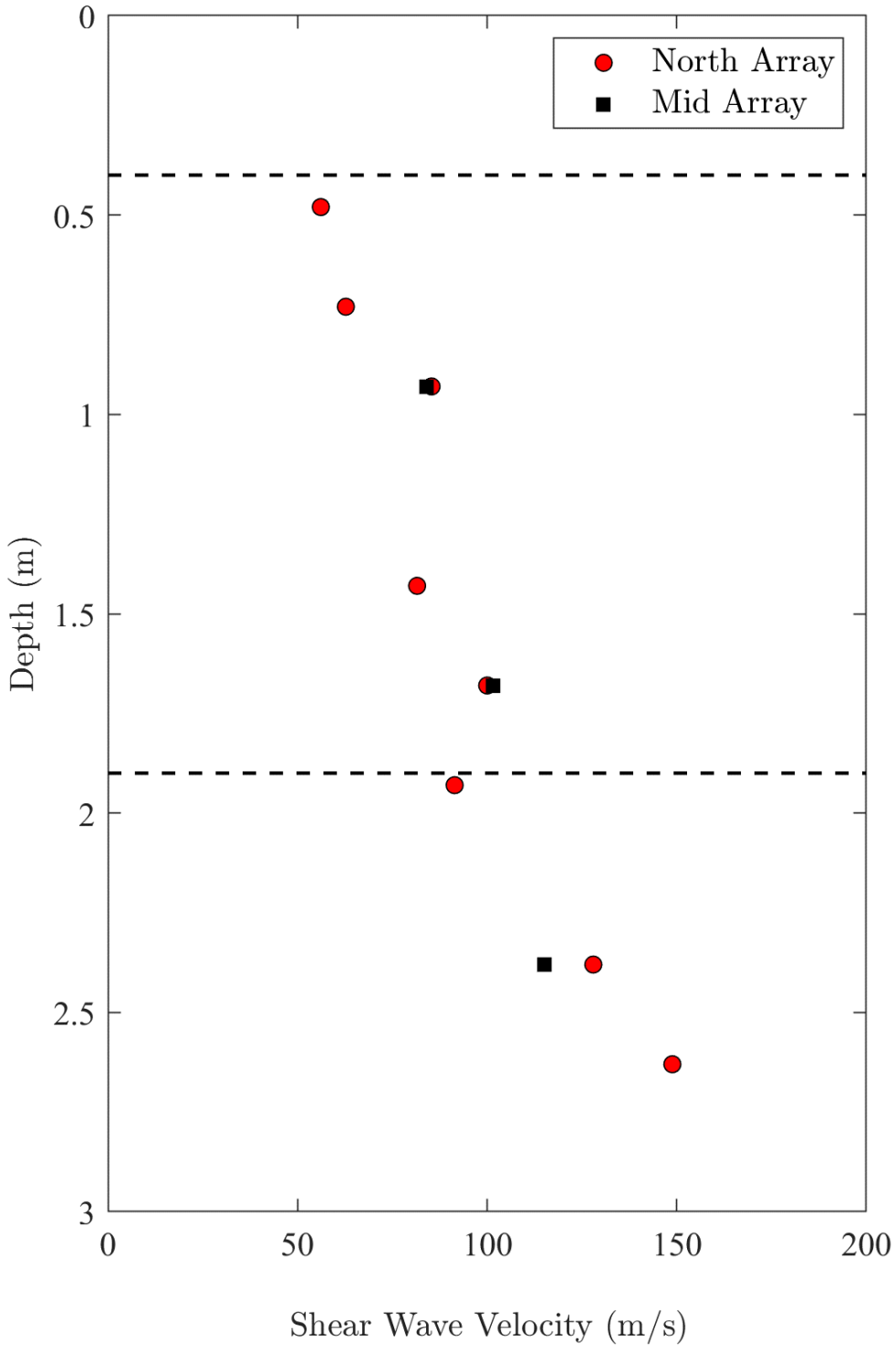

Figure 3.7. Estimate of Shear wave velocities from PCB accelerometers from WN01 (virgin model)

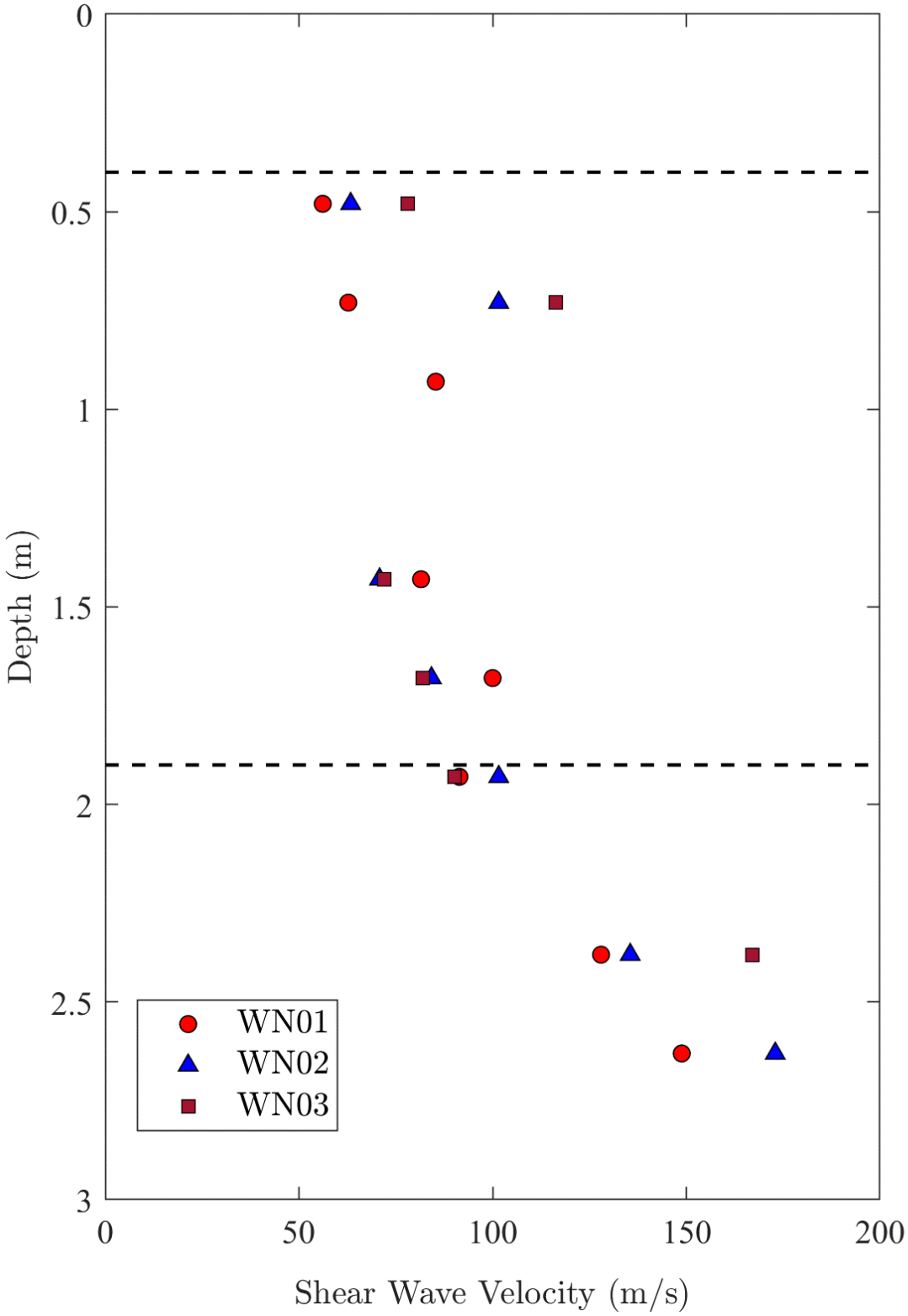

Figure 3.8. Shear wave velocities from PCB accelerometers from WN01, WN02 and WN03

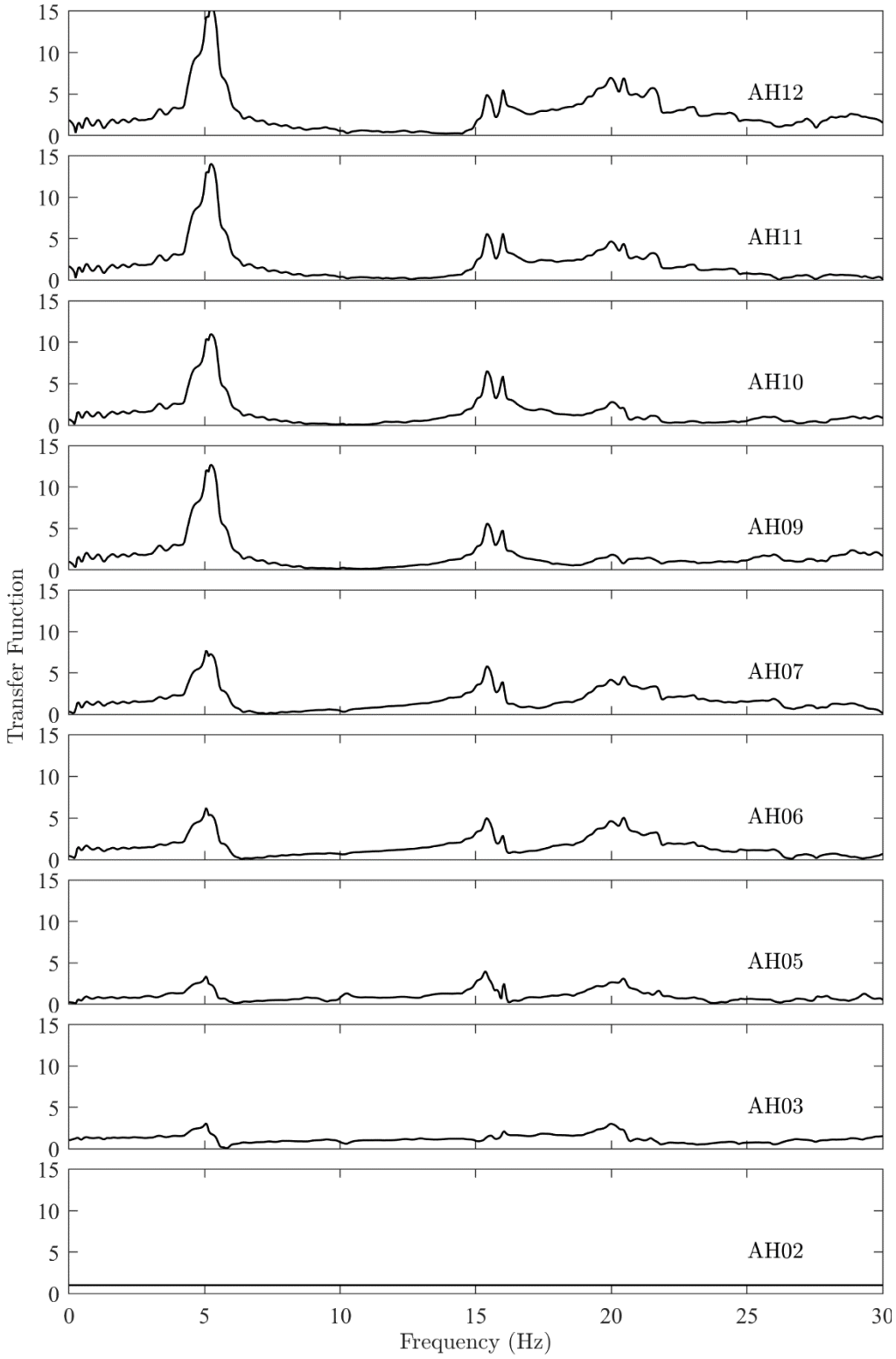

Figure 3.9. Estimated transfer functions between base and sensor location using north array PCB accelerometers for WN01

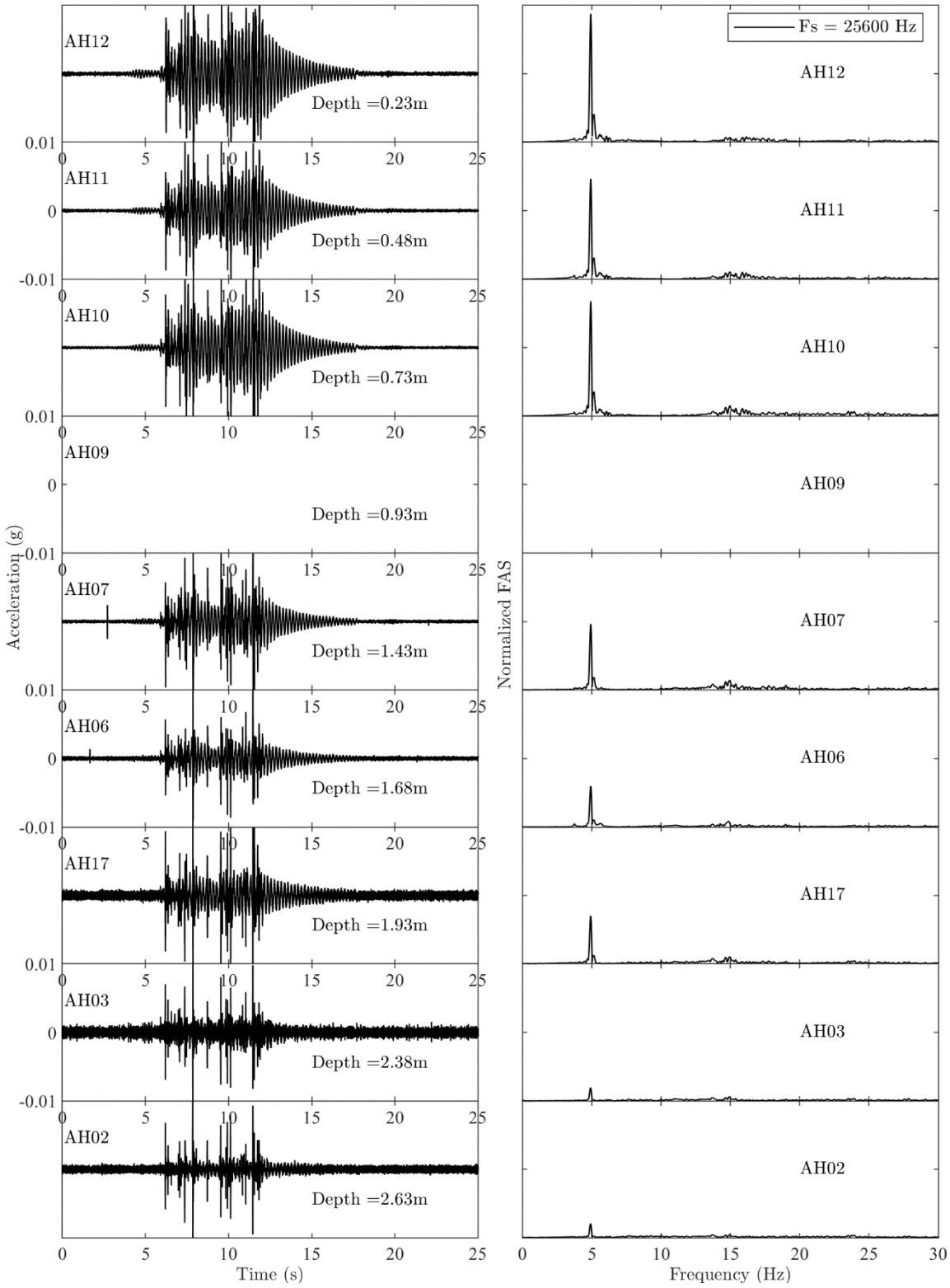

Figure 3.10. Recorded acceleration response and normalized Fourier amplitude spectra during WN02 (Fs refers to the sampling rate)

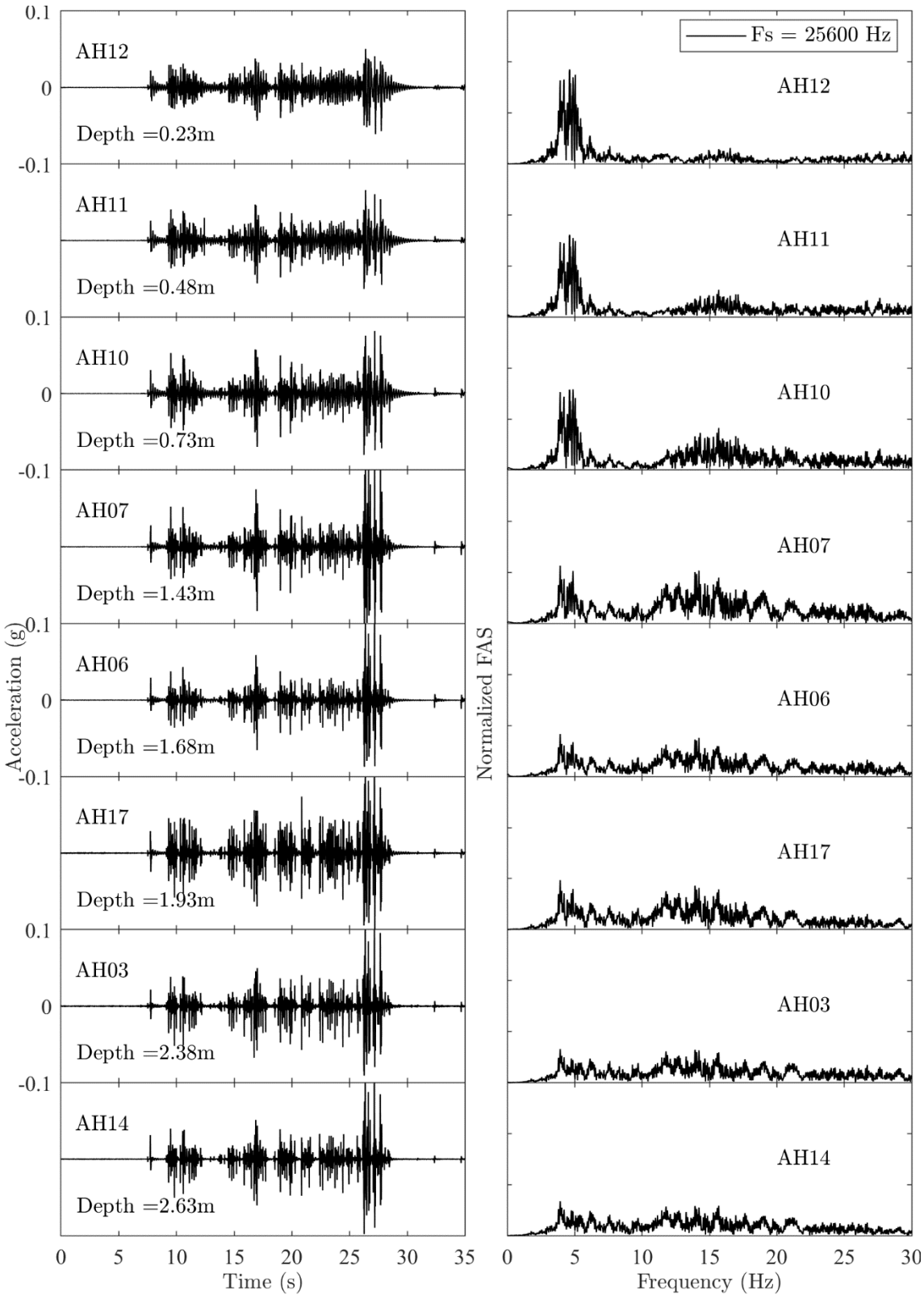

Figure 3.11. Recorded acceleration response and normalized Fourier amplitude spectra during WN03 (Fs refers to the sampling rate)

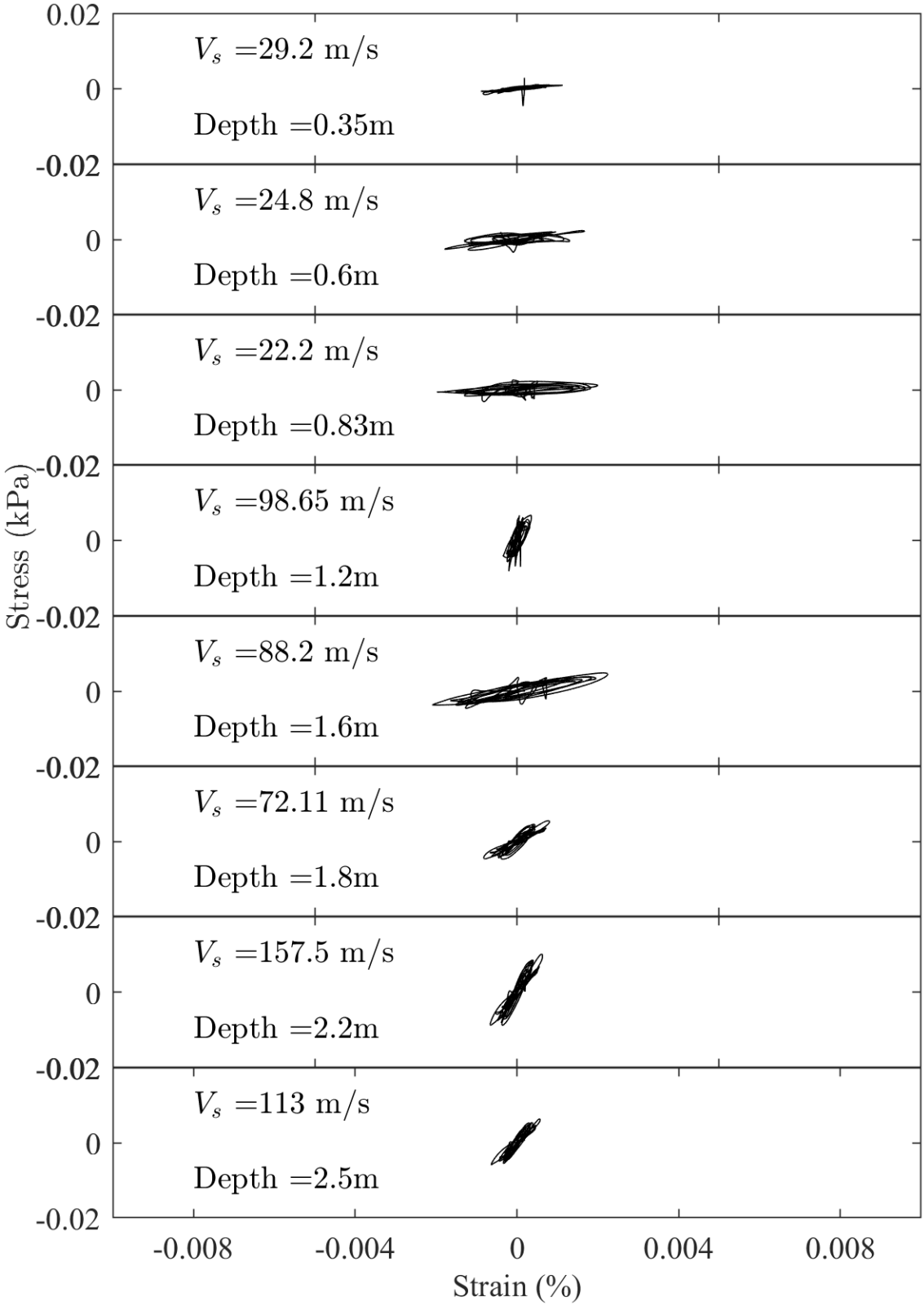

Figure 3.12. Shear stress strain loops obtained from WN01 using PCB accelerometers

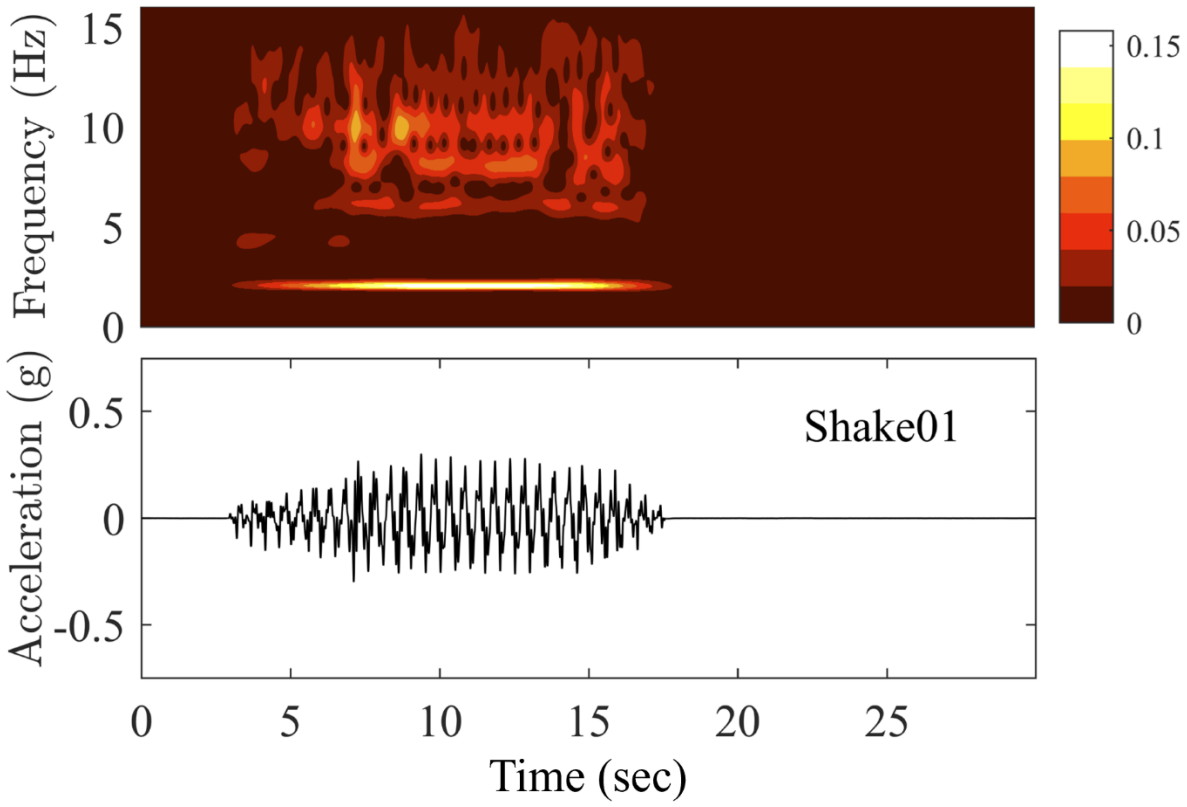

Figure 3.13. Imparted base excitation for shake table testing for Shake01

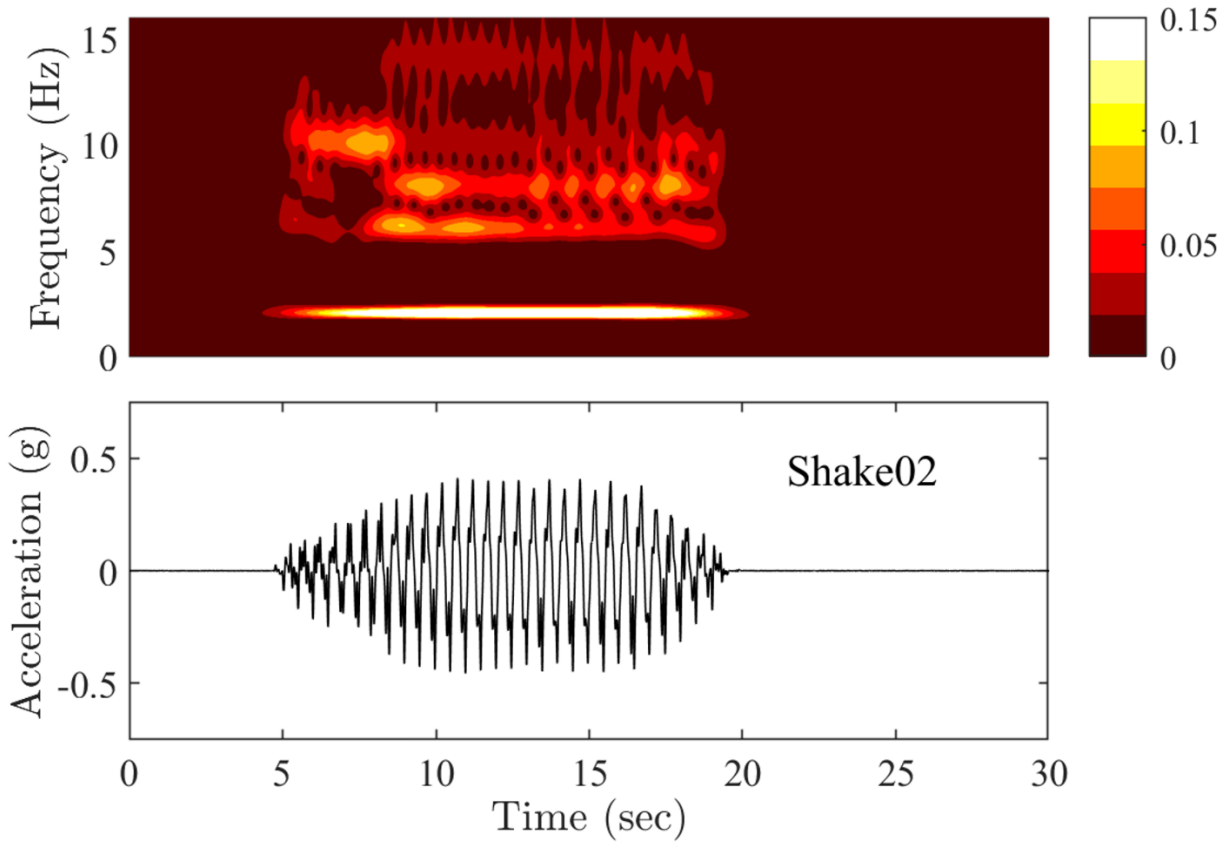

Figure 3.14. Imparted base excitation for shake table testing for Shake02 and Shake03

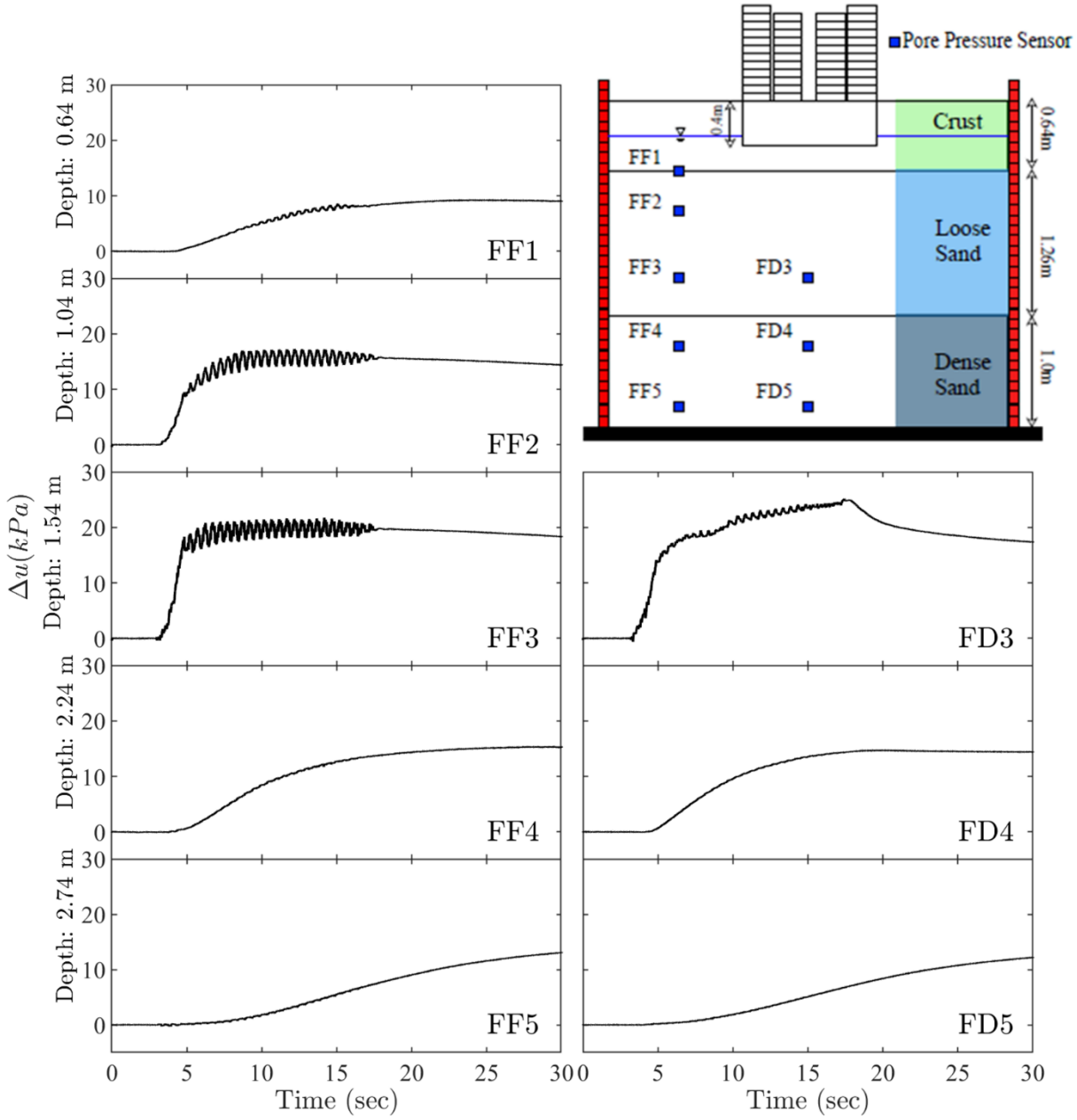

Figure 3.15. Excess pore pressure response in the baseline test during Shake01

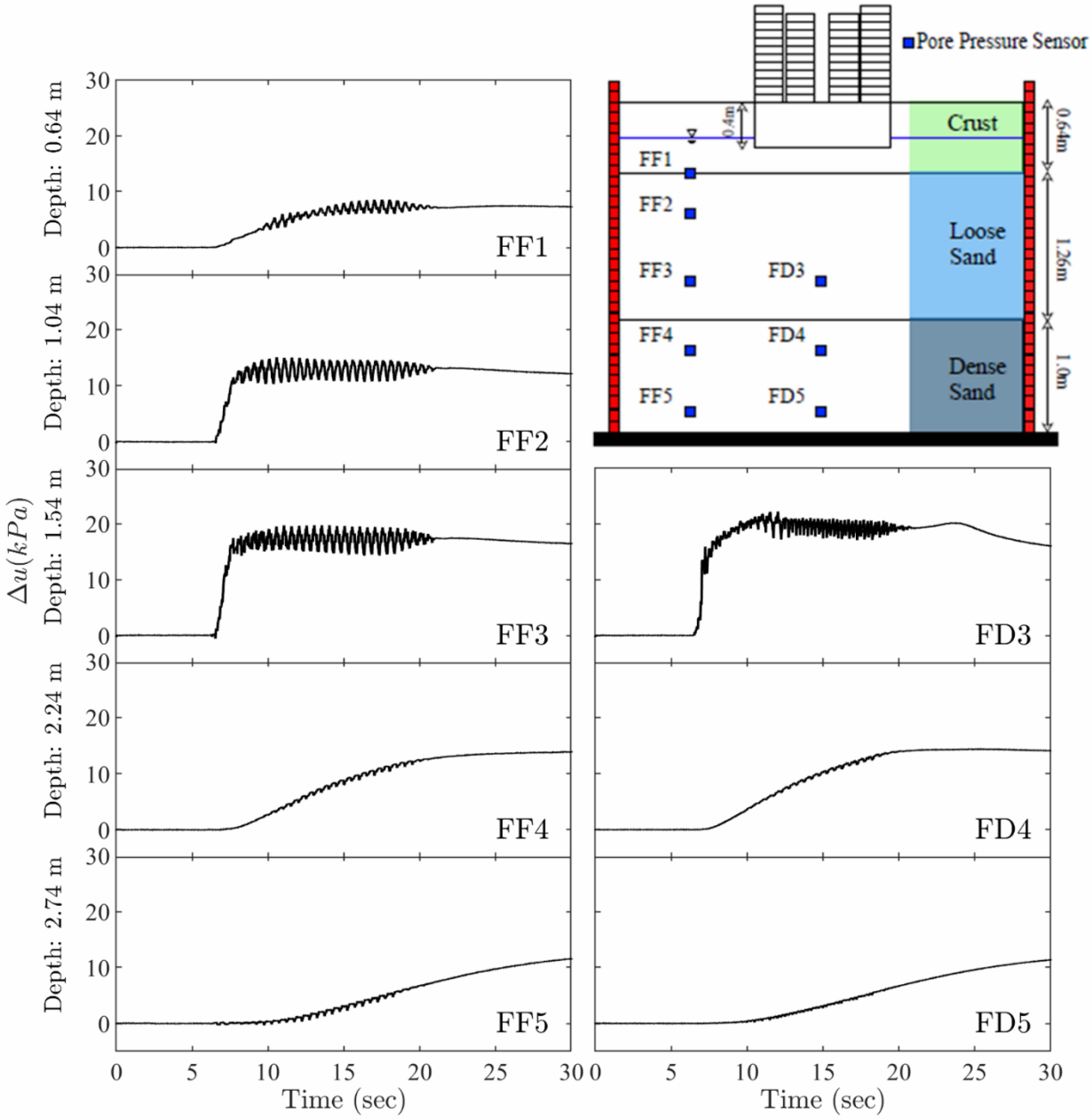

Figure 3.16. Excess pore pressure response in the baseline test during Shake02

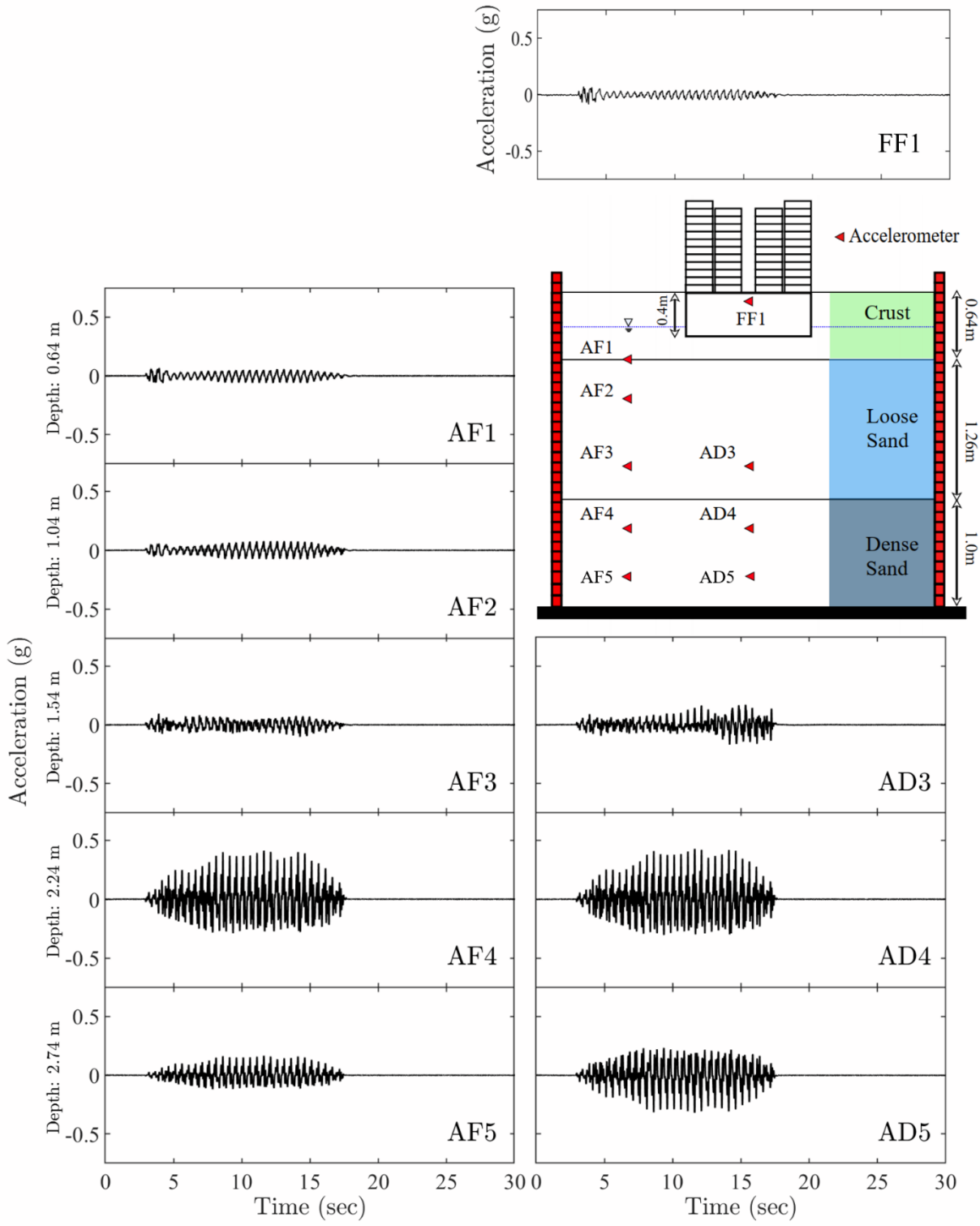

Figure 3.17. Acceleration response in the baseline test during Shake01

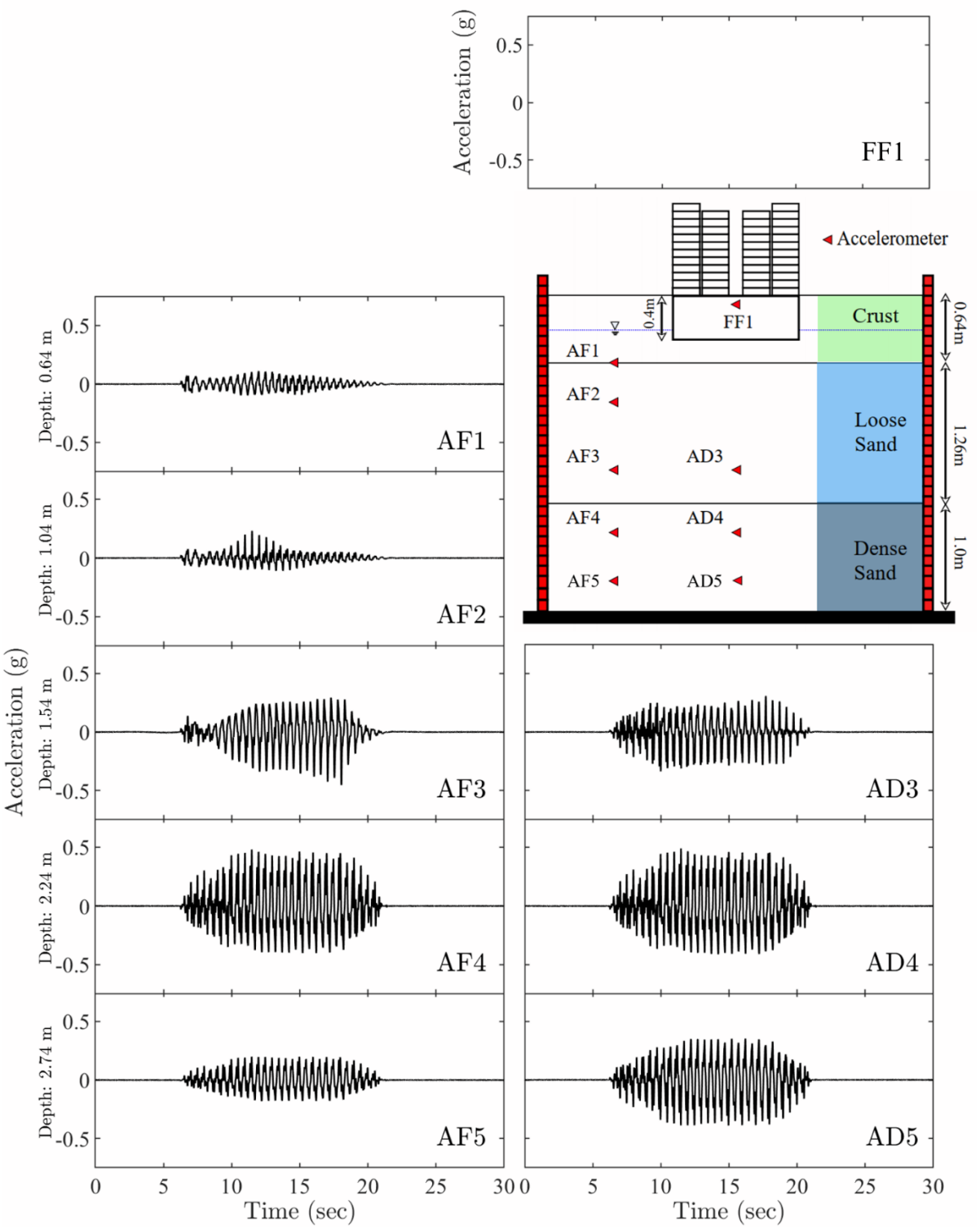

Figure 3.18. Acceleration response in the baseline test during Shake02

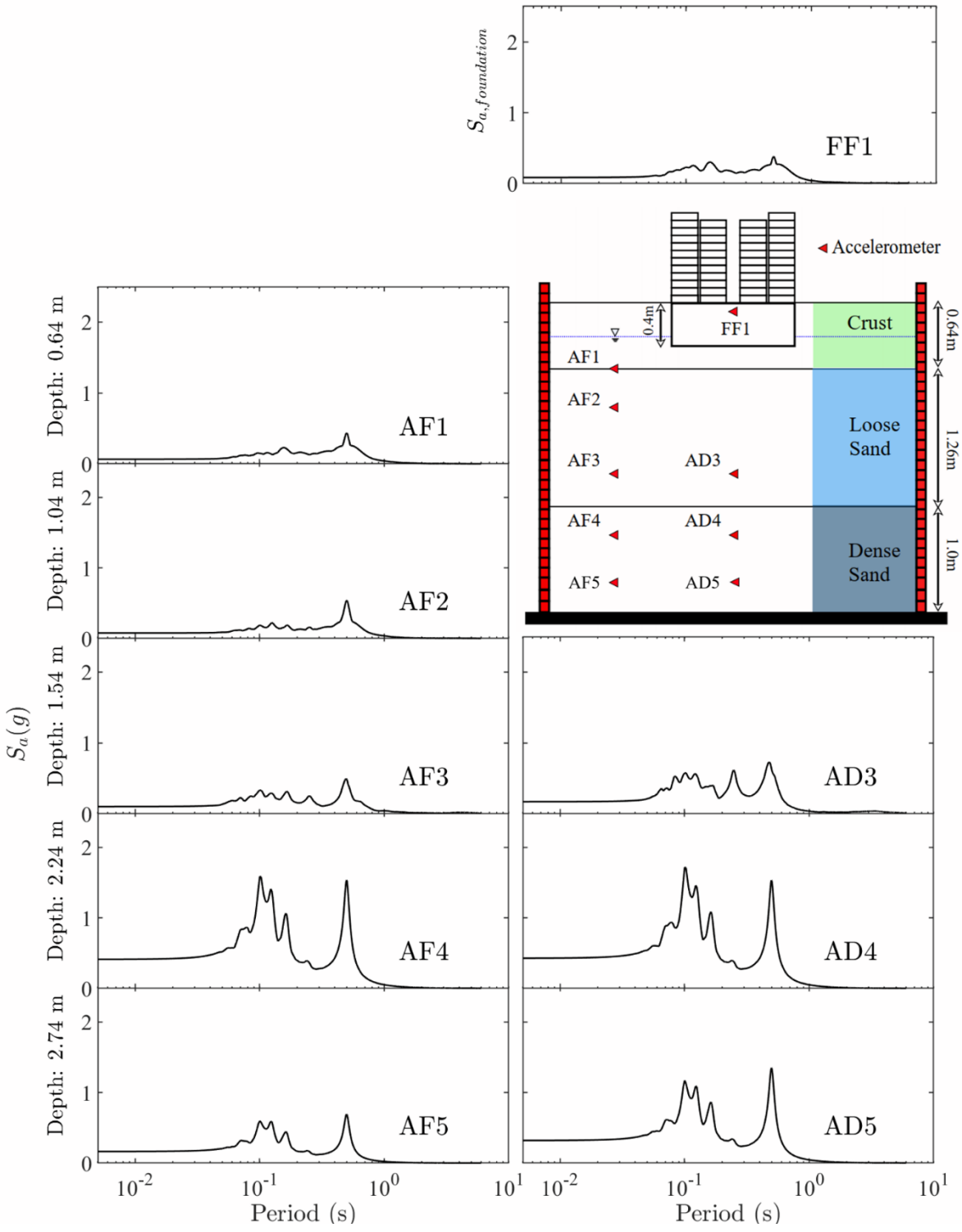

Figure 3.19. Response spectra in the baseline experiment during Shake01

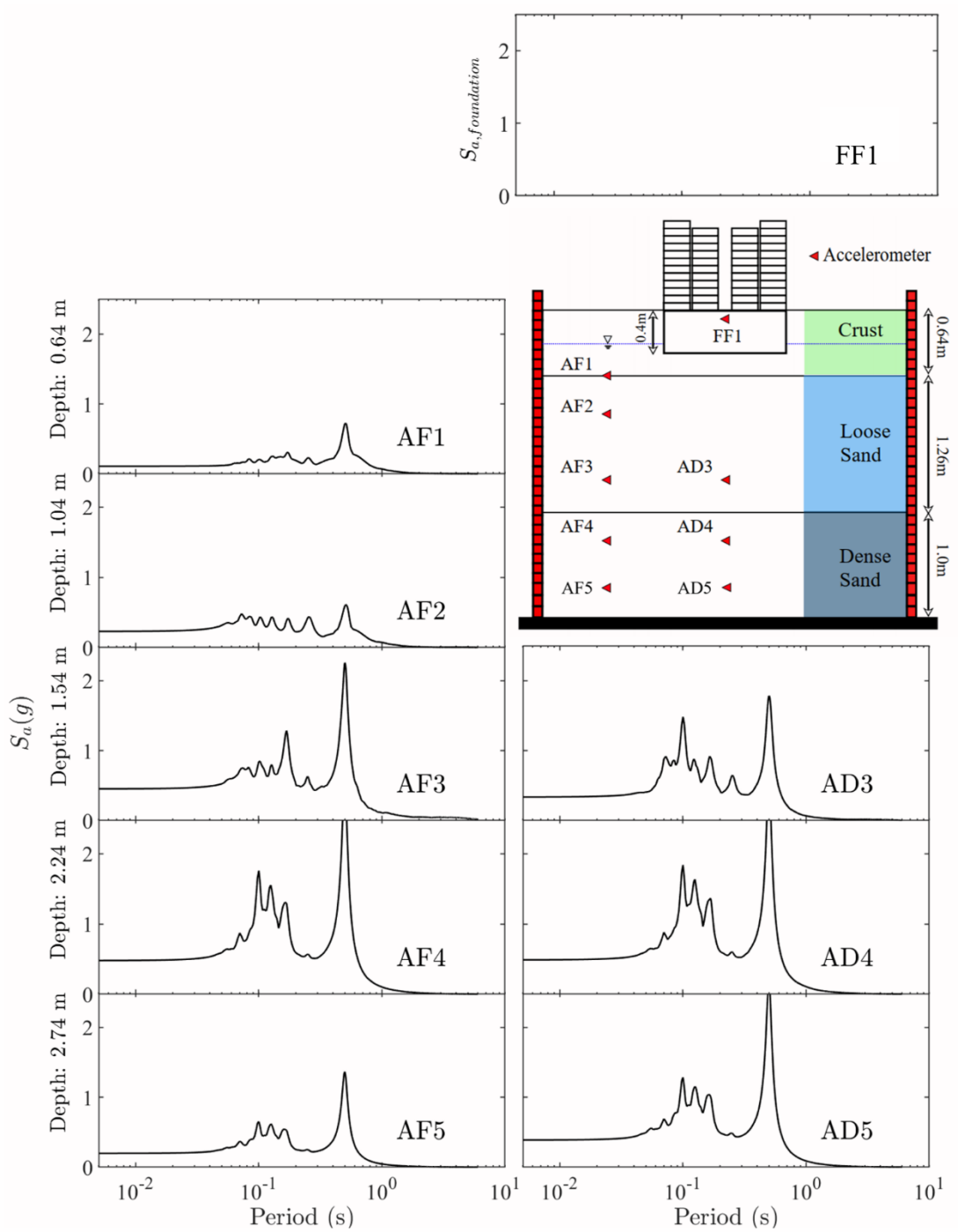

Figure 3.20. Response spectra in the baseline experiment during Shake02

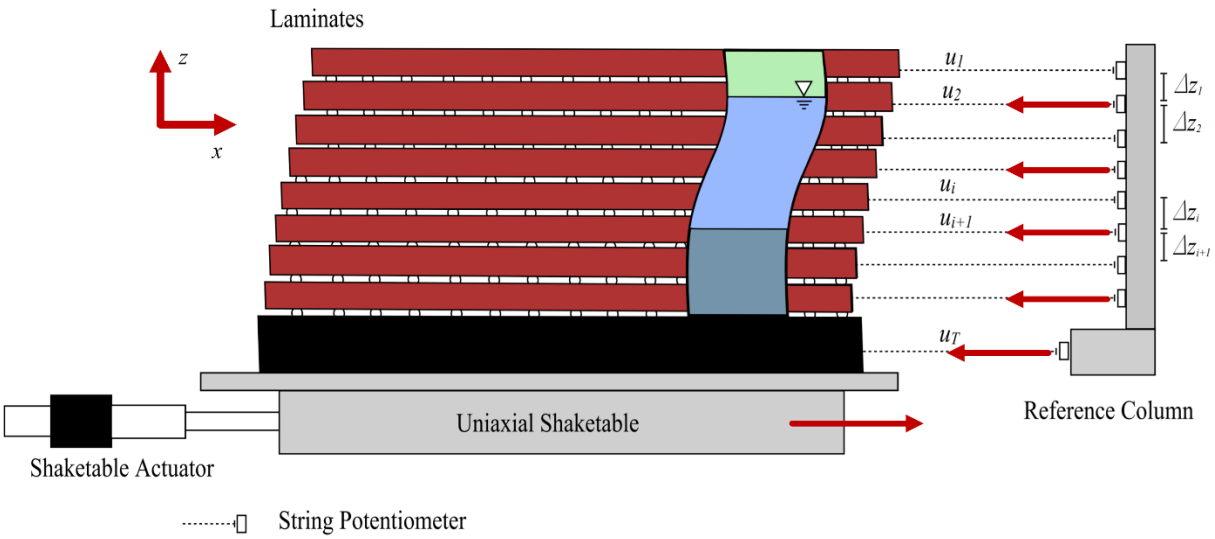

Figure 3.21. Sign convention for sensor data from lateral string potentiometers

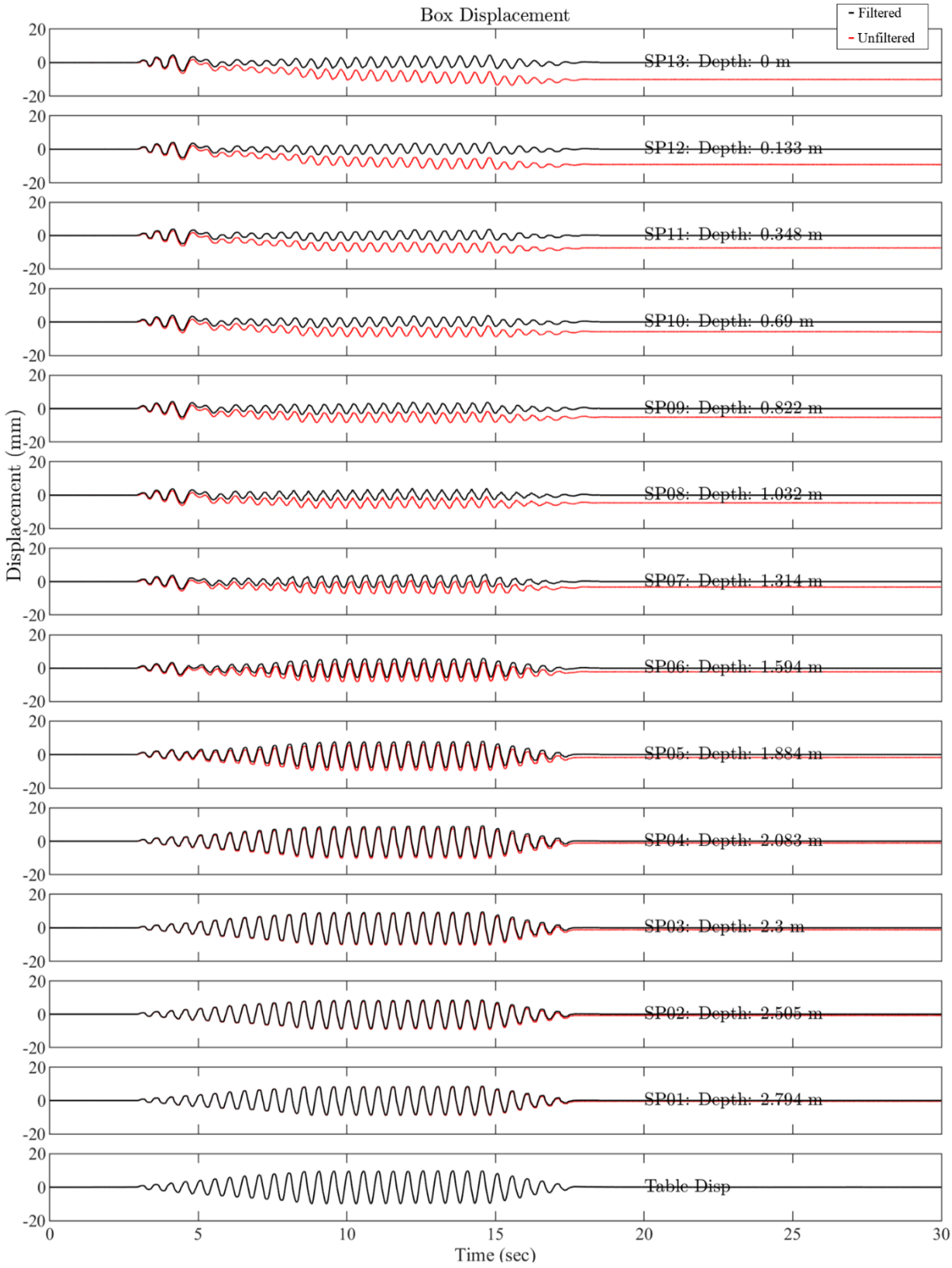

Figure 3.22. Lateral spring pot displacements (Total) during Shake01

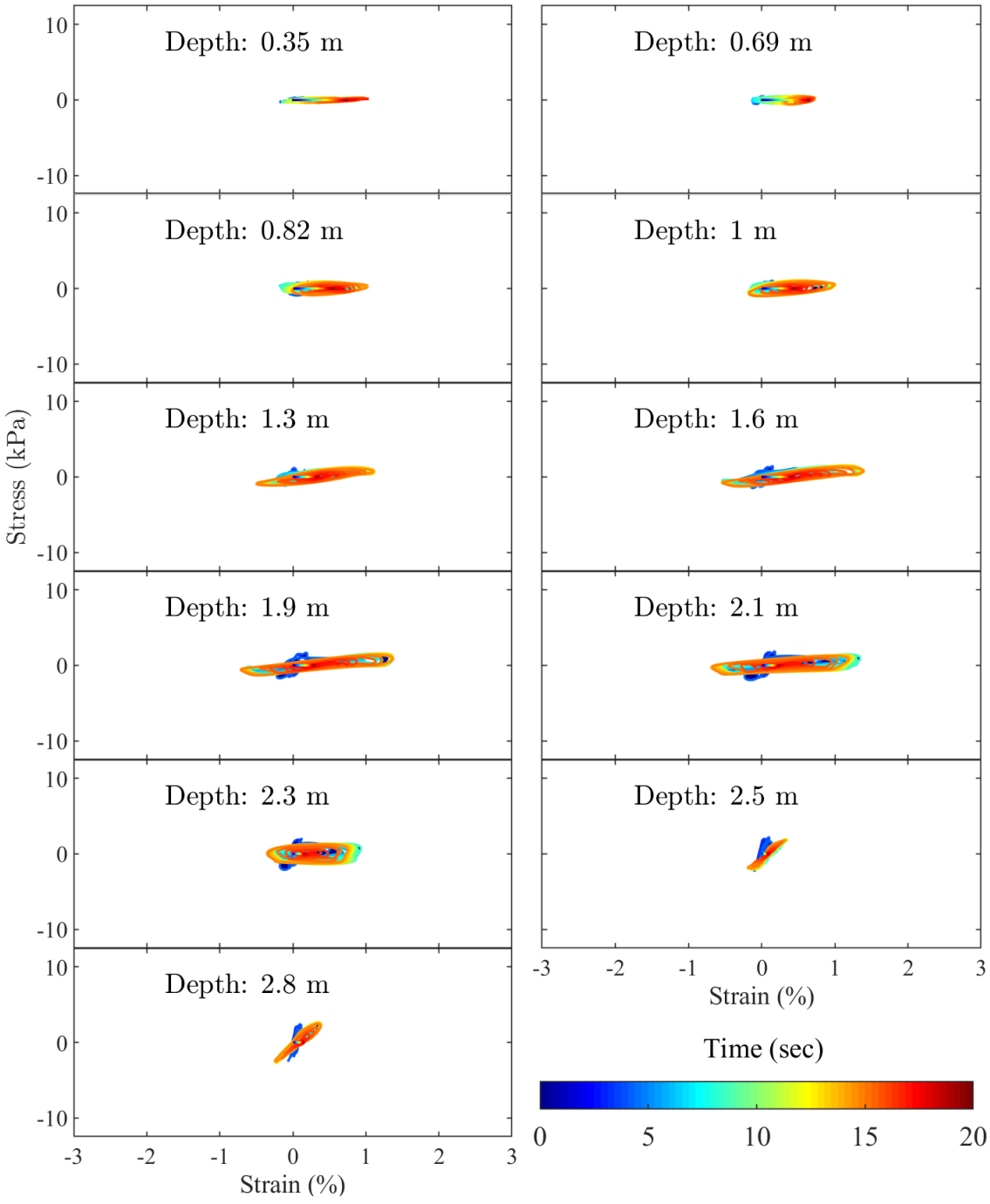

Figure 3.23. Stress strain response of deposit during Shake01

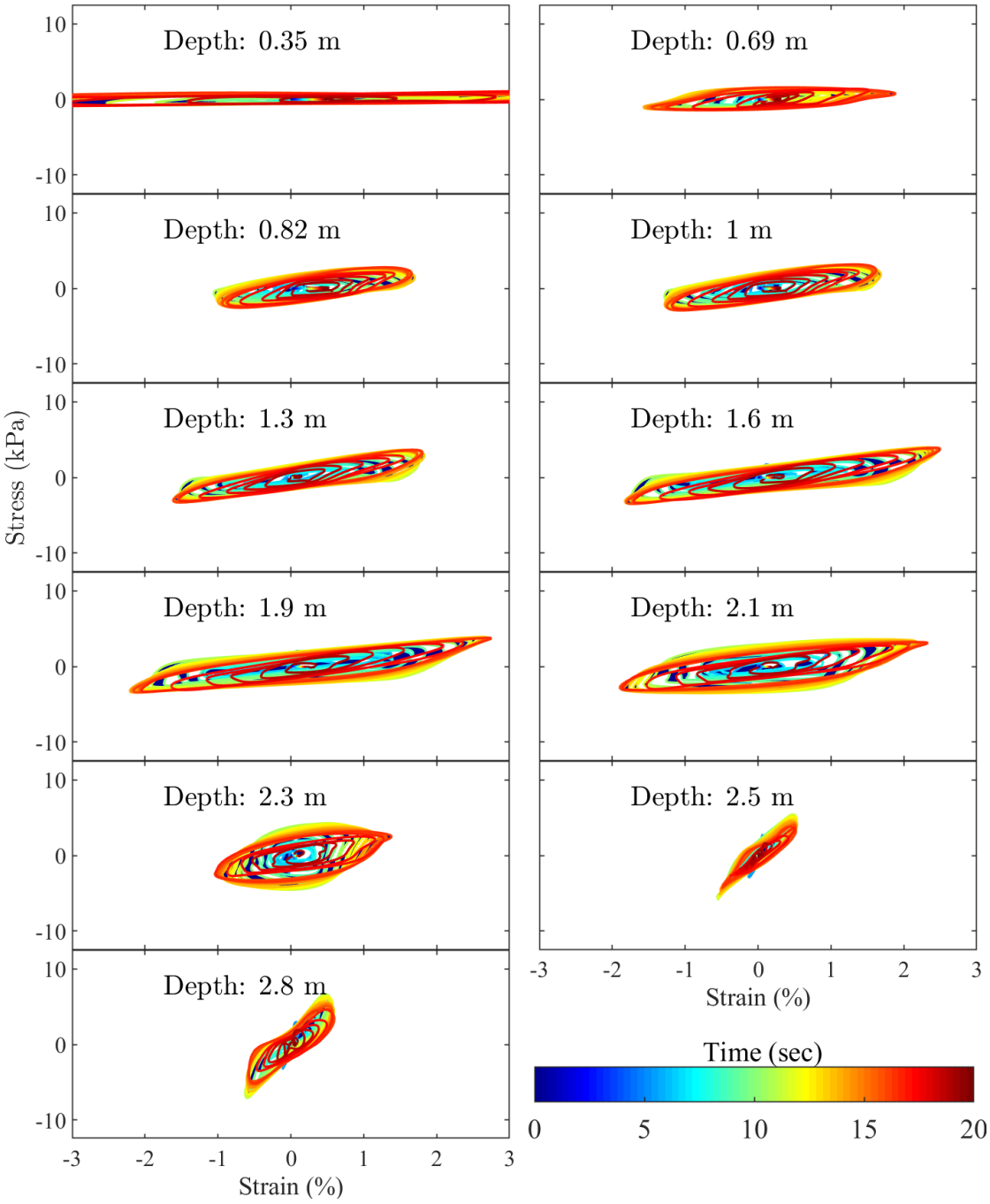

Figure 3.24. Stress strain response within liquefiable layer during Shake02

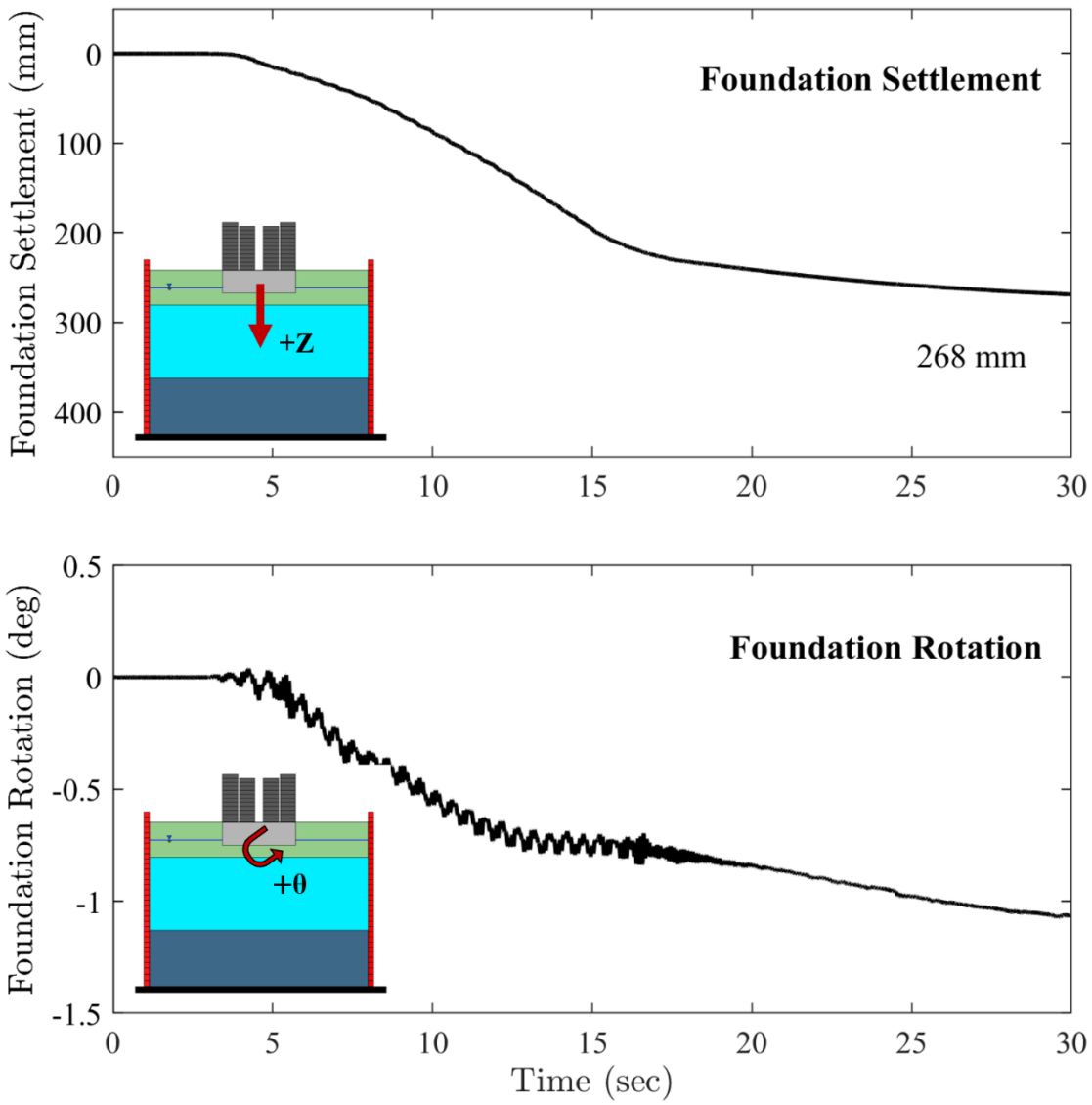

Figure 3.25. Foundation settlement and rotation time histories during Shake01

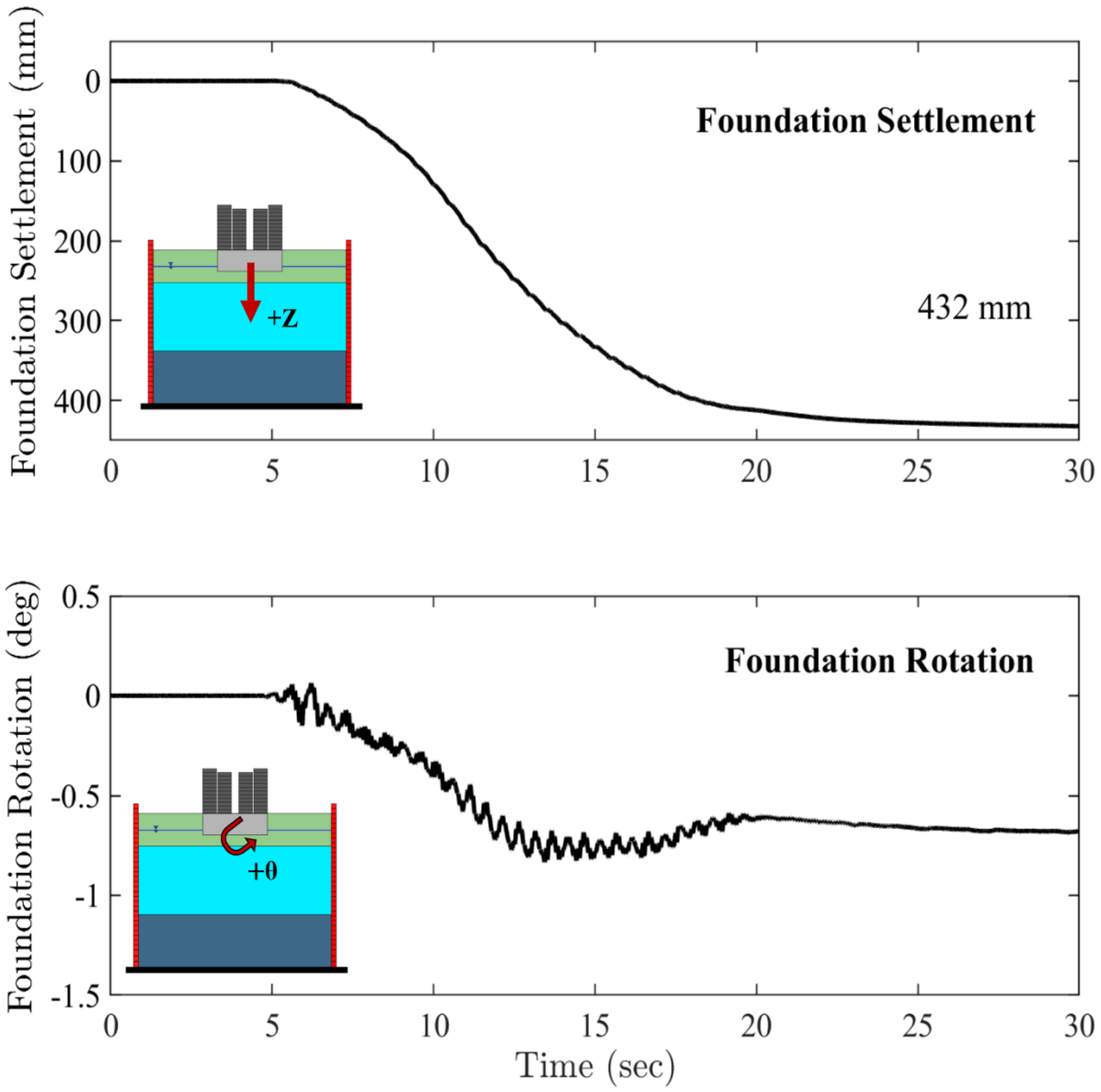

Figure 3.26. Foundation settlement and rotation time histories during Shake02

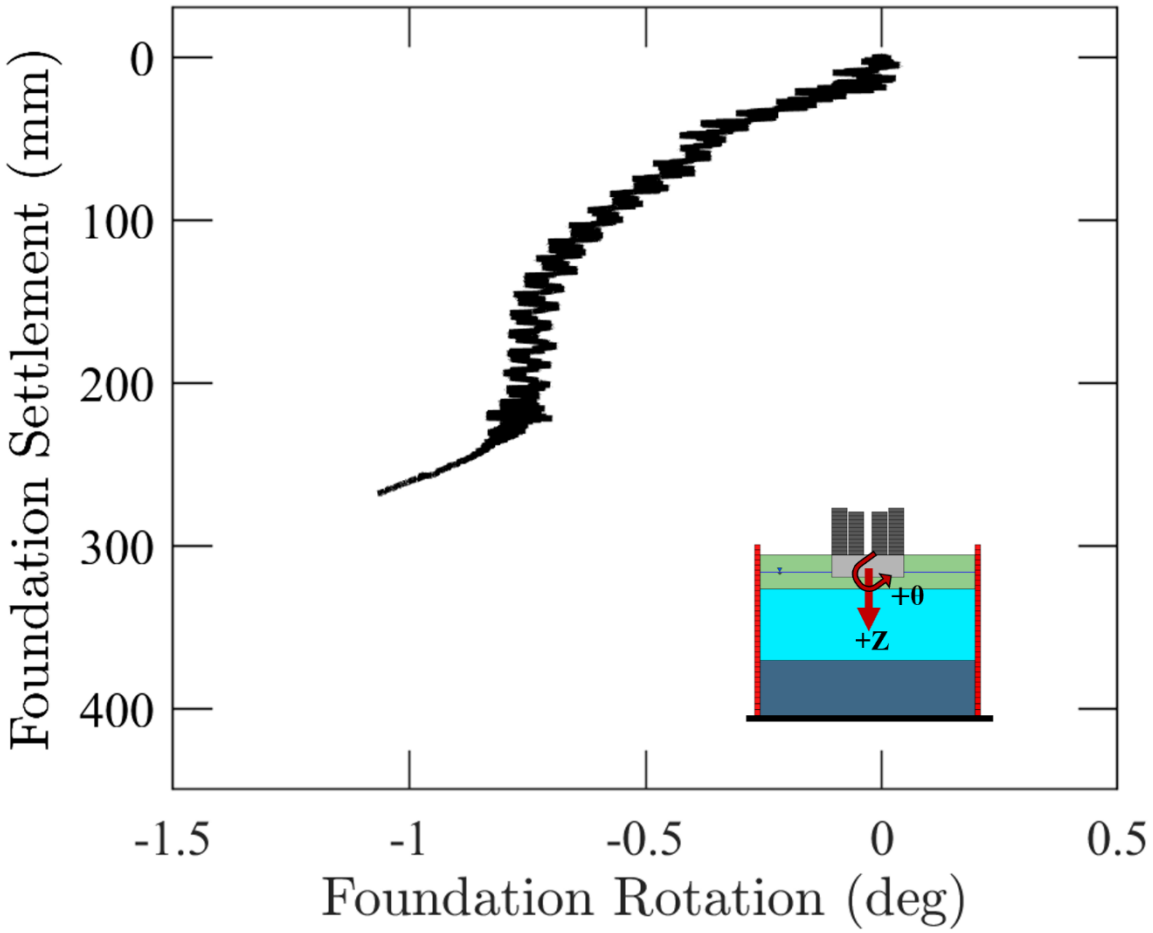

Figure 3.27. Foundation settlement - rotation behavior during Shake01

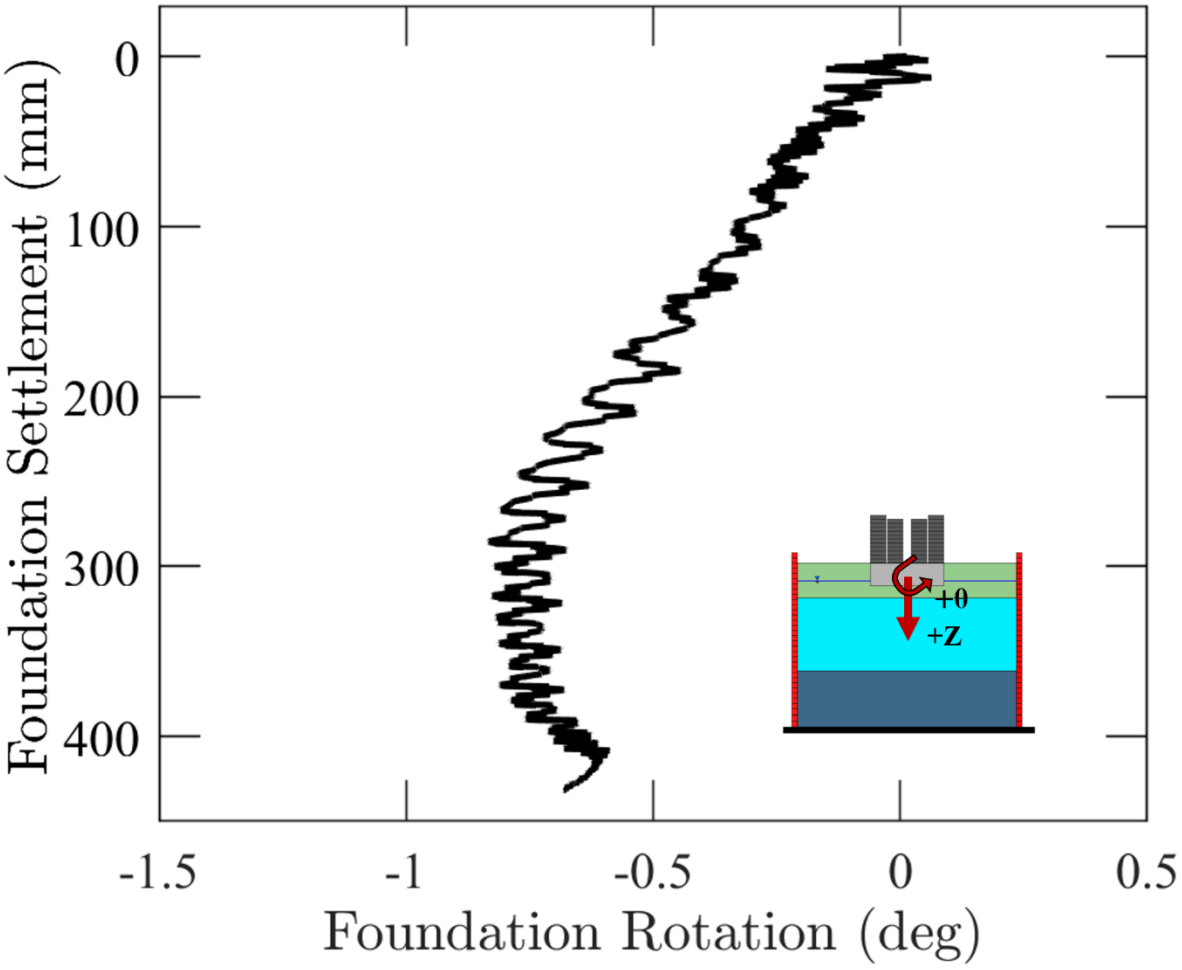

Figure 3.28. Foundation settlement - rotation behavior during Shake02

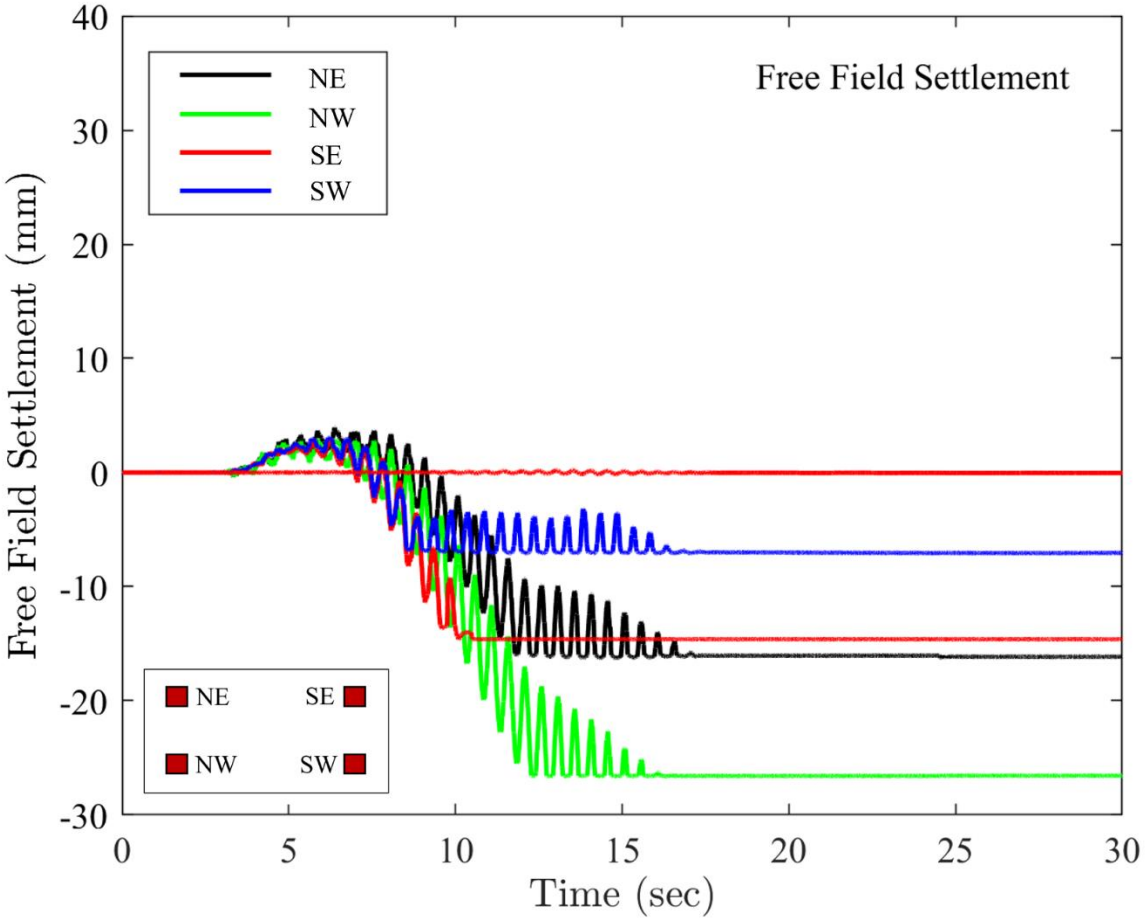

Figure 3.29. Free Field Settlement during Shake01

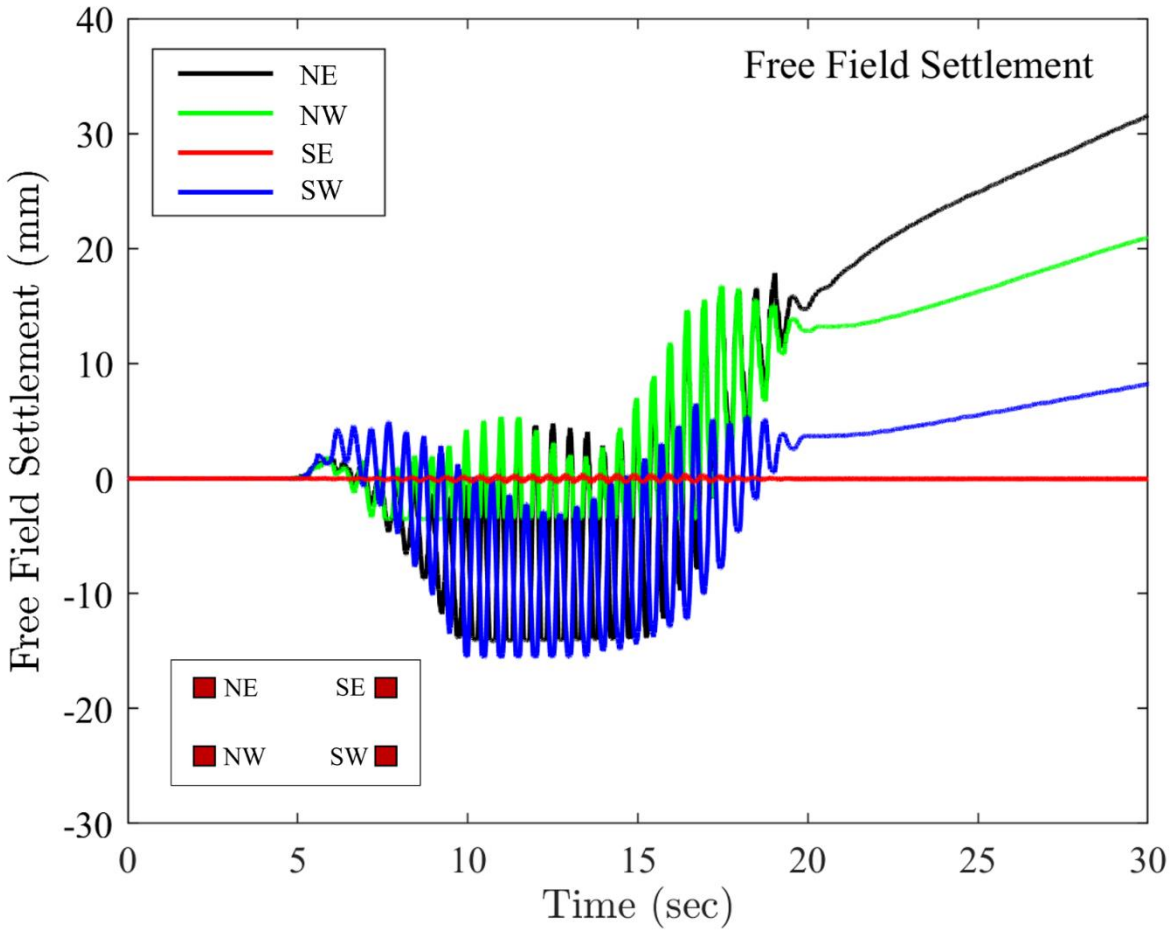

Figure 3.30. Free Field Settlement during Shake02

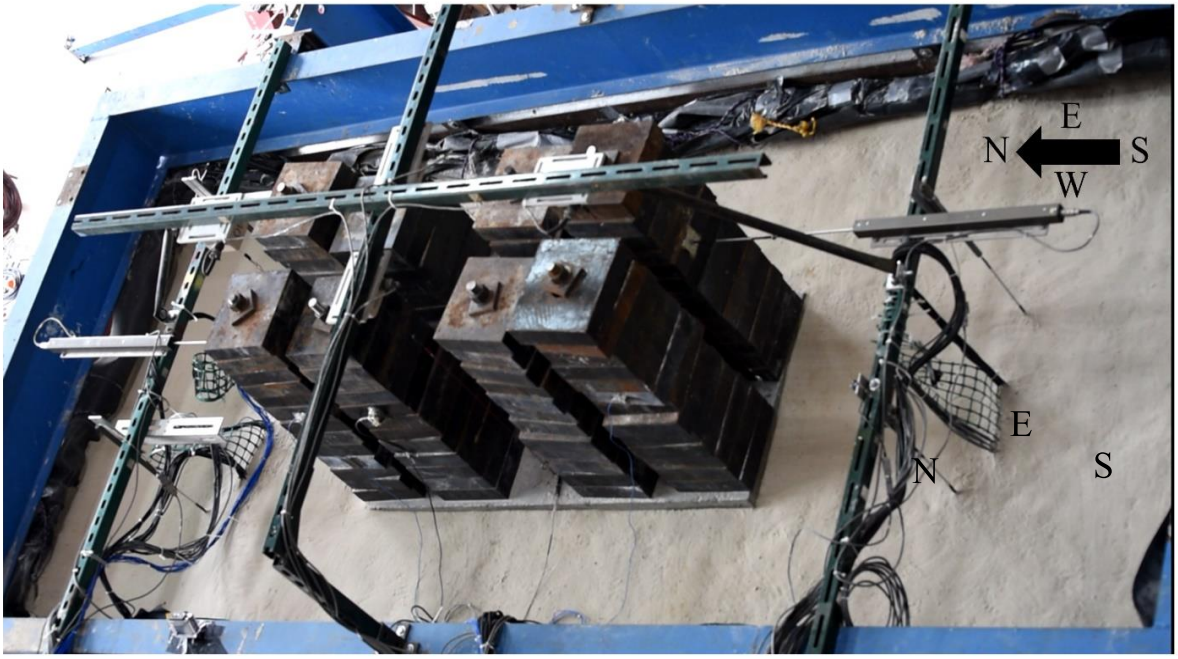

(a) Baseline model: before shaking

(b) Baseline model: after shaking (post Shake01)

Figure 3.31. Baseline model: (a) before shaking, (b) after shaking (post Shake01), (c) after shaking (post Shake02) and (d) after shaking (post Shake03)

(c) Baseline model: after shaking (post Shake02)

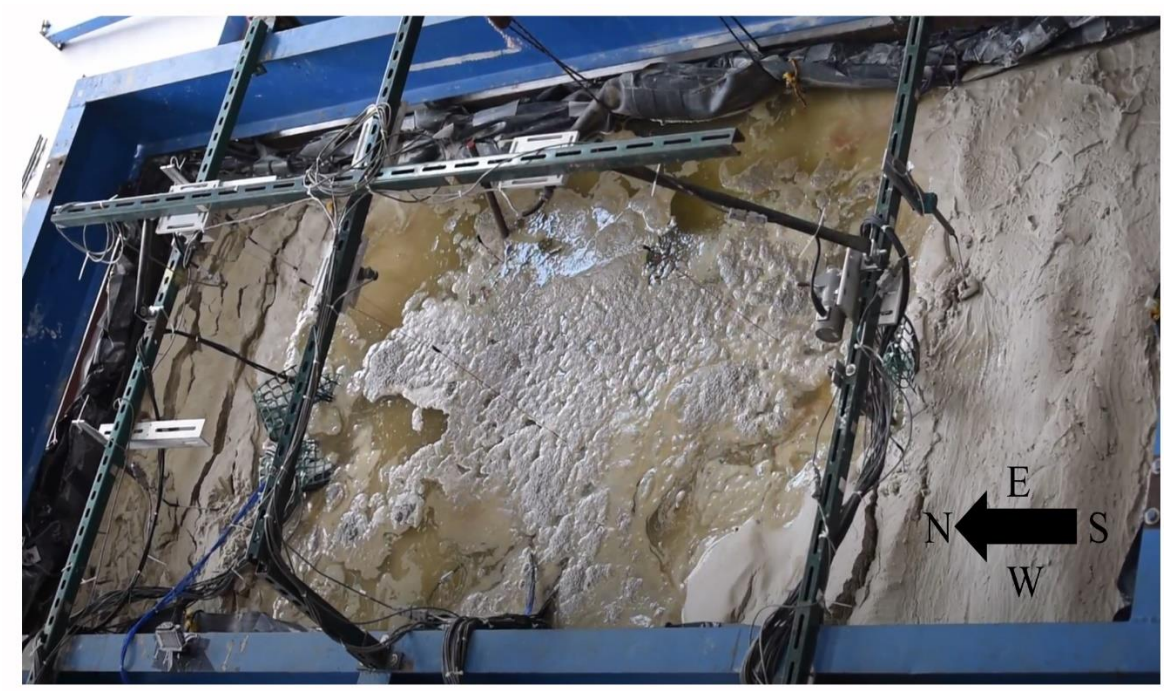

(d) Baseline model: after shaking (post Shake03)

Figure 3.31 (continued) Baseline model: (a) before shaking, (b) after shaking (post Shake01), (c) after shaking (post Shake02) and (d) after shaking (post Shake03)

Chapter 4. Polymer Injection and Liquefaction Induced Foundation Settlement: a Shake Table Test Investigation

4.1 Abstract

Shake table experiments are conducted to assess the potential of the polymer injection technique as a liquefaction countermeasure. A large 10 ft high (2.9 m) laminar soil container on a 13ft x 6 ft (3.9 m x 1.85 m) shake table is employed. Mitigation of liquefaction-induced settlement of a shallow foundation is explored. In a series of two shake table experiments, the system response is studied first without (baseline), and subsequently with polymer injected into the liquefiable stratum. Each test is instrumented to provide insights into the dynamic response of the soil and foundation system. Furthermore, Cone Penetration Tests (CPT) are performed pre- and post-injection to assess the extent of soil improvement. Strong base excitation is imparted by the shake table, resulting in liquefaction and excessive foundation settlement in the original baseline test. In the second test, after application of the polymer injection countermeasure, a major reduction is observed in the tendency for liquefaction, and the resulting foundation settlement. Careful excavation after the test provided additional insights as to configuration of the polymer within the deposit, increasing the overall soil confinement, and providing solidified paths for the shallow foundation load towards the lower more competent strata. As such, these mechanisms have the potential to provide for: i) an increase in the soil resistance to liquefaction, and ii) a significant reduction in settlement of overlying shallow foundations. Overall, this testing program is a first of its kind and offers insight into the behaviour of liquefiable ground remediated by the polymer injection technique. The potential for effective outcomes is highlighted, and efforts to establish analysis and design guidelines are warranted.

4.2 Introduction

Soil liquefaction is a mechanism that results in severe damage to buried structures and foundation systems during earthquakes as documented in Niigata 1964, Kobe 1995 and Tohoku 2011, Japan (Ishihara and Koga 1981, Hamada *et al.* 1996, Ashford *et al.* 2011), Kocaeli, 1999, Turkey (EERI 2000), Bhuj 2001, India (Jain *et al.* 2002), and 2010-2011 Canterbury earthquake sequence in New Zealand 2010-2011 (Cubrinovski *et al.* 2010). For instance, during the 2010-2011 Canterbury earthquake sequence, severe soil liquefaction affected 3,000 buildings within the Central Business District (CBD) of Christchurch, of which over 50% were to be demolished, being deemed economically unfit for further repairs (Cubrinovski 2013). Hence, in high seismic regions with loose saturated granular soils, it is vital that remediation measures be undertaken to minimize the consequences of soil liquefaction.

Various techniques currently exist to improve liquefaction susceptible soils during earthquakes, such as soil densification, cementation, drainage, and replacement (Adalier *et al.* 1998, Iai 2005, Yasuda and Harada 2014). Among such mitigation techniques, the injection of low viscosity polyurethane (polymer) has shown potential to be an effective countermeasure to remediate liquefaction susceptibility, particularly at locations that might otherwise be difficult to treat with conventional techniques (Traylen *et al.* 2016).

Several earlier laboratory studies demonstrated the beneficial effects of polymer remediation across various soil types (Maher *et al.* 1994, Yamazaki *et al.* 2005, Shigang *et al.* 2013, Lee *et al.* 2017a, Lee *et al.* 2017b, Kim *et al.* 2017, Liu *et al.* 2019). In addition to laboratory studies, field trials in Turkey (Erdemgil *et al.* 2007) reported significant increases in the post-injection standard penetration test blow counts (SPT-N value) at sites which suffered extensive damage in the 1999 Kocaeli earthquake. More recently, studies in New Zealand (Van Ballegooy

et al. 2016 and Traylen *et al.* 2017) observed clear increases in CPT tip resistance (q_c), shear wave velocity (V_s), and lateral earth pressure coefficient (K_o) over the improvement depth. As such, cyclic shear strains generated through a vibroseis machine were considerably reduced at the test site. Attention was paid to the mechanisms involved in the improved liquefaction resistance through a detailed excavation post-injection. The hardened composite (Traylen *et al.* 2017) was observed as dendritic veins/dykes, with thickness of few centimeters oriented along the direction of the lateral spread observed during the 2010-2011 Canterbury earthquake sequence.

As a complement to these earlier studies, this paper presents results from two large-scale shake table experiments performed to study the effectiveness of polymer injection in mitigating liquefaction-induced settlement of a shallow foundation. The foundation is placed on a sand layer, overlying a saturated liquefiable stratum. In a series of two shake table experiments, the system response is studied first without (baseline), and subsequently with polymer injected into the loose stratum. Effects of soil liquefaction including excess pore pressure generation, foundation settlement, and soil/foundation accelerations are targeted as key performance metrics to study the performance of polymer injection as a liquefaction countermeasure.

Extensive details of the baseline test can be found in (Jahed Orang *et al.* 2020). Results from the additional polymer test are presented in this paper and compared to the baseline counterpart. In the next sections, the following aspects are discussed: i) Experimental setup and model preparation, ii) Injected polymer configuration, iii) Model characterization, iv) Recorded dynamic response and comparison to baseline, and v) Characteristics of the polymer solidified zones and associated mitigation mechanisms. Finally, conclusions are presented with discussions towards adoption of this remediation technique in practice.

4.3 Specimen Characterization and Polymer Injection

4.3.1 Experimental Setup

Two shake table experiments were performed using the laminar soil container (Figure 4.1) of the Powell structural engineering laboratories at the University of California, San Diego. The uniaxial shake table platform has dimensions of 4.9 m by 3.1m and is designed for models that weigh up to 350 kN with an actuator of capacity 490 kN. Maximum table displacement is ±150 mm with a maximum nominal operating frequency of 20 Hz (Magenes 1989 and Trautner *et al.* 2018).

The soil deposit is prepared in the laminar soil container (Figure 4.1) with original internal dimensions of 3.9 m by 1.8 m by 1.9 m built by (Ashford and Jakrapiyanun 2001) and extended an additional 1m in height by (Ebeido 2019). In such a container, steel laminates are stacked on each other separated by roller bearings, to minimize lateral edge effects thus, facilitating the propagation of 1D horizontally polarized shear waves in a periodic boundary condition as noted by (Law and Lam 2001).

A 60 MIL thick Ethylene Propylene Diene Monomer (EPDM) rubber liner was placed to hold soil and water inside the laminar container. Two flexible perforated pipes were placed at the base of the laminar container and water was used to saturate the model. Further details about the shake table and laminar container are reported in Zayed (2020), and Motamed *et al.* 2020.

Each model was instrumented with three arrays of pore pressure sensors and accelerometers as shown in Figure 4.2. The laminar soil container, foundation, and free field soil surface were instrumented with vertical displacement transducers to obtain further insight into the performance of the system. Both experiments consisted of three arrays of sensor deployment within the soil deposit of which the north “free-field” and “under foundation” arrays are presented.

The soil surrounding the foundation at 0.6 m from edge of the foundation on each side is referred to as "free-field" condition through this paper (Jahed Orang *et al.* 2020). During both experiments, data were recorded at a sampling rate of 256 samples/s.

4.3.2 Model Preparation

The soil models for both tests were constructed in three phases using Ottawa F-65 sand (Parra Bastidas 2016), consisting of a saturated 1.00 m dense base layer underlying a 1.25 m thick saturated liquefiable deposit, overlain by a moist 0.64 m crust (Figure 4.2). The methodology of construction of all three layers is described in detail in the following sections.

i. **Dense base Layer**: The dense base layer was built dry in three sublayers, each densified using a plate compactor. Sand cone tests were performed to estimate relative density (D_r) of each sublayer (estimated at about 80 - 95 %). Post construction, this layer was saturated using a perforated piping system installed at the base of the laminar container with care in order to prevent soil disturbance.

ii. **Loose Middle Layer**: The 1.25 m liquefiable stratum was built using hydraulic pluviation to mimic the deposition of a loose young deposit (Dobry *et al.* 2010 and Whitman 1970). The sand was pluviated into the laminar container from a hopper through a number 6 sieve ensuring a clear water head of 0.25 m - 0.5 m, between the screen and the deposit. Estimated relative density (D_r) for this layer based on weight of the sand deposited was in the range of 35 – 44 %.

iii. **Top Crust**: The 0.64 m thick crust was built dry in two stages. An initial 0.24 m thick layer was deposited over the loose liquefiable strata, and the foundation was placed. Thereafter, the remaining 0.4 m layer was built around the foundation system. Upon construction, this crust

layer was in a moist state due to possible capillary action. The relative density of the top crust is estimated at about 50 – 55 % through sand cone tests.

iv. **Foundation System**: The foundation system (Figure 4.1b) consisted of a rigid concrete block of length 1.3 m, width 0.6 m and height 0.4 m, overlain by steel plates designed to produce a surcharge vertical pressure of 41.6 kPa. The concrete block (height of 0.4 m) was fully embedded into the crust.

A summary of properties of Ottawa F-65 sand and properties of the three-layered deposit is presented in Tables 4.1 and Table 4.2, respectively.

4.3.3 Polymer Remediation

The polyurethane (polymer) used in this study is a two-component chemically blown foam consisting of a curative phase (poly-isocyanate) and a resin phase (polyol), designated as EL077. Rapid polymerization occurs primarily due to two competing chemical reactions between the individual phases to form a cross-linked polyurethane which is then blown into a foam (Rao *et al.* 2017).

In this study, equal parts of both phases are mixed at a nominal temperature of 43°C and a controlled pressure of 5.5 MPa to produce the foam. The resulting structural foam has a free rise mass density of about 64 kg/m^3. Upon injection, the polymer used in this study has low viscosity and is specifically formulated for maximum permeation. Full details concerning the kinetics of the polymerization process are reported in Rao *et al.* 2017. Mechanical properties of the polymer used in this study are presented in Table 4.3.

In a preliminary testing phase based on volume replacement, the amount of polymer required to improve sand deposits of initial D_r = 35% to D_r = 80% was estimated. From this phase,

a volume replacement ratio of about 8% was recommended for the loose layer of this three-layered deposit.

4.3.4 Polymer Injection

In the polymer test (Figure 4.2a-b), 18 injection tubes of diameter 16 mm were inserted with relative ease into the soil using a small impact wrench (in about 1 hour). As shown in the figure, four tubes were also deployed at an angle from each lateral face of the foundation to its center. In this test, all tubes were inserted to a depth of 1.5 m into the model (0.9 m into the loose liquefiable layer). This target depth was selected to perform a bottom – up injection, close to the base of the liquefiable layer, thus allowing the polymer to spread throughout the loose layer as it permeates towards the soil surface.

At each injection point, a target injection volume was made a priori to achieve a relative density. On average, 21±11 kg of polymer was injected at each point. Significant variability within the amounts injected arises as lower volumes are required to cause refusal at points further from the first injection. In total, 327 kg of polymer in its liquid form was injected into the soil model.

Figure 4.3 presents the excess pore pressure response of the soil during the injection process. As seen in the figure, each injection resulted in the generation of excess pore pressure, followed by a dissipation phase, as the polymer mixes and expands, confirming that the injection process results in a partially drained type of soil response. As, such slight heave of the foundation (about 11 mm) and surrounding soil (about 50 mm) was observed (Figure 4.4)

4.4 Configuration of the Polymer-Sand Composite

Post shaking, the foundation was removed, and the model was carefully excavated to observe the distribution of the hardened polymer-sand composite formation within the treated ground (Figure 4.5). The final depth of permeation was observed between 1.60 m -1.65 m.

Several characteristic formations of the composite were observed within both the crust and the underlying loose layer. Within the loose layer, near the depth of injection (1.5m), a dense zone of the solidified polymer- sand composite around 100mm in thickness was observed. From this zone, veins of the polymer were seen to emanate into the upper strata, apparently oriented along the compliant longer direction of the laminar container as shown in Figure 4.5b. Such formations were also observed after polymer injection in the Avondale and Bexley red zone sites in New Zealand (Traylen *et al.* 2017), towards the direction of the lateral spread observed in the 2010-2011 Canterbury earthquake sequence.

During excavation, based on averaging slices of thicknesses of 100mm, a three-dimensional representative rendering was constructed to map the distribution of the polymer-sand composite (Figure 4.6). It is noted that this mesh does not represent thin isolated sections of the composite. However, salient aspects of its distribution were captured, including the dense zone observed at the depth of injection, veins/dykes in the loose layer and the overlying crust.

4.4.1 Polymer Characterization

Figure 4.7 presents cross-sections of the polymer-sand composite excavated from the upper crust and the liquefiable layer of the model. Within the composite, two distinct phases are observed.

i. **Solidified interface sand**: During injection, the polymer initially fractures through the soil model and then permeates into the sand. On curing, cementation occurs, and a portion of this sand mixes with the polymer and is hardened. This region is typically along the surface of the hardened composite.

ii. **Pure Polymer**: During the process of curing, the injected polymer expands from its initial liquid volume (based on the confinement). This leads to a separation of surfaces where zones

of the pure polymer are sandwiched between layers where soil cementation occurs, as seen in Figure 4.7.

Within the liquefiable sand, a dense zone of the polymer-sand composite was observed between a depth of 1.55 m - 1.65 m. Specimens of large densities were observed in this region, suggesting extensive permeation of the polymer within the sand layer. The formation can be attributed to the initial set time of the polymer, as the polymer could not permeate into deeper strata at a rate faster than the rate of curing. Further penetration could be attained, using either higher injection pressure or a polymer with a higher initial set time to attain higher permeation/mixing.

Within the crust, specimens of lower density are observed with thinner fractions of the polymer sand interface, suggesting a reduced extent of mixing and more expansion. The liquid polymer reaching the crust had significantly higher viscosity (hence slower flow) as compared to its initial liquid form, as the injected polymer started to harden. Thin interface zones with large zones of pure polymer were observed at shallow depths.

4.4.2 Model Characterization

Several techniques were used to characterize the soil deposit before injection, including relative density using sand cone tests, two cone penetration tests (CPT), and further, the weight/volume of the sand deposited (Figure 4.8a). The relative density (D_r) estimate from the sand cone tests and the weight of the sand deposited prior to injection is presented in Table 4.2. Cone Penetration tests (CPT) using a 15cm^2 piezocone were performed at two locations in the north and south parts of the laminar soil container pre-injection (Figure 4.8b). Upon fully curing of the polymer (72 hours post-injection), two CPT soundings were performed to obtain a measure of the soil properties after improvement. Post injection, the CPT's were performed only up to a

depth of about 1.55 m at both locations. As seen in Figure 4.6, a platform of the hardened polymer sand composite was obtained post-excavation throughout the area of the laminar soil container at a depth of 1.55 m - 1.65 m. Further investigation to deeper strata was restricted due to an uplifting tendency of the employed CPT rig.

From Figure 4.8b, clear improvement in the tip resistance is observed post remediation, particularly near the depth of injection. Prior to injection, the tip resistances in the liquefiable layer were recorded at around 0.18-0.3 MPa. Post improvement, values were recorded at 0.75-2.25 MPa at equivalent depths. According to Robertson and Wride (1998), the change in CPT values suggests about a fourfold increase in liquefaction triggering resistance of the initially loose liquefiable from a $CRR_{7.5}$ of 0.07 to a $CRR_{7.5}$ of 0.27. Specimens prior and post injection in the polymer test also compared reasonably well with the observed q_c values for a D_r of about 36 % and 79 % respectively (Dobry *et al.* 2019). Generally, higher values of the tip resistance and sleeve friction were in the southern CPT sounding, indicative of a higher level of soil improvement near this location. Figure 4.6 indicates that the composite polymer-sand formations were more prevalent and continuous in this vicinity.

The equivalent map presented in Figure 4.6, facilitated the estimation of the volume of the hardened composite (V_T) in each section. From each section, specimens of the hardened composite were obtained and their mass densities (ρ_T) were estimated (Figure 4.9). Furthermore, using estimates of the density of the pure polymer (ρ_P), and the solidified sand (ρ_S), it was possible to back-calculate the volume of pure polymer (V_P) and solidified sand at each section as.

$$\frac{V_{P,i}}{V_{T,i}} = \frac{\rho_{T,i} - \rho_{S,i}}{\rho_{P,i} - \rho_{S,i}}$$

where, $\rho_{T,i}$ is the measured density of hardened composite at section i, $\rho_{S,i}$ is the density of the solidified sand within the composite at section i (assumed between 1581 kg/m^3 to 1785

kg/m^3), $\rho_{P,i}$ is the density of the pure polymer within the composite at section i, (assumed to vary linearly between 405 kg/m^3 to 1530 kN/m^3), $V_{P,i}$ is the volume of pure polymer at section i, and $V_{T,i}$ is the estimated volume (using Figure 4.6) of the hardened polymer-sand composite at section i.

On this basis, assuming replacement occurs under constant volume, an estimate for the final relative density of the sand surrounding the composite inclusion is presented in Figure 4.9. Overall, these estimates suggest that the polymer expanded around 3 - 3.5 times its initial liquid volume within the soil mass.

4.5 Shake Table Testing

The baseline and polymer remediated models are both first subjected to a base excitation at a peak cyclic acceleration of 0.2 g (referred to as Shake01). The motion and its time-frequency spectra computed using the modified Stockwell transformation (George 2009 and Stockwell *et al.* 1996) are shown in Figure 4.10. This excitation was imparted 1.5 weeks after injection, with the polymer fully cured within the laminar soil container. After Shake01, with sufficient time allowed to assure full excess pore pressure dissipation, the baseline and polymer models were subjected to a further excitation at a peak cyclic acceleration of 0.4 g.

4.5.1 Excess Pore Pressure

Generally, in both the free-field (FF_i) and below foundation (FD_i) sensors, substantial excess pore pressure generation indicative of initial liquefaction was observed in the baseline test (Jahed Orang *et al.* 2020) as compared to its polymer remediated counterpart (Figure 4.11). Within the loose layer (FF_3, FF_2), soil reached initial liquefaction, within 1-2 cycles of strong shaking in the baseline test, whereas the polymer model achieves its maximum pore pressure response (below the value for initial liquefaction) after about 12 seconds (15-17 cycles) of shaking. Stronger dilative

tendency of the sand was also observed through transient drops in the free-field pore pressure transducers (FF_3) in the polymer test, indicative of the densification post injection.

The soil above the injection depth improved due to the injection and expansion of the polymer, and subsequently did not develop did not develop significant pore pressures as seen in sensors FF_{1-3} and FD_3 in the polymer test. However, significant excess pore pressure did eventually develop below the depth of injection, due to the upper layers effectively performing as a denser non-liquefiable layer increasing the shear demand on lower layers. Pore pressure response during Shake02 is presented in Figure 4.12.

4.5.2 Foundation and Soil Acceleration

Figure 4.13 displays a comparison between the recorded accelerations of the two test models during Shake01 for the free-field and under foundation arrays. All acceleration records presented here were filtered using a zero phase lowpass fourth order Butterworth with a cutoff of 15 Hz. In general, a significant reduction in the foundation and ground accelerations were observed in the baseline test as compared to the polymer test in both free-field and under foundation accelerometers. The ability of the soil to transfer high-frequency content is significantly reduced in the baseline model. This may be attributed to the extensive softening of the soil within the first few cycles of shaking in the baseline test.

In the polymer test, much higher acceleration values were transmitted to upper strata, indicative of the retention of soil stiffness for a much longer duration. After about 12 seconds of strong shaking (15-17 cycles), the acceleration response of the foundation (FF_1) in the polymer test indicated considerable period elongation, though higher in amplitude as compared to the baseline. The presence of the dense polymer-sand composite between 1.55 - 1.65 m was evidently visible in the acceleration response of the system Accelerometers (AF_4 and AD_4). showed a smaller

response in the polymer test as compared to the baseline indicative of the considerable shearing that occurred in the sand below the depth of injection and corroborating with the higher excess pore pressures generated at the same location.

As seen from Figure 4.14, a clear indication of de-amplification is observed in the baseline test in the 5 % damped acceleration response spectra. The de-amplified acceleration response in the baseline test is indicative of the reduction in the ability of the soil to transfer shear due to the significant degradation in stiffness that occurs post liquefaction. In the polymer remediated test, though the ability of the soil to effectively transmit high-frequency content does decrease, the time to effectively soften the response (time for initial liquefaction) is much slower as compared to the baseline test model. Soil accelerations at various depths during Shake02 is presented in Figure 4.15.

4.5.3 Soil Shear Stress-Strain

A second-order approach as proposed by Zeghal and Elgamal (1994) is used to estimate the shear stress/strain response of both experiments. The shear strain in the direction of shaking is estimated through the displacement transducers mounted on the laminates (Figure 4.16a and Figure 4.16b for Shake01 and Shake02 respectively). Further, these transducers are used to estimate the relative displacement and subsequently relative acceleration response at the location of each transducer. These acceleration histories are then used to estimate the shear stresses. Figures 4.17a and 4.17b present the calculated shear stress-shear strain loops during Shake01 and Shake02, respectively.

Salient response mechanisms contributing to the observations during Shake01 can be clearly observed in Figure 4.18, where the shear stress strain curves are plotted at two locations within the liquefiable and dense layers for the Baseline and Polymer tests. Similar curves at the

identical locations for Shake02 are presented in Figure 4.19. In the baseline test, significant softening of the system response is seen to occur within the first few cycles of shaking, corroborating with rapid rise in excess pore pressures seen in Figure 4.11. However, in the polymer experiment, soil softening occurs post 17-18 cycles of shaking in the denser stratum, while much less degradation is seen in the loose liquefiable layer indicative of the stiffer response of the soil after improvement. It is noted that kinematic constraints due to the shape of the polymer within the laminar soil container could play a major role in observed response in the liquefiable layer and pinning effects are observed, through which the remediated model develops lesser permanent shear strains, within the loose liquefiable layer.

Clear evidence of system response of the soil deposit can be observed from Figure 4.18, in both the polymer and baseline test models. Within the liquefiable layer in the baseline model, significant vertical continuity exists allowing for pore pressure redistribution, without any permeability contrasts. As pore pressure starts approaching initial liquefaction within the upper layers of the deposit, the ability of the layers to transmit shear stresses to deeper strata decreases. In the remediated test, the soil within the loose liquefiable layer retains sufficient stiffness during shaking and the deposit can effectively transmit higher shear stresses to lower strata as seen in Figure 4.18 and Figure 4.19.

4.5.4 Foundation and Soil Settlement

In the baseline experiment, as noted by (Jahed Orang *et al.* 2020) a local shear failure occurs in the foundation system resulting in the foundation punching through the soil. Post injection, a significant reduction in the liquefaction induced foundation settlement, tilt and free-field settlements was observed during Shake01 as seen in Figure 4.20 and Figure 4.21, respectively. Upon initial liquefaction, the loss of ground stiffness and strength is visible with a

reduction in the ability of the foundation system to undergo cyclic loading. Similar trends are observed for Shake02 and are presented in Figure 4.22 and Figure 4.23.

The soil structure interaction induced ratcheting mechanism (Dashti *et al.* 2010) is much more pronounced in the polymer remediated experiment indicative through the out of phase behavior in the cyclic response of displacement transducers on the foundation oriented along the shaking direction. In the baseline experiment, post liquefaction, a much-reduced tendency of cyclic ratcheting is observed, due to the loss of ground stiffness. Extensive tilts of the order of 1/60 rad are observed in the shaking direction and transverse directions respectively in the baseline experiment higher than the 1/300 rad prescribed in standard design codes (JGS 1996 and DFI 2013). In the polymer remediated model, tilts of the order of 1/350 rad are observed.

Heaving of the soil surface is observed in the baseline test, indicative of the local shear failure of the foundation system. In the polymer test factors contributing to the arrest of these primary settlement mechanisms are observed in greater detail after the excavation. As injection tubes were deployed at angles around the foundation, the presence of clear load paths, capable of transmitting the foundation load to deeper strata, once the soil beneath the foundation softened during shaking, were observed. Further evidence to the hypothesis that the foundation was supported on the composite is seen from Figure 4.24 and Figure 4.25, where the recorded free field and foundation settlement during Shake01 and Shake02 is presented for the polymer remediated model. The foundation and free field settlements are in phase during shaking till 8-9 s. However, after 9 s, during each cycle, the free field soil settlement is significantly higher than the settlement of the foundation, indicating that the foundation was supported vertically.

Post Shake01, the model is subjected to a further excitation, at a peak cyclic acceleration of 0.4 g, termed Shake02. Foundation settlement and rotation response of the baseline and polymer

remediated models post the second shake are presented in Figure 4.20 and Figure 4.21. This event manifested extensive liquefaction induced damage in the baseline experiment resulting in a cumulative settlement of about 660 mm compared to 27 mm of settlement in the polymer remediated model. The deformed configurations of the soil-foundation system in the Baseline and Polymer tests pre and post Shake02 are presented in Figure 4.26 and Figure 4.27.

4.6 Discussion

4.6.1 Ground Improvement Mechanisms

The ability to tailor polymers to a specific site condition offers significant advantages in the context of liquefaction mitigation. In this section, insight is provided into the characteristics of the polymer-sand composite and a few considerations towards the selection of polymers are discussed, which can be useful in adoption to field practice.

The degree of cementation and expansion is dependent on several factors including confinement, permeability of the sand, and initial viscosity of the polymer in its liquid form. In the context of liquefaction remediation, various mechanisms contribute to the increased liquefaction resistance after polymer injection including densification, soil cementation, polymer expansion and increased lateral earth pressure post expansion. The primary mechanism involved in soil improvement is densification and therefore the methodology seems to be best suited for non-cohesive granular soils with low silt/clay fractions. It is noted that a careful balance must be made between the initial viscosity of the polymer and its gel time, depending on the soil fabric and the required strategy of improvement. If the initial viscosity is low and gel time is large, the behavior is similar to stabilizer materials such as colloidal silica (Gallagher and Mitchell, 2002). However, unlike stabilizers, the polymer injection offers additional advantages due to its rapid expansion and increase in the lateral earth pressure.

The strategy for polymer selection should include the confinement involved at the depth of treatment. At deeper strata, remediation through aggressive expansion of the polymer would be restricted. However, cementation and the addition of shear reinforcement to the soil through the composite polymer-sand formations would provide additional resistance to soil liquefaction and subsequent consequences.

Further, in interbedded deposits, with thin zones of liquefaction susceptible soil at large depths, soil liquefaction and consequent loss of strength and stiffness inhibit the ability of the deposit to effectively transmit shear strain to upper strata. Such a layer of soil, if continuous, on the onset of liquefaction acts as a natural isolation system (Cubrinovski *et al.* 2019). Such effects may be beneficial in selecting the extent of ground remediation required, where a strategy of allowing a portion of the deposit to liquefy may be beneficial. A holistic design approach is however then required to reduce both the kinematic and inertial demands on the supporting structure.

4.6.2 Limitations of the current study

This experimental program is subjected to several limitations including:

1. The confinements offered by the laminar soil box are effective in studying issues involving shallow liquefaction.
2. The foundation system and surcharge were considered rigid in this study and may be subjected to increased demands if it were made flexible.
3. Polymer injection was performed only at one specified depth in this study.
4. Sides of the laminar soil container may provide additional shear resistance in the vertical direction along the boundary of the model.

5. The laminar soil container is designed for uniaxial shaking, however, due to asymmetry arising from the geometry of the polymer, slight torsional response observed.

4.7 Conclusions

Results from a two-stage shake table testing program to assess the potential of polymer injection technique as a countermeasure for liquefaction induced foundation settlement are presented. The test models consisted of a shallow foundation with a surcharge pressure seated on a three-layered liquefiable soil deposit. In the test series, the system response was studied first without (baseline test), and subsequently with the expansive polymer injected into the liquefiable stratum under identical base excitation.

1. From the investigation, extensive soil liquefaction and associated consequences were observed in the baseline test. A significant reduction in the foundation settlement was observed in the polymer remediated test compared to the baseline experiment.
2. A marked increase is observed in the soil resistance to liquefaction due to cementation and additional lateral confinement provided by the expansive polymer, after permeation. Such tendencies were evident with the CPT performed after injection and the slow rise in excess pore pressure and retention of soil stiffness observed in the polymer remediated test as compared to its baseline counterpart.
3. System performance was highlighted whereby improvement of the liquefiable layer was shown to increase shear demands on the underlying dense layer. Further, ground improvement increased the acceleration demands on the foundation system.
4. Channels of the composite polymer sand formations were observed to transmit foundation loads to deeper strata. Such shear reinforcement provides additional stiffness to loose liquefiable sites, reducing the shear transmitted to the in-situ soil.

5. Distinct phases of the polymer-sand composite were observed including a pure polymer phase sandwiched by phases of mixed sand as a result of the expansion of the polymer.
6. Due to ease of deployment in dense urban environments and the ability to tailor polymers to the requirements of each project, the polymer injection remediation measure shows considerable promise.

As such, this testing program demonstrated the potential of the polymer injection technique as a countermeasure against liquefaction induced settlement. Further efforts to establish routine analysis and design guidelines to adopt the methodology to conventional design practice are required. Additional testing to study the efficacy of the remediation measure for liquefaction induced lateral spreading effects are warranted.

4.8 Acknowledgement

Chapter 4, in part, is a reprint of the material as it appears in a forthcoming article: Prabhakaran, A., Kim, K., Orang, M. J., Qiu, Z., Ebeido, A., Zayed, M., Boushehri, R., Motamed, R., Elgamal, A., and Frazao, C. *Forthcoming*. "Polymer Injection and Liquefaction-Induced Foundation Settlement Mitigation: a Shake Table Testing Investigation". *Journal of Geotechnical and Geoenvironmental Engineering*, ASCE. The dissertation author was the primary investigator and author.

Chapter 4, in part, is a reprint of the material as it appears in the article: Prabhakaran, A., Kim, K., Orang, M. J., Qiu, Z., Ebeido, A., Zayed, M., Boushehri, R., Motamed, R., Elgamal, A., and Frazao, C. (2020). "Polymer Injection and Liquefaction-Induced Foundation Settlement: A Shake Table Test Investigation." *ASCE Geo-Congress 2020*, American Society of Civil Engineers, Minneapolis, MN. The dissertation author was the primary investigator and author.

4.9 References

Adalier, K., Elgamal, A.-W., and Martin, G. R. (1998). "Foundation Liquefaction Countermeasures for Earth Embankments." *Journal of Geotechnical and Geoenvironmental Engineering*, ASCE, 124(6), 500–517.

Ashford, S. A., Boulanger, R. W., Donahue, J. L., and Stewart, J. P. (2011). "Geotechnical Quick Report on the Kanto Plain Region during the March 11, 2011, Off Pacific Coast of Tohoku Earthquake, Japan." *Geotechnical Extreme Events Reconnaissance*, GEER-025a(April), 1–20.

Ashford, S. A., and Jakrapiyanun, W. (2001). *Design and verification of the UCSD laminar container (SSRP282 2001/07)*. La Jolla, CA.

Van Ballegooy, S., Williams, K., Fairclough, T., Phillips, R., Hunter, R., Coe, T., Stretton, M., Wynyard, T., and Walsh, J. (2016). *Residential Ground Improvement Findings from trials to manage liquefaction vulnerability*.

Cubrinovski, M. (2013). "Liquefaction-Induced Damage in The2010-2011 Christchurch (New Zealand) Earthquakes." *International Conference on Case Histories in Geotechnical Engineering*, Missouri University of Science and Technology, Chicago, Illinois.

Cubrinovski, M., Green, R. A., Allen, J., Ashford, S., Bowman, E., Brendon, Bradley, Cox, B., Hutchinson, T., Kavazanjian, E., Orense, R., Pender, M., Quigley, M., and Wotherspoon, L. (2010). "Geotechnical reconnaissance of the 2010 Darfield (Canterbury) earthquake." *Bulletin of the New Zealand Society for Earthquake Engineering*, 43(4), 243–320.

Dashti, S., Bray, J. D., Pestana, J. M., Riemer, M., and Wilson, D. (2010). "Mechanisms of seismically induced settlement of buildings with shallow foundations on liquefiable soil." *Journal of Geotechnical and Geoenvironmental Engineering*, American Society of Civil Engineers, 136(1), 151–164.

Dobry, R., Thevanayagam, S., El-Sekelly, W., Abdoun, T., and Huang, Q. (2019). "Large-Scale Modeling of Preshaking Effect on Liquefaction Resistance, Shear Wave Velocity, and CPT Tip Resistance of Clean Sand." *Journal of Geotechnical and Geoenvironmental Engineering*, American Society of Civil Engineers (ASCE), 145(10).

Dobry, R., Thevanayagam, S., Medina, C., Bethapudi, R., Elgamal, A., Bennett, V., Abdoun, T., Zeghal, M., El Shamy, U., and Mercado, V. M. (2010). "Mechanics of lateral spreading observed in a full-scale shake test." *Journal of Geotechnical and Geoenvironmental Engineering*, American Society of Civil Engineers, 137(2), 115–129.

EagleLift (2018). Personal Communication.

Ebeido, A. (2019). "Lateral-Spreading Effects on Pile Foundations: Large-scale Testing and Analysis." *PhD Thesis*, University of California San Diego

EERI. (2000). “Damage Patterns and Foundation Performance in Adapazari.” *Earthquake Spectra*, 16(SUPPL. A), 163–188.

Erdemgil, M., Sağlam, S., and Bakır, B. S. (2007). “Utilization of Highly Expansive Polymer Injection to Mitigate Seismic Foundation Failure for Existing Structures.” *8th Pacific Conference on Earthquake Engineering*, Singapore.

George, N. V. (2009). “S Transform: Time Frequency Analysis and Filtering.” National Institute of Technology , Rourkela.

Ground Improvement Committee. (2013). “Commentary on the Selection, Design and Specification of Ground Improvement for Mitigation of Earthquake-Induced Liquefaction.” *DFI Journal - The Journal of the Deep Foundations Institute*, Informa UK Limited, 7(1), 3–12.

Hamada, M., Isoyama, R., and Wakamatsu, K. (1996). “Liquefaction-induced ground displacement and its related damage to lifeline facilities.” *Soils and Foundations*, Japanese Soc of Soil Mechanics & Foundation Engineering, 36(Special), 81–97.

Iai, S. (2005). “Remediation of liquefiable soils for port structures in japan — analysis, design and performance.” *Journal of Earthquake Engineering*, Taylor & Francis Group , 9, 77–103.

Ishihara, K., and Koga, Y. (1981). “Case Studies of Liquefaction in the 1964 Niigata Earthquake.” *Soils and Foundations*, Elsevier BV, 21(3), 35–52.

Jahed Orang, M., Motamed, R., Prabhakaran, A., and Elgamal, A. (2020). “Large-scale shake table test on a shallow foundation in liquefied soils (in Review).” *Journal of Geotechnical & Geoenvironmental Engineering*.

Jain, S. K., Lettis, W. R., Murty, C. V. R., and Bardet, J.-P. (2002). “Bhuj, India Earthquake of January 26, 2001 Reconnaissance Report.” *Earthquake Spectra*, SAGE Publications, 18(1_suppl), 1–4.

Japanese Geotechnical Society (JGS). (1996). *Remedial measures against soil liquefaction*. Rotterdam, the Netherlands.

Kim, T. R., Shin, J. K., Goh, T. S., Kim, H. S., Lee, J. S., and Lee, C. S. (2017). “Modeling of elasto-viscoplastic behavior for polyurethane foam under various strain rates and temperatures.” *Composite Structures*, Elsevier Ltd, 180, 686–695.

Law, H. K., and Lam, I. P. (2001). “Application of Periodic Boundary for Large Pile Group.” *Journal of Geotechnical and Geoenvironmental Engineering*, American Society of Civil Engineers, 127(10), 889–892.

Lee, K. S., Choi, J. Il, Kim, S. K., Lee, B. K., Hwang, J. S., and Lee, B. Y. (2017a). “Damping and mechanical properties of composite composed of polyurethane matrix and preplaced aggregates.” *Construction and Building Materials*, Elsevier Ltd, 145, 68–75.

Lee, S. H., Lee, S. J., Park, J. G., and Choi, Y. T. (2017b). "An experimental study on the characteristics of polyurethane-mixed coarse aggregates by large-scale triaxial test." *Construction and Building Materials*, Elsevier Ltd, 145, 117–125.

Liu, K., Li, Y., Wang, F., Xie, H., Pang, H., and Bai, H. (2019). "Analytical and Model Studies on Behavior of Rigid Polyurethane Composite Aggregate under Compression." *Journal of Materials in Civil Engineering*, American Society of Civil Engineers (ASCE), 31(3).

Magenes, G. (1989). "Design, analysis and calibration of the UCSD shake table." University of California San Diego.

Maher, M. H., Ro, K. S., and Welsh, J. P. (1994). "High strain dynamic modulus and damping of chemically grouted sand." *Soil Dynamics and Earthquake Engineering*, Elsevier, 13(2), 131–138.

Motamed, R., Orang, M. J., Parayancode, A., and Elgamal, A. (2020). "Results of a Class C Blind Prediction Competition on the Numerical Simulation of a Large-Scale Liquefaction Shaking Table Test." *ASCE Geo-Congress 2020*, American Society of Civil Engineers (ASCE), 334–342.

Parra Bastidas, A. M. (2016). "Ottawa F-65 Sand Characterization." University of California Davis.

Prabhakaran, A., Kyungtae, K., Ebeido, A., Jahed Orang, M., Motamed, R., Elgamal, A., and Frazao, C. (2021). "Polymer injection and associated site liquefaction remediation mechanisms." *17th World Conference on Earthquake Engineering*, Sendai, Japan.

Rao, R. R., Mondy, L. A., Long, K. N., Celina, M. C., Wyatt, N., Roberts, C. C., Soehnel, M. M., and Brunini, V. E. (2017). "The kinetics of polyurethane structural foam formation: Foaming and polymerization." *AIChE Journal*, John Wiley and Sons Inc., 63(7), 2945–2957.

Robertson, P. K., and Wride, C. E. (1998). "Evaluating cyclic liquefaction potential using the cone penetration test." *Canadian Geotechnical Journal*, National Research Council of Canada, 35(3), 442–459.

Shigang, A., Liqun, T., Yiqi, M., Yongmao, P., Yiping, L., and Daining, F. (2013). "Effect of aggregate distribution and shape on failure behavior of polyurethane polymer concrete under tension." *Computational Materials Science*, Elsevier, 67, 133–139.

Stockwell, R. G., Mansinha, L., and Lowe, R. P. (1996). "Localization of the complex spectrum: the s transform." *IEEE Transactions on Signal Processing*, 44(4), 998–2001.

Trautner, C., Zheng, Y., McCartney, J. S., and Hutchinson, T. (2018). "An approach for shake table performance evaluation during repair and retrofit actions." *Earthquake Engineering & Structural Dynamics*, John Wiley and Sons Ltd, 47(1), 131–146.

Traylen, N. J., Van Ballegooy, S., and Wentz, R. (2016). "Liquefaction Mitigation beneath Existing Structures Using Polyurethane Grout Injection." *NZSEE Conference*, Christchurch.

Traylen, N. J., Wentz, R., Van Ballegooy, S., Hnat, T., and Wotherspoon, L. M. (2017). "Research Results from a Study into Resin Injection for Liquefaction Mitigation 2017 NZSEE Conference." *NZSEE Conference*, Wellington.

Whitman, R. V. (1970). "Hydraulic Fills to Support Structural Loads." *Journal of the Soil Mechanics and Foundations Division*, 96(1), 23–47.

Yamazaki, H., Hayashi, K., and Zen K. (2005). "New liquefaction countermeasure based on pore water replacement." *16th International Conference on Soil Mechanics and Geotechnical Engineering*, Osaka, 2741–2744.

Yasuda, S., and Harada, K. (2014). "Measures developed in Japan after the 1964 Niigata earthquake to counter the liquefaction of soil." *Tenth U.S. National Conference on Earthquake Engineering* , Earthquake Engineering Research Institute, Anchorage.

Zayed, M. (2020). "Large-Scale Seismic Response of Ground and Ground-Structure Systems." University of California San Diego.

Zeghal, M., and Elgamal, A. (1994). "Analysis of Site Liquefaction Using Earthquake Records." *Journal of Geotechnical Engineering*, American Society of Civil Engineers, 120(6), 996–1017.

4.10 Tables and Figures

Table 4.1. Basic Geotechnical Properties of Ottawa F-65 Sand

Specific Gravity	2.65
Maximum Void Ratio (e_{max})	0.853
Minimum Void Ratio (e_{min})	0.503
Coefficient of uniformity (C_u)	1.61
Coefficient of curvature (C_c)	0.96
Maximum and minimum voids ratio (e_{max}, e_{min})	0.853, 0.503
Maximum and minimum mass density ρ_{min}, ρ_{max} (kg/m^3)	1446, 1759
Coefficient of uniformity (C_u)	1.61

Table 4.2. Soil properties of three-layered model prior to injection

Property	**Crust layer**	**Liquefiable layer**	**Base layer**
Water/soil condition	Moist	Saturated	Saturated
Depth (m)	0-0.64	0.64-1.9	1.9-2.9
Thickness (m)	0.64	1.26	1.0
Estimated D_r (%)	50%-55%	35%-44%	80 – 95%

Table 4.3. Mechanical Properties of Pure Polymer (EagleLift, 2018)

Density (kg/m^3) (ASTM D-1622)	64-320
Compressive Strength (kPa) (ASTM D-1621)	550-689
Tensile Strength (kPa) (ASTM D-1623)	689-827
Shear Strength (kPa) (ASTM C273)	620
Flexural Strength (kPa) (ASTM D790)	2668
Water Absorption (kg/m^2) (ASTM D-2842)	0.2
Rise Time (s)	15-90

a

b

Figure 4.1. Laminar soil container at the Powell structural engineering laboratories at UC San Diego: (a) Side view, and (b) Foundation and soil model prior to experiment

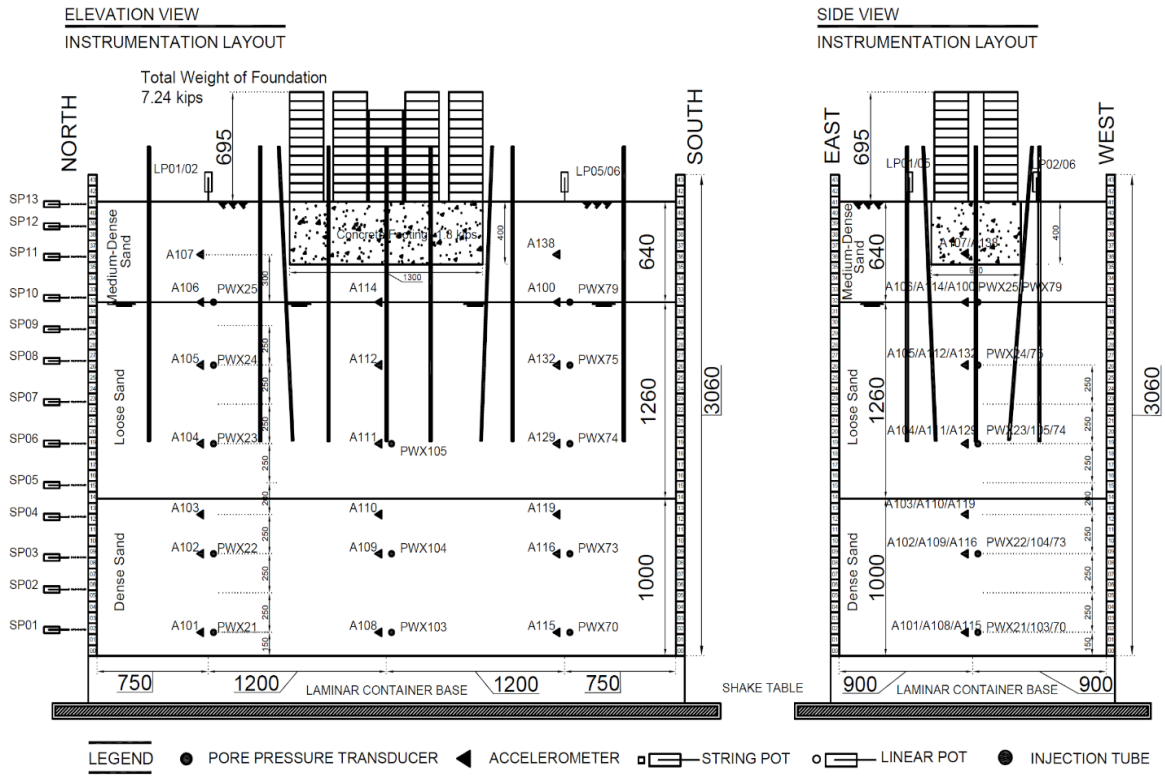

(a)

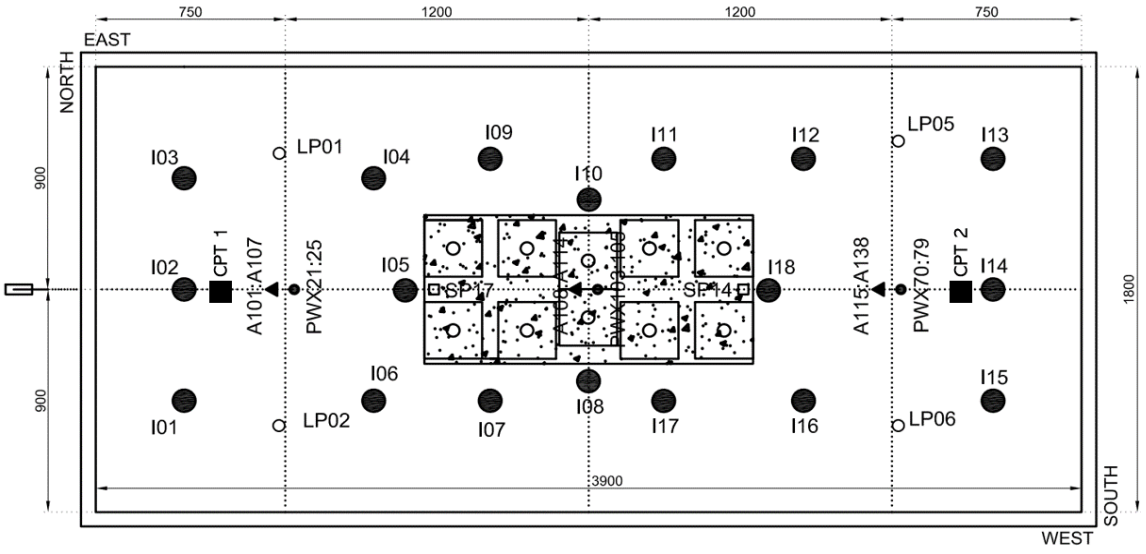

(b)

Figure 4.2. Instrumentation layout: (a) Elevation and side view, (b) Plan view depicting polymer injection locations (All units in mm)

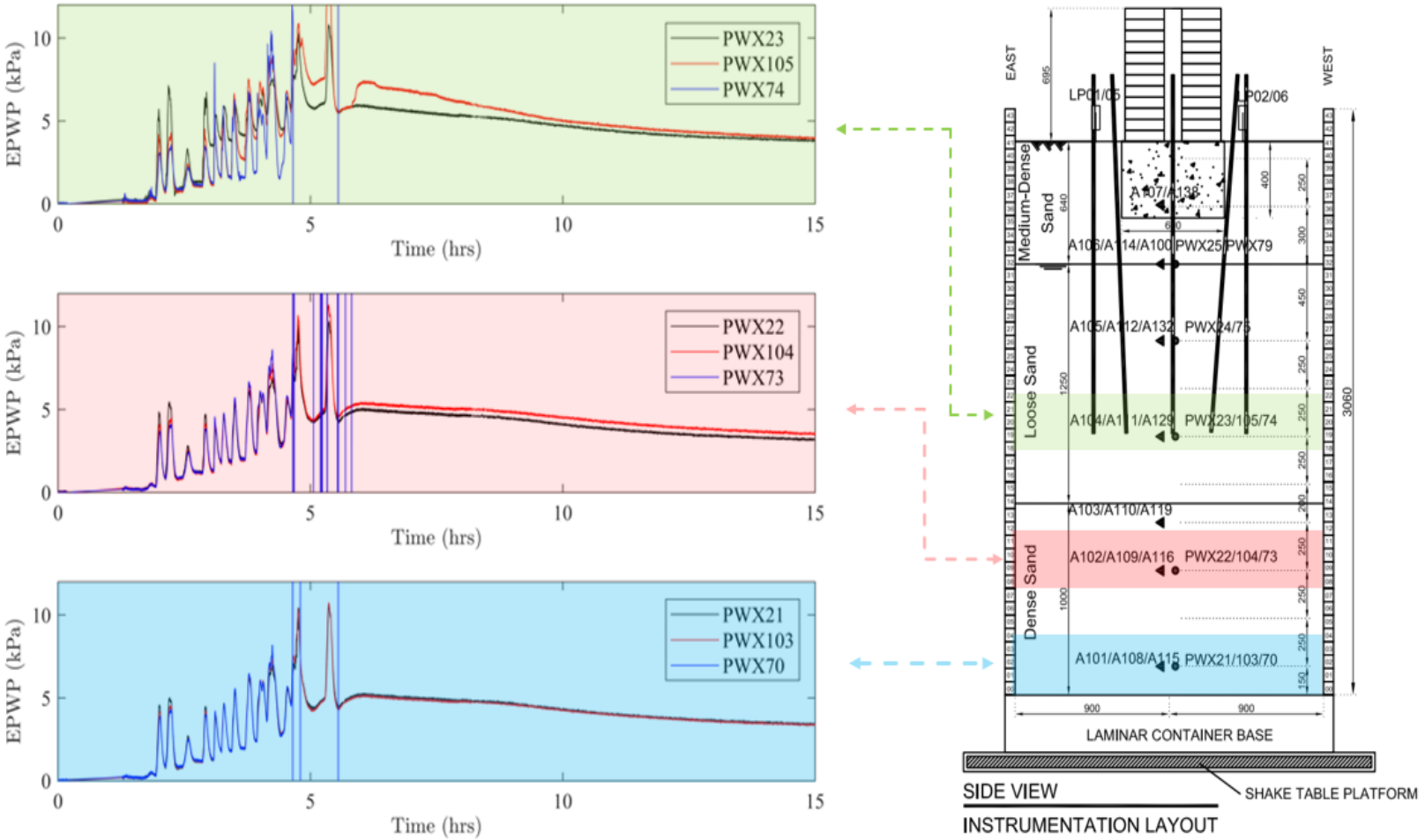

Figure 4.3. Recorded excess pore pressure rise during the injection process

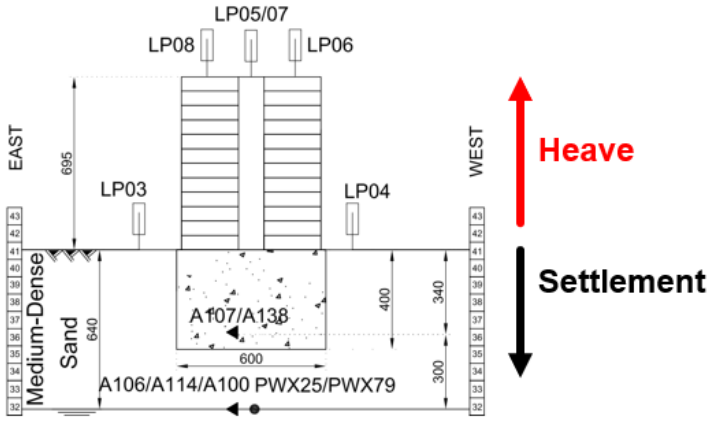

(a) Layout of displacement sensors

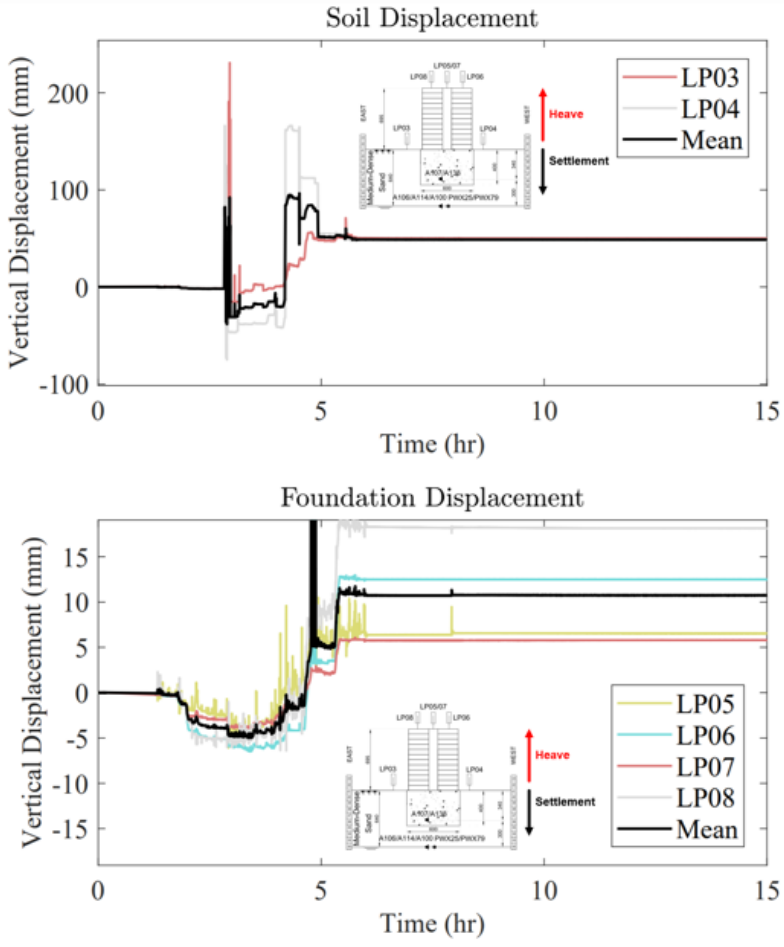

(b) Observed displacement response of foundation and surrounding soil during injection

Figure 4.4. Recorded excess pore pressure rise during the injection process

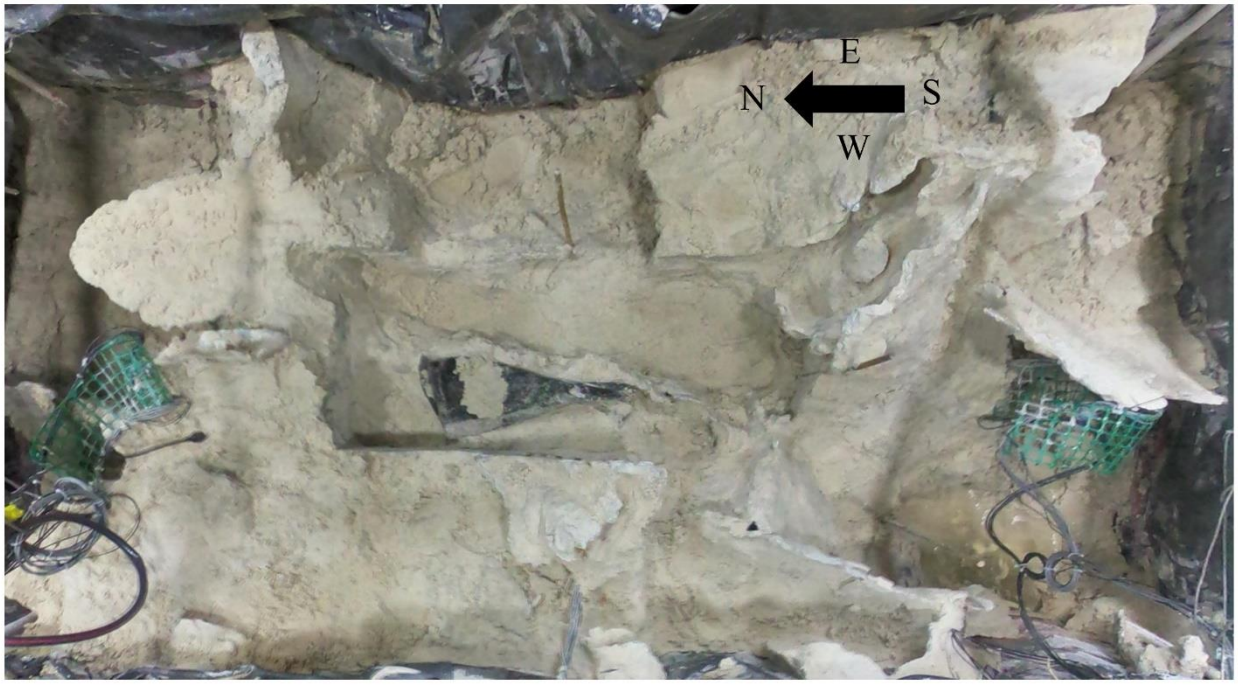

(a)

(b)

Figure 4.5. View of hardened polymer composite: (a) in crust and below foundation, (b) in liquefiable layer (c) perspective view in liquefiable layer

(c)

Figure 4.5 (continued). View of hardened polymer composite: (a) in crust and below foundation, (b) in liquefiable layer (c) perspective view in liquefiable layer

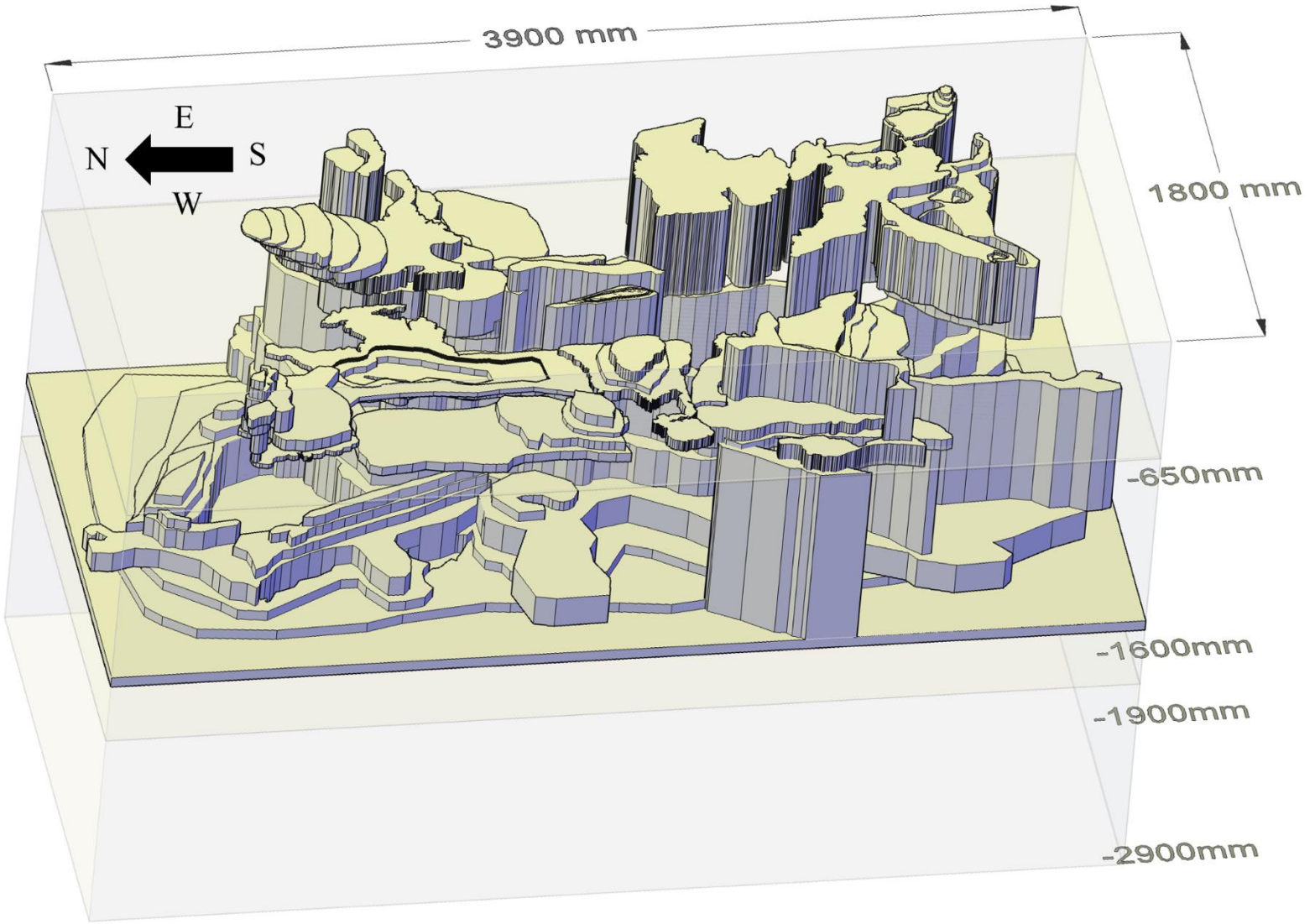

Figure 4.6. Mapped configuration of the polymer-sand composite

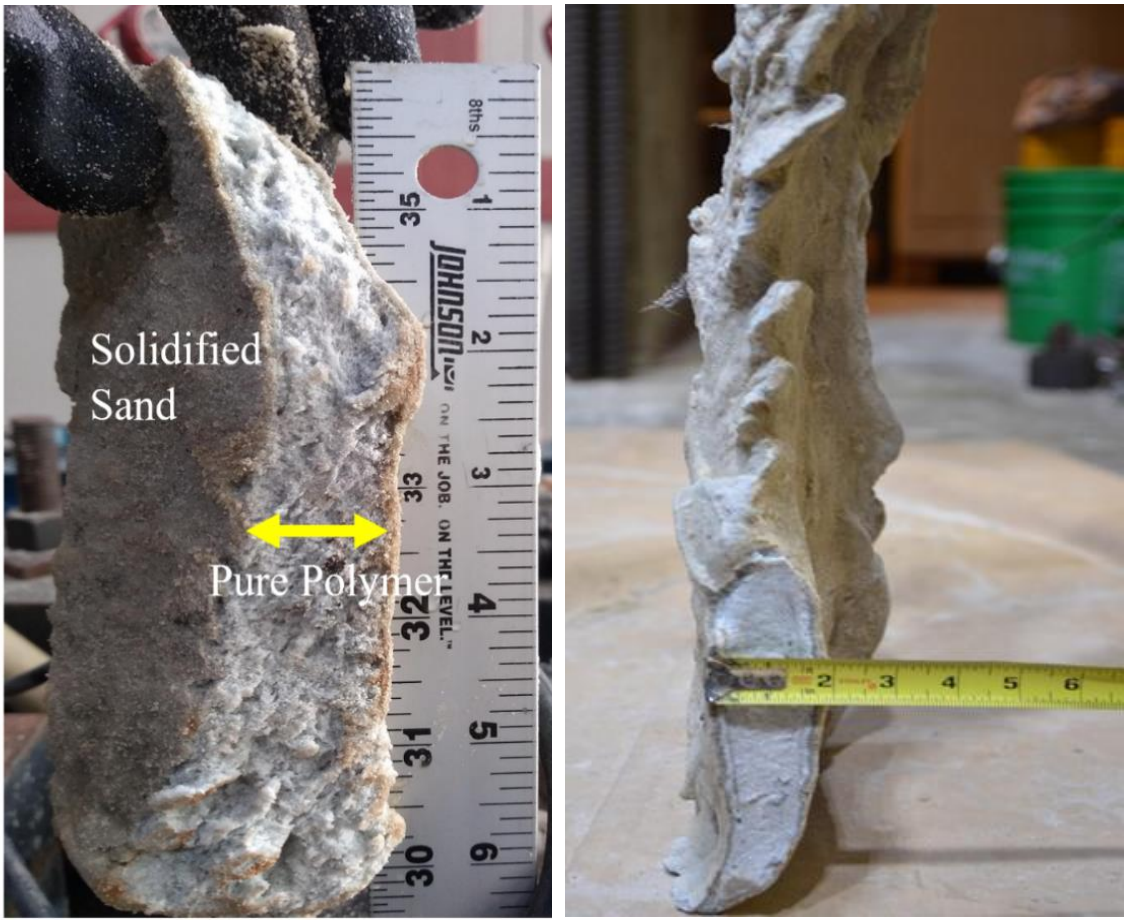

(a) (b)

Figure 4.7. Typical Cross-section of the hardened composite in the (a) crust and (b) liquefied layer

(a) Cone penetration test setup on top of the laminar soil container

Figure 4.8. Cone penetration test (a) rig and (b) soundings for model characterization

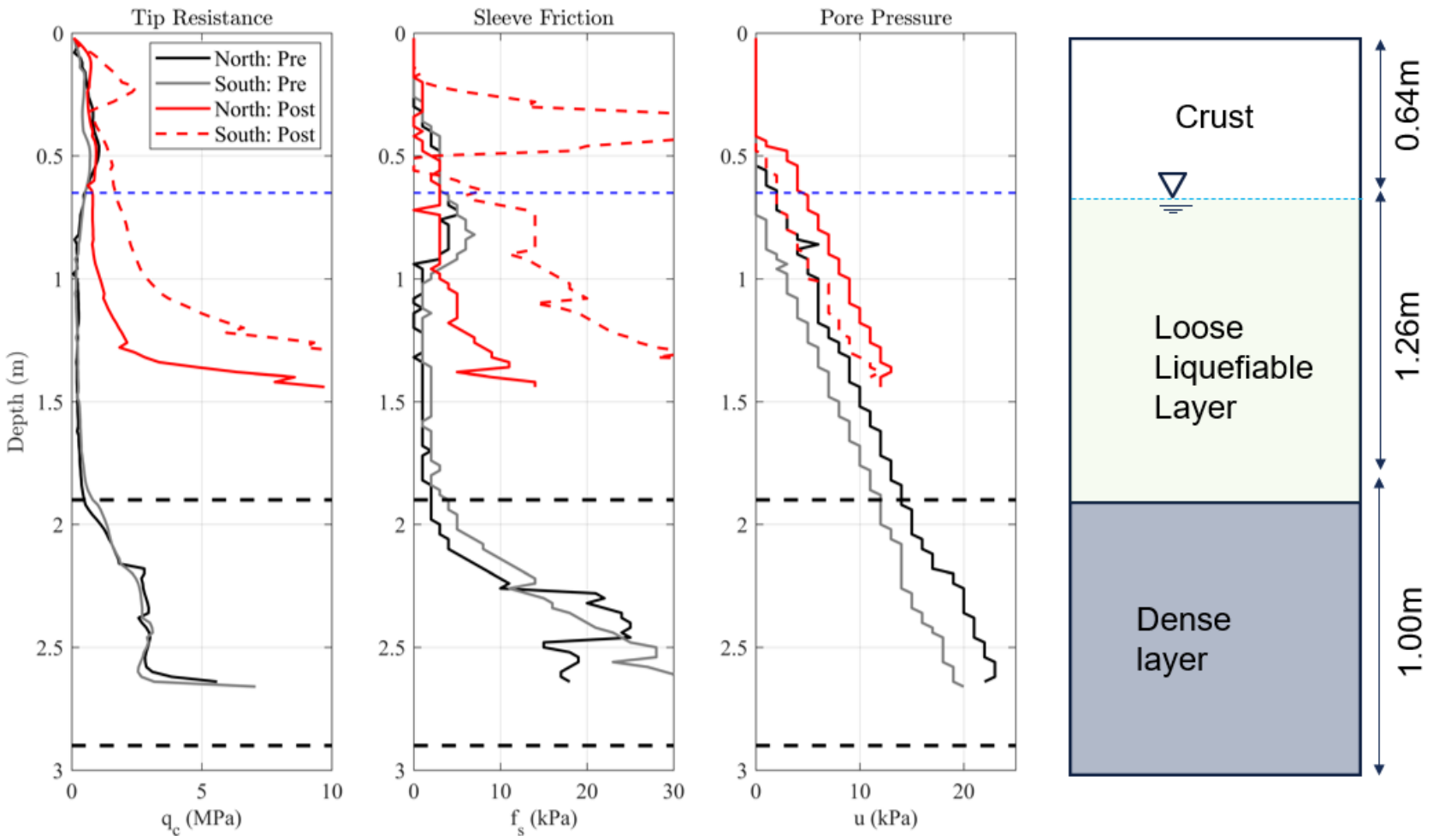

(b) Recorded CPT tip resistance, sleeve friction and pore pressure at cone tip pre and post injection

Figure 4.8 (continued). Cone penetration test (a) rig and (b) soundings for model characterization

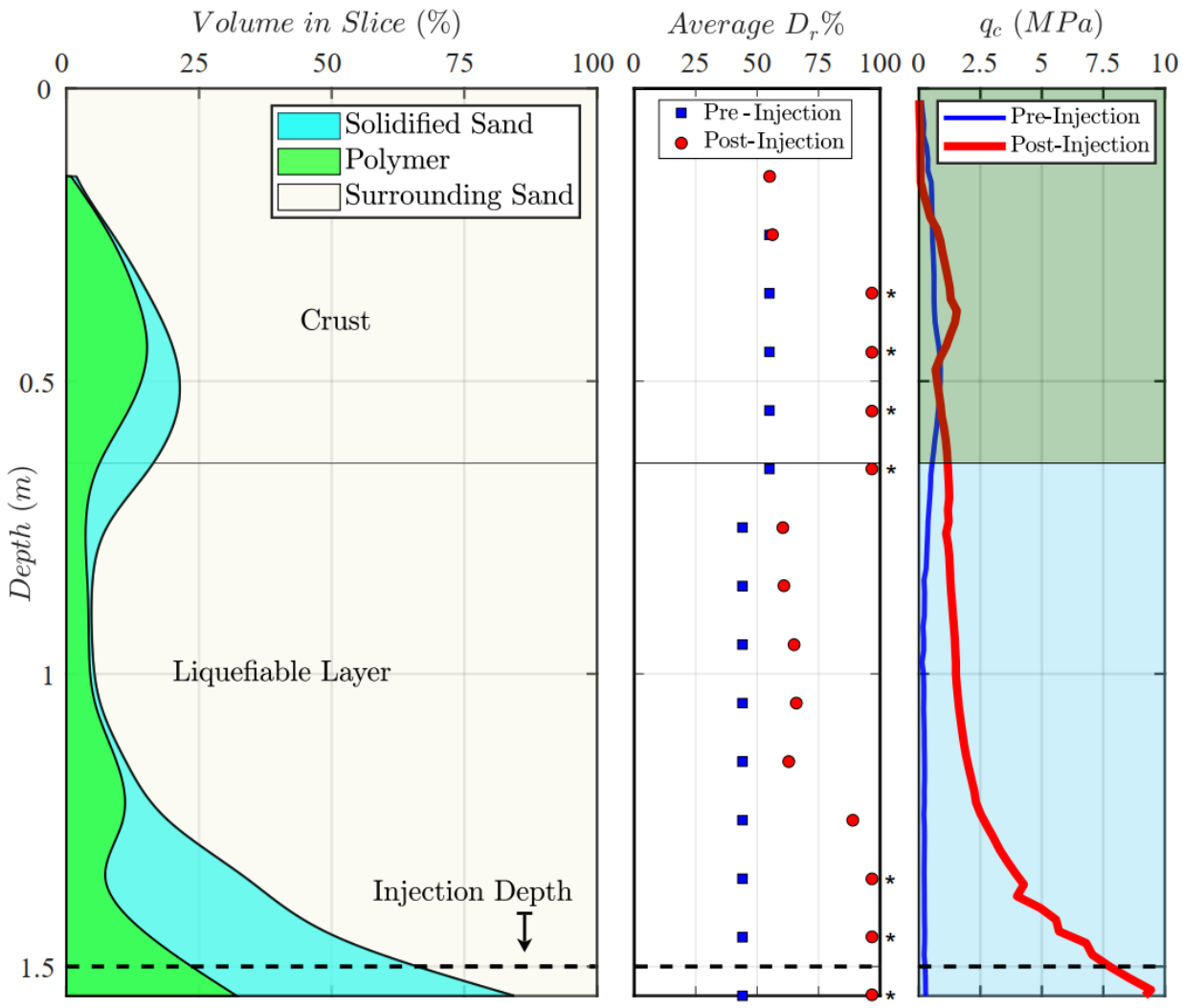

Figure 4.9. Estimation of percent volume of the solidified polymer sand composite, pure polymer within composite, and relative density of surrounding sand at different depths

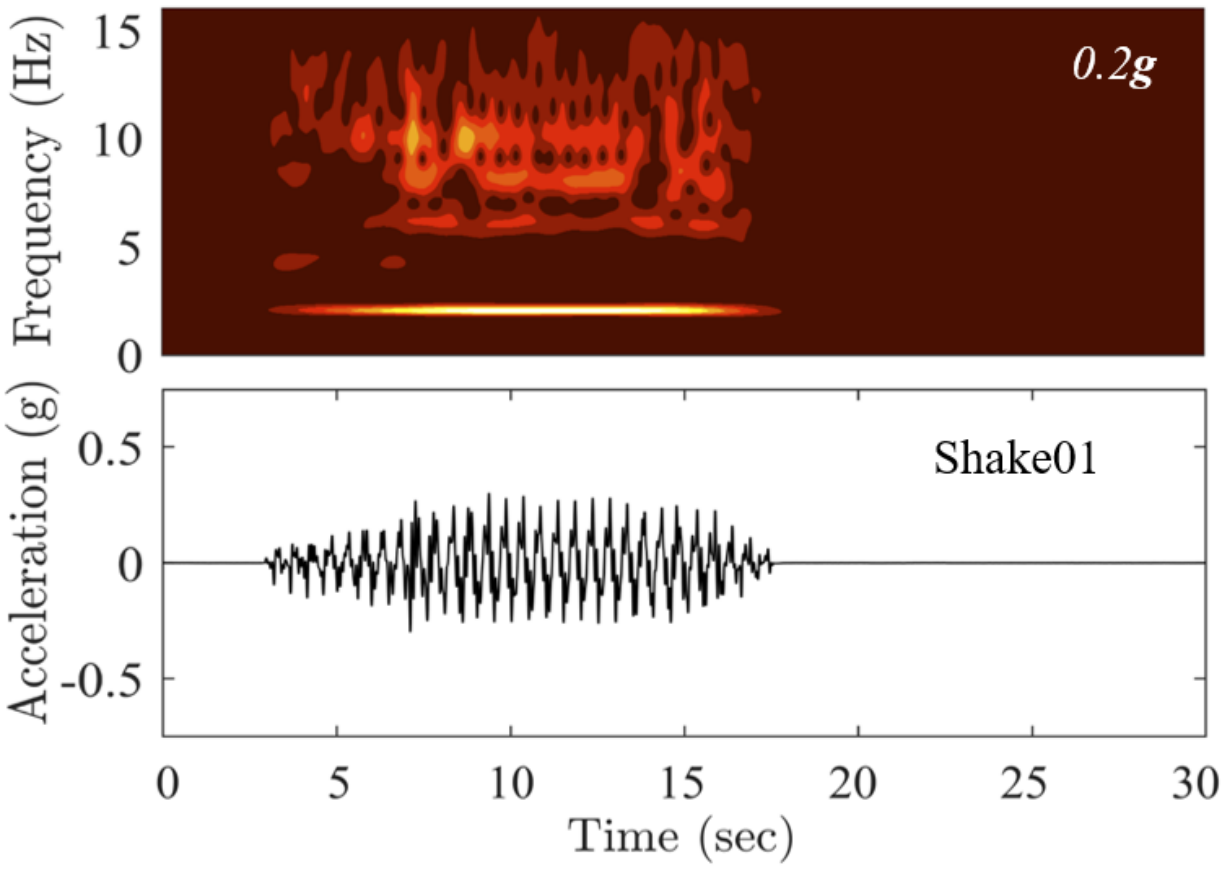

(a) Base excitation for Shake01

Figure 4.10. Recorded base excitation for shake table testing: (a) Shake01 and (b) Shake02

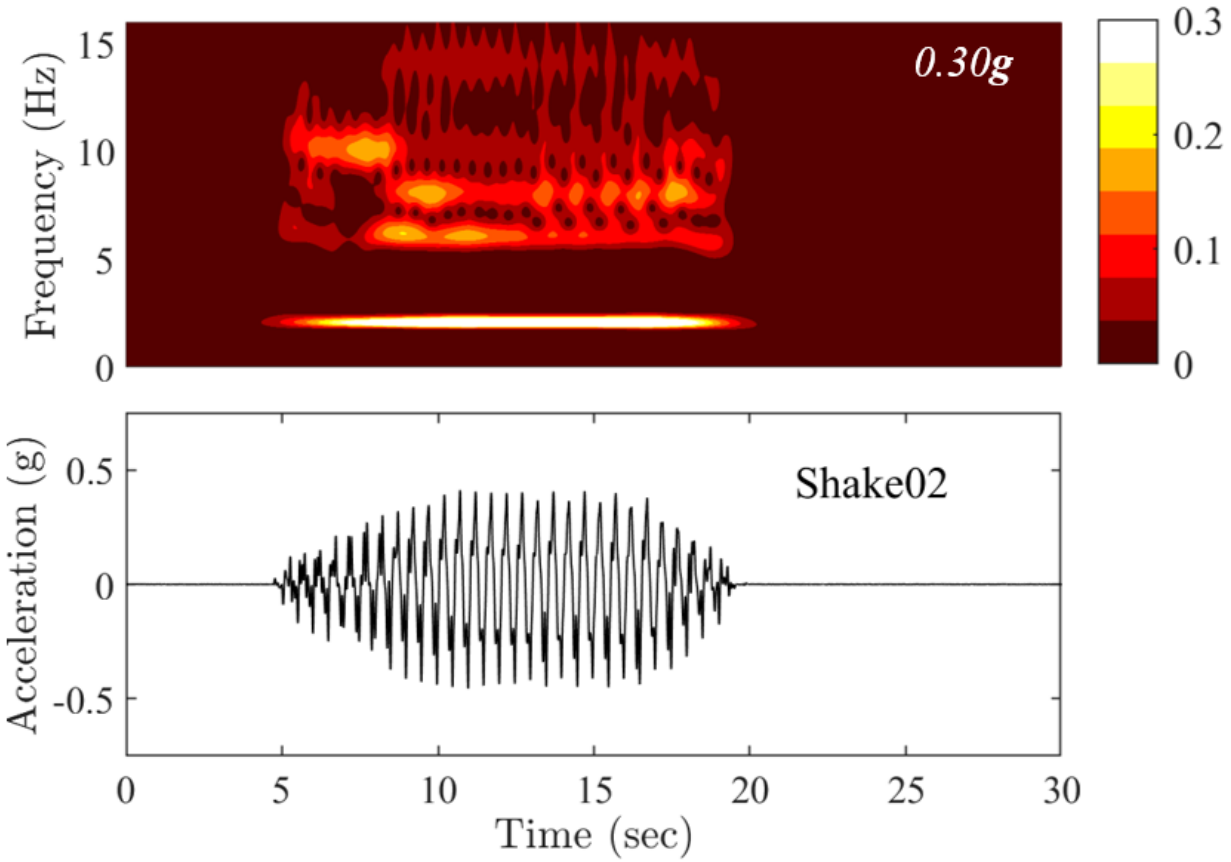

(b) Base excitation for Shake02

Figure 4.10 (continued). Recorded base excitation for shake table testing: (a) Shake01 and (b) Shake02

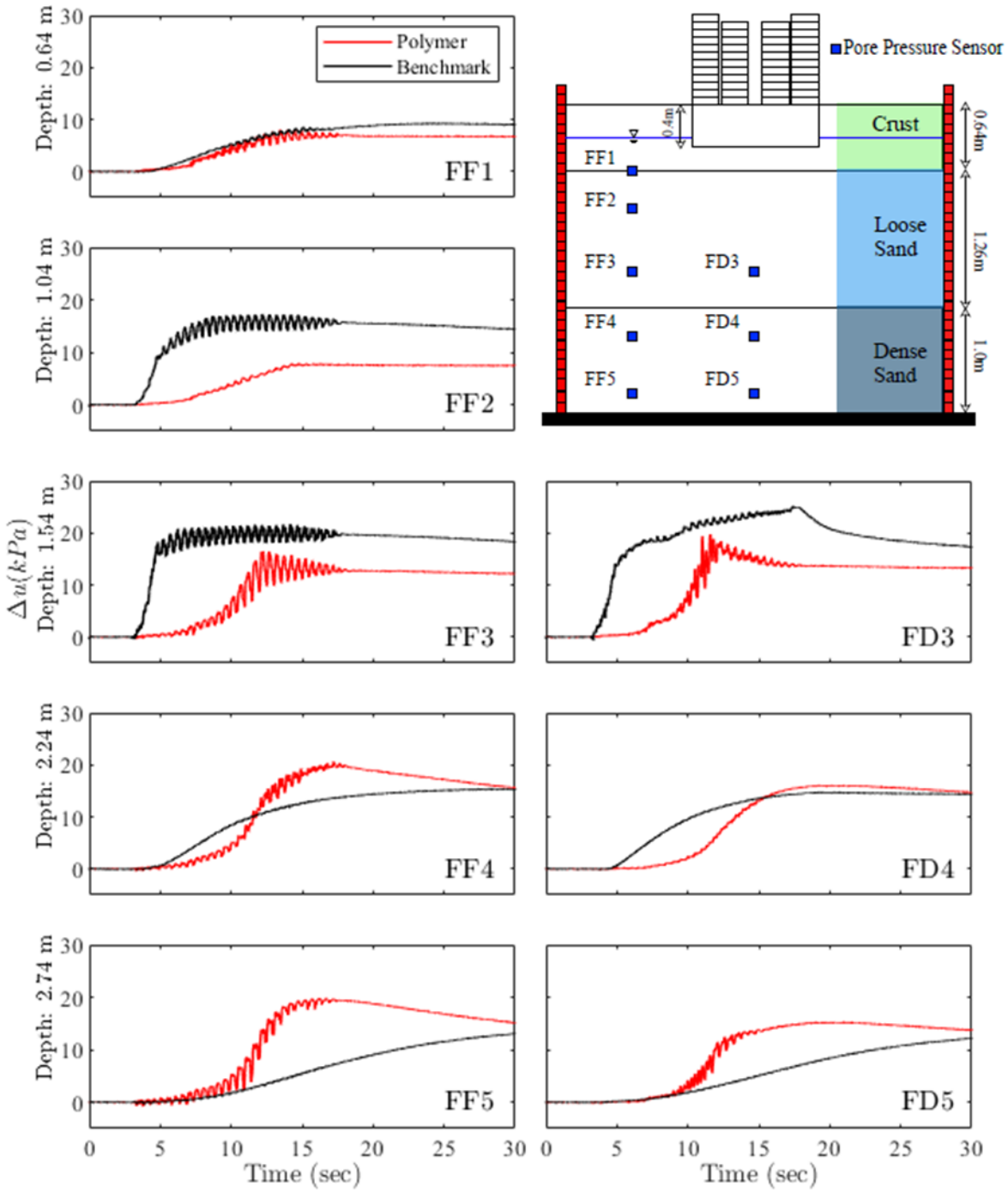

Figure 4.11. Comparison of excess pore pressure response in the baseline and polymer experiments during Shake01

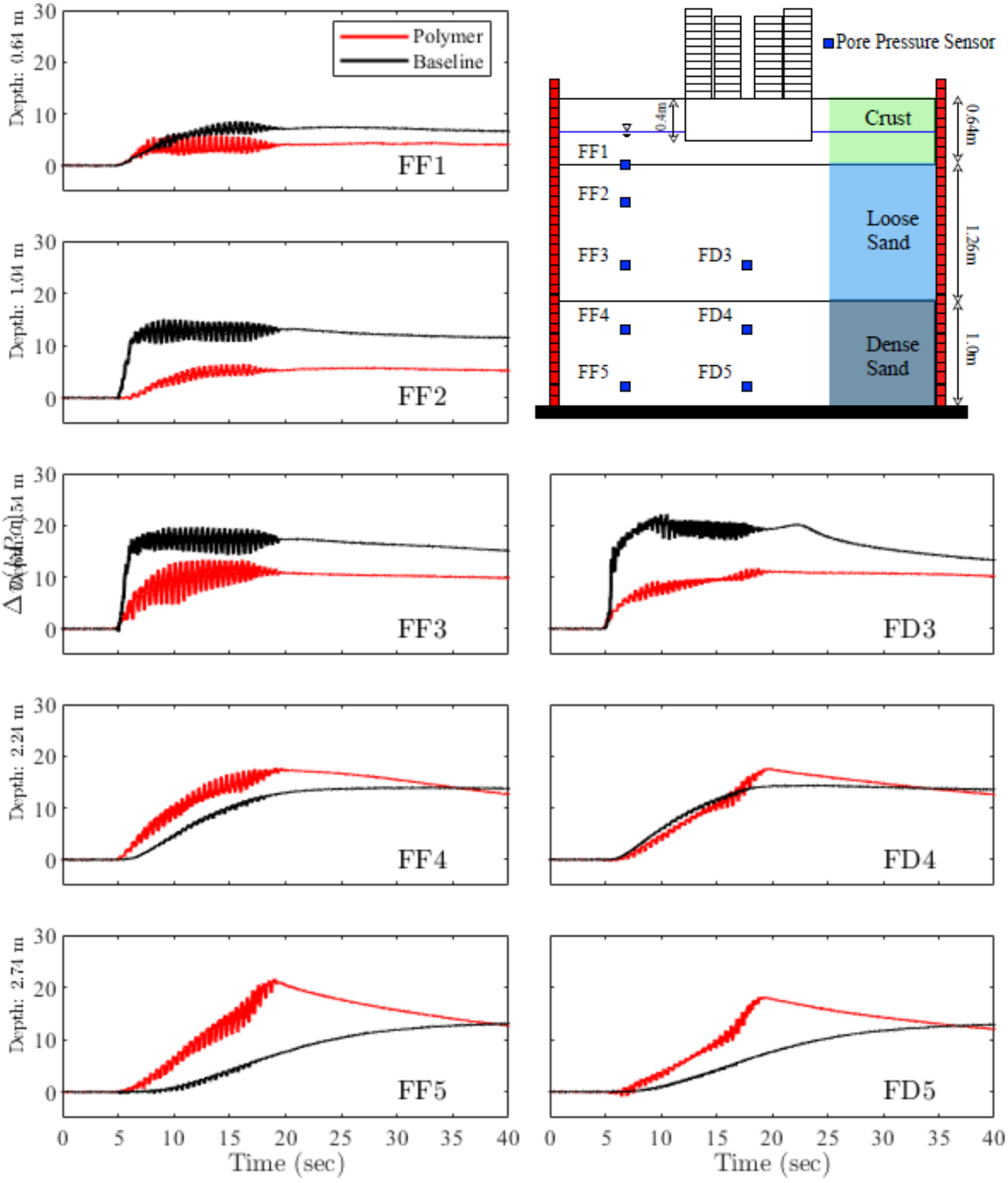

Figure 4.12. Comparison of excess pore pressure response in the baseline and polymer experiments during Shake01

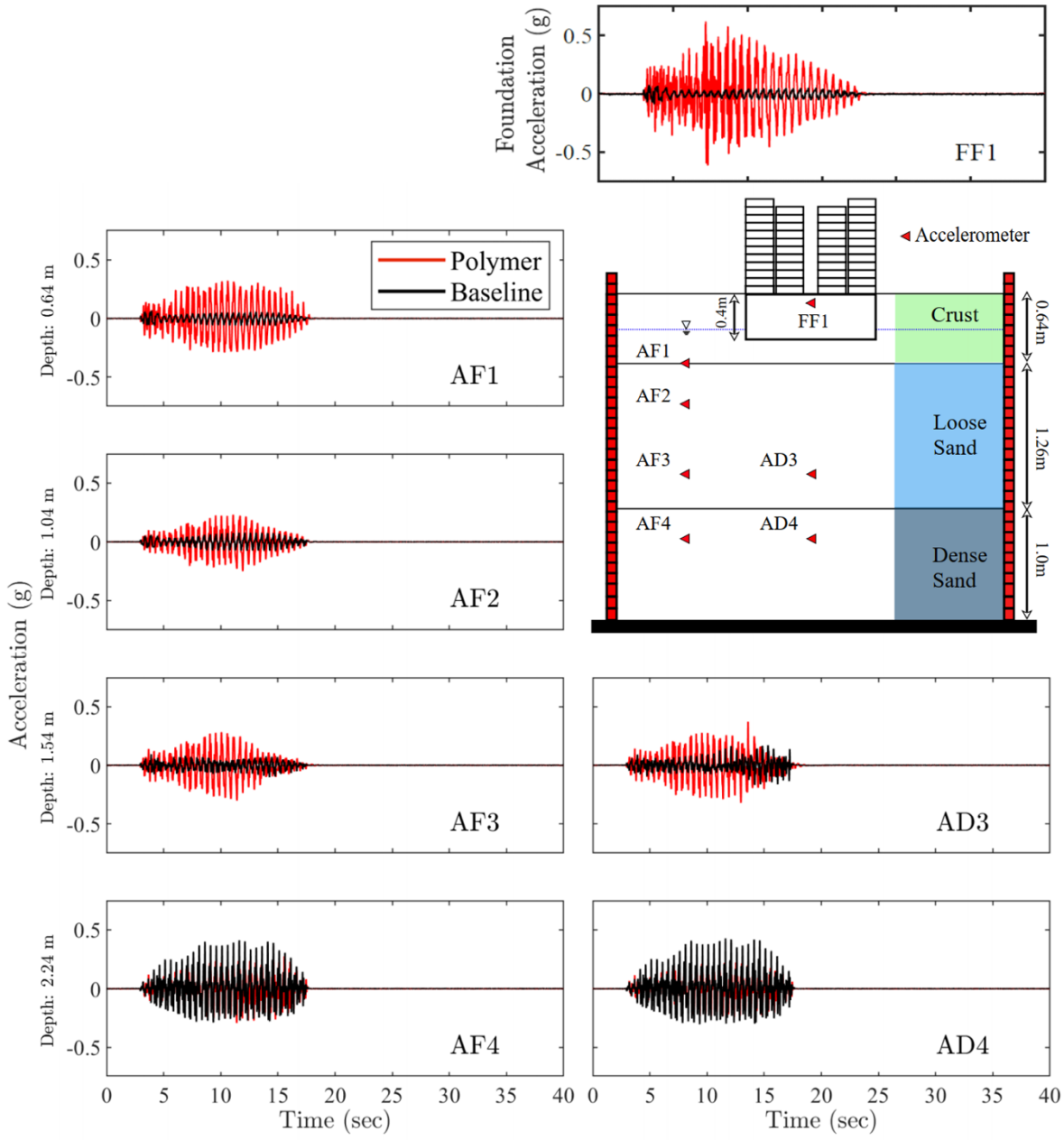

Figure 4.13. Comparison of acceleration response in the baseline and polymer experiments during Shake01

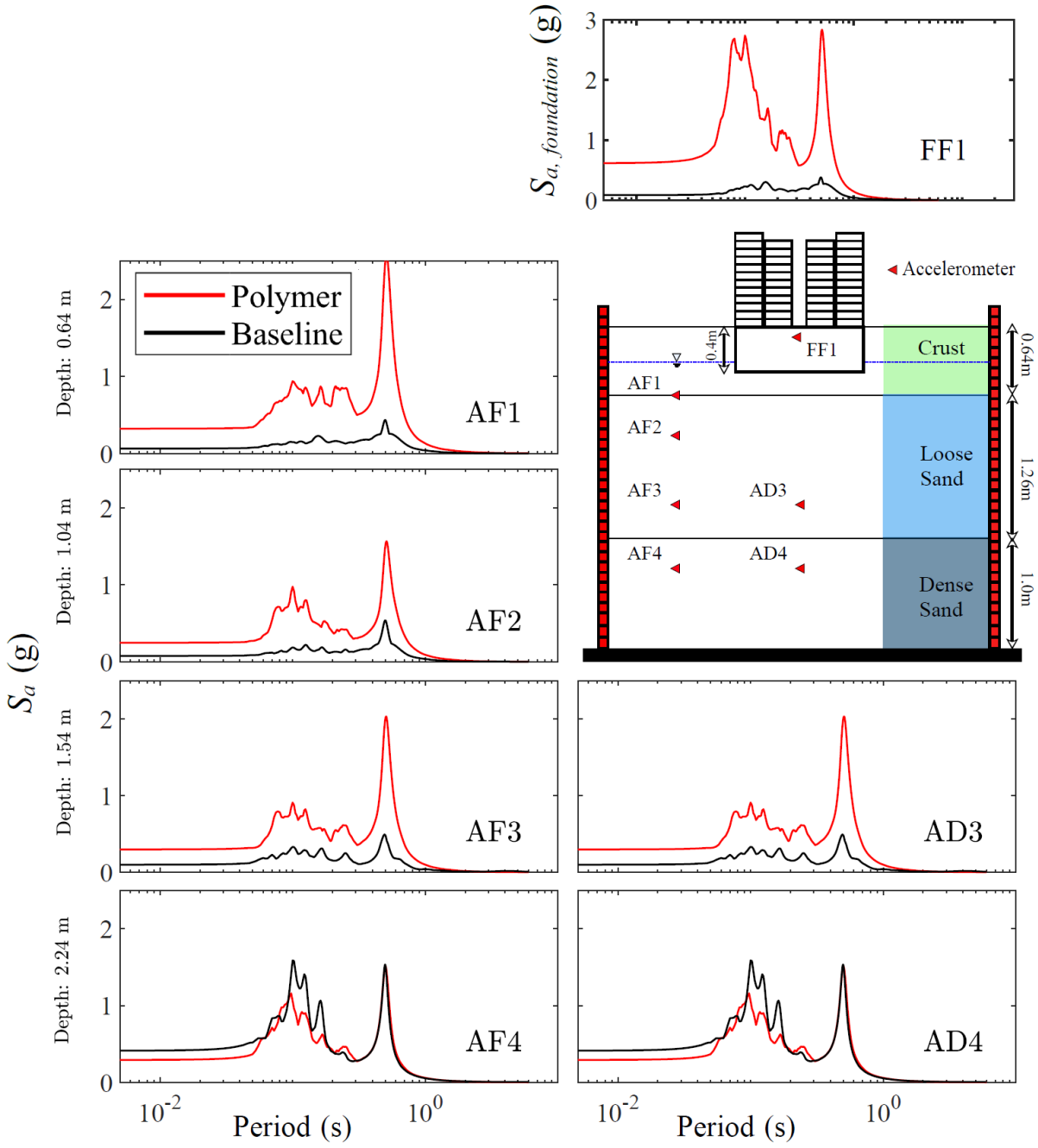

Figure 4.14. Comparison of acceleration response spectra in the baseline and polymer experiments during Shake01

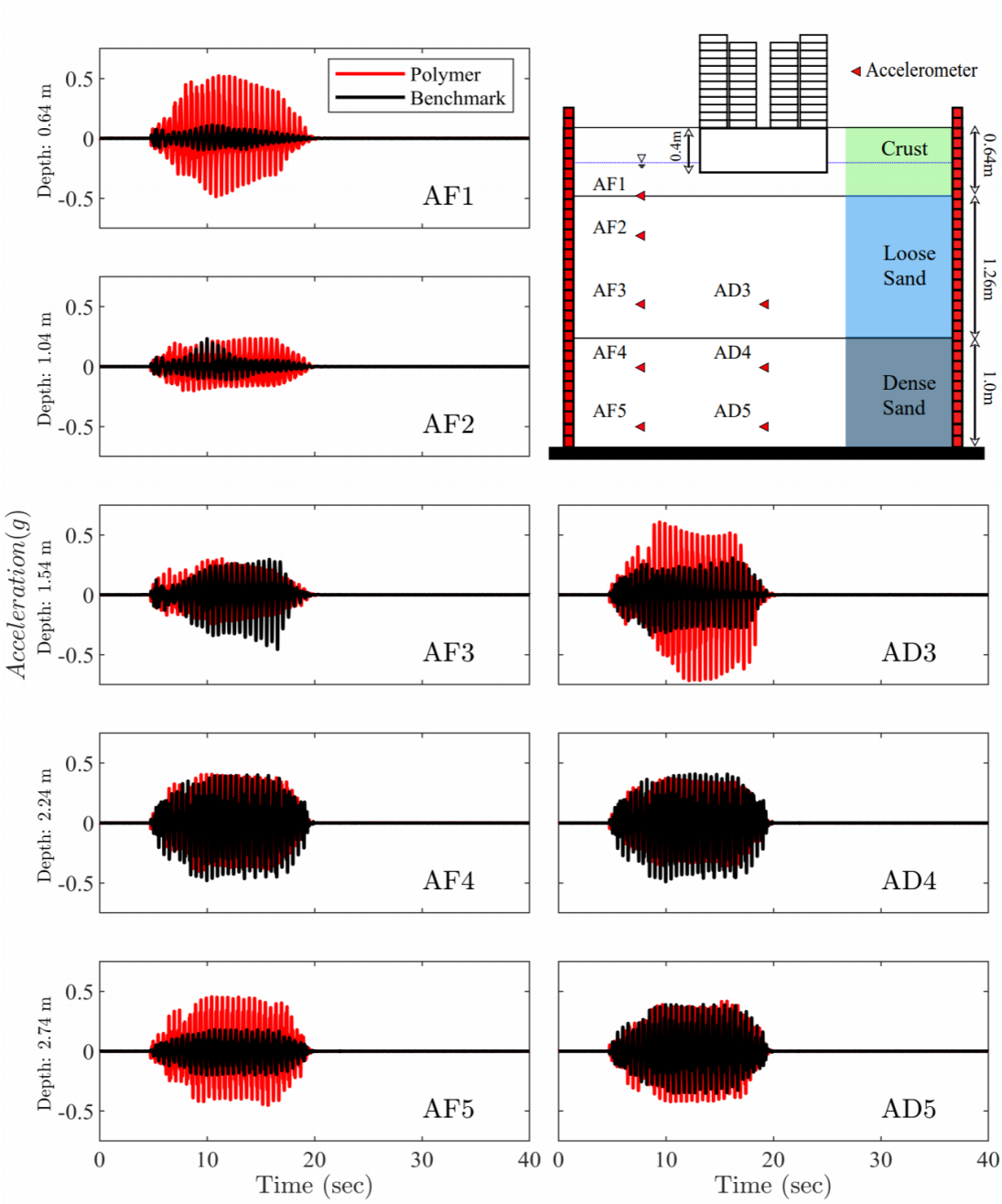

Figure 4.15. Comparison of acceleration response spectra in the baseline and polymer experiments during Shake02

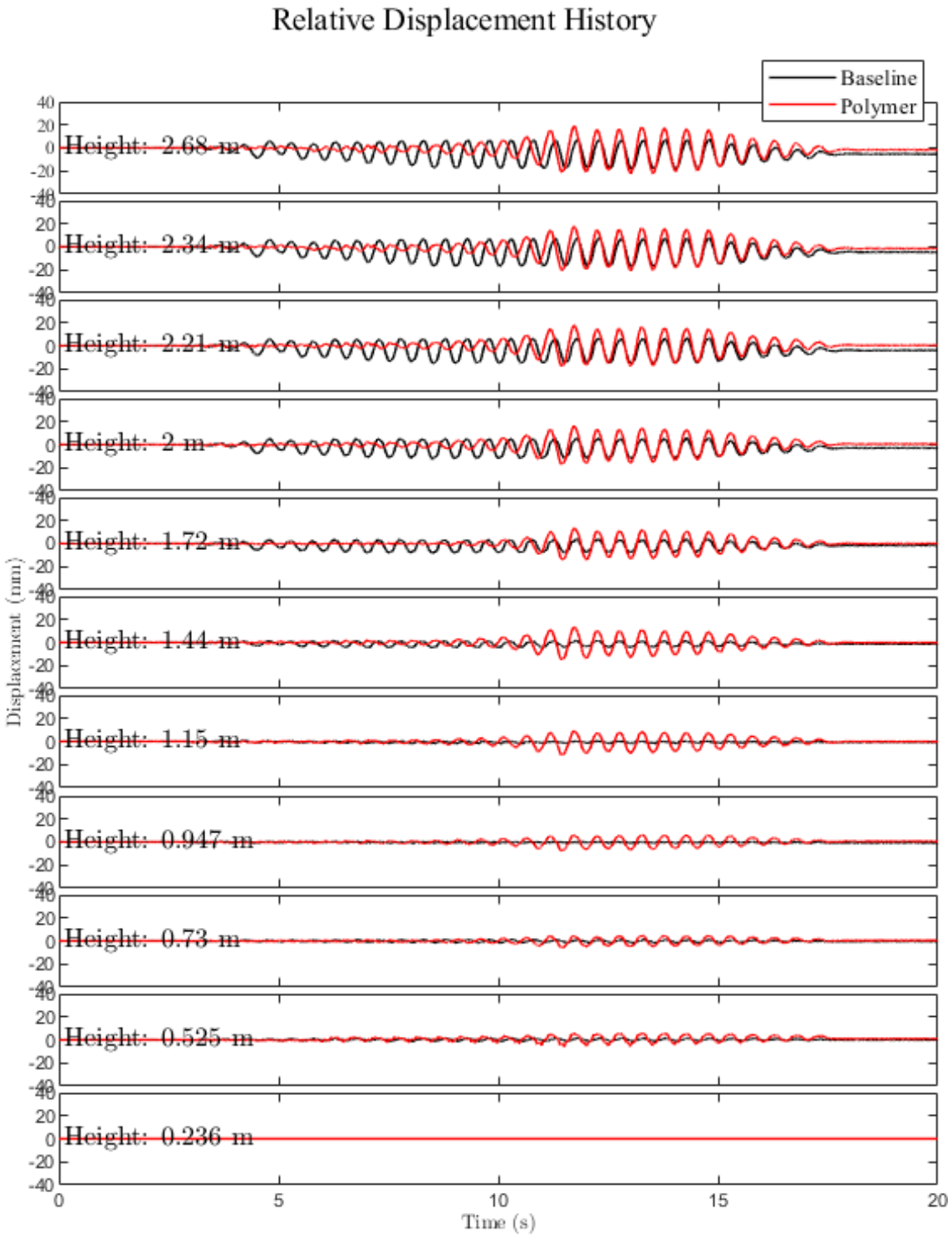

(a)

Figure 4.16. Baseline model: (a) before shaking, and (b) after shaking (post Shake02)

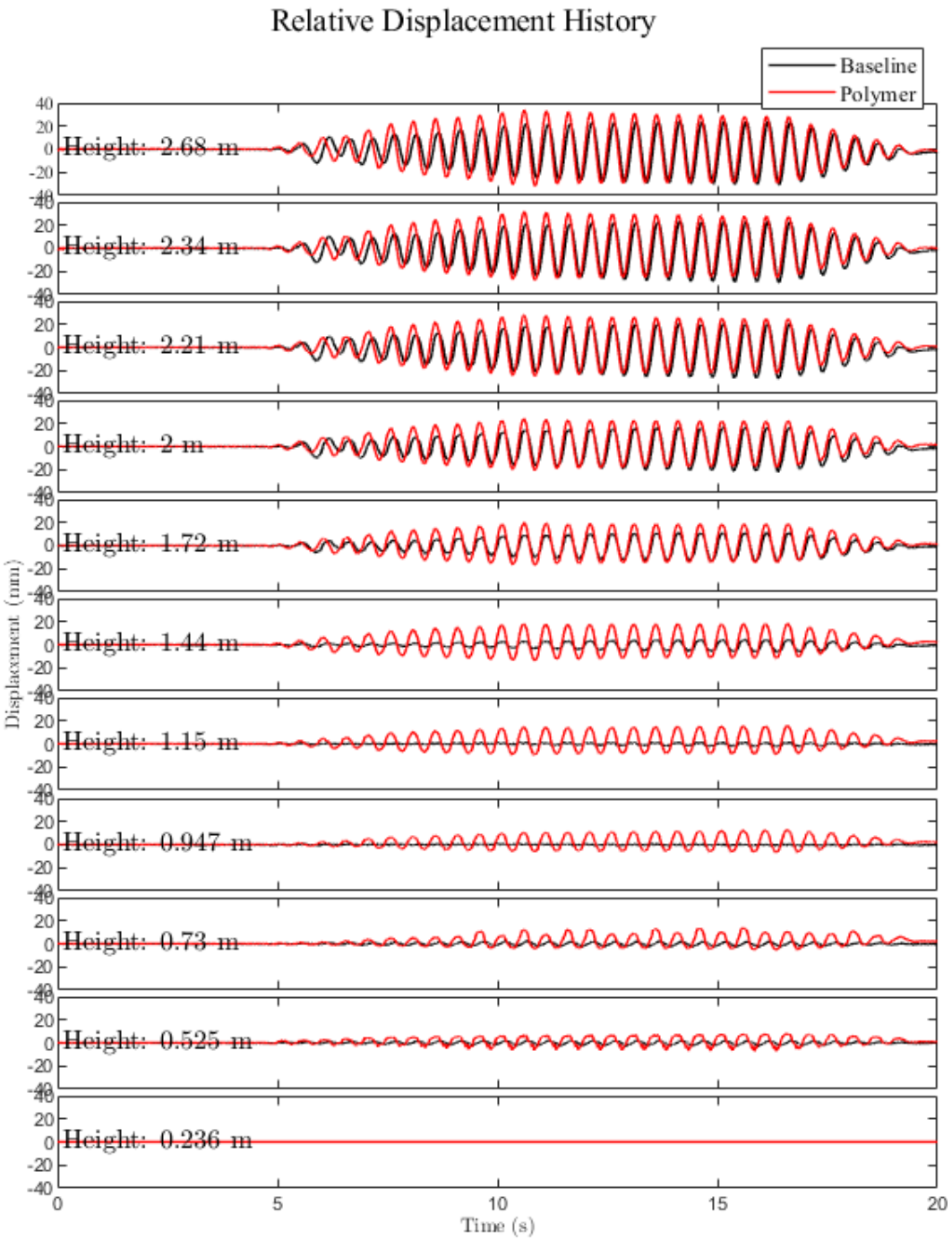

Figure 4.16 (continued). Baseline model: (a) before shaking, and (b) after shaking (post Shake02)

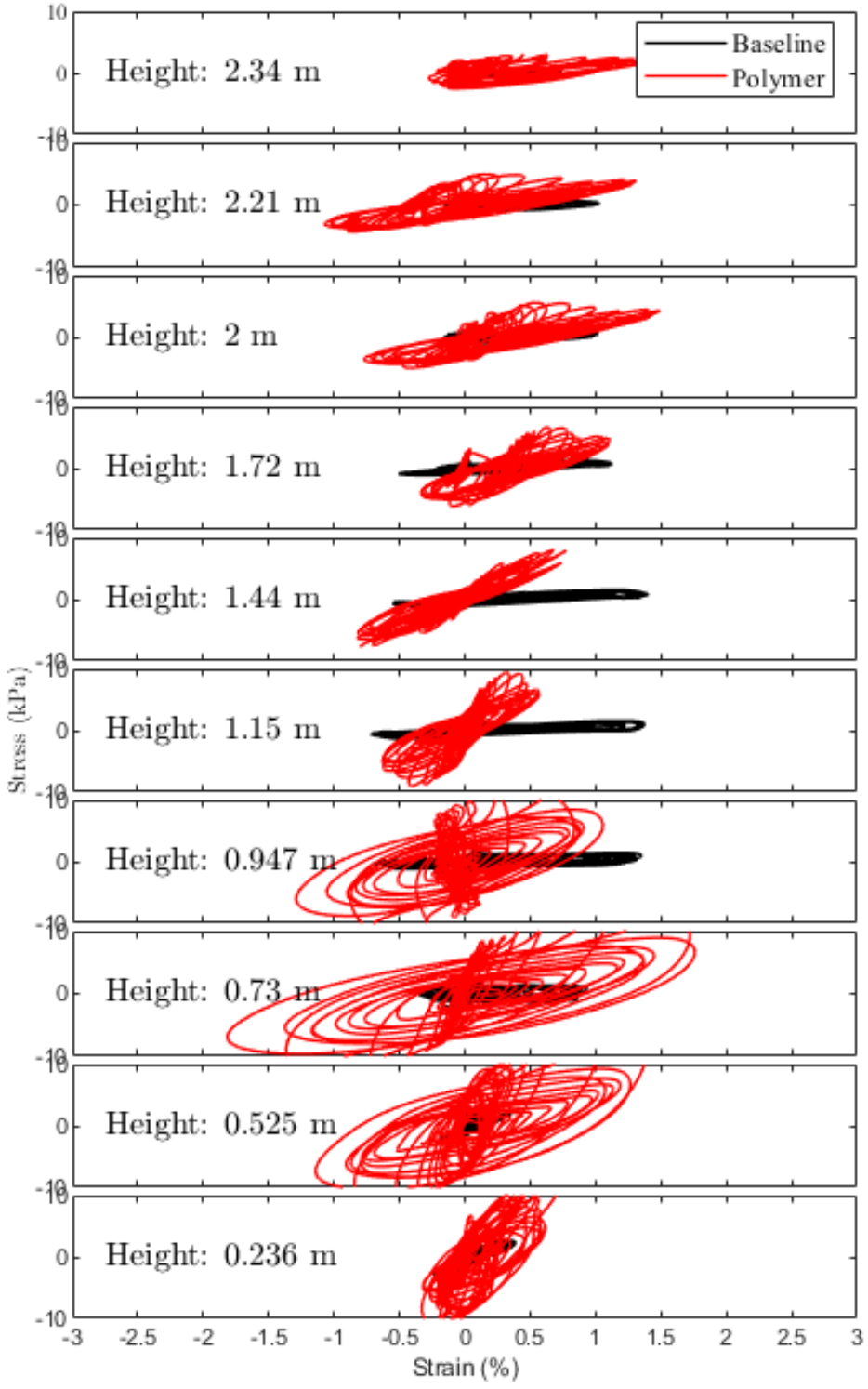

(a)

Figure 4.17. Comparison of stress strain response during (a) Shake01 and (b) Shake02

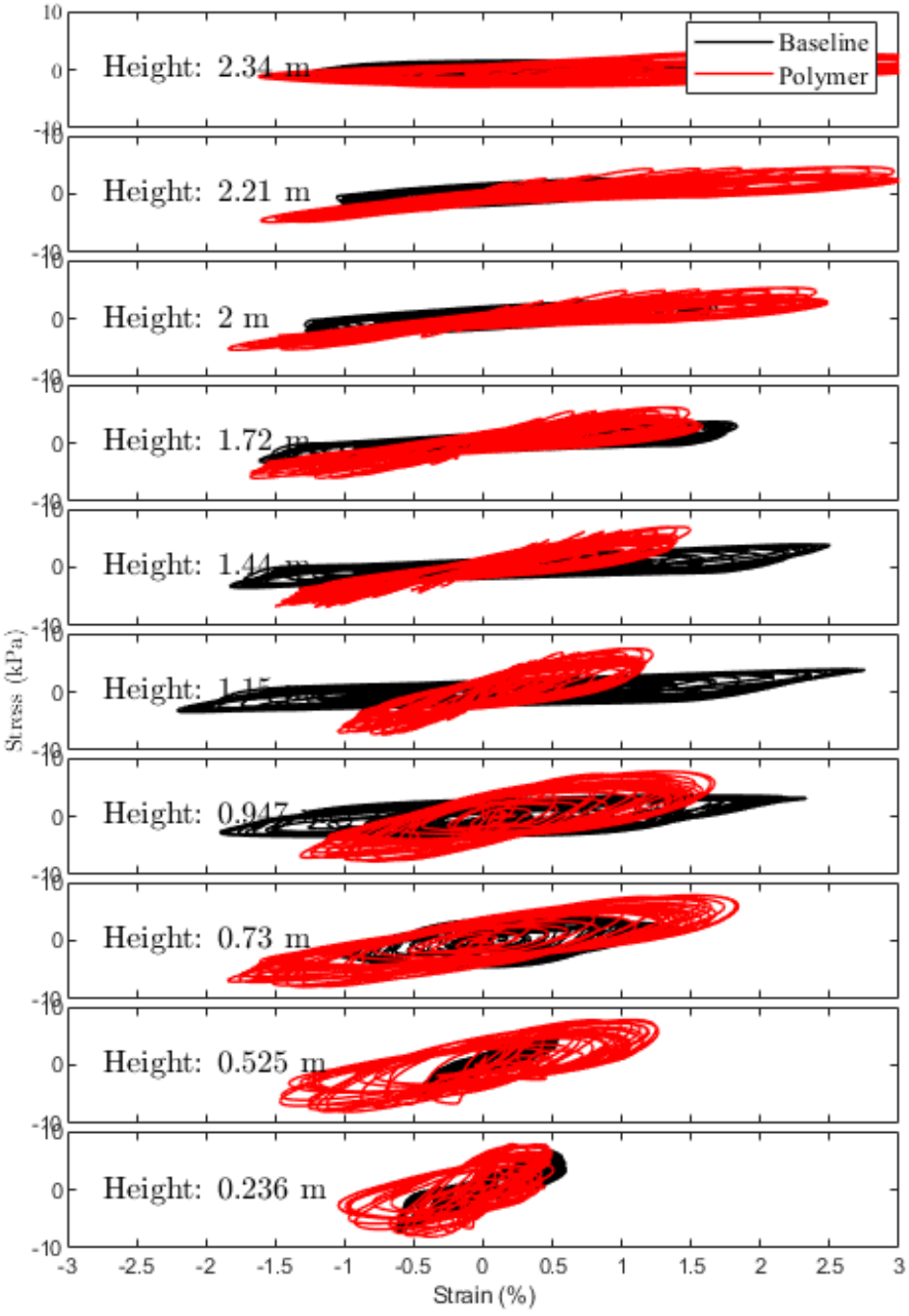

(b)

Figure 4.17 (continued). Comparison of stress strain response during (a) Shake01 and (b) Shake02

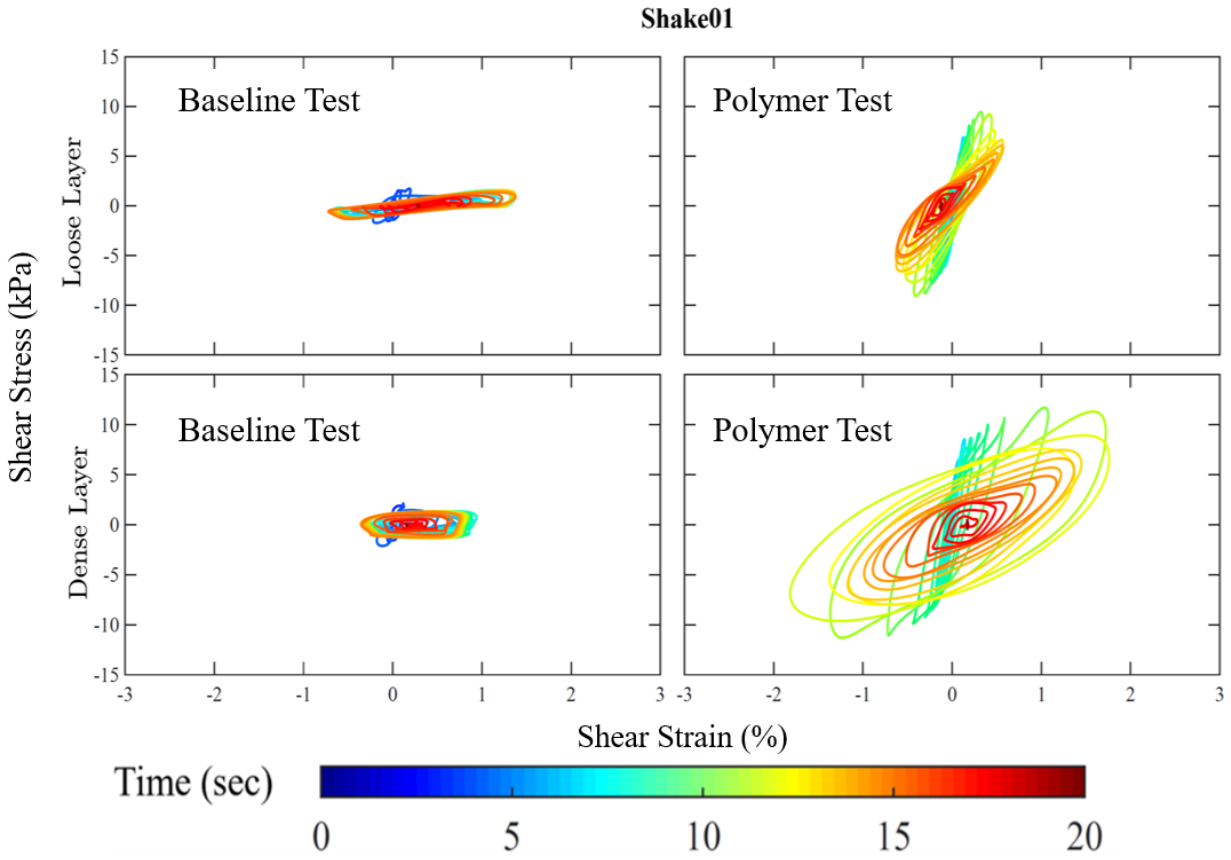

Figure 4.18. Comparison of stress strain response within liquefiable layer (Depth = 1.7m) and dense layer (Depth = 2.3m) during Shake01

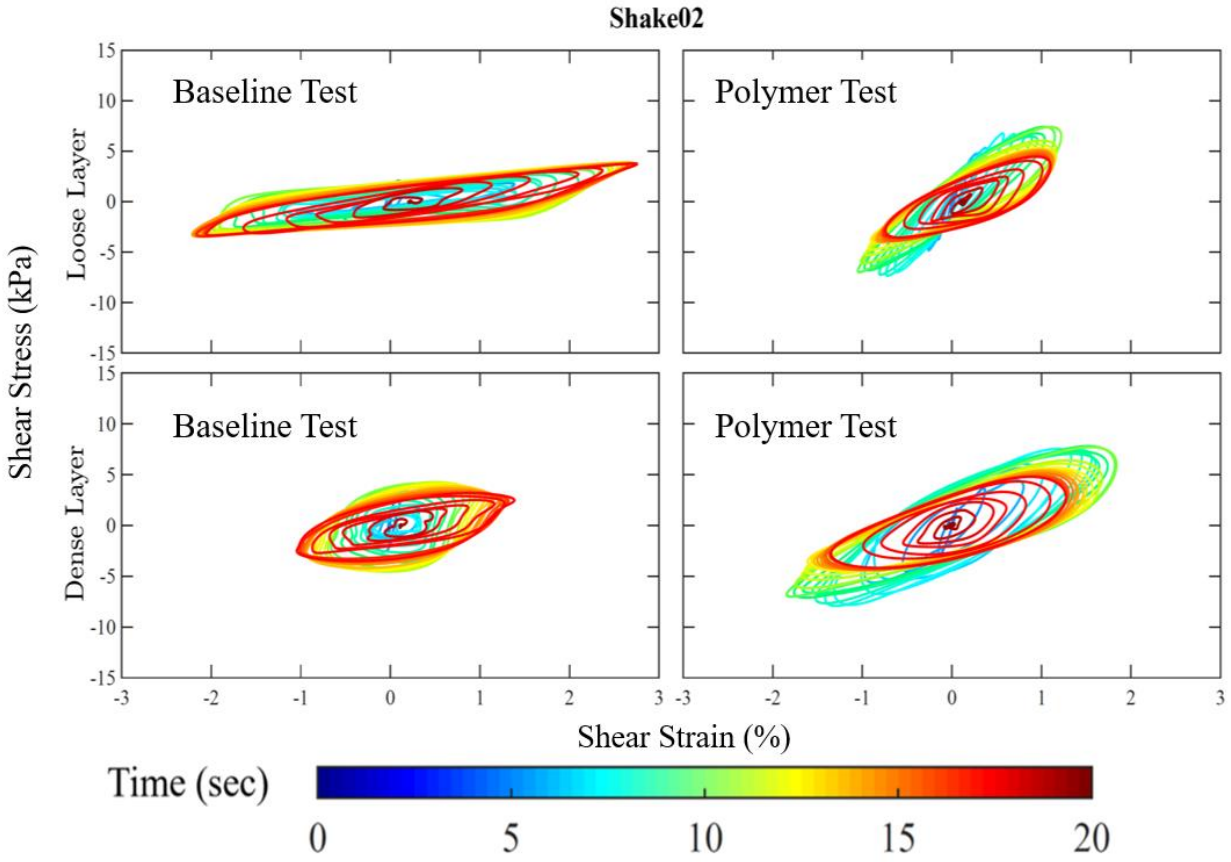

Figure 4.19. Comparison of stress strain response within liquefiable layer (Depth = 1.7m) and dense layer (Depth = 2.3m) during Shake01

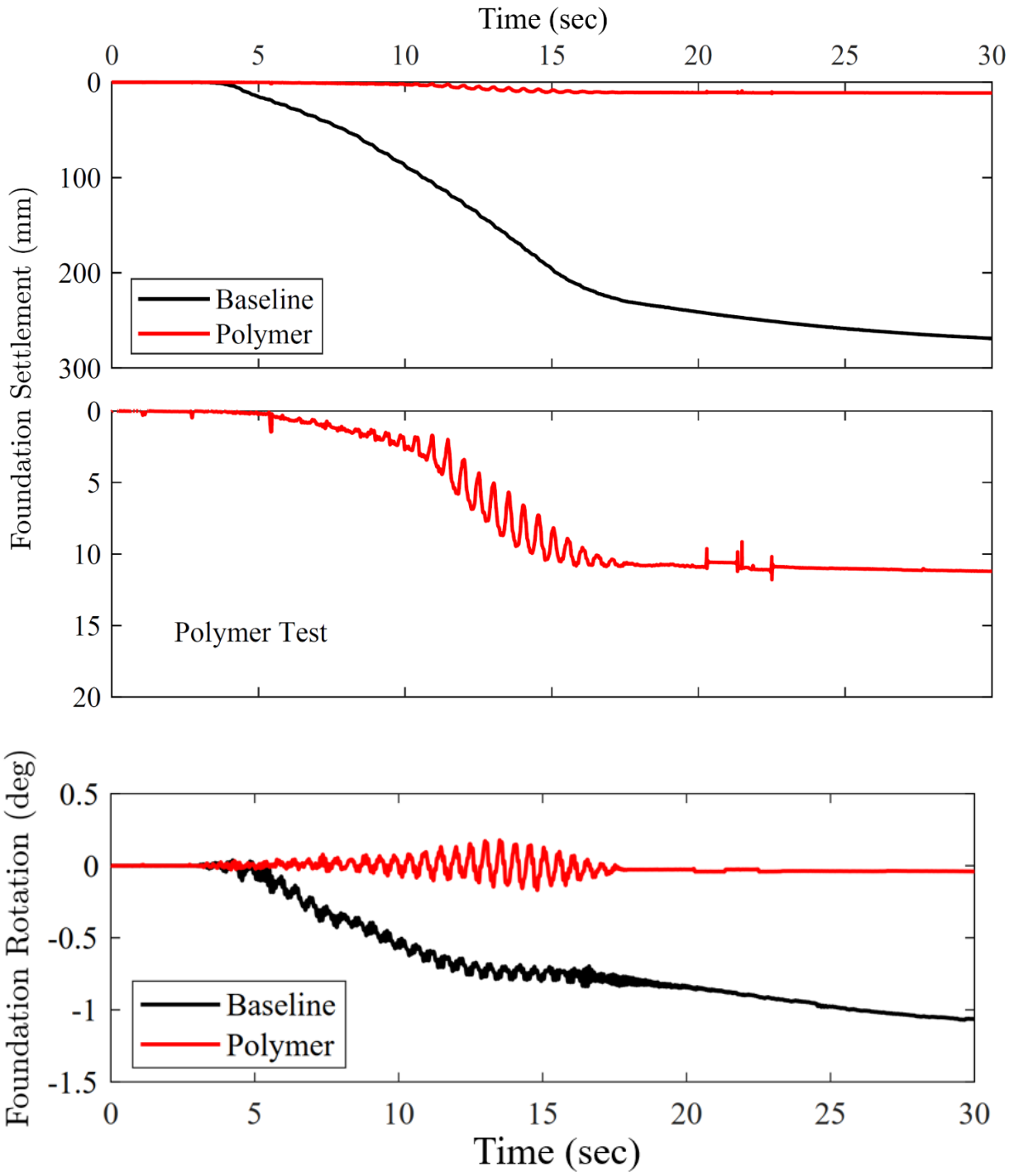

Figure 4.20. Foundation settlement and rotation time histories during Shake01

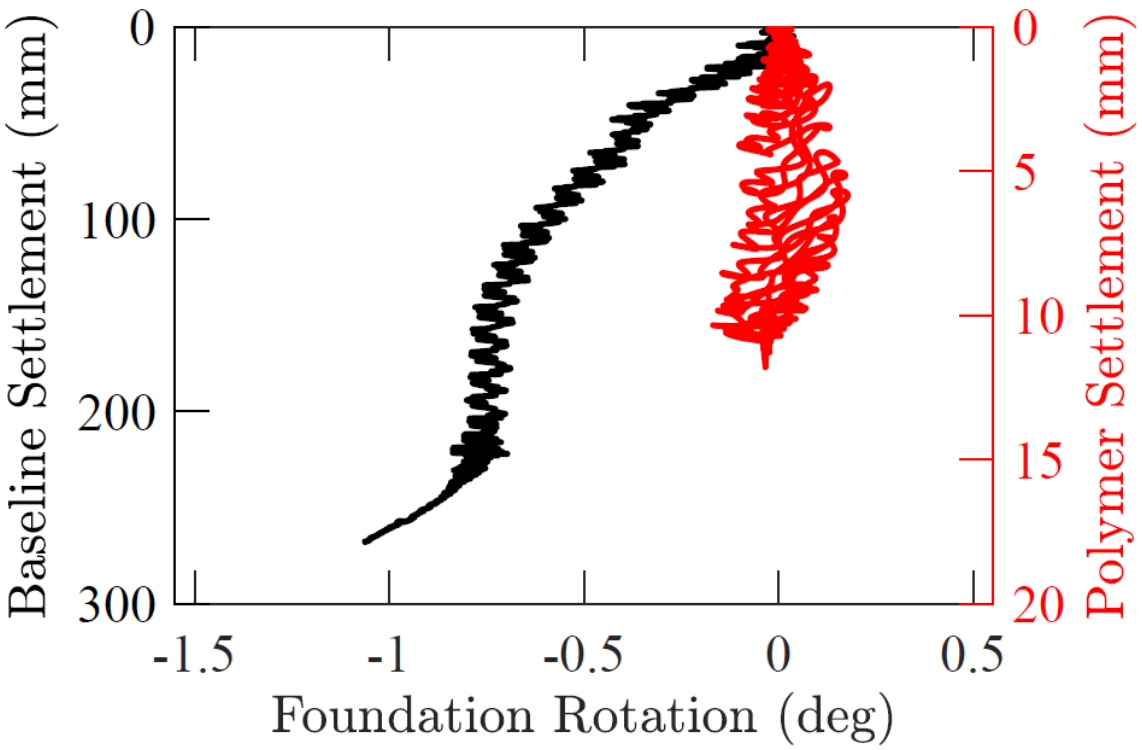

Figure 4.21. Foundation settlement - rotation behavior during Shake01

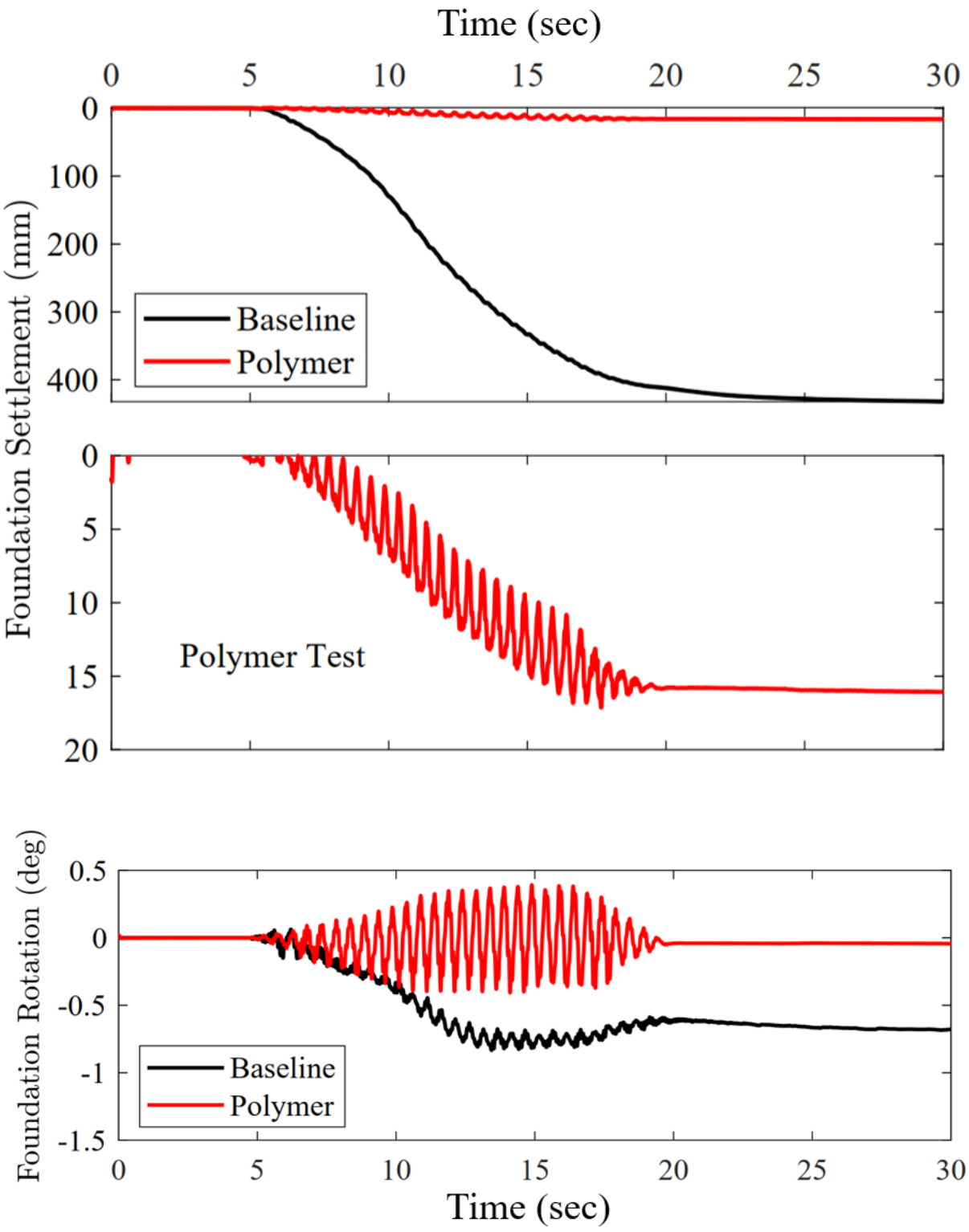

Figure 4.22. Foundation settlement and rotation time histories during Shake02

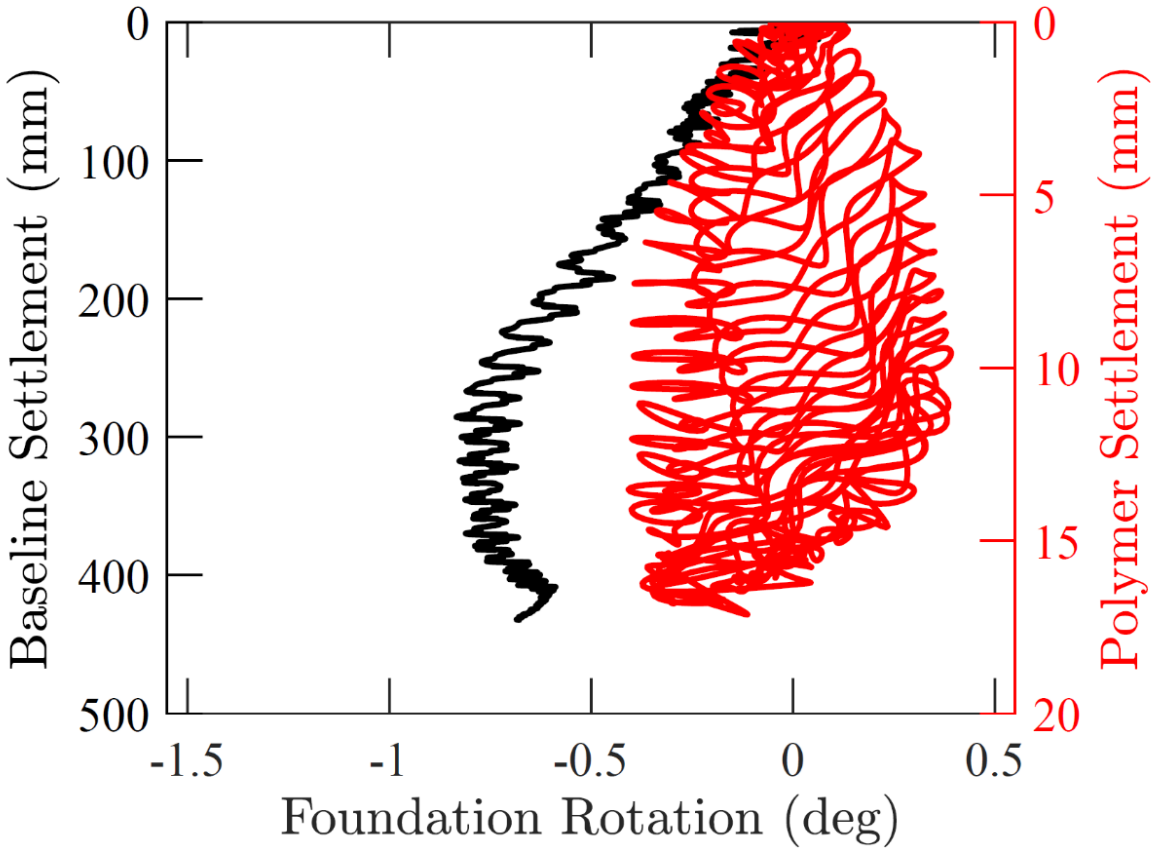

Figure 4.23. Foundation settlement - rotation behavior during Shake02

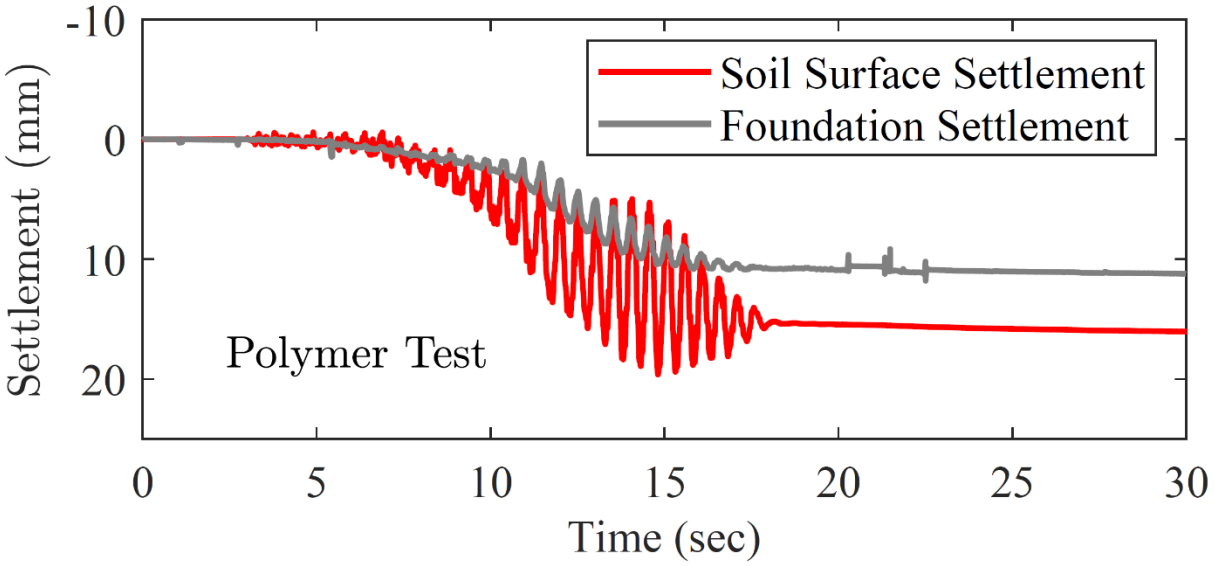

Figure 4.24. Free Field and Foundation Settlement during Shake01

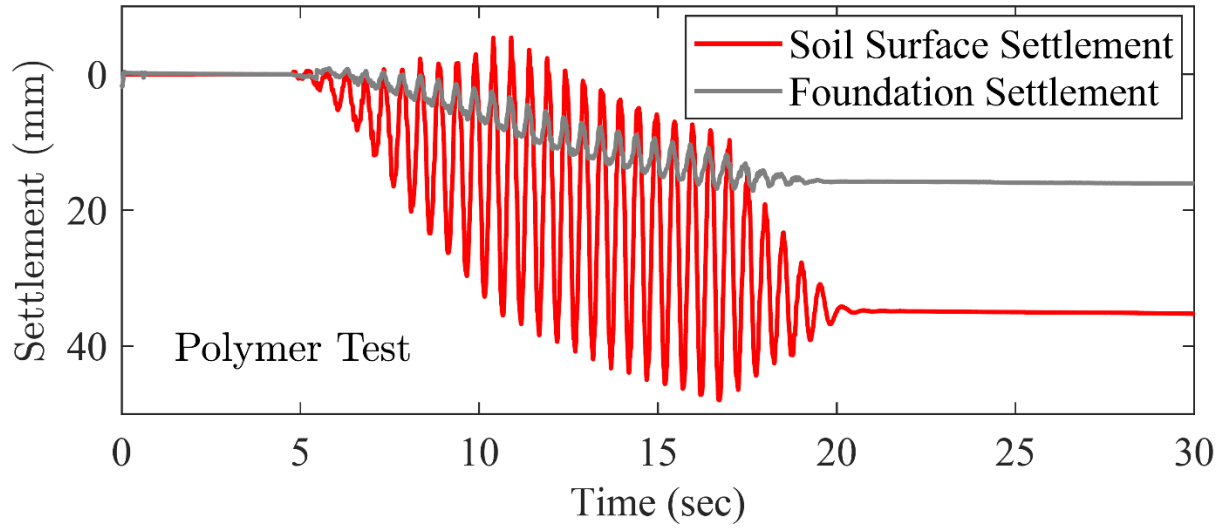

Figure 4.25. Free Field and Foundation Settlement during Shake02

(a)

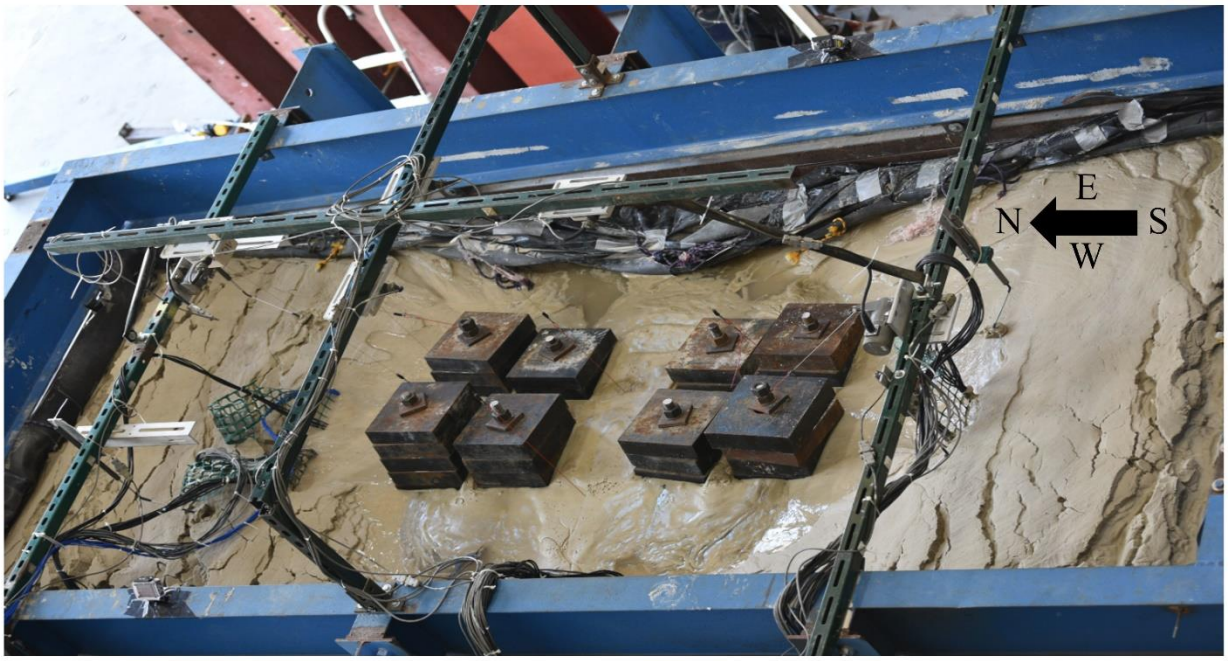

(b)

Figure 4.26. Baseline model: (a) before shaking, and (b) after shaking (post Shake02)

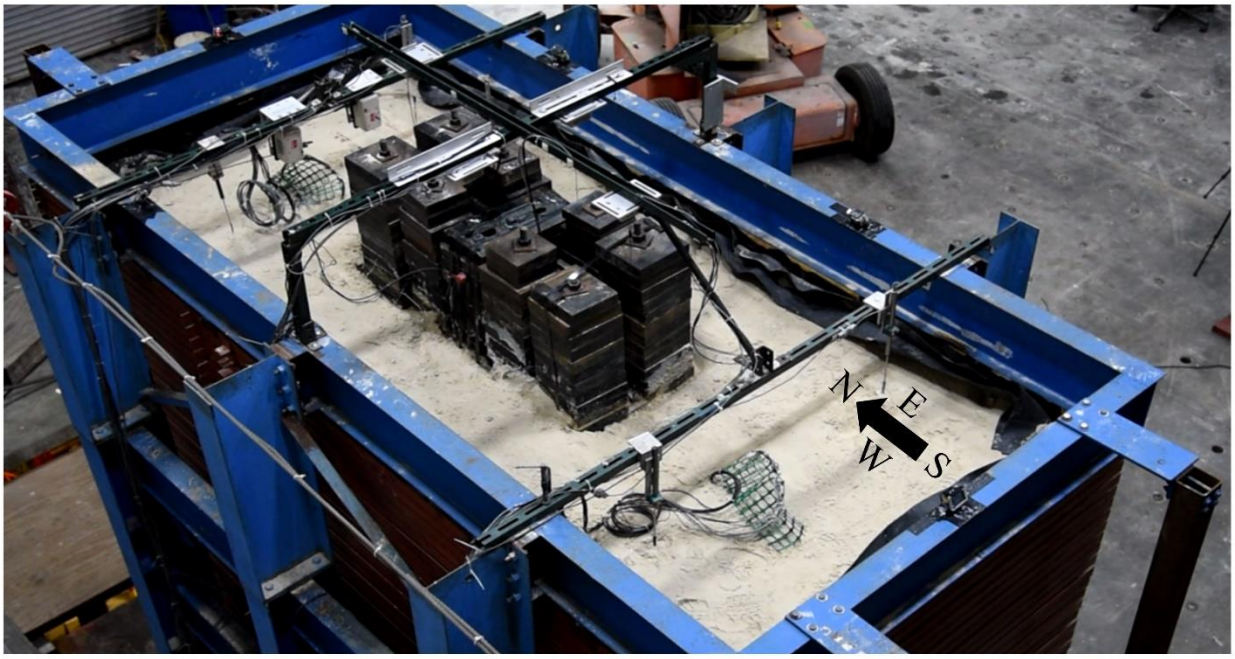

(a)

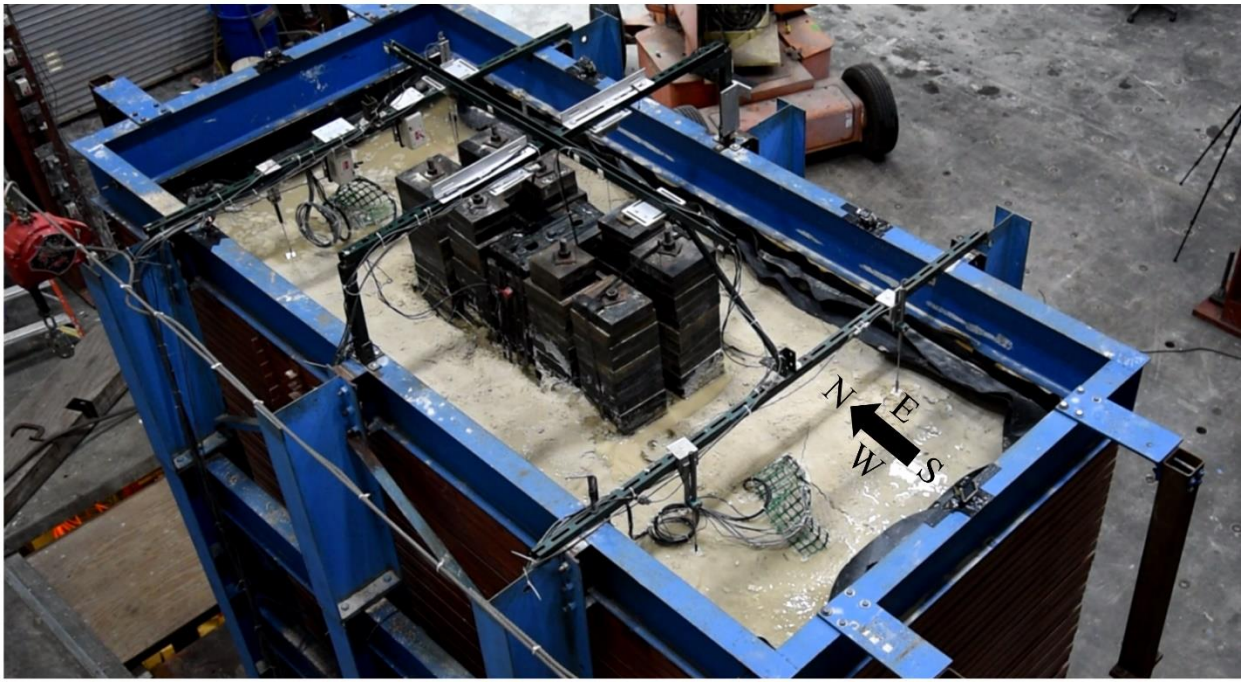

(b)

Figure 4.27. Polymer remediated model: (a) before shaking, and (b) after shaking (post Shake02)

Chapter 5. Liquefaction Induced Settlement of Shallow Foundations: Numerical Simulation of the Baseline Experiment

5.1 Abstract

This chapter presents results from a comprehensive system-level numerical calibration to a set of large-scale shake table tests performed to study the baseline response of a shallow foundation seated on a three-layered liquefiable deposit. Salient constitutive model parameters for the developed finite element model were obtained based on the calibration of a three-layered free-field experiment. With this parameter set, a set of Class C1 numerical simulations of these tests are presented using a 3D two-phase (solid fluid) fully coupled finite element model. Comparisons are made between computed and recorded engineering demand parameters (EDPs), including excess pore pressure, acceleration, and foundation settlement.

5.2 Introduction

Soil liquefaction is a mechanism that results in severe damage to buried structures and foundation systems during earthquakes as documented in Niigata 1964, Kobe 1995 and Tohoku 2011, Japan (Ashford *et al.* 2011, Hamada *et al.* 1996, Ishihara and Koga 1981), Kocaeli, 1999, Turkey (EERI 2000), Bhuj 2001, India (Jain *et al.* 2002), and 2010-2011 Canterbury earthquake sequence in New Zealand 2010-2011 (Cubrinovski *et al.* 2010). For instance, during the 2010-2011 Canterbury earthquake sequence, severe soil liquefaction affected 3,000 buildings within the Central Business District (CBD) of Christchurch, of which over 50 % were to be demolished, being deemed economically unfit for further repairs (Cubrinovski 2013).

Despite being a relevant aspect of shallow foundation response in liquefiable soils, the estimation of co-seismic settlement for engineering applications has been challenging.

Traditionally, the state of practice has utilized free-field based methods to predict shallow foundation settlement (Liu and Dobry 1997, Yoshimi and Tokimatsu 1977). Recent studies (Bertalot *et al.* 2013, Dashti *et al.* 2010, Karamitros *et al.* 2013) recognized the necessity to incorporate shear and drainage-based mechanisms that significantly contribute to the settlement estimate, particularly in deposits with thin liquefiable layers. Several experiments have been performed in this regard utilizing the centrifuge (Adamidis and Madabhushi 2018, 2022, Dashti *et al.* 2010, Kassas *et al.* 2021a, Tokimatsu *et al.* 2019) and shake table (Jahed Orang *et al.* 2020, Yoshimi and Tokimatsu 1977).

Numerical simulations using effective stress analyses have shown capabilities to capture salient response mechanisms. Once calibrated, these simulation frameworks have provided an avenue to leverage and scale experimental insights to perform parametric studies and large datasets (Dashti *et al.* 2018, Dashti and Bray 2013, Dimitriadi *et al.* 2017, Elgamal *et al.* 2005, Karamitros *et al.* 2013, Karimi and Dashti 2016, Kassas *et al.* 2021b, Shahir and Pak, 2010). Motamed *et al.* (2020) discussed the use of different numerical simulation techniques and their efficacy in predicting liquefaction-induced foundation and free field settlements. Researchers (Bray and Macedo 2017, Bullock *et al.* 2019) have further analyzed these datasets using predictable input variables, providing equations for the engineering assessment of settlement and tilt. However, before parametric analyses, each numerical model needs careful validation with the element level and system-level response results. As such, the majority of these numerical simulations have been calibrated on the system-level response obtained from centrifuge experiments.

As a complement to centrifuge tests, Jahed Orang *et al.* (2020) conducted a set of large-scale baseline shake table experiments (Figure 5.1) to study shallow foundations' response in a layered liquefiable stratum. This test series, a first of its kind in terms of scale, are used to perform

a system-level class C1 calibration to a finite element (FE) modeling framework to shed light on the response mechanisms. The numerical simulations are performed using a well-established, calibrated finite element (FE) modeling framework, developed, and implemented in OpenSees (McKenna *et al.* 2010) by Khosravifar *et al.* (2018) and Yang *et al.* (2003) The employed framework is particularly beneficial in studying cyclic mobility and its effect on shear-induced settlement mechanisms, which often have immense contributions to the observed liquefaction-induced foundation settlement during strong shaking.

In the sections below, the following aspects are discussed: (i) Summary of the experimental program, (ii) Model characterization and element level calibration, (iii) Numerical modeling procedure and framework, (iv) Computational response, comparison with the experimental observation and discussion, and (v) Parametric studies into associated deformation mechanisms. Finally, conclusions are presented with insights into the in-situ liquefaction mitigation measure.

5.3 Outline of Experimental Program

5.3.1 Free field Experiment

Zayed *et al.* (2021) performed a set of large-scale shake table experiments to study the accumulation of biased shear strains in level ground free field scenarios (Figure 5.2). The test series consisted of a three-layered soil system constructed with Ottawa F-65 sand (Basic soil properties are provided in Table 5.1, based on Parra Bastidas, 2016). The deposit was constructed with a 0.55 m moist crust layer (D_r estimated at about 75 – 85 %), overlying a 1.35 m loose liquefiable layer (D_r estimated at about 35 – 40 %) underlain by a 1.00 m dense bottom layer (D_r estimated at about 85 – 95 %). The soil properties and layering of the free field experiment are summarized in Table 5.2. The ground motion for this experiment was tailored to produce large, biased shear strains in a fixed direction to accumulate inertia driven shear induced lateral

deformations. An example of the motion is provided in Figure 5.3. Extensive pore pressures were observed in the free-field test resulting in large liquefaction induced lateral deformations.

5.3.2 Soil Foundation System Experiment

The deposit for this experimental stage consisted of a shallow foundation system supported on a three-layered stratified deposit. The deposit consisted of a saturated 1.00 m dense base layer (D_r estimated at about 80 – 95 %) underlying a 1.25 m thick saturated liquefiable layer (D_r estimated at range of 35 – 44 %), overlain by a moist 0.64 m crust (D_r estimated at range of 50-55%). The soil properties and layering of the soil foundation system experiment are summarized in Table 5.3. The foundation system (Figure 5.4) consisted of a rigid concrete block of length 1.3 m, width 0.6 m and height 0.4 m, overlain by steel plates designed to produce a surcharge vertical pressure of 41.6 kPa. The concrete block (height of 0.4 m) was fully embedded into the crust. Full details on the test models may be found in Jahed Orang *et al.* (2020).

i) Low Strain System Identification

Systematic geotechnical system identification procedures were performed to characterize the low strain shear modulus and damping ratio of the profile prior to each main excitation, Shake1. High resolution PCB accelerometers with a sampling rate of 25,600 Hz were used to track the wave propagation during white noise excitation. Further details can be obtained in Chapter 3 and a summary of employed base excitations are presented in Table 5.4. The shear wave velocity of the deposit is presented in Figure 5.5. The natural period of the system is estimated at 0.21 s (4.7 Hz - 5.03 Hz). An estimate of the low strain damping ratio was estimated from the logarithmic decrement method and estimates are summarized in Figure 5.6. Consistent estimates of (0.01 % - 4 %) are obtained following WN01, with an average estimate of about 1 %.

ii) Base Excitation

The model is first subjected to a base excitation at a peak cyclic acceleration of 0.2 g (referred to as Shake1). The motion and its time-frequency spectra computed using the modified Stockwell transformation (George 2009, Stockwell *et al.* 1996) are shown in Figure 5.7.

5.4 Simulation Framework

The set of 3-D nonlinear, fully coupled, finite element simulations were performed using OpenSees (McKenna *et al.* 2010) for both experimental datasets. The models were developed using the mixed, fully coupled *u-p* formulation of (Chan 1988) based on (Biot 1962). The soil domain was modelled using 8-noded hexahedral elements with the mean dilatational formation ($\bar{B}$ method) as per (Hughes 2008) to remove numerical issues associated with the incompressible fluid phase. A state-of-the-art plasticity-based stress strain constitutive models termed as Pressure Dependent Multi-Yield 02 (PDMY02) (Yang *et al.* 2003) were used to reproduce the liquefiable and non-liquefiable soil response in both experiments. A background into the constitutive model and associated parameters are provided in the following section.

5.4.1 Pressure Dependent Multi-Yield Model

The Pressure Dependent Multi-Yield (PDMY02) constitutive model developed by Parra (1996) and Yang *et al.* (2003) based on the original framework of Prevost (1985). Soil shear stress-strain behavior under cyclic mobility is modelled incorporating the contractive phase (as pore pressure develops), perfectly plastic phase and dilative phase (at shear strain excursions).

PDMY02 uses a set of nested yield conical yield surfaces apexed at the origin of the principal effective stress space to capture the soil response. A small positive intercept is provided (0.3 kPa, at the origin) to avoid numerical difficulties as soil approaches zero confinement during liquefaction. Each yield surface causes a change in the plastic modulus and thus gives the user

control of the shear stress-strain response. The yield surface is open along the hydrostatic axis and is not capped for large confining stresses. The model uses a set of phase transformation surfaces that lie below the yield surface to capture the contractive or dilative behavior of the soil. A purely kinematic hardening rule is employed to track the yield surface with plastic flow.

To couple the development of shear and volumetric plastic strains in soil behavior, a non-associative flow rule is used. The non-associativity is only attributed to the volumetric component of the plastic strain, whereas the deviatoric component of the strain is associative. The volumetric component of the plastic strain defines the extent of dilation and contraction and is only a function of the stress ratio (η), and a scalar valued function (Ψ) that determines the rate of contraction (based on soil type and D_r) and confinement (k_σ effect). It is noted that this model is unable to capture a consolidation path and therefore underestimates post liquefaction volumetric strains (Elgamal *et al.* 2003, Howell *et al.* 2015). Improvements can be made however, by varying the permeability as a function of the effective confinement as noted in (Shahir *et al.* (2012). Effects of the sedimentation/consolidation process can also be heuristically incorporated similar to Ziotopoulou and Boulanger (2013).

It is important to note that the calibrations for PDMY02 to a specific soil is not carried out for the critical state. Therefore, for each type of soil, calibration needs to be carried out for each D_r and confining pressure used in testing. Data for the calibration of Ottawa F-65 sand is obtained from Parra Bastidas (2016). Further parameters specific to the PDMY02 constitutive model are presented in Table 5.5.

5.4.2 Finite Element Modeling

The mesh for the free-field and soil-foundation system experiments are shown in Figure 5.8 and Figure 5.9, respectively. All nodes along the boundary of the laminar soil container

are tied to move together in the lateral direction. Nodes along the base of the model are fixed. Due to the symmetry, half meshes are used for both simulations. In the soil-foundation system simulation, the foundation is rigidly tied to the soil and no slip is allowed along the boundary. The loading was performed in 3 stages, including:

i) Application of gravity using linear elastic soil properties with a Poisson's ratio of 0.4. This stage ensures the static soil stage is imposed (to obtain confinement, static stresses). A large permeability (100 cm/s) is set to the soil domain to ensure a drained response.

ii) The soil properties are switched to plastic to obtain compatible strain levels to match the static stresses imposed in stage 1.

iii) The permeability is switched to the actual soil permeability and the time history is imposed at the base of the model.

Time stepping for the matrix equations are solved using a second order accurate two step TRBDF2 scheme (Bathe, 2007). The integrator is a composite scheme that uses the trapezoidal rule for the predictor step and a 3-point backward Euler scheme for the corrector step in an attempt to conserve momentum and energy. The rule also enables a specification of higher time increments post strong shaking allowing to simulate excess pore pressure dissipation. The resulting system of equations are solved using a modified Newton Raphson incremental iterative procedure with a Krylov subspace accelerator (Scott and Fenves, 2009) for faster convergence.

5.5 Computed Response

This section details the computed response in the free field and soil foundation system experiment for Shake1. The calibration for constitutive model parameters is performed using the free field experiment and a forward prediction is made for the soil-foundation system experiment using the calibrated properties. Due to the similarity in model construction and layering between

the two experiments, it is expected that a calibration for the free-field experiment would yield a sufficiently good model for the forward prediction of the experiment with the foundation system.

5.5.1 Free field Experiment

i) Pore Pressure Response

Comparisons between the simulated and experimentally recorded excess pore pressures at different sensor locations along the depth of the deposit are presented in Figure 5.10. Within the liquefiable layer, excess pore pressure rises after 1-2 cycles of strong shaking, followed by dilative spikes which lead to sudden dips. Generally, the employed simulations could track the cycle-by-cycle generation of excess pore pressure within the loose layer. System response was also evident in the stratified profile, where extensive once the liquefied layer developed high pore pressures, large accelerations were not transmitted to upper strata. This effect in turn reduced the shear demands on the liquefiable layer and reduced the rate of excess pore pressure generation.

ii) Acceleration Response

The simulated and experimentally recorded acceleration response of the deposit is presented in Figure 5.11. Within the liquefiable and dense layers, the simulation can reasonably estimate the acceleration response of the deposit. At shallow depth, the numerical simulation underestimates the observed acceleration response. This discrepancy in the FE simulation is attributed to the extensive softening of the liquefied layer, leading to a base isolation like effect.

iii) Relative Displacement Response

The comparison between the computed and experimental liquefaction induced ground deformations are presented in Figure 5.12. The cycle-by-cycle deformation mechanism, attributed to the pulse type input motion, is reasonably predicted by the FE simulation.

5.5.2 Soil Foundation System Experiment

This section presents the computed response for Shake1 in the soil foundation system experiment from the properties calibrated for the free-field experiment. Salient features of the response are discussed with the capabilities and limitations of the model.

i) Foundation Settlement

Foundation settlement and rotation computed during Shake1 are presented in Figure 5.13. The numerical model is able to capture the co-seismic shear induced settlements fairly well, is unable to capture the post liquefaction induced settlement. Post shaking, sedimentation and consolidation are the dominant mechanisms contributing to the observed foundation settlement (in the experiment). Post liquefaction and on reconsolidation, the PDMY02 model is excessively stiff and could not accumulate volumetric settlements post shaking. This is also observed in the pore pressure response discussed below, wherein immediately after strong shaking pore pressure dissipation occurs in the numerical model as opposed to the slow dissipation observed in the experiment. Post shaking no appreciable volumetric settlements were observed in the numerical model, and therefore a high rate of pore pressure dissipation was observed. The displacement configuration of the soil mesh at the end of shaking is presented in Figure 5.14.

ii) Pore Pressure Response

Figure 5.15 and Figure 5.16 present a comparison between the experimental and numerical excess pore pressure histories during Shake1 for the free field and below foundation arrays, respectively. The numerical model is largely able to capture the excess pore-pressure histories within the liquefiable layer. However, it underestimates the rate of pore pressure buildup within the dense layer. The dense layer continued to build excess pore pressure even after strong shaking to about 50s as noted in Jahed Orang *et al.* (2020). A low contraction parameter for the PDMY02

constitutive model (c_1 = 0.001) was specified for the bottom dense layer based on observations from the free-field test. Therefore, the layer was unable to generate any appreciable excess pore pressures of its own and the histories at depths below 2 m were reflective of the pressures generated within the upper loose layer.

From the simulation, we can observe that the excess pore pressures generated in the middle array (under foundation) are similar to those observed in the north array. Due to the presence of the foundation, higher confining stresses would be expected in the middle array, as opposed to the north array (at similar depth). Therefore, the soil underneath the foundation did not reach initial liquefaction and hence excess pore pressure ratios ($r_{u,foundation}$) underneath the foundation should be generally lower than the $r_{u,freefield}$. Once the soil in free field liquefies, it cannot provide any additional lateral confinement to the soil underneath the foundation and therefore the excess pore pressure beneath the foundation is capped by the value in the free field. Several researchers have commented on this issue including Adalier *et al.* (2003) and Karamitros *et al.* (2013).

The effect of permeability in the pore pressure dissipation time is presented in Figure 5.17. For a permeability of 1.1×10^{-4} m/s (measured permeability of Ottawa F-65 sand from Parra Bastidas, 2016) we observe that the simulated excess pore pressures dissipate fairly quickly (~30 s after strong shaking). This corroborates well with the low consolidation induced volumetric strains post shaking. Therefore, to reasonably capture the dissipation time, the permeability of sand is lowered post shaking to 0.4×10^{-5} m/s. Using this value, no appreciable difference in the co-seismic settlement rates were observed, however the simulation is able to adequately track the observed pore fluid dissipation in the experiment.

iii) Soil Acceleration Response

Figure 5.18 and Figure 5.19 present a comparison between the acceleration time histories observed from the experiment and simulations during Shake1 for the free-field and under foundation arrays. The numerical model is able to track the acceleration response fairly well in the dense layer. However, within the liquefiable layer, a good comparison is observed for the first 2-3 cycles, after which higher accelerations are observed from the simulation as compared to the experiment. This could be attributed to the relatively low hysteretic damping generated from the simulation as compared to the experiment post liquefaction. Within the liquefiable layer, we also observe a stronger dilative tendency for the numerical model as opposed to the experimental counterpart.

iv) Shear Stress-Strain Response

A second order method proposed by Zeghal and Elgamal (1994) was used to calculate the shear stress-shear strain behavior of the experiment during Shake1. Figure 5.20 and Figure 5.21 present a comparison between the developed cyclic shear stress and shear strain for the experiment and simulation, respectively. The simulation is able to track the developed shear stresses fairly well as observed in Figure 5.20 due to reasonable prediction of soil accelerations. The cyclic shear strains are presented in Figure 5.21, and the simulation is able to reasonably capture the cycle after cycle accumulation of shear strain within the liquefiable layer.

5.6 Conclusions

This chapter presented a calibration and a forward prediction of two large scale shake table experiments performed at the University of California San Diego. First, a calibration was performed to obtain consistent constitutive model parameters for a test conducted to study the response of a three-layered deposit under free field conditions (Zayed *et al.* 2021). The calibrated

parameters are then utilized to predict the system response of a soil foundation interaction experiment.

1. The PDMY02 constitutive model can reasonably capture the mechanism behind liquefaction induced ground deformations observed in both the free-field and soil foundation system experiments.
2. The calibrated constitutive model parameters (PDMY02 constitutive model) obtained for this test series can be used as a future benchmark to study the response of similar large scale shake table experiments.
3. The choice of permeability of sand (within the constitutive model) plays a major role in the accumulation of volumetric strains post shaking. Using the actual permeability of Ottawa F-65 sand results in a relatively fast dissipation of excess pore pressures and little to no volumetric strains after strong shaking. However, on further decreasing the permeability by an order of magnitude, a reasonable match in the excess pore pressure dissipation histories were obtained.
4. Reasonable estimates of the system response (ground/structure deformations, accelerations, and excess pore pressures) can be obtained using computational simulations for the design of structures founded on potentially liquefiable soil.
5. After strong shaking, the observed settlement in the experiment was driven by the consolidation sedimentation process. Reducing the soil permeability for PDMY02 can lead to better predictions of the consolidation process, however improvements must be made to physically capture the sedimentation process.

5.7 Acknowledgement

Chapter 5, in part, is in part a reprint of the material as it appears in Prabhakaran, A., Kim, K., Qiu, Z., Elgamal, A., and Frazao, C. (2022). "Polymer Injection to Remediate Liquefaction-Induced Foundation Settlement: Numerical Simulation of Shake Table Experiments." *ASCE Lifelines Conference*, American Society of Civil Engineers, Los Angeles, CA. The dissertation author was the primary investigator and author.

5.8 References

Adalier, K., Elgamal, A., Meneses, J., and Baez, J. I. (2003). "Stone columns as liquefaction countermeasure in non-plastic silty soils." *Soil Dynamics and Earthquake Engineering*, Elsevier BV, 23(7), 571–584.

Adamidis, O., and Madabhushi, S. G. (2018). "Deformation mechanisms under shallow foundations on liquefiable layers of varying thickness." *Geotechnique*, ICE Publishing, 68(7), 1–13.

Adamidis, O., and Madabhushi, S. P. G. (2022). "Rocking response of structures with shallow foundations on thin liquefiable layers." *Geotechnique*, ICE Publishing, 72(2), 127–145.

Ashford, S. A., Boulanger, R. W., Donahue, J. L., and Stewart, J. P. (2011). "Geotechnical Quick Report on the Kanto Plain Region during the March 11, 2011, Off Pacific Coast of Tohoku Earthquake, Japan." *Geotechnical Extreme Events Reconnaissance*, GEER-025a(April), 1–20.

Bathe, K. J. (2007). "Conserving energy and momentum in nonlinear dynamics: A simple implicit time integration scheme." *Computers and Structures*, Pergamon, 85(7–8), 437–445.

Bertalot, D., Brennan, A. J., and Villalobos, F. A. (2013). "Influence of bearing pressure on liquefaction-induced settlement of shallow foundations." *Geotechnique*, Thomas Telford Ltd , 63(5), 391–399.

Biot, M. A. (1962). "Mechanics of deformation and acoustic propagation in porous media." *Journal of Applied Physics*, American Institute of PhysicsAIP, 33(4), 1482–1498.

Bray, J. D., and Macedo, J. (2017). "6th Ishihara lecture: Simplified procedure for estimating liquefaction-induced building settlement." *Soil Dynamics and Earthquake Engineering*, Elsevier, 102, 215–231.

Bullock, Z., Karimi, Z., Dashti, S., Porter, K., Liel, A. B., and Franke, K. W. (2019). "A physics-informed semi-empirical probabilistic model for the settlement of shallow-founded structures on liquefiable ground." *Geotechnique*, ICE Publishing, 69(5), 406–419.

Chan, A. (1988). “A unified Finite Element Solution to Static and Dynamic Geomechanics problems.” *Department of Civil Engineering*, University College of Swansea, Swansea.

Cubrinovski, M. (2013). “Liquefaction-Induced Damage in the 2010-2011 Christchurch (New Zealand) Earthquakes.” *International Conference on Case Histories in Geotechnical Engineering*, Missouri University of Science and Technology, Chicago, Illinois.

Cubrinovski, M., Green, R. A., Allen, J., Ashford, S., Bowman, E., Brendon, Bradley, Cox, B., Hutchinson, T., Kavazanjian, E., Orense, R., Pender, M., Quigley, M., and Wotherspoon, L. (2010). “Geotechnical reconnaissance of the 2010 Darfield (Canterbury) earthquake.” *Bulletin of the New Zealand Society for Earthquake Engineering*, 43(4), 243–320.

Dashti, S., and Bray, J. D. (2013). “Numerical Simulation of Building Response on Liquefiable Sand.” *Journal of Geotechnical and Geoenvironmental Engineering*, American Society of Civil Engineers, 139(8), 1235–1249.

Dashti, S., Bray, J. D., Pestana, J. M., Riemer, M., and Wilson, D. (2010). “Mechanisms of Seismically Induced Settlement of Buildings with Shallow Foundations on Liquefiable Soil.” *Journal of Geotechnical and Geoenvironmental Engineering*, American Society of Civil Engineers, 136(1), 151–164.

Dashti, S., Bullock, Z., Porter, K., Liel, A., and Karimi, Z. (2018). “Key predictors of structure settlement on liquefiable ground: a numerical parametric study.” *Soil Dynamics and Earthquake Engineering*, Elsevier, 113, 286–308.

Dimitriadi, V. E., Bouckovalas, G. D., and Papadimitriou, A. G. (2017). “Seismic performance of strip foundations on liquefiable soils with a permeable crust.” *Soil Dynamics and Earthquake Engineering*, Elsevier, 100, 396–409.

EERI. (2000). “Damage Patterns and Foundation Performance in Adapazari.” *Earthquake Spectra*, 16(SUPPL. A), 163–188.

Elgamal, A., Lu, J., and Yang, Z. (2005). “Liquefaction-induced settlement of shallow foundations and remediation: 3d numerical simulation.” *Journal of Earthquake Engineering*, Taylor & Francis Group, 9(1), 17–45.

Elgamal, A., Yang, Z., Parra, E., and Ragheb, A. (2003). “Modeling of cyclic mobility in saturated cohesionless soils.” *International Journal of Plasticity*, Pergamon, 19(6), 883–905.

George, N. V. (2009). “S Transform: Time Frequency Analysis and Filtering.” National Institute of Technology, Rourkela.

Hamada, M., Isoyama, R., and Wakamatsu, K. (1996). “Liquefaction-induced ground displacement and its related damage to lifeline facilities.” *Soils and Foundations*, Japanese Soc of Soil Mechanics & Foundation Engineering, 36(Special), 81–97.

Howell, R., Rathje, E. M., and Boulanger, R. W. (2015). “Evaluation of Simulation Models of Lateral Spread Sites Treated with Prefabricated Vertical Drains.” *Journal of Geotechnical*

and Geoenvironmental Engineering, American Society of Civil Engineers, 141(1), 04014076.

Hughes, T. J. R. (2008). "The Finite Element Method: Linear Static and Dynamic Finite Element Analysis: Thomas J. R. Hughes." *Computer-Aided Civil and Infrastructure Engineering*, Prentice-Hall, 4(3), 245–246.

Ishihara, K., and Koga, Y. (1981). "Case Studies of Liquefaction in the 1964 Niigata Earthquake." *Soils and Foundations*, Elsevier BV, 21(3), 35–52.

Jahed Orang, M., Motamed, R., Prabhakaran, A., and Elgamal, A. (2020). "Large-scale shake table test on a shallow foundation in liquefied soils (in Review)." *Journal of Geotechnical & Geoenvironmental Engineering*.

Jain, S. K., Lettis, W. R., Murty, C. V. R., and Bardet, J.-P. (2002). "2001 Bhuj, India Earthquake Reconnaissance Report." *Earthquake Spectra*, SAGE Publications, 18(1_suppl), 1–4.

Karamitros, D. K., Bouckovalas, G. D., and Chaloulos, Y. K. (2013). "Insight into the Seismic Liquefaction Performance of Shallow Foundations." *Journal of Geotechnical and Geoenvironmental Engineering*, American Society of Civil Engineers, 139(4), 599–607.

Karimi, Z., and Dashti, S. (2016). "Numerical and Centrifuge Modeling of Seismic Soil–Foundation–Structure Interaction on Liquefiable Ground." *Journal of Geotechnical and Geoenvironmental Engineering*, American Society of Civil Engineers (ASCE), 142(1), 04015061.

Kassas, K., Adamidis, O., and Anastasopoulos, I. (2021a). "Shallow strip foundations subjected to earthquake-induced soil liquefaction: Validation, modelling uncertainties, and boundary effects." *Soil Dynamics and Earthquake Engineering*, Elsevier, 147, 106719.

Kassas, K., Adamidis, O., Gerolymos, N., and Anastasopoulos, I. (2021b). "Numerical modelling of a structure with shallow strip foundation during earthquake-induced liquefaction." *Geotechnique*, ICE Publishing, 71(12), 1099–1113.

Khosravifar, A., Elgamal, A., Lu, J., and Li, J. (2018). "A 3D model for earthquake-induced liquefaction triggering and post-liquefaction response." *Soil Dynamics and Earthquake Engineering*, Elsevier, 110, 43–52.

Liu, L., and Dobry, R. (1997). "Seismic Response of Shallow Foundation on Liquefiable Sand." *Journal of Geotechnical and Geoenvironmental Engineering*, American Society of Civil Engineers, 123(6), 557–567.

McKenna, F., Scott, M. H., and Fenves, G. L. (2010). "Nonlinear Finite-Element Analysis Software Architecture Using Object Composition." *Journal of Computing in Civil Engineering*, American Society of Civil Engineers, 24(1), 95–107.

Motamed, R., Orang, M. J., Parayancode, A., and Elgamal, A. (2020). "Results of a Class C Blind Prediction Competition on the Numerical Simulation of a Large-Scale Liquefaction Shaking

Table Test." *ASCE Geo-Congress 2020*, American Society of Civil Engineers (ASCE), 334–342.

Parra Bastidas, A. M. (2016). "Ottawa F-65 Sand Characterization." *PhD Thesis*, University of California Davis.

Parra, E. (1996). "Numerical modeling of liquefaction and lateral ground deformation including cyclic mobility and dilation response in soil systems." Rensselaer Polytechnic Inst.

Prevost, J. H. (1985). "A simple plasticity theory for frictional cohesionless soils." *International Journal of Soil Dynamics and Earthquake Engineering*, Elsevier, 4(1), 9–17.

Scott, M. H., and Fenves, G. L. (2009). "Krylov Subspace Accelerated Newton Algorithm: Application to Dynamic Progressive Collapse Simulation of Frames." *Journal of Structural Engineering*, American Society of Civil Engineers, 136(5), 473–480.

Shahir, H., and Pak, A. (2010). "Estimating liquefaction-induced settlement of shallow foundations by numerical approach." Computers and Geotechnics, Elsevier, 37(3), 267–279.

Shahir, H., Pak, A., Taiebat, M., and Jeremić, B. (2012). "Evaluation of variation of permeability in liquefiable soil under earthquake loading." *Computers and Geotechnics*, Elsevier, 40, 74–88.

Stockwell, R. G., Mansinha, L., and Lowe, R. P. (1996). "Localization of the complex spectrum: the s transform." *IEEE Transactions on Signal Processing*, 44(4), 998–2001.

Tokimatsu, K., Hino, K., Suzuki, H., Ohno, K., Tamura, S., and Suzuki, Y. (2019). "Liquefaction-induced settlement and tilting of buildings with shallow foundations based on field and laboratory observation." *Soil Dynamics and Earthquake Engineering*, Elsevier, 124, 268–279.

Yang, Z., Elgamal, A., and Parra, E. (2003). "Computational Model for Cyclic Mobility and Associated Shear Deformation." *Journal of Geotechnical and Geoenvironmental Engineering*, American Society of Civil Engineers (ASCE), 129(12), 1119–1127.

Yoshimi, Y., and Tokimatsu, K. (1977). "Settlement of Buildings on Saturated Sand During Earthquakes." *Soils and Foundations*, Elsevier, 17(1), 23–38.

Zayed, M., Ebeido, A., Prabhakaran, A., Qiu, Z., and Elgamal, A. (2021). "Asymmetric input motion for accumulation of lateral ground deformation in laminar container shake table testing." *Canadian Geotechnical Journal*, Canadian Science Publishing, 58(2), 210–223.

Zeghal, M., and Elgamal, A. W. (1994). "Analysis of site liquefaction using earthquake records." *Journal of Geotechnical Engineering*, American Society of Civil Engineers, 120(6), 996–1017.

Ziotopoulou, K., and Boulanger, R. W. (2013). "Numerical Modeling Issues in Predicting Post-Liquefaction Reconsolidation Strains and Settlements." *10th International Conference on*

Urban Earthquake Engineering (10CUEE), Tokyo, (1992), 469–475.

5.9 Tables and Figures

Table 5.1. Basic Geotechnical Properties of Ottawa F-65 Sand (Parra Bastidas, 2016)

Specific Gravity	2.65
Maximum Void Ratio (e_{max})	0.853
Minimum Void Ratio (e_{min})	0.503
Coefficient of uniformity (C_u)	1.61
Coefficient of curvature (C_c)	0.96
Maximum and minimum voids ratio (e_{max}, e_{min})	0.853, 0.503
Maximum and minimum mass density ρ_{min}, ρ_{max} (kg/m^3)	1446, 1759
Coefficient of uniformity (C_u)	1.61

Table 5.2. Soil properties and layering of free field experiment

Property	**Crust layer**	**Liquefiable layer**	**Base layer**
Water/soil condition	Moist	Saturated	Saturated
Depth (m)	0-0.55	0.55-1.9	1.9-2.9
Thickness (m)	0.64	1.26	1.0
Estimated D_r (%)	50%-55%	35%-44%	80 – 95%

Table 5.3. Soil properties and layering of soil foundation system experiment

Property	**Crust layer**	**Liquefiable layer**	**Base layer**
Water/soil condition	Moist	Saturated	Saturated
Depth (m)	0-0.64	0.64-1.9	1.9-2.9
Thickness (m)	0.64	1.26	1.0
Estimated D_r (%)	50%-55%	35%-44%	80 – 95%

Table 5.4. Base Excitation Sequence

Shake#	**Shake Identifier**	**PGA (g)**	**uration (s)**	**Comments**
1	WN01	0.05 (RMS)	5 s	(5-20) Hz
2	**Shake1**	0.15g	18 s	Main Shake1
3	WN02	0.05g (RMS)	20 s	(5-20) Hz
4	**Shake02**	0.3g	18 s	Main Shake02
5	WN03	0.05g (RMS)	20 s	(5-20) Hz
6	WN05	0.05g (RMS)	20 s	TestDay2: Top Layer Saturated
7	**Shake03**	0.3g	18 s	Main Shake03
8	WN06	0.05g (RMS)	20 s	(5-20) Hz

Table 5.5. Employed properties for the soil constitutive PDMY02 model

Model Parameters	***Crust***	***Liquefiable layer***	***Dense layer***
Relative Density (D_r)	55%	40%	85%
Element Type		B-Bar brick u-p	
Reference mean effective pressure, p'_r (kPa)	8.9	18.7	30.3
Total mass density, ρ (t/m^3)	2.00	1.9	2.1
Maximum shear strain at reference pressure, $\gamma_{max,r}$		0.10	
Shear modulus at reference pressure, G_r (MPa)	7.5	5	25
Stiffness dependence coefficient *d*		0.5	
Poisson's ratio *v* for dynamics		0.4	
Friction angle ϕ, with resulting strength defined as $p' \sin\phi$	32	29.5	36
Phase transformation angle, ϕ_{PT}	31	29.5	28.5
Contraction coefficient, c_1	0	0.18	0.001
Dilation coefficient, d_1	0	0	0.2
Permeability (m/s)		1.1×10^{-5}	
Initial stiffness damping coefficient		0.003	
Convergence criteria based on norm of energy increment		10^{-6}	

(a)

(b)

Figure 5.1. Laminar soil container at the Powell structural engineering laboratories at UC San Diego: (a) Side view, and (b) Foundation and soil model prior to experiment

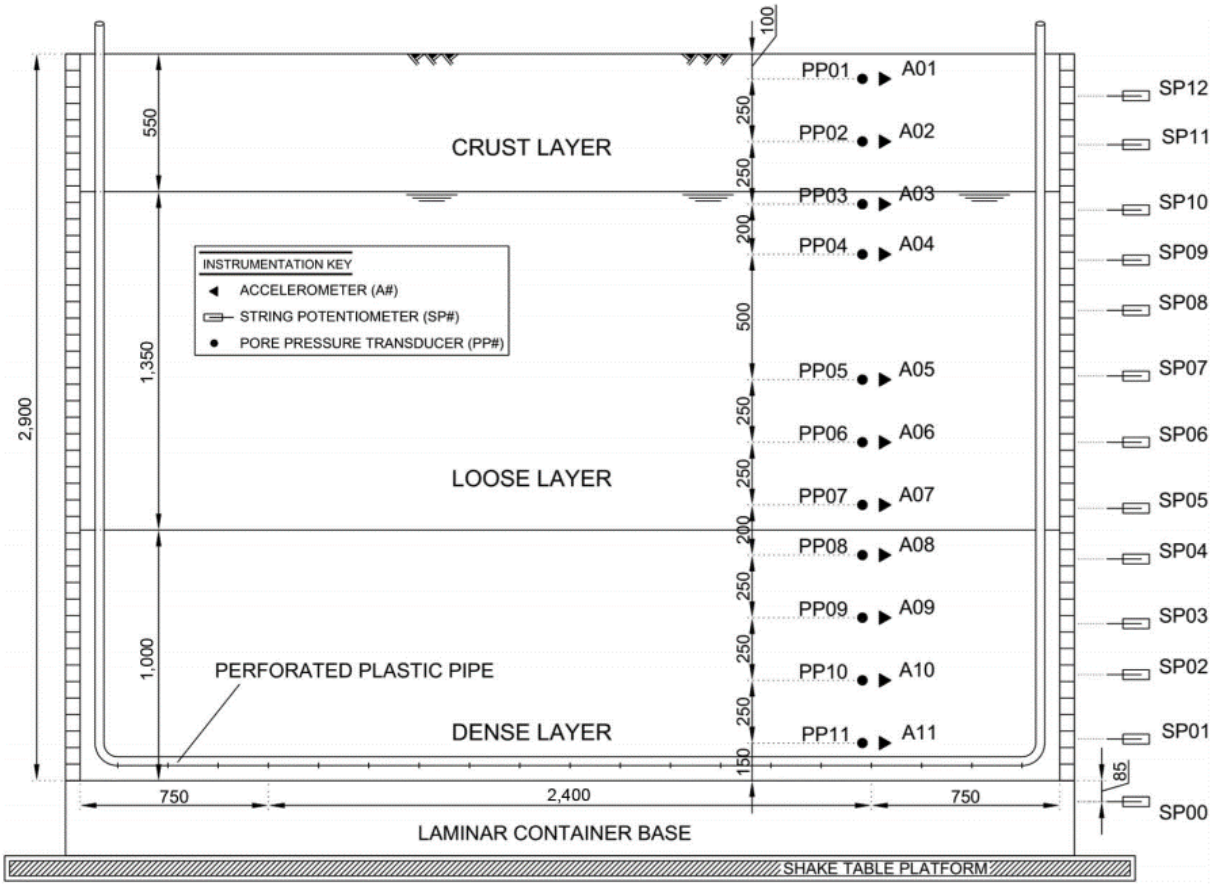

Figure 5.2. Instrumentation layout of free field experiment (Zayed *et al.* 2020) (All units in mm)

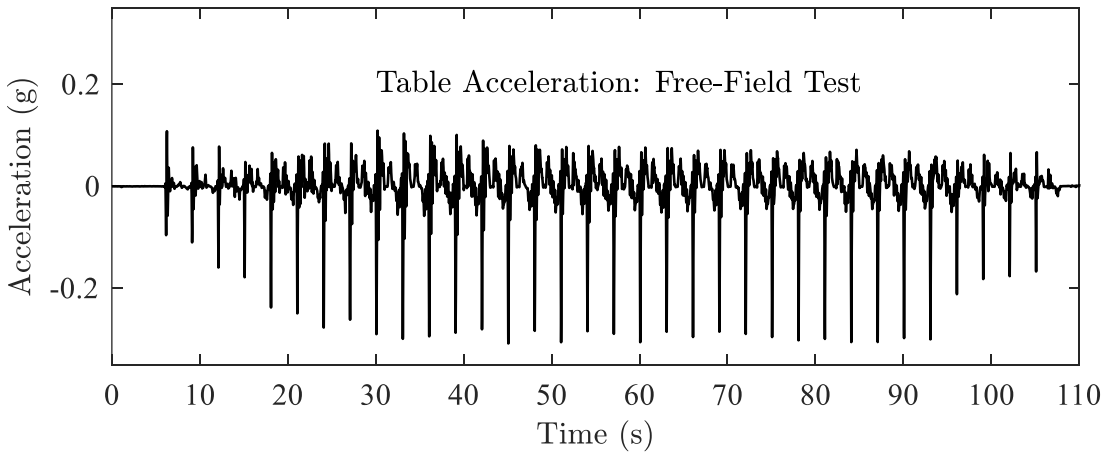

Figure 5.3. Input base excitation for the free field experiment based on Zayed *et al.* (2021)

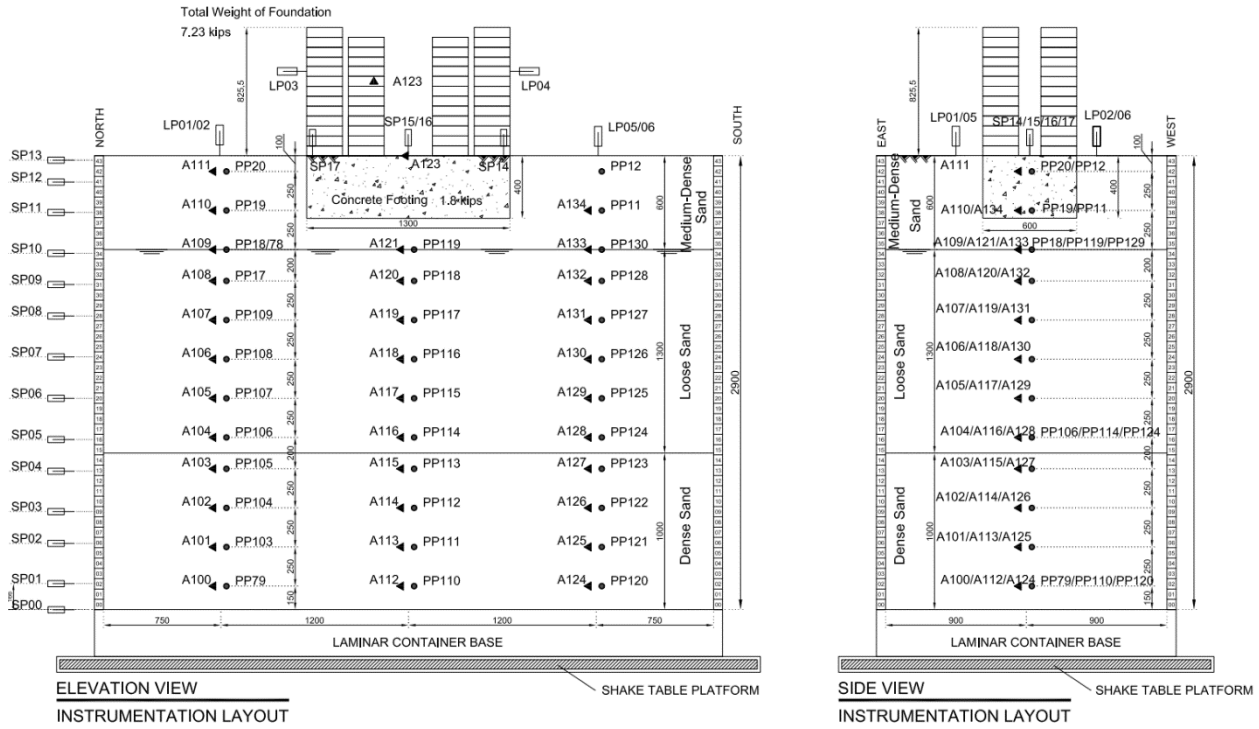

(a)

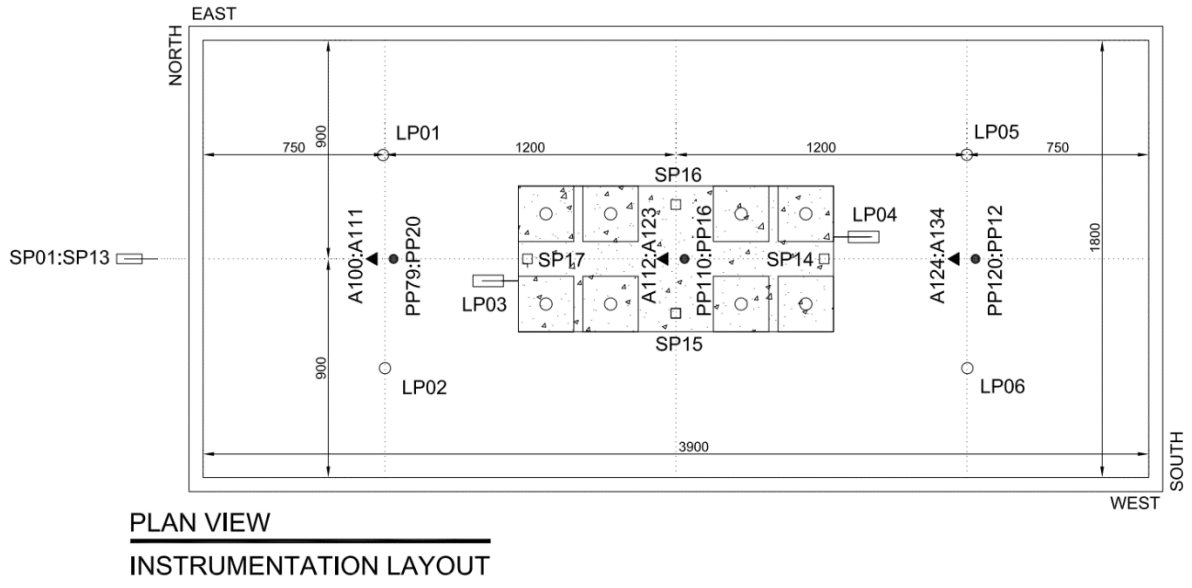

(b)

Figure 5.4. Instrumentation layout of baseline experiment: (a) Elevation and side view, (b) Plan view of baseline model (All units in mm)

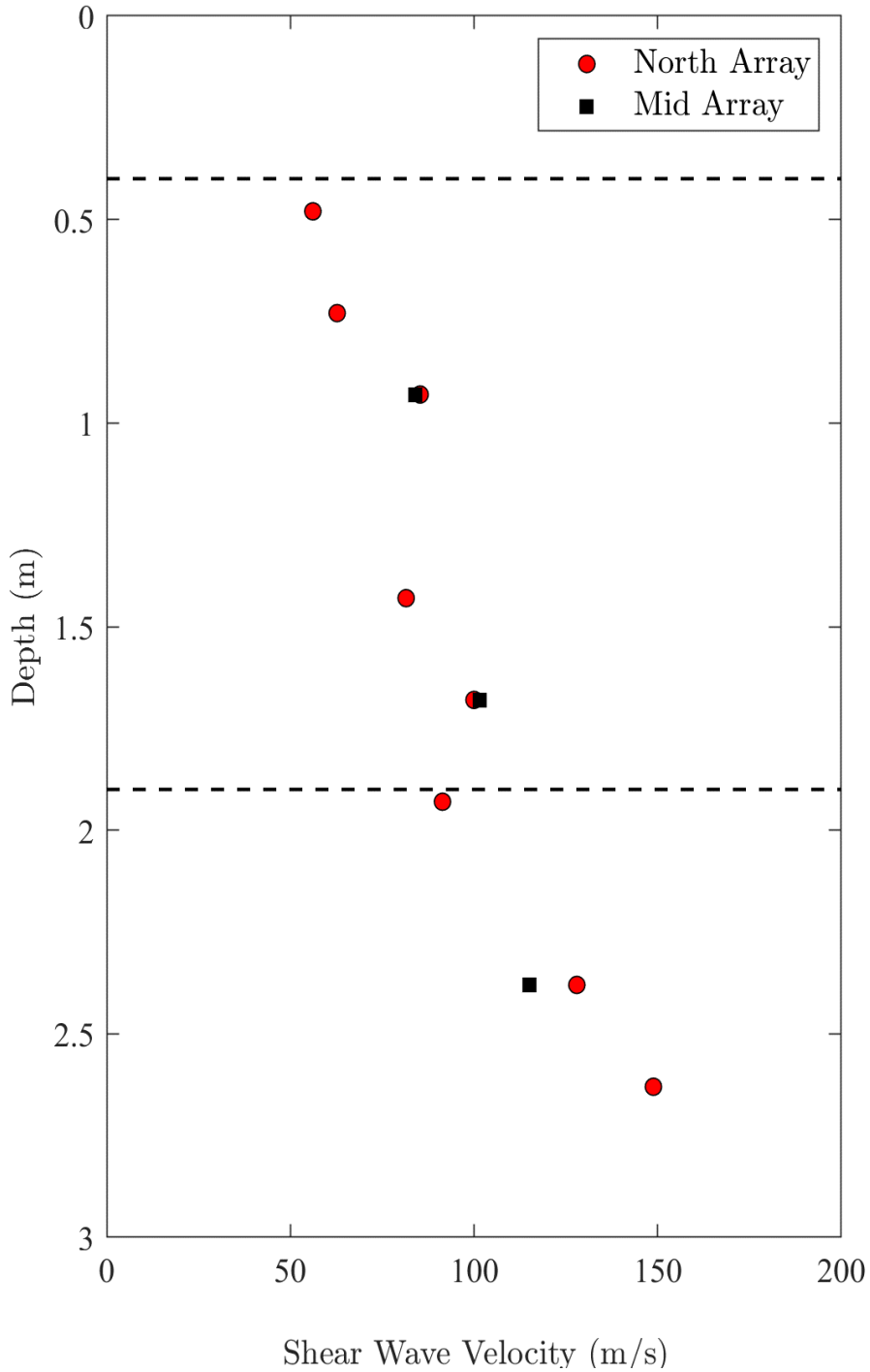

Figure 5.5. Estimate of Shear wave velocities from PCB accelerometers from WN01 (virgin model)

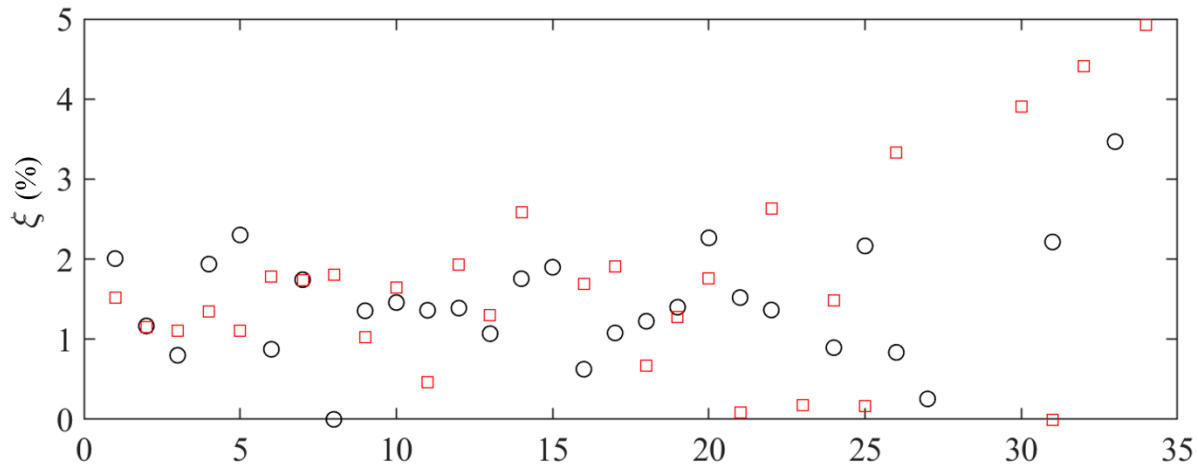

Figure 5.6. Computed low strain damping ratio estimates based on the log decrement method

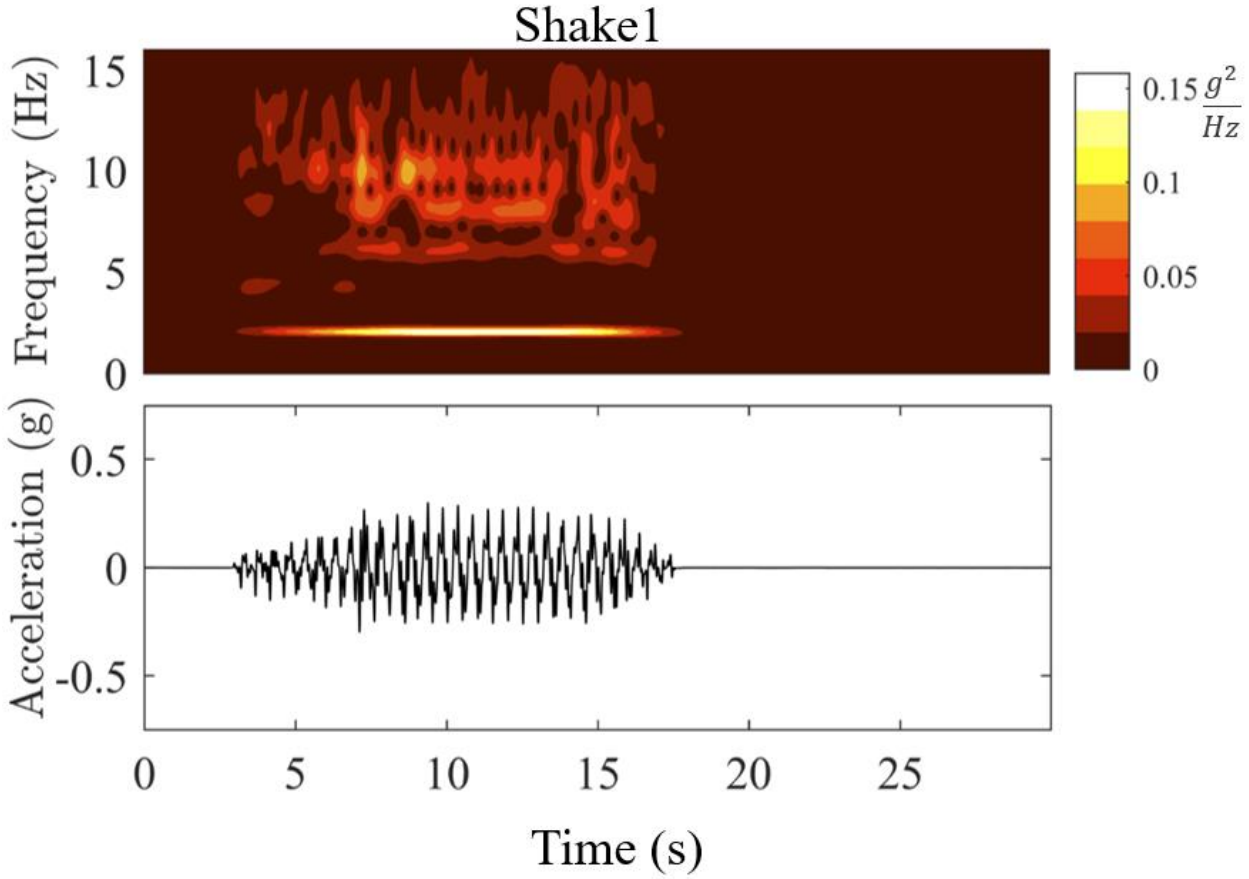

Figure 5.7. Imparted base excitation for shake table testing for Shake1 (soil-foundation system experiment)

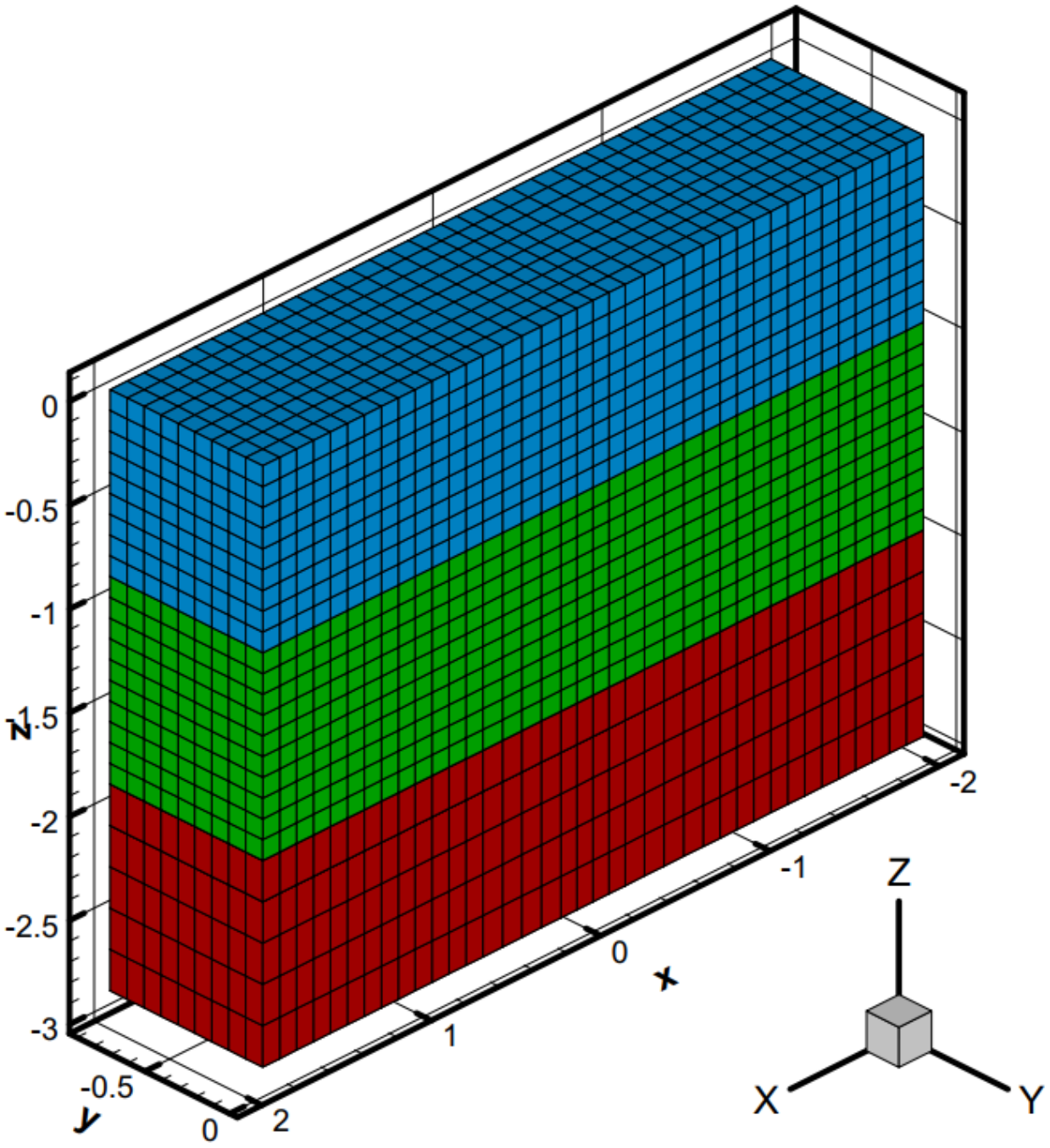

Figure 5.8. Finite element model and soil mesh for the free field experiment

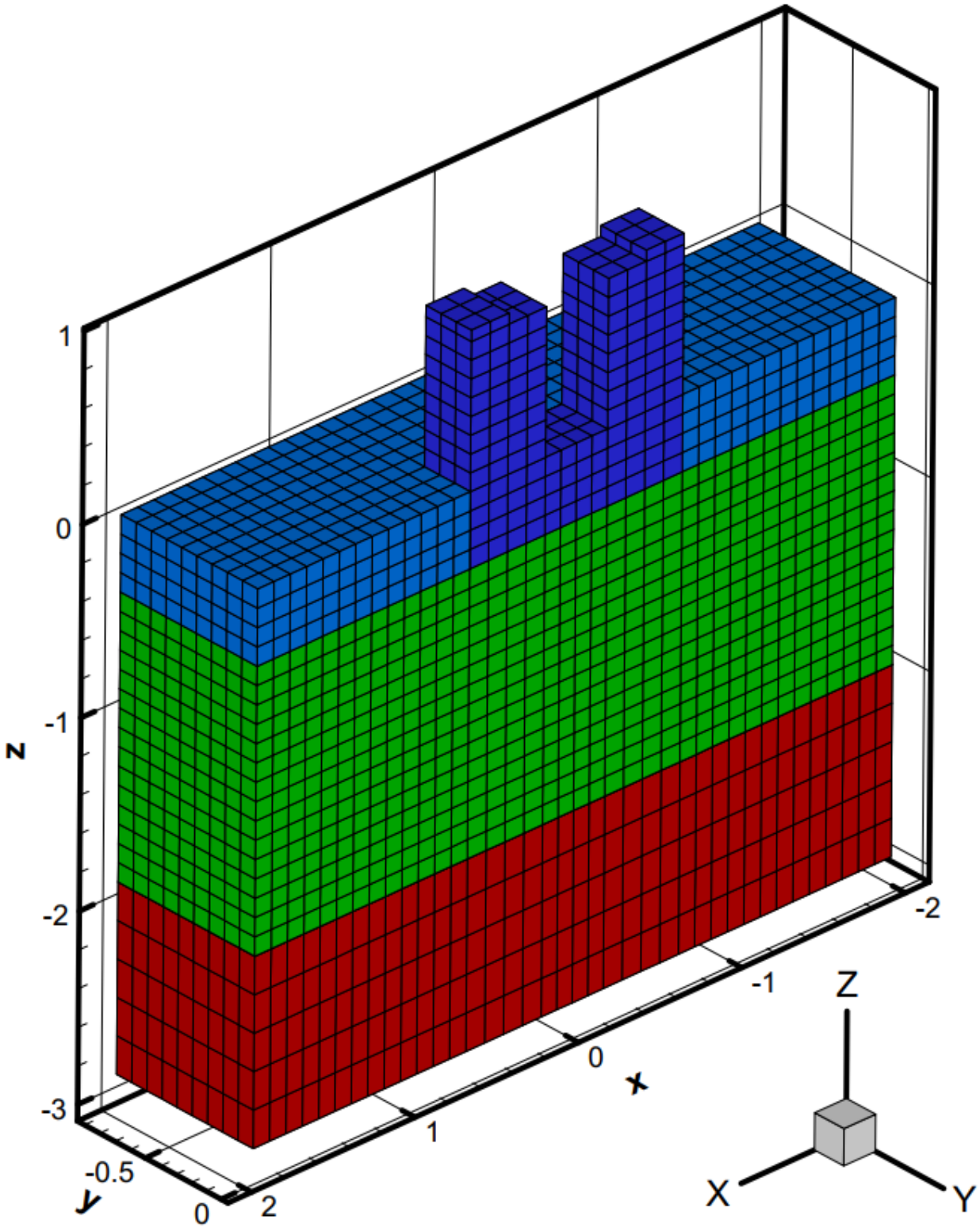

Figure 5.9. Finite element model and mesh for the soil-foundation system experiment

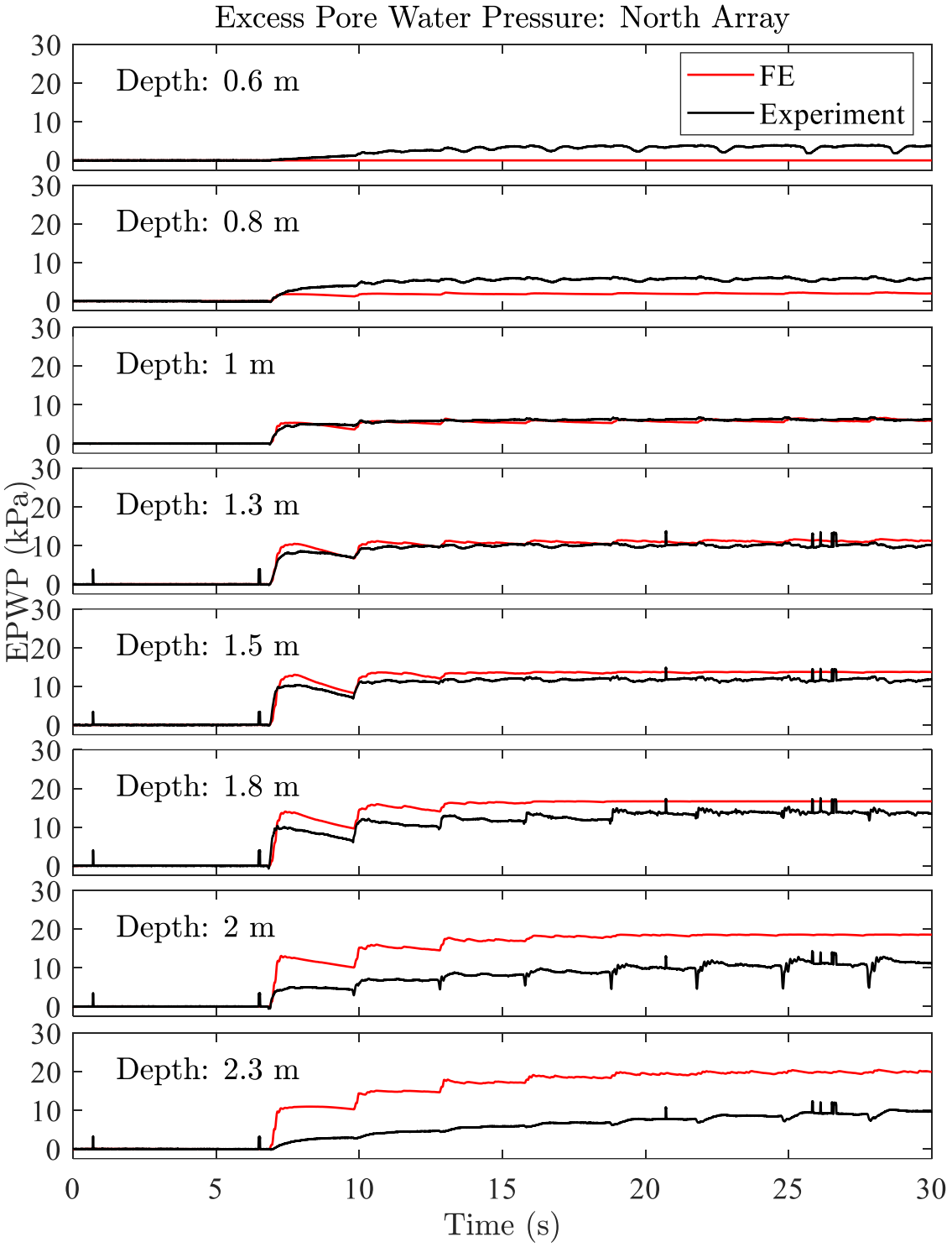

Figure 5.10. Measured and computed excess pore pressure response of the free field experiment

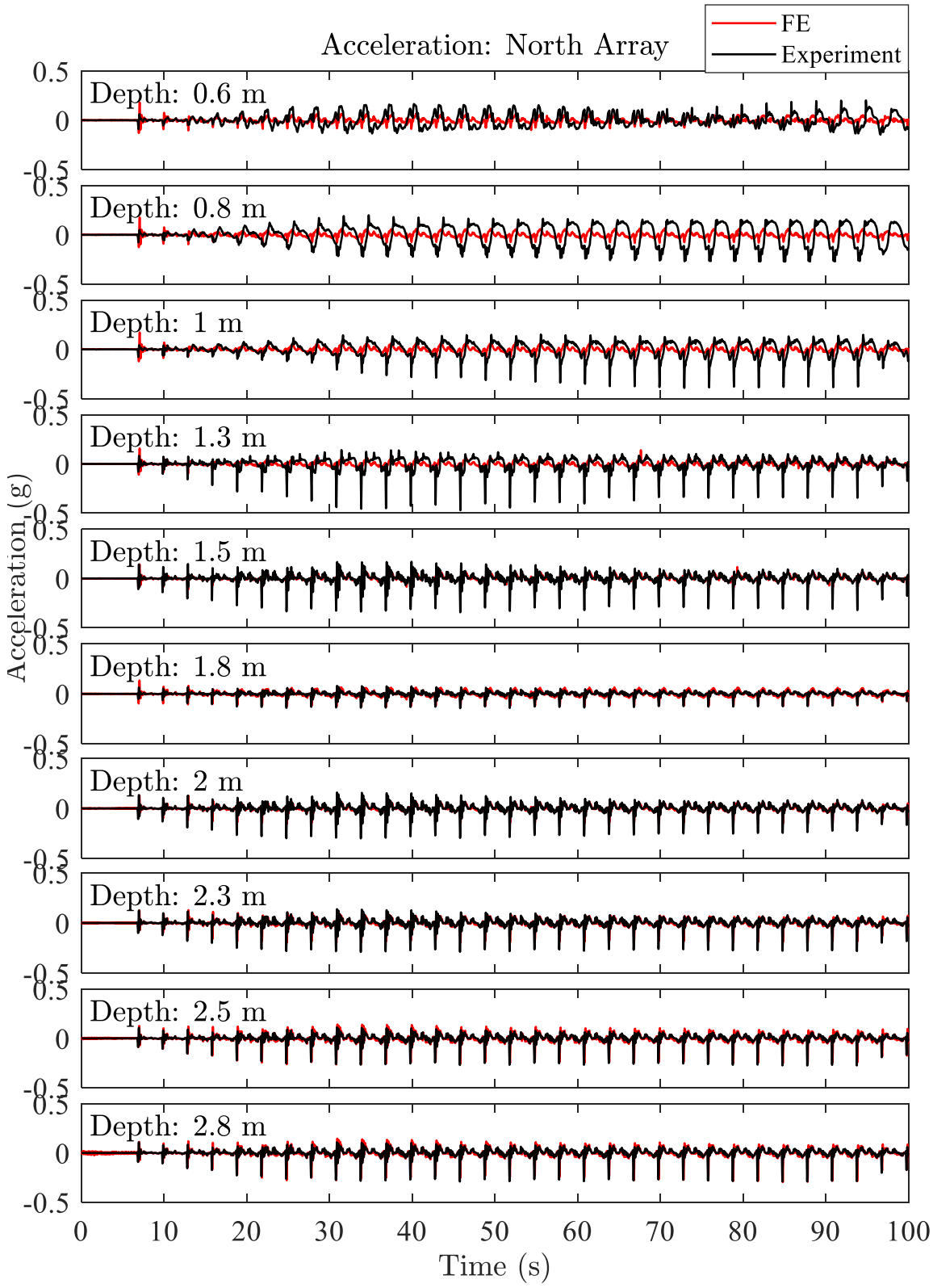

Figure 5.11. Measured and computed soil accelerations for the free field experiment

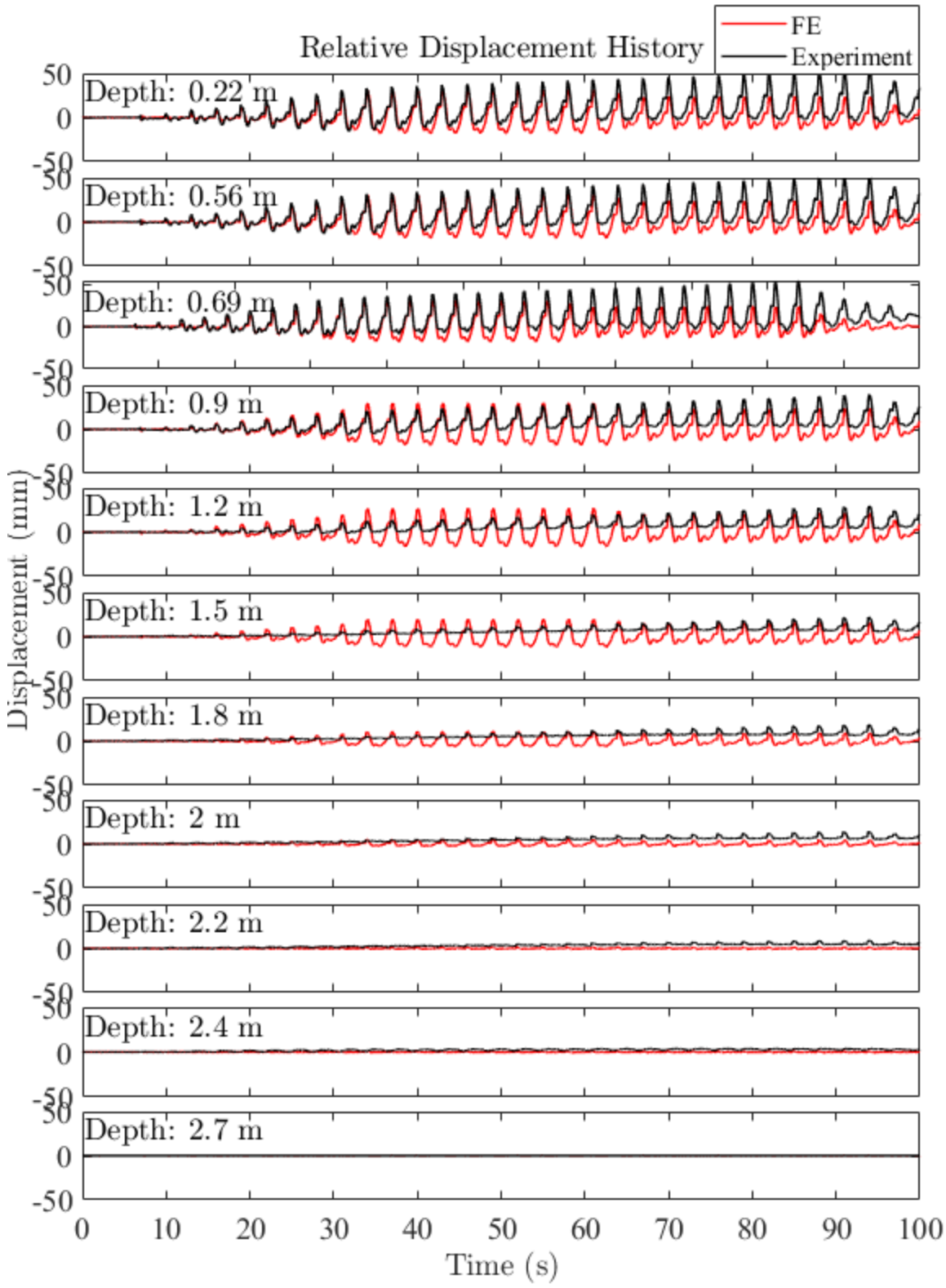

Figure 5.12. Measured and computed soil displacements for the free field experiment (along the laminates of the container)

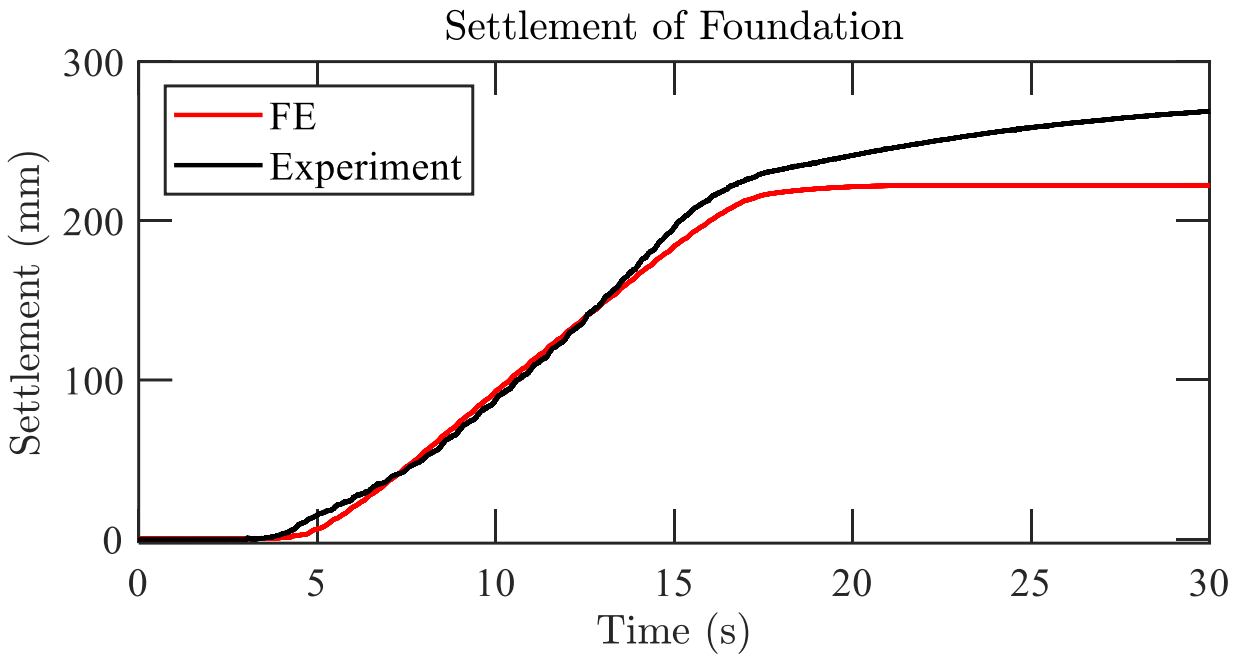

Figure 5.13. Measured and computed foundation settlement for the soil-foundation system experiment

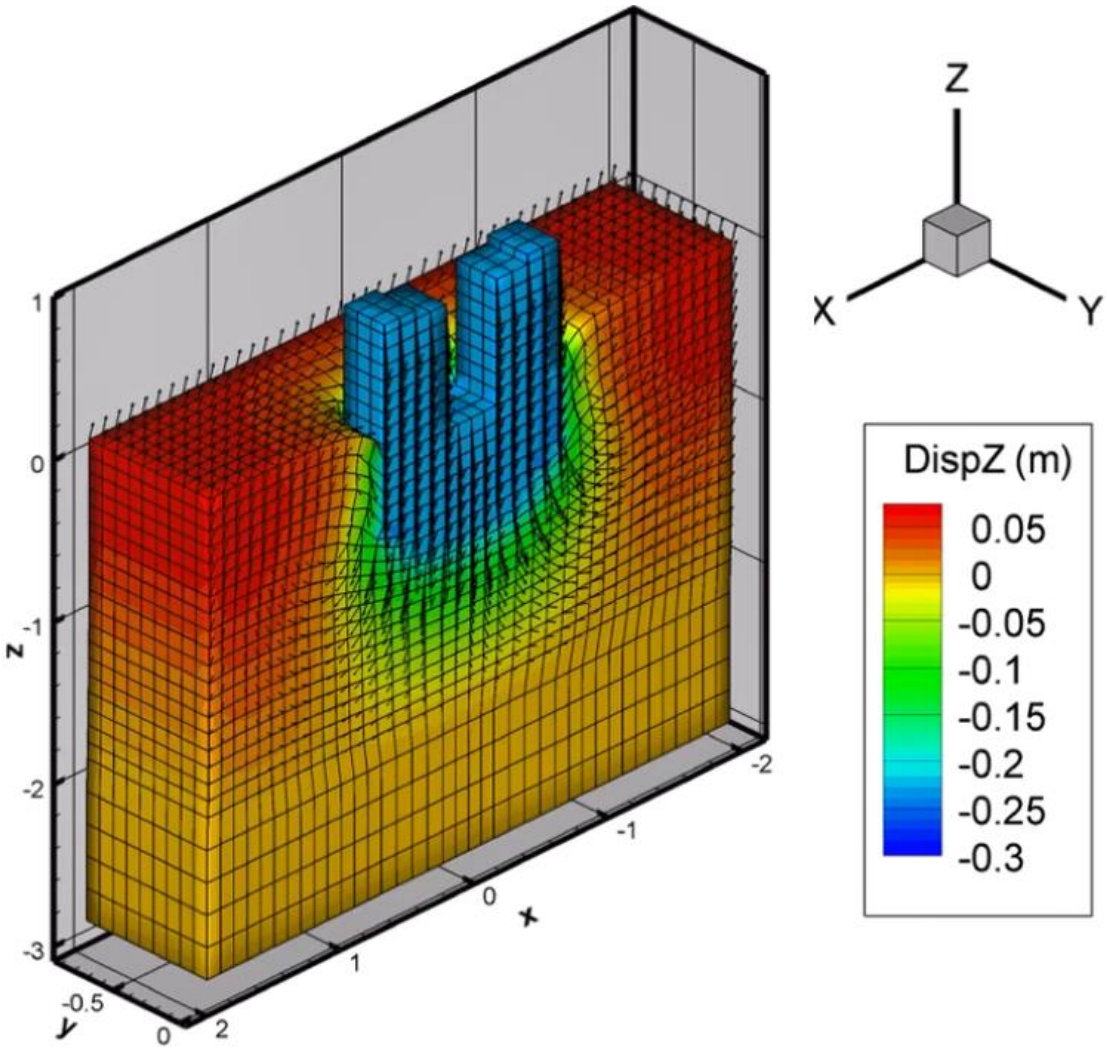

Figure 5.14. Displaced configuration of soil mesh at the end of Shake1 for the soil-foundation system experiment

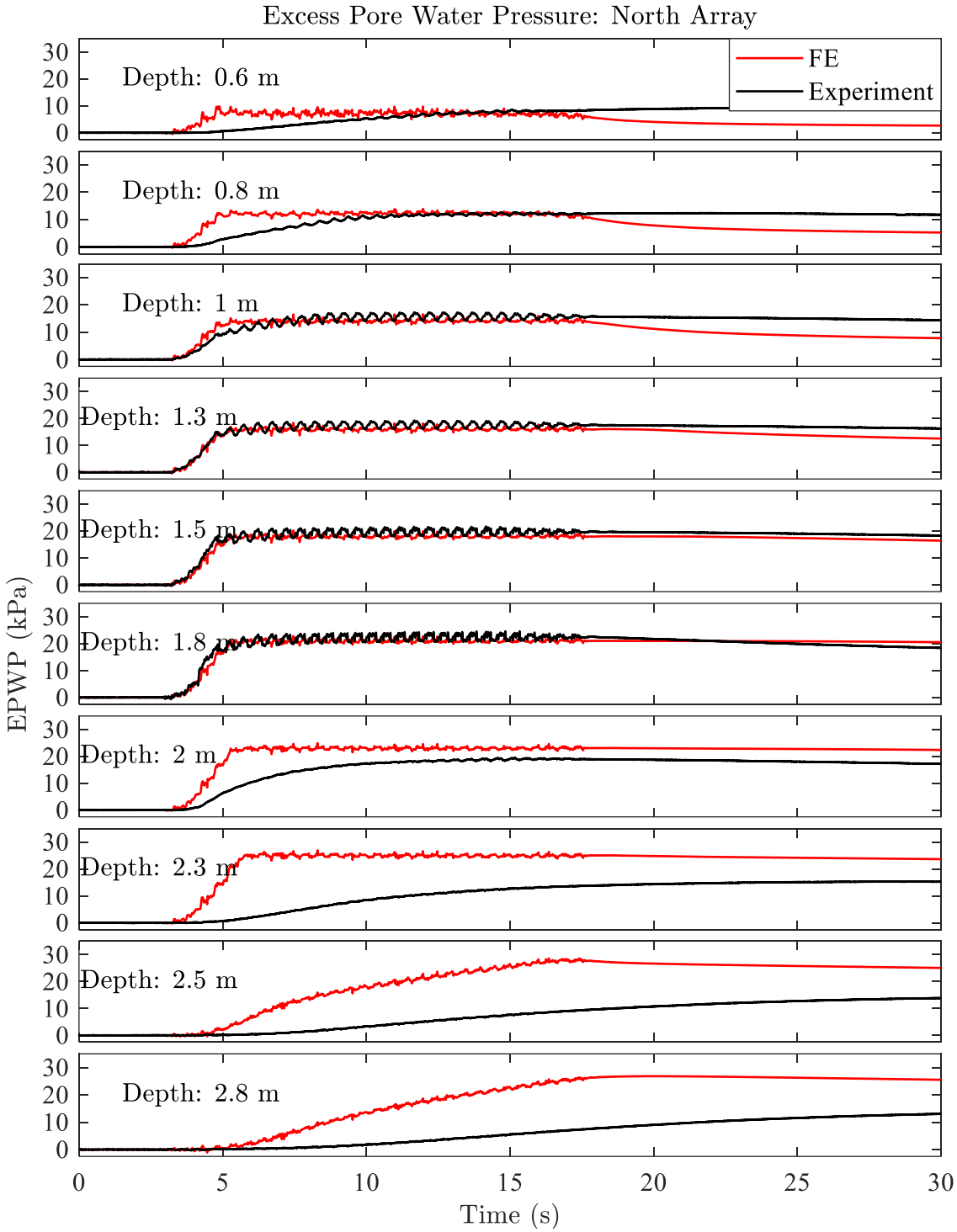

Figure 5.15. Measured and computed excess pore pressure response in the north array for the soil-foundation system experiment (along soil nodes at different depth)

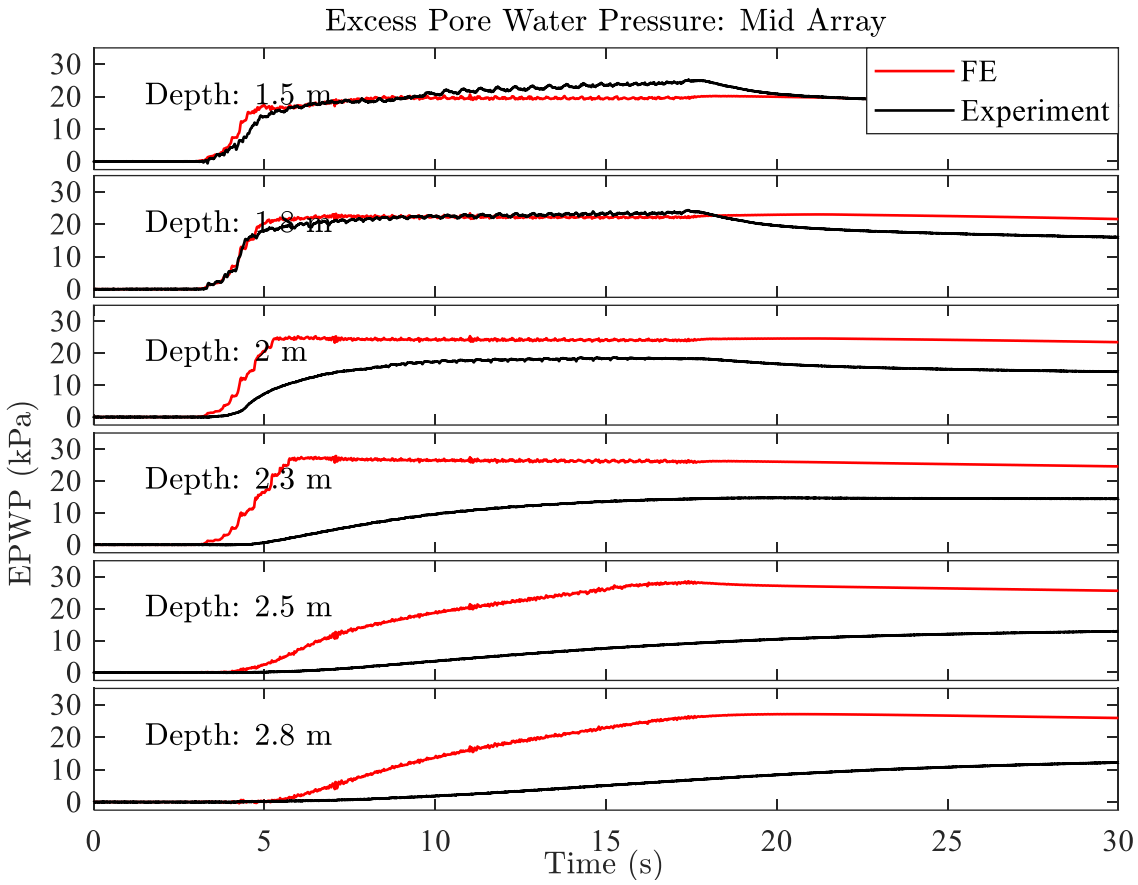

Figure 5.16. Measured and computed excess pore pressure response in the under-foundation array for the soil-foundation system experiment (along soil nodes at different depth)

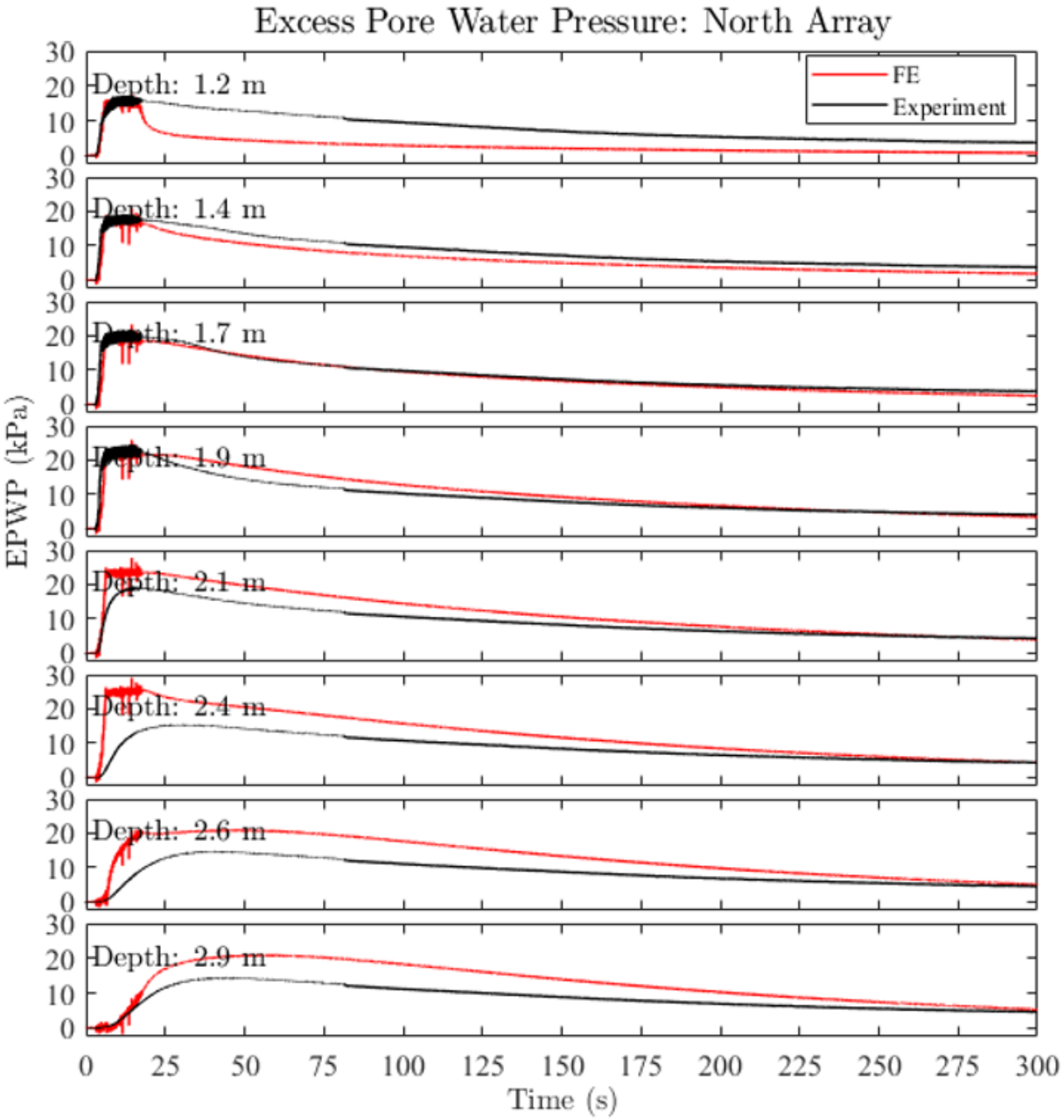

Figure 5.17. Measured and computed excess pore pressure response in the north array for the soil-foundation system experiment (with permeability of 0.4×10^{-5} m/s post shaking)

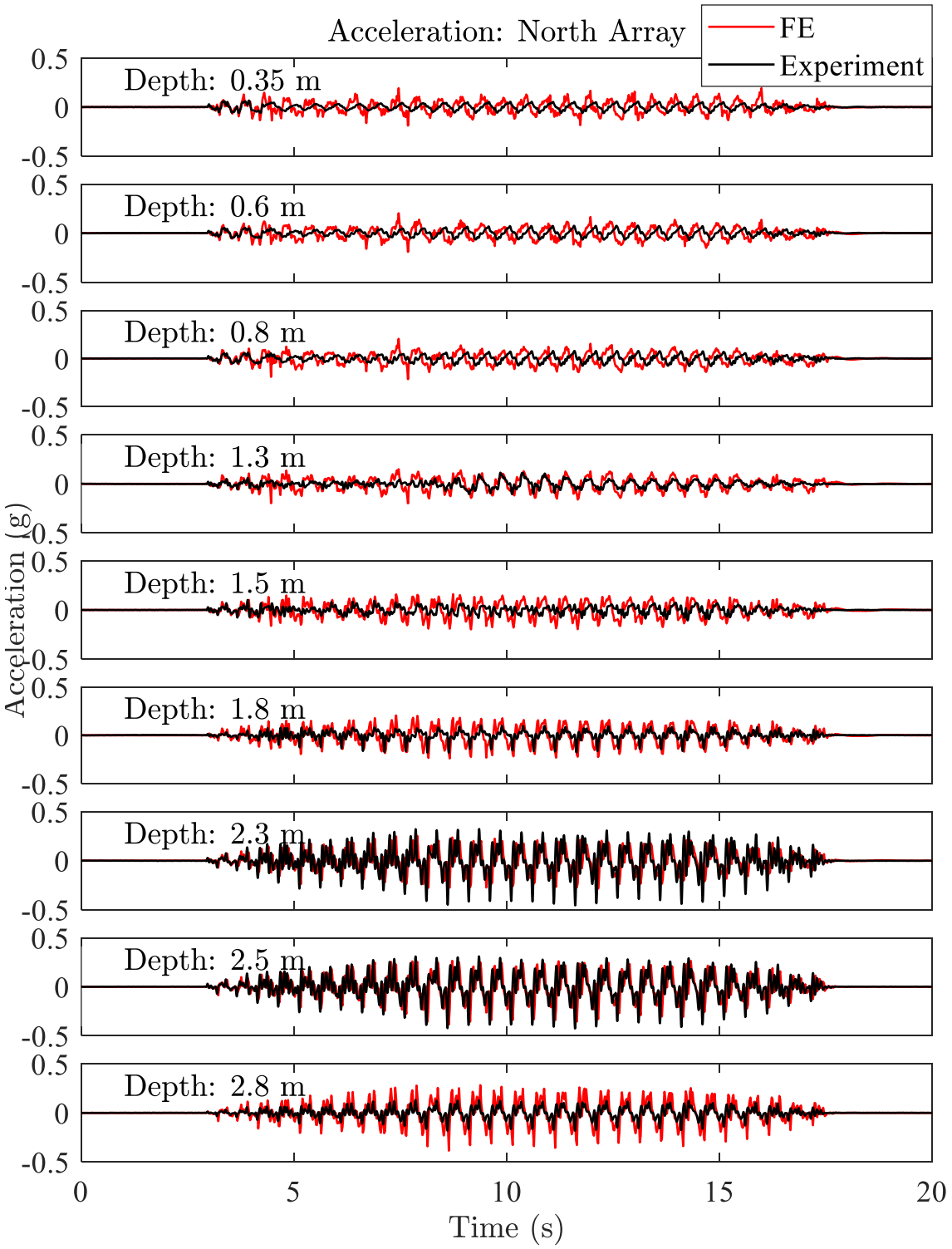

Figure 5.18. Measured and computed soil accelerations for the soil-foundation system experiment along the north array

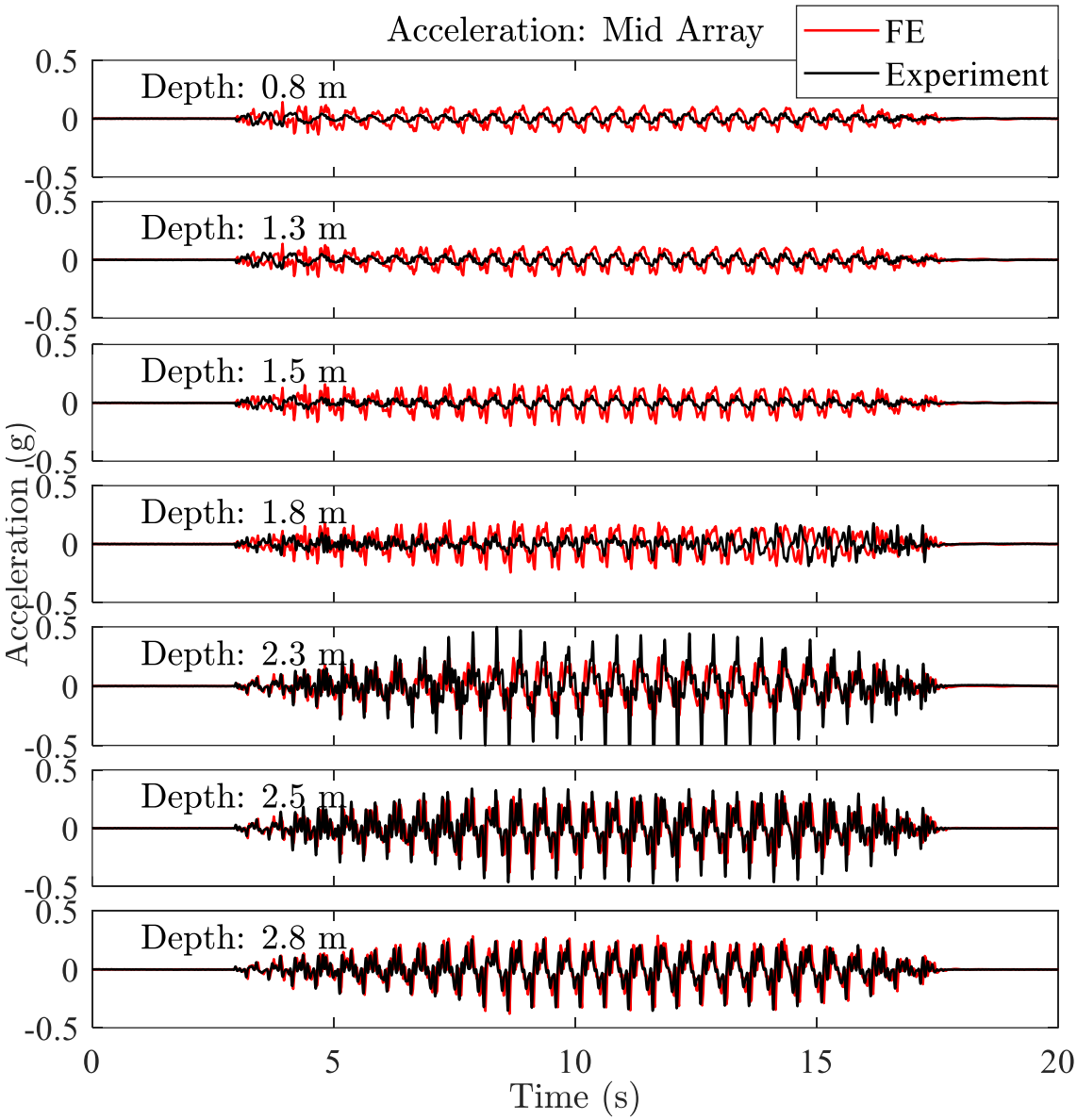

Figure 5.19. Measured and computed soil accelerations for the soil-foundation system experiment along the under-foundation array

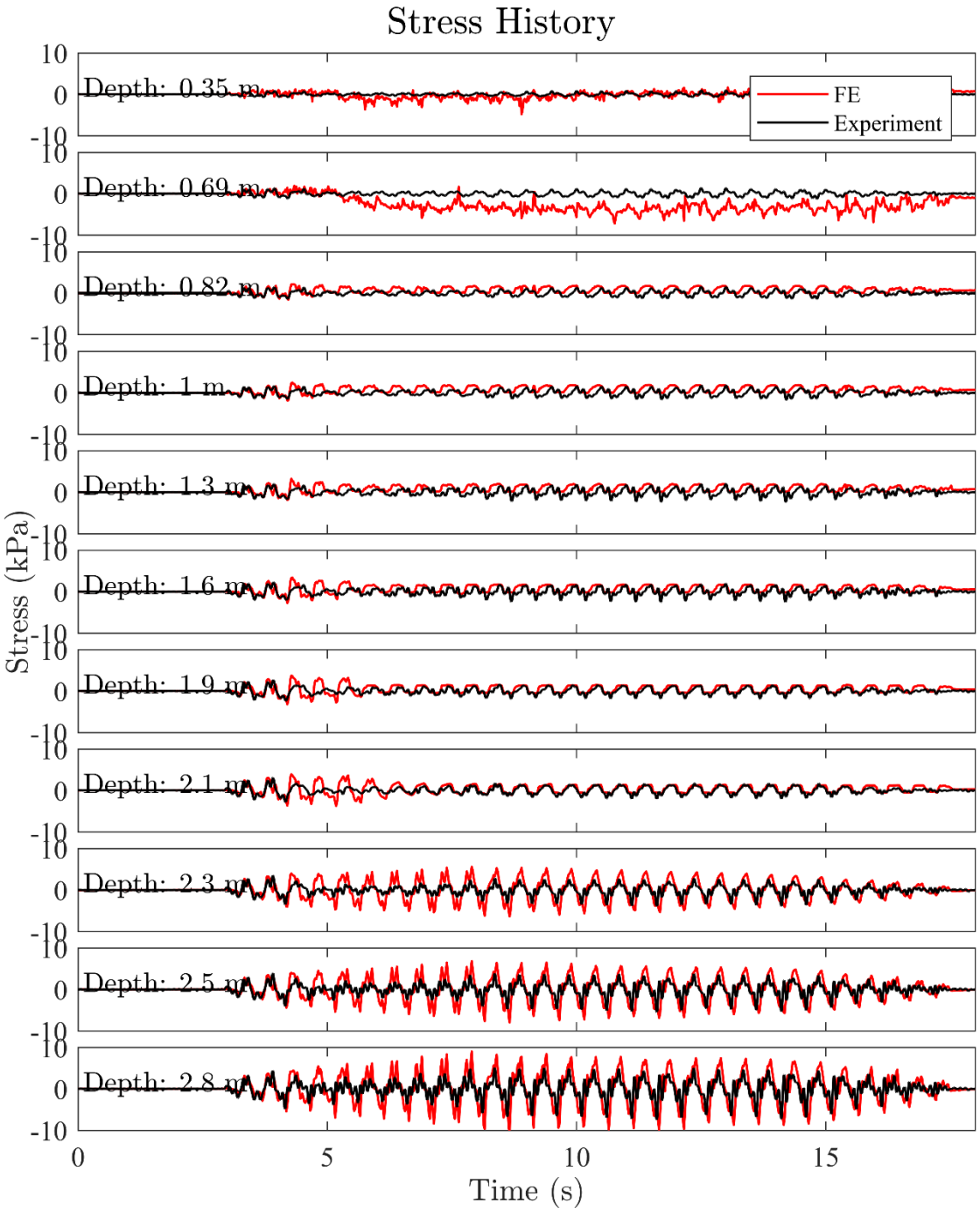

Figure 5.20. Estimated and computed soil shear stress histories for the soil-foundation system experiment

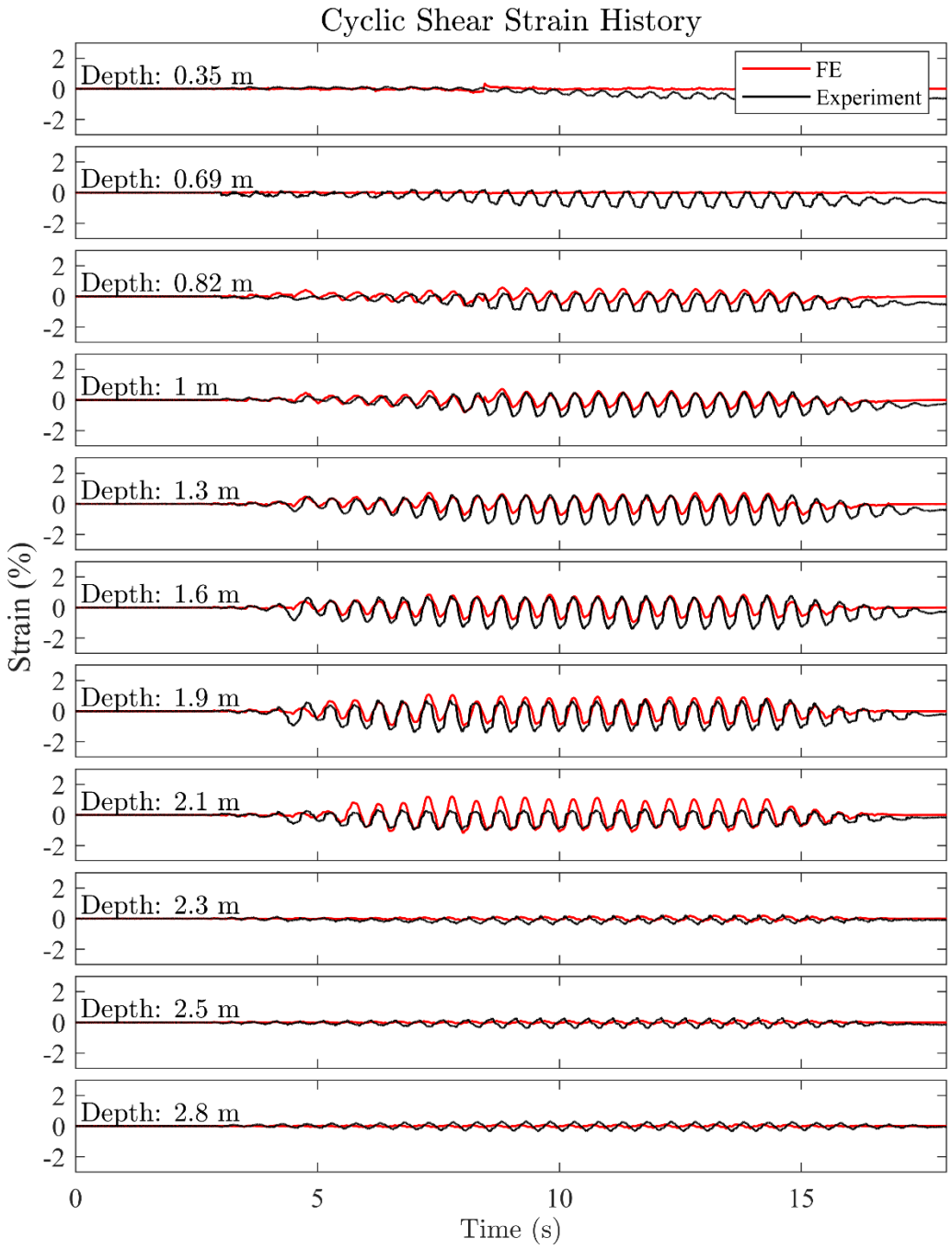

Figure 5.21. Estimated and computed soil shear strain histories for the soil-foundation system experiment

Chapter 6. Polymer Injection to Remediate Liquefaction Induced Ground Displacement and Foundation Settlement: Numerical Simulation of Shake Table Tests and Parametric Studies

6.1 Abstract

A series of two large scale shake table tests was performed to investigate the efficacy of the polymer injection technique in remediating liquefaction induced foundation settlement. In these tests, system response was studied first without, and subsequently with polymer injected into the liquefiable stratum resulting in a set of unique and comprehensive datasets. Here, Class C1 numerical simulations of these tests are presented using 3D solid-fluid fully coupled finite element models with constitutive model parameters partially calibrated based on earlier experimental studies. The physical and numerical models indicate a possible substantial reduction in the liquefaction-induced ground deformations and foundation settlement due to the injection and associated stiffening/strengthening of the treated soil strata. Comparisons are made between computed and recorded engineering demand parameters (EDPs) including excess pore pressure, acceleration, and foundation settlement. A reasonable match is observed to the physical response, and the calibrated model is further used to run additional scenarios, where contributing mechanisms to the reduced foundation settlement are explored in detail. In addition, parametric studies are presented to further understand effects of the geometric configuration of the polymer and associated behavior of the overall system.

6.2 Introduction

Seismically induced soil liquefaction is a mechanism that results in severe damage to structures and foundation systems as documented Niigata 1964, Kobe 1995 and Tohoku 2011,

Japan (Ishihara and Koga 1981, Hamada *et al.* 1996, Ashford *et al.* 2011, Kocaeli, 1999, Turkey (EERI 2000), Bhuj 2001, India (Jain *et al.* 2002), and 2010-2011 Canterbury earthquake sequence in New Zealand 2010-2011 (Cubrinovski *et al.* 2010). For instance, during the 2010-2011 Canterbury earthquake sequence, severe soil liquefaction affected 3,000 buildings within the Central Business District (CBD) of Christchurch, of which over 50 % were to be demolished, being deemed economically unfit for further repairs (Cubrinovski 2013). Such liquefaction hazards necessitate the development of approximate remediation measures of which existing techniques include soil densification, cementation, drainage, and replacement (Adalier *et al.* 1998, Iai 2005, Yasuda and Harada 2014). However, in the context of liquefaction mitigation under existing structures, studies are relatively limited.

A number of studies exist that address liquefaction mitigation under existing structures, including model tests using both the centrifuge (Conlee *et al.* 2012, Kirkwood and Dashti 2019, García-Torres and Madabhushi 2019, Paramasivam *et al.* 2020) and shake table experiments (Rasouli *et al.* 2016, Jahed Orang *et al.* 2020). These techniques allow for the verification, analysis paradigms, and design of countermeasures. Among the mitigation techniques, the injection of low viscosity polyurethane (polymer) using permeation grouting has proven to be an effective measure for remediation at locations which might otherwise be difficult to treat with conventional techniques (Erdemgil *et al.* 2007 and Traylen *et al.* 2017).

The efforts discussed in this chapter is targeted at calibration and modelling of a series of shake table tests performed to study the effects of liquefaction induced foundation settlement, particularly under existing structures. Using the Powell Structural Engineering Laboratories at UC San Diego laminar soil container at the, a baseline test is first conducted to document the dynamic soil and foundation system response of the under strong shaking without any mitigation measures.

Under the same shaking conditions, an additional model is constructed to study the effectiveness of polymer injection (using the two-component expansive polymer EagleLift^{TM} EL077) as a liquefaction remediation measure. Each model is instrumented with accelerometers, pore pressure sensors, and displacement transducers to offer insight into the dynamic response of the soil and foundation. The experimental results are used to calibrate a finite element (FE) modelling framework to shed light on the response mechanisms observed at the system level. The numerical simulations are performed using a well-established, calibrated finite element (FE) modelling framework developed, and implemented in OpenSees (McKenna *et al.* 2010) by Yang *et al.* (2003).

Herein, the authors discuss a set of Class C1 numerical simulation results are discussed, regarding two large scale shake table tests performed to study effectiveness of the polymer injection technique to mitigate effects of soil liquefaction under an existing structure. Emphasis is placed on demonstrating post liquefaction system response characteristics and comparisons to its experimental counterpart. In addition, the calibrated FE models are extended to study effects of the geometric configuration of the polymer and the associated densification of the compacted sand.

Full details of the baseline and polymer tests can be found in Chapter 3 and Chapter 4, respectively. The experimental results are used to calibrate a finite element (FE) modeling framework to shed light on the response mechanisms observed at the system level. The numerical simulations are performed using a well-established, calibrated finite element (FE) modelling framework, developed, and implemented in OpenSees (Mckenna *et al.* 2010) by Yang *et al.* (2003) and Khosravifar *et al.* (2018). The employed framework is particularly beneficial in studying the effect of cyclic mobility and its effect on shear induced settlement mechanisms which often have large contributions to the observed liquefaction induced foundation settlement during

strong shaking (Karimi *et al.* 2018). In the sections below, the following aspects are discussed: (i) Summary of the experimental program, (ii) Model characterization, configuration, and element level calibration, (iii) Numerical modeling procedure and framework, (iv) Computational response, comparison with the experimental observation and discussion, (v) Parametric studies regarding associated deformation mechanisms with emphasis on geometric configuration of the polymer and densification of the compacted sand. Finally, conclusions are presented with insights into the in-corresponding situ liquefaction mitigation approach.

6.3 Experimental program

The response of a shallow foundation supported on saturated sand is systematically studied through two identical large-scale shake table experiments, with and without polymer injection (as the liquefaction countermeasure). A foundation with a surcharge load of 41.6 kPa is seated on a three-layered soil deposit built in a laminar soil container of internal dimensions 3.9 m by 1.8 m by 2.9 m. The deposit was built using Ottawa F-65 sand and consisted of a saturated 1.00 m dense bottom layer (D_r: 80 – 90 %) underlying a 1.25 m (D_r: 35 – 44 %) thick, saturated liquefiable deposit overlain by a partially saturated 0.64 m crust (D_r: 45 % - 55 %). The foundation system consists of a concrete block of dimensions 1.3 m by 0.6 m by 0.4 m, embedded 0.4 m in the partially saturated crust, and overlain by additional steel weights to provide the prescribed surcharge pressure. As such, a foundation system on a three-layered soil deposit was constructed for both experiments. The foundation system (Figure 6.1 and Figure 6.2) consisted of a rigid concrete block of length 1.3 m, width 0.6 m and height 0.4 m, overlain by steel plates designed to produce a surcharge vertical pressure of 41.6 kPa. The concrete block (height of 0.4 m) was fully embedded into the crust.

6.3.1 Baseline Test

The soil models for both tests were constructed in three phases using Ottawa F-65 sand (Parra Bastidas 2016), consisting of a saturated 1.00 m dense base layer (D_r estimated at about 80-95%) underlying a 1.25 m thick saturated liquefiable deposit (D_r estimated at range of 35-44 %), overlain by a moist 0.64 m crust (D_r estimated at range of 50 – 55 %). Salient properties of Ottawa F-65 sand are presented in table 6.1. Stratigraphy pre-injection is summarized in Table 6.2. The foundation system (Figure 6.1) consisted of a rigid concrete block of length 1.3 m, width 0.6 m and height 0.4 m, overlain by steel plates designed to produce a surcharge vertical pressure of 41.6 kPa. The concrete block (height of 0.4 m) was fully embedded into the crust. Full details on the test models may be found in Jahed Orang *et al.* (2020) and in Chapters 3 and 5.

6.3.2 Polymer Test

The polyurethane (polymer) used in this study is a two-component chemically blown foam consisting of a curative phase (poly-isocyanate) and a resin phase (polyol), designated as EL077. In the polymer test (Figure 6.2), 18 injection tubes of diameter 16 mm were inserted to a depth of 1.5 m into the model (0.9 m into the loose liquefiable layer). This target depth was selected in order to perform a bottom – up injection, close to the base of the liquefiable layer, thus allowing the polymer to spread throughout the loose layer as it permeates towards the soil surface. In this study, equal parts of two-component polyurethane to produce a structural foam having a free rise mass density of about 64 kg/m^3. Upon injection, the polymer used in this study has low viscosity and is specifically formulated for high permeation. Upon injection, the two components mix, and the resulting polymer permeates into the surrounding soil. The polymer expands in volume depending on its surrounding state of confinement. Post shaking, the foundation was removed, and the model was carefully excavated to observe distribution of the polymer within the laminar

container. Figure 6.1b presents a cross-section of the polymer from the upper crust of the model. Within the hardened polymer composite, two distinct phases of a solidified interface sand and a polymer rich core were observed.

Each model was instrumented with three arrays of pore pressure sensors and accelerometers as shown in Figure 6.2. The laminar soil container, foundation, and free field soil surface were instrumented with vertical displacement transducers to obtain further insight into the system performance. Both experiments consisted of three arrays of sensor deployment within the soil deposit of which the north "free field" and "under foundation" arrays are presented. The soil surrounding the foundation at 0.6 m from edge of the foundation on each side is referred to as "free field" condition through this chapter (Jahed Orang *et al.* 2020). During both experiments, data were recorded at a sampling rate of 256 samples/s. In the following sections, selected recorded responses will be presented to compare the system response across the two experiments. In a preliminary testing phase based on volume replacement, the amount of polymer required to improve sand deposits of initial D_r = 35 % to D_r = 80 % was estimated. From this phase, a volume replacement ratio of about 8 % was recommended for the loose layer of this three-layered deposit (Prabhakaran *et al.* 2021).

6.3.3 Geometric Configuration of the Polymer-Sand Composite

Post shaking, the foundation was removed, and the model was carefully excavated to observe the distribution of the hardened polymer-sand composite within the treated ground (Figure 6.3). The final depth of polymer permeation was observed between 1.60 m -1.65 m. Several characteristic formations of the composite were observed within both the crust and the underlying loose layer. Within the loose layer, near the depth of injection (1.5 m), a dense zone of the solidified polymer- sand composite around 100 mm in thickness was observed. From this zone, dendritic

veins of the polymer were seen emanating into the upper strata, apparently oriented along the compliant longer direction of the laminar container. Such vein formations were also observed after polymer injection in the Avondale and Bexley red zone sites in New Zealand (Traylen *et al.* 2017), towards the direction of the lateral spread observed in the 2010 - 2011 Canterbury earthquake sequence. During excavation, based on averaging slices of thicknesses of 100 mm, a three-dimensional representative rendering was constructed to map the distribution of the polymer-sand composite. It is noted that this rendering does not represent thin isolated sections of the composite but captures salient aspects of its distribution. Using the mapped configuration, based on volume replacement, the volume of the polymer-sand composite, polymer within the composite and relative density of the surrounding sand were estimated as shown in Figure 6.4.

6.3.4 Characterization of the Polymer-Sand Composite

The polyurethane (polymer) used in this study is a two-component chemically blown foam consisting of a curative phase (poly-isocyanate) and a resin phase (polyol), designated as EagleLift^{TM} EL077. Figure 6.1b presents a cross-section of the polymer-sand composite excavated from the upper crust of the model. Within the composite, two distinct phases are observed.

i) Solidified interface sand.

During injection, the polymer initially fractures through the soil model and then permeates into the sand. On curing, cementation occurs, and a portion of this sand mixes with the polymer and is hardened. This region is typically along the surface of the hardened composite.

ii) Polymer-sand composite.

The injected polymer expands from its initial liquid volume (based on the confinement) and starts to harden. This leads to a separation of surfaces where zones of the pure polymer are sandwiched between layers where soil cementation occurs, as seen in Figure 6.1b.

Within the liquefiable sand, a dense zone of the polymer-sand composite was observed between a depth of 1.55 m-1.65 m. Specimens of large density (about 970 kg/m^3) were observed in this region, suggesting extensive permeation of the polymer within the sand layer. The formation can be attributed to the initial set time of the polymer, as the polymer could not permeate into deeper strata at a rate faster than the rate of curing. Further penetration could be attained, using either higher injection pressure or a polymer with a higher initial set time to attain higher permeation/mixing.

Within the crust, specimens of lower density (about 210 kg/m^3) are observed with thinner fractions of the polymer sand interface, suggesting a reduced extent of mixing and more expansion. The liquid polymer reaching the crust had significantly higher viscosity (hence slower flow) as compared to its initial liquid form, as the injected polymer becomes cooler and starts to harden. Thin interface zones with large zones of pure polymer were observed at shallow depths (seen in Figure 6.1b and Figure 6.4).

6.3.5 Element Level Characterization of the Polymer-Sand Composite

Following the excavation, intact specimens of the polymer-sand composite were removed from the laminar soil contained and stored. From these specimens (obtained from different depths of the laminar soil box), cores of the polymer- sand composite were obtained (Figures 6.5 to 6.7). Estimates of mass density of each core were obtained prior to further testing (210 kg/m^3- 970 kg/m^3). Unconfined compression tests were performed using these polymer-sand composite specimens to identify their element level response. Typical axial stress-axial strain curves for the polymer-sand composite specimen can be seen in Figure 6.8. From the axial stress-strain curves, estimates of the shear strength and shear modulus of these cores were obtained (using a Poisson's ratio of 0.38 based on Gatto *et al.* 2020) and are presented in Figures 6.9 and 6.10. For the

specimens obtained, shear strengths between 30 kPa-410 kPa were observed near the surface (initial confinement of about 3 kPa) and at a depth of about 1.5 m (initial confinement of about 30 kPa) respectively. It is noted that these specimens were obtained from the model test specimens, therefore contain different degrees of polymer fractions, leading to the observed variability (potentially also impacted by different confinement levels due to the imparted polymer injection sequence process). As such, the actual insitu confinement at the specimen locations after each injection could be significantly different, due to the entire grouting process.

6.4 Finite element model

The set of 3-D nonlinear, fully coupled, finite element simulations were performed using OpenSees (McKenna *et al.* 2010 for both experimental datasets. The models were developed using the mixed, fully coupled formulation of (Chan 1988) based on (Biot 1962). The soil domain was modelled using 8-noded hexahedral elements with the mean dilatational formulation ($\bar{B}$ method) as per (Hughes 2008) to remove numerical issues associated with the incompressible fluid phase. Multi surface plasticity-based stress strain constitutive models (Elgamal *et al.* 2003) were used to reproduce the liquefiable and non-liquefiable soil response in both experiments.

6.4.1 Baseline Test

Full details regarding the baseline test calibration are provided in Chapter 5. Salient aspects of modelling are repeated below.

i) Liquefiable Sand

In the original baseline experiment, the soil response is simulated using an established confinement dependent, multi surface constitutive model (PDMY02). Further details on PDMY02 are available from (Elgamal *et al.* 2003). The model has been calibrated in earlier studies by (Parra 1996) and (Yang *et al.* 2003) for the relative densities encountered in the experiment. The saturated

loose sand displays a contractive tendency during partially drained/undrained loading. However, due to the moderate confinement conditions in the shake table, several parameters were modified on the basis of engineering judgement to best fit the observed response due to the lack of data for the Ottawa F-65 at the relative densities and confining pressures involved. Employed soil properties pre improvement are listed in Table 6.3.

6.4.2 Polymer Test

i) Liquefiable Sand

In the remediated test, based on post injection cone penetration testing and assuming replacement of the soil by polymer occurs at constant volume, the relative density (D_r) of the liquefiable layer was seen to increase, on average, from 30 % - 40 % pre injection to 60 % - 70 % post injection as seen in Figure 6.4. As with the liquefiable soil in the baseline test, the PDMY02 constitutive model was used, however with parameters modified to match soil of D_r of about 70 %, post improvement. Figure 6.11 displays the discretization of the soil foundation system employed in the simulation. Employed soil properties of the surrounding sand post improvement are listed in Table 6.4.

ii) Solidified Polymer-Sand Composite

From the excavation, zones of solidified sand were delineated and mapped. This map was further discretized (Figure 6.12) to model the solidified polymer sand composite within the loose layer. The sand-polymer composite was modelled using a confinement independent, multi surface constitutive model (PIMY), typically used to model monotonic or cyclic response of organic soils or clays under undrained loading. By virtue of its synthesis, sand-polymer composite specimens obtained from larger depths display higher strength and stiffness (Golpazir *et al.* 2016). However, to simulate this dependence on initial confinement, the PIMY model is demarcated into 5 zones

along the depth (designated Polymer 1-5). Employed modeling properties of the composite (using the PIMY material model) are provided in Table 6.5.

6.4.3 Model Development

Due to the asymmetric distribution of the polymer-sand composite within the laminar soil container, a full mesh is employed to simulate the polymer test (as seen in Figure 6.11). All nodes along the boundary of the laminar soil container are tied to move together to represent the relatively rigid laminar soil box perimeter. In addition, nodes along the base of the model are fixed. The foundation is rigidly tied to the soil and no slip is allowed along the boundary between the surface of the foundation and the adjacent soil nodes. Loading was performed in 3 stages (as shown in Figure 6.13a), including:

i) Application of gravity using linear elastic soil properties with a Poisson's ratio of 0.4. This stage ensures the static soil stress is imposed (to obtain confinement, static stresses). A large permeability (100 cm/s) is set to the soil domain to ensure a drained response.

ii) Soil properties are switched to plastic to obtain compatible strain levels to match the static stresses imposed in stage 1.

iii) Permeability is switched to the actual value and the shaking time history is imposed at the model base.

It is noted that a more realistic simulation would involve a detailed 5-step process, where the process of polymer injection is directly modeled (in an undrained analysis), followed by the curing of the polymer (drained analysis). The stages are highlighted in Figure 6.13b. As noted in Chapter 4, the process of polymer injection led to an increase in excess pore pressures, followed by pore pressure dissipation as the polymer starts to cure. Therefore, the soil around vicinity of the injection depth experiences transient loads during the relatively undrained grouting process. During this

phase, the foundation loads are partially carried by the developed water pressure. As excess pore pressures dissipate and the polymer begins to cure, stress redistribution occurs where the stiffer inclusions of the polymer start to resist the foundation loads. A more refined analysis, which reflects the explicit change in the state of soil stress near the injection depth, can theoretically be performed.

Time stepping for the matrix equations is undertaken using a second order accurate two step TRBDF2 scheme (Bathe, 2007). The integrator is a composite scheme that uses the trapezoidal rule for the predictor step and a 3-point backward Euler scheme for the corrector step in an attempt to conserve momentum and energy. The rule also enables a specification of higher time increments post strong shaking allowing to simulate excess pore pressure dissipation. The resulting system of equations are solved using a modified Newton Raphson incremental iterative procedure with a Krylov subspace accelerator for faster convergence.

6.5 Dynamic response of baseline and polymer tests

The baseline and polymer remediated models were both first subjected to a base excitation at a peak cyclic acceleration of 0.2 g (referred to as Shake1). The motion and its response spectrum are shown in Figure 6.14. This excitation was imparted 1.5 weeks after injection, with the polymer fully cured within the laminar soil container. Representative dynamic system response including excess pore pressure, acceleration, and foundation settlement is presented, for a few key locations, in the following sections.

6.5.1 Pore Pressure Response

Figures 6.15 (a,b) compare the experimental and simulated excess pore pressure response in the baseline test in the free field and under foundations sensor arrays. Figure 6.16 (a, b) present a similar response for the polymer remediated test. The comparisons show reasonable agreement

in both test models. Levels indicative of liquefaction were observed in the original baseline test (Figure 6.15). In contrast, much lower levels of excess pore pressure were observed in the polymer remediated counterpart (Figure 6.16), indicative of a substantial increase in liquefaction resistance and reduction in contraction tendency. This aspect of response is captured well by the numerical models.

6.5.2 Foundation Settlement

Figures 6.17 and 6.18 present a comparison between the experimental and numerical liquefaction induced foundation settlement in the baseline and polymer remediated tests, respectively. Significant liquefaction-induced settlement and tilt were observed in the original baseline test as compared to the polymer test, for the same base excitation The numerical models could generally capture the observed levels of settlement during the shaking phase in both experiments.

6.5.3 Soil Acceleration

Figures 6.19 and 6.20 present comparisons between the experimental and numerical responses in the baseline and polymer remediated tests, respectively. The results are presented for a depth of 1.1m (within liquefiable layer) in the free field and under the foundation. Extensive base isolation was observed in the acceleration response of the soil within the crust in the original baseline experiment due to the pore pressure induced softening of the liquefiable layer. In the polymer remediated experiment, the stiff stratum could transmit much higher accelerations to upper strata as is effectively captured by the numerical model.

6.6 Mechanisms contributing to reduced foundation settlement

The reduction in liquefaction induced foundation settlement, following polymer injection is attributed to:

i) Improvement in the resistance to soil liquefaction due to a) cementation of sand during the injection, and b) densification, and subsequent increase in confinement following the injection process.

ii) Geometry and physical configuration of the polymer-sand composite.

Each aspect above is explored in the following sections using the calibrated finite element model of the polymer test.

6.6.1 Soil densification due to the injection process

Following the injection process, the polymer expands based on the ambient confinement, whereby the surrounding soil densifies. If injections are first performed around the perimeter of the structure and adequate confinement is provided to minimize volume expansion (laterally by the perimeter grout and vertically by the surcharge weight/superstructure loads), the injections occur at reasonably constant volume. Therefore, the chart presented in chapter 2, was employed to obtain estimates of the degree of improvement of the surrounding sand. A case is presented (as shown in Figure 6.21), with D_r within the liquefiable layer improved from about 40 % to about 80 % (corresponding to an $(N_1)_{60}$ of 29) respectively. In addition, Appendix 3 presents preliminary results illustrating the potential of the polymer injection technique (using smeared properties) in facilitating geotechnical base isolation, whereby leaving a small portion of the deposit untreated reduces both structural accelerations, and co-seismic foundation settlement.

Injections are performed such that the D_r of the sand in the liquefiable layer reaches about 80% (Table 6.6) following the curve. This scenario represents a case where initial liquefaction is precluded (Figure 6.22 for the north array). As seen in Figure 6.23, significant reduction in the foundation settlement is observed. However even at this relatively high D_r value, the co-seismic settlement still does not closely approach the measurement in the polymer test. This aspect of

response indicates the consideration of additional mechanisms, in conjunction with the densification of the sand (related to the geometric configuration of the polymer), in explaining the observed settlement response of the polymer test.

6.6.2 Physical configurations of the polymer-sand composite

The geometric configuration of the polymer-sand composite can play a critical role in the extent of foundation settlement reduction. Using the calibrated finite element model of the baseline test (Figure 6.24a), additional scenarios are explored varying the location of the injected polymer (within the confines of the laminar soil container) to develop specific configurations of the polymer-sand composite inclusions. Each configuration discussed below leverages the physical geometry of the inclusion to remediate liquefaction induced foundation settlement (*i.e.*, densification of the surrounding sand is not explicitly accounted for in the analyses below for further focus on the role of polymer geometry). Three different configurations (Figure 6.24) are discussed in detail below including *i)* piles, *ii)* grout curtain walls and *iii)* load bearing curtain walls. In these scenarios, the composite was modelled with a strength of 400 kPa, and a shear stiffness of 2.8 MPa (identical to Polymer5 in Table 6.5).

i) Piles

In this scenario, the injection tubes are deployed directly below the foundation to develop structural piles (inclusions), capable of transmitting the foundation loads to the lower competent denser layer (Figure 6.24b). Figure 6.25 presents time history of vertical effective stress for the soil beneath the foundation and the top of piles. Prior to the onset of liquefaction (around 5-seconds), both the soil and piles carry an equal portion of the load from the foundation. After liquefaction, the soil loses strength and stiffness (vertical effective stress approaches zero) and the entire foundation load is carried by the piles. Figure 6.26 presents the deformed configuration of

the soil (at free field) and each pile at different points during shaking. The figure clearly indicates that as the load on the piles increase (post liquefaction), each pile tends to deflect outward, while moving in conjunction with the free-field soil. As seen in Figure 6.28, the settlement of the foundation is observed to reduce from about 0.23 m in the baseline experiment to about 0.07 m, after adding the piles.

ii) Grout curtain walls

Grout curtain walls are commonly employed by the polymer injection industry as a barrier to reduce groundwater/soil movement. Figure 6.24c, presents the deployed grout curtain around the shallow foundation. Such a grout curtain is not connected to the foundation. As such, after onset of soil liquefaction, the curtain minimizes the lateral outflow (to the free field) of the soil and water beneath the structure (Figure 6.27) and reduces the co-seismic foundation settlement (Figure 6.28). The foundation settlement is reduced to about 0.11 m compared to the baseline (about 0.23 m). Of interest as well is the permeability barrier offered by the grout curtain to prevent pore pressure migration from the free field towards the foundation.

iii) Load-bearing grout curtains

Figure 6.24d presents the load-bearing grout curtain, similar to case *ii).* However, in this case, the curtain is structurally connected to the foundation and, after soil liquefaction, can carry the structural loads to the competent dense layer. In addition to minimizing lateral outflow after soil liquefaction, a part of the structural load is carried by the curtains. In this case, the foundation settlement reduces to about 0.05 m (Figure 6.28) as compared to 0.23 m in the baseline scenario.

6.6.3 Discussion

Figure 6.27 presents the computed excess pore pressure ratios along the north (Figure 6.27a) and middle arrays (Figure 6.27b) respectively. Results from a one-dimensional shear beam

run is added for comparison. Away from the foundation, all simulations predict similar values of peak excess pore pressure (comparable to that of the free field). As such, when the soil away from the foundation (North and South arrays) liquefies, the horizontal resistance of the soil underneath the foundation is reduced. Therefore, the peak excess pore pressure response of the middle array is similar to that of the free field. However, the excess pore pressure responses from the curtain and load bearing grout curtain models are in general higher (Figure 6.27 b) underneath the foundation. The grout curtains provide an impervious boundary separating the soil within the curtain (lattice type structure) and the free field. As such, the soil underneath the foundation can develop peak excess pore pressures higher than the free field, once confined with such a curtain.

Figure 6.28 presents the foundation settlement for the three remediation measures (piles, curtain, and load bearing curtain) along with the baseline experiment. As seen in the figure, the load bearing grout curtains, if connected to the foundation, appears to be the most effective in reducing the foundation settlement. The deformed configuration of each case at the end of shaking is presented in Figure 6.29. It is noted that these configurations do not alone explain the observed foundation settlement of the polymer test (about 11 mm). As such, a combination of the densification of the surrounding compacted sand, and the physical (geometric) configuration of the polymer accounted for the observed settlement of the polymer test.

6.7 Simplified logic towards for practical applications

The insights obtained from the experimental and numerical simulations were used to develop simplified recipes for practicing engineers employing the polymer injection technique. Two illustrative scenarios are presented: (a) reduction in liquefaction induced settlement of a free field level ground site, and (b) reduction in liquefaction induced lateral spreading.

6.7.1 Simplified analysis of soil free field settlement

This example presents precluding initial liquefaction for a site with a normalized standard penetration test blow count $(N_1)_{60}$ of about 8.

1. A preliminary step is to confine the site to prevent escape of the polymer to surrounding areas. As such, injections using a high viscosity polymer can be made along the perimeter of the site, to create a curtain wall.
2. Use the simplified chart (such as that presented in Figure 6.21) to estimate the volume of liquid polymer required for injection. It is noted that the chart presented in Figure 6.21 is based on an average expansion ratio of 2.7. Based on preliminary test pits, such charts can be developed for the observed expansion ratio at the specific site. In this example, a choice of $(N_1)_{60}$ of about 30 would preclude initial liquefaction at the site. As such for a site with an $(N_1)_{60}$ of about 8, a volume ratio of about 8% (volume of liquid polymer to soil) would result in a site where the surrounding sand has an $(N_1)_{60}$ of about 30.
3. Based on the obtained $(N_1)_{60}$ value, a simplified liquefaction triggering analysis can be performed (Youd *et al.* 2002) to obtain the factor of safety against liquefaction triggering (FS_{Liq}). It is noted that pre/post injection CPTs are commonly employed by the industry to measure the extent of remediation and such datasets can additionally inform the degree of improvement.
4. The site is a free field deposit, therefore the post liquefaction sedimentation – consolidation process will govern resulting ground settlement. As such, the volumetric strain can be obtained from procedures such as Ishihara and Yoshimine (1992) or Tokimatsu and Seed (1987) based on FS_{Liq} and $(N_1)_{60}$ of the improved site.

6.7.2 Simplified analysis for mitigating lateral soil deformations in sloping ground

The example presents a simplified strategy for remediating lateral soil deformations in a gently inclined slope (with an infinite out of plane thickness). The slope considered in this study is presented in Figure 6.30a.

1. A preliminary step is to characterize properties of the soil and slope geometry and determine liquefaction susceptibility using a triggering analysis.
2. Perform a limit equilibrium type slope stability analysis to obtain the yield coefficient of the slope (k_y) using liquefied soil properties. Based on the obtained k_y, estimates of slope displacement can be obtained from Newmark type sliding block models (for example Bray and Macedo, 2019)
3. A schematic of a possible remediation strategy using polymer injection is presented in Figure 6.30b. As such, representative properties of the polymer-sand composite and improved properties of the sand around the composite can be employed in a limit equilibrium analysis to determine an improved k_y (and following a sliding block analysis, displacement) for the slope.
4. As such, high fidelity computational simulations can also be employed on a case - by- case basis to determine the degree of remediation. Appendix 3 presents an illustration remediating for liquefaction induced lateral spreading using the calibrated models of the baseline and polymer tests presented earlier in the chapter (in a gently inclined slope of 4 degrees). Further, it is noted that for polymers of higher strength readers are referred to Baez (1995) or Rayamajhi *et al.* (2016) where the inclusions can effectively behave as structural piles with sufficient flexural stiffness.

6.8 Conclusions

Results from a set of class C1 numerical simulations of a two-stage shake table test investigation were presented for evaluating the potential of the polymer injection technique, as a countermeasure for liquefaction-induced foundation settlement. The test models consisted of a shallow foundation with a surcharge pressure seated on a three-layered liquefiable soil deposit with and without an expansive polymer (EagleLift EL007) injected into the liquefiable stratum and further subjected to identical base excitation.

The physical and numerical models indicate an extensive reduction in the liquefaction induced foundation deformations due to the injection and associated stiffening of the ground. Time histories of excess pore pressures, soil acceleration and foundation settlement are presented for a few key locations and compared to their experimental counterparts. Generally, the numerical simulations were able to reliably capture key response characteristics at the system level. As such, the simulations demonstrated potential of computational tools to replicate system-level response mechanisms, once calibrated with experimental datasets.

The calibrated model was then extended to explore additional scenarios beyond the scope of the original test series. Effects of geometric configuration of the solidified polymer zones, and state of compacted soil around the solidified zones were explored in detail. It is shown that the deployed geometry of injected polymer can play a significant role in foundation settlement reduction, along with those offered by the resulting increase in soil relative density and confinement.

6.9 Acknowledgement

Chapter 6, in part, is a reprint of the material as it appears in Prabhakaran, A., Kim, K., Qiu, Z., Elgamal, A., and Frazao, C. (2022). “Polymer Injection to Remediate Liquefaction-

Induced Foundation Settlement: Numerical Simulation of Shake Table Experiments." *ASCE Lifelines Conference*, American Society of Civil Engineers, Los Angeles, CA. The dissertation author was the primary investigator and author.

6.10 References

Adalier, K., Elgamal, A.-W., and Martin, G. R. (1998). "Foundation Liquefaction Countermeasures for Earth Embankments." *Journal of Geotechnical and Geoenvironmental Engineering*, ASCE, 124(6), 500–517.

Ashford, S. A., Boulanger, R. W., Donahue, J. L., and Stewart, J. P. (2011). "Geotechnical Quick Report on the Kanto Plain Region during the March 11, 2011, Off Pacific Coast of Tohoku Earthquake, Japan." *Geotechnical Extreme Events Reconnaissance*, GEER-025a(April), 1–20.

Baez, J. I. (1995). "A design model for the reduction of soil liquefaction by using vibro-stone columns." *PhD Thesis*, University of Southern California, Los Angeles.

Bathe, K. J. (2007). "Conserving energy and momentum in nonlinear dynamics: A simple implicit time integration scheme." *Computers and Structures*, Pergamon, 85(7–8), 437–445.

Biot, M. A. (1962). "Mechanics of deformation and acoustic propagation in porous media." *Journal of Applied Physics*, American Institute of PhysicsAIP, 33(4), 1482–1498.

Bowles, J. E. (1977). "Foundation Analsis and Design", McGraw Hill, Inc., New York.

Bray, J. D., and Macedo, J. (2019). "Procedure for Estimating Shear-Induced Seismic Slope Displacement for Shallow Crustal Earthquakes." *Journal of Geotechnical and Geoenvironmental Engineering*, American Society of Civil Engineers, 145(12), 04019106.

Chan, A. H.-C. (1988). "A Unified Finite Element Solution to Static and Dynamic Problems of Geomechanics." University College of Swansea, Swansea.

Conlee, C. T., Gallagher, P. M., Boulanger, R. W., and Kamai, R. (2012). "Centrifuge Modeling for Liquefaction Mitigation Using Colloidal Silica Stabilizer." *Journal of Geotechnical and Geoenvironmental Engineering*, American Society of Civil Engineers, 138(11), 1334–1345.

Cubrinovski, M. (2013). "Liquefaction-Induced Damage in The2010-2011 Christchurch (New Zealand) Earthquakes." *International Conference on Case Histories in Geotechnical Engineering*, Missouri University of Science and Technology, Chicago, Illinois.

Cubrinovski, M., Green, R. A., Allen, J., Ashford, S., Bowman, E., Brendon, Bradley, Cox, B., Hutchinson, T., Kavazanjian, E., Orense, R., Pender, M., Quigley, M., and Wotherspoon, L. (2010). "Geotechnical reconnaissance of the 2010 Darfield (Canterbury) earthquake." *Bulletin of the New Zealand Society for Earthquake Engineering*, 43(4), 243–320.

Dickenson, S. E. (1994). “Dynamic Response of Soft and Deep Cohesive Soils during the Loma Prieta Earthquake of October 17, 1989.” *PhD Thesis*, University of California, Berkeley.

EERI. (2000). “Damage Patterns and Foundation Performance in Adapazari.” *Earthquake Spectra*, 16(SUPPL. A), 163–188.

Elgamal, A., Yang, Z., Parra, E., and Ragheb, A. (2003). “Modeling of cyclic mobility in saturated cohesionless soils.” *International Journal of Plasticity*, Pergamon, 19(6), 883–905.

Erdemgil, M., Sağlam, S., and Bakır, B. S. (2007). “Utilization of Highly Expansive Polymer Injection to Mitigate Seismic Foundation Failure for Existing Structures.” *8th Pacific Conference on Earthquake Engineering*, Singapore.

García-Torres, S., and Madabhushi, G. S. P. (2019). “Performance of vertical drains in liquefaction mitigation under structures.” *Bulletin of Earthquake Engineering*, Springer Netherlands.

Gatto, M. P. A., Lentini, V., Castelli, F., Montrasio, L., and Grassi, D. (2021). “The use of polyurethane injection as a geotechnical seismic isolation method in large-scale applications: A numerical study.” *Geosciences (Switzerland)*, Multidisciplinary Digital Publishing Institute, 11(5), 201.

Golpazir, I., Ghalandarzadeh, A., Jafari, M. K., and Mahdavi, M. (2016). “Dynamic properties of polyurethane foam-sand mixtures using cyclic triaxial tests.” *Construction and Building Materials*, Elsevier Ltd, 118, 104–115.

Hamada, M., Isoyama, R., and Wakamatsu, K. (1996). “Liquefaction-induced ground displacement and its related damage to lifeline facilities.” *Soils and Foundations*, Japanese Soc of Soil Mechanics & Foundation Engineering, 36(Special), 81–97.

Hughes, T. J. R. (1987). *The Finite Element Method: Linear Static and Dynamic Finite Element Analysis - Thomas J. R. Hughes - Google Books*. Prentice-Hall.

Iai, S. (2005). “Remediation of liquefiable soils for port structures in japan — analysis, design and performance.” *Journal of Earthquake Engineering*, Taylor & Francis Group , 9, 77–103.

Ishihara, K., and Yoshimine, M. (1992). “Evaluation of settlements in sand deposits following liquefaction during earthquakes.” Soils and Foundations, Elsevier, 32(1), 178–188.

Ishihara, K., and Koga, Y. (1981). “Case Studies of Liquefaction in the 1964 Niigata Earthquake.” *Soils and Foundations*, Elsevier BV, 21(3), 35–52.

Jahed Orang, M., Motamed, R., Prabhakaran, A., and Elgamal, A. (2021). “Large-Scale Shake Table Tests on a Shallow Foundation in Liquefiable Soils.” *Journal of Geotechnical and Geoenvironmental Engineering*, American Society of Civil Engineers, 147(1), 04020152

Jain, S. K., Lettis, W. R., Murty, C. V. R., and Bardet, J.-P. (2002). “Bhuj, India Earthquake of January 26, 2001 Reconnaissance Report.” *Earthquake Spectra*, SAGE Publications,

18(1_suppl), 1–4.

Karimi, Z., and Dashti, S. (2016). "Numerical and Centrifuge Modeling of Seismic Soil–Foundation–Structure Interaction on Liquefiable Ground." *Journal of Geotechnical and Geoenvironmental Engineering*, American Society of Civil Engineers (ASCE), 142(1), 04015061.

Kirkwood, P., and Dashti, S. (2019). "Influence of prefabricated vertical drains on the seismic performance of similar neighbouring structures founded on liquefiable deposits." *Géotechnique*, ICE Publishing, 69(11), 971–985.

McKenna, F., Scott, M. H., and Fenves, G. L. (2010). "Nonlinear Finite-Element Analysis Software Architecture Using Object Composition." *Journal of Computing in Civil Engineering*, American Society of Civil Engineers, 24(1), 95–107.

Paramasivam, B., Dashti, S., and Liel, A. B. (2020). "In-Ground Gravel–Rubber Panel Walls to Mitigate and Base Isolate Shallow-Founded Structures on Liquefiable Ground." *Journal of Geotechnical and Geoenvironmental Engineering*, American Society of Civil Engineers (ASCE), 146(9), 04020087.

Parra Bastidas, A. M. (2016). "Ottawa F-65 Sand Characterization." *PhD Thesis*, University of California Davis.

Prabhakaran, A., Kyungtae, K., Ebeido, A., Jahed Orang, M., Motamed, R., Elgamal, A., and Frazao, C. (2021). "Polymer injection and associated site liquefaction remediation mechanisms." *17th World Conference on Earthquake Engineering*, Sendai, Japan.

Rasouli, R., Towhata, I., and Akima, T. (2016). "Experimental Evaluation of Drainage Pipes as a Mitigation against Liquefaction-Induced Settlement of Structures." *Journal of Geotechnical and Geoenvironmental Engineering*, American Society of Civil Engineers (ASCE), 142(9), 04016041.

Rayamajhi, Deepak, Scott A. Ashford, Ross W. Boulanger, and Ahmed Elgamal. "Dense granular columns in liquefiable ground. I: Shear reinforcement and cyclic stress ratio reduction." *Journal of Geotechnical and Geoenvironmental Engineering*, American Society of Civil Engineers (ASCE), 142, (7): 04016023.

Sabatini P. J., Bachus, R. C., Mayne, P. W., Schneider, J. A., Zettler, T. E. (2002). "Geotechnical Engineering Circular #5. Evaluation of Soil and Rock Properties". US Department of Transportation, Federal Highway Administration (FHWA), Publication N. FHWA-IF-02-034.

Schmertmann , J. H. (1975). "In-Situ Measurement of Shear Strength"-State-of-the art-paper, Third International Conference on Insitu Measurement of Soil Properties, American Society of Civil Engineers, Rayleigh, 57-138.

Tokimatsu, K., and Seed, H. B. (1987). "Evaluation of settlements in sands due to earthquake shaking." Journal of Geotechnical Engineering, American Society of Civil Engineers, 113(8),

861–878.

Traylen, N. J., Wentz, R., Van Ballegooy, S., Hnat, T., and Wotherspoon, L. M. (2017). "Research Results from a Study into Resin Injection for Liquefaction Mitigation 2017 NZSEE Conference." *NZSEE Conference*, Wellington.

Wair R. B, DeJong, J. T., and Shantz, T. (2012). "Guidelines for Estimation of Shear Wave Velocity Profiles." PEER Rep. 2012/80, Pacific Earthquake Engineering Research Center, Univ. of California, Berkeley, CA, 95

Yang, Z., Elgamal, A., and Parra, E. (2003). "Computational Model for Cyclic Mobility and Associated Shear Deformation." *Journal of Geotechnical and Geoenvironmental Engineering*, American Society of Civil Engineers, 129(12), 1119–1127.

Yasuda, S., and Harada, K. (2014). "Measures developed in Japan after the 1964 Niigata earthquake to counter the liquefaction of soil." Tenth U.S. National Conference on Earthquake Engineering , Earthquake Engineering Research Institute, Anchorage.

6.11 Appendix 1: Mechanical Properties of the Polymer-Sand Composite

Upon injection, the polymer cements a portion of the insitu soil, expands and increases the ambient confinement, and provides shear reinforcement after solidification. As such, mechanical properties of the resulting polymer-sand composite are dependent on the depth of injection (initial confinement), strength characteristics of the insitu sand and solidified polymer, degree of mixing (extent of permeation), rate and temperature of injection (injection pressure), and the injection sequence. Figure 6.30 presents the stress state in the surrounding soil, during injection. In the experiments performed, it was observed that the injection process was relatively undrained, and led to rise in excess pore pressure, shifting the Mohr's circle toward the failure surface. During expansion, the principal stresses (particularly σ'_3) increase and move the Mohr's circle to the right, leading to improved confinement and reduced shear (as compared to the initial stress state). Therefore, the pressure and sequence of injection, and rate of polymer expansion dictate the mechanical properties of the improved ground. As such, it can be difficult to establish exact mechanical properties of the polymer-sand composite in a field setting.

This appendix contains a summary of the mechanical properties of the polymer-sand composite for preliminary computational modeling and analysis. Two strategies are presented, including the treated ground with: 1) mechanical properties of the composite, 2) smeared properties of the remediated ground.

6.11.1 Properties of Sand Polymer Composite

The geometric configuration of the resulting polymer-sand composite was shown to play a significant role in the performance of treated ground. As such, if a targeted geometric configuration is employed, the mechanical properties of the polymer-sand composite are paramount. Figure 6.32 presents the variation of polymer- sand composite cohesion and mass density with

confinement. At modest confinement (about 30 kPa), the polymer-sand composite had a shear strength of about 400 kPa (as seen in Figure 6.32a). As such a preliminary approach to modeling the composite is to employ a confinement dependent cohesion intercept (as shown in Figure 6.32a) with the friction angle of the insitu sand, if the injection is performed along the entire height of the deposit. In the absence of further information, empirical correlations can be employed to relate the low strain shear modulus (Wair *et al.* 2012, Dickenson 1994) to the developed shear strength. For instance, the equation ($V_s = 23\ {s_u}^{0.475}$, where V_s is in m/s and s_u is in kPa) by Dickenson (1994) can be employed.

6.11.2 Smeared properties of treated ground

In first approximation, the chart presented in Figure 6.21 may be employed to obtain smeared properties of the treated ground, without modeling the actual geometry of the polymer-sand composite. Such a chart is based on replacement under constant volume and relates $(N_1)_{60}$ of treated ground to the volume of polymer injected in its liquid form. It is noted that these curves are specific to the polymer used in this test series, and similar charts can be made based on preliminary trials (test pits) insitu. In a field setting, the assumption of constant volume might be difficult to achieve. In such scenarios, a perimeter grout curtain, could be created to help containment and prevent polymer escape. Additionally, if the vertical surcharge is inadequate, a top-down injection sequence can be deployed, where injection is first performed at shallow depth to create a capping layer followed by injection at depth.

Further, empirical correlations can be employed to relate the increase in $(N_1)_{60}$ (Bowles 1977, Sabatini *et al.* 2002) or corresponding D_r (Schmertmann 1975) to the improved friction angle and shear modulus (Wair *et al.* 2012) of the treated ground.

An alternate approach is proposed in Figure 6.33, based on area replacement ratio *(A_r)*, to determine the strength of treated ground, if a highly permeable polymer is deployed. As such, the strength envelope of the native soil can be increased based the degree of treatment. Figure 6.33 presents the increase in shear strength of treated ground for A_r ranging from about 5% to about 30%. It is noted that such an approach is approximate and requires judicial engineering judgement, when used in design.

6.12 Appendix 2: Conceptual illustration of geotechnical base isolation

Using smeared properties for treated ground, two illustrative scenarios are presented (Figure 6.34) within the confines of the laminar soil container, whereby: (1) the entire liquefiable layer deposit (about 1.5m) is improved (simulation is termed 'Dense') and (2) about 1.3 m of the liquefiable layer is improved and a portion of (0.2 m) is left untreated (simulation is termed 'Weak Layer'). These preliminary simulations aim to highlight beneficial effects of leaving a thin liquefiable layer untreated, when performing ground modification. Upon soil liquefaction and associated loss of stiffness, such weak layers have the potential to localize shear strains, restrict development of shear stresses and in effect limit transfer of accelerations to ground surface, allowing for a natural base isolation mechanism.

Figure 6.35 presents the computed acceleration response histories and 5% damped acceleration response spectra of the foundation for the 'Dense' and 'Weak Layer' simulations. As seen in the figure, remediating the entire deposit (in the 'Dense' simulation) results in amplification of the input motion, particularly at higher frequencies (lower periods). Of interest is the amplification of the input motion particularly between 0.01-0.25s (4 Hz - 100 Hz), which significantly affects the foundation response (foundation is essentially rigid in these simulations). After leaving a portion of the deposit untreated (in the 'Weak Layer' simulation), acceleration attenuation is observed. Similar observations can be noted in Figure 6.36 and Figure 6.37, which present the acceleration response history and the 5% damped acceleration response spectra along the North array for the two simulations. Figure 6.38 presents time histories of Arias Intensity along the deposit (north array). As such, the profile of Arias intensity (I_a) and Cumulative Absolute Velocity (*CAV*) at the end of shaking is presented in Figure 6.39. Amplification can clearly be observed in the Dense simulation, whereas a significant reduction (compared to input) is observed

in the Weak Layer simulation. Of interest, is the I_a and *CAV* profiles between ground surface and 1.6 m in the Weak Layer simulation, where the deposit essentially behaves as a rigid body *i.e.,* moving with near constant acceleration.

Figure 6.40 presents the excess pore pressure response along the north array for the 'Dense' and 'weak layer' simulations. The untreated layer (depth of 1.8 – 2.0m) liquefies in 1-2 cycles of strong shaking and redistributes the developed excess pore pressure along the deposit. Figure 6.41 presents the corresponding shear stress-shear strains along the north array for the two simulations. As seen in the figure, shear strains localize in the untreated zone (depth of 1.8m), and thereby: (1) limit transfer of shear stresses to the top of the deposit after the onset of soil liquefaction, and (2) reduce shear demands on the underlying dense sand, leading to the observed soil isolation effects. As such, the untreated layer can transmit accelerations to the ground surface as long as it maintains sufficient stiffness (and strength), somewhat analogous to a Newmark type sliding block (where the yield strength is limited to the residual strength of the liquefied layer). As such, due to the attenuated accelerations of the foundation, reduced co-seismic settlements are observed (Figure 6.42).

Overall, these simulations illustrate potentially beneficial effects of leaving thin liquefiable layers untreated (in level ground sites), when remediating soil liquefaction under existing structures. As such, further studies are warranted in this direction exploring the effect of soil permeability (and its variation along the deposit), residual strength of liquefied soil, and integrity of the upper nonliquefiable (or treated) crust.

6.13 Appendix 3: Illustration for a lateral spreading scenario

With the calibrated parameters for both experiments, a further scenario is run to illustrate the response of polymer remediation on a mildly inclined slope (4 degrees). Identical models, as shown in Figure 6.11 and Figure 6.12, were subjected to the same base excitation, however, in the presence of a static lateral shear stress. The lateral displacement of the soil surface along the direction of the static shear stress is presented in Figure 6.43. As seen, polymer remediation was able to reduce development of biased shear strains within the liquefiable layer.

6.14 Appendix 4: Illustration for a lateral spreading scenario

Photos of the polymer-sand composite obtained after excavation is presented in Figure 6.44 and Figure 6.45. These photos illustrate the complexity in identifying mechanical properties of the composite with different degrees of permeation (cementation of insitu sand), and expansion (of pure polymer) observed after the injection sequence.

6.15 Tables and Figures

Table 6.1. Basic Geotechnical Properties of Ottawa F-65 Sand (Parra Bastidas, 2016)

Specific Gravity	2.65
Maximum Void Ratio (e_{max})	0.853
Minimum Void Ratio (e_{min})	0.503
Coefficient of uniformity (C_u)	1.61
Coefficient of curvature (C_c)	0.96
Maximum and minimum voids ratio (e_{max}, e_{min})	0.853, 0.503
Maximum and minimum mass density ρ_{min}, ρ_{max} (kg/m^3)	1446, 1759
Coefficient of uniformity (C_u)	1.61

Table 6.2. Properties of three-layered model prior to injection

Property	**Crust layer**	**Liquefiable layer**	**Base layer**
Water/soil condition	Moist	Saturated	Saturated
Depth (m)	0-0.64	0.64-1.9	1.9-2.9
Thickness (m)	0.64	1.26	1.0
Estimated D_r (%)	50%-55%	35%-44%	80 – 95%

Table 6.3. Employed Properties for the PDMY02 soil model for the Baseline test

Model Parameters	***Crust***	***Liquefiable layer***	***Dense layer***
Relative Density (D_r)	55%	40%	85%
Element Type		B-Bar brick u-p	
Reference mean effective pressure, p'_r (kPa)	8.9	18.7	30.3
Total Mass density, ρ (t/m^3)	2.00	1.9	2.10
Maximum shear strain at reference pressure, $\gamma_{max,r}$		0.10	
Shear modulus at reference pressure, G_r (MPa)	7.5	5	25
Stiffness dependence coefficient d		0.5	
Poisson's ratio v for dynamics		0.4	
Friction angle ϕ, with resulting strength defined as $p'\sin\phi$	32	29.5	36
Phase transformation angle, ϕ_{PT}	31	29.5	28.5
Contraction coefficient, c_1	0	0.18	0.001
Dilation coefficient, d_1	0	0	0.2
Permeability (m/s)		10^{-5}	
Initial stiffness damping coefficient		0.003	
Convergence criteria based on norm of energy increment		10^{-6}	

Table 6.4. Employed Properties for the PDMY02 soil model for the Polymer test

Model Parameters	***Crust***	***Liquefiable layer***	***Dense layer***
Relative Density (D_r)	65%	65%	85%
Element Type		B-Bar brick u-p	
Reference mean effective pressure, p'_r (kPa)	8.9	18.7	30.3
Total mass density, ρ (t/m^3)	2.0	2.0	2.1
Maximum shear strain at reference pressure, $\gamma_{max,r}$		0.10	
Shear modulus at reference pressure, G_r (MPa)	10	10	25
Stiffness dependence coefficient *d*		0.5	
Poisson's ratio for dynamics, *v*		0.4	
Friction angle ϕ, with resulting strength defined as $p' \sin\phi$	33	33	36
Phase transformation angle, ϕ_{PT}	31	31	28.5
Contraction coefficient, c_1	0	0.005	0.001
Dilation coefficient, d_1	0	0	0.2
Permeability (m/s)		10^{-5}	
Initial stiffness damping coefficient		0.003	
Convergence criteria based on norm of energy increment		10^{-6}	

Table 6.5. Employed Properties for the PIMY soil model for the Polymer test

Model Parameters	***Polymer1***	***Polymer2***	***Polymer 3***	***Polymer 4***	***Polymer 5***
Element Type			B-Bar brick u-p		
Total mass density, ρ (t/m^3)	0.2	0.2	0.6	1.0	1.2
Low strain shear modulus, G_0 (MPa)	0.2	0.4	1.5	2	2.8
Poisson's ratio for dynamics, *v*			0.38		
Cohesive Strength, s_u (kPa)	30	120	240	290	400
Permeability, *k* (m/s)			10^{-9}		
Maximum shear strain at reference pressure, $\gamma_{max,r}$			0.10		

Table 6.6. Smeared properties for the liquefiable soil in the Polymer test (using PDMY02)

Model Parameters	**$(N_1)_{60}$ = 29**
Relative Density (D_r) From Idriss and Boulanger (2008)	80%
Total mass density, ρ (t/m^3)	2.1
Shear modulus at reference pressure, G_r (MPa)	19.6
Friction angle ϕ, with resulting strength defined as $p' \sin\phi$	36
Phase transformation angle, ϕ_{PT}	28.5
Contraction coefficient, c_1	0.001
Dilation coefficient, d_1	0.2

(a)

(b)

Figure 6.1. (a) Laminar soil container at the UC San Diego and (b) excavated polymer specimen

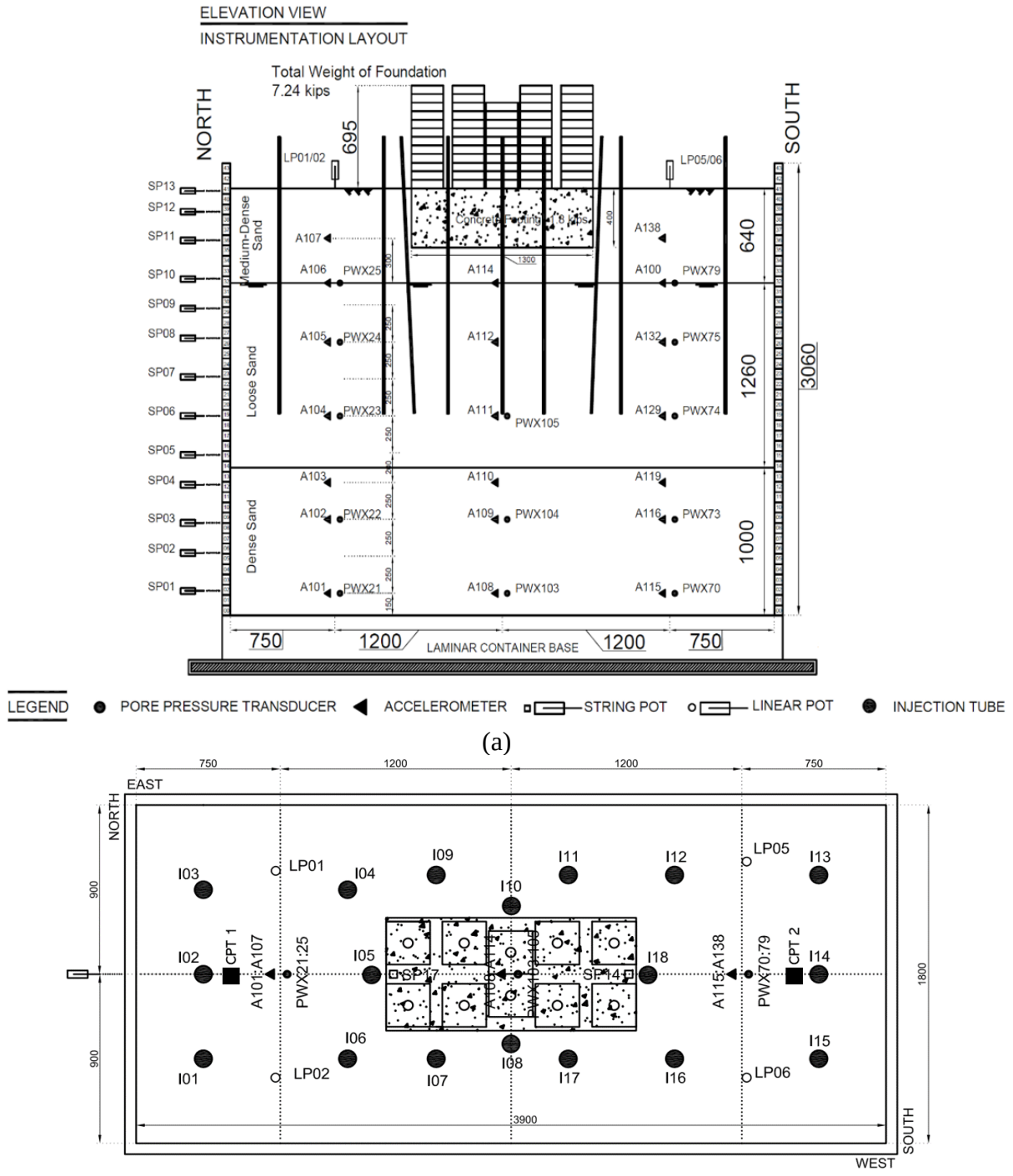

Figure 6.2. Instrumentation layout of Polymer Test: (a) Elevation and side view, (b) Plan view depicting polymer injection locations (All units in mm)

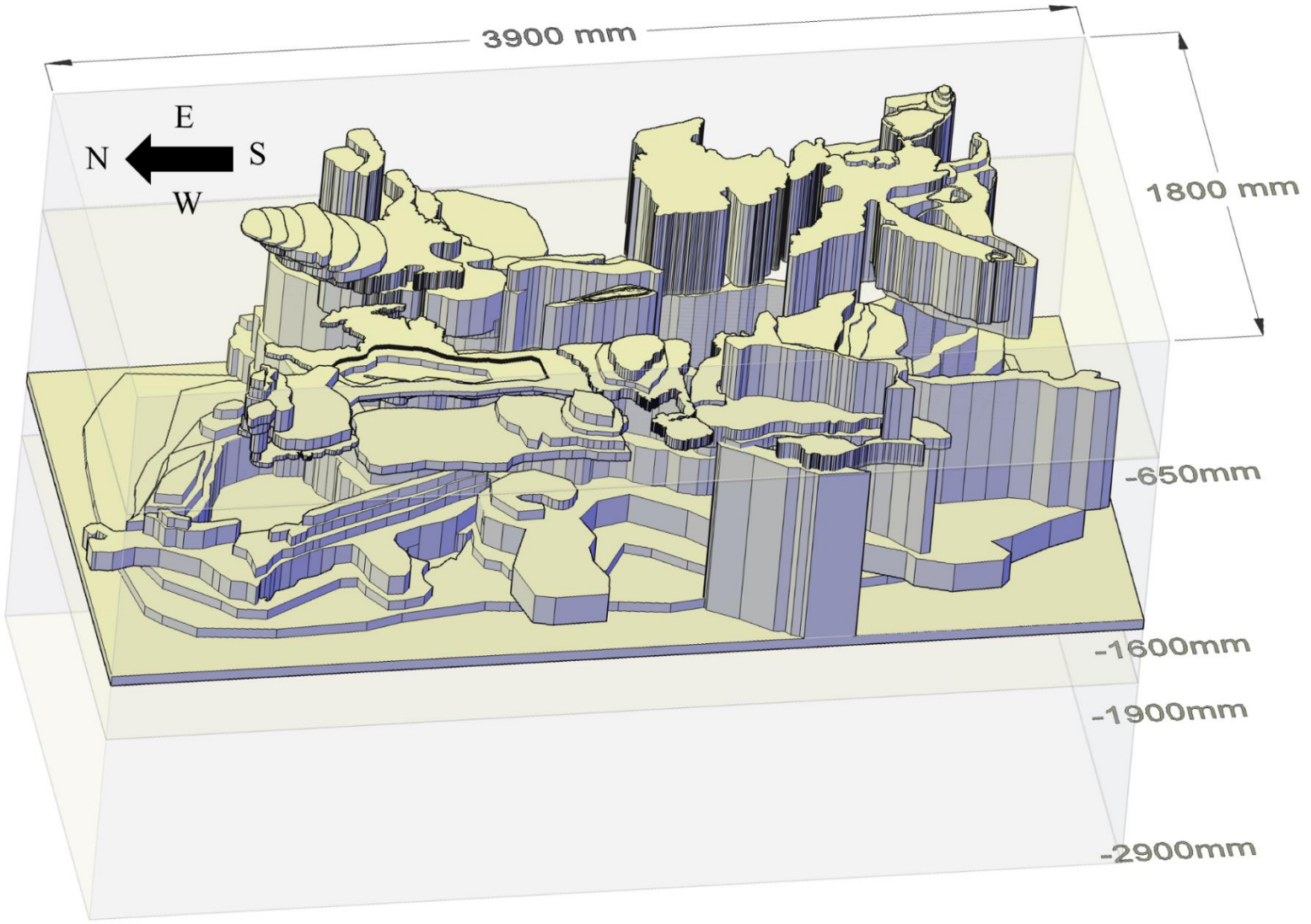

Figure 6.3. Mapped configuration of the polymer-sand composite

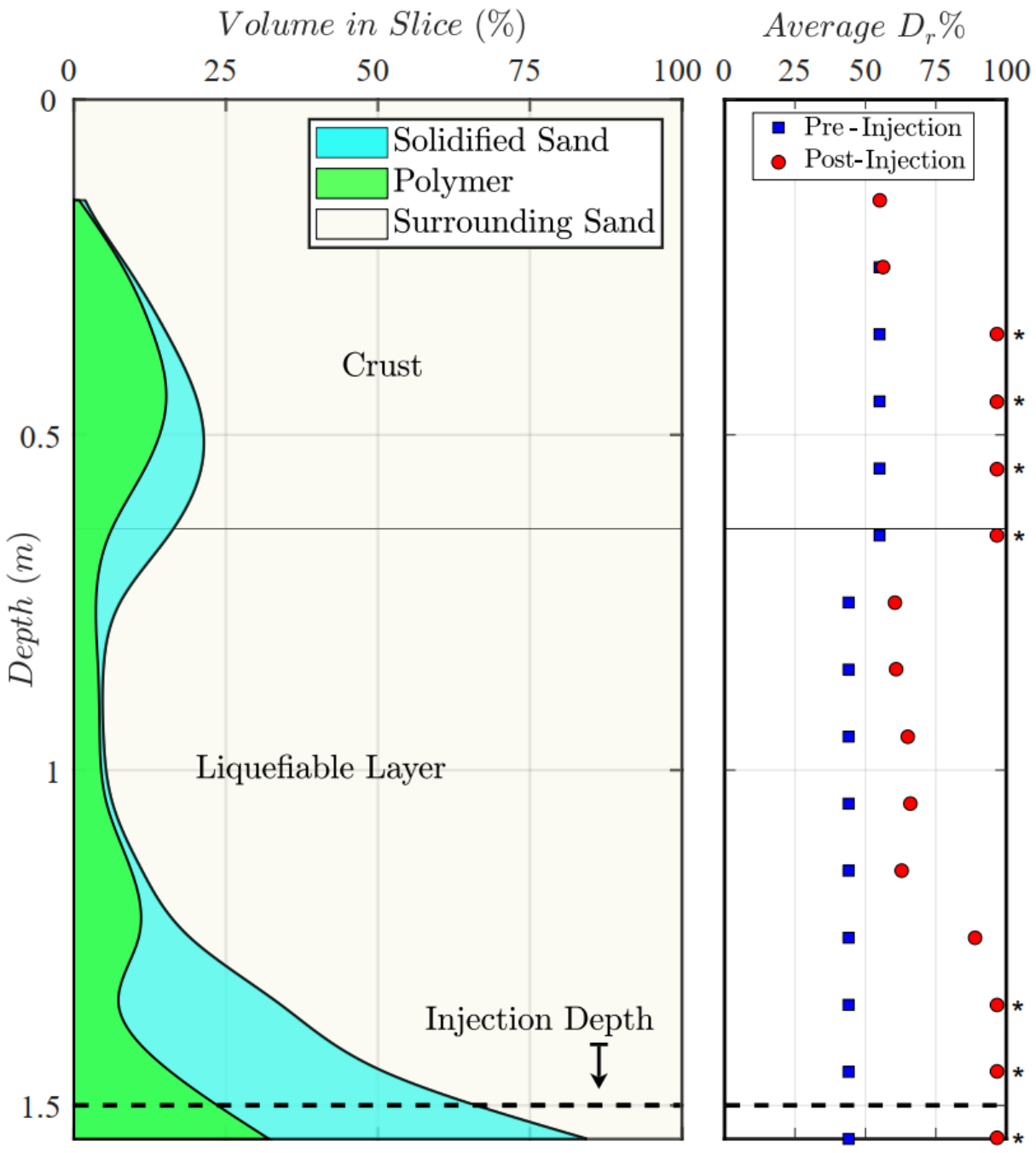

Figure 6.4. Estimation of percent volume of the solidified polymer sand composite, pure polymer within composite, and relative density of surrounding sand at different depths (* estimated D_r exceeds 100%, due to movement of soil across layers).

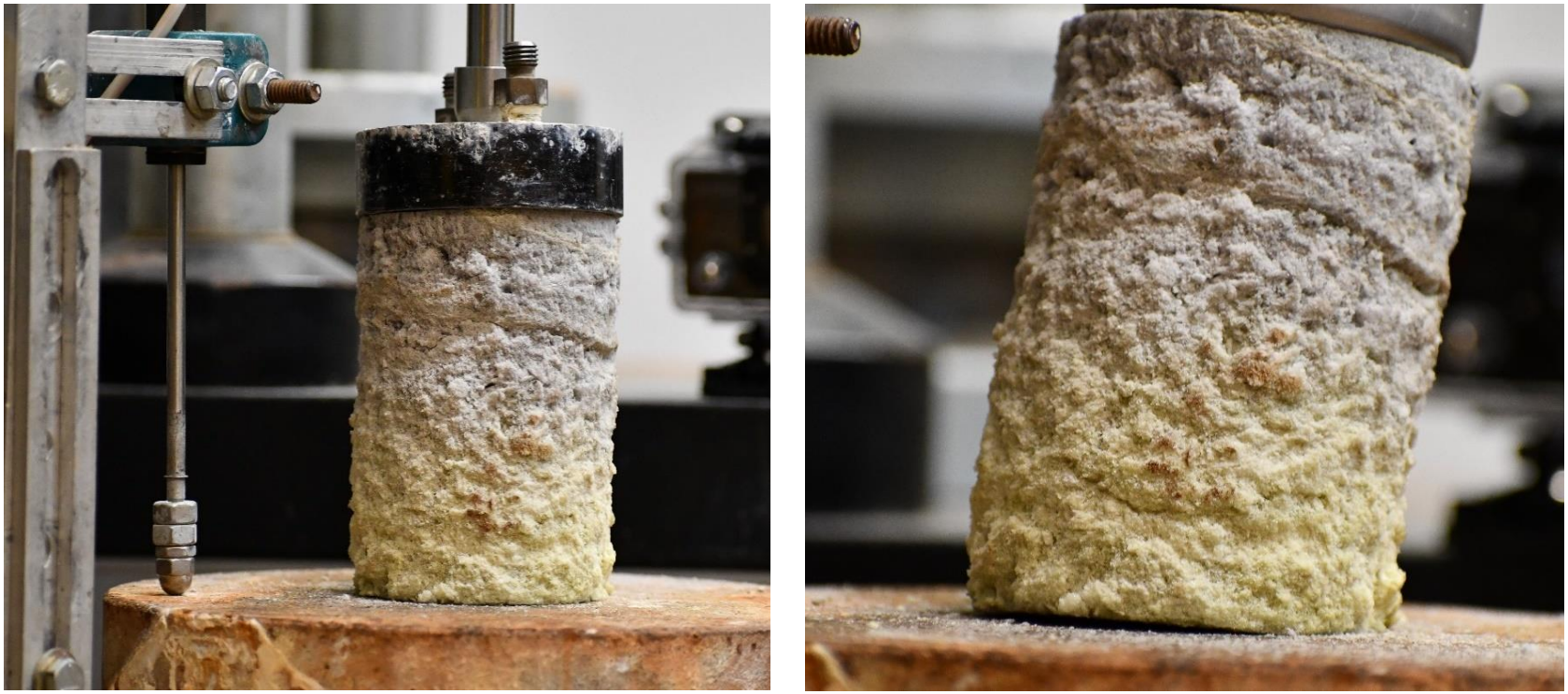

(a) (b)

Figure 6.5. Cored polymer-sand composite specimen at ground surface (a) prior to test, and (b) after test

(a) (b)

Figure 6.6. Cored polymer-sand composite specimen at a depth of about 1.5m (a) prior to test, and (b) after test

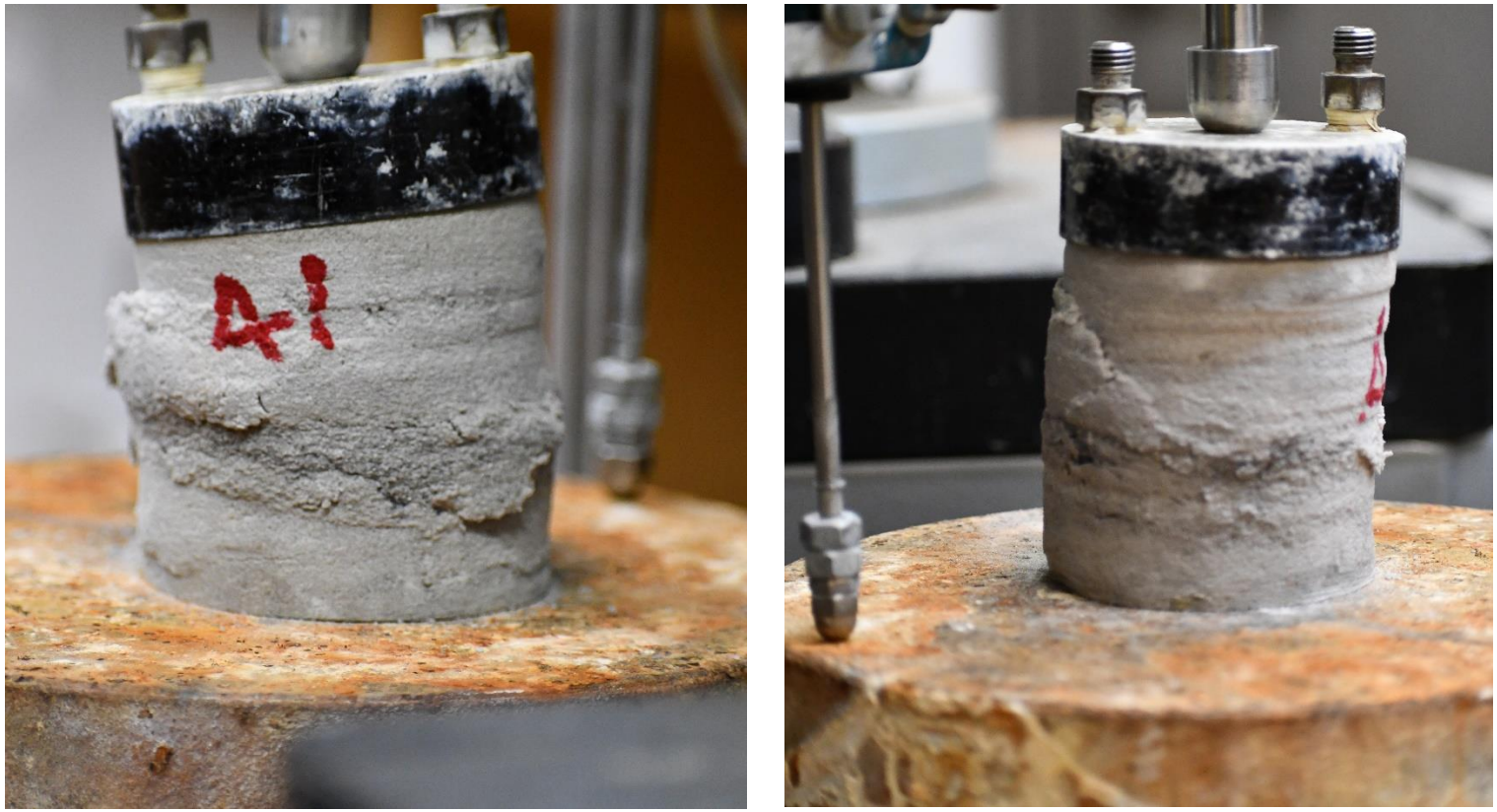

(a) (b)

Figure 6.7. Cored polymer-sand composite specimen at a depth of about 1.3m (a) prior to test, and (b) after test

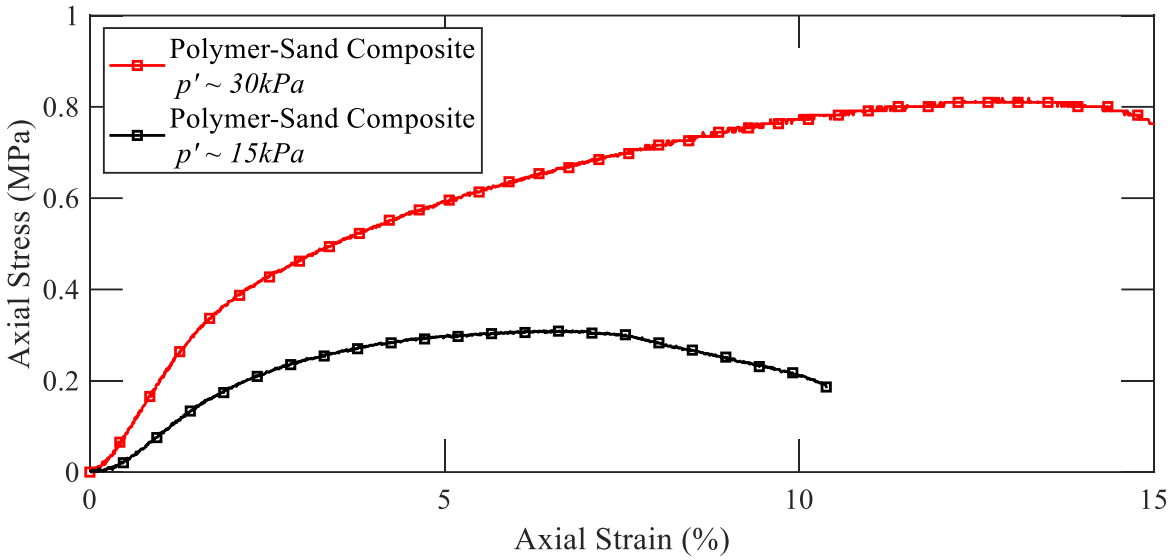

Figure 6.8. Typical stress-strain curves of the polymer-sand composite

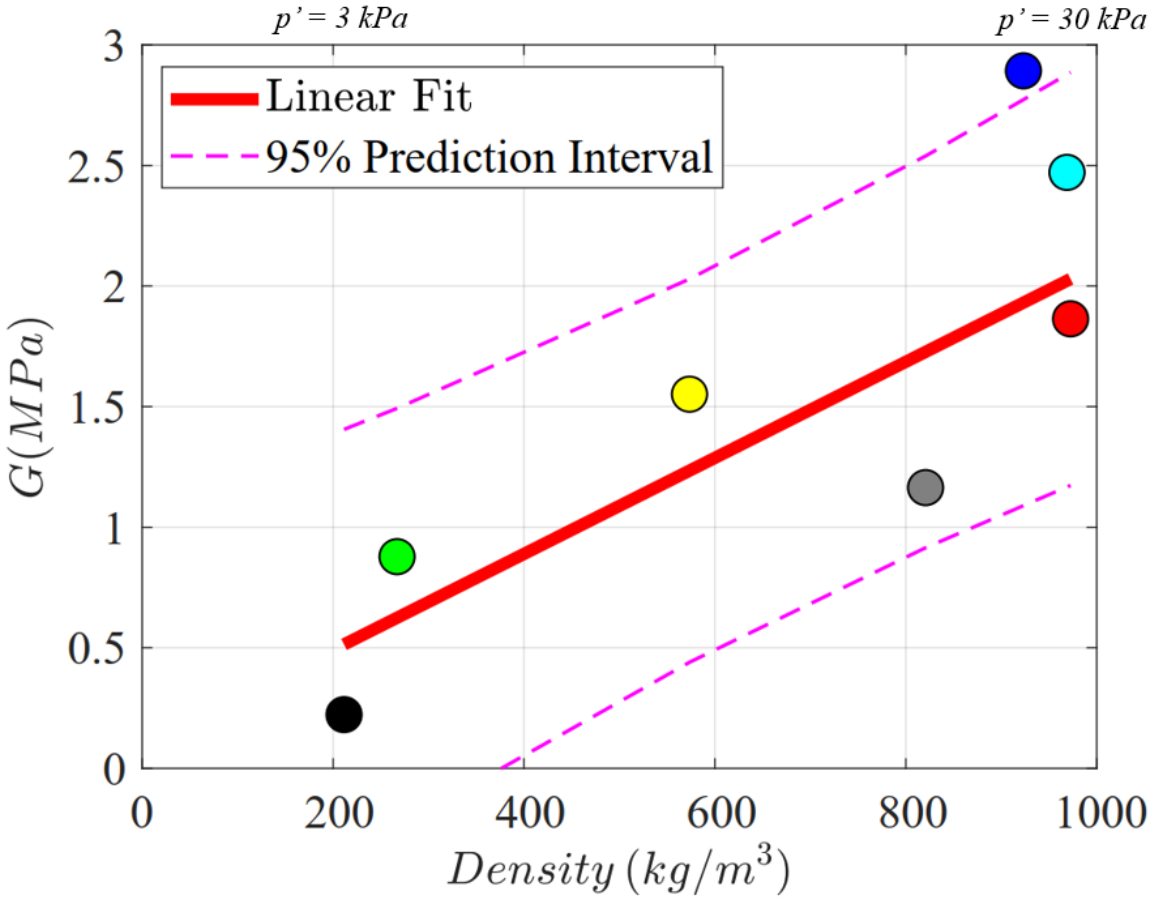

Figure 6.9. Variation of shear modulus (G) with density of the sand-polymer composite

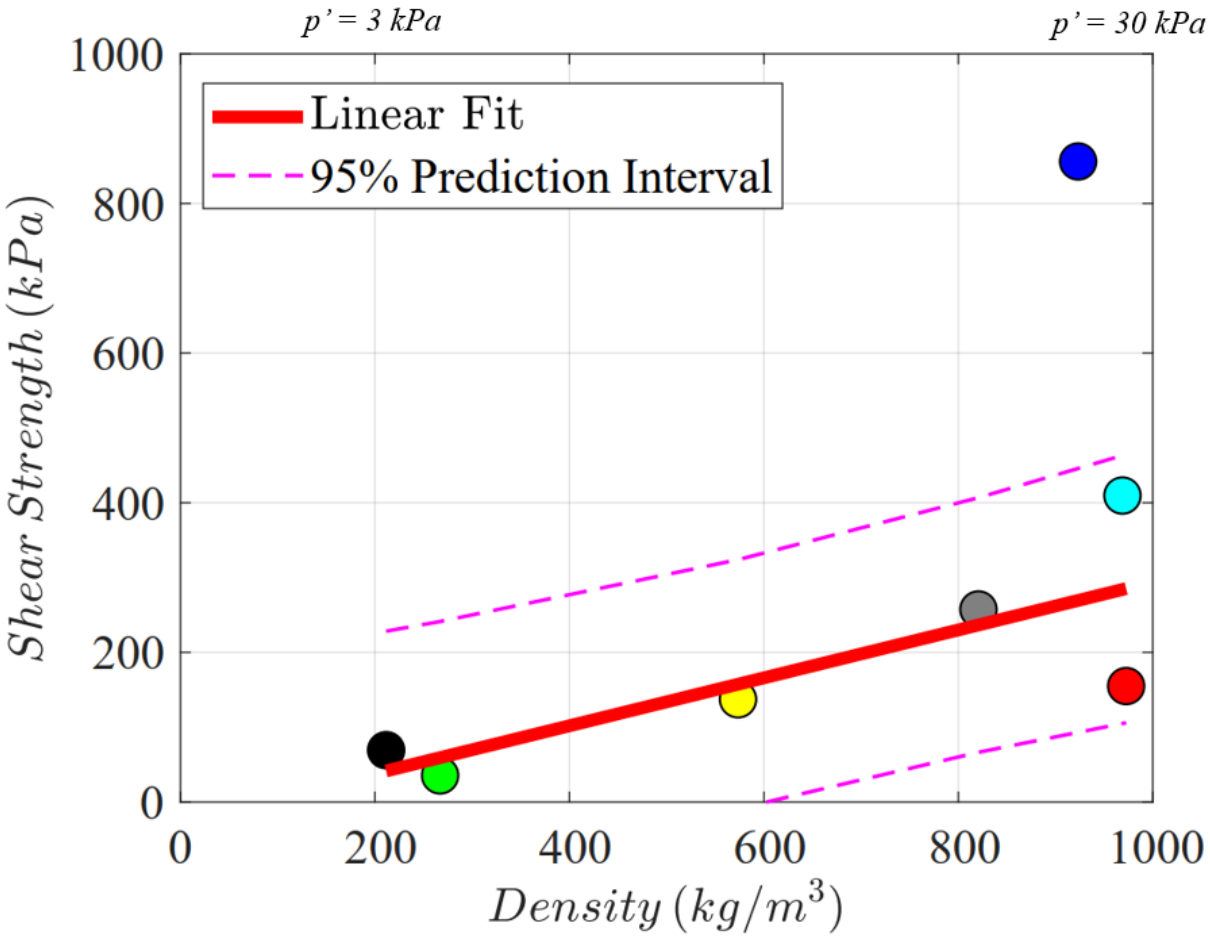

Figure 6.10. Variation of shear strength with density of the sand-polymer composite

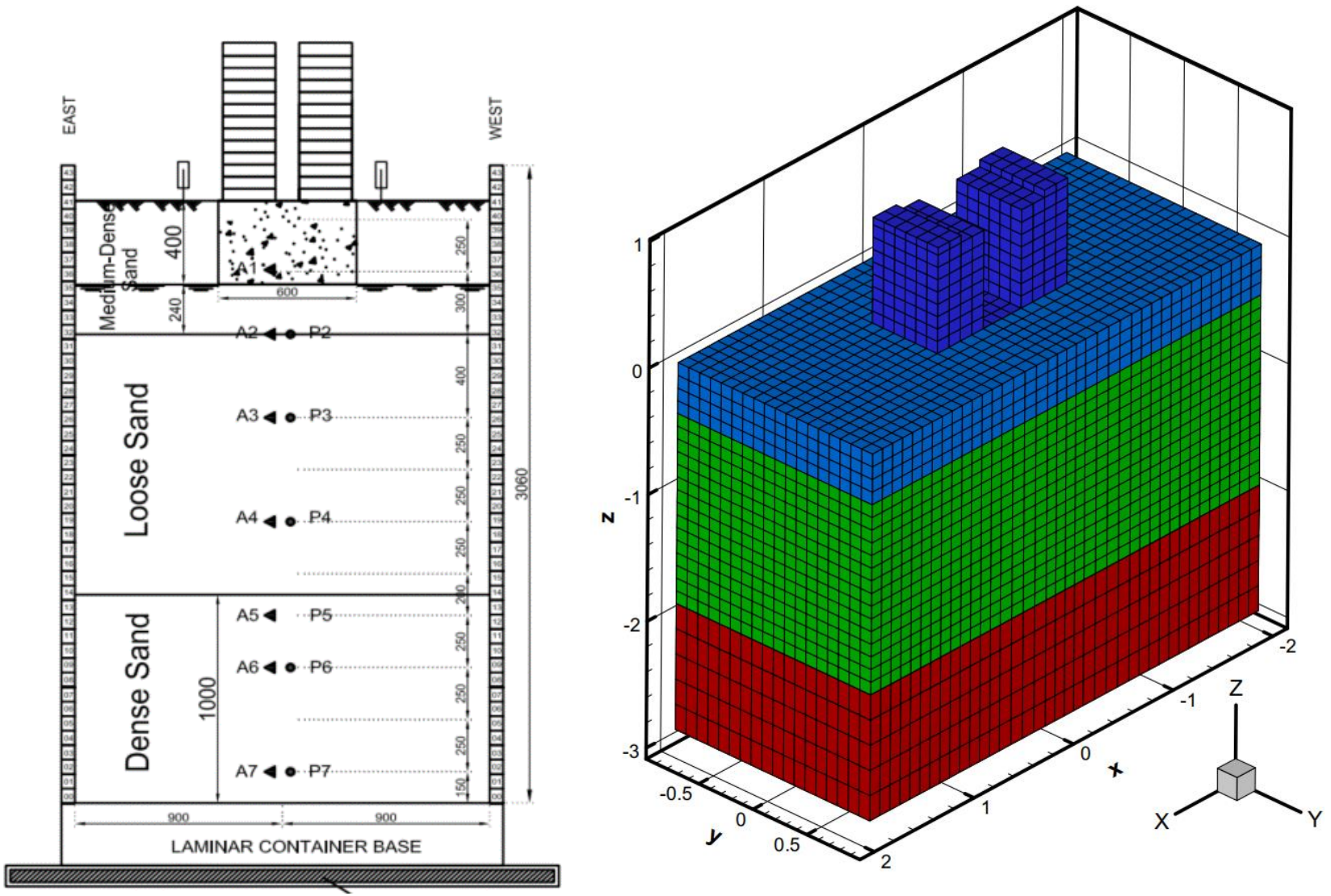

(a) (b)

Figure 6.11. Instrument layout (left) and employed discretization (right) of the polymer test

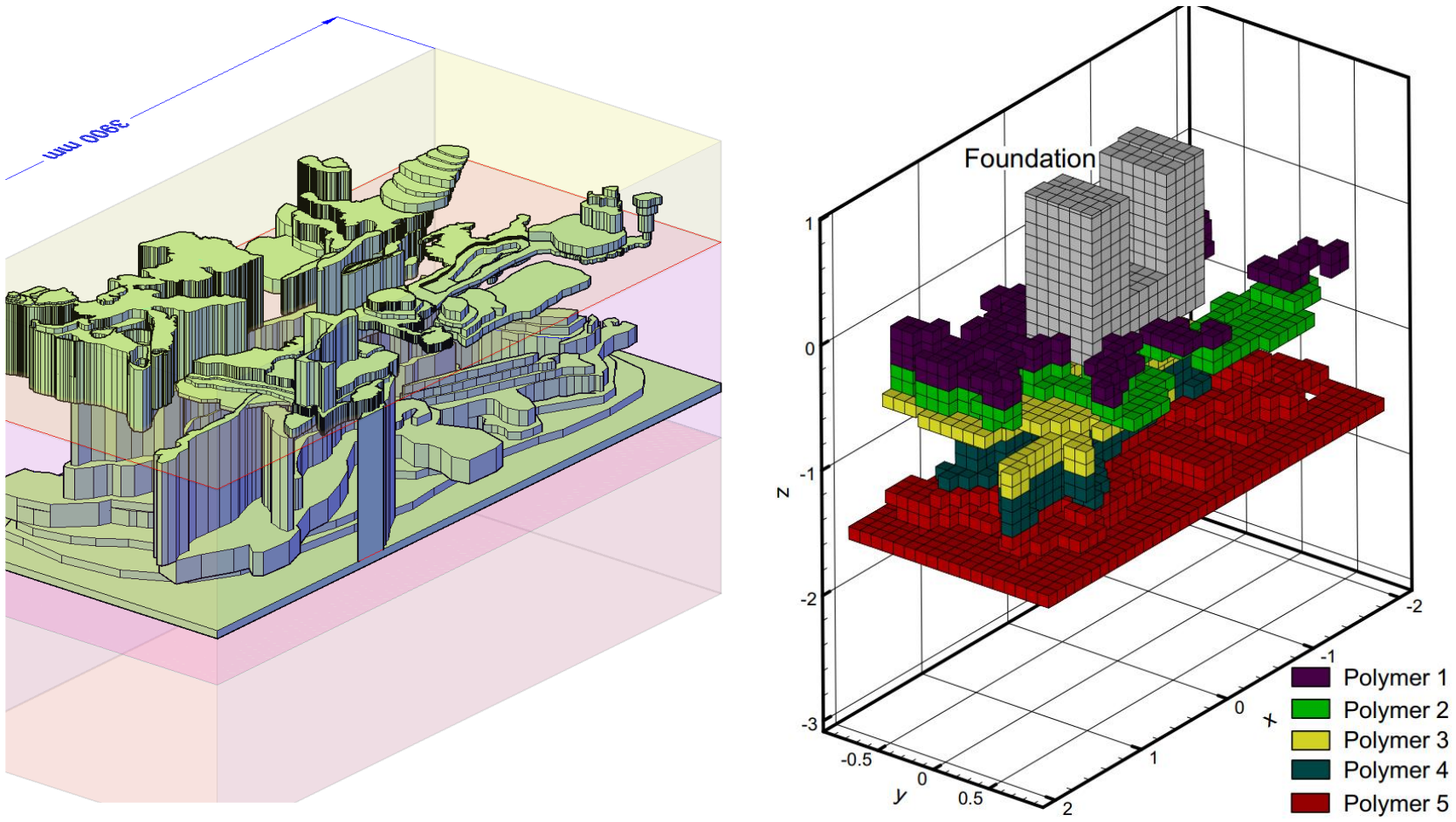

(a) (b)

Figure 6.12. Mapped polymer formation (left) and discretization (right)

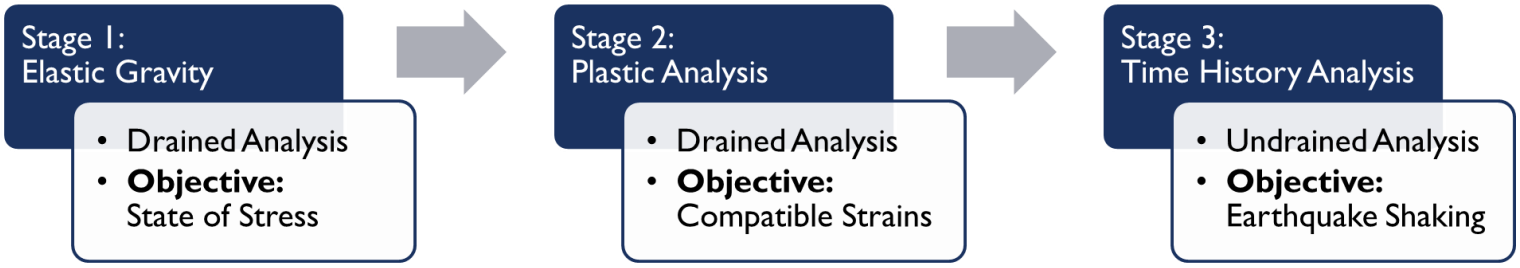

(a)

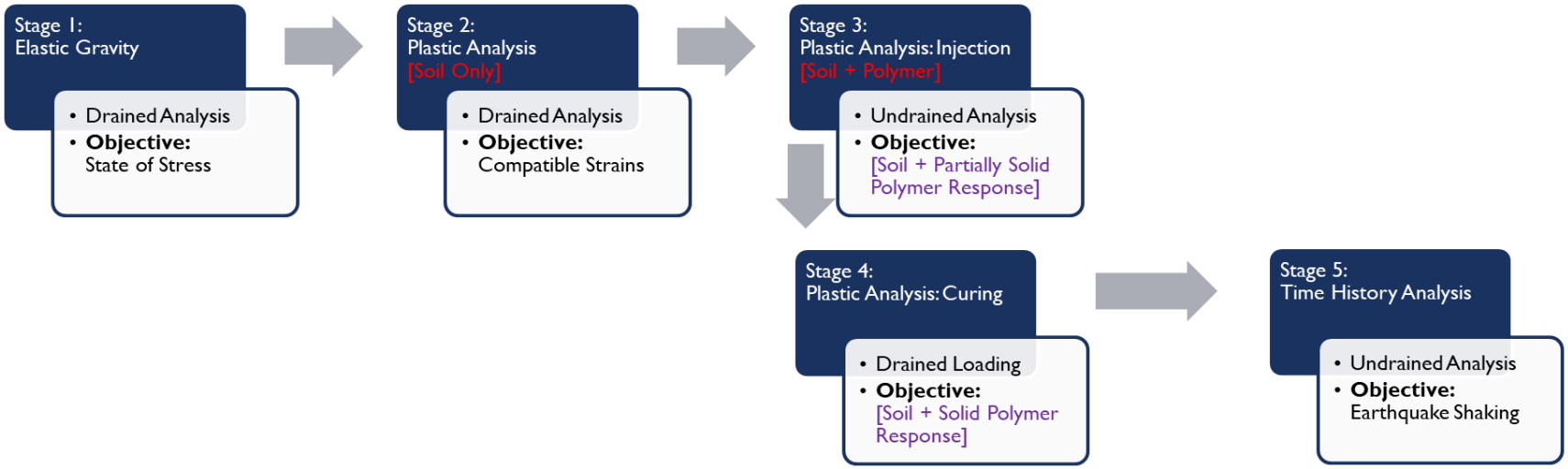

(b)

Figure 6.13. Staged Analysis: (a) currently employed three staged methodology, and (b) Refined 5 staged methodology

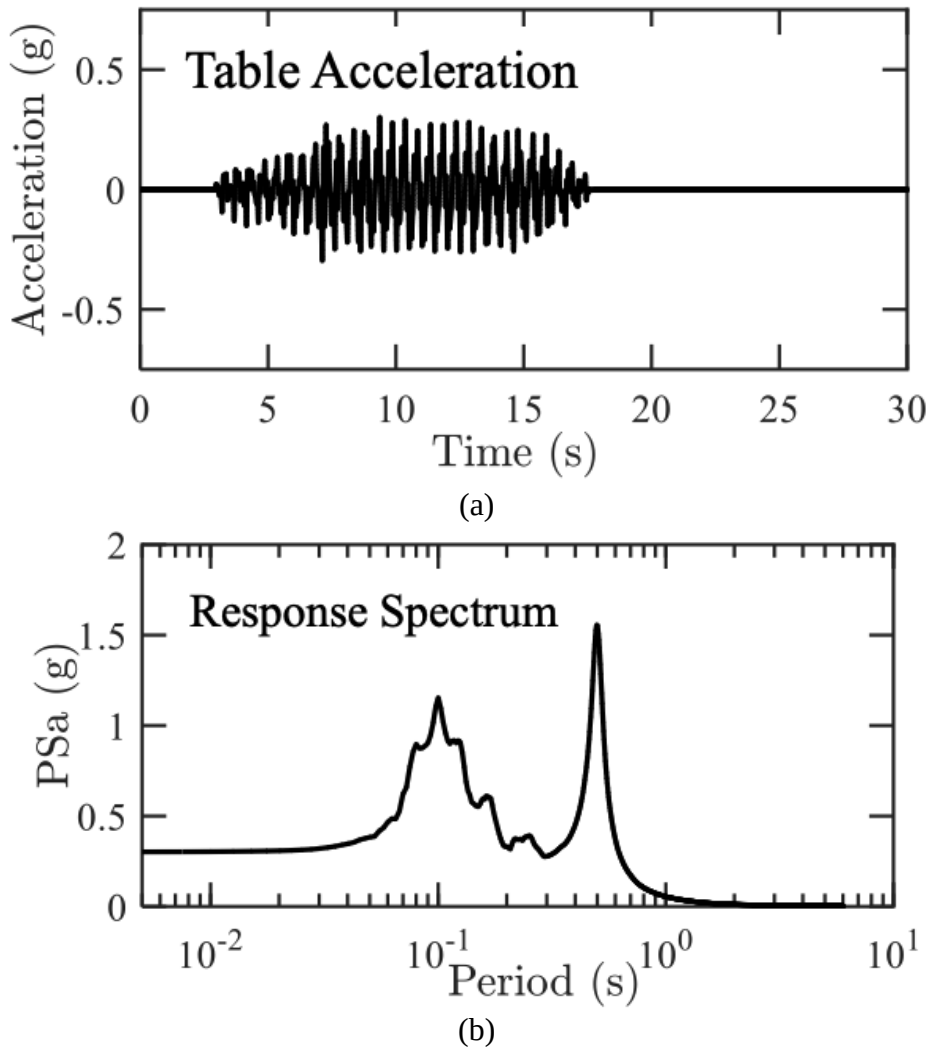

Figure 6.14. (a) Base excitation and (b) input acceleration response spectra in the experiments

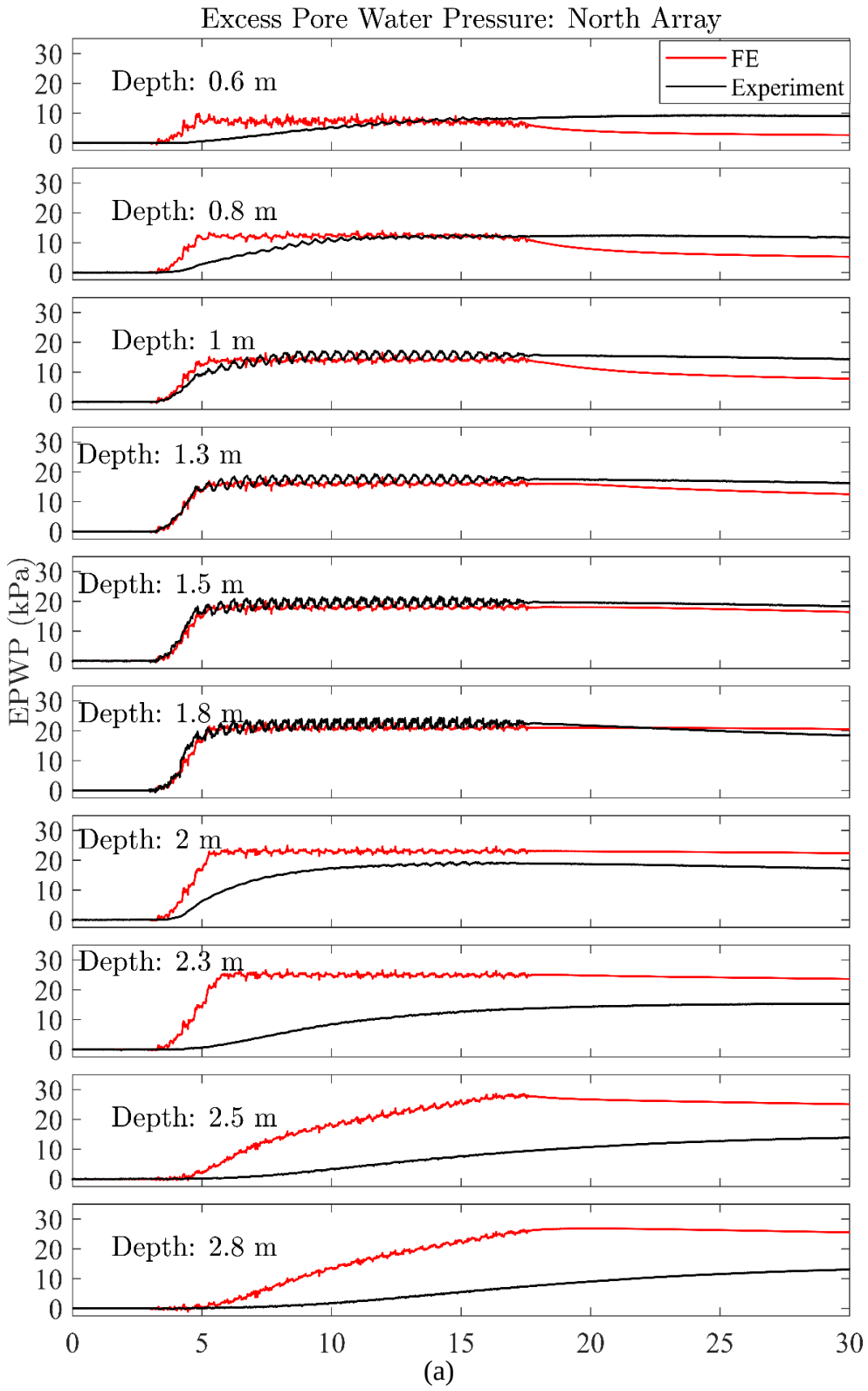

Figure 6.15. Excess pore pressure within the liquefiable layer for (a) free-field and (b) under foundation (right) arrays for the baseline experiment

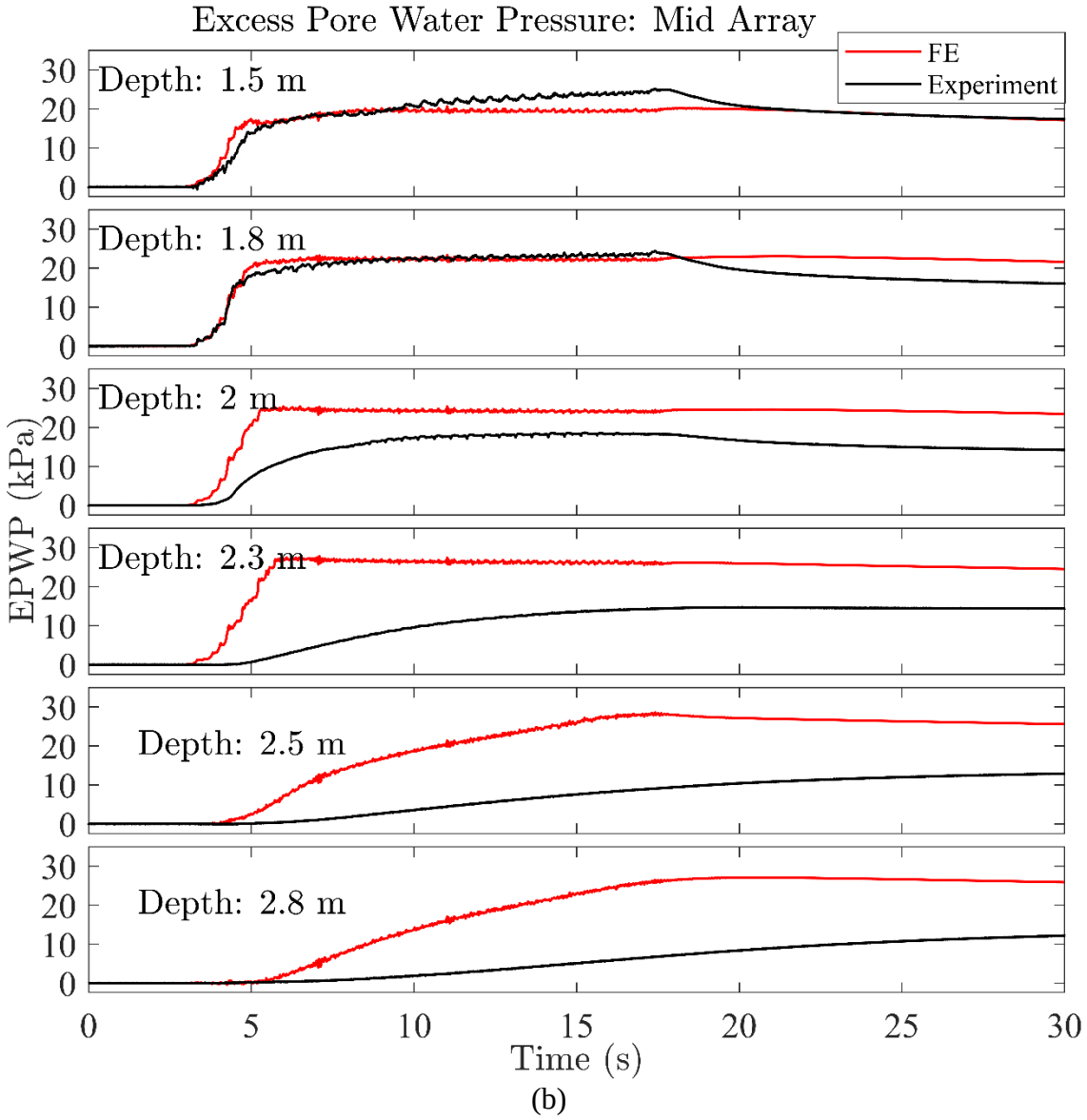

(b)

Figure 6.15 (continued). Excess pore pressure within the liquefiable layer for (a) free-field and (b) under foundation (right) arrays for the baseline experiment

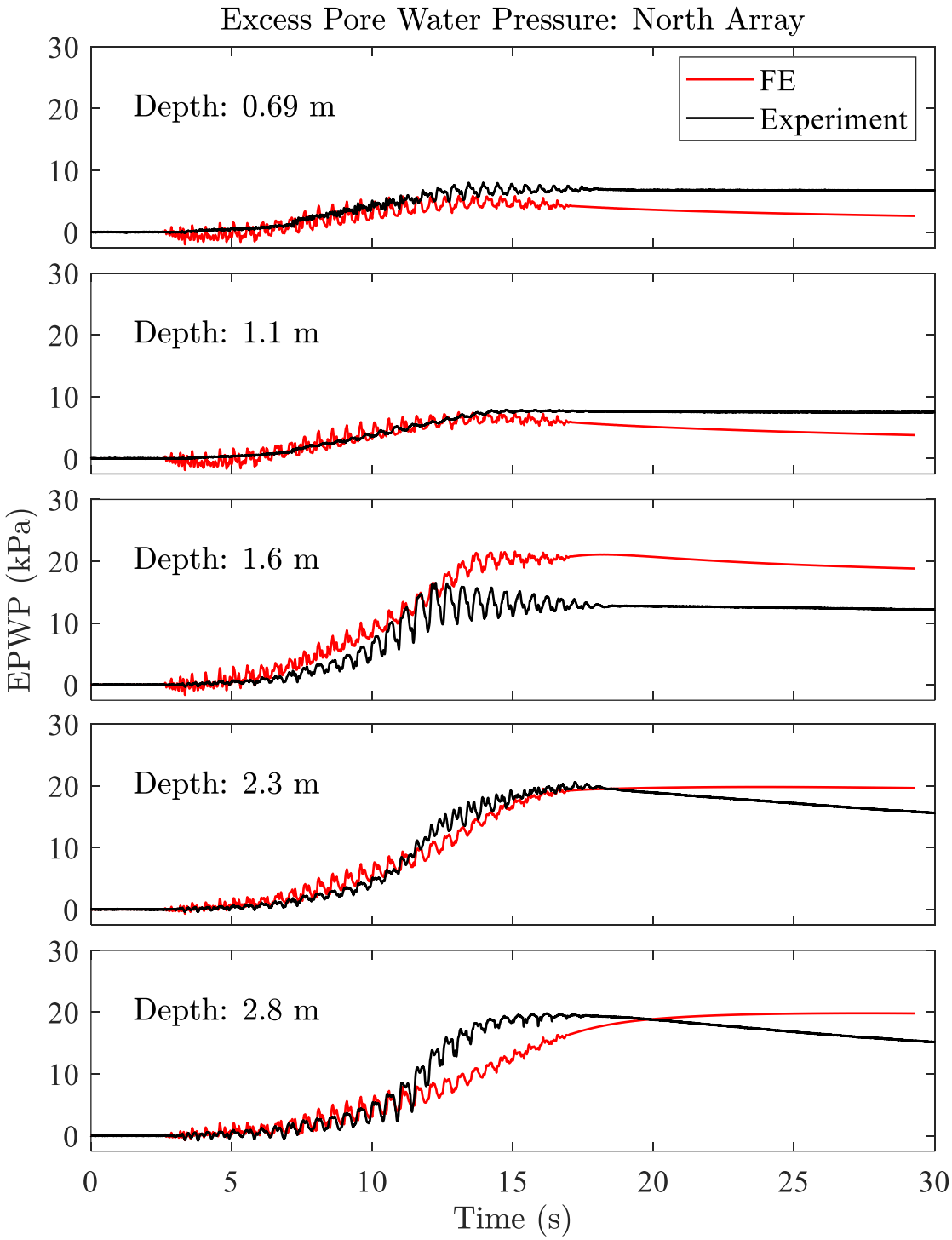

(a)

Figure 6.16. Excess pore pressure within the liquefiable layer for (a) free-field and (b) under foundation (right) arrays for the polymer remediated experiment

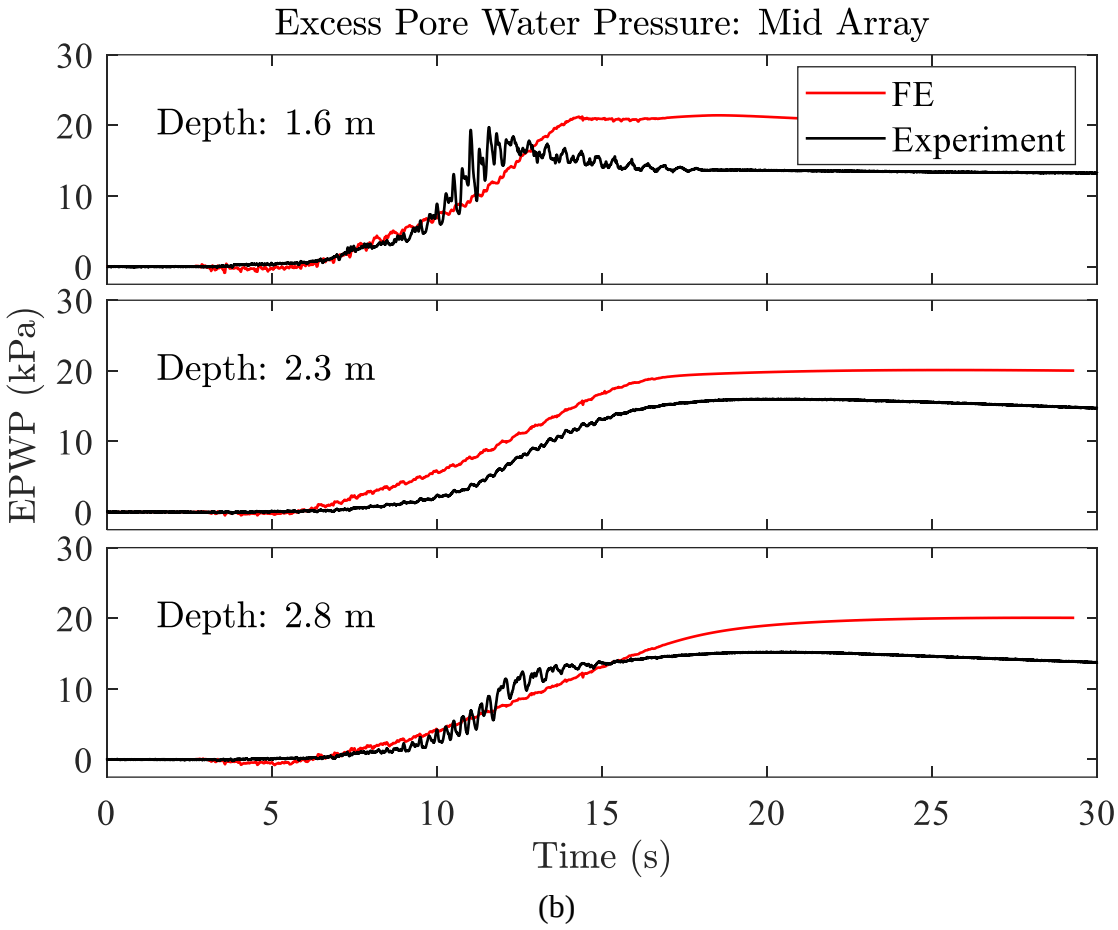

(b)

Figure 6.16 (continued). Excess pore pressure within the liquefiable layer for (a) free-field and (b) under foundation (right) arrays for the polymer remediated experiment

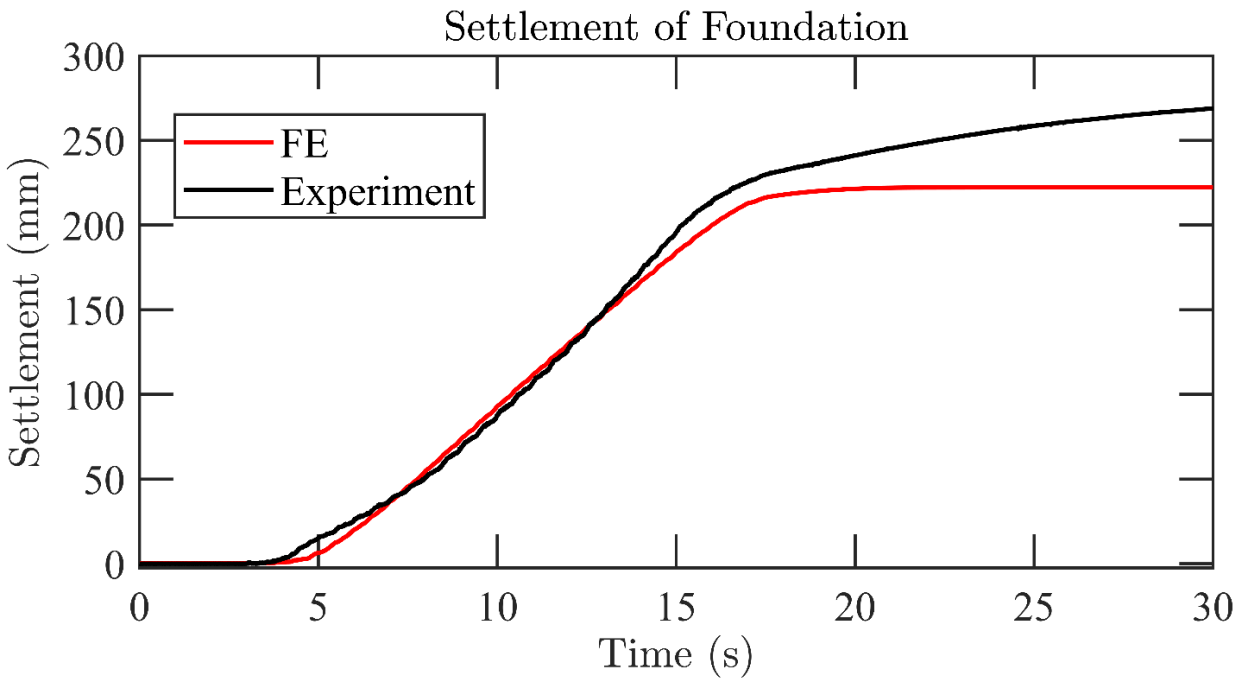

Figure 6.17. Foundation settlement during Shake1 for the baseline experiment

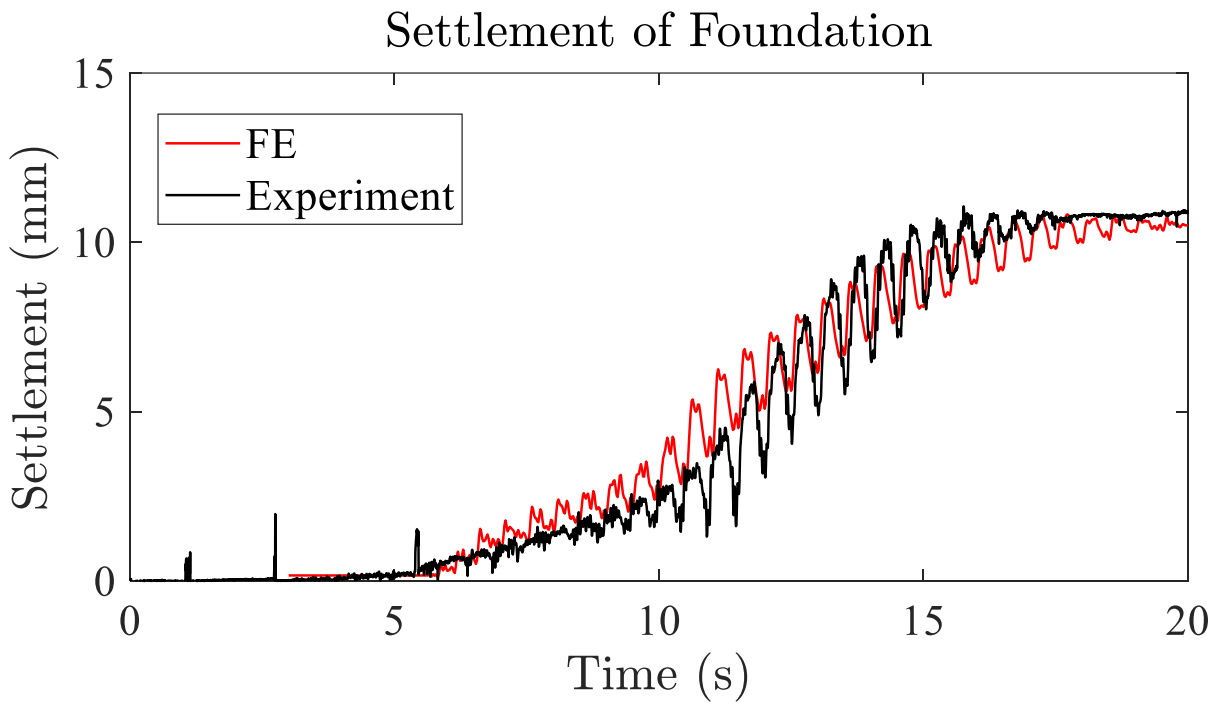

Figure 6.18. Foundation settlement during Shake1 for the polymer experiment

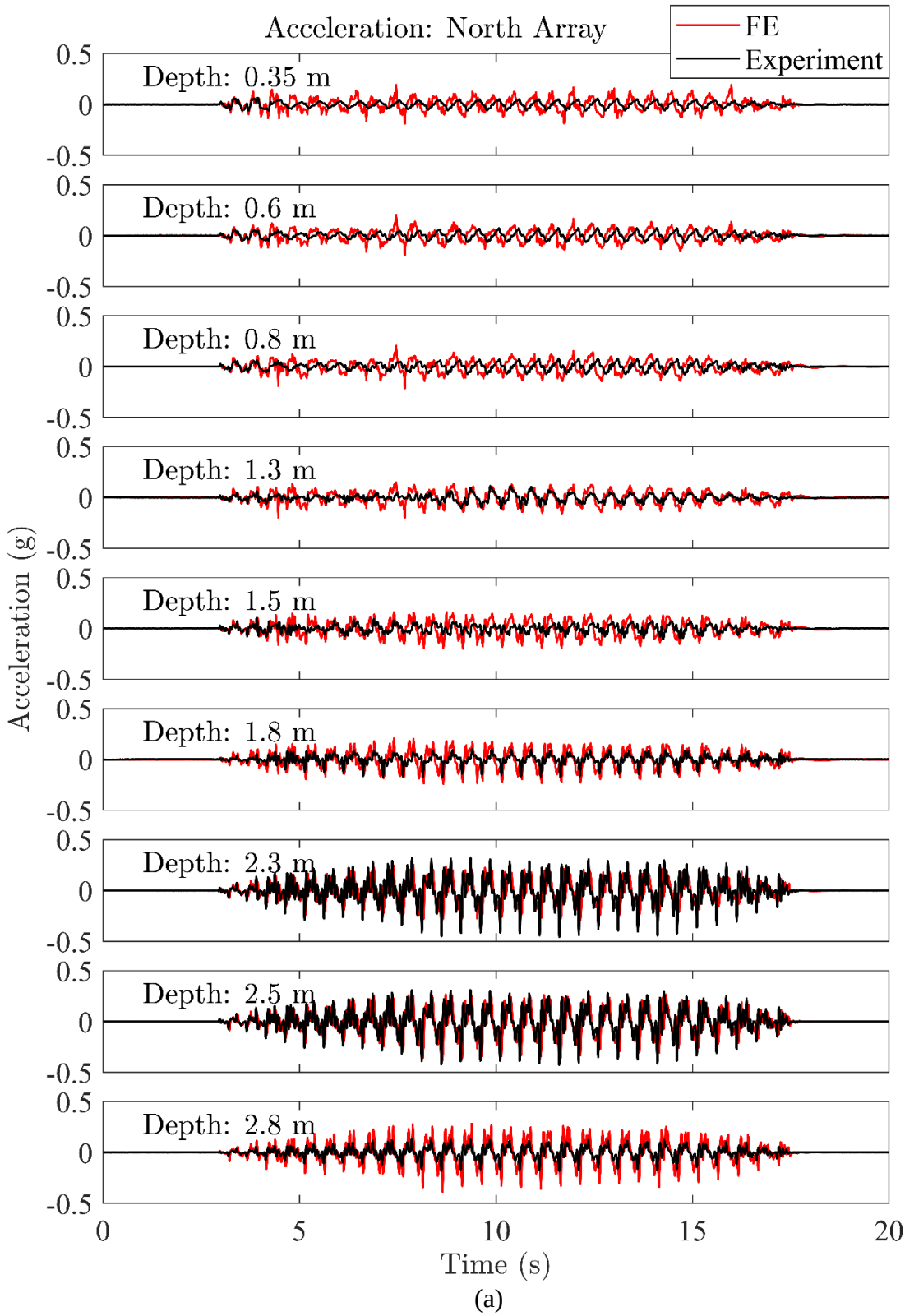

(a)

Figure 6.19. Soil acceleration within the liquefiable layer for (a) free-field and (b) under foundation (right) arrays for the baseline experiment

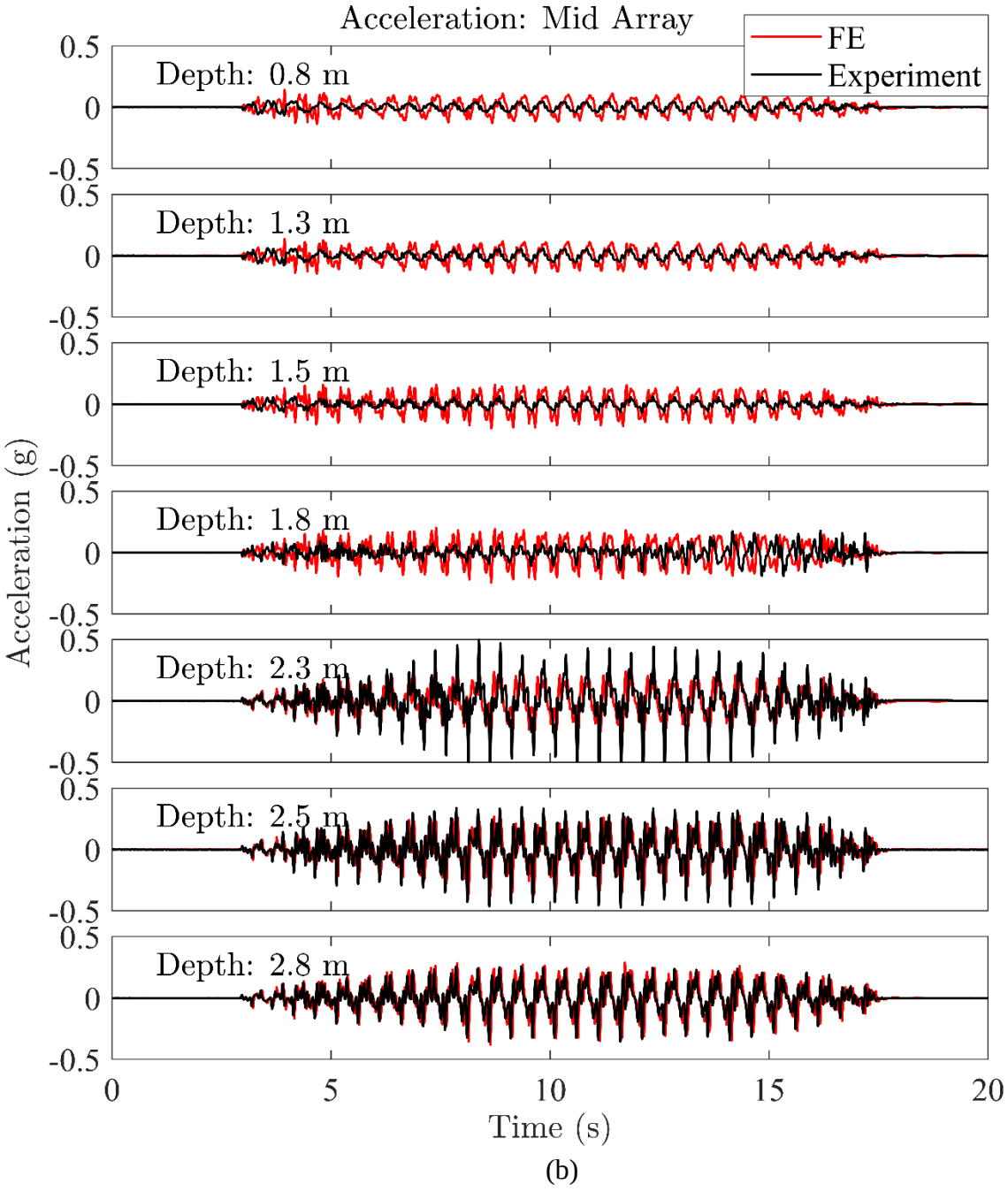

(b)

Figure 6.19 (contunied). Soil acceleration within the liquefiable layer for (a) free-field and (b) under foundation (right) arrays for the baseline experiment

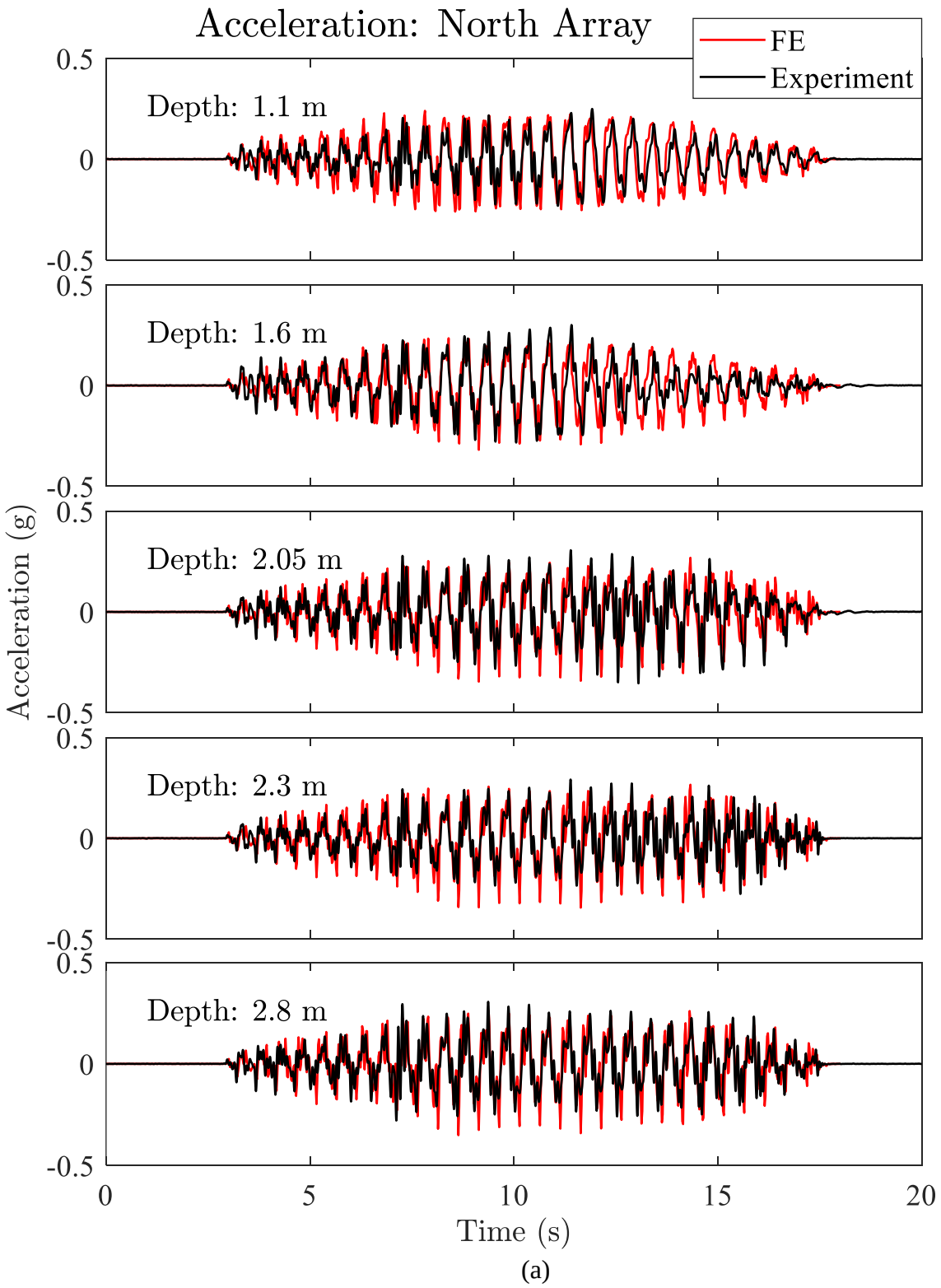

Figure 6.20. Soil acceleration within the liquefiable layer for (a) free-field and (b) under foundation (right) arrays for the polymer experiment

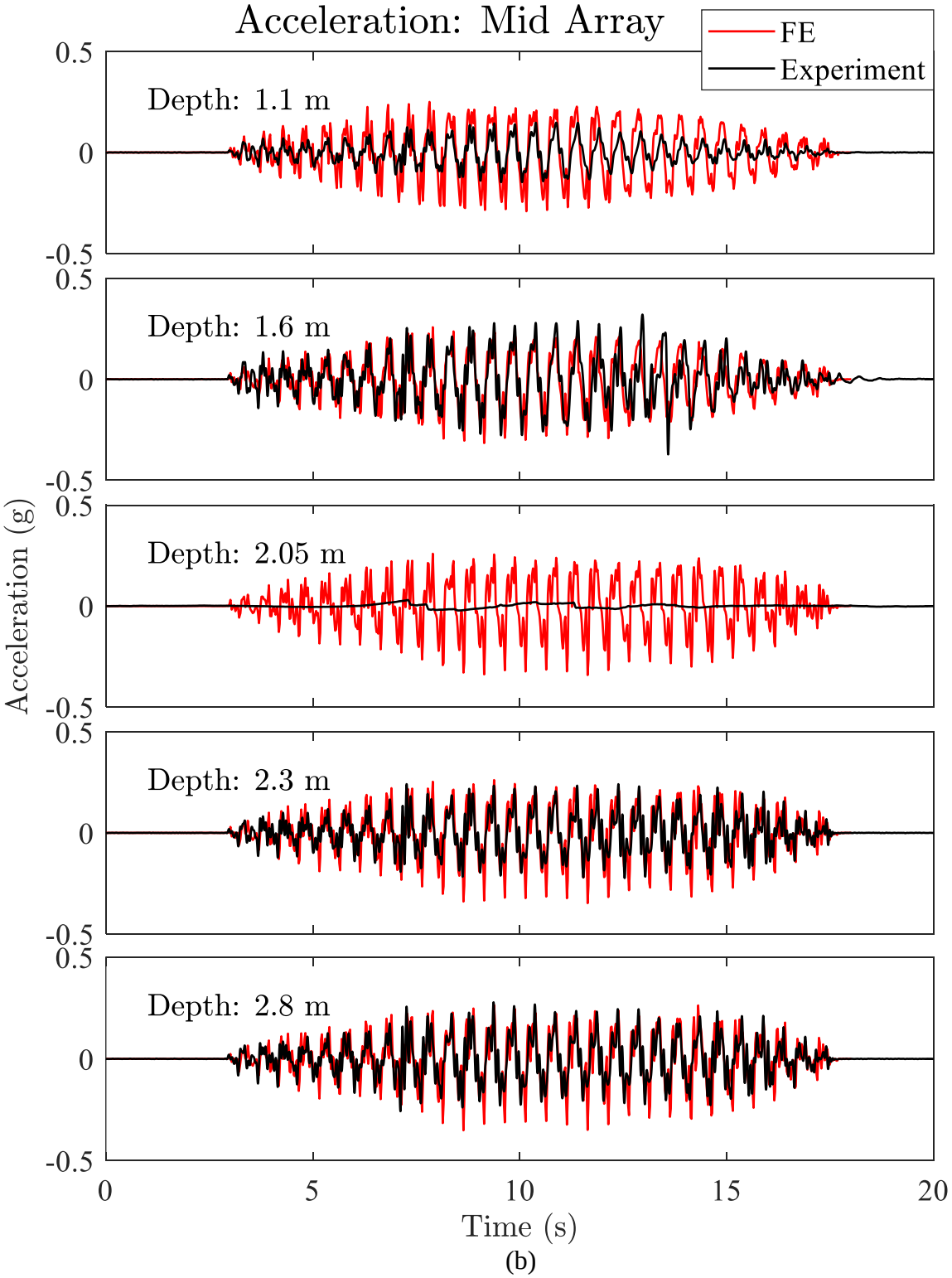

(b)

Figure 6.20 (continued). Soil acceleration within the liquefiable layer for (a) free-field and (b) under foundation (right) arrays for the polymer experiment

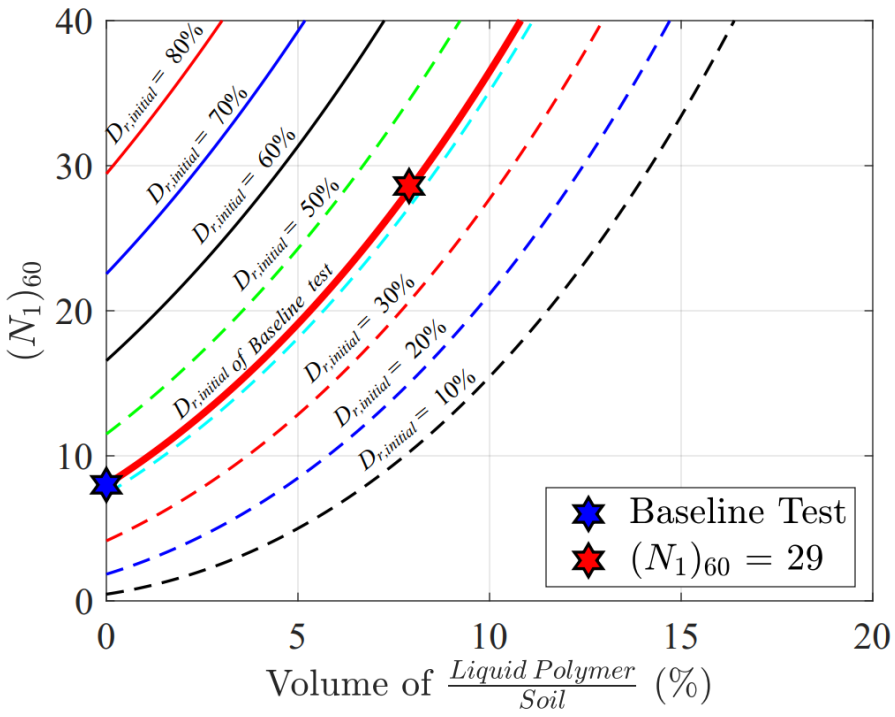

Figure 6.21. Extent of remediation in the treated ground using smeared properties

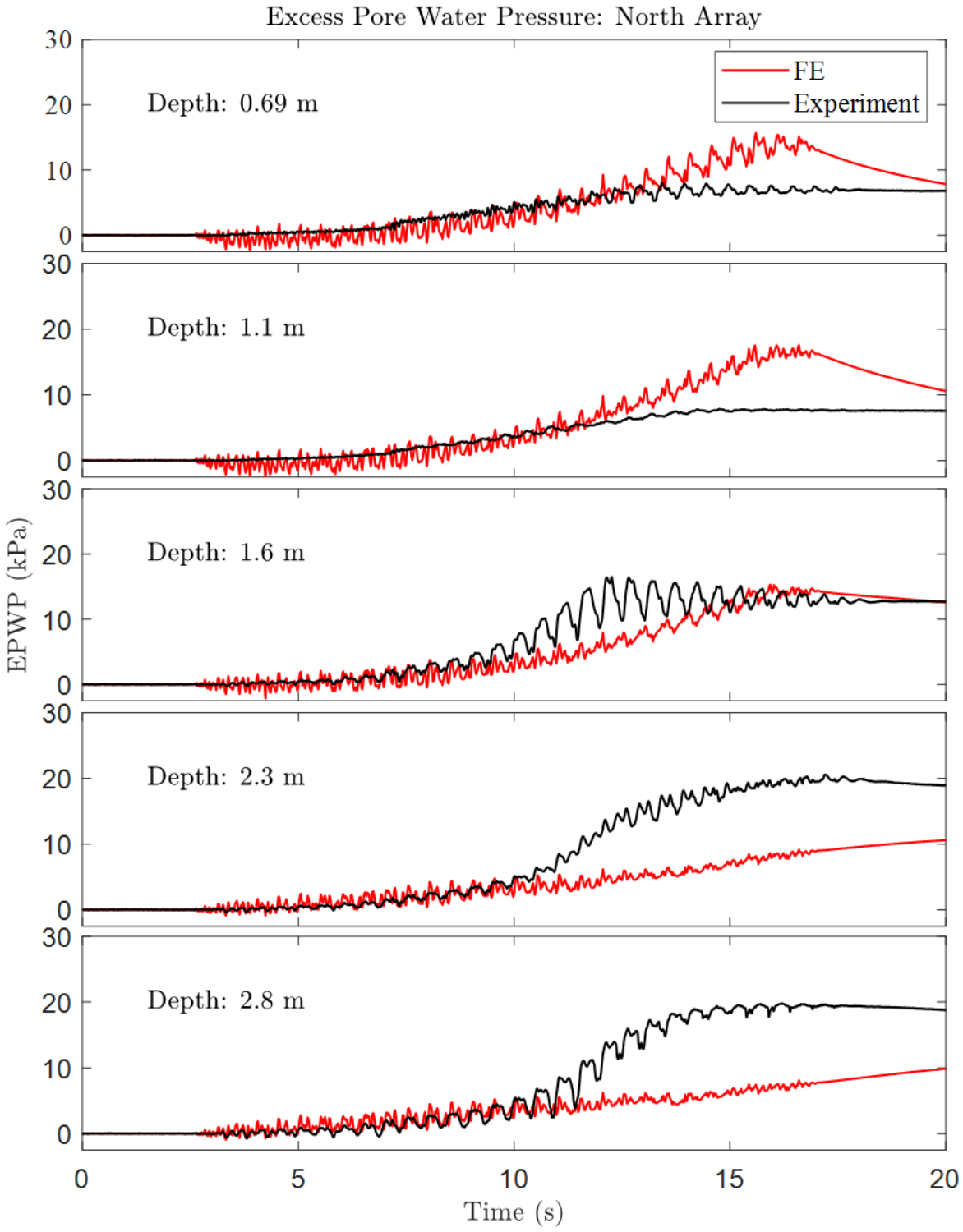

(b)

Figure 6.22. Developed excess pore pressure response within the north array using smeared properties for treated ground

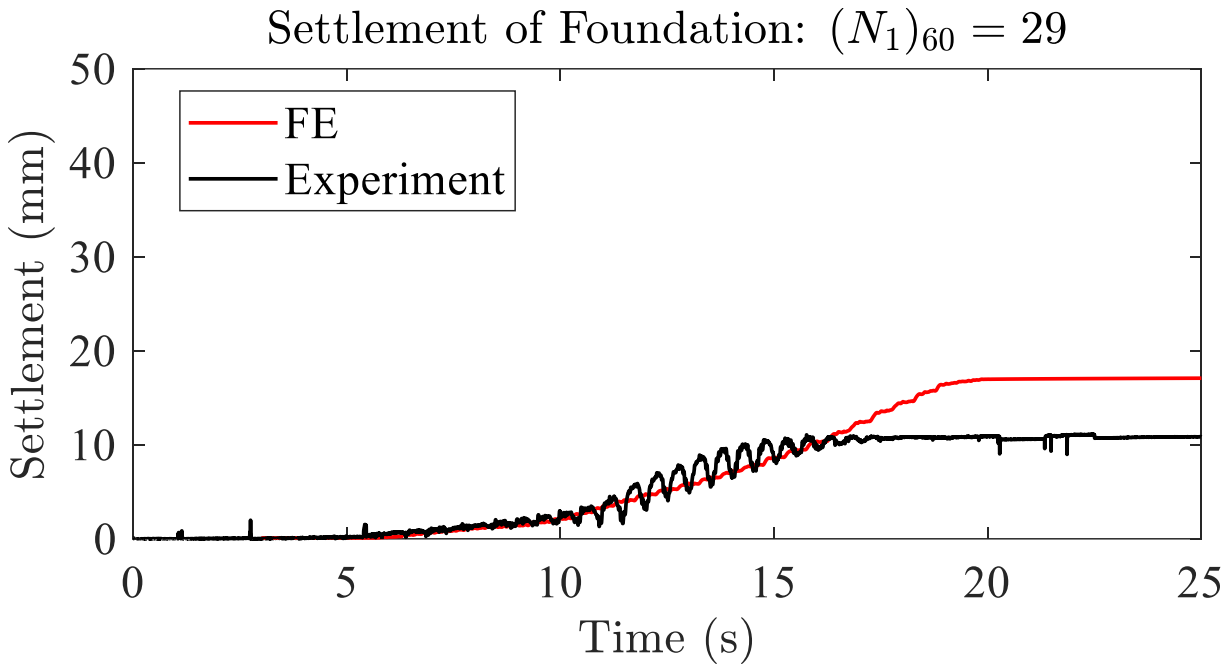

Figure 6.23. Foundation settlement for using smeared properties for treated ground

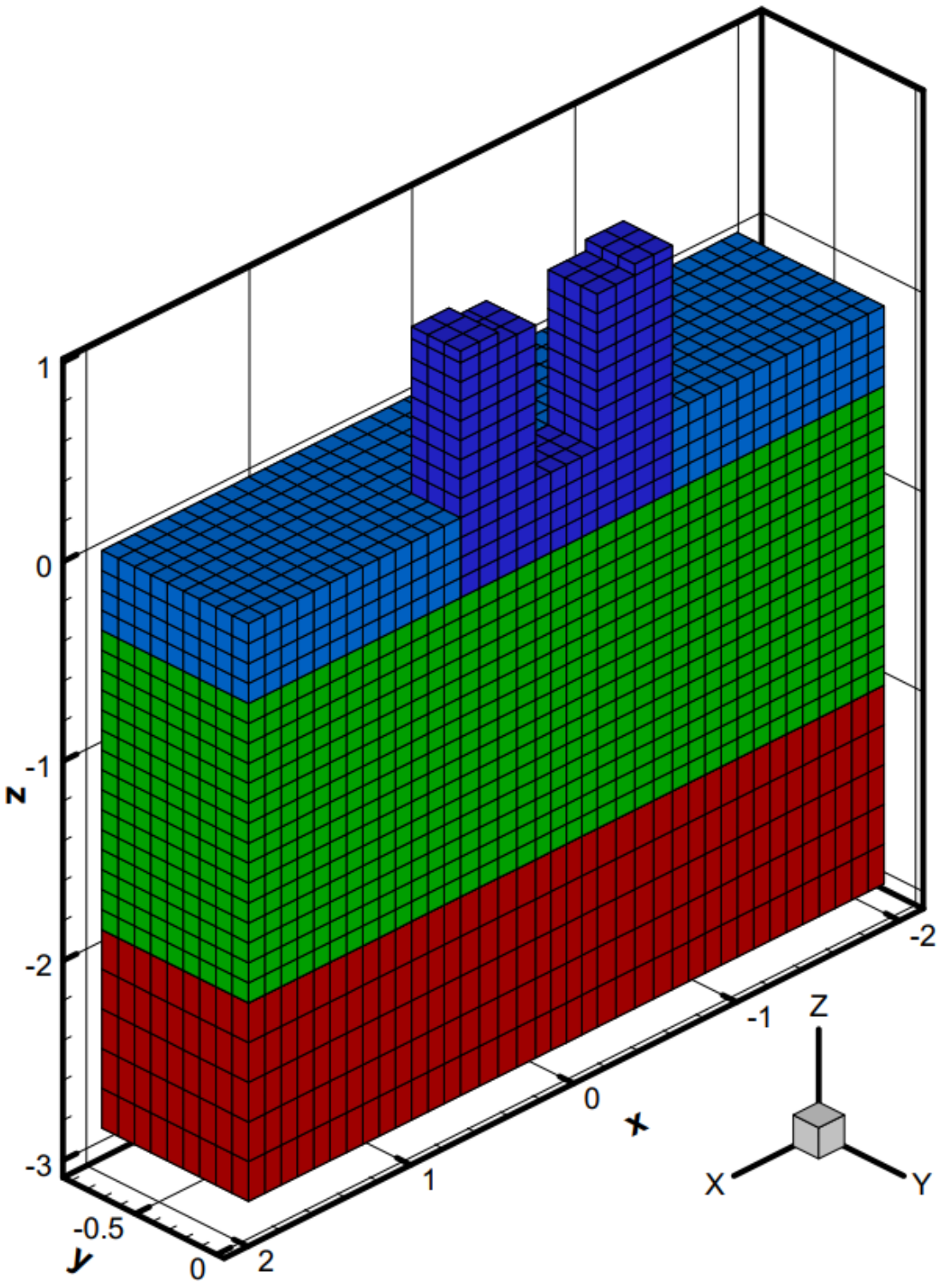

(a)

Figure 6.24. Polymer-sand composite configurations (a) baseline model, (b) piles underneath foundation, (c) grout curtain, and (d) load supporting grout curtain

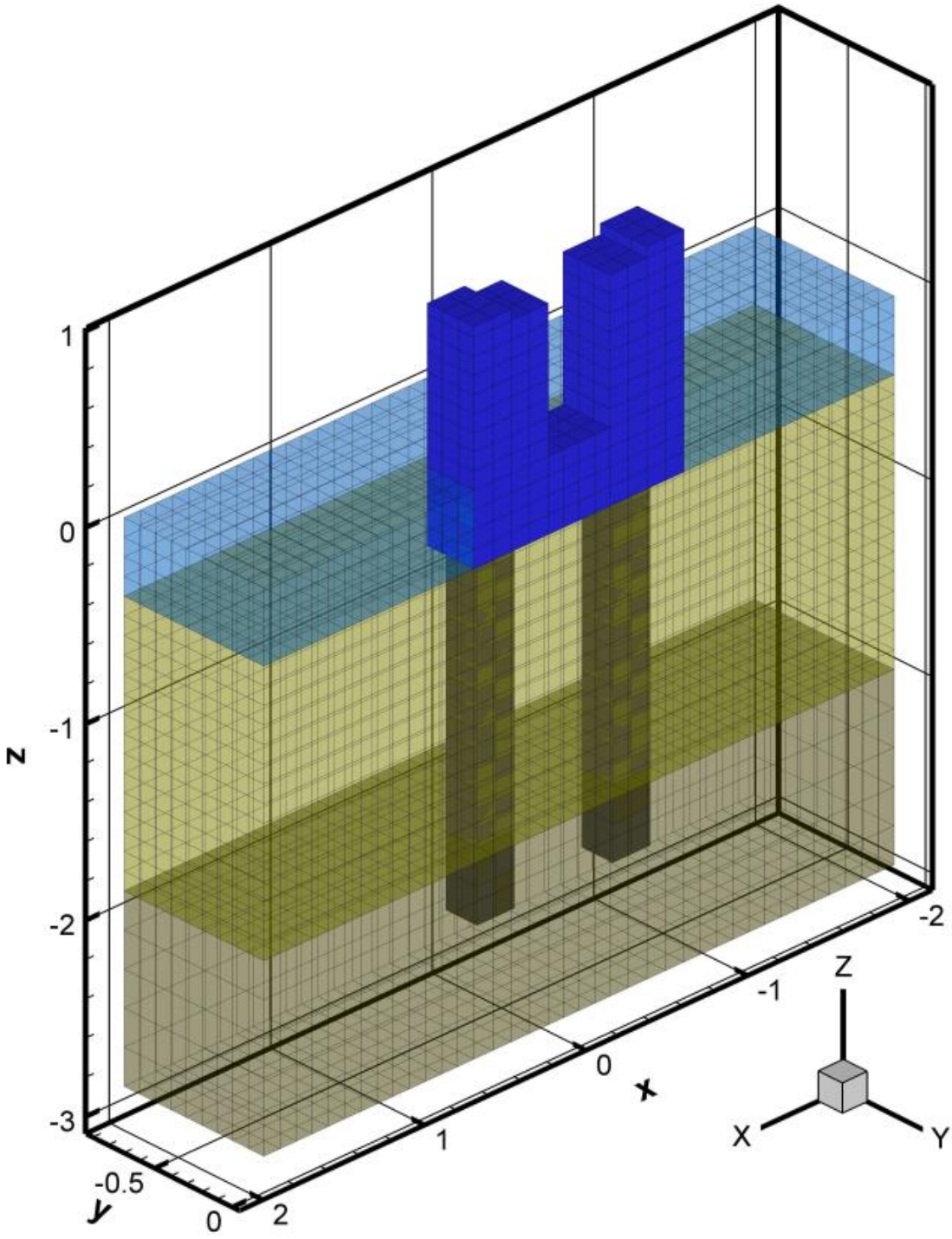

(b)

Figure 6.24 (continued). Polymer-sand composite configurations (a) baseline model, (b) piles underneath foundation, (c) grout curtain, and (d) load supporting grout curtain

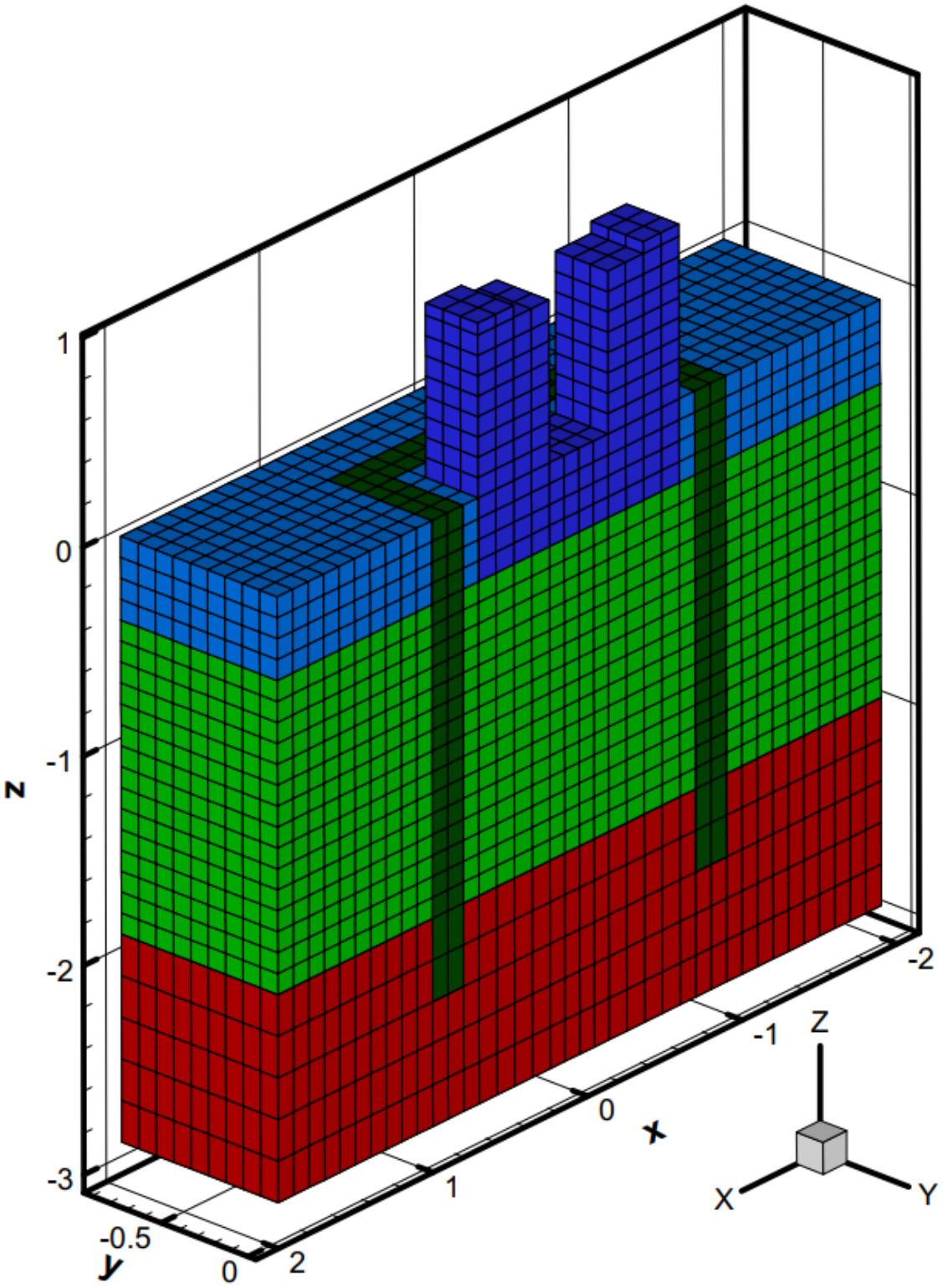

(c)

Figure 6.24 (continued). Polymer-sand composite configurations (a) baseline model, (b) piles underneath foundation, (c) grout curtain, and (d) load supporting grout curtain

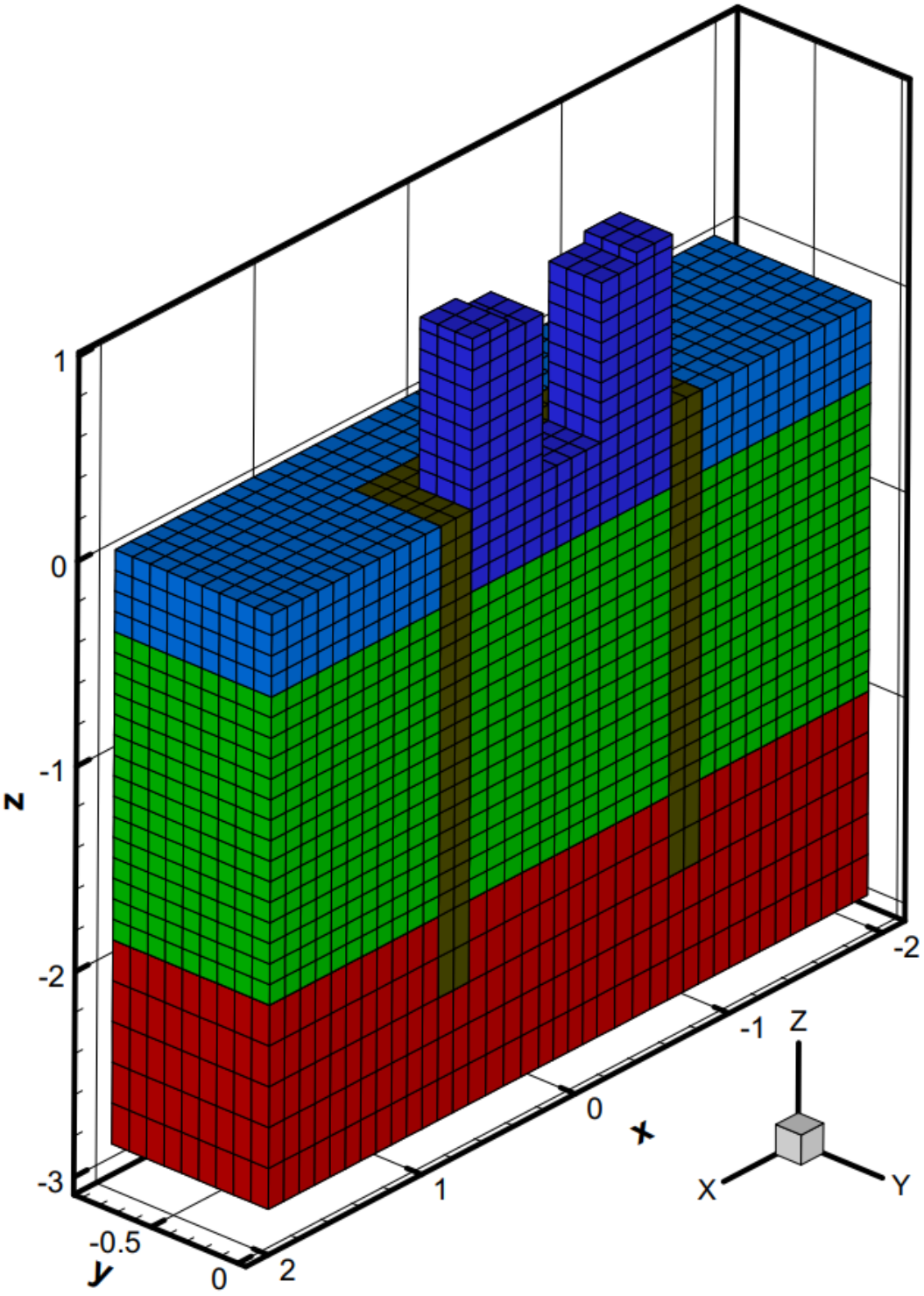

(d)

Figure 6.24 (continued). Polymer-sand composite configurations (a) baseline model, (b) piles underneath foundation, (c) grout curtain, and (d) load supporting grout curtain

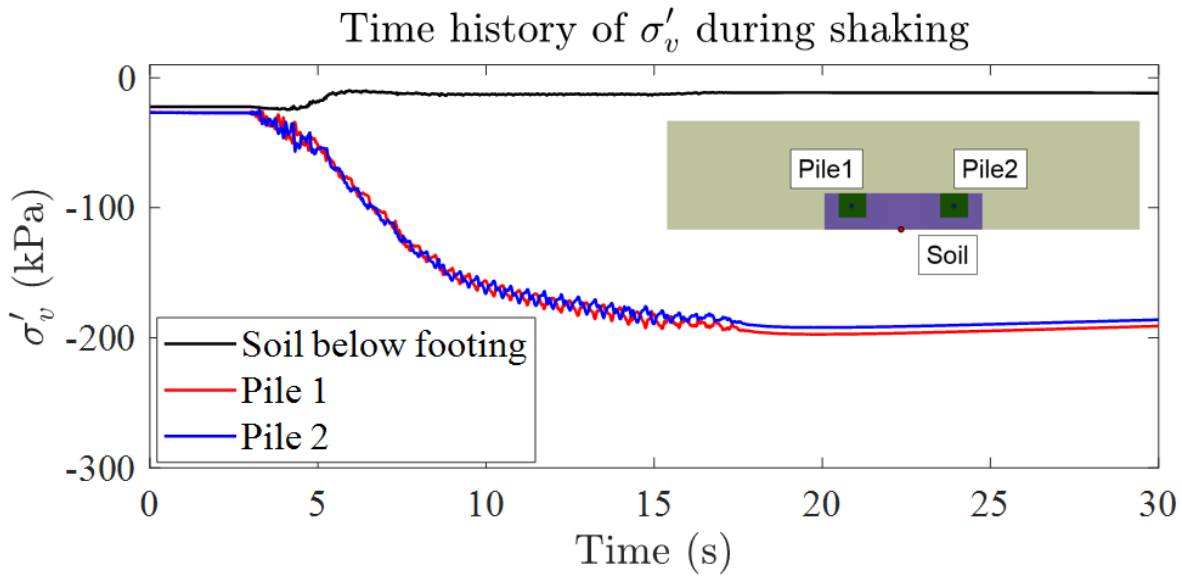

Figure 6.25. Load bearing response of the polymer-sand composite pile during soil liquefaction

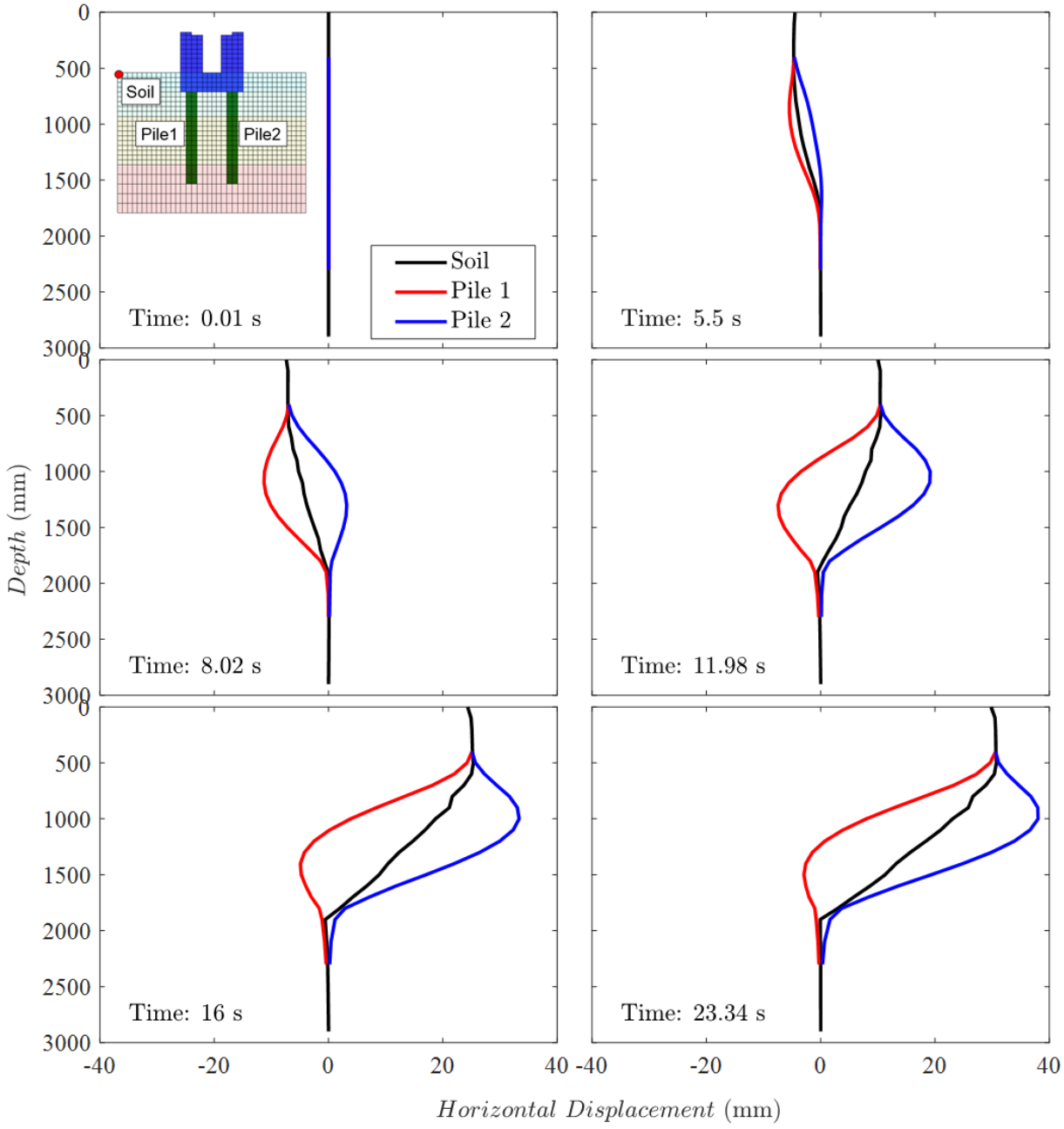

Figure 6.26. Load bearing response of the polymer-sand composite pile during soil liquefaction

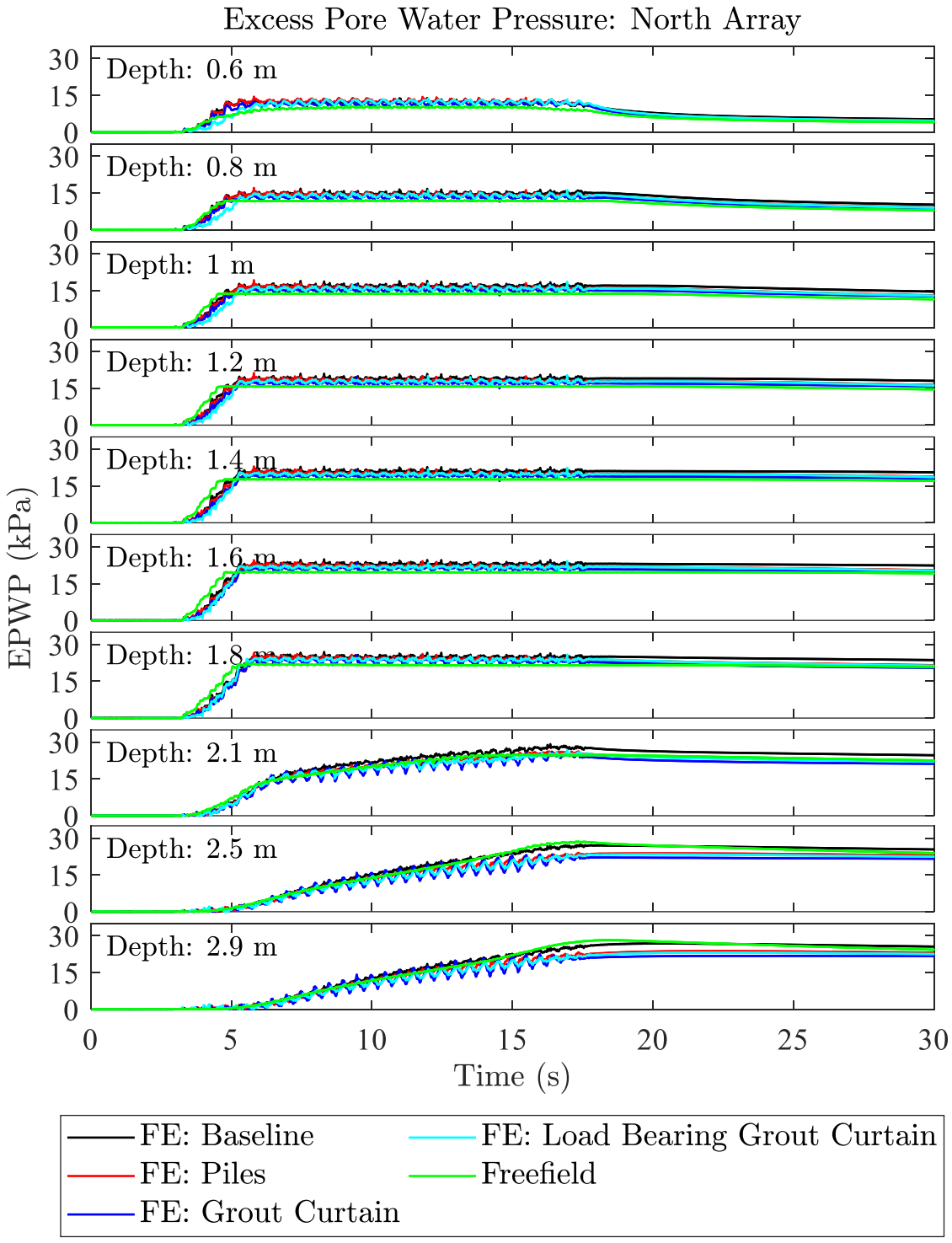

(a)

Figure 6.27. Developed excess pore pressure response in the (a) Middle array, and (b) North array in the employed configurations

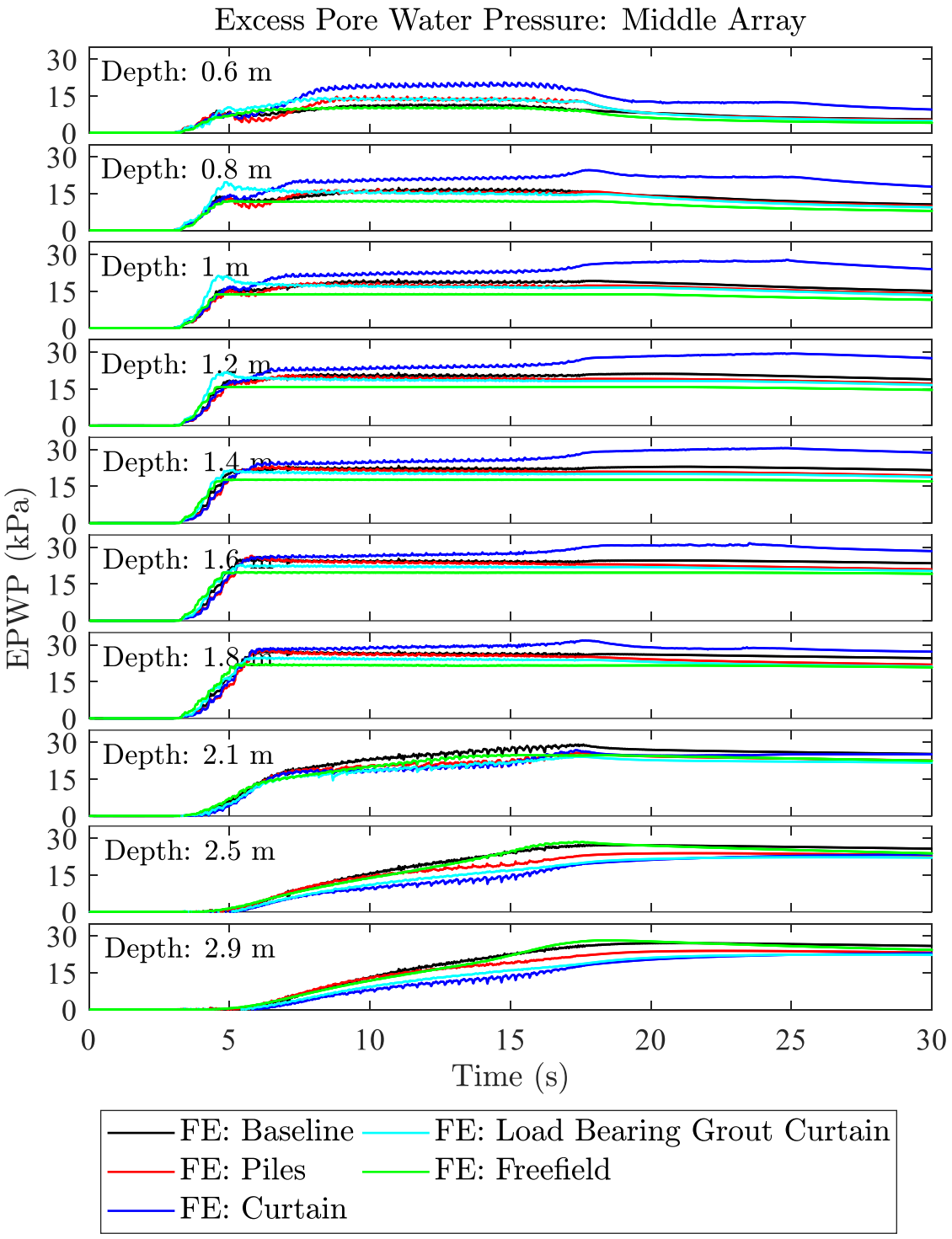

(b)

Figure 6.27 (continued). Developed excess pore pressure response in the (a) Middle array, and (b) North array in the employed configurations

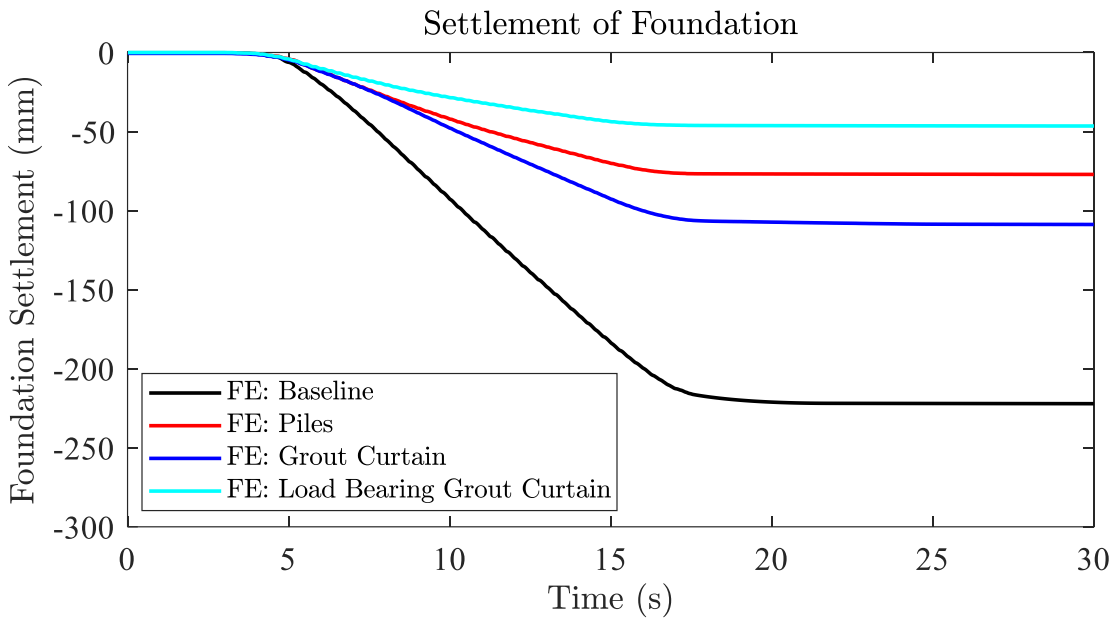

Figure 6.28. Foundations settlement in the varied configurations

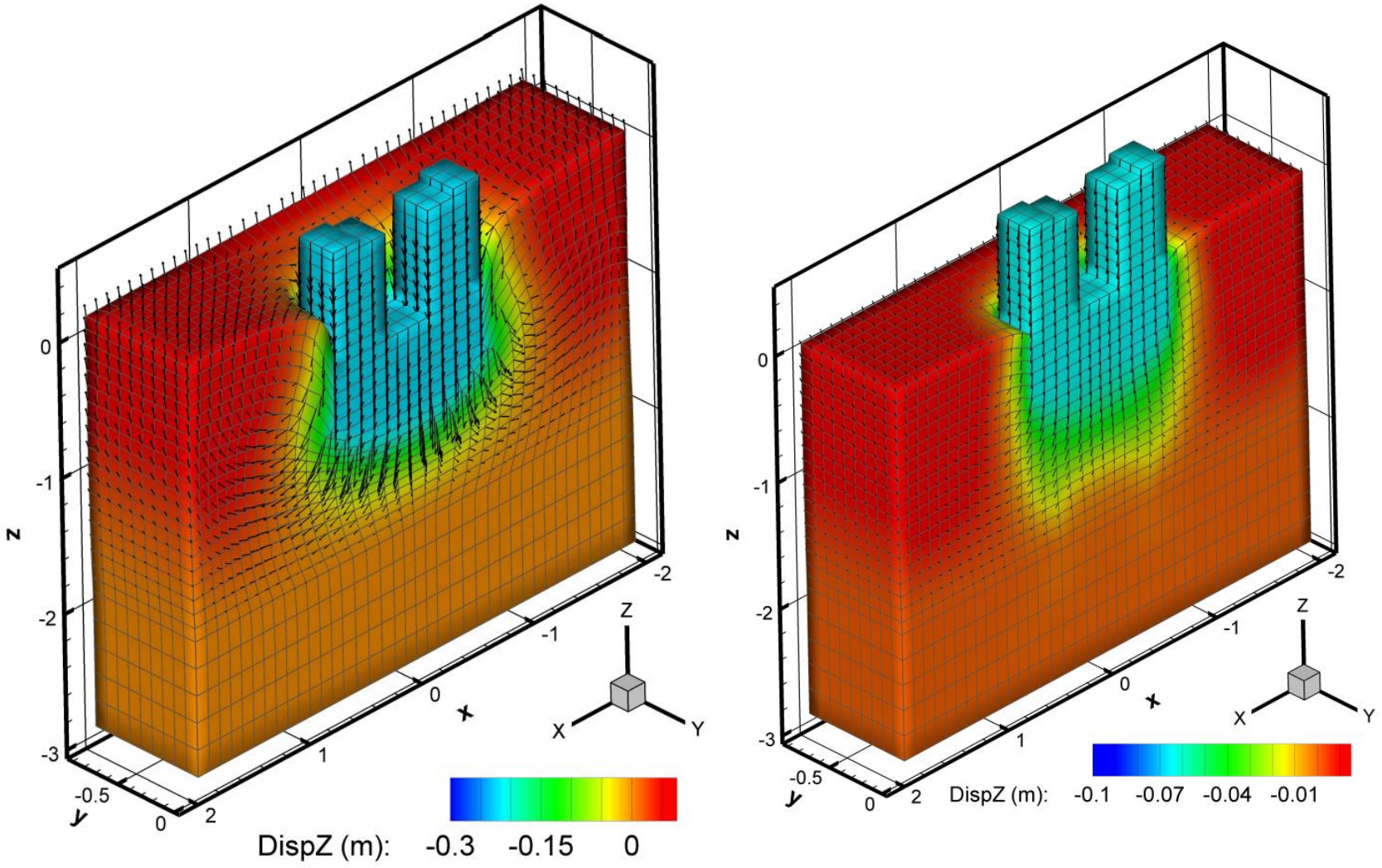

(a) Baseline

(b) Piles

Figure 6.29. Foundations settlement in the varied configurations (deformations exaggerated by 2): (a) Baseline, (b) Piles, (c) Grout Curtain, (d) Load Bearing Grout Curtain

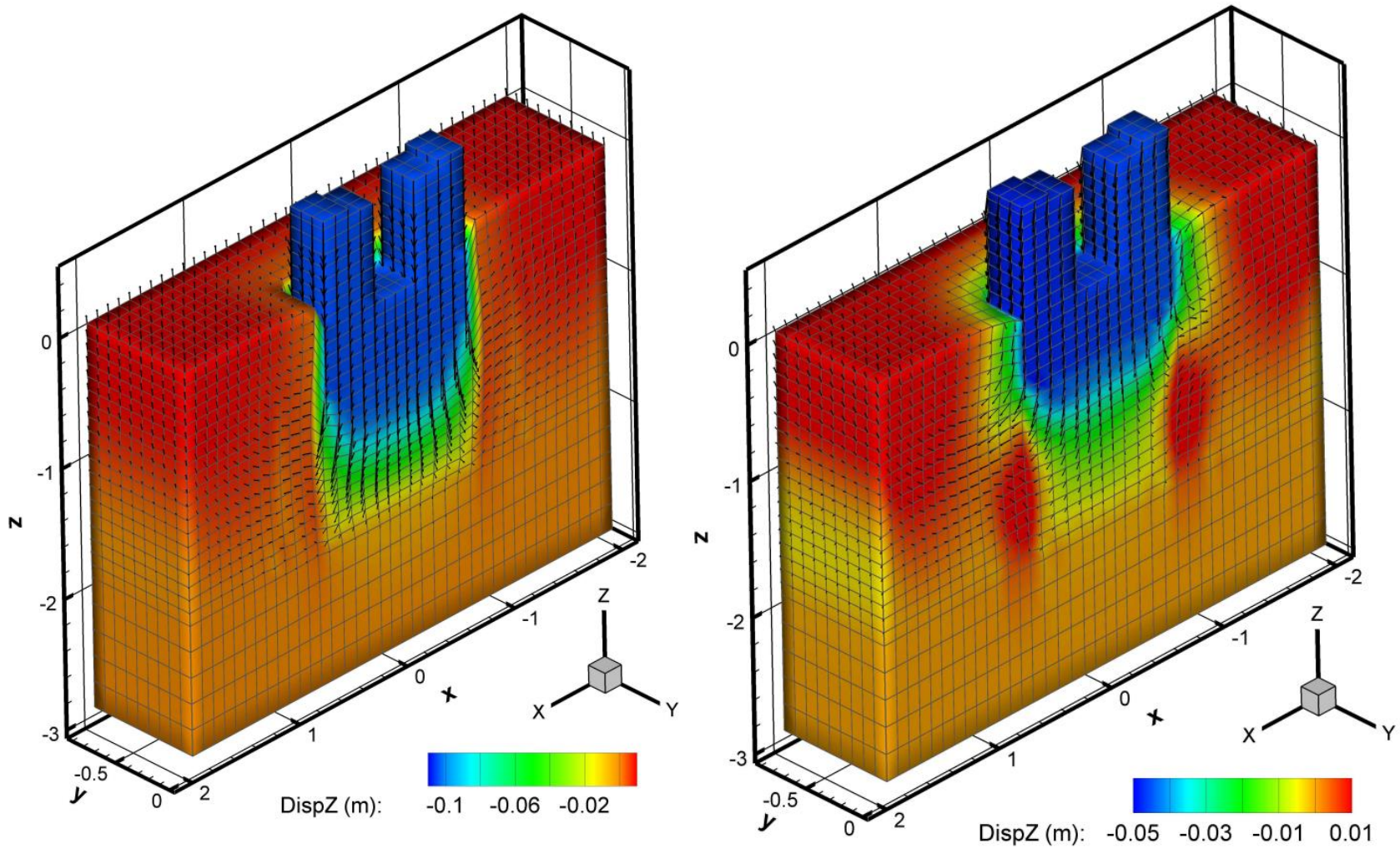

(b) Grout Curtain

(d) Load Bearing Grout Curtain

Figure 6.29 (continued). Foundations settlement in the varied configurations (deformations exaggerated by 2): (a) Baseline, (b) Piles, (c) Grout Curtain, (d) Load bearing grout curtain

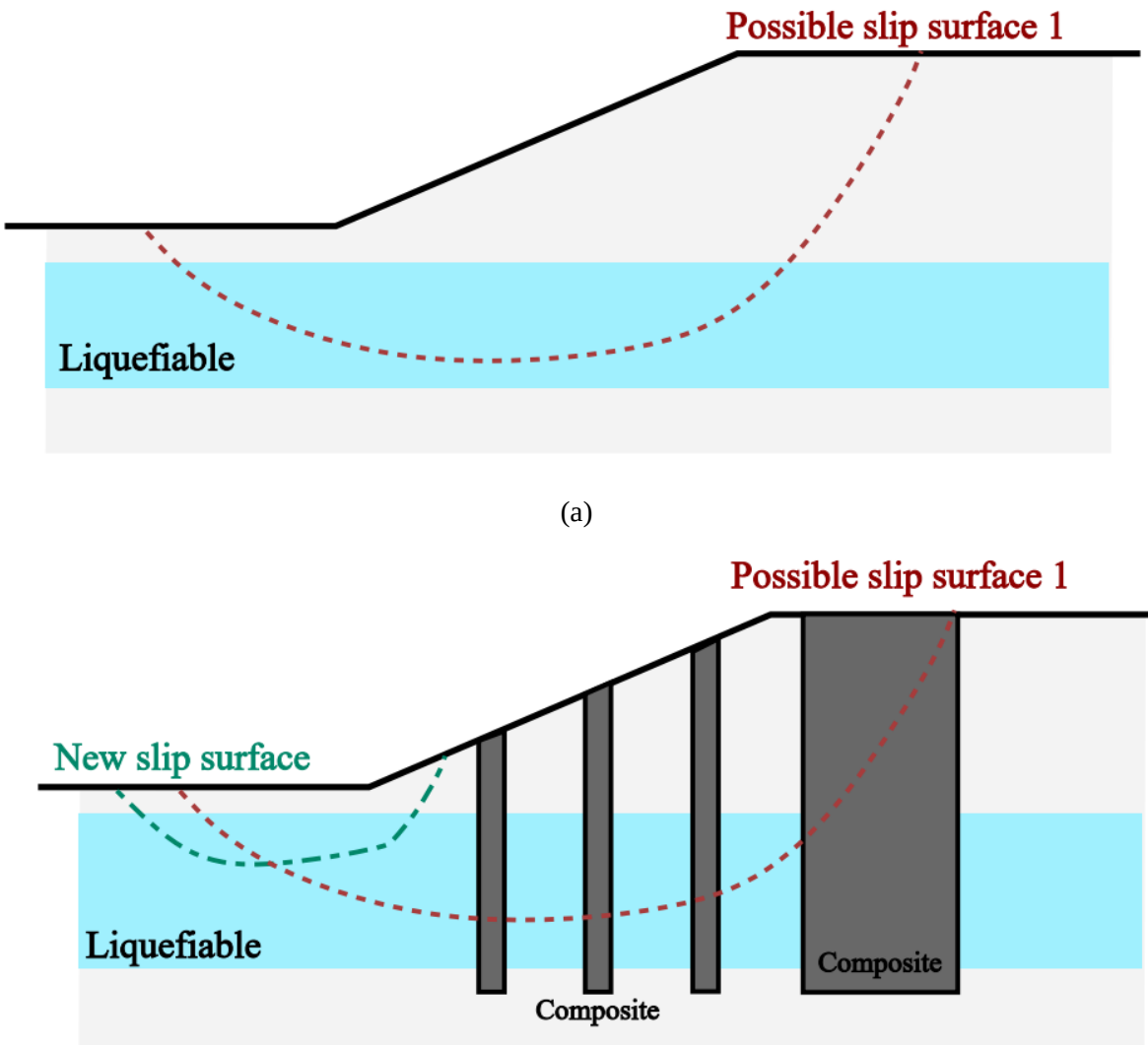

Figure 6.30. Remediation of lateral soil deformations post liquefaction using polymer injection: (a) Illustrative slope, and (b) remediation strategy

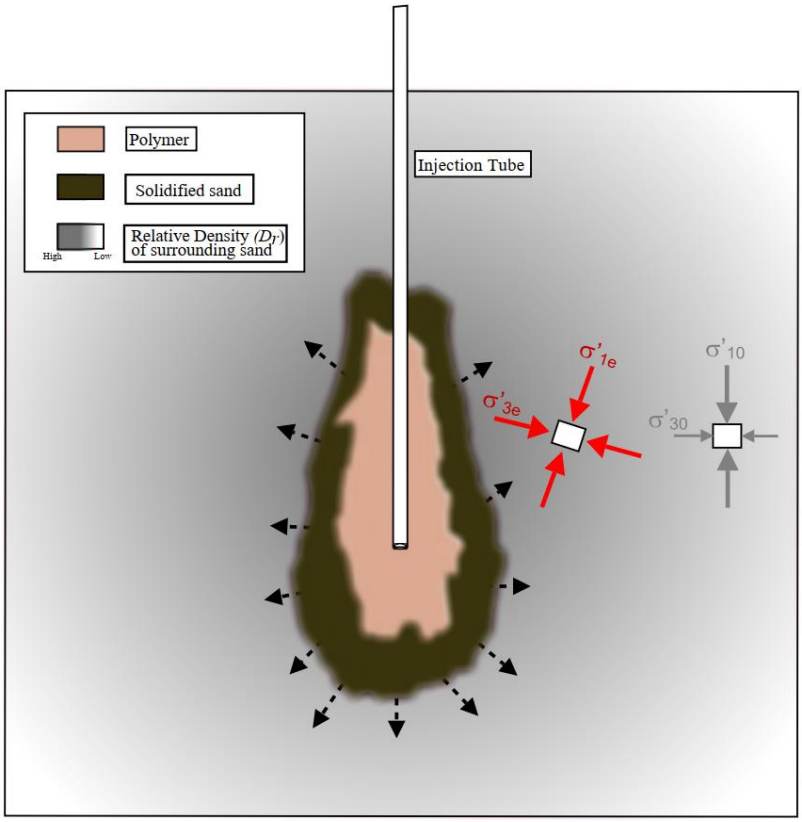

(a)

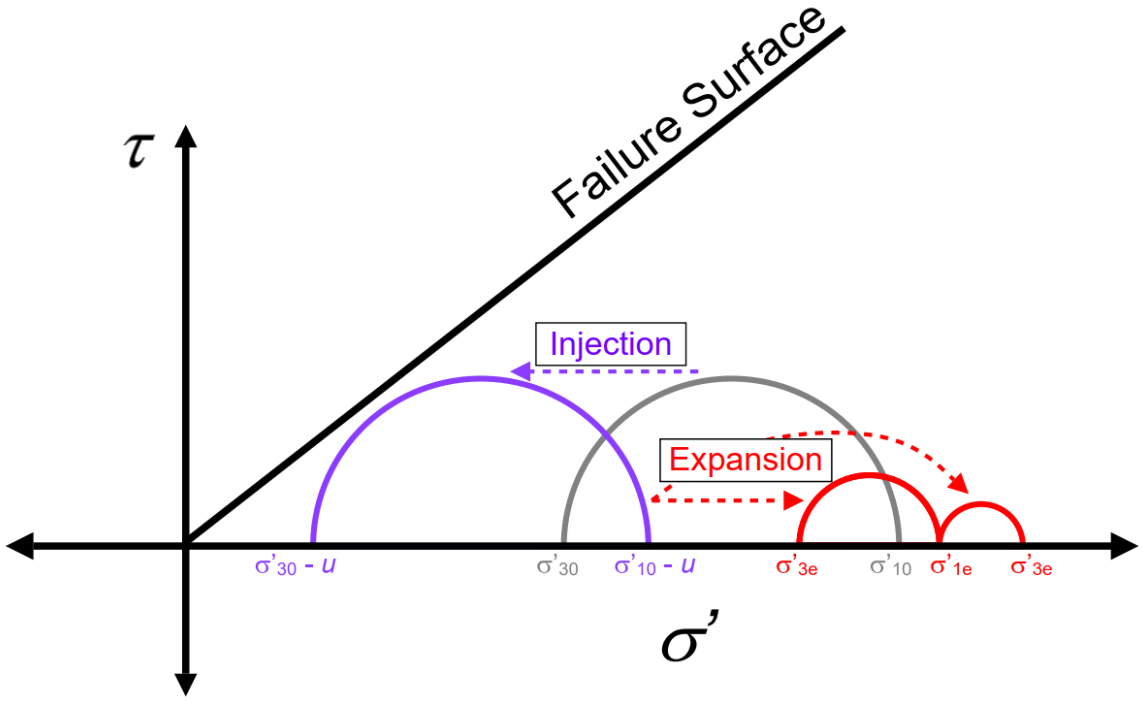

(b)

Figure 6.31. (a) Schematic of polymer expansion post injection and (b) stress state in the soil around the polymer-sand composite during and post injection

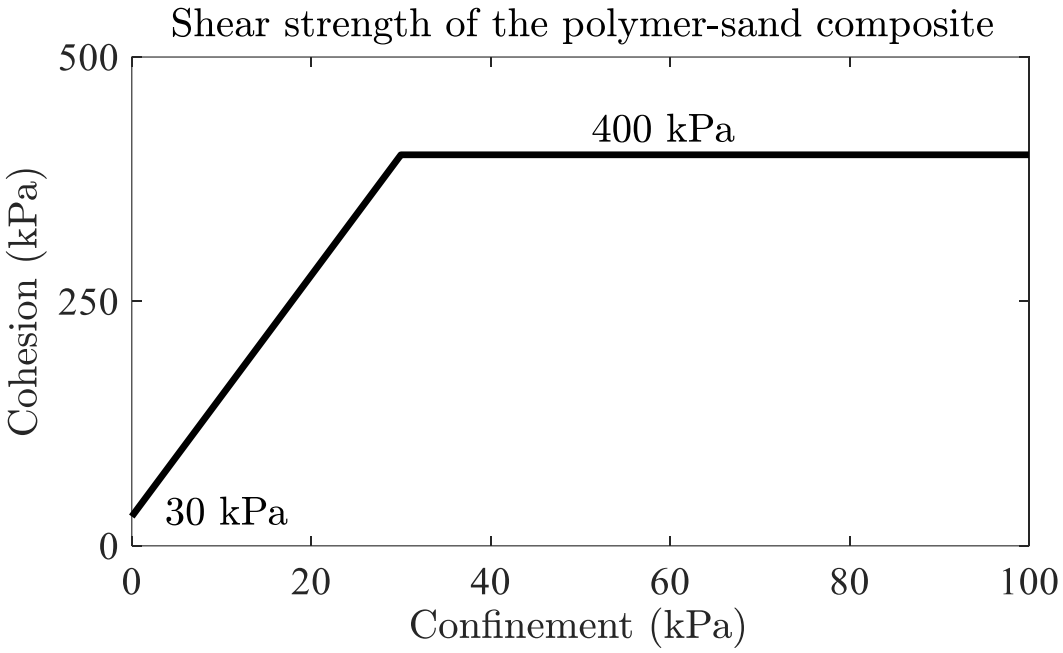

(a)

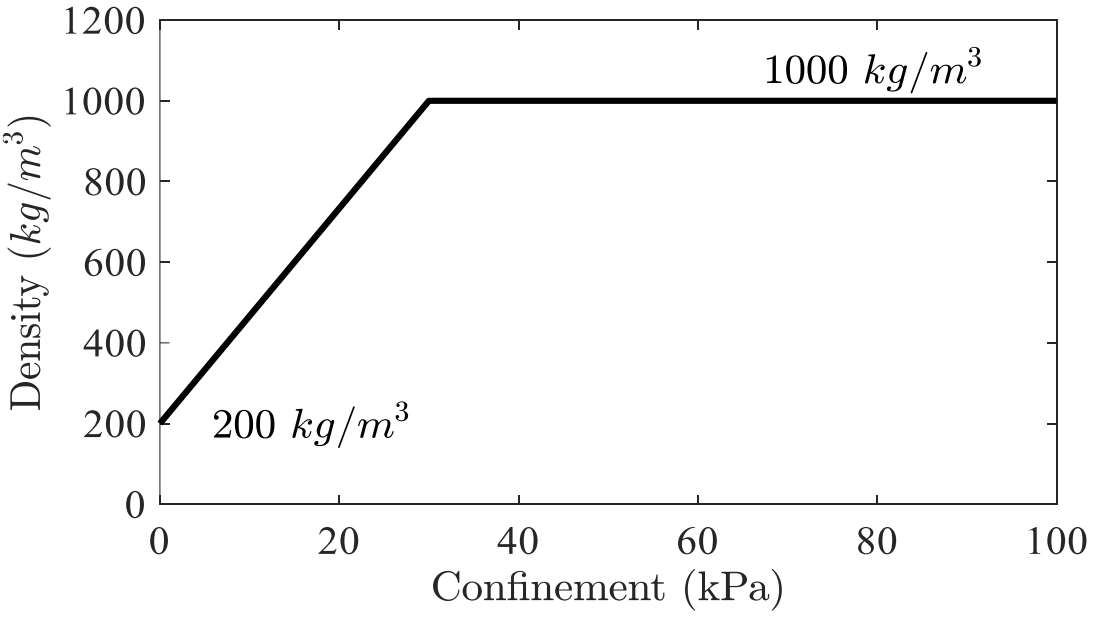

(b)

Figure 6.32. Variation of (a) cohesion and (b) mass density of the polymer-sand composite with confinement

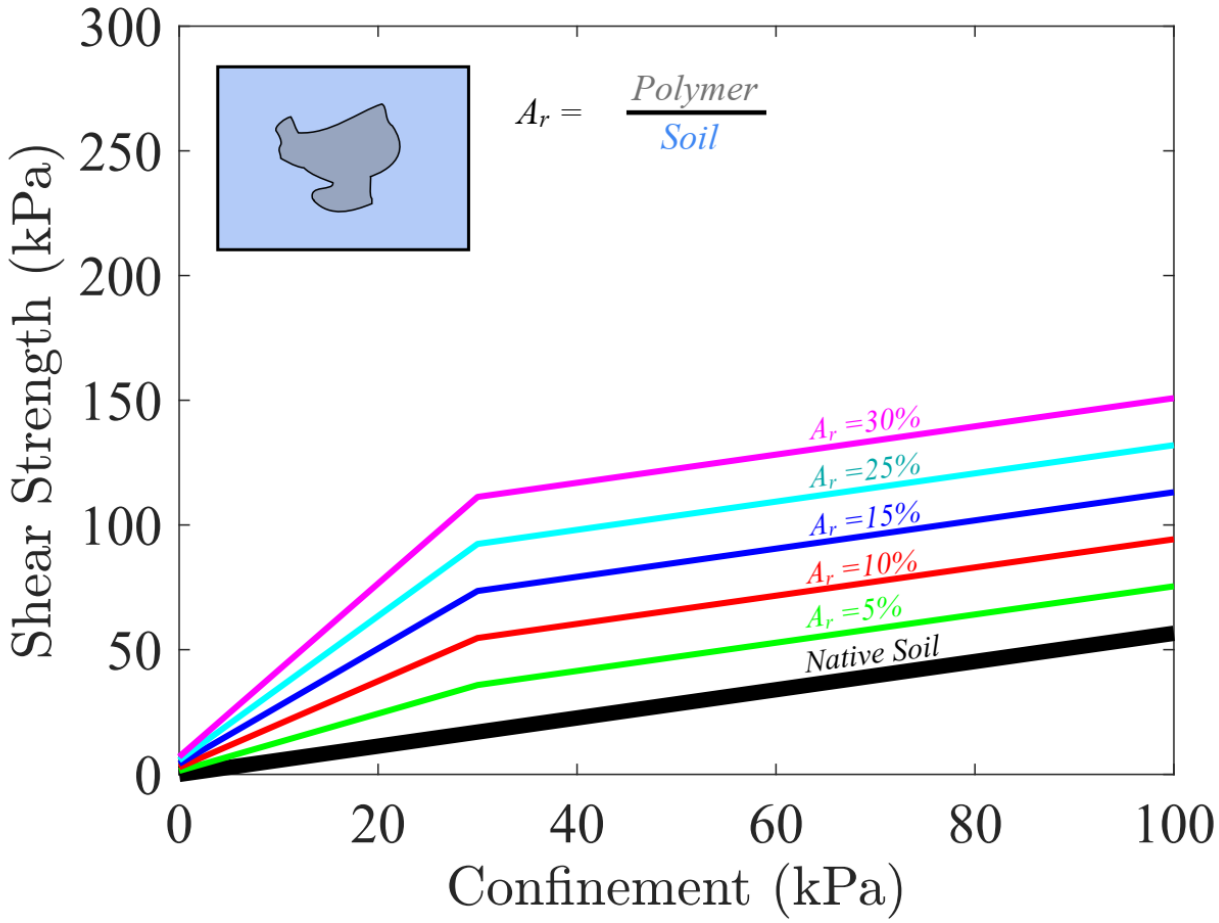

Figure 6.33. Smeared shear strength envelope of treated ground when a permeable polymer is deployed

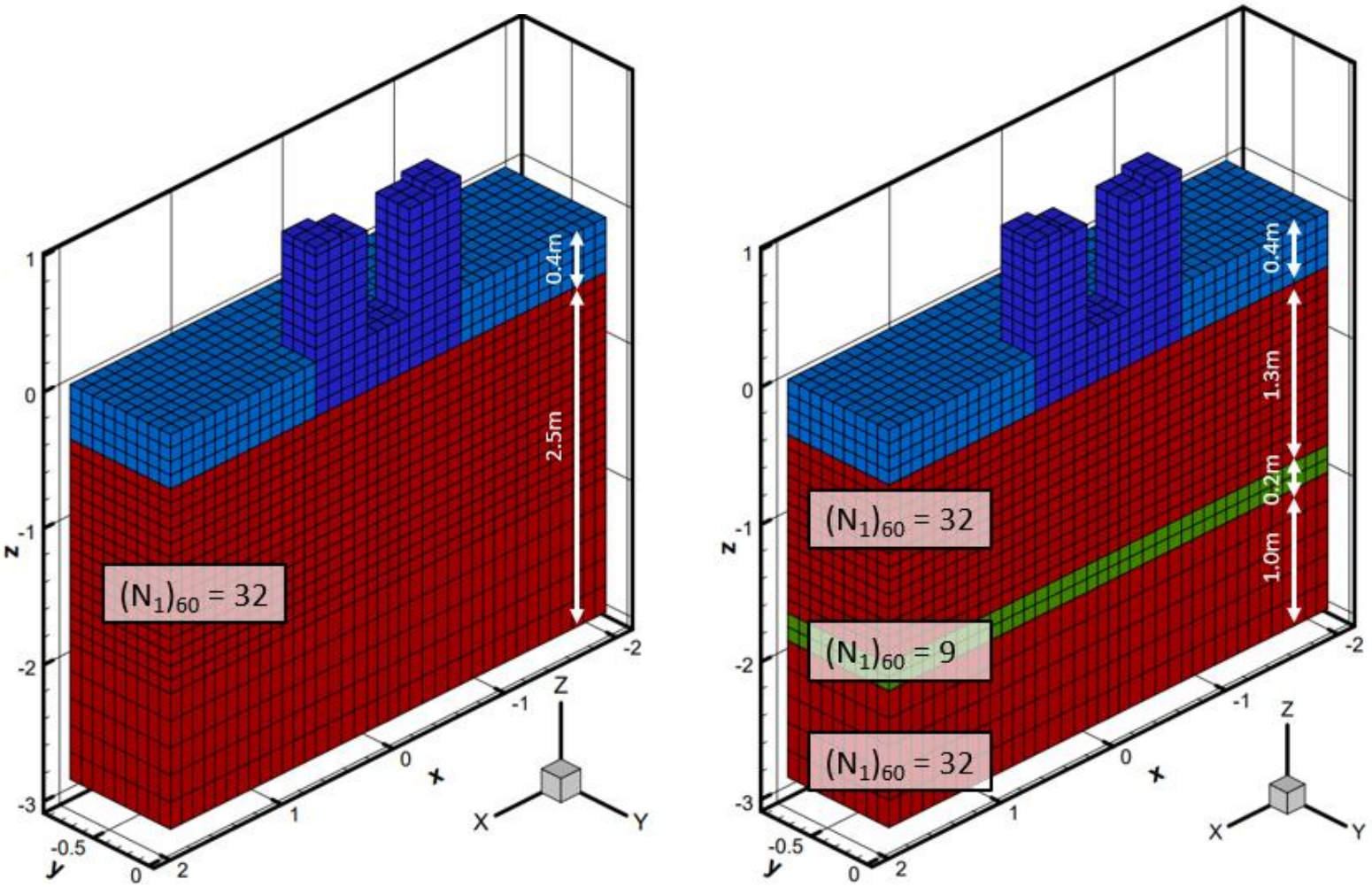

(a) Remediation along entire liquefiable layer (FE run is termed Dense)

(b) Remediation, leaving a portion of the liquefiable layer intact (FE run is termed weak layer)

Figure 6.34. Illustration of geotechnical base isolation using polymer injection: (a) Remediation is performed along entire deposit (FE run is termed Dense), and (b) remediation is performed along a portion of the deposit (leaving 0.2 m of liquefiable soil)

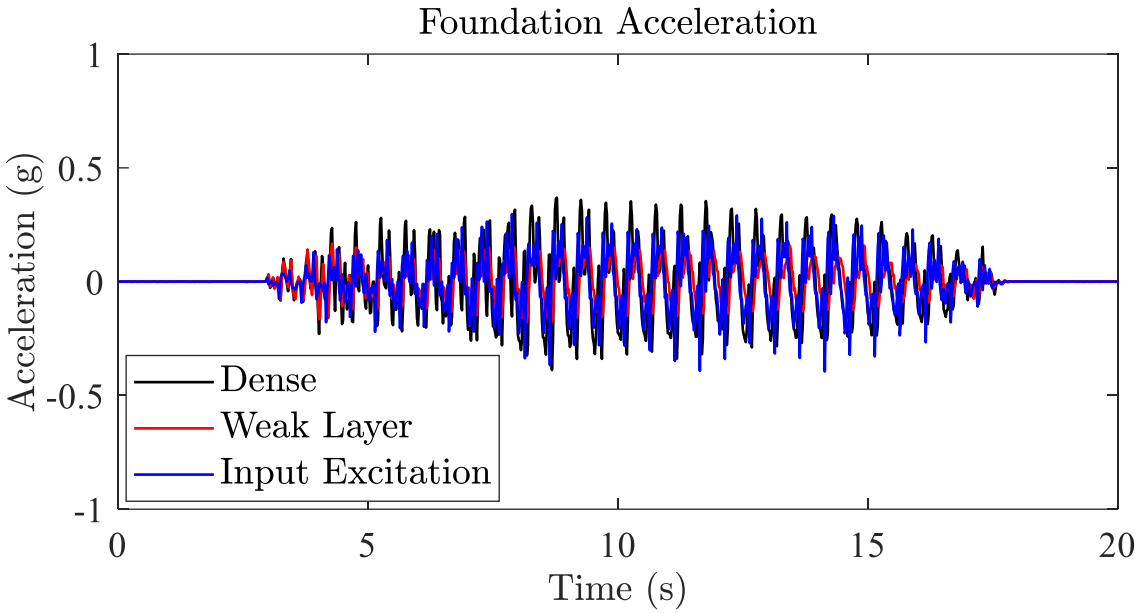

(a)

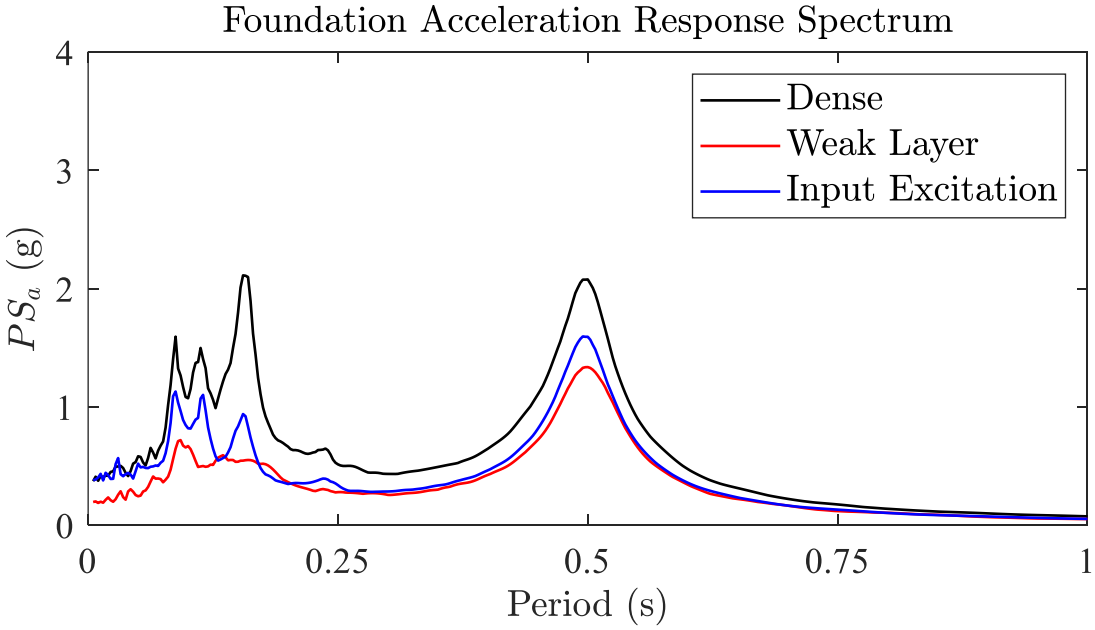

(b)

Figure 6.35. Foundation acceleration and 5% damped acceleration response spectra

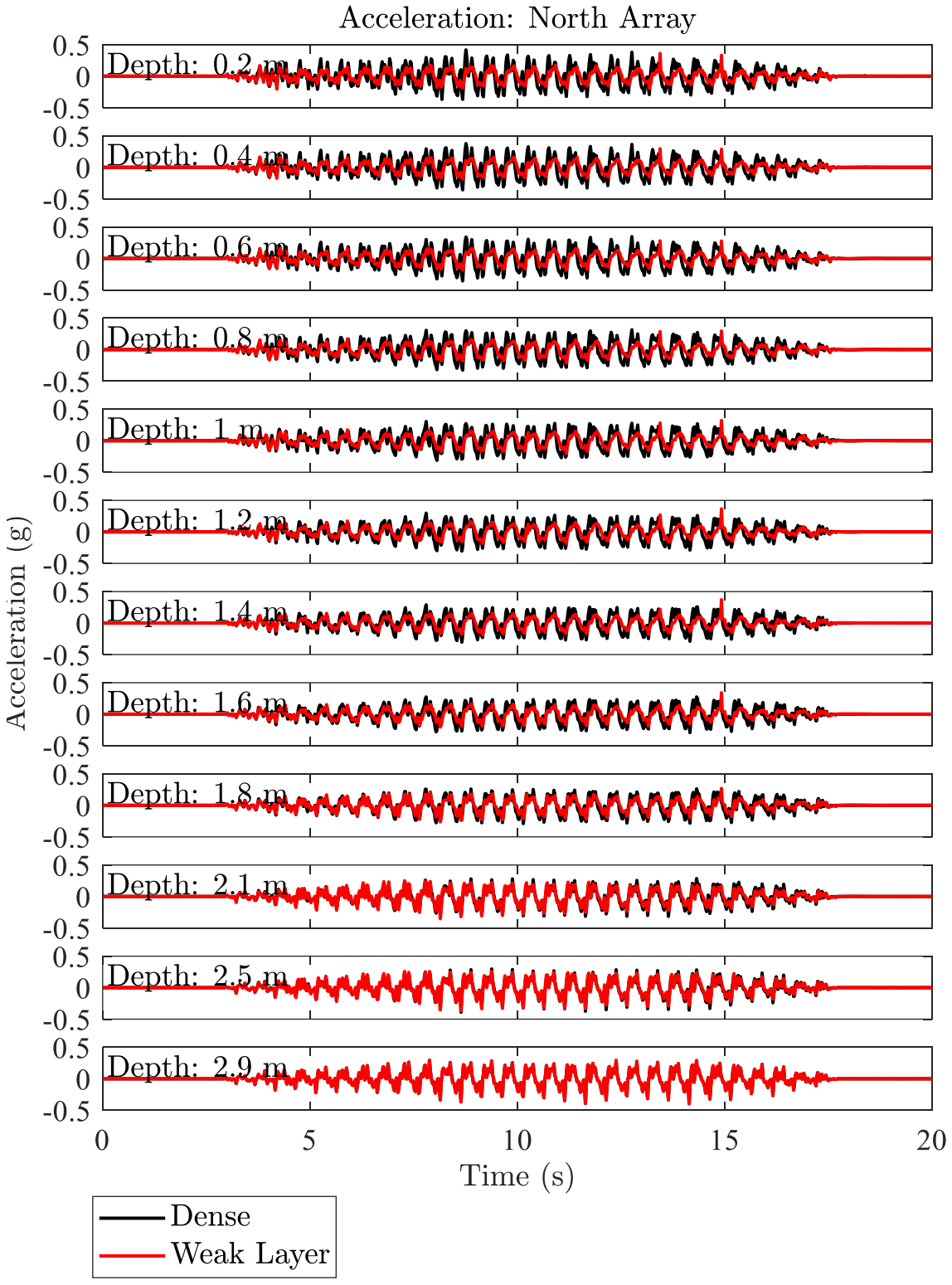

Figure 6.36. Soil acceleration response in the North array along the height of the deposit

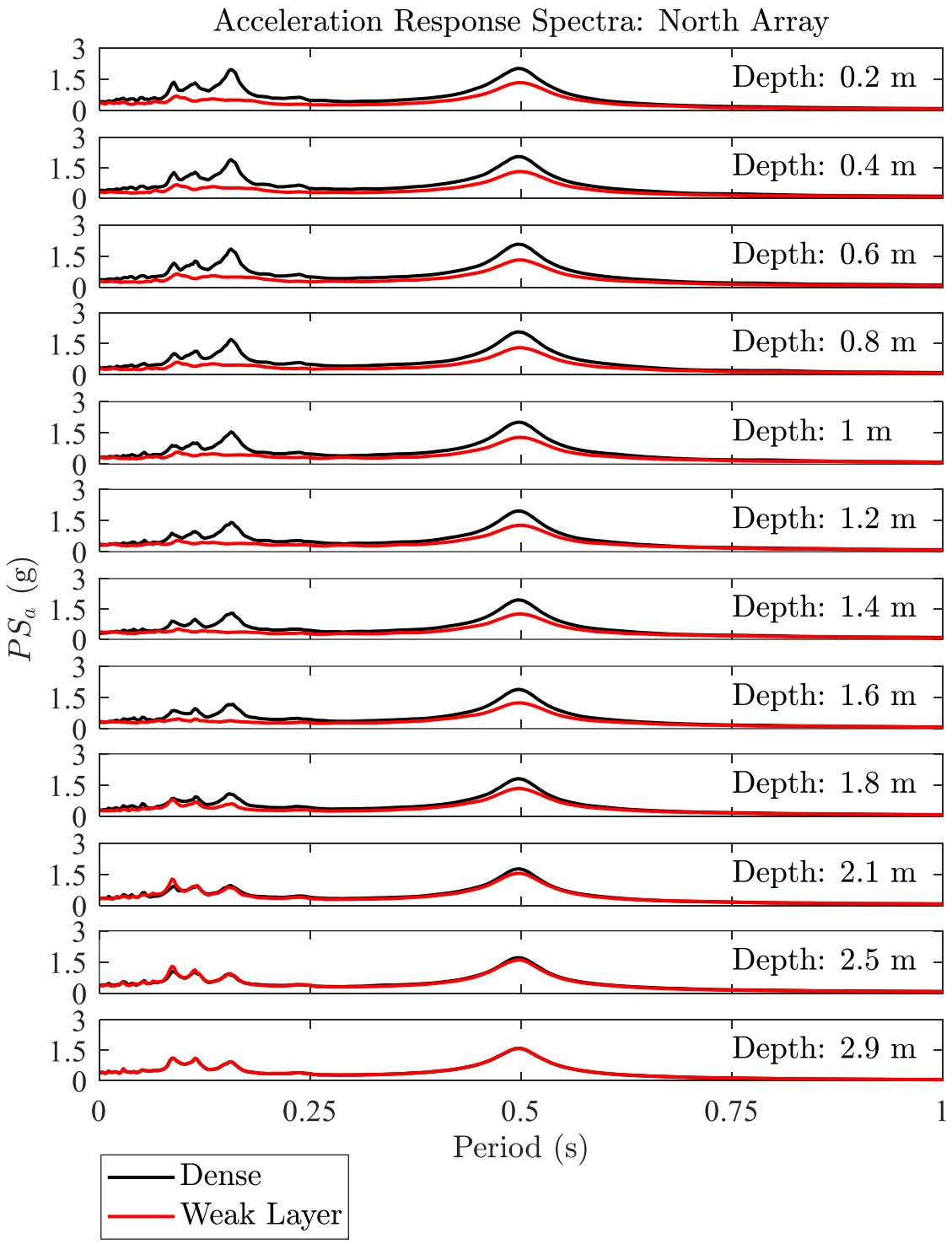

Figure 6.37. Soil acceleration response spectra in the North array along the height of the deposit

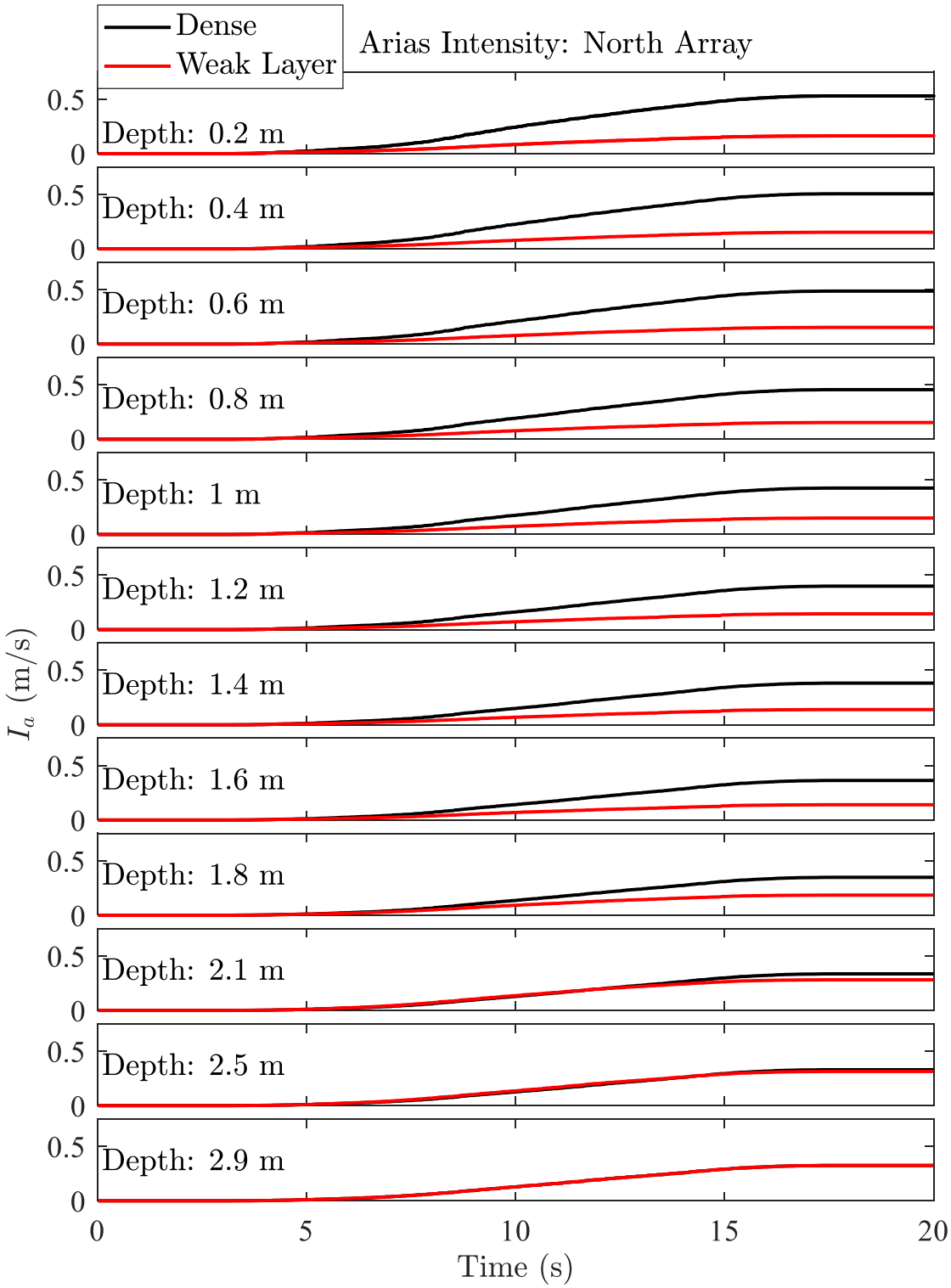

Figure 6.38. Arias Intensity in the North array along the deposit

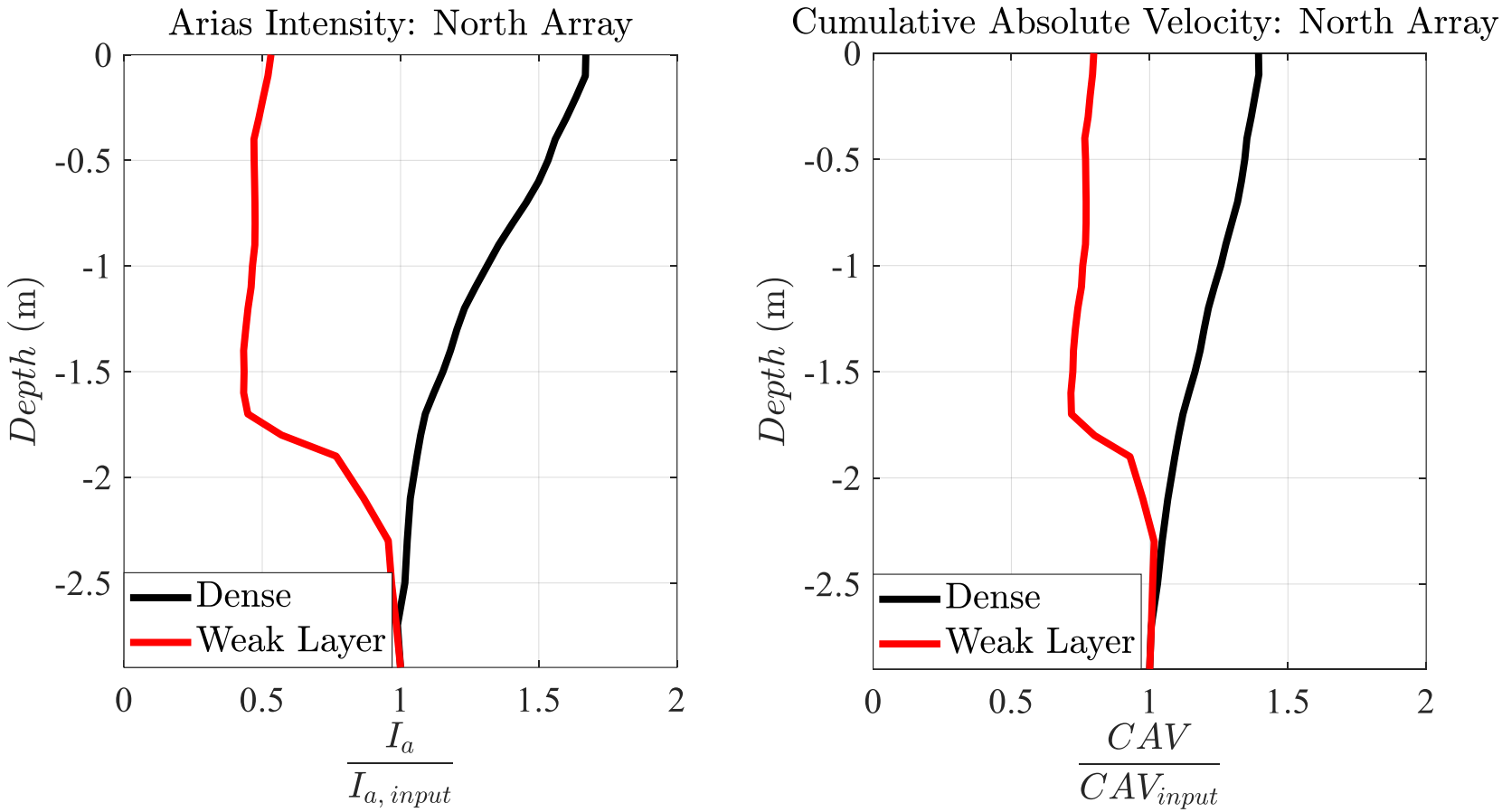

Figure 6.39. Variation of (a) Arias Intensity (Ia) and (b) Cumulative Average Velocity (*CAV*) along deposit ($I_{a,\,input}$ and CAV_{input} refers to Arias intensity and Cumulative Absolute Velocity of the input motion)

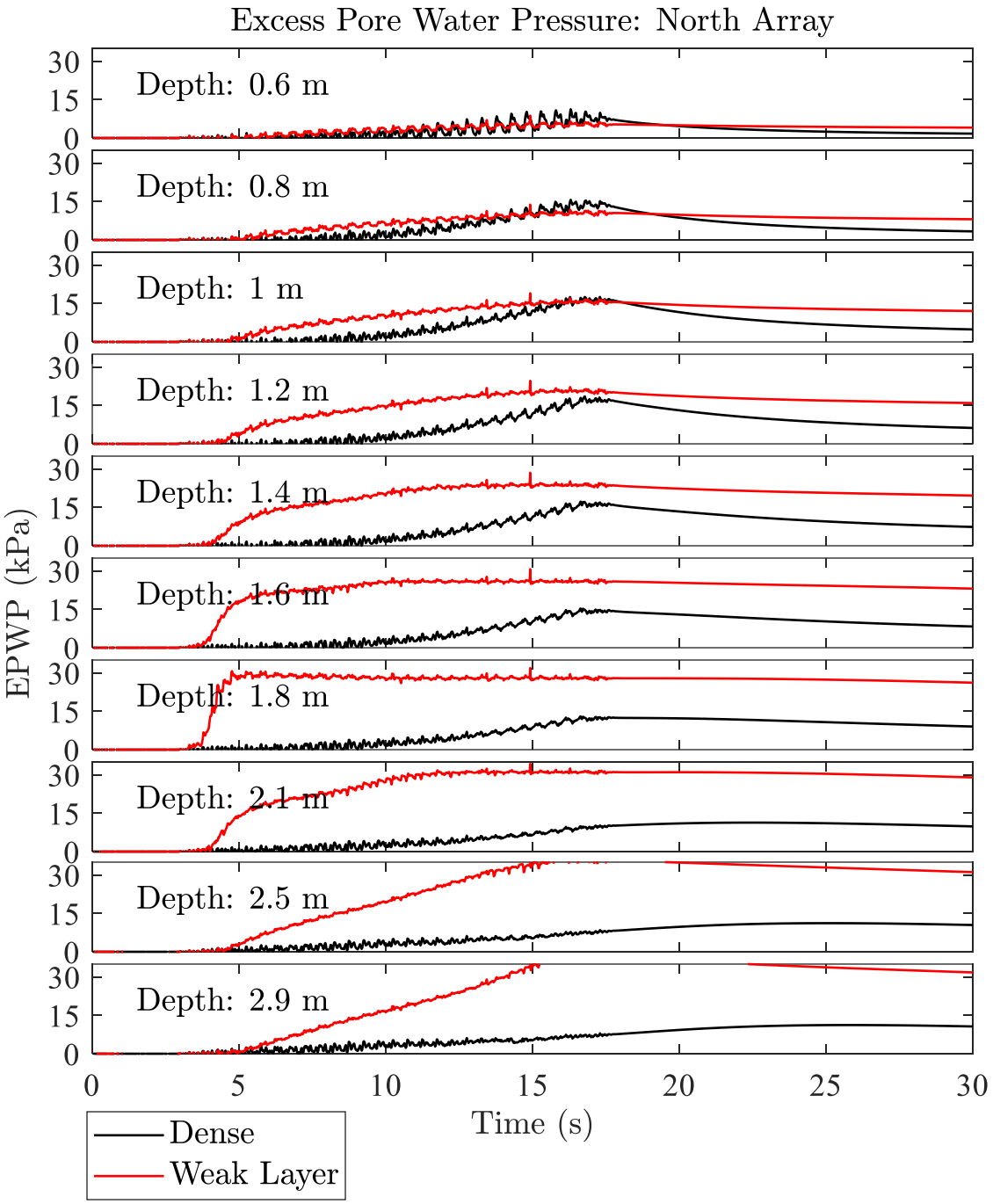

Figure 6.40. Excess pore pressure response in the North array along the height of the deposit

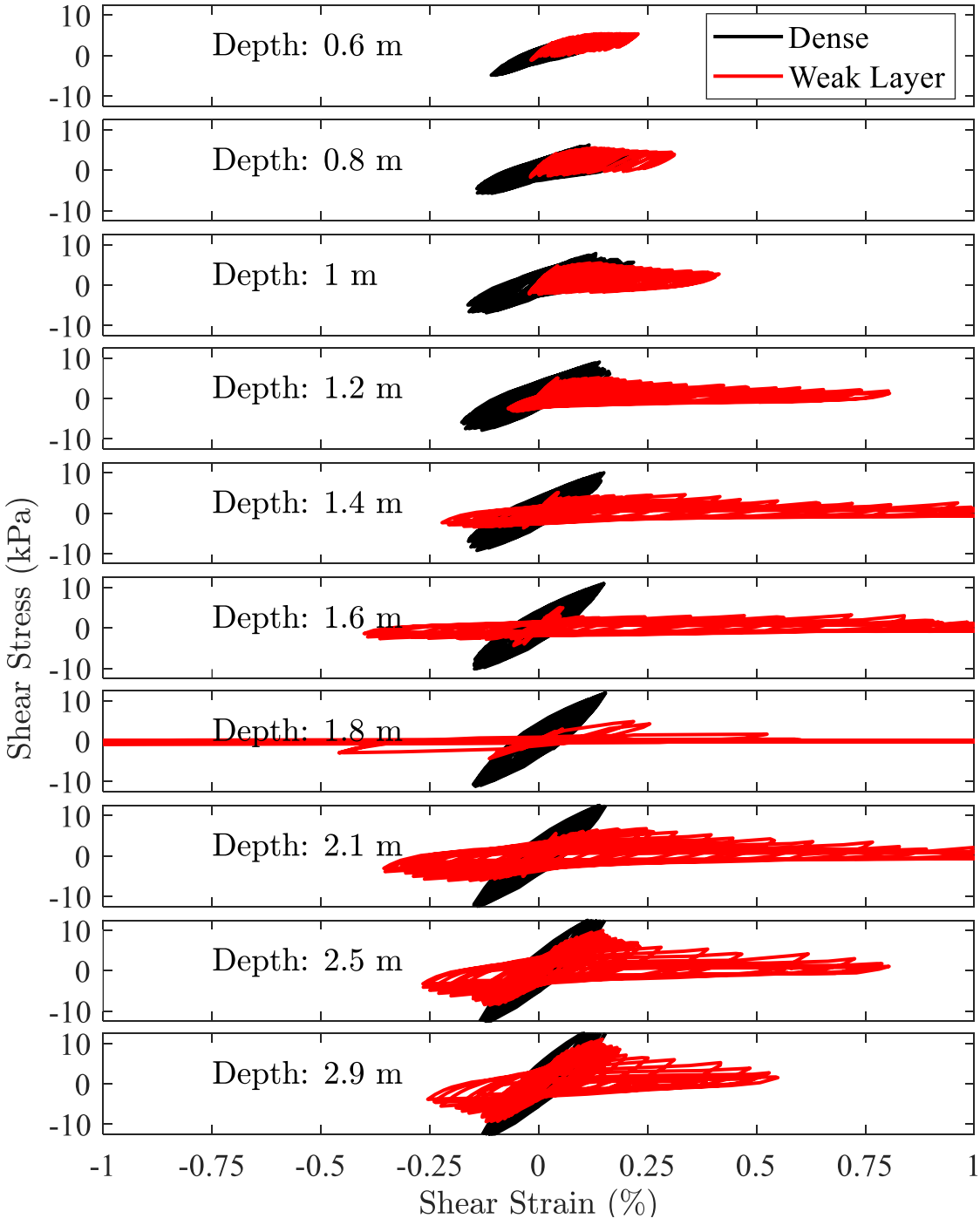

Figure 6.41. Shear stress-strain response in the North array along the height of the deposit

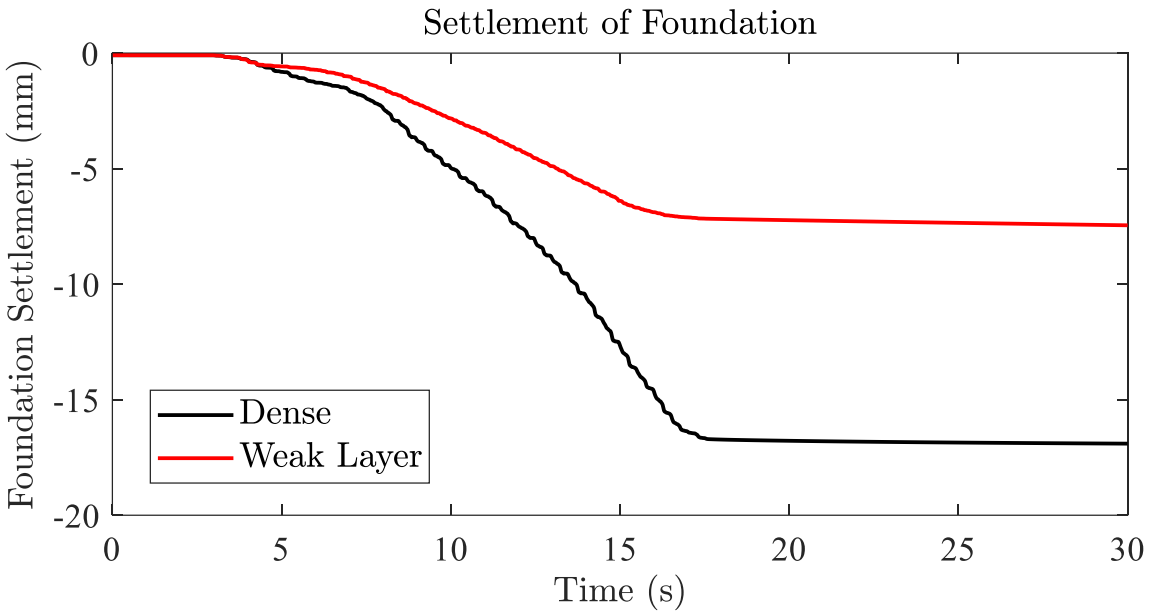

(a)

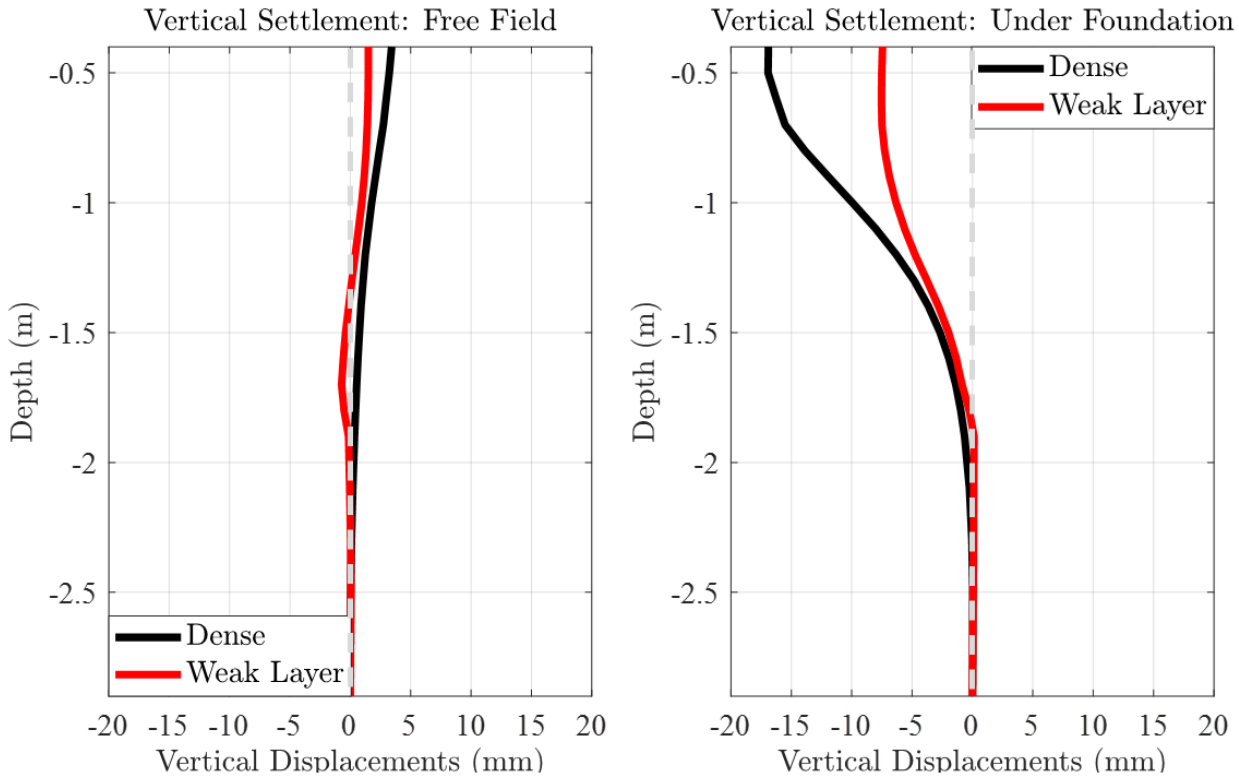

(b)

Figure 6.42. (a) Foundation settlement, (b) Vertical soil displacement at free field and under foundation

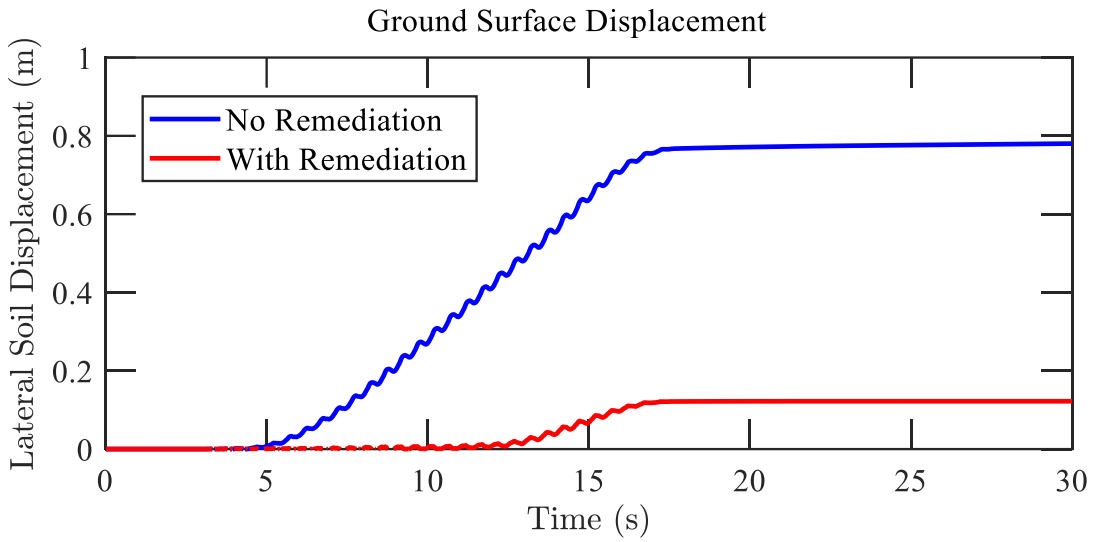

Figure 6.43. Lateral soil displacement of the ground surface during liquefaction induced lateral spreading with and without remediation

(a)

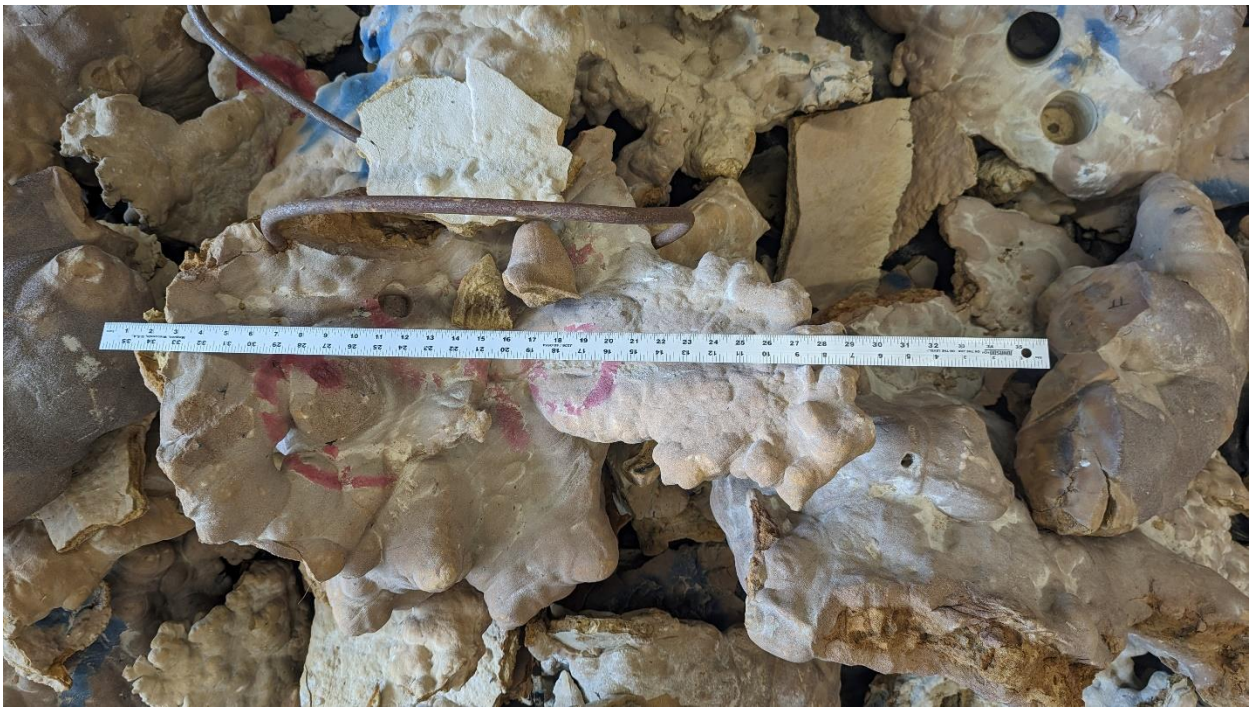

(b)

Figure 6.44. Extracted specimens of the polymer-sand composite (a-g)

(c)

Figure 6.44 (continued). Extracted specimens of the polymer-sand composite (a-g)

(d)

(e)

Figure 6.44 (continued). Extracted specimens of the polymer-sand composite (a-g)

(f)

Figure 6.44 (continued). Extracted specimens of the polymer-sand composite (a-g)

(g)

Figure 6.44 (continued). Extracted specimens of the polymer-sand composite (a-g)

(a)

(b)

Figure 6.45. Extracted polymer-sand composite specimens (a-l)

(c)

(d)

Figure 6.45 (continued). Extracted polymer-sand composite specimens (a-l)

(e)

(f)

Figure 6.45 (continued). Extracted polymer-sand composite specimens (a-l)

(g)

(h)

Figure 6.45 (continued). Extracted polymer-sand composite specimens (a-l)

(i)

(j)

Figure 6.45 (continued). Extracted polymer-sand composite specimens (a-l)

(k)

(l)

Figure 6.45 (continued). Extracted polymer-sand composite specimens (a-l)

Chapter 7. Response of the San Felipito bridge-ground system during the 2010 El Mayor-Cucapah Earthquake: Computational Simulation, Insights and Remediation

7.1 Abstract

Liquefaction-induced lateral spreading demands on a pair of adjacent parallel bridges during the 2010 7.2 M_w El Mayor-Cucapah earthquake is explored through detailed finite element (FE) analyses. During this earthquake, liquefaction and consequent loss of soil strength resulted in large accumulated downslope ground displacements of as much as 5 m in the free field. As such, a railroad bridge (RRB), built in 1962, experienced severe damage with unseating of one of its spans, while the adjacent highway bridge (HWB), constructed in 1999, only displayed minor flexural column cracks. Data from reconnaissance surveys and earlier related studies is used to build an idealized model for each bridge, supported on an interbedded multilayered soil profile. Within the scope of available data and information, developed idealized model properties aim to capture the salient deformation/damage features of the actual observed response. With these models, additional studies are undertaken to address shortcomings of the current railroad bridge configuration, in terms of extensions to the seat width, structural retrofit to enhance deck-bent connectivity, and insitu ground modification using polymer injection.

7.2 Introduction

Lateral spreading induced damage to bridge foundations has been observed in many major earthquakes (Youd 1993, Hamada *et al.* 1996, Tokimatsu and Asaka 1998, Berrill *et al.* 2001, Ledezma and Bray 2010, Arduino *et al.* 2010, Wotherspoon *et al.* 2011, Ledezma *et al.* 2012, Verdugo *et al.* 2012, Cubrinovski *et al.* 2011, 2014, and Turner *et al.* 2013, 2016). Reconnaissance

surveys from these events have demonstrated that consideration of the global bridge-ground system as an integral entity highly influenced the observed response. As such, global analysis is paramount in realistically evaluating the performance of bridge-ground systems due to lateral spreading.

On this basis, idealized 3D finite element (FE) models were developed herein, motivated by the performance of two adjacent parallel bridges during the 2010 El Mayor Cucapah earthquake (Turner 2016, Stewart and Brandenberg 2010, EERI 2010). Attention is paid to the consequences of liquefaction-induced ground deformation on the resulting salient deformation/damage characteristics of the bridges and their foundations.

The following sections outline the: 1) seismological aspects of the 2010 El Mayor Cucapah earthquake, 2) specifics and model properties of each bridge-ground system, 3) simplified limit equilibrium-based assessment of the free field soil deformation, 4) finite element model development, 5) conducted computations and salient bridge system response mechanisms, and 6) discussion of computed response and analysis methods. Finally, conclusions are presented and discussed.

7.3 2010 El Mayor Cucapah earthquake

The 7.2 M_w El Mayor-Cucapah earthquake occurred on 4th April 2010 near the Imperial County-Baja California border at a focal depth of about 10 km, on a previously unknown strike-slip fault parallel to the main San Andreas fault system (Stewart and Brandenberg 2010, EERI 2010). Historically, the region is seismically active, and the epicenter was in close proximity to that of the 1934, 1940 El Centro, and 1979 Imperial Valley earthquakes. Both sides of the US-Mexico border experienced strong shaking, and the main event was recorded by the dense instrumentation along the Baja California region.

The Imperial County/Baja California sedimentary basin includes large areas of prime agricultural land, with soft alluvium, characterized by upper 30 m averaged shear wave velocities (V_{s30}) less than 250 m/s, and shallow groundwater. Coupled with the proximity to faults, this region is particularly vulnerable to soil liquefaction. Associated soil liquefaction in the alluvial planes of Mexicali valley (along the Rio-Colorado) caused severe damage to agricultural/water infrastructure systems, including irrigation systems, earth dams, water, and wastewater treatment facilities, canals, and levees. Further, transportation infrastructure systems, including bridges, roadways, and railroad lines experienced post-earthquake severe damage and loss of functionality. Overall, direct losses of about 520 million USD were reported in the region. Further details are reported in Stewart and Brandenberg (2010) and EERI (2010). Figure 7.1 depicts location of the earthquake epicenter, along with the two parallel bridges under investigation herein.

Configuration of the parallel bridges

Full details regarding the bridge configurations and observed seismic response are presented in EERI (2010), Turner *et al.* (2014), Turner *et al.* (2016), and Turner (2016). Located about 25 km west of the epicenter, the two parallel bridges span the Rio Colorado, with a center-to-center distance (deck spacing) of about 12 m. Crossing the river at this location, are a highway bridge (HWB) built in 1999 and a railroad bridge (RRB) built in 1962. The bridges were built such that the columns of the highway bridge were aligned to match piers of the railroad bridge. The section below briefly discusses the recorded strong motion, site configuration, as well as the observed damage patterns for the free field.

7.3.1 Strong Motion

The main event of the 2010 El Mayor-Cucapah earthquake generated over 490 strong motion records in Baja California and Mexico. The maximum recorded peak ground acceleration

was about 0.56g near El Centro, California. Herein, we use ground motion records from the Riito strong-motion station (station RII) maintained by the Mexican Northwest Accelerometer Network (RANM), which is the closest available recording station (about 12km) to the bridges (PEER NGAWest2: https://ngawest2.berkeley.edu). This strong motion and 5% damped acceleration response spectra for the recorded fault normal and fault parallel components are presented in Figure 7.2, along with a prediction by the Boore *et al.* (2014) attenuation relationship.

Following estimates of H/V spectral ratios, Liao and Meneses (2013) estimated a V_{s30} of approximately 210 m/s at this station. For simplicity, the fault parallel component of the input motion recorded at the Riito station, scaled by 0.5, and imparted at a depth of 40 m was used as the input motion.

7.3.2 Soil Stratigraphy at River Crossing

Figure 7.3 presents the two parallel bridges and an idealized configuration of the river channel and soil layering following Turner *et al.* (2014). This cross-section presented by Turner *et al.* (2016) was used along with the CPT data from Turner (2016) to generate the idealized stratigraphy shown in Figure 7.3. About 200 m in length, both bridges traverse the 180 m channel across the Rio Colorado. The active river channel is about 50 m wide throughout the year, and the two abutments (A1 and A2) raise the grade of the deck, providing an average 10 m clearance. Within the active channel, the western slope is approximately 1.5H:1V, whereas the eastern slope is about 4H:1V at this location. Water table at the site was estimated based on Turner *et al.* (2016) following the river surface elevation.

Towards the abutments, the site consists of a 1.5-2 m loose upper fill, composed primarily of silty sand, above the groundwater table. Within the active channel, a loose sand layer extends

from below the groundwater table to a depth of about 6 m near the river. Below this layer, the stratigraphy consists of interbedded silty-sand layers up to a depth of 17 m.

Simplified liquefaction triggering analysis was performed following Robertson and Wride (1998) to identify liquefiable layers within the interbedded strata. As shown in Figure 7.3, CPT 1, CPT 2, and CPT 3 represent three CPT soundings from the eastern bank of the channel from west to east. The PGA at the Riito strong-motion station was used along with the specified groundwater table to estimate Cyclic Stress Ratio (CSR) at the river crossing. The triggering analysis shown in Figure 7.4 identifies interbedded liquefiable and nonliquefiable layers, which were used in addition to the cross-section mentioned above to generate the site soil profile. Below the liquefiable layer (at about 15 m near center of the active channel), the soil domain is deemed as dense, and not susceptible to liquefaction.

Figure 7.5 presents the observed performance of the east and west slopes of the active channel (GEER 2010) in the free field (about 60 m north of the bridge site). About 4-5 m of liquefaction induced lateral spreading deformation on the eastern slope and about 1-2 m on the western slope, as observed by Turner *et al.* (2014).

7.4 Simplified Limit Equilibrium Assessment

Slope stability analyses were performed to identify potential regions of strain localization and obtain estimates of the yield coefficient (k_y) using the idealized soil profile shown in Figure 7.3. Estimates of liquefied soil shear strength ($s_{u,liq}$) using the provided CPT data were employed following Robertson *et al.* (2010). For the LS and MS layers, a normalized residual shear strength ratio $\left(\frac{s_{u,liq}}{\sigma'_{v0}}\right)$ of about 0.12 was employed. Figures 7.6 (a, b) present results of the slope stability analysis on the western and eastern slopes of the active river channel. In general, the analyses

identified regions of observed strain localization with reasonable accuracy on both (east and west) slopes of the active river channel.

Coupled with a Newmark-type sliding block analysis, estimates of k_y for each slope in the active channel were used to obtain a simplified assessment of the free field soil displacement (Figure 7.7) following Bray and Macedo (2019). The fundamental period of the sliding mass was obtained through the measured shear wave velocity (V_s) at the site, and the acceleration demand was obtained through the response spectrum of the fault parallel motion at the Riito station, resulting in.

$$T_{n,east} = 4H/V_s = 4(8)/120 = 0.27s$$

$$PS_{a,east}(1.3T_{n,east}) \approx 1g$$

The simplified limit equilibrium analysis coupled with Newmark sliding block analyses from Bray and Macedo (2019) reasonably predicted (Figure 7.7) the expected levels of free field deformations that occurred (1.4 - 6.1m). However, the analyses are sensitive to the choice of residual shear strength ($s_{u,liq}$), the intensity of ground shaking, and the estimated period of the sliding mass. Therefore, selection of the input parameters in Bray and Macedo (2019) requires caution, and consideration should be made concerning the uncertainty of the predicted free field displacement from such sliding block models.

7.5 Bridge Configurations and Observed Performance

The two parallel bridges are constructed such that their corresponding piers are aligned. The structural configuration of both bridges is summarized along with their observed performance in the following section. Readers are referred to Turner *et al.* (2014) for further details.

7.5.1 Highway Bridge

The highway bridge (HWB) was constructed in 1998 and consists of ten 20 m long spans, each with seven 1.15 m deep I-section girders. The deck slab was cast in place with a width of about 11 m. Laminated elastomeric bearings transferred deck loads to the 1.6 m wide bent cap from the girders. The bent cap was supported by four extended shaft columns, each 1.2 m in diameter, which continued to four drilled shaft foundations with the same reinforcement detailing. Figure 7.8 presents salient structural features of the HWB. Elastomeric bearings transfer deck loads to the bent cap in all bents except spans between B3-B4, B7-B8, and abutment ends (Turner *et al.*, 2014). At all other bents, anchorage by rectangular shear tabs restricts longitudinal and transverse movement to prevent unseating. A fixity of all ten spans is considered simply supported. Further details can be found in Turner *et al.* (2016).

The HWB remained in operation following the earthquake and suffered low-moderate damage, including column flexural cracking near the active river channel and settlement of bent B6 due to liquefaction.

7.5.2 Railroad Bridge

The single-track railroad bridge (RRB) was constructed in 1962 and is currently operated by a private rail consortium. Figure 7.9 presents salient structural features of the RRB. Similar to the HWB, the RRB consisted of ten 20 m long spans, each with three 1.2 m deep I-section girders. All spans are considered simply supported and rest on oblong sectioned reinforced concrete piers. It is noted that no anchorage exists between the deck and piers to prevent unseating. Construction drawings and foundation details are not available for the RRB.

Unlike the HWB, the RRB experienced severe damage. Columns closer to the active river channel translated due to lateral spreading induced soil movement along the riverbanks. The span

between bents B5-B6 unseated at B5 and collapsed into the river. Similarly, the translation of bents B1-B2 led to a near collapse of the deck between these bents.

Figure 7.10a presents the B5 pier at (pier closest to the active river channel on the east bank), which displaced further towards the river than B6, leading to the deck collapse. Inadequate anchorage of the deck to bents B5 and B6 resulted in reduced lateral stiffness of the individual piers. Therefore, each pier performed as an individual unrestrained (at top) column at these two bents. Figure 7.10b presents the nearly unseated span at bent B2. Similar to B5, the inadequate anchorage led to the pier sliding beneath the deck, nearly unseating the span between B1-B2 (temporary steel shoring connected to bent B2, to support the deck is also visible in the figure). The displaced pier at bent B6 indicates that the stiff column did not deform.

7.6 Finite Element Modeling

The models were developed using the mixed, fully coupled *u-p* formulation (Chan 1988) based on (Biot 1962). The saturated soil domain was modeled using 8-noded hexahedral elements with the mean dilatational formation ($\bar{B}$ method) as per (Hughes 2008) to remove numerical issues associated with the incompressible fluid phase. Implementation of this u-p element is based on the following assumptions: 1) small deformation and rotation, 2) solid and fluid density is constant in time and space, 3) porosity is locally homogeneous and constant, 4) soil grains are incompressible, 5) solid and fluid phases are accelerated equally. Hence, soil represented by these fully coupled elements accounts for deformations and changes in pore-water pressure during seismic excitation. In this study, a 3.6 m slice of the bridge canyon system is considered for analyzing the longitudinal response of the bridge-ground system (Figure 7.11). This slice encompasses 1 column per bent of the HWB, and the entire width of the RRB. At the boundary, response is dictated by tying nodes to a large shear beam to enforce free field response (Qiu *et al.* 2020).

The loading was performed in 4 stages, including:

1. Application of gravity using linear elastic soil properties with a Poisson's ratio of 0.4. This stage ensures the static soil stage is imposed (to obtain confinement, static stresses). A large permeability (1 m/s) is set to the soil domain to ensure a drained response. At the end of this step, the displacements under self-weight were reset to zero using InitialStateAnalysis in OpenSees.
2. The soil properties are switched to plastic to obtain compatible strain levels to match the static stresses imposed in stage 1.
3. The bridge-foundation system (beam column elements) was added, and the self-weight of bridge was imposed.
4. The permeability is switched to the actual soil permeability, and the time history is imposed at the base of the model.

The FE matrix equation of the bridge-ground system is integrated in time using a single-step predictor multi-corrector scheme of the Newmark type with integration parameters γ = 0.6 and β = 0.3025. The resulting system of equations is solved using a modified Newton Raphson incremental, iterative procedure with a Krylov subspace accelerator (Scott and Fenves 2009) for faster convergence. A relatively low level of stiffness proportional viscous damping was used to enhance numerical stability (coefficient = 0.003), with the main damping emanating from the soil's nonlinear shear stress-strain hysteresis response.

7.6.1 Piers, Pile and Soil-Pile Interface

Three-dimensional nonlinear force-based beam-column elements with fiber sections were employed to represent the piers, deck, and piles for the purpose of this liquefaction-induced lateral

spreading investigation. Figure 7.12 presents the employed section and the corresponding moment-curvature response of the reinforced concrete piers for the HWB and RRB, respectively.

The piers of the HWB extend below the ground and perform as a Caltrans Type 1 shaft. Therefore, the same moment-curvature relationship presented in Figure 7.12a is used for the piles in the HWB. Due to the lack of structural drawings of the RRB foundation system, this study employed the following moment-curvature relationship (Figure 7.13) for a super-pile based on the most likely configuration reported in Turner *et al.* (2016). In order to represent the geometric space occupied by the pile in the soil domain, rigid beam-column links ($EI = 10^4$ times the linear EI of the pile) are used normal to the vertical axis of the pile, effectively defining its surface for friction along its length and end bearing at its base (Qiu *et al.* 2020). The 3D brick elements representing the soil are connected to the pile geometric configuration at the outer nodes of these rigid links by using zerolength elements, zerolengthSection elements, and the OpenSees equalDOF translation constraint. The zerolength and zerolengthSection elements are employed to axially connect the rigid links to adjacent soil nodes and provide yield shear force in each link according to the soil-pile interface friction angle and adhesion. As such, the yield shear force is limited by $F = [c_A + k\sigma' \tan(\phi)] \cdot l \cdot h / N$, where l is the perimeter of the pile, h is center to center contributing height (according to the adjacent soil element heights), c_A is the soil-pile adhesion, ϕ is the soil-pile friction angle, $k\sigma'$ is the effective lateral stress and N is the number of zeroLengthSection elements along the pile perimeter.

7.6.2 Deck to Bent Interface

The anchorage in the HWB is modeled by transferring moments at the top of the bents to the deck. Since no anchorage exists in the RRB, the deck is connected to the top of the pier wall using an elastic-perfectly plastic spring in the longitudinal direction, with a stiffness corresponding

to frictional resistance (coefficient of 0.15) offered by the vertical load from the deck to girders. In addition, deck-to-deck separation and pounding were modeled with an elastic-no tension spring (Figure 7.14). After convergence (at every time step), the elongation of each friction spring (Figure 7.14) was checked against the current seat width (about 0.85m for a single deck at a bent). If the seat width is exceeded, the updateMaterials command was employed in OpenSees to essentially eliminate stiffness and strength of the corresponding friction element to phenomenologically model the unseating, after which the analysis was continued.

7.6.3 Employed Soil Constitutive Models

State-of-the-art multi-surface plasticity-based stress-strain constitutive models termed PressureDependMultiYield03 (PDMY03), and PressureIndependentMultiyield (PIMY) were used to reproduce the liquefiable and non-liquefiable soil response. The hyperbolic relationship represents the shear stress-strain backbone curve in these models. It is noted that PressureDependMultiYield03 has been calibrated in earlier studies (Khosravifar *et al.* 2018) and includes recent modifications to more closely capture established liquefaction triggering guidelines. Model parameters specific to PDMY03 are presented in Table 7.1. The fill is modeled using the PIMY model specified with a V_s of 210 m/s, Poisson's ratio of 0.4, and cohesion of 40 kPa. Monotonic undrained response of each soil layer at a confinement of 1 atm is presented in Figure 7.15. Additionally, stress controlled simple shear responses of each cohesionless layer (LS, MS, SS and DS) at different cyclic stress ratio levels (at a vertical stress of 1 atm) are presented in Figure 7.16.

7.6.4 Limitations of the employed models

Limitations of the above developed models are briefly discussed below:

1. Soil properties and layering are idealized, based on limited available CPT data.

2. Ground motion derived from the nearest recording station, about 12 km away from the bridges is employed in the analysis.
3. A 3.6 m slice is used for each bridge models, with the HWB modeled with a single column per bent and the RRB modeled in full (with limited free field soil around the bridge)
4. Shadowing effects of the much stiffer HWB to the RRB are not explicitly accounted for. Each bridge is studied in isolation.
5. RRB foundation pile configuration is not known. As such, a super-pile is used to model the RRB span with approximate moment curvature behavior (on stronger side of what is assumed by Turner *et al.* 2014).
6. Connections between RRB bent and deck are approximated with a friction spring (coefficient of 0.15). Resulting deformations are rather sensitive to the choice of this friction yield coefficient.
7. Connection of deck to abutments is similar to that at bents (only through friction) for the RRB.

Considering all the above-mentioned limitations, it is deemed that the models use reasonable engineering judgement where necessary, aiming to capture the essential features of observed deformations.

7.7 Computed Response

This section presents the computed response from FE analysis of the free field, HWB, and RRB, with attention paid to mechanisms contributing to the observed deformations.

7.7.1 Accelerations

Figure 7.17 presents the computed acceleration along the east and west free-field boundaries of the FE model for the free-field, HWB, and RRB. The massive shear beam on either boundary enforces 1D shear beam response conditions for all three models. In the first mode

(Turner 2016) period range of both bridge bridges (1.7 - 2.3 s), the computed motion at the soil surface shows good agreement with the recorded motion.

7.7.2 Shear Strain Demands

Figure 7.18 presents the change in soil confinement (normalized to the initial confinement) and shear stress-strain (normalized with the vertical effective stress) demands within different locations of the canyon for the RRB, HWB, and free field models. Figure 7.19 (a-c) presents shear strain contours of the ground at the free field, vicinity of HWB, and vicinity of RRB.

Free field

Loss in soil confinement (due to excess pore pressure buildup) and development of large shear strains (order of >1%) are evident from Figure 7.19a. In the free field, the eastern side of the active river channel experiences a greater loss in confinement attributed to thicker liquefiable layers. In the free field (Figure 7.19a), localized shear bands can be seen, generally agreeing with the observed slip planes on either side of the active river channel. Further away from the channel, much lower shear strains are distributed over a larger area. The soil at the center of the river channel undergoes a slumping-like deformation pattern. On the eastern bank of the river channel (Location C), shear strains of about 20 % are observed.

Highway Bridge

Much reduced shear strains are observed (Figure 7.19b) compared to the free field in the vicinity of the HWB. The presence of the HWB system pins the soil at either end of the active river channel and effectively reduces localized slip. In addition, soil in the middle of the active river channel is not observed to slump and deform due to the presence of the bridge bent. On the eastern riverbank (Location C), shear strains of about 3 % are observed due to the restraining effect offered by the HWB.

Railroad Bridge

The RRB (Figure 7.19c) is not able to arrest localized shear strains along the active river channel as effectively as the HWB. Further, the shear strains are distributed over a larger area than soil in the vicinity of the HWB. On the eastern bank (Location C), the RRB is able to reduce free field deformations (with shear strains of about 10 %), to a lesser degree as compared to the HWB.

7.7.3 Structural Demands

Computed demands on the foundation systems of the HWB and RRB are presented in this section (Figure 7.20). Attention is paid to foundations supporting Bent 2 and Bent 5 for both bridges (*i.e.*, bents near either side of the active river channel and local slope faces). In addition, time histories of the computed deck displacements are presented (Figure 7.21).

Highway Bridge

Typical moment-curvature response of HWB foundations at Bent 2 and 5 are shown in Figure 7.20a. In addition, the structural drawings of the HWB foundation estimates of ϕ_y (curvature where extreme steel fiber starts to yield) are presented. The moment-curvature responses indicate cracking for both bent 2 and bent 5 foundations (on the side of columns facing the river) and slight yielding of the extreme rebar fiber. Further, deck displacements (Figure 7.21) indicate low deformations, suggesting the overall good performance of the HWB.

Railroad Bridge

Typical moment-curvature response of RRB foundations at Bent 2 and 5 are shown in Figure 7.20b. Compared to the HWB, each bent of the RRB acts in isolation (due to inadequate anchorage) and undergoes much larger deck displacements. Further, the span would be expected to collapse around 46 s into the shaking when the seat width of 0.85 m is surpassed.

7.7.4 Deformations

Free field

Soil displacement histories in the free field *i.e.,* without the bridges, are presented in Figure 7.22. The geometry of the canyon and thicker liquefiable layers on the eastern slope of the active river channel leads to about 3-4 m of lateral soil displacement in the free field. About 1-2 m of soil displacement towards the river is observed on the western bank. In general, these simulations reasonably agree with the observations (*i.e.,* about 3-4.5 m and 1-2 m on the east and west riverbanks, respectively).

Highway Bridge

The deformed configuration for the structural system in the HWB is presented in Figure 7.23. The figure shows that anchoring bents into the bridge deck leads to increased lateral resistance of individual bents and reduced deformations compared to the RRB. The analysis predicts distress in bents B2 and B5, having a double curvature type deformed shape (as observed in reconnaissance surveys) attributed to the significant restraint offered by the bridge deck. Therefore, flexural cracking is expected on the inward face of the columns (away from the river) in bents B2 and B5 towards the interface of layers SS (silty sand) and MS (medium sand) and continuing to the LS layer (upper loose sand).

Figure 7.24 presents the deformed configuration of soil in the free field, soil near bridge, and bents B5 and B6 at the end of shaking. The figure indicates the large shear strains developed in the LS layer (loose sand) near the ground surface for bent B5. It is noted that this bent was placed at the tail end of a local slope (near failure surface) within the active river channel, and therefore undergoes much larger displacements than soil near bent B6. The bridge offers

substantial lateral stiffness and reduces the free field soil displacements by about 50 %. Continuity of the deck leads to the double curvature type deflected shape as seen in the figure.

Railroad Bridge

Figure 7.25 presents the deformed configuration of the soil in the free field, soil near the bridge, and bents B5 and B6 of the RRB. Absence of anchorage of pier walls to the deck leads to inadequate frame action, and consequently, softer lateral resistance in each bent. Therefore, each bent performs in isolation.

Prior to unseating on the eastern bank, it is shown that bents B5 and B6 displaced 1 m and about 0.5 m, respectively, towards the river. The difference in the deformations of the individual piers during lateral spreading leads to the collapse of the span at bent B5. On the western bank, bents B2 and B1 displaced about 0.7m and 0.3m towards the river, nearly leading to the collapse of the span between B1-B2.

The presence of the bridge is clearly shown to arrest soil displacement within the active river channel, as seen in the figure. An almost 50% reduction is observed in the free field soil displacements near bents B5 and B6 attributed to pile pinning effects from the bridge structure.

7.8 Discussion

Figure 7.26(a-c) presents the free field response of the channel, HWB-ground system, and the RRB-ground system at the end of shaking. Post lateral spreading, free field geometry of the canyon is observed to slump and deform towards the Rio Colorado at both riverbanks (Figure 7.26a). In this particular channel, the geometry and layering resulted in about 3-4 m of lateral spreading induced soil displacement on the eastern riverbank and about 1-2 m on the western riverbank at the free field. The deformation patterns observed generally indicate presence

of local (concentrated) flow type failures over the global lateral spreading deformations on either side of the active river channel.

In general, limit equilibrium-based (LE) methods coupled with Newmark sliding block analyses reasonably agree with the FE analysis and the observed deformation patterns from reconnaissance surveys in the free field. However, the limit equilibrium method predicts a concentrated failure (flow slide type) surface on the east and west riverbanks and not one observed during lateral spreading (where slumping and strain redistribution over a larger spatial extent is observed).

Estimates for the free-field slope displacements were computed using slope stability analysis (with liquefied residual shear strength) coupled with a sliding block model. The current equations for estimating $s_{u,liq}$ (Robertson 2010, Idriss and Boulanger 2015, Kramer and Wang 2015) are based on flow-type failure mechanisms and are not intended for lateral spreading (Kramer and Wang 2015). Herein, the deterministic normalized residual strength model of Robertson (2010) is employed using the provided CPT data. However, the LE analyses show sensitivity in yield acceleration (k_y) to choice of the liquefied residual shear strength ($s_{u,liq}$). Further, given a value of k_y (corresponding to a choice of $s_{u,liq}$), employing the sliding block model of Bray and Macedo (2019) leads to significant uncertainty in the predicted displacement of the slope due to the natural variability of employed ground motions. Therefore, practicing engineers must be aware of the uncertainty involved in the predicted free field slope displacement (16^{th}-84^{th} percentile corresponding to 1-6 m) from such methods, particularly for sites governed by a distributed lateral spreading type mechanism.

Both bridges reduce the free field soil deformations, including the local (flow type) and distributed (lateral spreading type) failure mechanisms. In the HWB, significant restraint is offered

by the continuity of the deck and deformations closer to 1 m are observed on either side of the river channel at the end of shaking. In contrast, each pier of the RRB acts as an individual system, leading to similar deformations at the instant of unseating (around 46 s into strong shaking).

Of interest as well are the deformation patterns in the RRB- ground system at the end of shaking. Due to the lower RRB overall lateral stiffness, strain redistribution was observed over a much larger region on the eastern riverbank (as far as east of bent B6) compared to the HWB-ground system.

7.9 Structural Retrofit Measures

A number of structural retrofit measures were adopted to prevent the unseating of the railroad bridge span, including: 1) increasing friction between the deck to bents, and 2) expanding seat width.

7.9.1 Increasing friction at deck-bent connection

Figure 7.27 presents the effect of friction at the deck-bent connection on the displacement response (at the top) of bents B2 and B5. The displacement at the top of bents B2 and B5 (normalized to the available seat width i.e., 0.85 m) at the end of shaking is presented. The coefficient of friction is varied from 25 % - 400 % of the reported value in Turner (2016). A strong nonlinear relationship is observed, where increasing the coefficient of friction by about 110% (from 0.15 to 0.33), using appropriate bearing pads prevents unseating of the span at bent B5. In the existing railroad bridge, the concrete deck was directly placed on each bent. The resistance to soil movement, after liquefaction, is capacity limited by the degree of friction at the bent-deck connection. Therefore, increasing the frictional resistance at the deck-bent connection directly affects the extent of soil deformations, post-liquefaction. Figure 7.28 presents the displacement of the railroad bridge-ground system, at the end of shaking, for a coefficient of friction of 0.075, 0.15,

0.3, and 0.6. As seen in the figure, a greater degree of friction reduces the magnitude and spatial extent of ground deformations, highlighting the need to adequately model connections between the deck and bents into characterizing lateral resistance of the structural system**.**

7.9.2 Seat width expansion

To calculate the necessary width to avoid unseating of the railroad bridge span between bents B5 and B6, an additional simulation was performed that precludes the collapse of the B5-B6 span (Figure 7.29). As noted in the figure, increasing the seat width (at bent B5) by about 45 % could have prevented the unseating of the span (*i.e.*, seat width of about 1.25 m instead of 0.85 m).

7.10 Insitu Ground Remediation

In addition to the structural retrofit measures presented above, insitu ground remediation measures were employed to reduce lateral soil deformations. To this extent, the potential of the polymer injection technique was explored.

Due to its ease of deployment in dense urban environments, the polymer injection remediation measure is commonly used for re-leveling of roadways and foundations (Naudts 2003, Buzzi *et al.* 2010, Xiao *et al.* 2014, Xiao *et al.* 2018, Saleh *et al.* 2019). Such polymers are usually deployed using a two-component chemically blown foam consisting of a curative phase (poly-isocyanate) and a resin phase (polyol). Upon mixing, rapid polymerization occurs forming polyurethane, which expands (due to released CO_2 as a by-product), and cures into a hardened foam. A summary of polymer-sand composite properties is discussed below:

7.10.1 Polymer sand composite properties

Post injection and subsequent expansion, the resulting improvement in mechanical properties of the remediated ground might be attributed to the combined effects of: i) soil replacement and cementation by the created expanding composite inclusion, ii) soil densification,

and increase in confinement around these inclusions. The shear strength characteristics of the polymer-sand composite are based on testing results from Xiao *et al.* (2014), and the unconfined compression tests presented in Chapter 5 where a cohesion intercept of 400 kPa is introduced to the insitu soil (with the friction angle of the insitu sand left unchanged). It is noted that unconfied compression tests of the pure polymer (Figure 7.30) indicate similar responses. Monotonic shear stress-strain curves employed in the computational simulations are presented in Figure 7.31. The stiffness of the composite is varied with confinement and is presented in Figure 7.32 (alongside the in situ soil's shear wave velocity). A mass density of 1200 kg/m^3 (for the composite) was employed in all simulations.

Three strategies of soil improvement were adopted including 1) Improvement of the LS layer, through polymer injection and subsequent cementation to improve soil shear strength, 2) improvement of the LS and MS layers, through polymer injection, and 3) addition of polymer-sand composite inclusions to effectively pin the slopes along the active river channel. Schematics of the proposed remediation layouts are presented in Figure 7.33 and is elaborated in Figure 7.34 for the polymer-sand composite inclusions. The depicted injection techniques emphasize various mechanisms that contribute to the extent of soil improvement. The first two approaches primarily focus on remediation of an areal zone through densification. The third strategy employs structural inclusions, where the polymer-sand composite effectively pins the ground to anchor the lateral spreading ground.

The railroad bridge-ground mesh presented in Figure 7.11 is modified to increase the slice width (out-of-plane width) to 20 m. The modified mesh is presented in Figure 7.35. The proposed remediation strategies along the full railroad bridge-ground system are presented in Figure 7.36.

7.10.2 Remediation of Layer LS

In this approach (Figure 7.36a), polymer injection is performed in the LS layer (Loose Sand) along the footprint of the bridge (based on an out of plane width of 3.6 m). Injection is performed such that the $(N_1)_{60}$ (normalized standard penetration blow count), of remediated zone is increased from about 9 to about 29 using the methodology presented in Prabhakaran *et al.* (2020). As such, about 8% volume of liquid polymer to soil was employed (Figure 7.37) resulting in the injection of about 120 tons of polymer of the sand. It is noted that remediation is primarily attributed to the densification of the sand around the composite inclusions. Updated parameters of the PDMY03 soil constitutive model are presented in Table 7.2 (case 1).

Figure 7.38a and Figure 7.38b present the response of the railroad bridge-ground system in the absence of any remediation measure and following remediation of the LS layer, respectively. As seen in the figures, the deformations of the bridge structure are notably reduced. Of interest as well, is the displacement of the B5-B6 span at bent B5, reducing from about 1.8 m (prior to improvement) to about 0.7 m post remediation. Consequently, the remediation measure effectively prevented unseating, albeit with persistence of substantial deformations.

7.10.3 Remediation of Layers LS and MS

In this scenario (Figure 7.36b), both liquefiable layers LS (Loose Sand) and MS (Medium Sand) layers are improved along the footprint of the bridge. About 8% volume of the liquid polymer to soil was employed, similar to the previous case, such that the $(N_1)_{60}$ of LS and MS layers is increased from about 9 and 13 to about 29 and 33 respectively. As such, about 440 tons of liquid polymer is injected for this illustrative scenario. Updated parameters of the PDMY03 soil constitutive model are presented in Table 7.2 (case 2).

Figure 7.38c presents the response of the system after remediation of both liquefaction susceptible layers (LS and MS Layers). As seen in the figure, the deformations of the bridge structure are reduced. In this illustrative scenario, the displacement of the B5-B6 span at bent B5, reduces from about 1.8 m (without improvement) to about 0.35 m after remediation, effectively precluding unseating of the span.

7.10.4 Remediation using composite inclusions

In the third illustrative scenario (Figure 7.36c), the polymer is injected to form structural inclusions to effectively pin the ground during liquefaction induced lateral spreading. As such about 60 tons of the polymer is injected (based on the layout presented in Figure 7.34) along the active river channel.

Figure 7.38d presents the response of the system after addition of the composite inclusions. As seen in the figure, deformations of the bridge structure are reduced as compared to the case without remediation. In this case, the displacement of the B5-B6 span at Bent B5, reduces from about 1.8 m (without improvement) to about 0.8 m after remediation. The unseating of the B5-B6 span at bent B5 is prevented. However, the bridge undergoes significant damage due to the incurred large deformations.

7.11 Conclusions

Longitudinal response of the San Felipito bridges spanning the Rio Colorado during the 7.2 M_w 2010 El Mayor Cucapah earthquake is revisited in this study. The bridge-ground systems were analyzed with simplified limit equilibrium type analyses and followed up with detailed finite element simulations. The models, with judicial engineering judgement, replicate the observed global deformation patterns and reasonably predict the performance of both bridges.

Specific conclusions and observations include:

1. The structural system of the bridge (piles, piers, and deck) is shown to potentially reduce free-field soil deformations significantly. In this regard, continuity of the deck (through adequate anchorage) increases lateral resistance of individual piers, enforcing a frame-like response emanating from the strut action of the bridge deck. In addition, attention must be paid to connections between the bridge pier and deck to adequately characterize the lateral resistance of piers.

2. Deformation patterns consisting of a localized failure mechanism overlain by a more distributed lateral spreading-type mechanism are shown to control the overall system response. Both bridges were able to reduce the free field deformations. However, the much stiffer HWB was able to pin the ground and effectively reduce the formation of localized shear zones.

3. The slice-based back analysis can capture salient response mechanisms in the longitudinal direction. The conducted FE analyses predict unseating of the RRB span between B5-B6 and near failure of the deck between bents B1-B2.

4. Computed structural demands on the bridges indicate flexural cracking (on the side of columns facing the active river channel) and slight yielding of the HWB foundations and suggest likely failure of the RRB foundation system. Further, the analysis indicates that unseating of the RRB span between bents B5-B6 could have been prevented if the seat width was increased by about 45 %, and/or if friction between the pier and deck was increased. In such a case, the increased demands on the RRB foundation system warrant further scrutiny.

5. Limit equilibrium (LE) based methods coupled with Newmark sliding block models can bound estimates of local slope deformations. However, attention must be paid to their sensitivity to the choice of k_y (given an $s_{u,liq}$) and the aleatory uncertainty provided by ground motions.

Further work should be performed to assess sensitivity of the computed results to the choice of input parameters in both the FE and LE-based analyses.

6. Noted by Turner and Brandenberg (2015), proximity of the much stiffer HWB led to somewhat reduced deformations near the RRB. Such an analysis cannot be performed by a slice-based model, and efforts toward full 3D FE analysis with both the HWB and RRB are warranted.

7. Following the comprehensive calibration of the railroad bridge-ground system, various illustrative structural and geotechnical retrofit measures were proposed. These included enhancing deck-bent friction, expanding seat width, and injecting an expansive polymer along the footprint of the bridge. To emphasize the potential of the polymer injection technique in mitigating liquefaction induced lateral deformations, three representative scenarios were studied, and system response was discussed. In the studied scenarios, it was shown that injections of the order of 10 % (volume of liquid polymer to soil) resulted in a reduction of lateral spreading deformations, precluding the observed unseating of the bridge-deck span. As such, this chapter presented a comprehensive framework that highlights feasibility of utilizing the polymer injection technique for liquefaction mitigation in practical scenarios, while also assessing the resulting outcomes.

7.12 Acknowledgement

The work presented in this paper was partially supported by the California Department of Transportation. The authors are grateful for the detailed post-earthquake surveys conducted by the Geotechnical Extreme Events Reconnaissance (GEER) and EERI teams following the 2010 El Mayor Cucapah earthquake. The authors are grateful to the Pacific Earthquake Engineering Research Center (PEER) NGAWest2 team for providing the recorded strong motions used in this

study. The authors would also like to thank Professor Scott Brandenberg and Dr. Benjamin Turner for personal communications, and for their input, photographs, and excellent documentation of the case history.

Chapter 7, in full, is currently being prepared for submission for publication of the material as it may appear in the following publication: Prabhakaran, A., Qiu, Z., and Elgamal, A. "Response of the San Felipito bridge-ground system during the 2010 El Mayor-Cucapah Earthquake: Computational Simulation, Insights and Remediation". The dissertation author will be the primary investigator and author of this paper.

7.13 References

Biot, M. A. (1962). "Mechanics of deformation and acoustic propagation in porous media." *Journal of Applied Physics*, American Institute of Physics(AIP), 33(4), 1482–1498.

Boore, D. M., Stewart, J. P., Seyhan, E., and Atkinson, G. M. (2014). "NGA-West2 Equations for Predicting PGA, PGV, and 5% Damped PSA for Shallow Crustal Earthquakes:" *Earthquake Spectra*, SAGE Publications, Sage UK: London, England, 30(3), 1057–1085.

Bray, J. D., and Macedo, J. (2019). "Procedure for Estimating Shear-Induced Seismic Slope Displacement for Shallow Crustal Earthquakes." *Journal of Geotechnical and Geoenvironmental Engineering*, American Society of Civil Engineers, 145(12), 04019106.

Buzzi, O., Fityus, S., and Sloan, S. W. (2010). "Use of expanding polyurethane resin to remediate expansive soil foundations." *Canadian Geotechnical Journal*, 47(6), 623–634.

Chan, A. (1988). "A unified Finite Element Solution to Static and Dynamic Geomechanics problems.", *PhD Dissertation*, Department of Civil Engineering, University College of Swansea, Swansea.

EERI (Earthquake Engineering Research Institute). (2010). "The El Mayor Cucapah, Baja California earthquake, April 4, 2010." EERI Reconnaissance Rep. 2010-02, Oakland, CA.

Esri Inc. (2020). *ArcGIS Pro* (Version 2.9). Esri Inc. https://www.esri.com/en-us/arcgis/products/arcgis-pro/overview.

GEER (Geotechnical Extreme Event Reconnaissance). (2010). "Preliminary report on seismological and geotechnical engineering aspects of the April 4, 2010, Mw 7.2 El Mayor-Cucapah (Mexico) earthquake." Rep. No. GEER-023, Oakland, CA

Hughes, T. J. R. (2008). "The Finite Element Method: Linear Static and Dynamic Finite Element Analysis: Thomas J. R. Hughes." *Computer-Aided Civil and Infrastructure Engineering*, Prentice-Hall, 4(3), 245–246.

Idriss, I. M., and Boulanger, R. W. (2015). "2nd Ishihara Lecture: SPT- and CPT-based relationships for the residual shear strength of liquefied soils." *Soil Dynamics and Earthquake Engineering*, Elsevier, 68, 57–68.

Idriss I M, Boulanger R W (2008). Soil liquefaction during earthquakes. *Earthquake Engineering Research Institute Monograph* (12). Earthquake Engineering Research Institute, Oakland, CA, USA

Kleinfelder (2019). Personal Communication.

Kramer, S. L., and Wang, C.-H. (2015). "Empirical Model for Estimation of the Residual Strength of Liquefied Soil." *Journal of Geotechnical and Geoenvironmental Engineering*, American Society of Civil Engineers, 141(9), 04015038.

Khosravifar, A., Elgamal, A., Lu, J., and Li, J. (2018). "A 3D model for earthquake-induced liquefaction triggering and post-liquefaction response." *Soil Dynamics and Earthquake Engineering*, Elsevier, 110, 43–52

Liao, Y., and Meneses, J. (2013). "Engineering Characteristics of Ground Motion Records from the 2010 Mw 7.2 El Mayor–Cucapah Earthquake in Mexico", SAGE Publications, Sage UK: London, England, 29(1), 177–205.

McKenna, F., Scott, M. H., and Fenves, G. L. (2010). "Nonlinear Finite-Element Analysis Software Architecture Using Object Composition." *Journal of Computing in Civil Engineering*, American Society of Civil Engineers, 24(1), 95–107.

Naudts, A. (2003). "Irreversible Changes in the Grouting Industry Caused by Polyurethane Grouting: An Overview of 30 Years of Polyurethane Grouting." Third Internatioanl Conference on Grouting and Ground Treatment, American Society of Civil Engineers, New Orleans, 1266–1280.

Olson, S. M., and Johnson, C. I. (2008). "Analyzing Liquefaction-Induced Lateral Spreads Using Strength Ratios." *Journal of Geotechnical and Geoenvironmental Engineering*, American Society of Civil Engineers, 134(8), 1035–1049.

PEER (Pacific Earthquake Engineering Research Center). (2013). "NGAWest2 database" ⟨https://peer.berkeley.edu/ngawest2⟩ (Feb. 24, 2022).

Qiu, Z., Ebeido, A., Almutari, A., Lu, J., Elgamal, A., Shing P. B., and Martin, G. (2020). "Aspects of bridge-ground seismic response and liquefaction-induced deformations." *Earthquake Engineering Structural Dynamics*, 49(4):675-93.

Prabhakaran, A., Kyungtae, K., Ebeido, A., Jahed Orang, M., Motamed, R., Elgamal, A., and Frazao, C. (2021). "Polymer injection and associated site liquefaction remediation mechanisms." *17th World Conference on Earthquake Engineering*, Sendai, Japan.

Robertson, P. K. (2010). "Evaluation of Flow Liquefaction and Liquefied Strength Using the Cone Penetration Test." *Journal of Geotechnical and Geoenvironmental Engineering*, American Society of Civil Engineers, 136(6), 842–853.

Robertson, P. K., and Wride, C. E. (1998). "Evaluating cyclic liquefaction potential using the cone penetration test." *Canadian Geotechnical Journal*, NRC Research Press Ottawa, Canada,

35(3), 442–459.

Saleh, S., Yunus, N. Z. M., Ahmad, K., and Ali, N. (2019). “Improving the strength of weak soil using polyurethane grouts: A review.” *Construction and Building Materials*, Elsevier, 202, 738–752.

Naudts, A. (2003). “Irreversible Changes in the Grouting Industry Caused by Polyurethane Grouting: An Overview of 30 Years of Polyurethane Grouting.” Third Internatioanl Conference on Grouting and Ground Treatment, American Society of Civil Engineers, New Orleans, 1266–1280.

Scott, M. H., and Fenves, G. L. (2009). “Krylov Subspace Accelerated Newton Algorithm: Application to Dynamic Progressive Collapse Simulation of Frames.” *Journal of Structural Engineering*, American Society of Civil Engineers, 136(5), 473–480.

Turner, B., Brandenberg, S. J., and Stewart, J. P. (2014). “Evaluation of collapse and non-collapse of parallel bridges affected by liquefaction and lateral spreading.” PEER Rep. 2014/10, Pacific Earthquake Engineering Research Center, Univ. of California, Berkeley, CA, 122.

Turner, B. J. (2016). “Kinematic Pile-Soil Interaction in Liquefied and Nonliquefied Ground.”, *PhD Dissertation*, University of California Los Angeles.

Turner, B. J., and Brandenberg, S. J. (2015). “Pile pinning and interaction of adjacent foundations during lateral spreading.”, *DFI-Journal, Deep Foundations Institute*, Taylor & Francis, 9(2), 92–102.

Turner, B. J., Brandenberg, S. J., and Stewart, J. P. (2016). “Case Study of Parallel Bridges Affected by Liquefaction and Lateral Spreading.” *Journal of Geotechnical and Geoenvironmental Engineering*, American Society of Civil Engineers, 142(7), 05016001.

Xiao, Y., Liu, H., and Desai, C. S. (2015). “New Method for Improvement of Rockfill Material with Polyurethane Foam Adhesive.” *Journal of Geotechnical and Geoenvironmental Engineering*, American Society of Civil Engineers (ASCE), 141(2), 02814003.

Xiao, Y., Stuedlein, A. W., Chen, Q., Liu, H., and Liu, P. (2018). “Stress-Strain-Strength Response and Ductility of Gravels Improved by Polyurethane Foam Adhesive.” *Journal of Geotechnical and Geoenvironmental Engineering*, American Society of Civil Engineers (ASCE), 144(2), 04017108.

Zhang, G., Robertson, P. K., and Brachman, R. W. I. (2011). “Estimating liquefaction-induced ground settlements from CPT for level ground.”, *Canadian Geotechnical Journal*, NRC Research Press Ottawa, Canada , 39(5), 1168–1180.

7.14 Tables and Figures

Table 6.1. Properties of the PDMY03 constitutive model employed in the analysis.

Model Parameters	*LS*	*MS*	*SS*	*DS*
	D_r = 45%	D_r = 55%	D_r = 75%	D_r = 85%
Normalized Standard Penetration blowcount, $(N_1)_{60}$ (based on Idriss and Boulanger, 2008)	9	13	26	33
Reference mean effective pressure, p'_r (kPa)	170	180	210	270
Total mass density, ρ (t/m^3)	1.8	1.9	2.1	2.2
Maximum shear strain at reference pressure, $\gamma_{max,r}$	0.10			
Shear modulus at reference pressure, G_r (MPa)	80	95	120	160
Stiffness dependence coefficient *d*	0.5			
Poisson's ratio for dynamics, *v*	0.4			
Shear strength at zero confinement, *c* (kPa)	1.73			
Friction angle ϕ, with resulting strength defined as $p' \sin\phi$	24	25	27	30
Phase transformation angle, ϕ_{PT}	24	25	25	27
Contraction coefficient, c_1	0.1	0.1	0.035	0.015
Contraction coefficient, c_2	5	5	3	1
Contraction coefficient, c_3	0.05	0.1	0.2	0.45
Dilation coefficient, d_1	0.10	0.12	0.15	0.2
Dilation coefficient, d_3	0.05	0.1	0.2	0.45
Permeability (m/s)	10^{-5}			
Initial stiffness damping coefficient	0.003			
Convergence criteria based on norm of energy increment	10^{-4}			

Table 6.2. Smeared properties of PDMY03 constitutive model (for LS MS layers) after remediation

Model Parameters	***LS-R*** D_r = 80%	***MS-R*** D_r = 85%
Normalized Standard Penetration blowcount, $(N_1)_{60}$ (based on Idriss and Boulanger, 2008)	29	33
Reference mean effective pressure, p'_r (kPa)	170	180
Total mass density, ρ (t/m^3)	2.0	2.2
Shear modulus at reference pressure, G_r (MPa)	110	127
Friction angle ϕ, with resulting strength defined as $p' \sin\phi$	28	30
Phase transformation angle, ϕ_{PT}	25	27
Contraction coefficient, c_1	0.003	0.0015
Contraction coefficient, c_3	0.25	0.45
Dilation coefficient, d_1	0.15	0.20
Dilation coefficient, d_3	0.25	0.45

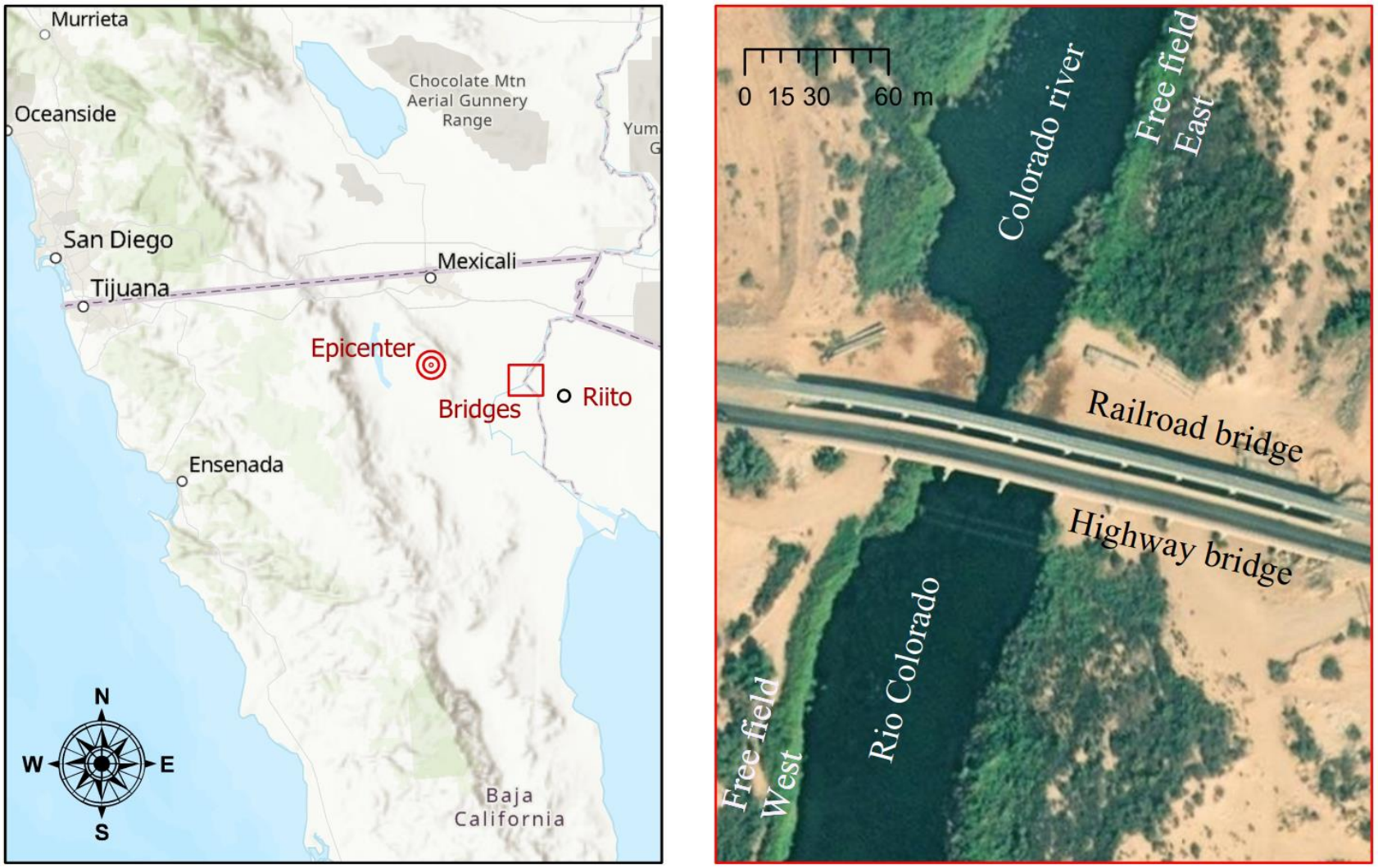

Figure 7.1. Location and layout of the San Felipito bridges (Esri Inc., 2020). The map also shows the location of the closest available strong motion recording station (Riito, about 14km away from the bridge) employed in the analysis

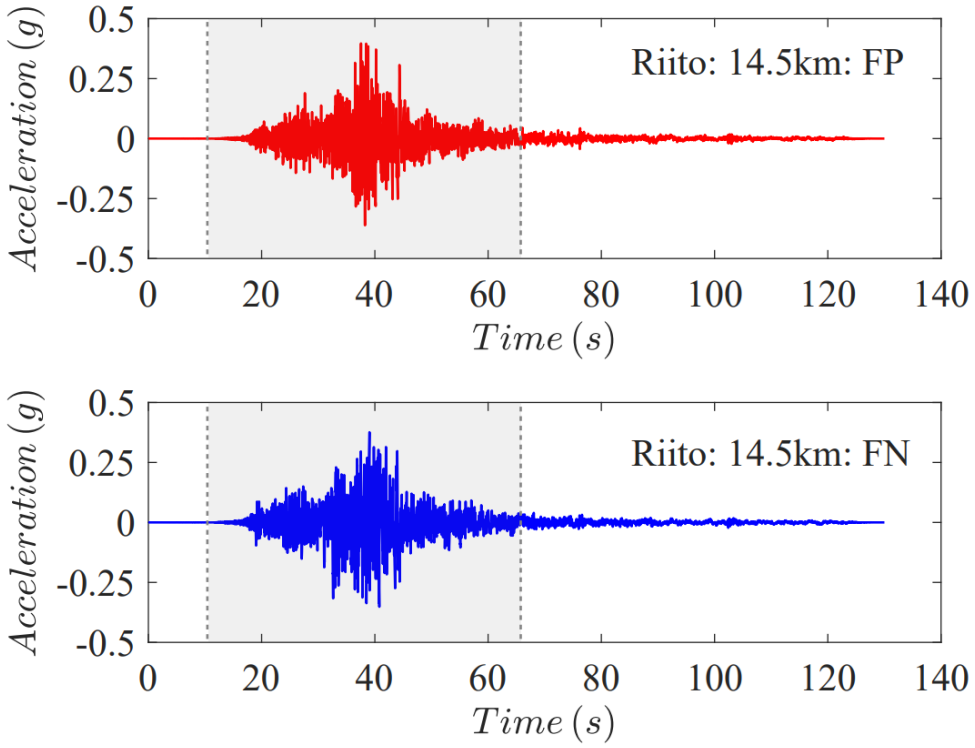

(a) Recorded motion at Riito station (dashed lines represent analysis duration based on 5% to 95% Arias Intensity). Fault parallel component was employed in the analysis.

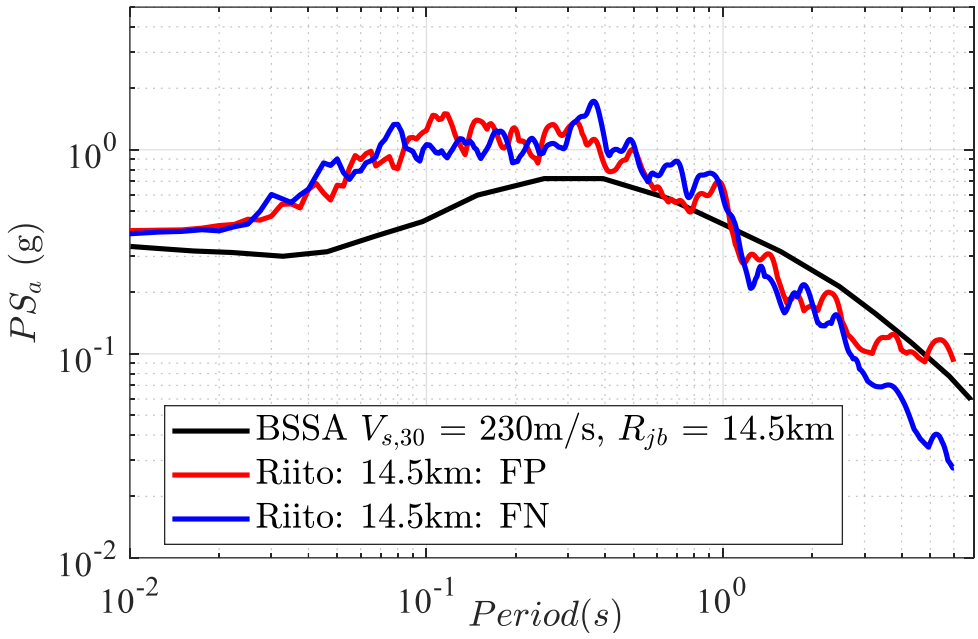

n

(b) Recorded and estimated 5% damped acceleration response spectra

Figure 7.2. (a) Recorded time history (b) Recorded and estimated response spectra estimated 5% damped acceleration response spectra at the Riito station (PEER NGAWest2)

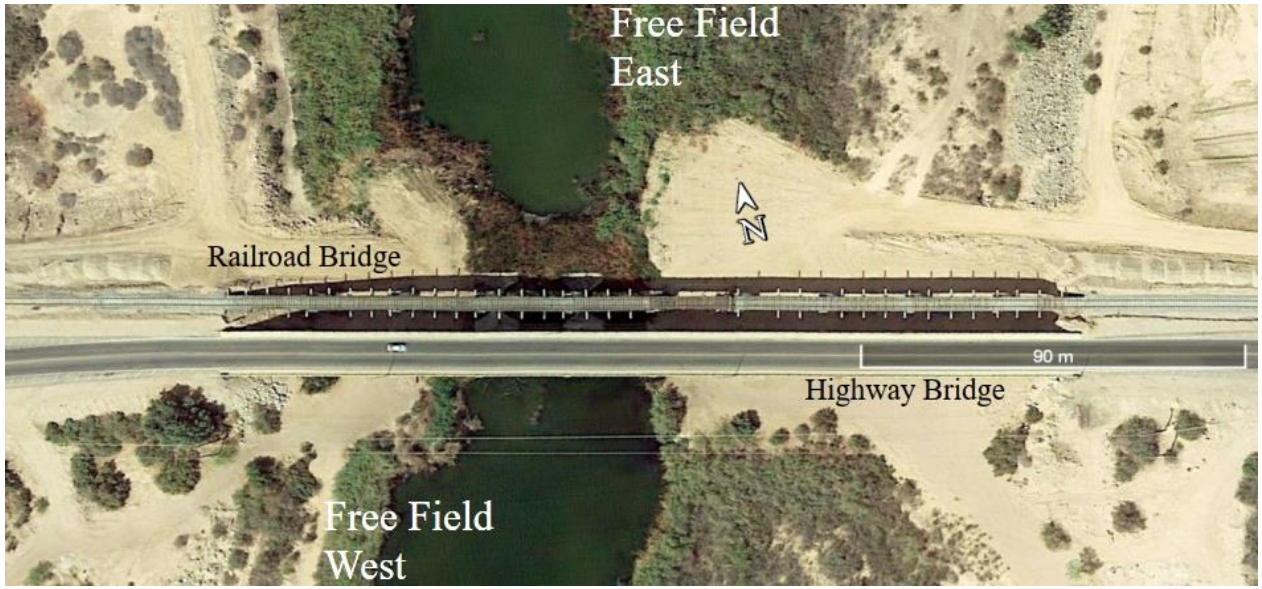

(a)

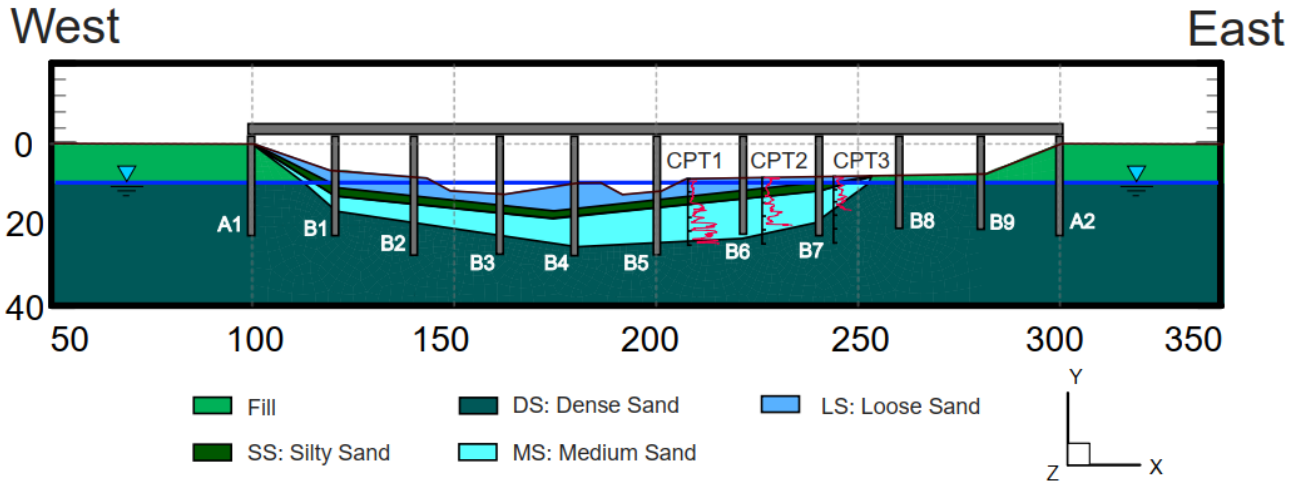

(b)

Figure 7.3. (a) Satellite view and (b) simplified layering of the soil profile at the river channel. (dimensions are in m)

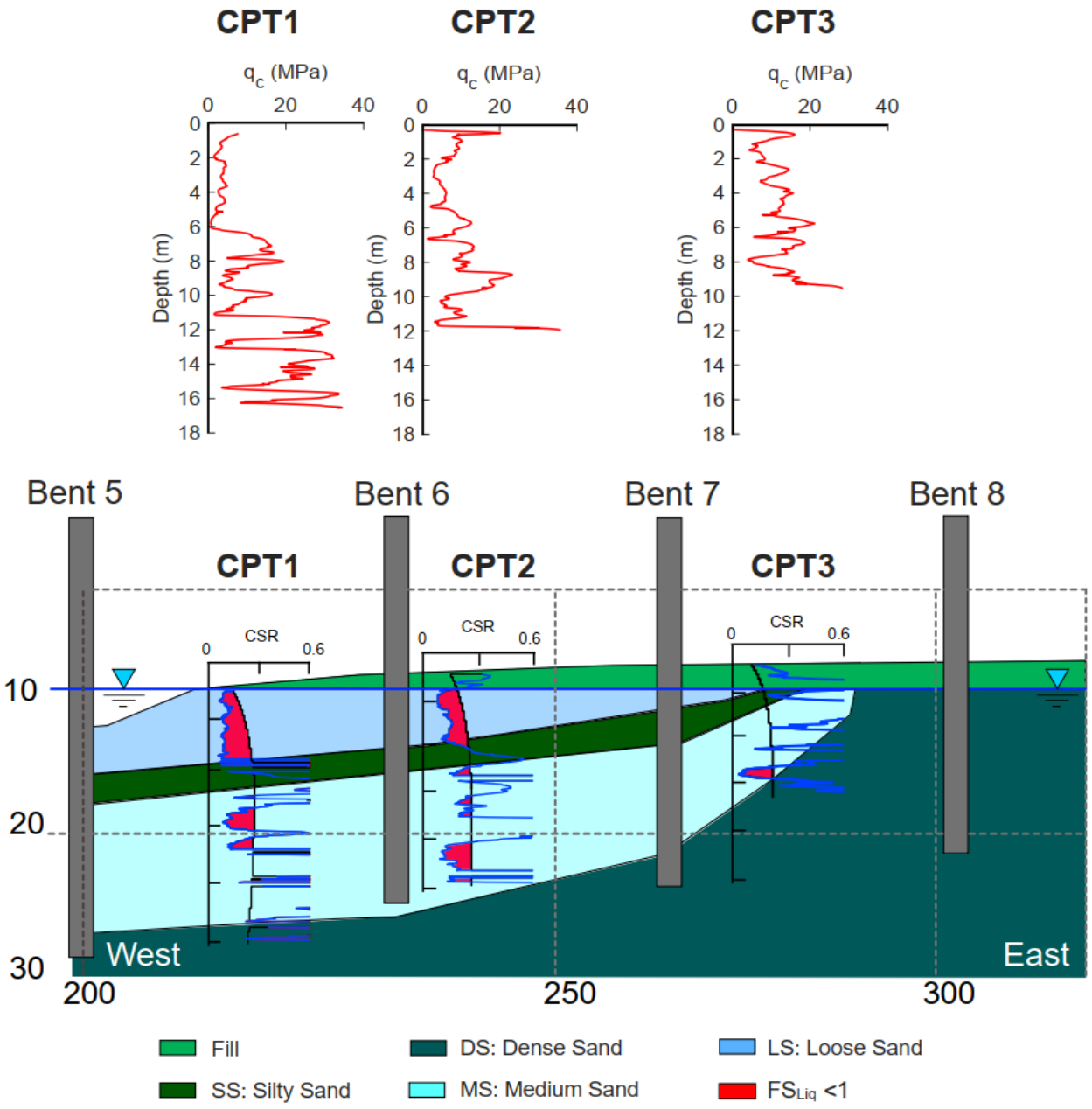

Figure 7.4. Observed cone tip resistance (q_c) and Simplified liquefaction triggering assessment with the cyclic stress ratio (CSR) of the eastern bank of the active river channel following Robertson and Wride (1998) (all dimensions are in m)

(a)

(b)

Figure 7.5. Observed lateral spreading induced deformations at (a) free field east bank (photograph by Scott Brandenberg) and (b) free field west bank of the active river channel at the free field (photograph by James Gingery) (GEER 2010)

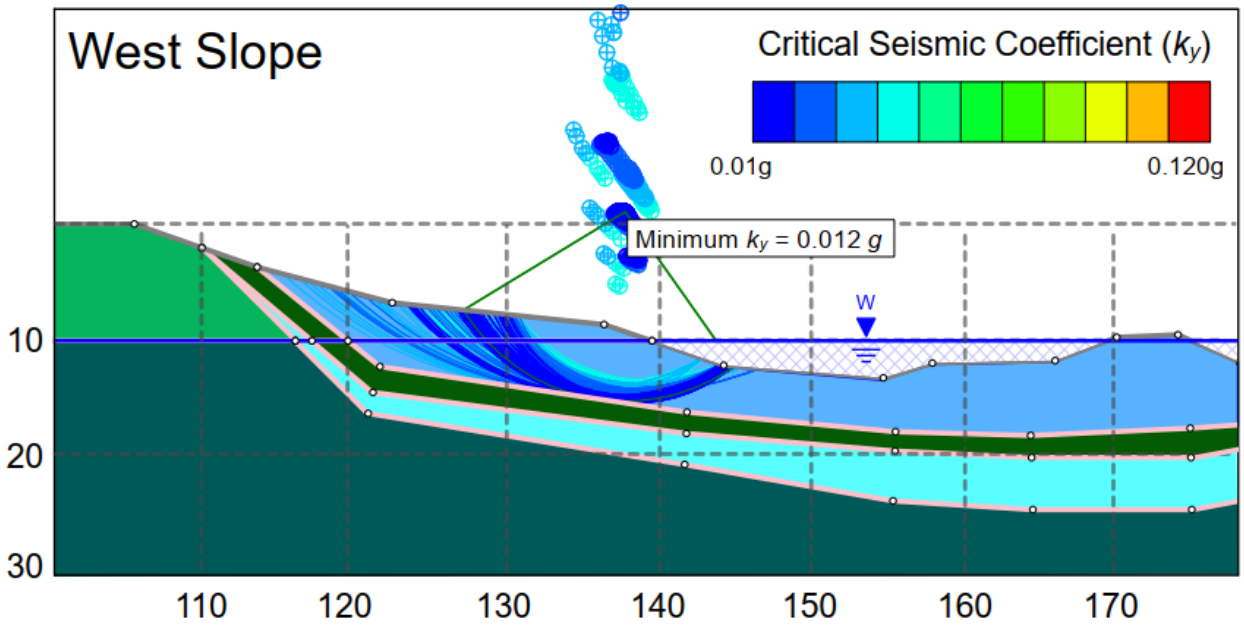

(a)

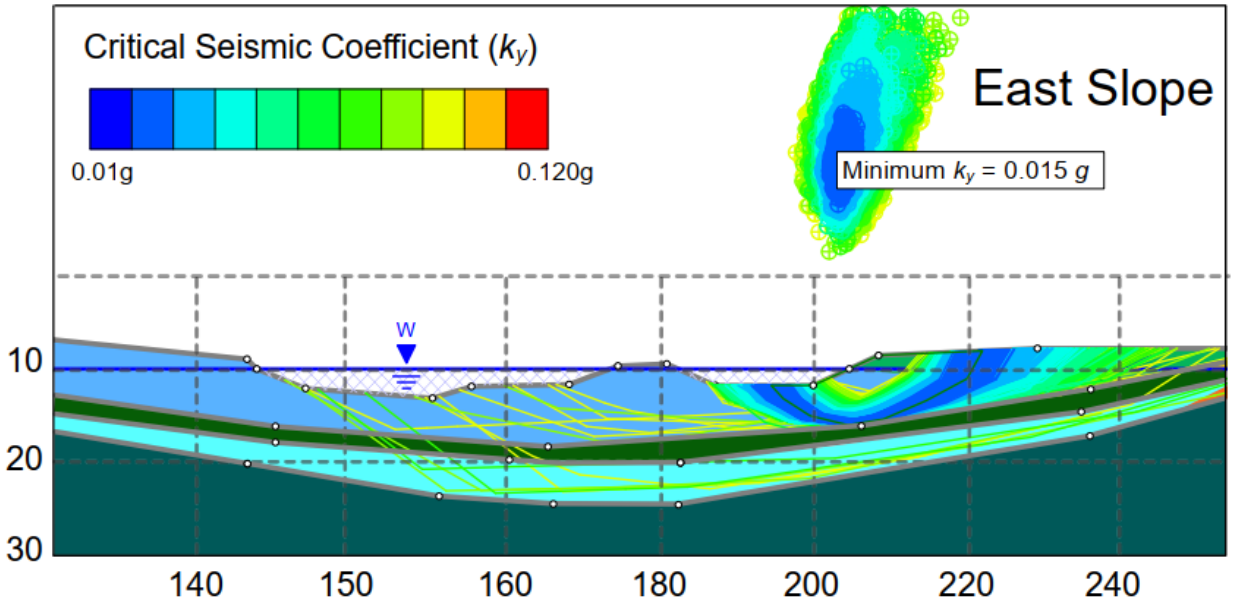

(b)

Figure 7.6. Slope stability analysis of the (a) western slope and (b) eastern slope in the active river channel (all dimensions are in m)

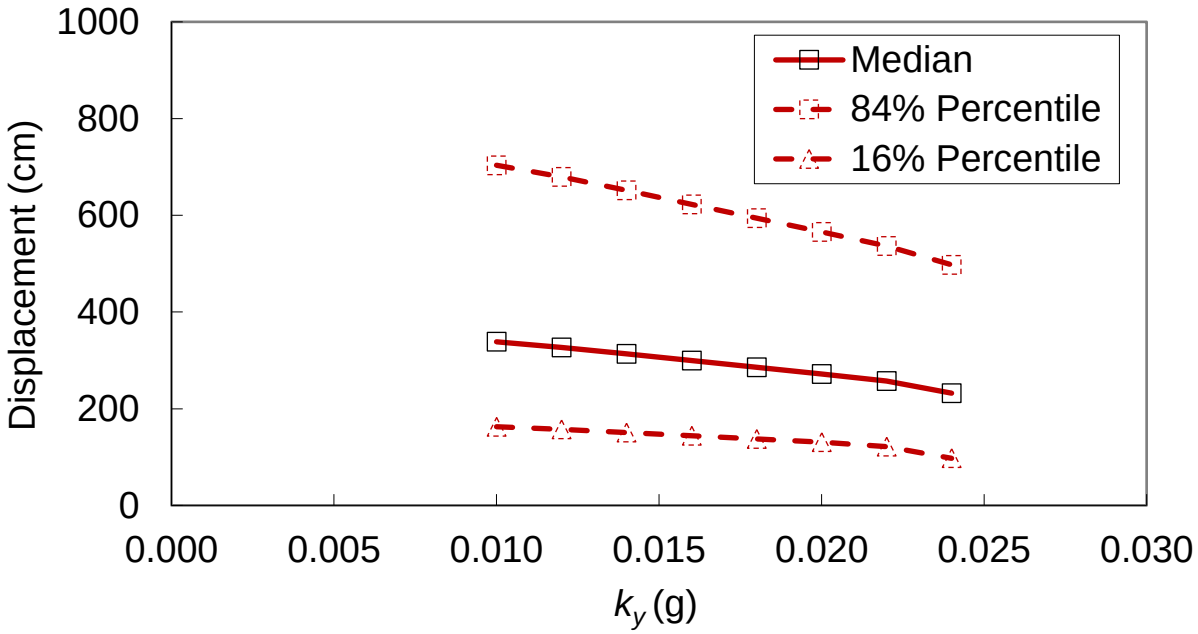

Figure 7.7. Estimates of slope displacement for the eastern slope of active river channel following Bray and Macedo (2019)

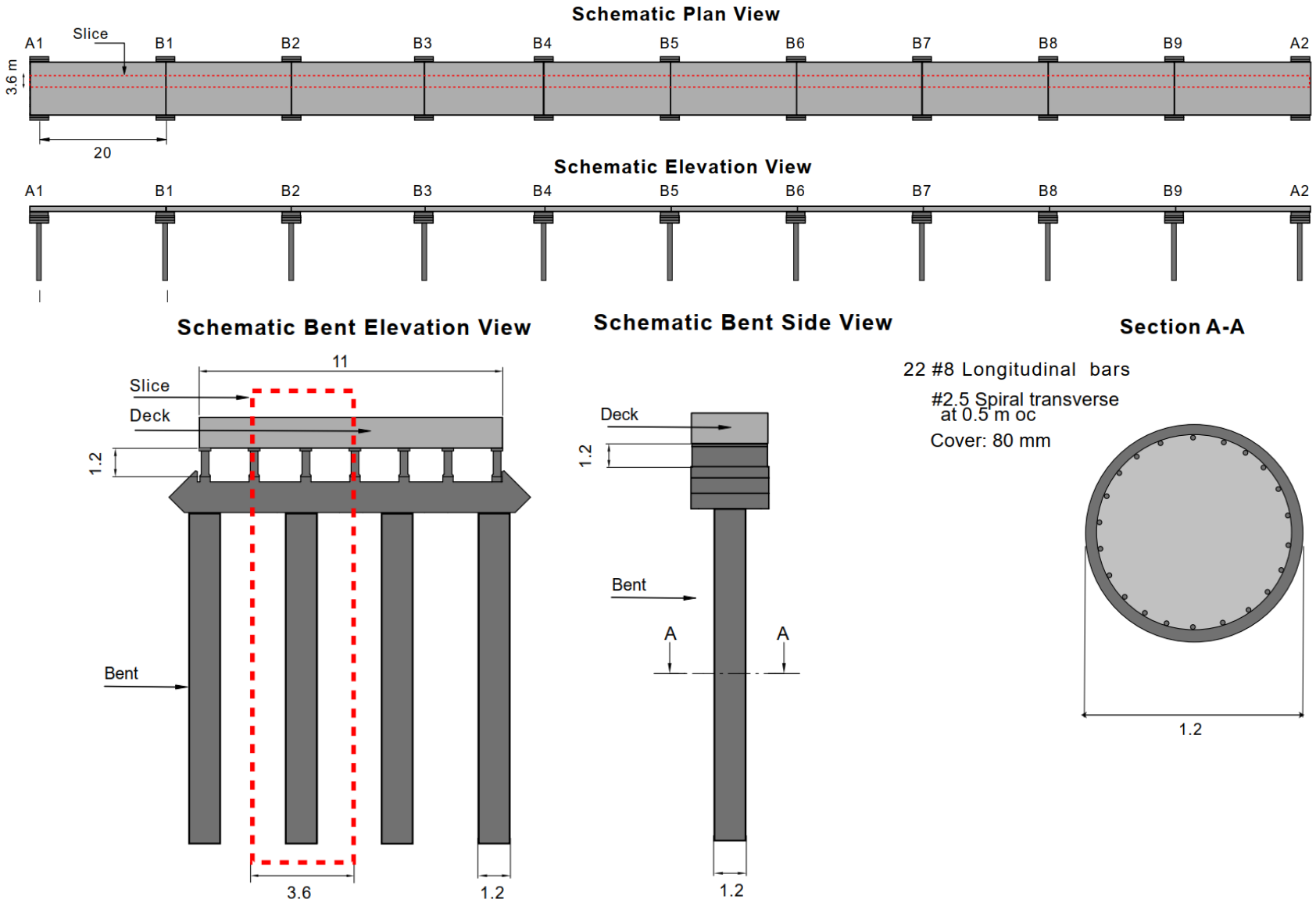

Figure 7.8. Salient structural features of the highway bridge (all dimensions are in m)

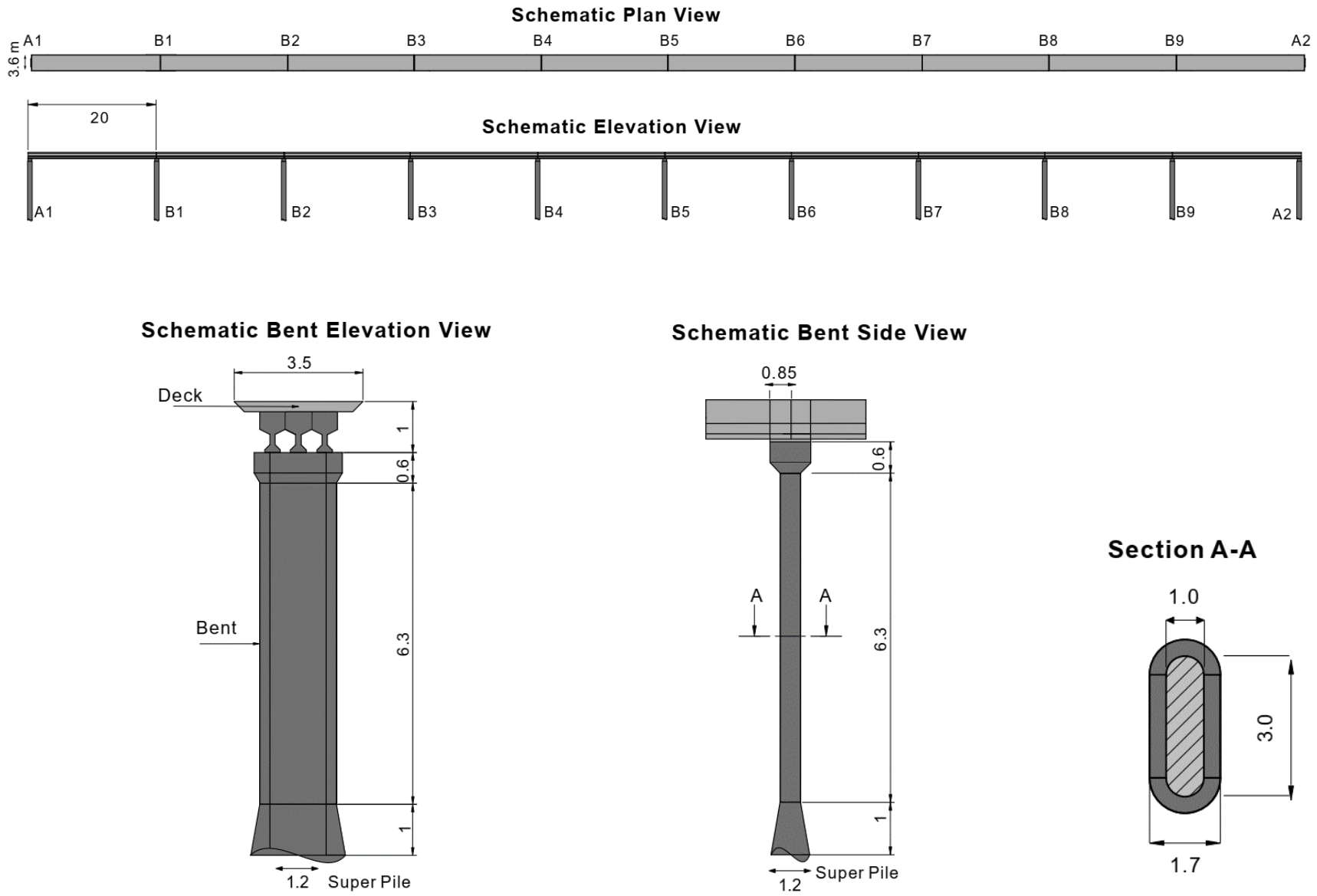

Figure 7.9. Salient structural features of the railroad bridge (all dimensions are in m)

(a) Nearly unseated Span at Bent B2 of Railroad bridge (b) Unseated Span at Bent B5 of Railroad bridge

Figure 7.10. Unseated span at (a) nearly unseated B1-B2 span at Bent B2, and (b) unseated B5-B6 span of the railroad bridge at Bent B5 (Photos by Scott Brandenberg)

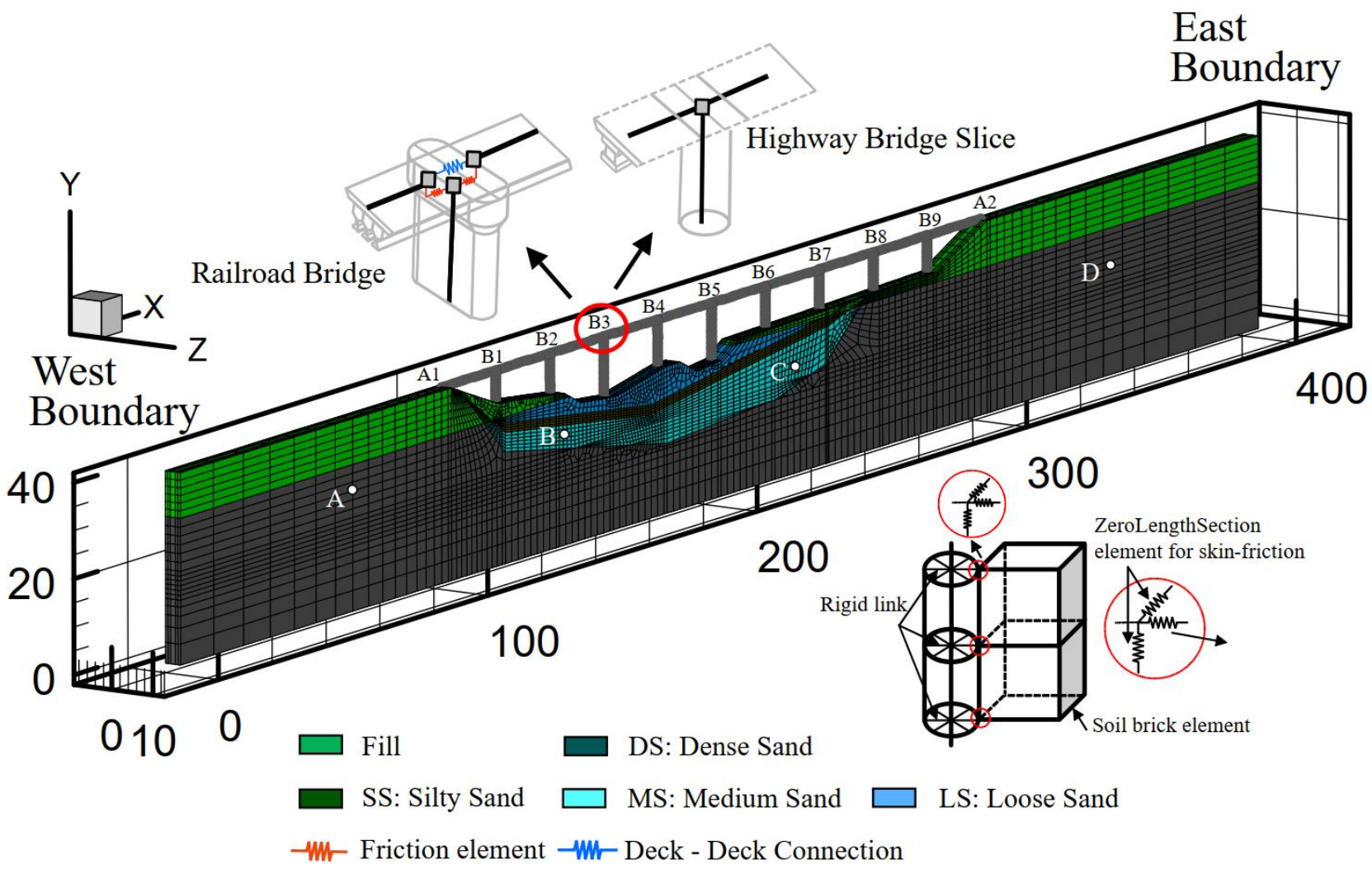

Figure 7.11. Mesh of the bridge ground system used in the analysis (colors represent soil layers)

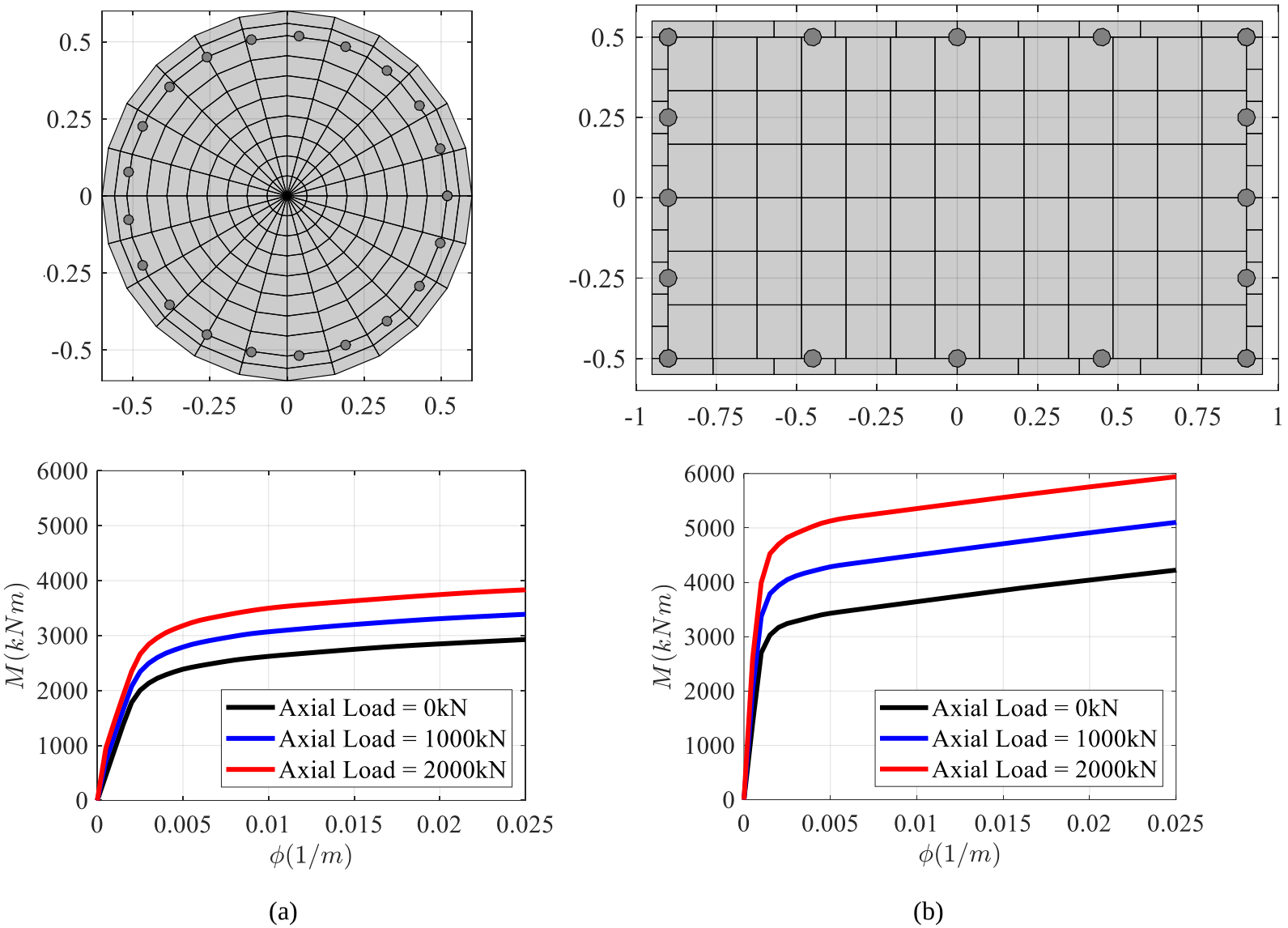

Figure 7.12. Section and the moment-curvature response of the piers of the (a) HWB and (b) RRB

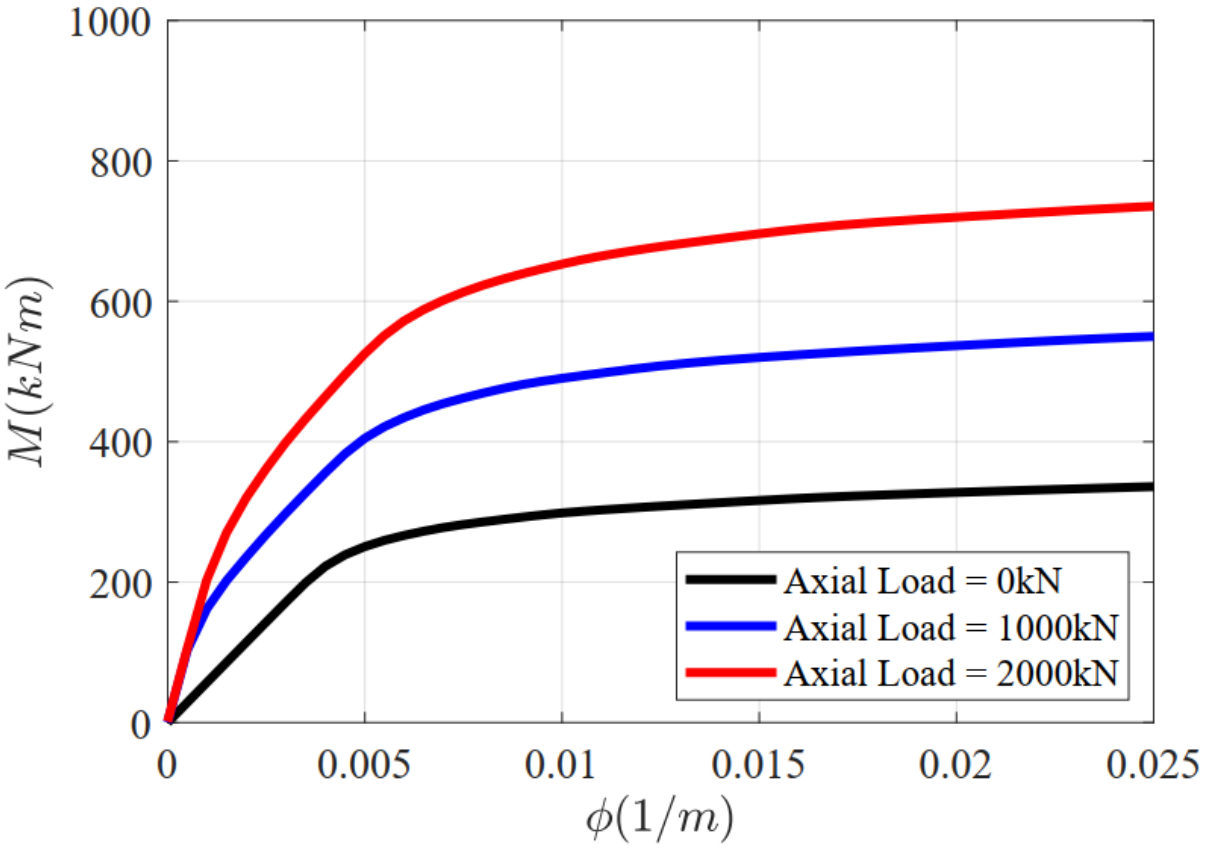

Figure 7.13. Employed moment-curvature relationship for the railroad bridge super pile.

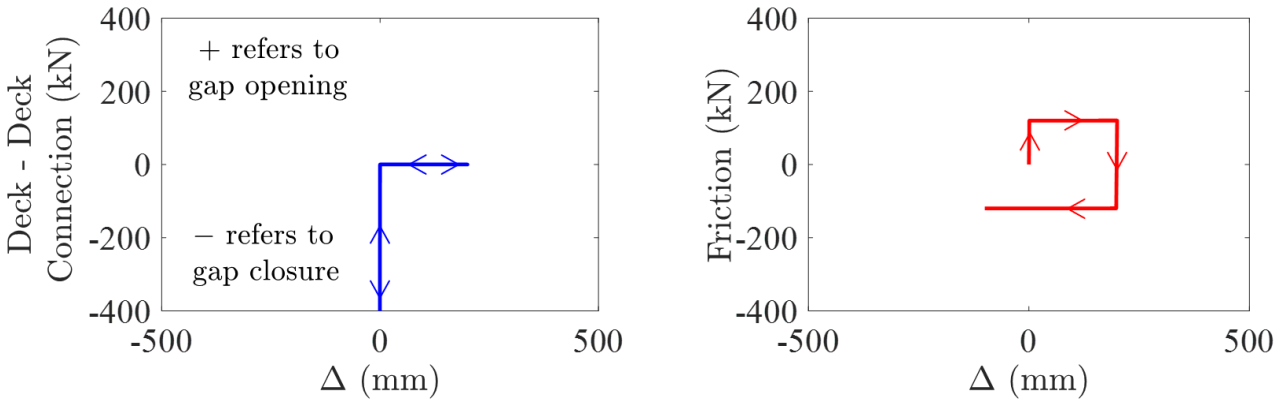

Figure 7.14. Interface elements between bent and deck of railroad bridge (a) deck-deck connection and (b) friction element

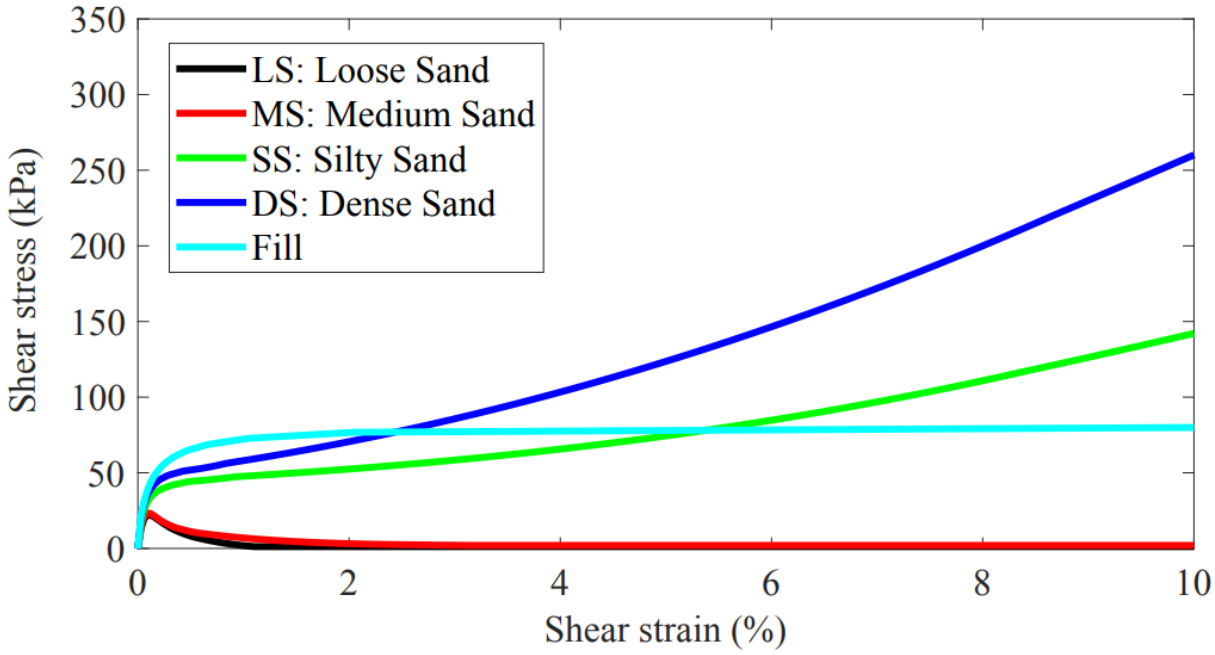

Figure 7.15. Undrained monotonic shear stress strain curves for each layer at a vertical stress of 1 atm

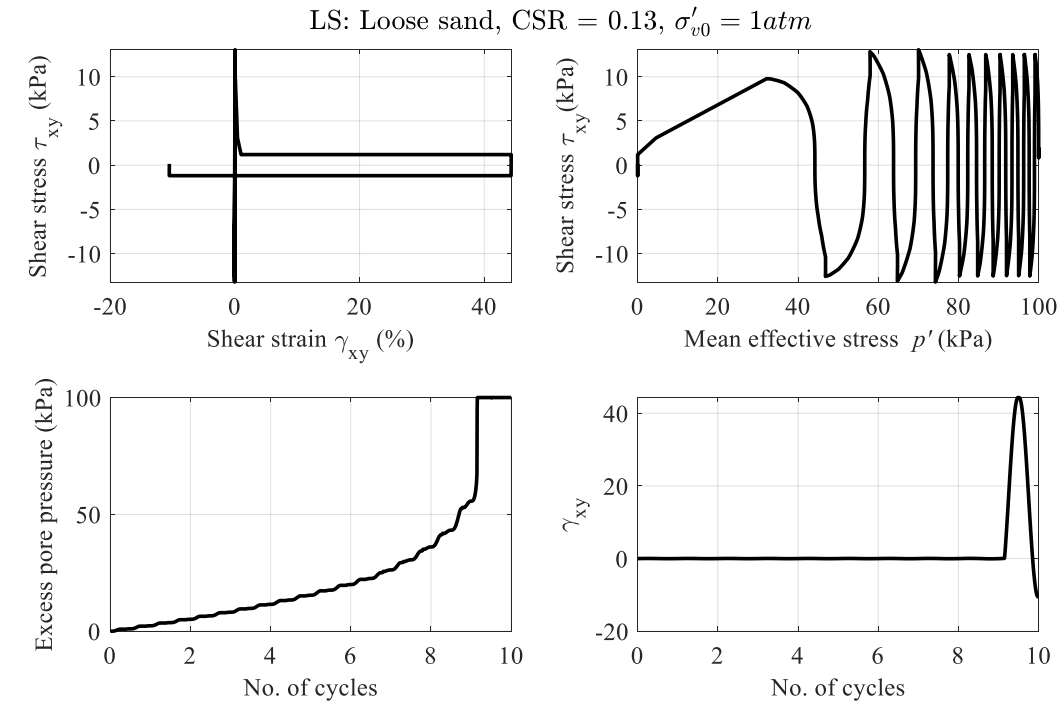

(a) LS (at a CSR of 0.13)

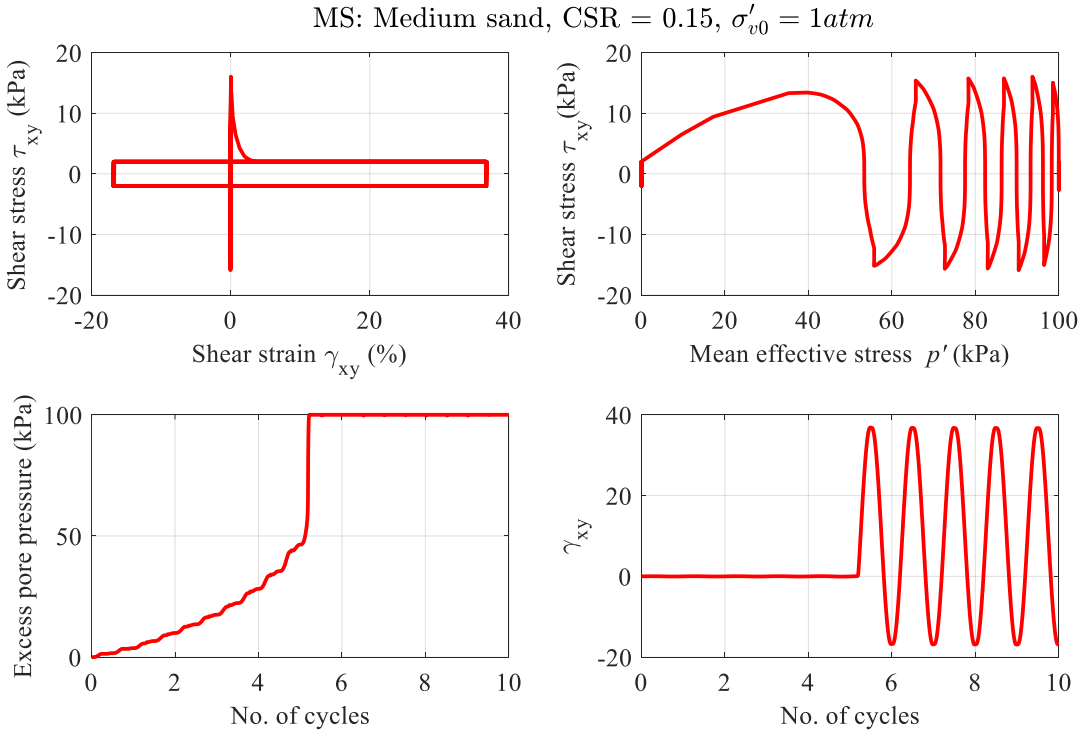

(b) MS (at a CSR of 0.15)

Figure 7.16. Cyclic stress controlled simple shear element simulations for (a) LS (at a CSR of 0.13), (b) (b) MS (at a CSR of 0.15), (c) SS (at a CSR of 0.2), and (d) DS (at a CSR of 0.4)

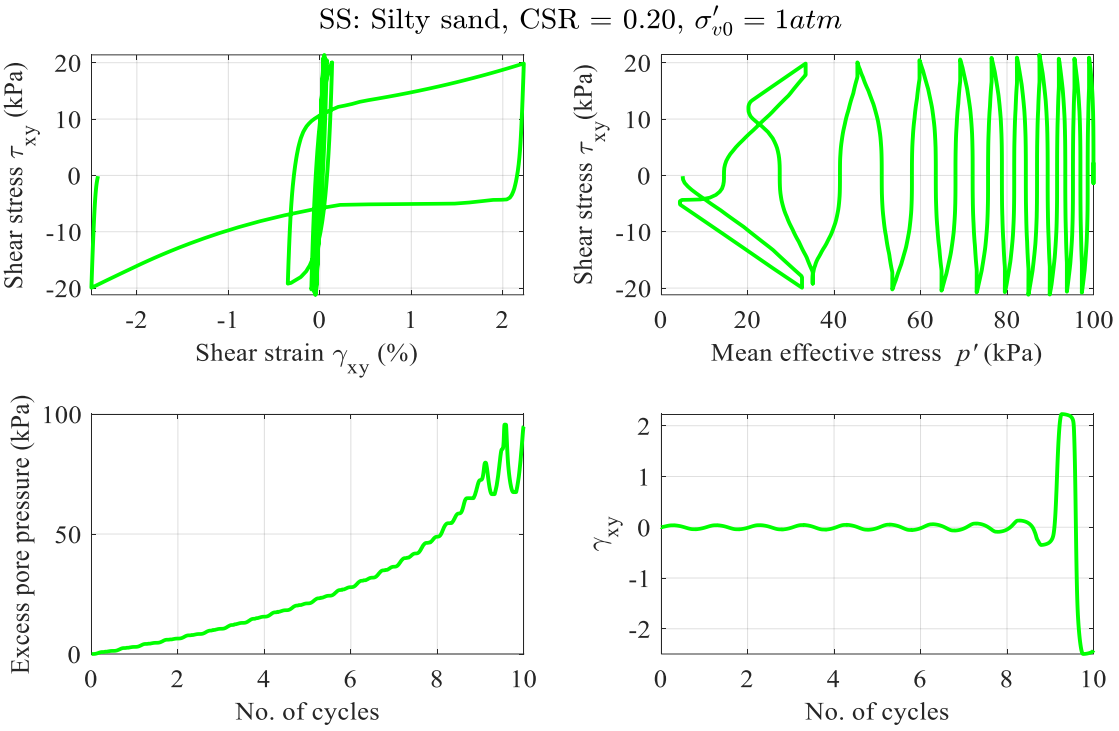

(c) SS (at a CSR of 0.2)

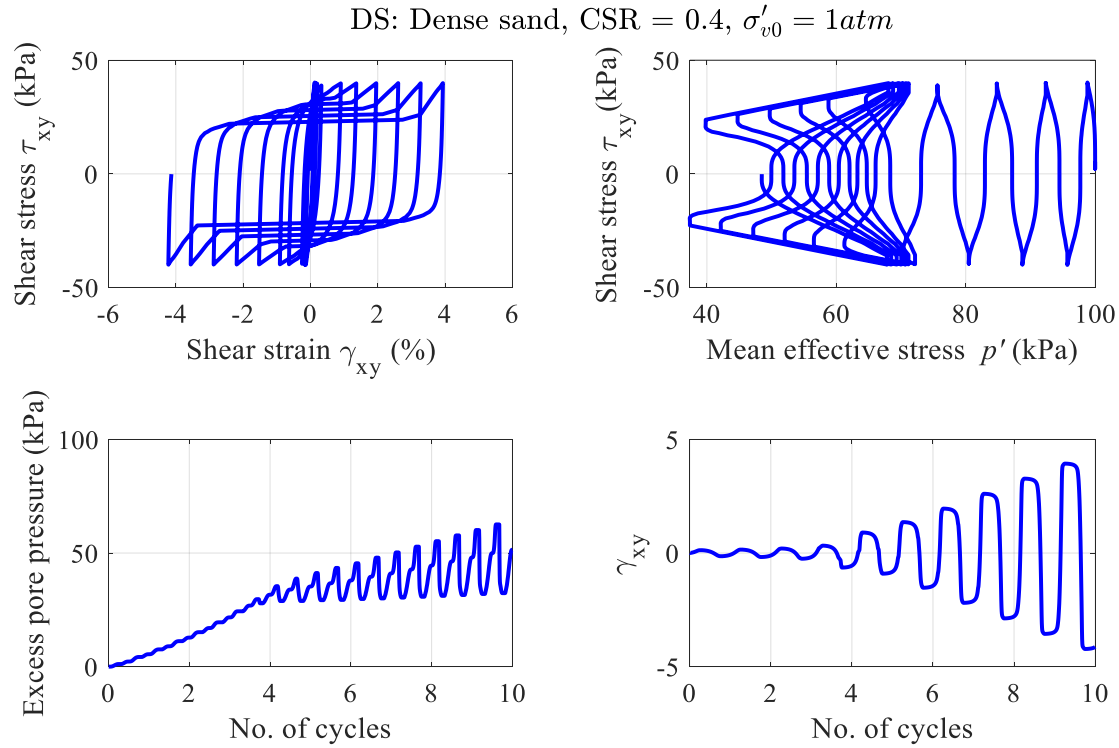

(d) DS (at a CSR of 0.4)

Figure 7.16 (continued). Cyclic stress controlled simple shear element simulations for (a) LS (at a CSR of 0.13), (b) (b) MS (at a CSR of 0.15), (c) SS (at a CSR of 0.2), and (d) DS (at a CSR of 0.4)

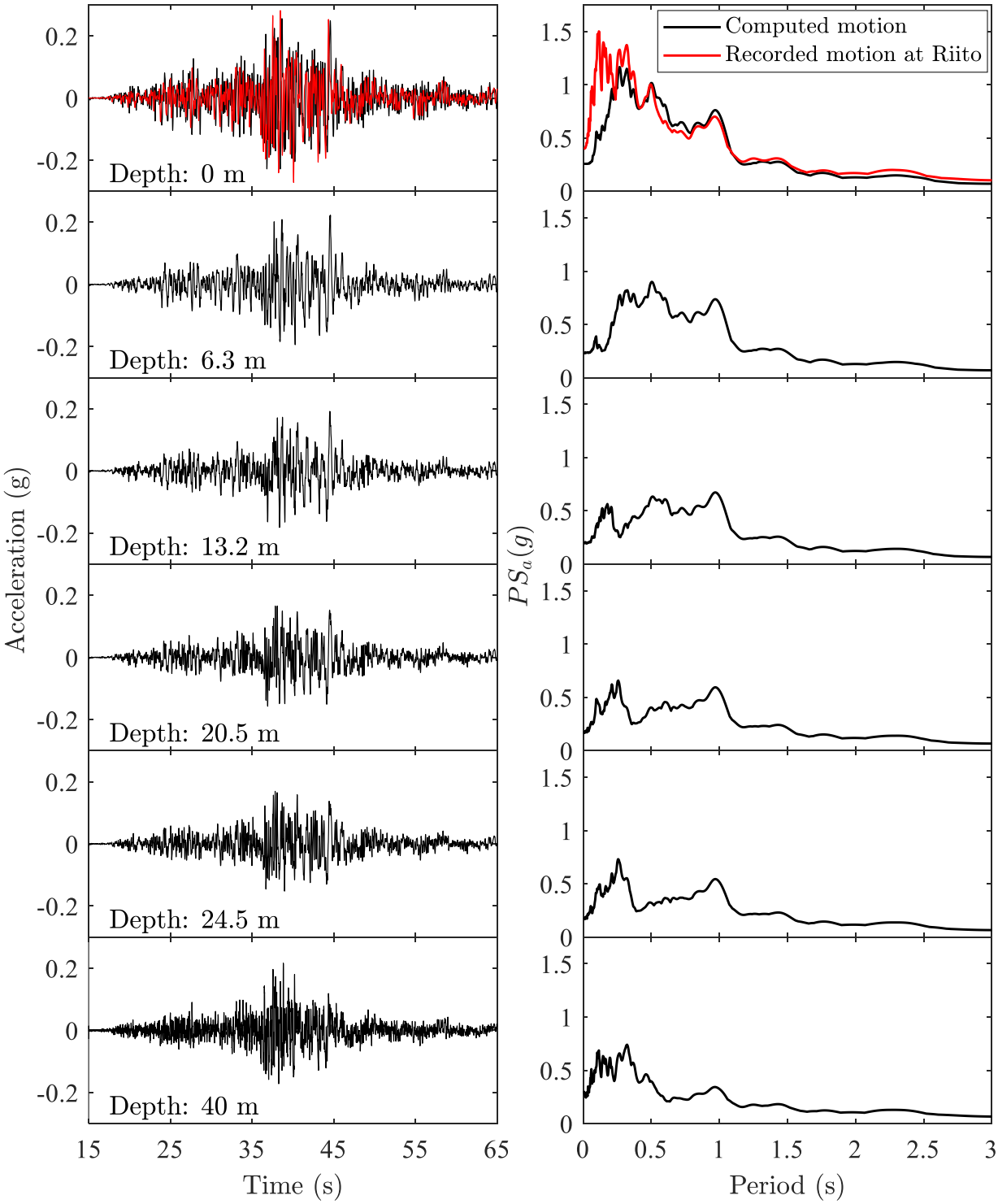

Figure 7.17. Computed acceleration at east and west boundaries of the model along shear beam (recorded motion at top is lowpass filtered at 20 Hz)

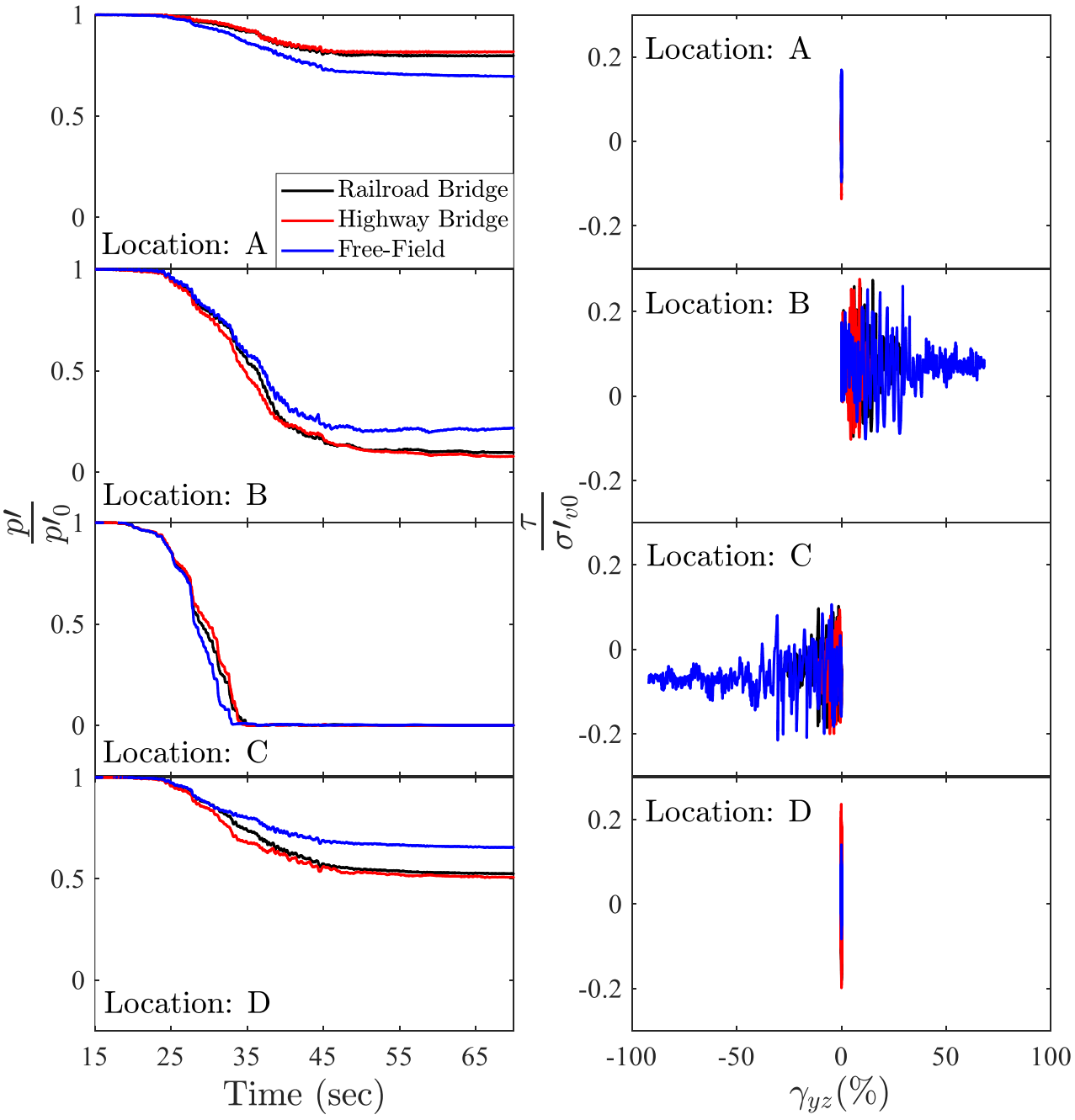

Figure 7.18. Computed soil confinement histories and shear stress-strain response for the Railroad bridge, Highway bridge, and free field at different locations within the canyon (locations are shown in Figure 7.11)

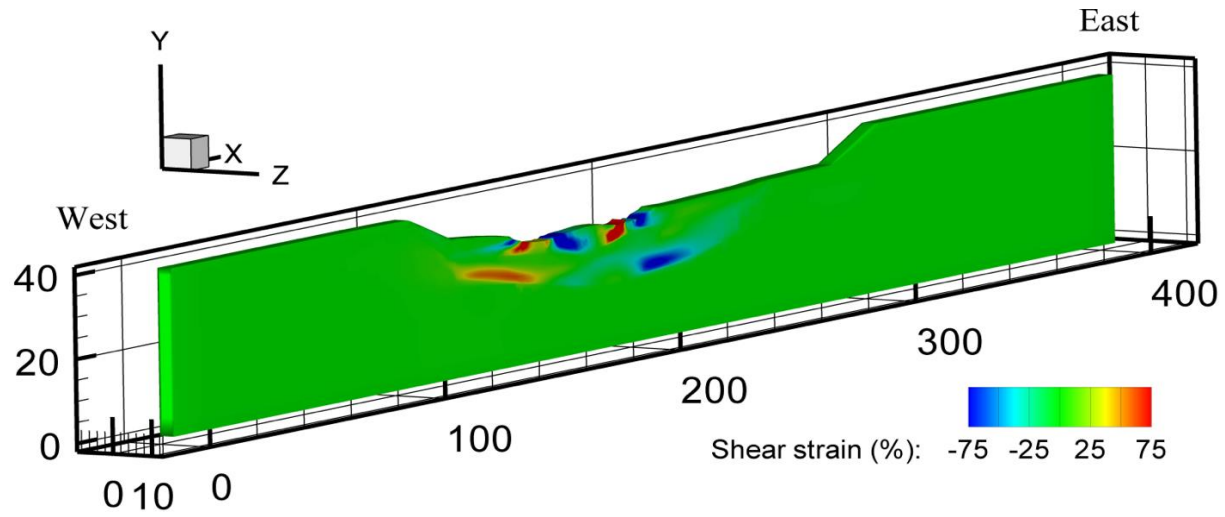

(a) Shear strains at freefield at the end of shaking.

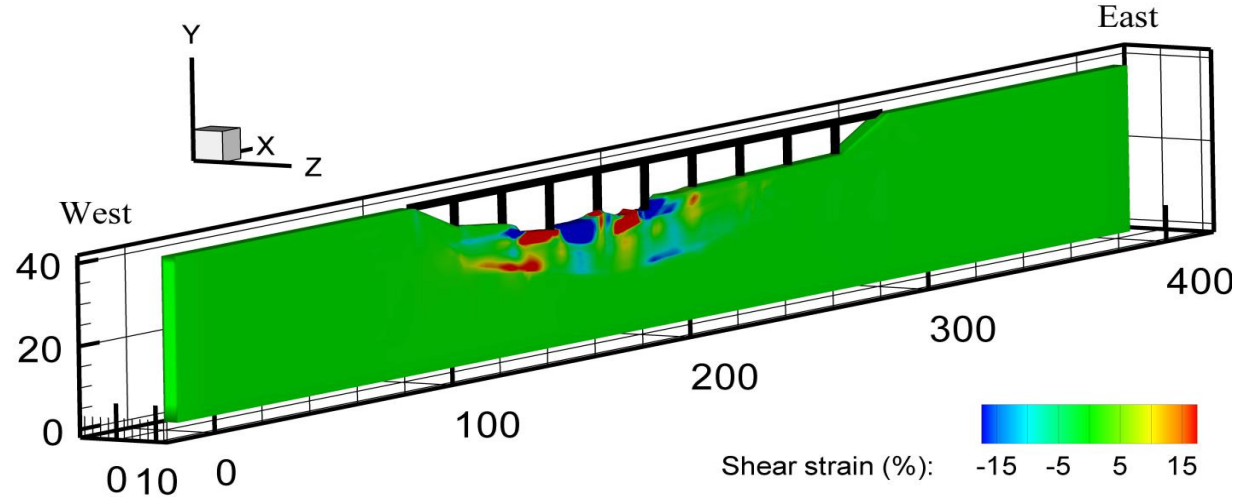

(b) Shear strains at highway bridge-canyon system at end of shaking

Figure 7.19. Shear strain profiles at (a) free field (without influence of bridge), (b) highway bridge-canyon system at end of shaking, and (c) railroad bridge at end of shaking

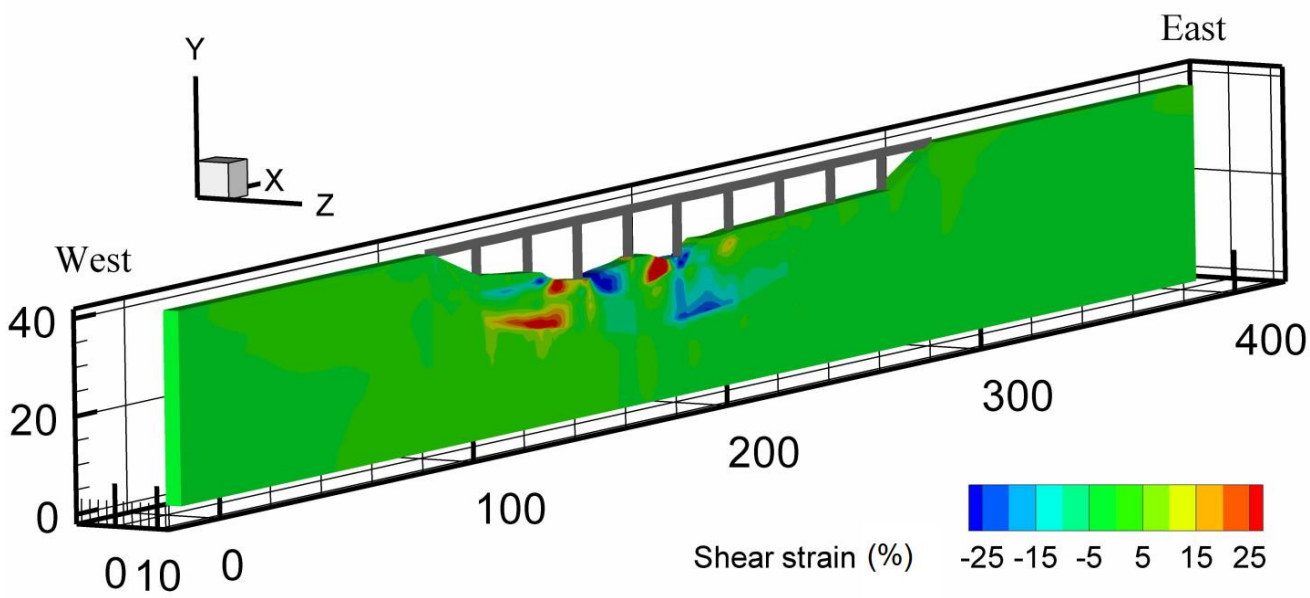

(c) Shear strains at railroad bridge at end of shaking

Figure 7.19 (continued). Shear strain profiles at (a) free field (without influence of bridge), (b) highway bridge-canyon system at end of shaking, and (c) railroad bridge at end of shaking

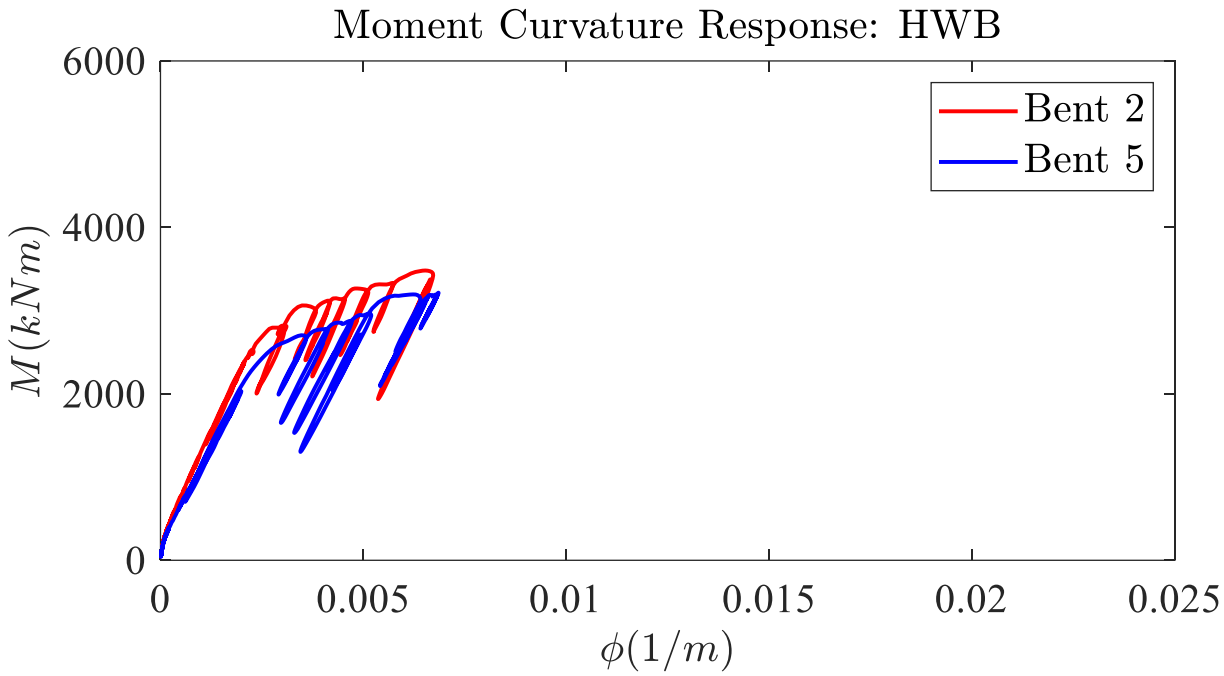

(a) Moment curvature demands on foundation of highway bridge

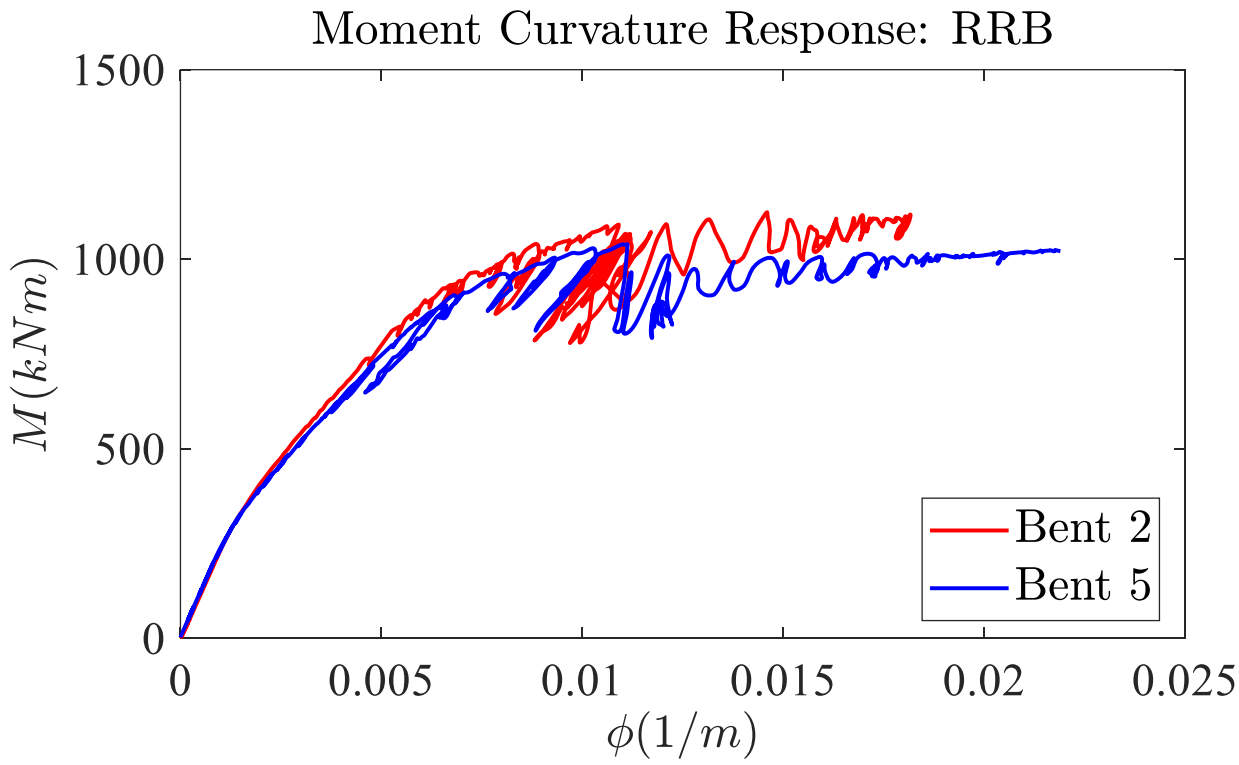

(b) Moment curvature demands of railroad bridge piles (at the location of peak moment)

Figure 7.20. Moment curvature demands on foundations of (a)highway bridge and (b) railroad bridge

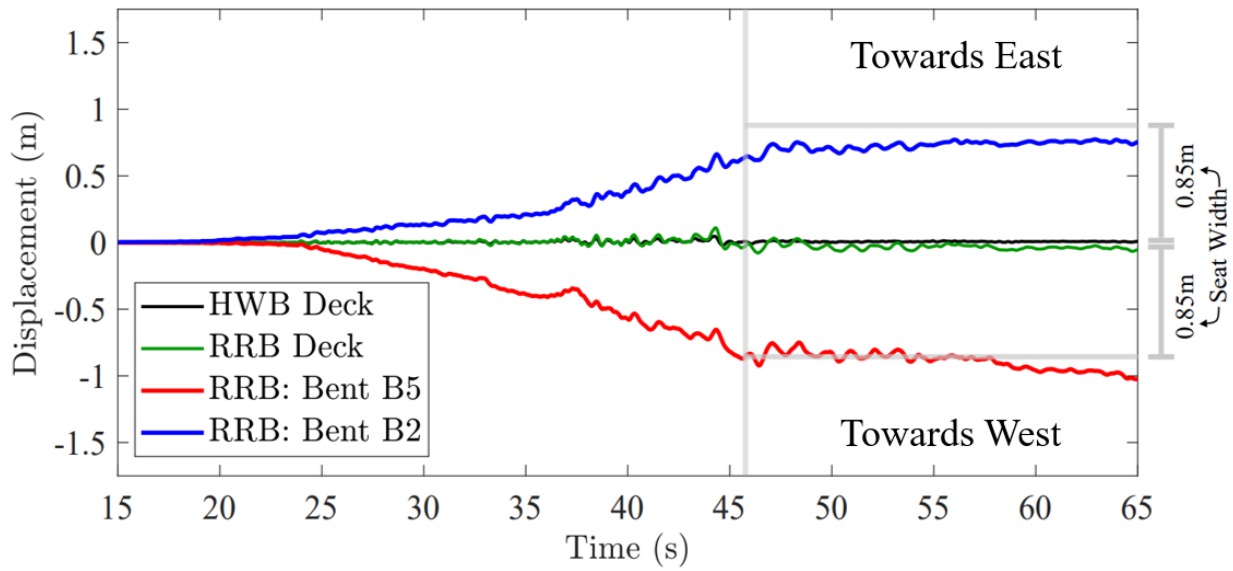

Figure 7.21. Computed deck displacements for the HWB, RRB and top of RRB bents B2 and B5 towards river channel.

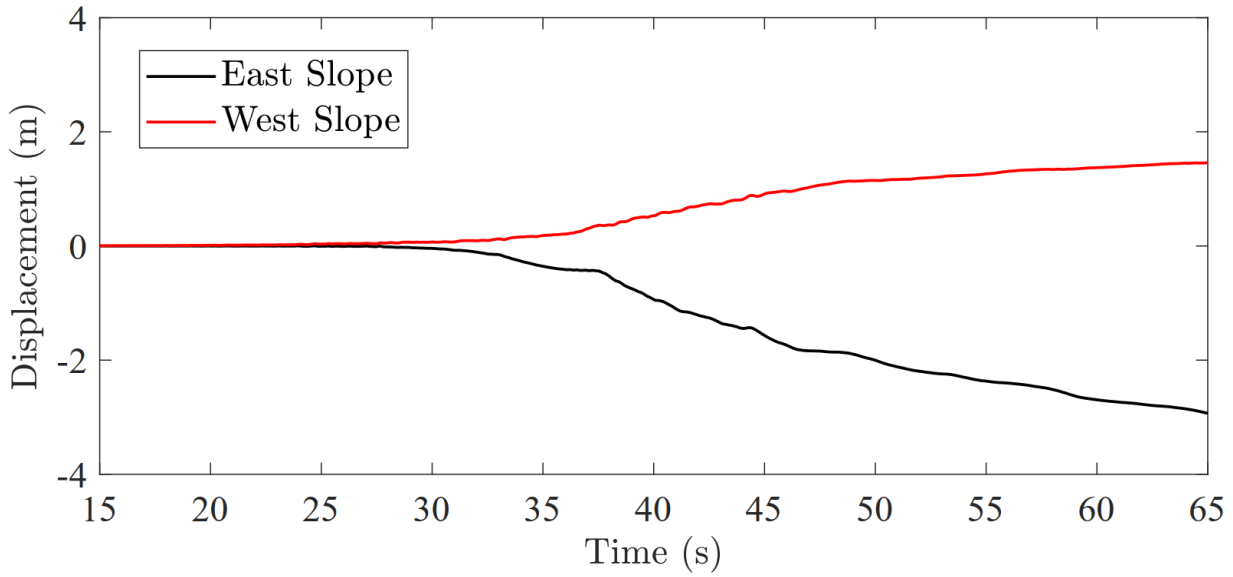

Figure 7.22. Computed soil displacement histories on east and west slopes of the active river channel

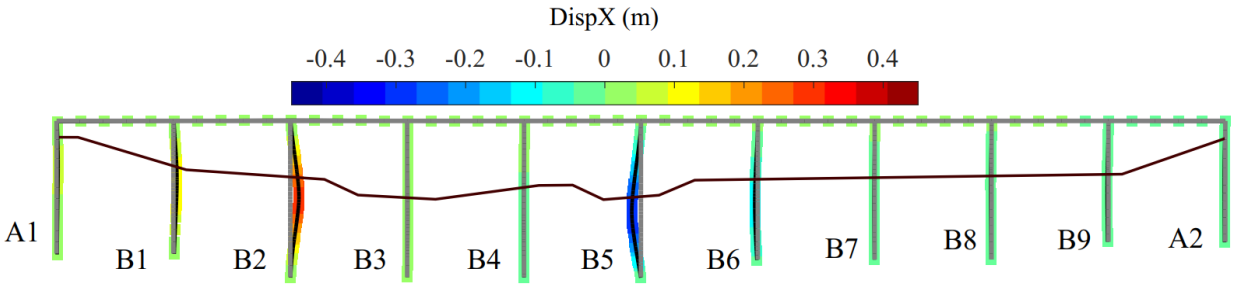

Figure 7.23. Deformed configuration of the highway bridge at the end of shaking. (Deformations scaled by a factor of 5 in figure)

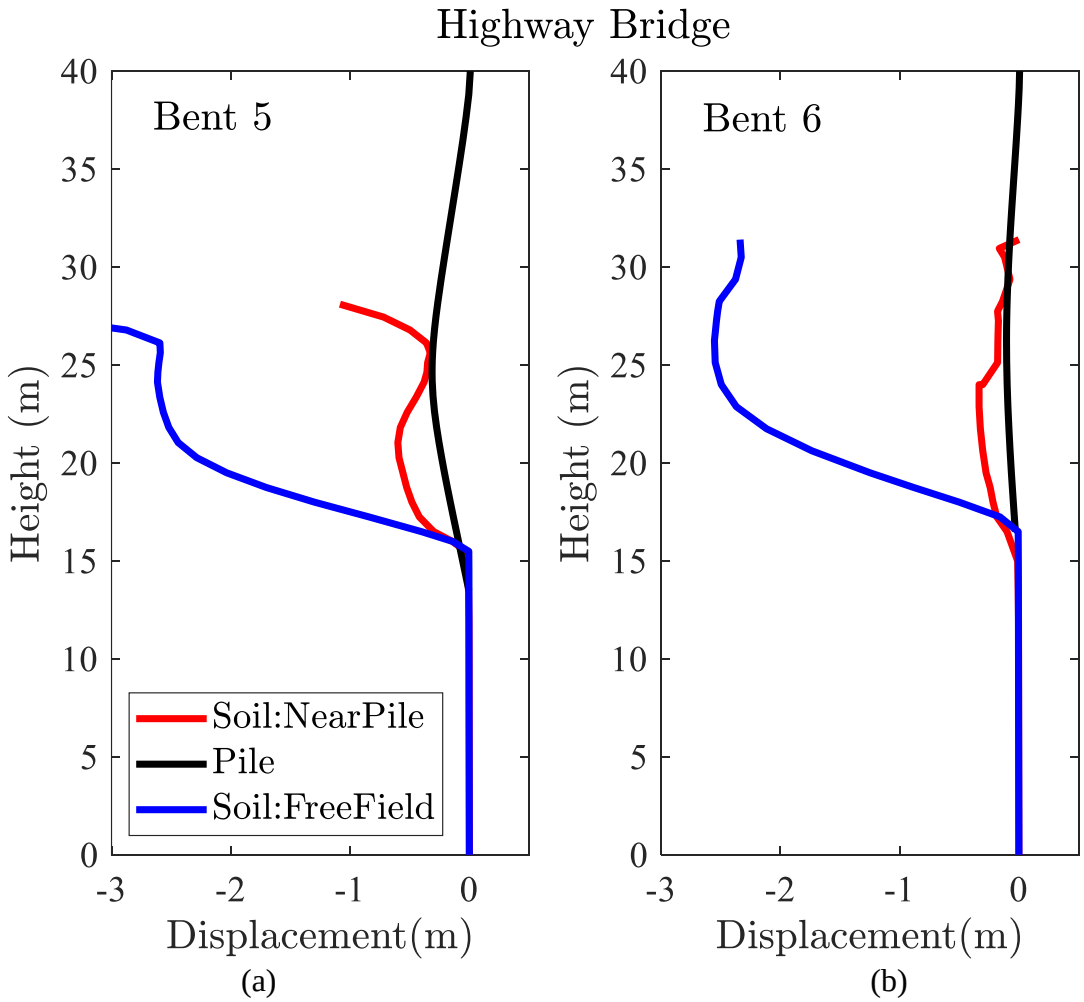

Figure 7.24. Configuration of deformed soil in free field, near pile and piers for bents (a) B5 and (b) B6 at the end of shaking for the highway bridge

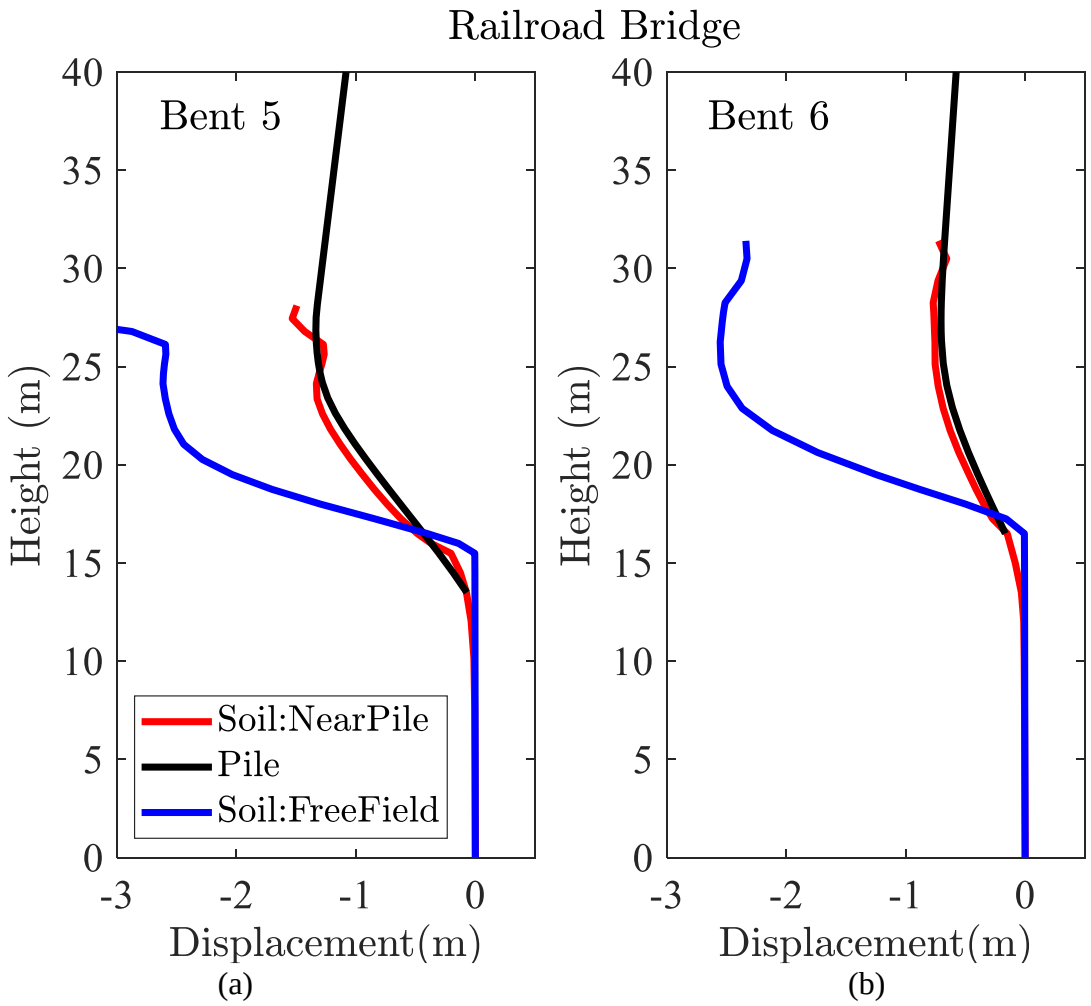

Figure 7.25. Configuration of deformed soil in free field, near pile and piers for bents (a) B5 and (b) B6 at end of shaking for the railroad bridge

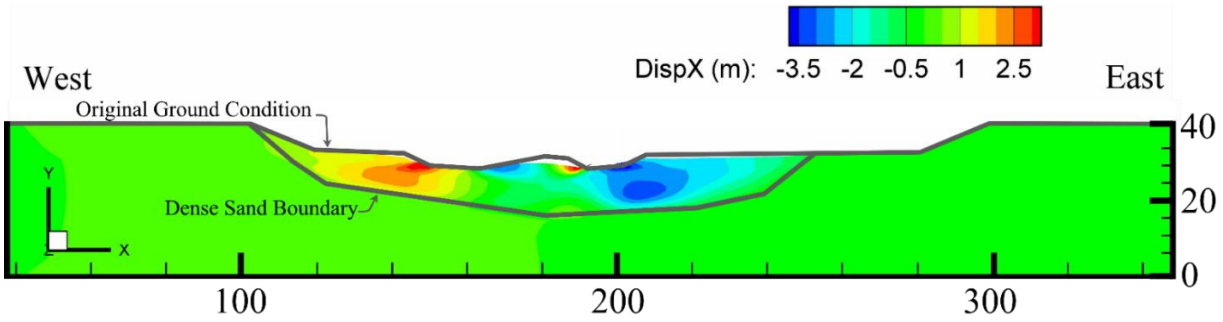

(c) Free field (without influence of bridge)

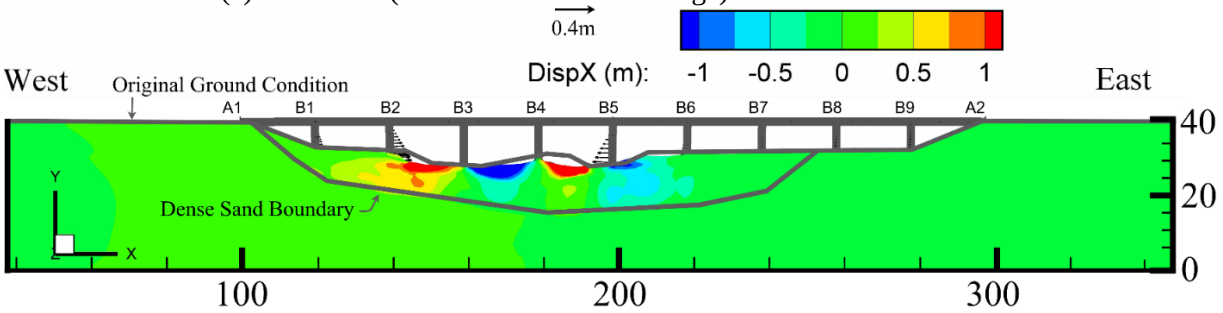

(d) Highway bridge-canyon system at end of shaking

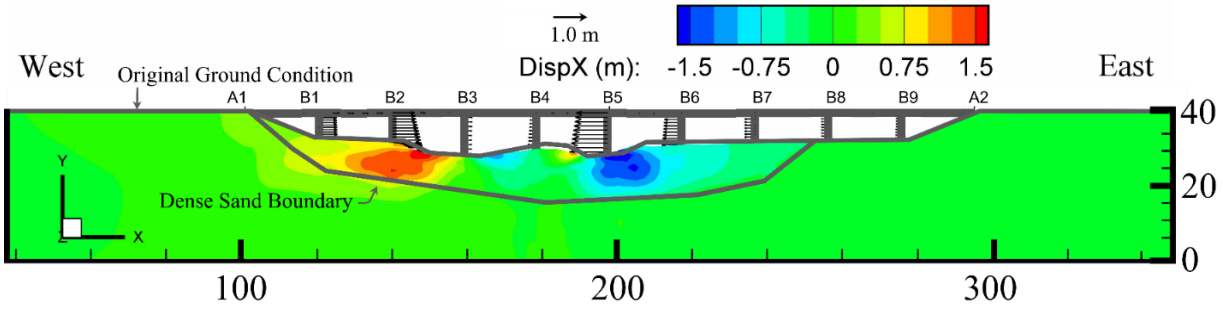

(e) Railroad bridge-canyon system at end of shaking

Figure 7.26. Displaced Configurations at end of shaking (a) free field (without influence of bridge), (b) highway bridge-canyon system, and (c) railroad bridge-canyon system

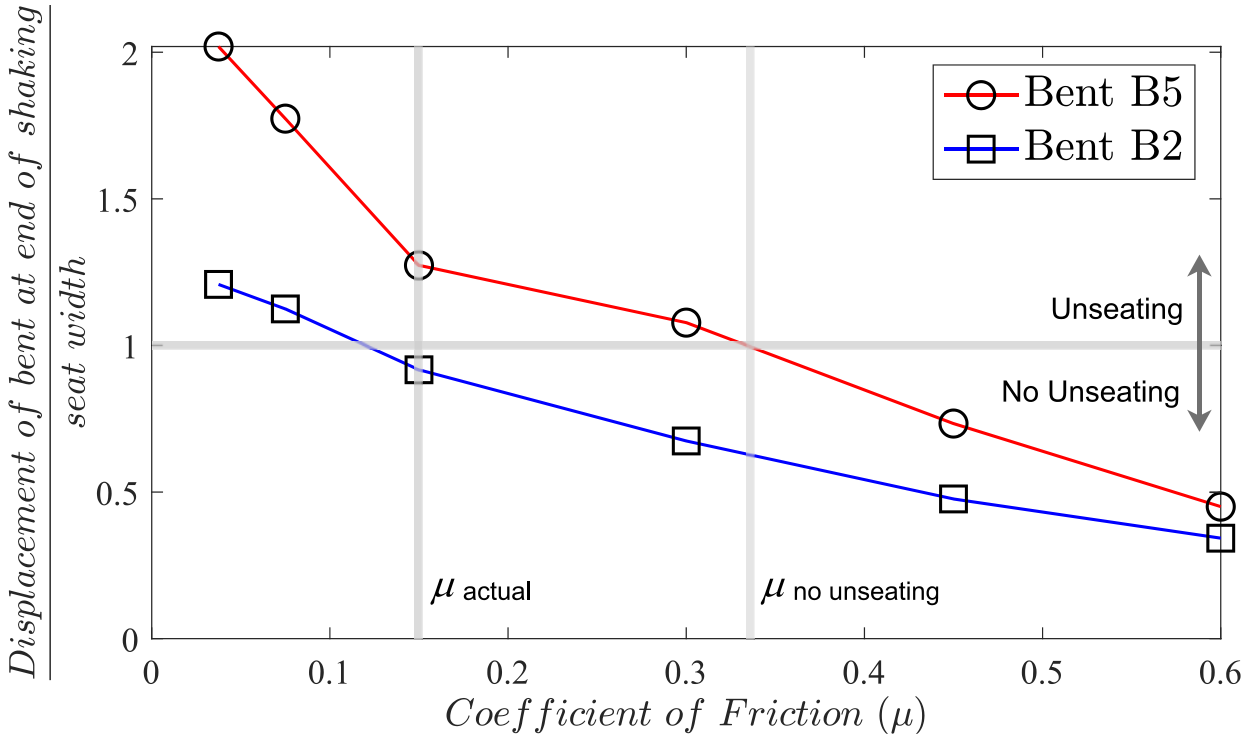

Figure 7.27. Displacement at the top of Bents 2 and 5 of the railroad bridge with different levels of friction.

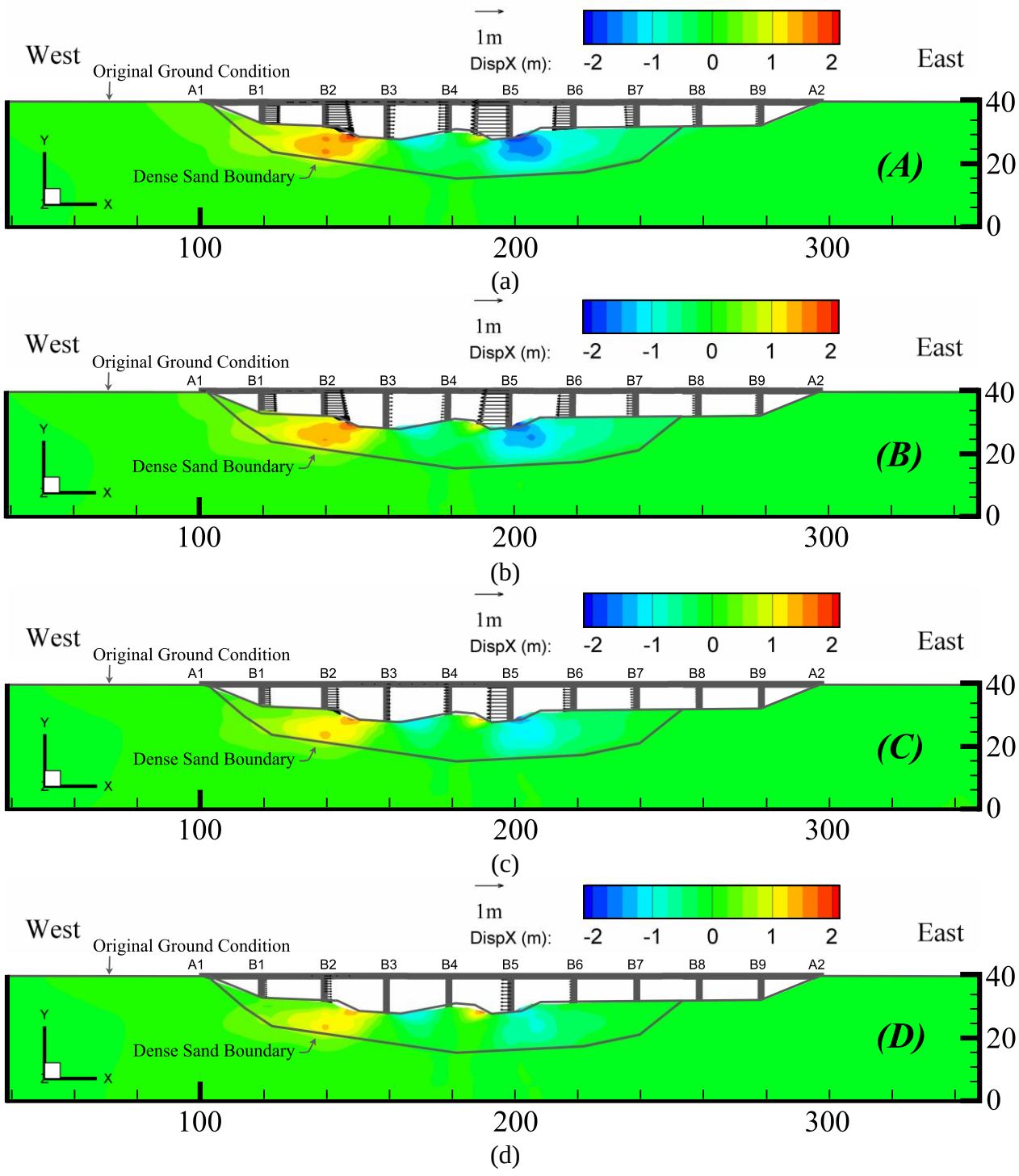

Figure 7.28. Deformed profiles of the railroad bridge-canyon system at end of shaking for a deck-bent friction coefficient of (a) 0.075, (b) 0.15, (c) 0.3, and (d) 0.6. (all dimensions are in m)

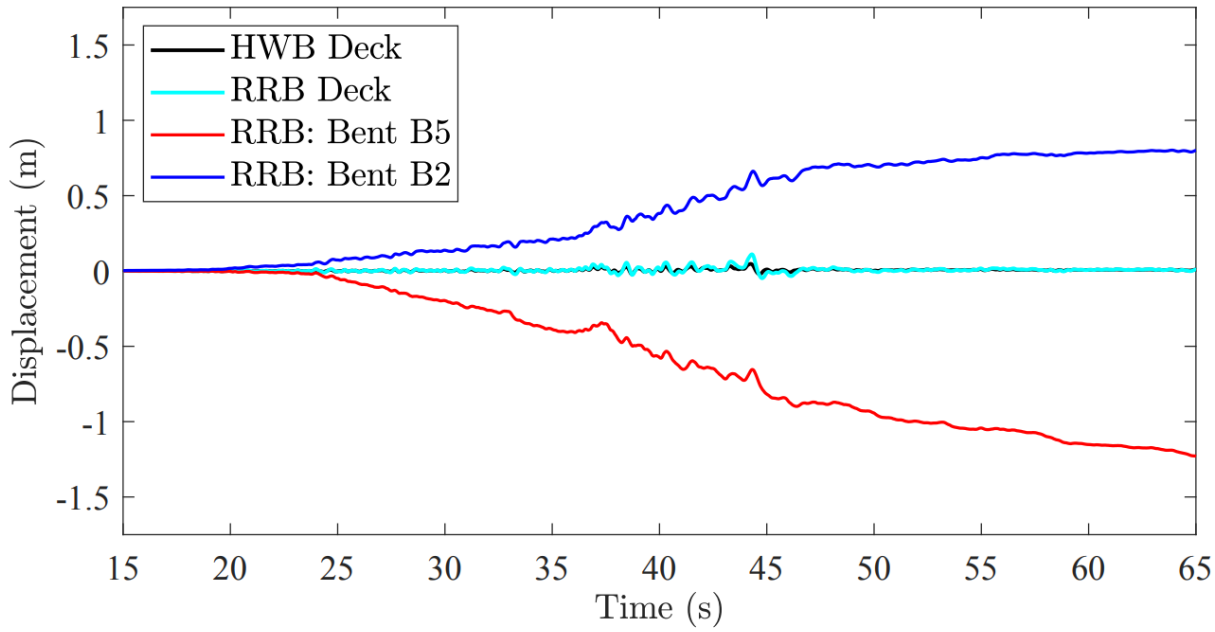

Figure 7.29. Computed deck displacements for the HWB, RRB and top of RRB bents B2 and B5 towards river channel (precluding unseating of span B5-B6).

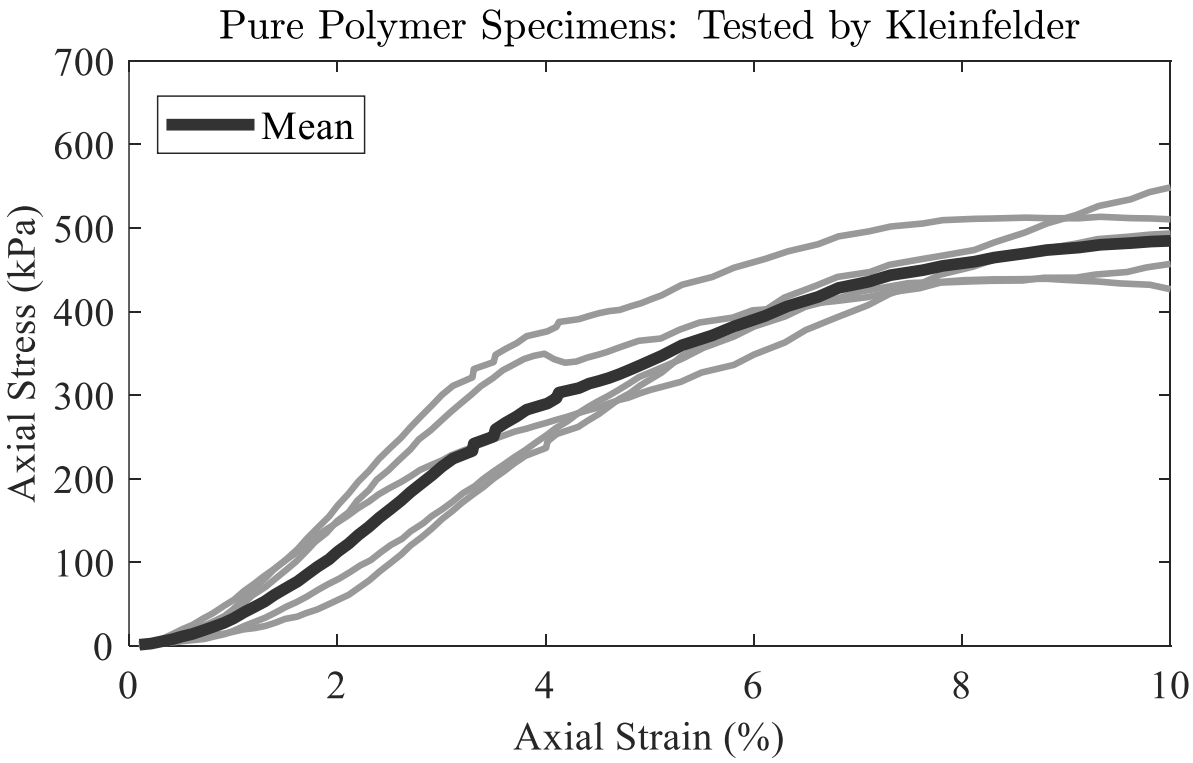

Figure 7.30. Stress strain response of pure polymer specimens (from Kleinfelder 2019)

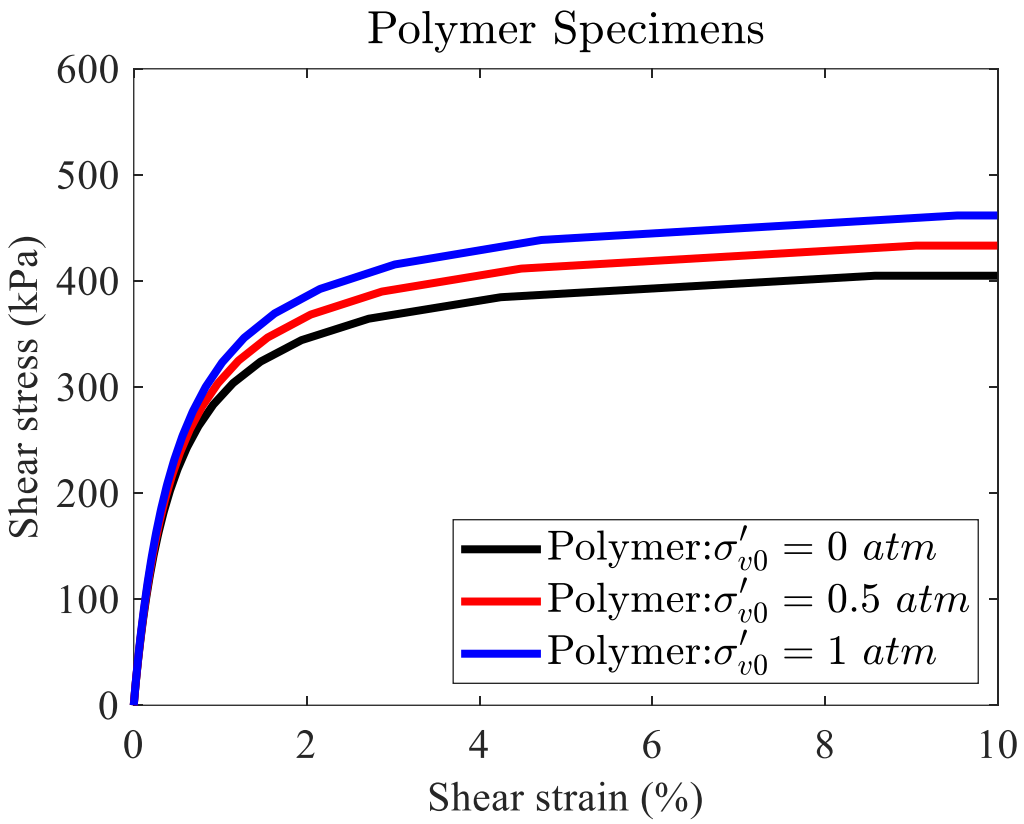

Figure 7.31. Monotonic shear stress-strain curves for the polymer-sand composite

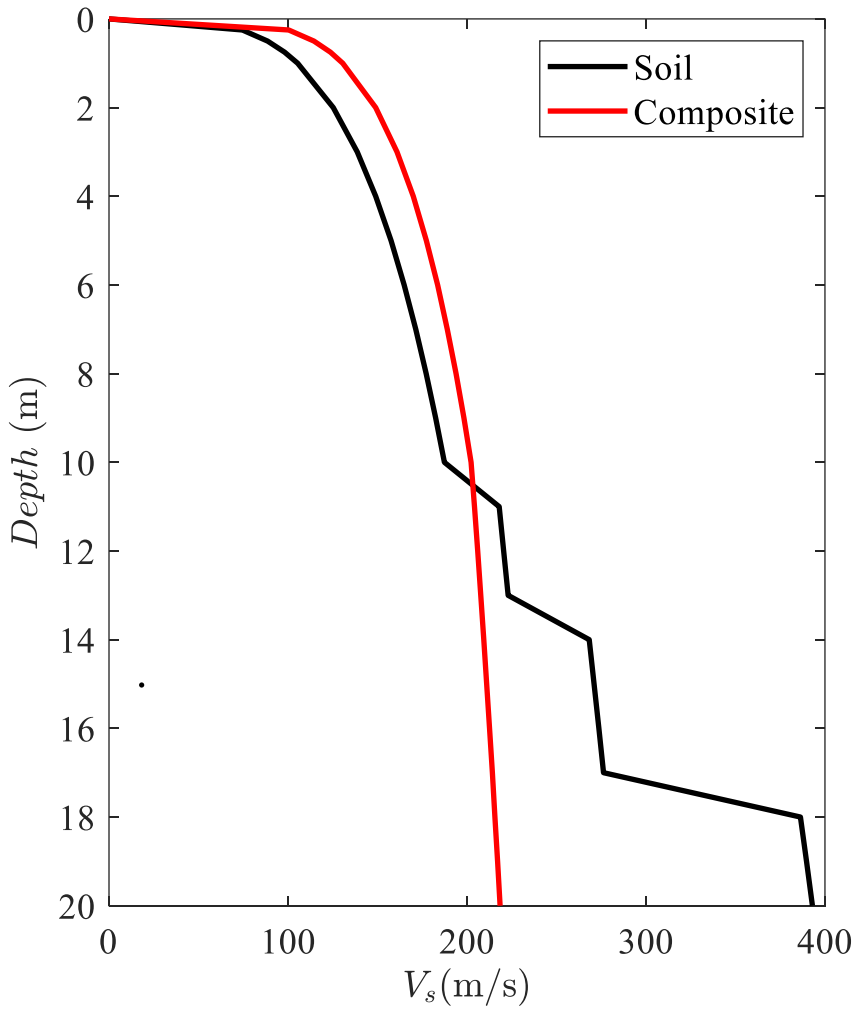

Figure 7.32. Shear wave velocity (V_s) of deposit and polymer-sand composite

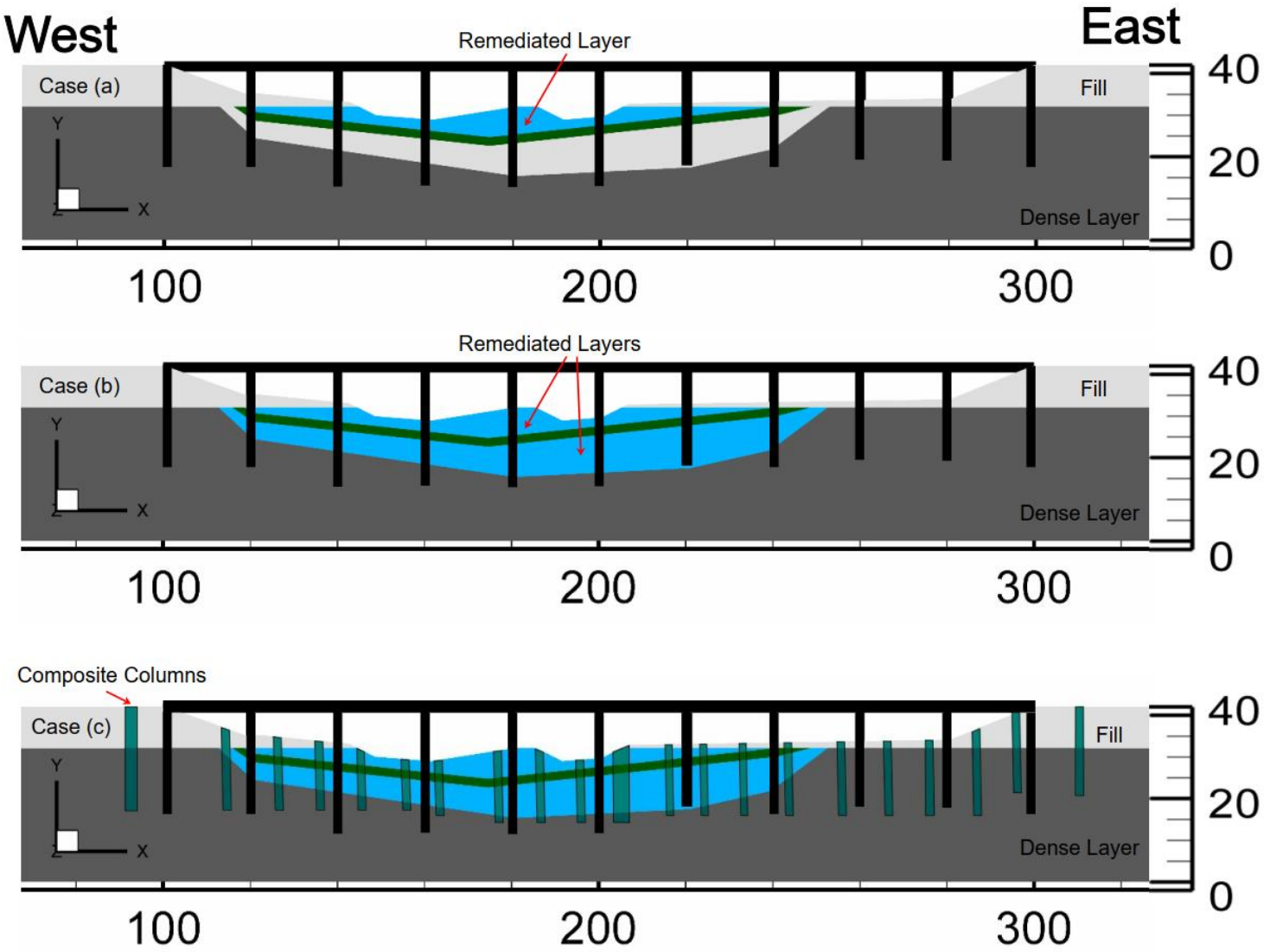

Figure 7.33. Insitu ground modification measures for the railroad bridge: remediation of (a) Layer LS (shallow liquefiable layer) along bridge footprint, (b)Layers LS, SS, and MS (along bridge footprint (c) grout inclusions.

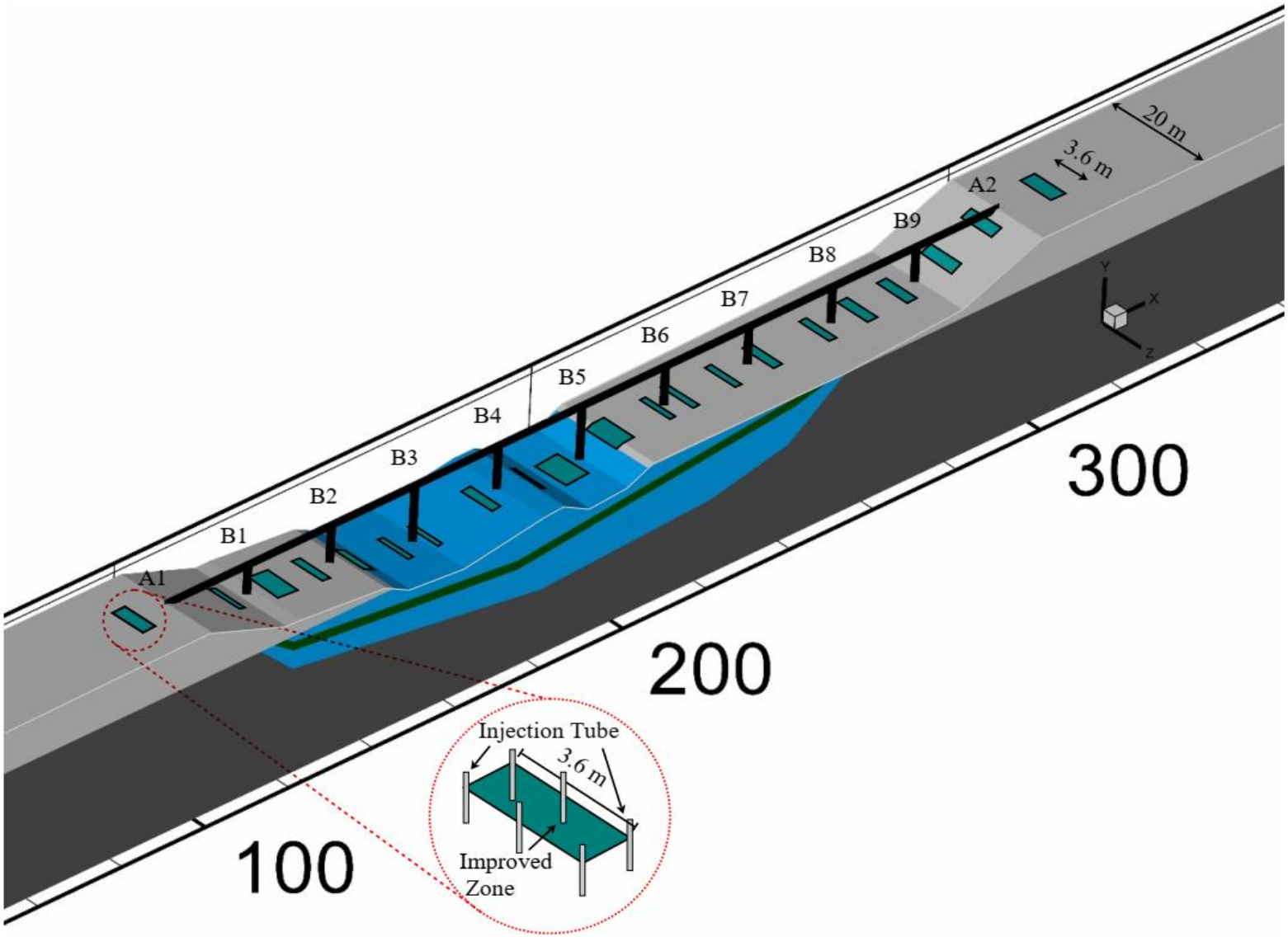

Figure 7.34. Insitu ground modification using grout inclusions (layout of injection is presented)

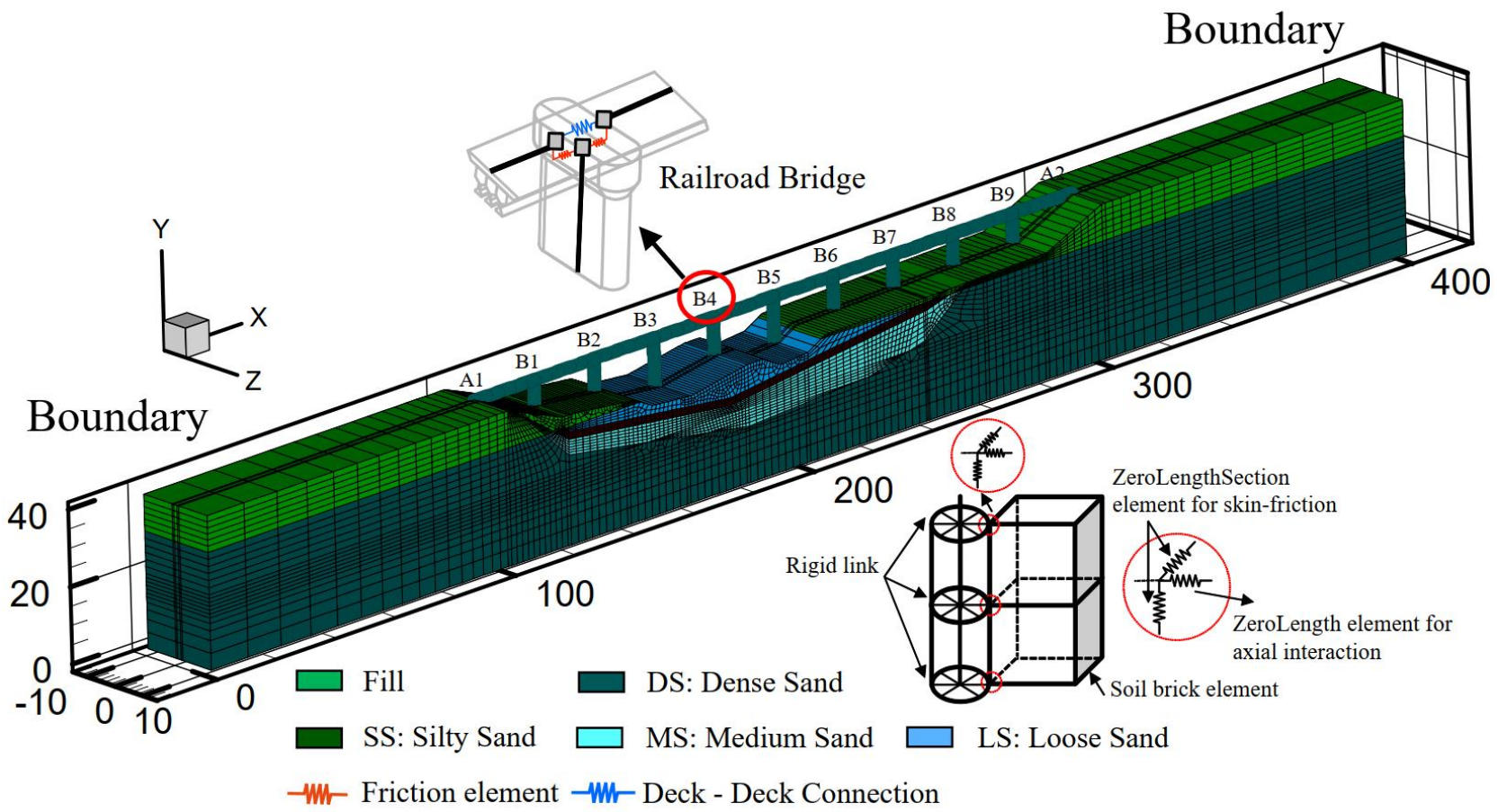

Figure 7.35. Expanded mesh of the railroad bridge -ground system employed in the simulations with ground remediation

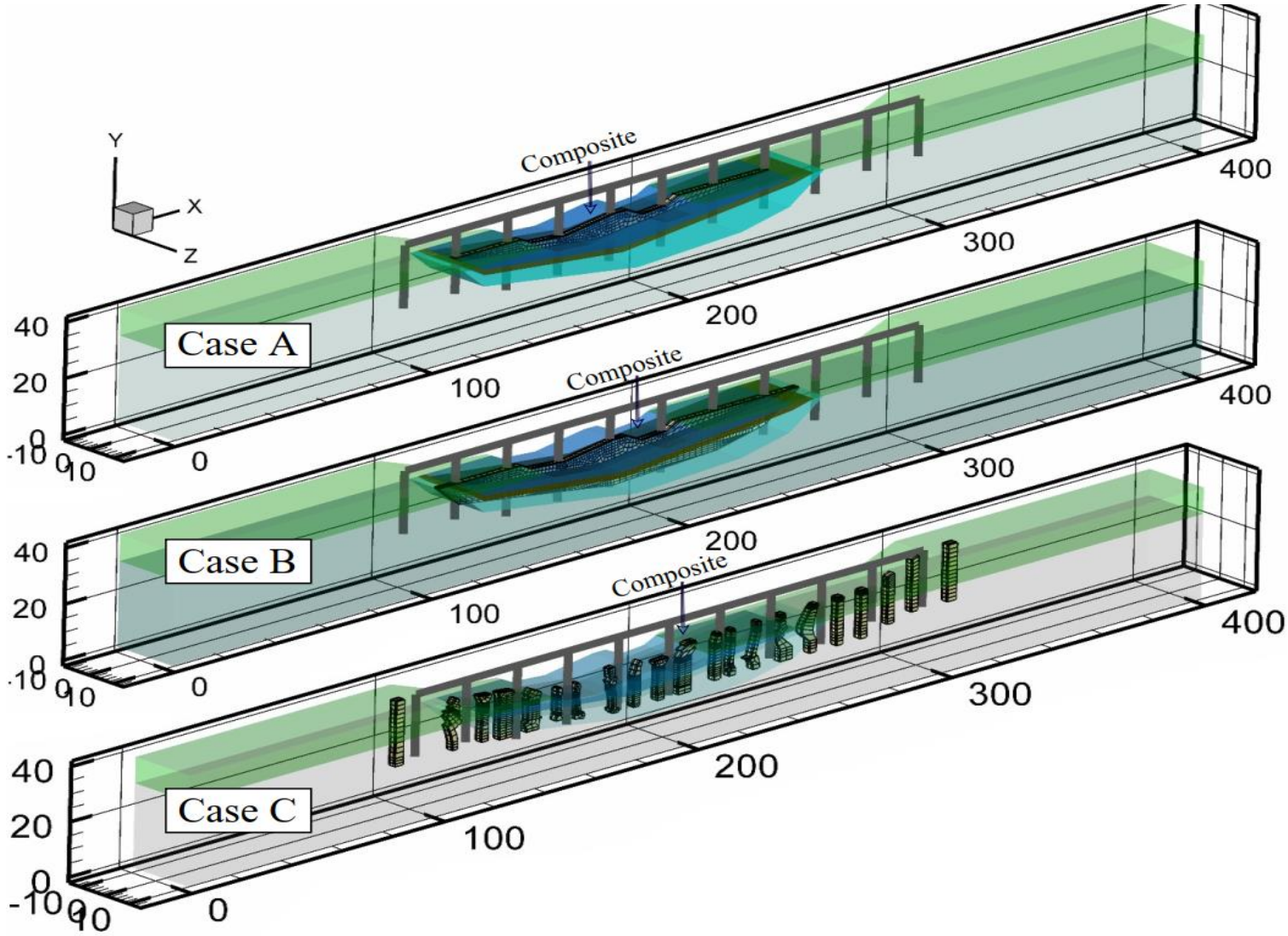

Figure 7.36. Employed remediation measures for the railroad bridge: remediation of (a) Layer LS (shallow liquefiable layer) along bridge footprint, (b)Layers LS, SS, and MS (along bridge footprint (c) grout inclusions

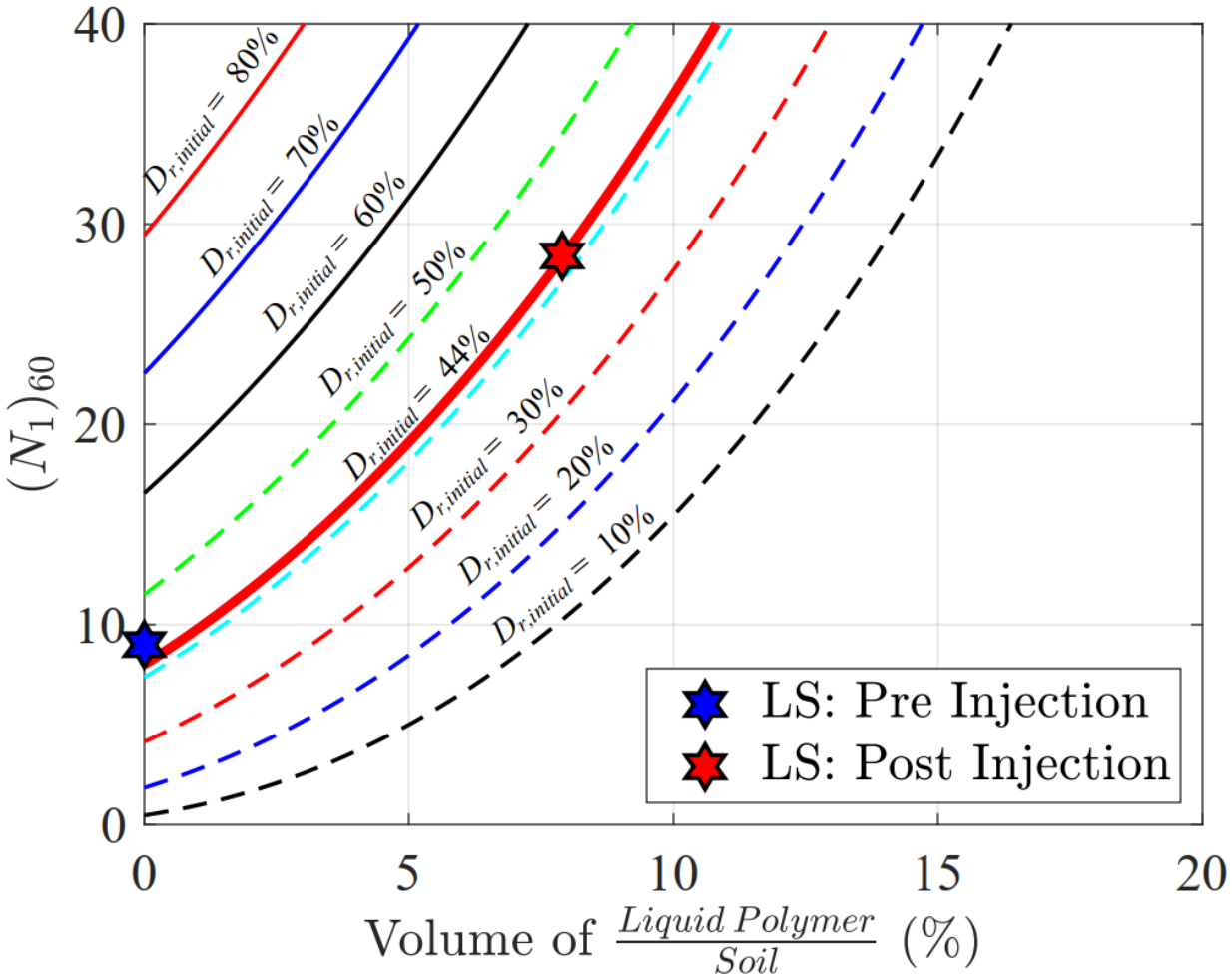

Figure 7.37. Degree of soil improvement pre and post injection into the LS (Loose Sand) layer

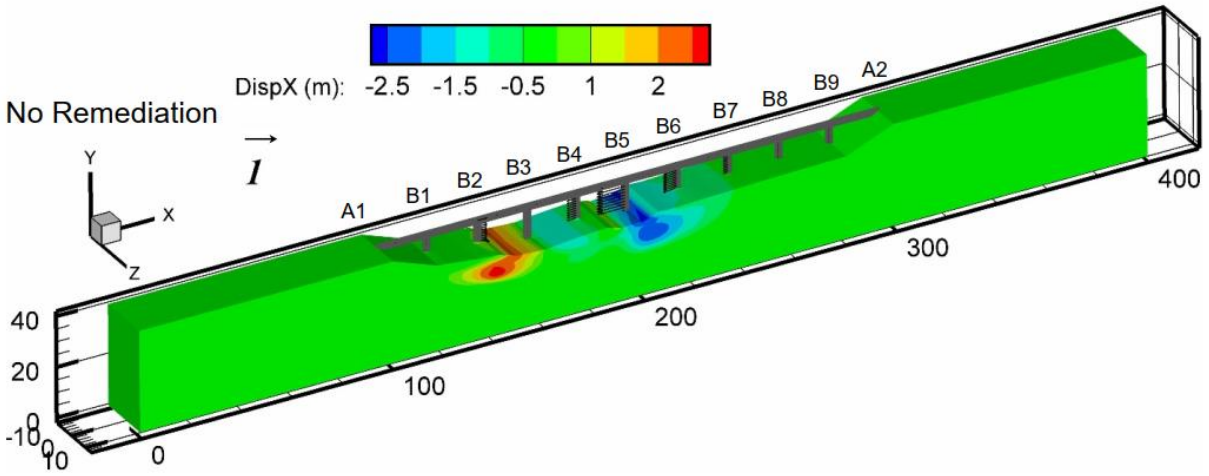

(a) Railroad bridge-ground system without remediation

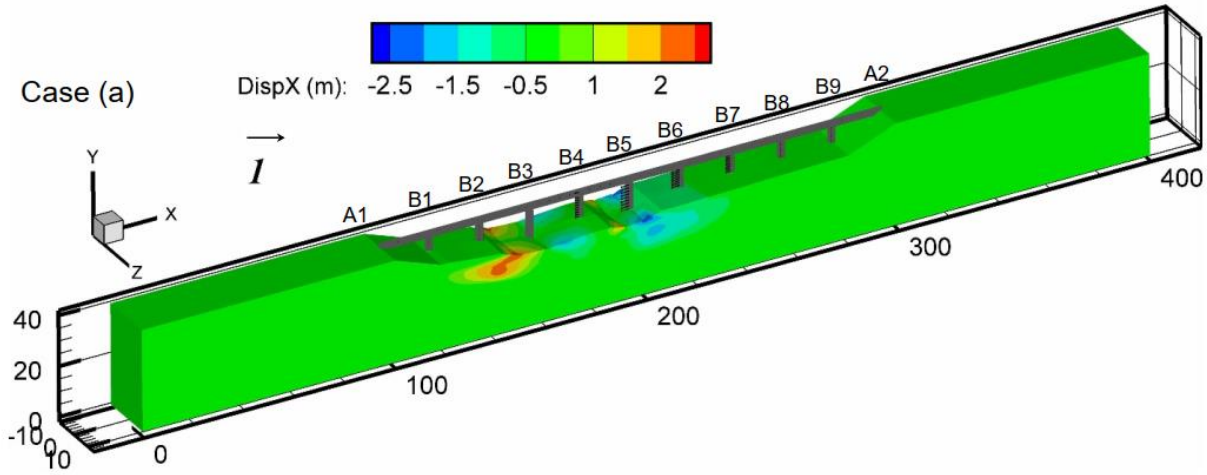

(b) Railroad bridge-ground system after remediation of the LS Layer

Figure 7.38. Deformed configuration of the railroad bridge -ground system at end of shaking: (a) without remediation, (b) improving LS Layer, (c) improving LS and MS layers, and (d) adding composite inclusions

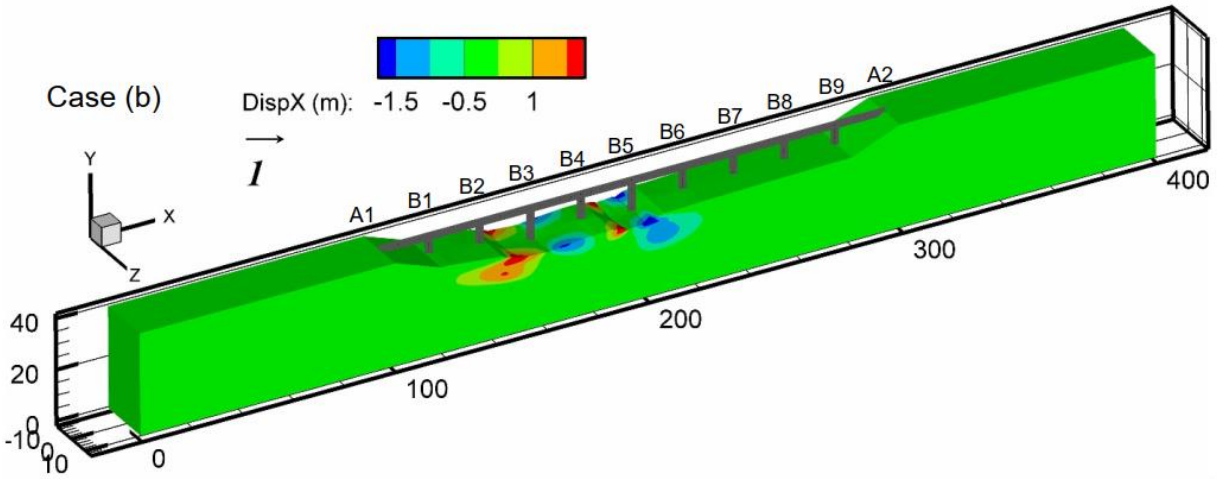

(c) Railroad bridge-ground system after remediation of the LS and MS layers

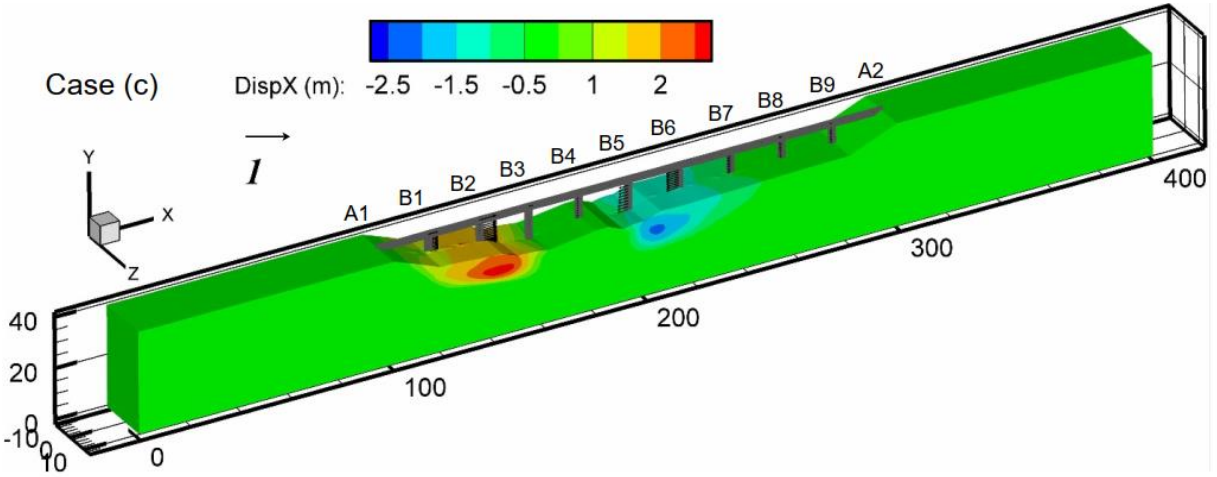

(d) Railroad bridge-ground system after remediation using composite inclusions

Figure 7.38 (continued). Deformed configuration of the railroad bridge -ground system at end of shaking: (a) without remediation, (b) improving LS Layer, (c) improving LS and MS layers, and (d) adding composite inclusions

Chapter 8. Summary and Conclusions

This chapter presents an overall summary and conclusions of the conducted research effort. In addition, a number of suggestions for future research are provided.

8.1 Summary

The overarching objective of this dissertation was to explore viability of the polymer injection technique as a countermeasure for ground liquefaction and associated deformations. This objective was achieved through:

1. Large scale experimental testing to identify governing mechanisms contributing to the degree of soil remediation. Specifically, mitigation of settlement for a shallow foundation supported on a liquefiable sand deposit was explored. In a series of two shake table experiments, system response was studied first without and subsequently with the injection of polymer into the liquefiable stratum. Upon application of the polymer injection countermeasure, results showed a significant reduction in the tendency for liquefaction and resulting foundation settlement. After the test, careful excavation of the deposit provided additional insights into the injected polymer's configuration, creating solidified zones that further support the shallow foundation load and increasing the overall stratum strength (relative density and confinement).

2. Leveraging insights from the experiments to calibrate computational models capable of reproducing observed mechanisms, and thereby extending the simulations to additional scenarios beyond the scope of the original test series. In this regard, stress-strain properties of the solidified polymer zones and surrounding strengthened ground were developed. This calibrated model was then extended to explore effects of geometric configuration of the solidified polymer zones, and state of compacted soil around the solidified zones in detail.

3. Application of the proposed methodology to a well-documented full-scale bridge ground system that suffered lateral spreading damage during the 7.2 M_w 2010 El Mayor Cucapah earthquake. Detailed post-earthquake reconnaissance surveys and observations were used to computationally simulate the bridge-ground system and capture documented damage mechanisms. Three different polymer injection configurations were studied, and the response of the remediated bridge-ground system was explored.

As such, it was demonstrated that the polymer injection technique shows considerable promise for liquefaction remediation, due to its ease of application in dense urban environments.

8.2 Conclusions

The following section summaries some of the overall conclusions of this dissertation. Additional details are included in each individual chapter.

1. The experimental and computational simulations described in this dissertation clearly highlight potential of the polymer injection technique as a soil liquefaction countermeasure.

2. A first of its kind, the conducted two-stage experiment program with and without polymer injection demonstrated potential of the technique as a countermeasure for liquefaction induced foundation settlement.

3. Remediation is attributed to increased liquefaction resistance, increased ground stiffness and strength, and the ability of the solidified polymer below the foundation to provide load paths to the underlying competent strata.

4. Along with the reduction in settlement, an increase in acceleration transmitted to the foundation and ground surface was noted. In this regard, the achieved reduction in settlement objective comes with increased inertial loads on the supported superstructure.

5. A simplified methodology was proposed for estimating smeared mechanical properties of ground remediated using the polymer injection technique. A family of curves was presented, relating the increase in corrected SPT blow count $(N_1)_{60}$ to the volume of polymer injected in its liquid form. Such a family of curves is specific to the polymer used in this experimental program. The presented methodology provided a rational basis to inform computational simulations of the shake table test response. Furthermore, it might be considered as preliminary guidance for practical applications.

6. Mechanical properties of the solidified polymer (polymer-sand composite) were proposed. Two modeling strategies were presented using: 1) smeared properties for response of the entire treated ground (based on replacement under constant volume conditions), and 2) stress strain curves of the polymer-sand composite. As such, a preliminary approach to modeling the shear strength of the injected polymer is to employ a cohesion of about 250 kPa – 400 kPa, and friction angle of the native sand. These strategies furnish a framework for evaluating response of ground treated using this technique.

7. At present, employing cone penetration test (CPT) or standard penetration test (SPT) soundings, pre- and post-injection appear to be the best technique for evaluating the extent of soil remediation, due to inhomogeneities generated by the injection process.

8. Calibrated computational models highlighted beneficial effects that can stem from controlling the geometric configuration of injected polymer. As such, the deployed geometry of the injected polymer can play a significant role in foundation settlement reduction, along with those offered by the resulting increase in soil relative density and confinement.

9. A computational framework based on a well-documented bridge-ground seismic response case history, was presented to illustrate utilization of the polymer injection technique for

liquefaction mitigation in a practical setting. This framework allowed for the assessment of outcomes in terms of ground and structural deformations. In the studied scenarios, it was shown that injections of the order of 10 % (volume of liquid polymer to soil) resulted in a reduction of lateral spreading deformations, precluding the observed unseating of the bridge-deck span.

10. The presented results illustrate the value of large-scale shake table testing, calibrated computational modeling, and documented field case histories in significantly improving our understanding of the salient system level response mechanisms.

8.3 Avenues for Future Research

This dissertation explored and demonstrated the potential of the polymer injection technique as a soil liquefaction mitigation measure. Few directions for future research are presented below:

1. Physical configuration of the injected polymer was shown to play a significant role in reducing liquefaction induced foundation settlement. As such, more accurate mapping of the actual injected geometric configuration is needed for field applications. In addition, this will provide valuable insights concerning changes in relative density and lateral confinement of the surrounding soil.

2. The extent of polymer expansion and permeation depends on its own properties, as well as the porosity of the soil and the ambient confinement (as dictated by the depth of the stratum). To achieve a target increase in relative density, higher confinement restricts the extent of polymer expansion requiring additional volume to be injected. As such, further research should adequately characterize the interplay between injected liquid polymer properties (gel time, viscosity), amount of injected polymer, and characteristics of the surrounding soil.

3. Further research efforts are warranted to more accurately estimate mechanical properties of the solidified polymer and their dependence on the degree of permeation (upon mixing with the native soil) and ambient confinement.

4. In the conducted experiment, polymer was injected at a single depth near the bottom of the liquefiable layer. In practice, different injection sequence protocols can be adopted, including: 1) remediation around the perimeter of the area first (to provide additional lateral confinement), followed by injection at interior zones, and 2) first remediating at shallow depth to create a capping layer (essentially a stiffer surficial crust) followed by injection at depth.

5. In the experiments outlined in this dissertation, polymer was injected through thin tubes with a single opening. Future studies can deploy tubes with multiple perforations distributed along their length.

6. Future studies should investigate the influence of parameters such as injection pressure, layout, and spacing on the overall soil improvement outcomes.

7. The chemical kinetics of the polymeric reaction play a significant role in the extent of remediation. Injection at elevated temperatures leads to a faster chemical reaction resulting in accelerated expansion (and curing) and therefore limited permeation into the soil matrix. Injection at lower temperatures will reduce the rate of viscosity increase and promote mixing. Consequently, further research should focus on determining optimal ranges of injection temperature and pressure, as well as other factors influencing the chemical kinetics of the process, in order to tailor polymers for site-specific applications.

8. Advancements in monitoring systems for automated, real-time control of the injection process (including measurement of excess pore pressures in the deposit) have the potential to improve the effectiveness of the polymer injection technique.

9. During the injection process, the polymeric reaction actively releases carbon dioxide (CO_2) into the surrounding soil. As such, the soil can become partially saturated during this process. The long-term effects of desaturation can be explored in additional laboratory and field experiments.

10. Computational models, once calibrated to experiments, provide an avenue to extend the scope of performed tests to additional scenarios. As such, further research can extend the calibrated computational models to remediate liquefaction induced lateral spreading demands on pile foundations. In addition, studies into uncertainty quantification, sensitivity of constitutive model parameters on system response, and input motion characteristics are warranted.

11. Simulation of the parallel railroad highway bridge-ground system: The analyses performed in Chapter 7 studied the performance of each bridge-ground system in isolation. In reality, the proximity of the much stiffer highway bridge led to reduced deformations near the railroad bridge. As such, further efforts to model the full parallel railroad bridge-highway bridge-ground system is warranted, albeit requiring significantly more computational effort.

12. Remediation measures for the parallel railroad highway bridge-ground system: Due to its versatility, additional scenarios employing the polymer injection technique for soil remediation can be explored, including: 1) injection around piles (effectively increasing pile diameter), 2) addition of curtain walls or lattice shaped grids along the active river channel, and 3) extending the remediation zone beyond the footprint of the bridge.

13. Synthesis and deployment of novel bio-based polymers: The polymer used in this study was a petroleum byproduct. Several researchers from NREL (National Renewable Energy Laboratory, https://www.nrel.gov/news/program/2021/nrel-developed-renewable-polyurethane-concept-takes-step-forward.html) and UC San Diego (California Center for Algae Biotechnology, https://renewablematerials.ucsd.edu/research/polyurethanes.html) have explored the possibility of

employing bio-based polymers (derived from algae) to generate structural polyurethane. As such, future research can focus on the development and deployment of innovative, eco-friendly polymers. The exploration of bio-based and biodegradable polymers as alternatives to conventional synthetic materials could lead to more sustainable and environmentally friendly soil improvement methods.

14. Additional documentation of field trials in practice: This research had significant input from industry partners (EagleLift). Documentation and analysis of field trials (including documenting pre and post improvement soil properties) involving the polymer injection technique can provide valuable insights. As such, further industry – academia collaborations are warranted to enhance current guidelines for the design, execution, and monitoring of polymer injection projects to facilitate widespread adoption of this technique for soil liquefaction mitigation.